

This item was submitted to Loughborough University as a PhD thesis by the author and is made available in the Institutional Repository (<https://dspace.lboro.ac.uk/>) under the following Creative Commons Licence conditions.



For the full text of this licence, please go to:
<http://creativecommons.org/licenses/by-nc-nd/2.5/>

Pilkington Library

Author/Filing Title WISHART, M

Accession/Copy No.

040147096

Vol. No.

Class Mark

LOAN COPY

0401470962



Impact Properties and Finite Element Analysis of a Pultruded Composite System

by

M. Wisheart

A Doctoral Thesis

submitted in partial fulfilment
of the requirements for the award of the degree of

Doctor of Philosophy

of

Loughborough University


October 1996

Supervisor : Dr M.O.W. Richardson

Director of Research : Dr P.K. Freakley

Institute of Polymer Technology and Materials Engineering

© M. Wisheart 1996

 Loughborough University Pitt Rivers Library	
Date	June 97
Class	
Acc No	040147096

99102392

Acknowledgements

Firstly, I would like to express my gratitude to the sponsoring companies for this project; European Intermodal Products, Maunsell Structural Plastics, and Loughborough University.

I must also thank my supervisor, Dr Richardson for his support and also the other members of staff, and students within IPTME who have advised and encouraged.

I have been very fortunate to have a great deal of contact in industry and would particularly like to pay tribute Gordon Bishop, Tony Reynolds, Mick Parma, and Charles Bream at Pera, who were always very helpful. Regarding the finite element analysis research FEA Ltd, were quick to advise, whilst my brief collaboration with Professor Crisfield and Mi at Imperial College was very fruitful.

Once again, my family support me in whatever direction I am going. Thank you.

Loughborough, 1996.

Abstract

This project was sponsored by two companies interested in promoting the use of pultruded glass fibre/polyester composites in the construction of freight containers. Thus, the research was to understand and quantify the damage mechanisms caused by low velocity impact on the composite system and to produce a finite element impact model to further the understanding of these events.

The empirical impact behaviour of the system was evaluated using instrumented falling weight impact testing (IFWI) in conjunction with ultrasonic C-Scan, optical microscopy and thermal deply techniques to detect delamination, matrix cracking, and fibre breakage. Strain-rate effects were concluded to be negligible over the range tested on introduction of the new term "total impact energy" rather than using "impact energy" ($1/2mv_0^2$), which has been employed traditionally. Since the detailed impact response and damage modes of pultruded composites have not been reported previously in the literature, the impact test programme was designed so that all the major damage modes were induced. By testing over the energy range from elastic impact to final failure, damage mode initiation, propagation, and interactions were related to the impact response, thus enabling the impact behaviour of the typical CFM/UD/CFM pultruded lay-up to be characterised. The geometrical complexity of the coupons was increased from simple plates to the complete pultruded section to study the effect of the double-skin/web design. A transition from local to remote damage response was observed as the impact site moved from simple to complex geometry under the impactor. Simple geometry response was dictated by the local deflection under the impactor, whereas the response resulting from an impact on, or near, the web was dominated by remote and unpredictable damage modes as determined by the global deflection.

The finite element analysis was performed using a commercial code, which was extended to enable modelling of delamination using a novel interface element technique. This new element was fully verified under Mode I, Mode II, and mixed-mode loading, and then used to model the experimentally observed delaminations as induced by matrix or CFM cracking. The predicted delamination shapes compared well with those obtained from experiment. Static mechanical testing of the composite was performed to obtain the material properties for the elastic FE analyses, whose predictions correlated closely with the experimental data.

Keywords: fibre composite, impact, pultrusion, finite element method, interface element modelling, delamination, freight containers, instrumented falling weight impact (IFWI).

Contents

Abstract	i
Notation	vi

PART I - INTRODUCTION AND LITERATURE REVIEW

Chapter 1. Introduction	1
Chapter 2. Literature Review	5
2.1 The Application	5
2.1.1 The Advanced Composite Construction System	5
2.1.2 The Pultrusion Manufacturing Technique	6
2.1.3 Freight Containers	8
2.1.4 Composite Materials in Freight Container Construction	10
2.2 Impact Properties of Composite Materials	11
2.2.1 Definition of Low Velocity Impact	12
2.2.2 Modes of Failure in Low Velocity Impact	14
2.2.3 Damage Modes in Randomly Oriented Fibre Laminates	20
2.2.4 Infl. of Constit. on the Impact Response of Composite Materials	21
2.2.5 Impact Performance of Complex Geometry Specimens	25
2.2.6 Post Impact Residual Strength	26
2.3 Experimental Procedures	28
2.3.1 Static versus Dynamic Testing for Low Velocity Impact	28
2.3.2 Dynamic Impact Testing of Composite Materials	29
2.3.3 Impact Damage Detection Techniques	31
2.3.4 Relating Experimental Impact Test Results to "Real" Structures	33
2.4 Analytical Techniques Applied to Aspects of Impacts of Composites	34
2.4.1 Spring-Mass Models	34

2.4.2	Energy Balance Models	36
2.4.3	Contact Analyses	37
2.4.4	Scaling Laws	39
2.5	Modelling the Impact Event	40
2.5.1	Finite Element Analysis	40
2.5.2	Finite Element Analysis of Composite Materials	41
2.5.3	Impact Analysis of Composite Materials by the FE method	42
2.5.4	Progressive Failure Finite Element Analysis.	44
2.5.5	Modelling Residual Strength	56
2.6	Conclusions.	56

PART II - METHODOLOGY

Chapter 3. Static Mechanical Testing	59
3.1 Materials and Environmental Conditioning	59
3.2 Test Equipment and Data Acquisition	60
3.2.1 "Dartec" Servo Hydraulic Test Machine	60
3.2.2 "Lloyd" Materials Testing L1005 Machine	60
3.2.3 In-Plane Shear Rail Assembly	62
3.3 Strain Measurement Techniques	63
3.3.1 Crosshead Displacement	63
3.3.2 Extensometer	63
3.3.3 Strain Gauge	64
3.4 Test Specimen Preparation, Geometry, and Procedure	65
3.4.1 Tensile Tests	65
3.4.2 In-Plane Shear Tests.	67
3.4.3 Flexural Tests.	68
3.4.4 Critical Strain Energy Release Rate Tests	69
 Chapter 4. Impact Testing and Damage Assessment	 73
4.1 Materials and Environmental Conditioning	73
4.2 Test Equipment and Techniques	73
4.2.1 Instrumented Falling Weight Impact Test Machine	73
4.2.2 Damage Assessment	78
4.2.3 High Speed Video Camera	81
4.3 Test Strategy	82
4.3.1 Preliminary Impact Tests	82
4.3.2 Strain-Rate Tests	84

4.3.3	Coupon Tests	86
4.3.4	Box Section Tests	88
4.3.5	Full "Plank" Cross-Section Tests	90
Chapter 5. Finite Element Analysis of Impact		91
5.1	Elastic Impact Models	92
5.1.1	Geometric Configurations and Boundary Conditions	92
5.1.2	Modelling Strategy	92
5.1.3	Material Properties	95
5.1.4	Loading	96
5.1.5	Software	96
5.2	Development of the Damage Model - Delamination	97
5.2.1	Two-Dimensional Models	100
5.2.2	Three-Dimensional Models	104
5.2.3	Delamination in the ACCS "Plank"	105
5.3	Non-Linear Impact Models	106
5.3.1	Lower Interface Delamination Induced by Longitudinal Bending	107
5.3.2	Upper Interface Delamination Induced by Transverse Bending	107
5.3.3	Lower Interface Delamination Induced by Shear Loading	108

PART III - RESULTS AND DISCUSSION

Chapter 6. Static Mechanical Test Results and Analysis		109
6.1	Static Mechanical Test Results	109
6.1.1	Tensile Tests	109
6.1.2	In-Plane Shear Tests	112
6.1.3	Flexural Tests	114
6.1.4	Critical Strain Energy Release Rate Tests	116
6.2	Reduction of Laminate Moduli to Obtain Individual Ply Properties	122
6.2.1	Classical Laminated Plate Theory	122
6.2.2	Moduli Calculations	125
Chapter 7. Impact Test Results and Discussion		128
7.1	Preliminary Impact Tests	128
7.1.1	Effect of Specimen Thickness	128
7.1.2	Effect of Filtering the Characteristic Impact Curve	129
7.1.3	Effect of the Delay Function	130
7.2	Strain-Rate Tests	131

7.3 Coupon Tests	134
7.3.1 Shear Coupon	134
7.3.2 Transverse Coupon	145
7.3.3 Longitudinal Coupon	148
7.4 Box Section Tests	153
7.4.1 Three-Box Section	153
7.4.2 Five-Box Section	169
7.5 Full Plank Cross-Section Tests	173
7.6 Comparisons Between Impact Test Configurations	174
7.6.1 Comparison of Damage Data for all the Impact Specimens	175
7.6.2 Comparison Between the Transverse Coupon, and Central Impacts from Three- and Five-box Sections	177
7.6.3 Comparison of Three- and Five-box Sections	179

Chapter 8. FE Results and Discussion 181

8.1 Elastic Impact Models	181
8.1.1 Convergence Exercise	181
8.1.1 Correlation of Coupon Impact Analyses with Experimental Data	182
8.2 Development of the Damage Model - Delamination	186
8.2.1 Two-Dimensional Models	187
8.2.2 Three-Dimensional Models	206
8.2.3 Delamination of the ACCS "Plank"	209
8.3 Non-Linear Impact Models	211
8.3.1 Lower Interface Delamination Induced by Longitudinal Bending	212
8.3.2 Upper Interface Delamination Induced by Transverse Bending	214
8.3.3 Lower Interface Delamination Induced by Shear Loading	216

PART IV - CONCLUSIONS AND FURTHER WORK

Chapter 9. Conclusions 219

9.1 Static Mechanical Testing and Elastic Finite Element Analysis	219
9.2 Experimental Impact Test Results	219
9.3 Non-Linear Finite Element Analysis	221

Chapter 10. Recommendations for Further Work 224

References 226

Appendices

Notation

Scalars

ν	Poisson's ratio
δ	central displacement
α	indentation
ρ	density
a, a_0	crack length, initial crack length
da	change in crack length
A	area
C	compliance
d	diameter
E	Young's modulus
F	force
G	shear modulus
G_c	fracture energy (critical strain energy release rate)
h	drop height
K	stiffness
m	mass
P	load
Q	in-plane reduced stiffness
R	resistance, radius
ΔR	change in resistance
S	span
t, t_c, t_p, t_d	time, contact time, time to peak force, peak deflection
t_{rel}	relative thickness
U, U_0	impact energy, initial impact energy
w, L, t	dimensions - width, length, thickness
x	displacement
X	longitudinal failure stress
Y	transverse failure stress
z	thickness co-ordinate
Z	normal (through-thickness) failure stress

Vectors

ϵ	strain
γ	curvature
$\Delta\epsilon$	change in strain
σ	stress
v	velocity
v_0	initial velocity

Matrices

A	membrane (in-plane) stiffness matrix
B	membrane-plate coupling stiffness matrix
C	damping matrix
D	material stiffness, or plate bending stiffness matrix
F	applied load matrix
M	mass matrix, or bending moment matrix
K	stiffness matrix

Indices

I, II, III	Modes I, II, and III of fracture
X-input, X-output	input, output fracture energy for the interface element
c	indicates critical/failure value
C	compression
11	longitudinal in-plane
22	transverse in-plane
33	normal (through-thickness)
12	transverse shear
13	through-thickness longitudinal shear
23	through-thickness transverse shear
i	impactor
p	plate
T	tension

Acronyms

BVID	Barely Visible Impact Damage
CFM	Continuous Filament Mat
DCB	Double Cantilever Beam
DOF	Degree Of Freedom
ENF	End Notched Flexure
FE	Finite Element
FM	Fracture Mechanics
FRP	Fibre Reinforced Plastic
IE	Impact Energy
IFWI	Instrumented Falling Weight Impact
ILSS	Interlaminar Shear Stress
GRP	Glass Reinforced Plastic
MMB	Mixed-Mode Bending
OM	Optical Microscopy
PFFEA	Progressive Failure Finite Element Analysis
PICS	Post Impact Compression Strength
SDOF	Single Degree Of Freedom
SERR	Strain Energy Release Rate
TIE	Total Impact Energy
UD	Unidirectional

PART I

INTRODUCTION

AND

LITERATURE REVIEW

Chapter 1

Introduction

The term 'composite material' refers to a material that is formed from two or more constituents on a macroscopic scale. Fibre reinforced plastic (FRP) is a particular type of composite which has a fibre phase (glass, carbon, kevlar, etc.) within a polymer resin matrix. Where the term composite material is used in this work, it is used in reference to a fibre reinforced composite. Composite materials are often fabricated as laminates, where the individual lamina are bonded together by the resin. The fibres carry most of the axial load, with the resin transferring the load via shear stresses and protecting the fibres which lose their strength very quickly when damaged.

Composite materials are therefore heterogeneous and anisotropic, resulting in the design of composite structures being very flexible when compared with traditional isotropic materials, e.g. metals. The fibres can be aligned in the direction of principal stresses which results in more efficient structures. Some of the other properties of composites that are advantageous are, strength- and stiffness-to-weight ratio, corrosion resistance, thermal properties, fatigue life, wear, and fire retardance. Composite materials are therefore finding applications in a wide variety of roles including, aircraft and space structures, automobile components, sports equipment, and medical prosthetic devices. As materials technology makes further advances, the potential markets for composite systems is growing to include more secondary and primary structural applications. The pultrusion manufacturing technique is an automated continuous process which is particularly suited to the production of composite profiles, and has brought down production costs and times, enabling the material property advances to be taken advantage of.

As well as the advantages mentioned above, composites do have a number of inherent weaknesses. One of the major weaknesses is a poor resistance to impact damage and the dramatic strength reductions which occur in the presence of barely visible impact damage. Transverse impact resistance is particularly low due to the lack of through-thickness reinforcement. Impact damage modes are complex and varied and include matrix cracking, delamination and fibre breakage, and interactions between the three.

One possible market which is opening up to the application of composites is the freight container industry. Due to changes in the market regarding traditionally used materials to fabricate containers, and container floors in particular, the door has been opened to the introduction of novel materials technology. A major obstacle to be overcome in the acceptance of composite materials into this market is the poor impact properties of composites. An improvement in the understanding of impact damage mechanisms is required to enable engineering designs to minimise the risk of impact damage. As pultrusion could hold the key, in terms of mass marketing of composite structural profiles, the understanding of pultruded laminates is particularly important. Pultrusions normally consist of layers of randomly oriented fibre mats, to provide transverse strength, sandwiched around unidirectional layers of fibres parallel to the draw direction, and therefore are quite different to the angle-ply laminates which dominate impact response reported in the literature.

The present work was performed to develop the understanding of the impact response of the pultruded Advanced Composite Construction System (ACCS) which is currently available as glass reinforced plastic cellular modules based on E-glass reinforced isophthalic polyester resin and is representative of a typical pultruded section. This type of system could be applied to the construction of freight containers - either whole (monocoque) containers or aspects of the floor, walls or roof. Containers made of composite materials would also open the possibility of dual functionality e.g. for hovercraft, the container could be employed first as the transportation module, which would then be capable of conversion to a hangar at the point of delivery. The investigation has concentrated on the ACCS "plank" which is the primary element of the system, with the overall objective of this aspect of the work being to understand and quantify the damage mechanisms caused by low velocity impact. A detailed and comprehensive series of impact tests were performed on increasingly complex specimens, taken from the ACCS "plank". The impact response of complex geometry sections was researched, with a completely different damage response being observed for impacts between the webs than occurred when the impact site was over the webs. Strain-rate effects were also investigated by performing impacts at a constant impact energy but with varying mass and velocity combinations.

Design of composite structures provides a new challenge to engineers. Optimisation of metallic, or other traditional isotropic material, structures is well understood and the tools to do so are well developed. Replacing metal by a composite in a structure requires redesign of the structure with several choices to be made, including: fibre and resin type, orientation of reinforcement, lay-up sequence, and processing method. Direction dependent material properties opens up a new area of design optimisation, requiring a detailed understanding of the likely loading the structure will be subject to. Unless numerous expensive experiments are to be performed, which may result in the preclusion of composite materials in economic terms, computer aided engineering tools are required, but these techniques need further development. One such technique is finite element analysis.

As computer hardware costs reduce and computational times are lowered, computational analyses can be performed on more complex structures. The finite element method is currently the most powerful numerical method for predicting the response of composite structures and was chosen for the computational analyses in this research. When analysing a real structure the individual fibres and surrounding matrix cannot be modelled due to the number of elements that would be required, and therefore smeared fibre/matrix properties are employed. In impact analyses where damage is often induced at low energies, it is of vital importance to be able to model the failure modes and delamination is especially important causing low post impact residual compressive strength. Delaminations occur due to poor through-thickness impact properties of laminates and low interlaminar strengths, which results in the layers in the laminate becoming separated. Delaminations are generally induced by an intralaminar failure mechanism such as matrix cracking.

Composite damage models are required within finite element analysis to simulate both intra- and interlaminar failure and this research has focused on the latter, in the form of a novel interface element technique to model delamination. The investigation into the behaviour of the interface element was performed initially at a nodal level, with both two- and three-dimensional models being verified, quantitatively and qualitatively, under various modes of loading. The work culminated in modelling the types of delamination, reported from the damage assessment of the impacted test specimens. All the material data, both elastic and failure, employed within the finite element analyses was obtained from a series of static mechanical tests performed on specimens taken from the "plank".

The research was carried out in collaboration with the sponsoring companies, an industrial research consortium, and other universities. There were two sponsoring companies; The first being Maunsell Structural Plastics Ltd. which is a wholly owned subsidiary of the

International Maunsell Group of Consulting, Civil, and Structural Engineers. The Group is engaged in a wide cross-section of the civil and structural engineering field, whilst MSP Ltd has concentrated on the development of composite material technology, and developed the Advanced Composite Construction System which is the focus for this project. The second sponsor was European Intermodal Products Ltd., who design, manufacture, and refurbish a wide range of freight container systems including ISO marine containers, swap-bodies, bulk dry goods (reefers), and one-off special designs. They are also interested in looking at new materials in order to capitalise on opportunities created by a changing market. A consortium of companies researching the area of impact properties of composite materials, managed by PERA International was also joined. The finite element analysis research was performed using LUSAS in close association with the software designers, FEA Ltd. and a research group at Imperial College.

This thesis covers three main areas. Part I is a review of the field of knowledge surrounding impact properties of composite materials, experimental techniques, and non-linear FE modelling. Part II (Chapters 3 to 5) covers the methodology behind the experimental and analytical work performed: Chapter 3 describes a series of static mechanical tests performed to obtain the material properties required to fully define the composite laminate within the finite element analysis. The impact test programme is detailed in Chapter 4, whilst Chapter 5 outlines the finite element work regarding the design of the elastic models and the use of the interface element in modelling delamination. Part III consists of Chapters 6 to 8 which report and discuss the results obtained, and finally conclusions are drawn and recommendations for further work made in Chapters 9 and 10 respectively (Part IV).

Chapter 2

Literature Review

2.1 The Application

This research was concerned with the application of a typical pultruded composite to the manufacture of freight containers, made possible by advances in material and production technology and changes in the freight container market.

2.1.1 The Advanced Composite Construction System

Recent advances in pultrusion technology (section 2.1.2) have provided the means for manufacturing thin wall cellular systems, and by incorporating high volumes of glass fibres high performance structures can be produced. Furthermore fibrous cellular structures, as often found in nature, can provide very efficient design concepts for pultrusions. Geometrical tolerancing has also improved, enabling complex components to be designed for structurally critical applications.

Commercial companies such as Maunsell Structural Plastics Ltd. have taken advantage of these advances to design systems of interlocking pultruded components. One such example is called the Advanced Composite Construction System (ACCS), which can be joined together quickly to build up two- or three-dimensional lightweight structures. Appendix I contains the basic data sheet for the ACCS detailing the seven component cross-sections which can be produced to the desired length. The "plank", "three-way connector", "groove connector" and "toggle connector" are pultruded components, whilst the "flat trimmer" and "channel connector" are moulded. This system has already been used as the primary load bearing structure in a number of diverse civil engineering projects (footbridge (Figure 2.1),

pontoon systems, bridge enclosures^{1,2,3}) including the world's first advanced composites road bridge⁴. The designs are based on the Limit State Design Philosophy⁵, also developed by Maunsell Structural Plastics Ltd. The "plank" is the panelling section and has been chosen as the focus for this project (Figure 2.2).

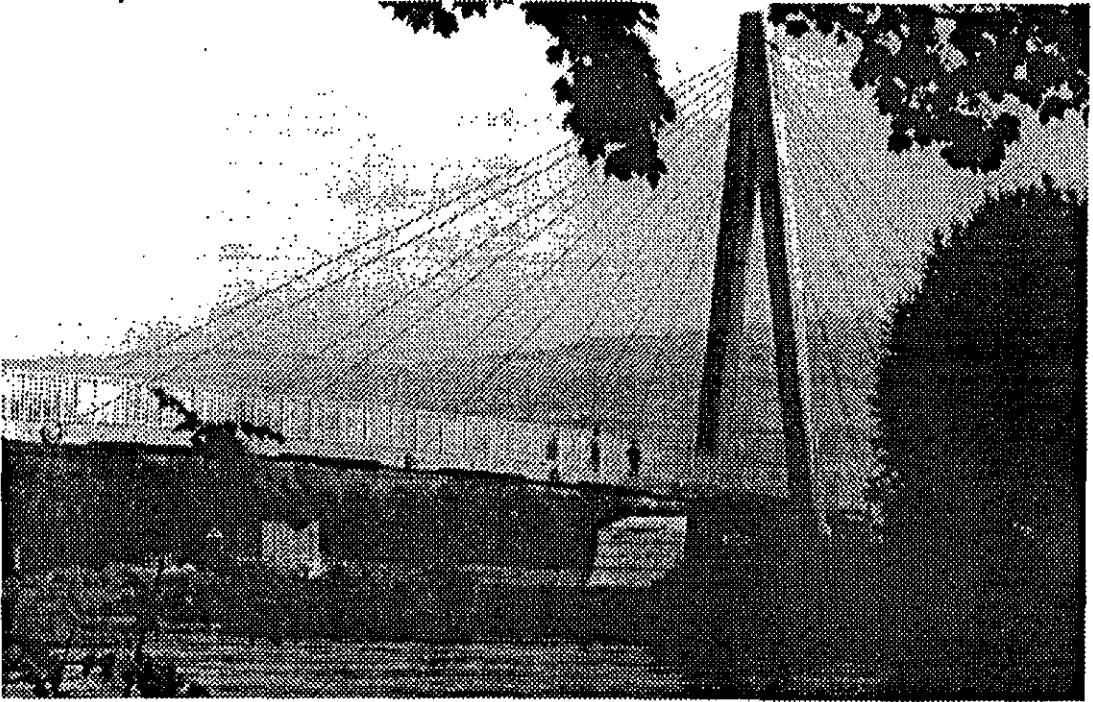


Figure 2.1 Footbridge in Scotland constructed from ACCS.

The primary material components of the ACCS are E-glass fibres and isophthalic polyester resin⁶. The outer skins of the "plank" consist of unidirectional fibres (UD) sandwiched between continuous filament mats (CFM) to provide the transverse strength and stiffness, with a polymeric veil on the outer surface to improve the appearance. The webs consist of unidirectional fibres sandwiched between two needle mat layers.

2.1.2 The Pultrusion Manufacturing Technique

Pultrusion is a fast growing automated manufacturing method which is capable of producing fibre reinforced plastics (FRPs) of high structural integrity⁷. Further development of the pultrusion process will allow even more complex systems to be produced in the future⁷⁻¹⁰. Pultrusions are characterised by exceptional longitudinal mechanical properties provided by high volumes of glass (typically 45 to 60% by weight). The material used in a pultruded section consists of the reinforcement (fibre), the polymer matrix (resin) and additives.

The reinforcement fibres are usually glass (normally E-glass, though S-glass is also used) but the more expensive high modulus graphite and aramid fibres are also employed (often as hybrids in combination with glass)⁸. The fibres are used in the form of unidirectional rovings (which provide the longitudinal strength and stiffness necessary for the section to be pulled through the die) and chopped strand or continuous filament mats which provide the transverse strength of the section. Due to the low pressure in the process, the fibres tend to rise to the surface of the section and so surface mats or polymeric veils are used to suppress this tendency and to provide an improved surface finish⁸.

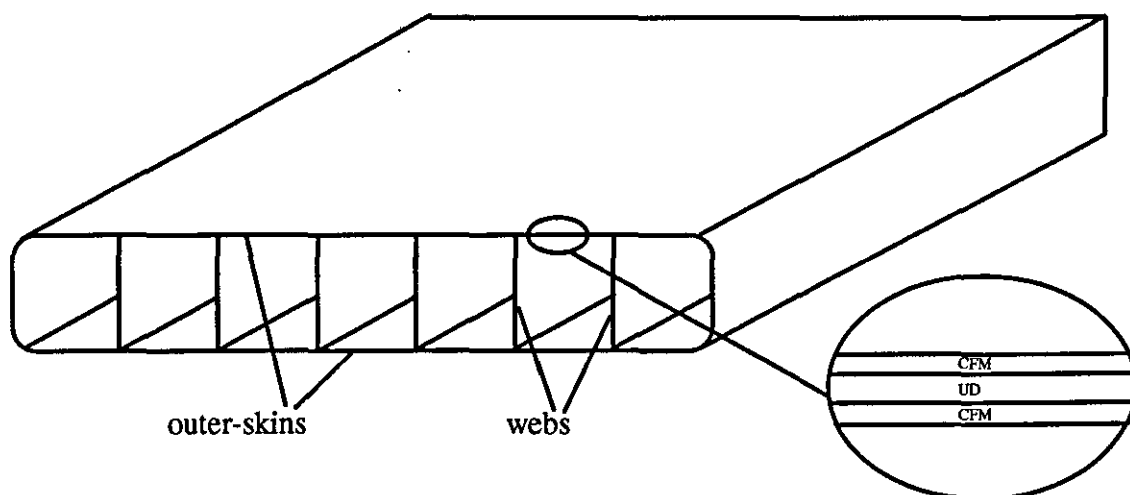


Figure 2.2 Simplified diagram of the ACCS "plank".

The majority of pultrusions (85%) employ unsaturated polyesters of which there are approximately thirty commercially available types. Vinyl esters are used in applications where the need for better physical properties outweighs the higher cost. Epoxy resins are inherently difficult to process due to the low shrinkage on curing which results in high frictional forces with the die⁸. Pultrusion of thermoplastic systems is difficult due to their high melt viscosity but they are currently being developed which will increase the toughness of pultruded products and allow easier post-forming and welding^{8,11}.

Additives are used to tailor the mechanical and in-service properties of the component and also to improve the efficiency of the manufacturing process. Common additives include organic peroxides as cross-linking agents, internal release agents to minimise the effects of shrinkage and adhesion forces in the die, and pigments to provide self colouring. Fillers alter the viscosity, flame retardance, and chemical and UV resistance⁸.

During the pultrusion process (Figure 2.3), the rovings are fed off creels, which are designed to ensure that the fibres do not damage themselves. The rovings are guided

through a resin wet-out tank whilst being kept in alignment by grid plates. On exiting the tank, excess resin is removed before the reinforcement passes onto the pre-forming die. This die guides the reinforcement towards the final desired configuration which is provided by the heated chrome-plated dies⁷.

The pultruded section is pulled through the system by continuous caterpillar belts and the section is cut off at the desired length with a conventional, water spray cooled, diamond rimmed saw which clamps the profile and traverses with it to allow continuous processing. Line speeds now achievable are in the order of 2m/minute for thermosets (up to 10m/minute for thermoplastics¹¹), with the limiting factors being reaction kinetics within the section (for thicker profiles) and the mechanics of the line (for thin sections)⁹.

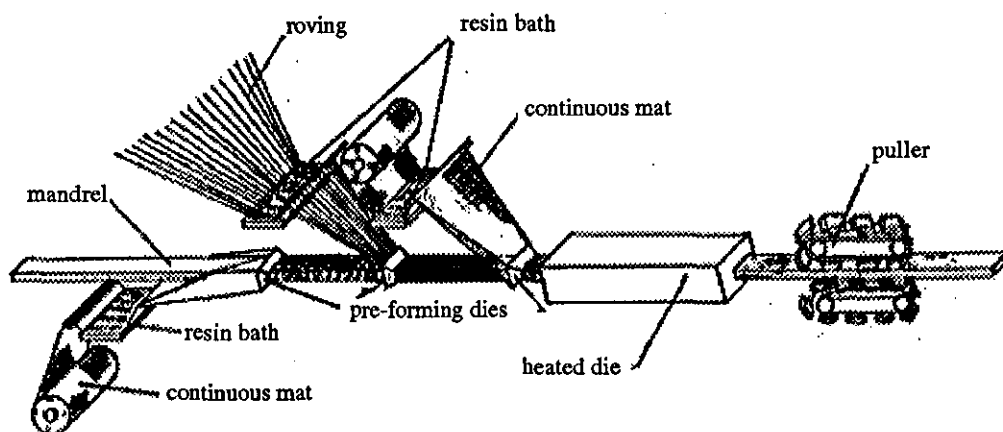


Figure 2.3 The pultrusion process for a hollow section⁷.

The use of a mandrel extending through both sets of dies, enables hollow profiles to be pultruded. The process is usually carried out horizontally whilst vertical machines avoid out-of-plane bending of mandrels and/or profiles under their own weight, but the length of the section is limited by the height of the die above the floor⁸. Curved and/or twisted products are now being developed by pre-form or post-form techniques, whilst pull-winding allows unidirectional fibres to be combined with wound or hoop fibres. New markets for pultruded products and the ACCS in particular are being sought and one possibility is to apply this system to the construction of freight containers.

2.1.3 Freight Containers

Freight containers (Figure 2.4) were developed from the need to transport cargo quickly and carefully, usually involving a combination of rail, road and sea. Standard units have

enabled the transportation vehicles to be optimised for space and reduce transfer times between modes of transport. Therefore, due to the inherent nature and philosophy that containerisation has been developed on, it has become a highly standardised industry¹². Twenty different ISO standards¹³ cover "Series One" freight containers (i.e. international marine containers covering general purpose, thermal, tank, dry bulk and platform containers), however the materials to be used are not specified in order to encourage innovative design and development of new materials¹².

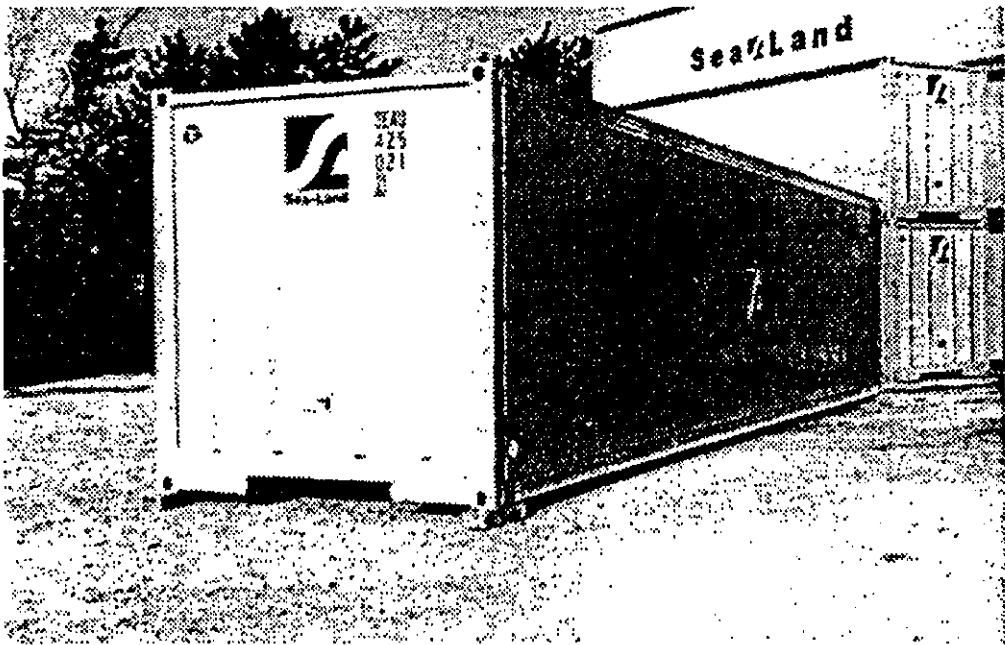


Figure 2.4 A typical freight container.

Designs of containers made from traditional materials from marine containers (world-wide transportation) to Swap-bodies¹⁴, (European road rail and sea) are highly optimised with respect to weight, within the strict stiffness and strength specifications laid down. As demands for improved intermodal efficiency increase, the industry still calls for yet lighter containers (reduced Tare mass) allowing a greater portion of the container's gross mass (Rating) to be the payload¹⁵. Composite materials are a candidate to achieve this goal, and in the past some GRP/plywood/GRP sandwich panel section's have been used to this end, but only in limited volumes. Traditionally steel or aluminium has been used for the chassis and panelling sections with cast iron corner fittings and floors made of wood.

The freight container market is becoming more open to new materials with container floors being an area of particular opportunity^{16,17}. There are a number of categories which container floor designs must satisfy, with seven areas being highlighted as particularly important: strength, durability, "nail-ability", "clean-ability", odour, weather resistance, and fatigue strength^{18,19}. In the past, wood floors have achieved these requirements

economically. The popularity of hardwood over softwood, in either plywood or solid format has fluctuated over the last two decades. However, availability of irreplaceable tropical hardwoods has suddenly decreased because of legal restrictions placed on the logging industry in 1992 by the Malaysian government (the worlds largest tropical hardwood exporter). In combination with restrictions already imposed in Indonesia in 1980 (and tightened in 1993), the shortage in hardwood resulted in sudden price rises in the order of 50%^{16,17}. This has opened the market to materials which were previously too expensive.

Strict corrosion/weather resistance specifications apply to all components, not just container floors. Dry goods containers must maintain a good appearance over long periods (the refurbishment life is on average 3.5 years) with the container finishing being resistant to corrosion under marine conditions in temperate and tropical conditions, able to withstand -40°C to +40°C rapid temperature changes, have a good appearance despite handling conditions, and be flexible and resistant to impact due to handling²⁰.

2.1.4 Composite Materials in Freight Container Construction

Composite materials are becoming a practical alternative to traditional materials in structural applications as they are lightweight, corrosion resistant, and have good strength and stiffness properties. Out of all the manufacturing techniques available pultrusion is well suited to the production of structural beams and members²¹. Of all their advantageous properties, the most widely taken advantage of is the strength to weight ratio, which has resulted in rapid growth in the use of composites in the aerospace industry where high performance lightweight properties are essential. In the freight container market it is this property in particular, which makes composite materials attractive.

In order to meet the corrosion resistance requirements, traditional metal containers often use zinc based coatings but costs have risen sharply, but FRPs would not require these coatings. In terms of refrigerated containers, the advantage of composites is that they have thermal conductivity coefficients thirty to fifty times less than steel²², and many composite sections are double-skinned which enables them to be filled with insulating foam²³.

In regard to new flooring materials, due to the inertia of the industry, much of the current research remains focused on new wood combinations or use of non-traditional hardwood supplies (Finnish Birch¹⁸). However, other materials under review include a bamboo/plywood floor^{17,24}, bamboo/pine²⁵: softwood covered with composite material¹⁷ (carpet fibres and textile waste) and Strato-Stock^{16,25}, which is a polypropylene/wood/aluminium floor composite. Enviro-dek²⁵⁻²⁷ is an extruded HDPE

based floor design, C-Board²⁶ is composed of pressure and heat treated textile waste materials. The number of innovative floor designs being developed is indicative of the seriousness with which the industry views the wood floor situation. Genstar, one of the world's leading container lessors, sees technological change as being fundamental to the survival of the container industry²⁸ and is spear-heading the use of Azdel²⁹, a thermoplastic composite/wood (with the wood soon to be replaced) floor system which is already on one hundred of its open topped containers.

Recently the worlds first 20ft dry freight marine container built from composite materials (including the floor) passed the required ISO standards^{23,30}. It uses both carbon and glass reinforced pultrusions. The only metal components are predictably the corner castings, some door-gear components, and reinforcements to the lift pockets, i.e. the areas most likely to be damaged by impact. This container has a tare weight of 1496kg compared to 1750kg (aluminium) and 2250kg (steel).

Pultruded composite components or entire composite containers are being introduced to the freight container industry. However, the poor impact resistance of composite materials is an area of weakness which holds back acceptance. Containers are open to a wide range of impacts especially in the handling sequences between modes of transport (i.e., from lorry to rail, from rail to dock yard, from dock yard to ship) and whilst the container itself is being loaded and unloaded. The resulting damage was observed both at EIP Ltd., Rotherham, and the maintenance yard for United Transport, Hull, during a detailed investigation of in-service containers. With steel containers, relatively large energy impacts can be absorbed through plastic deformation with structural integrity being maintained and the resulting impact damage is addressed during annual maintenance or during its three to five yearly refurbishment. The following section reviews the area of composite material performance under impact loading.

2.2 Impact Properties of Composite Materials

Freight containers have traditionally been metal constructions and extensive research has been performed on the impact response of metals over a wide range of velocities. Impact damage in metals is easily detected as damage starts at the impacted surface, however damage in composites often begins on the non-impacted face or in the form of an internal delamination.

Impact damage is generally not considered to be a threat in metal structures because, due to the ductile nature of the material, large amounts of energy may be absorbed. At yield stress the material may flow for very large strains (up to 20%) at constant yield before work hardening (Figure 2.5). In contrast, composites can fail in a wide variety of modes and contain barely visible impact damage (BVID) which nevertheless severely reduces the structural integrity of the component. Most composites are brittle and so can only absorb energy in elastic deformation and through damage mechanisms, and not plastic deformation. Clearly, the vast majority of impacts on a composite plate will be in the transverse direction but due to the lack of through-thickness reinforcement, transverse damage resistance is particularly poor. Interlaminar stresses - shear and tension - are often the stresses which cause first failure due to the correspondingly low interlaminar strengths. As a result, design failure strains of 0.5% are used to guard against impact failure, resulting in the excellent in-plane strength and stiffness properties of composites not being fully taken advantage of.

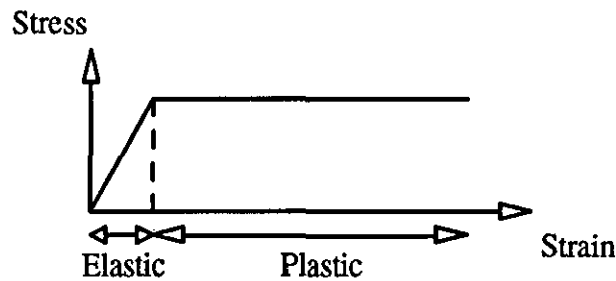


Figure 2.5 Stress-strain response of a ductile material.

Two terms used commonly in the area of impact of composite materials are *Damage resistance*, which refers to the amount of damage incurred on impact by the system, and *Damage tolerance*, which describes the system's ability to perform post-impact (i.e. in the presence of damage)^{31,32}. In the literature there is a great deal of information regarding the impact response of composites and much work has been performed over a wide range of velocities. It is therefore necessary to ensure that the correct velocity range is considered as this affects both the structural and material response.

2.2.1 Definition of Low Velocity Impact

Generally, impacts are categorised into either low or high velocity (and sometimes hyper velocity) but there is no clear transition between categories and authors disagree on their definition.

Sjöblom et al³³ and Shivakumar and co-workers³⁴ defined low velocity impact as events which can be treated as quasi-static, whose upper limit can vary from one to tens of m/s depending on the target stiffness, material properties and the impactor's mass and stiffness. High velocity impact response is dominated by stress wave propagation through the material, in which the structure does not have time to respond, leading to very localised damage. Boundary condition effects can be ignored because the impact event is over before the stress waves have reached the edge of the structure. In low velocity impact, the dynamic structural response of the target is of utmost importance as the contact duration is long enough for the entire structure to respond to the impact and in consequence more energy is absorbed elastically.

Cantwell and Morton³⁵ conveniently classified low velocity as up to 10m/s, by considering the test techniques which are generally employed in simulating the impact event (Instrumented Falling Weight Impact (IFWI) Testing, Charpy, Izod etc.) whilst, in contrast, Abrate³⁶ in his review of impact on laminated composites stated that low velocity impacts occur for impact speeds less than 100m/s.

Liu and Malvern³⁷ and Joshi and Sun³⁸ suggest that the type of impact can be classed according to the damage incurred, especially if damage is the prime concern. High velocity being characterised by penetration-induced fibre breakage, and low velocity by delamination and matrix cracking.

Davies and Robinson^{39,40} define a low velocity impact as being one in which the through-thickness stress wave plays no significant part in the stress distribution and suggest a simple model to give the transition to high velocity. A cylindrical zone under the impactor is considered to undergo a uniform strain as the stress wave propagates through the plate giving the compressive strain as³⁹:

$$\epsilon_c = \frac{\text{impact velocity}}{\text{speed of sound in the material}} \quad (2.1)$$

For failure strains between 0.5% and 1% this gives the transition to stress wave dominated events at 10 to 20 m/s for epoxy composites.

Despite the wide ranging variation in definitions, the impacts experienced by a freight container certainly fall into the low velocity category - impacts up to 10m/s, producing strain-rates of 1 to 10/s⁴¹. From a damage viewpoint low velocity impact introduces a wide variety of failure modes preceding ultimate failure which will be discussed in the next section.

2.2.2 Modes of Failure in Low Velocity Impact

The heterogeneous and anisotropic nature of FRP laminates, gives rise to four major modes of failure (although many others could be cited):

Matrix Mode - cracking parallel to the fibres due to tension, compression, or shear.

Delamination Mode - separation of plies produced by interlaminar stresses.

Fibre Mode - in-tension fibre breakage, and in-compression fibre buckling.

Penetration - the impactor completely perforates the impacted surface.

It is very important to identify the mode of failure because this will yield information not only about the impact event, but also regarding the structure's residual strength. Interaction between failure modes is also very important in understanding damage mode initiation and propagation³⁷.

2.2.2.1 Matrix Damage

The majority of low velocity impact testing which has been reported in the literature has involved low energy testing (i.e. that which causes only minimal damage in the range of 1 to 5J approximately). It is this work which has revealed information concerning matrix cracking and delamination initiation. Matrix damage is the first type of failure induced by transverse low velocity impact, and usually takes the form of matrix cracking but also debonding between fibre and matrix. Thermosetting resins are in general brittle, therefore little deformation occurs prior to fracture⁴². Matrix cracks occur due to property mismatching between the fibre and matrix, and are usually oriented in planes parallel to the fibre direction in unidirectional layers. Joshi and Sun⁴³ reported a typical crack and delamination pattern shown in Figure 2.6.

The matrix cracks in the upper layer (Figure 2.6a) and middle layer (Figure 2.6b) start under the edges of the impactor. These *shear cracks*⁴⁴ are formed by the very high transverse shear stress through the material, and are inclined at approximately 45°. The transverse shear stresses are related to the contact force and contact area. The crack on the bottom layer of Figure 2.6a is termed a *bending crack* because it is induced by high tensile bending stresses and is characteristically vertical. The bending stress is closely related to the flexural deformation of the laminate⁴⁵. Lee and Sun⁴⁶ reached the same conclusions in their analyses, whilst Cantwell and Morton⁴⁷ emphasised that the type of matrix cracking which occurs is dependent on the global structure of the impacted specimens. For long thin specimens bending cracks in the lower layers occur due to excessive transverse deflection

and subsequent membrane effects predominate, whereas short thick specimens are stiffer and so higher peak contact forces induce transverse shear cracks under the impactor in the upper plies.

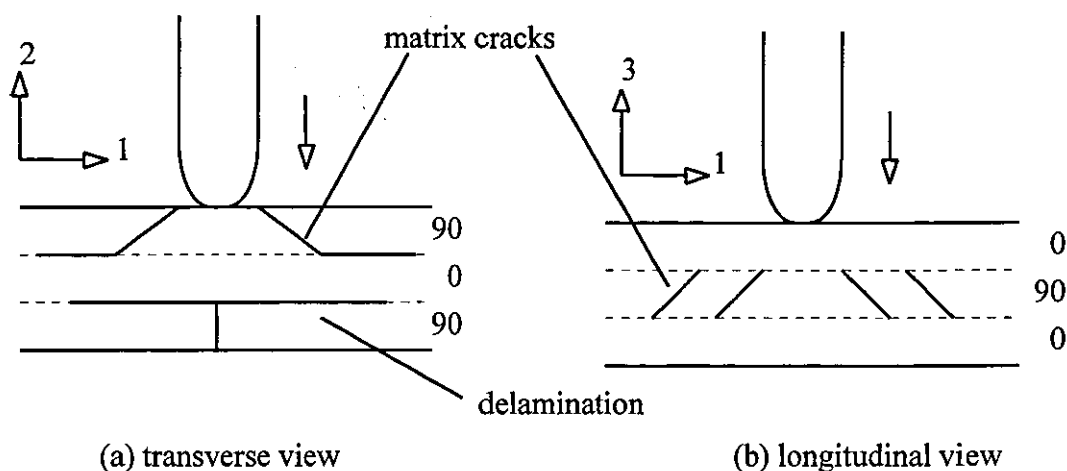


Figure 2.6 Initial damage in an impacted 0/90/0 composite plate.

Liu and Malvern³⁷ presented a detailed view of matrix cracking which agreed with the above, whilst Wu and Springer⁴⁸ reported detailed locations of matrix cracking for graphite/epoxy plates of various stacking sequences.

F.K. Chang, F.-Y. Chang, and co-workers^{44,49-53} have performed much research in this area, and postulated that the bending crack in the 90° layer is caused by a combination of σ_{33} , σ_{11} , and σ_{13} (Figure 2.7) stresses for line-loading impact damage. Their analysis also concluded that the σ_{33} was very small relative to σ_{11} and σ_{13} throughout the impact event, and that there was a critical energy below which no damage occurred.

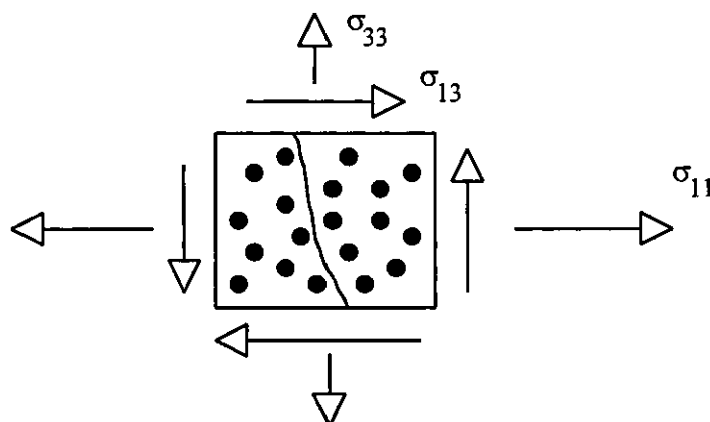


Figure 2.7 Diagram of the stress components contributing to a bending matrix crack in a transverse layer.

2.2.2.2 Delamination

A delamination is a crack which runs in the resin rich area (approximately 0.0007mm in graphite epoxy laminates⁵⁴) between plies of different fibre orientation and not between lamina in the same ply group^{48,55,56}. A crack propagating through a ply is arrested at an interface due to a change in fibre orientation with high stresses at the crack tip causing the crack to run along the interface⁴².

Liu and Malvern³⁷ compiled detailed connections between delaminations and the areas over which matrix cracks were found, for various lay-ups. Liu⁵⁷ explained that delamination was a result of the bending stiffness mismatch between adjacent layers, (i.e. the different fibre orientation between the layers). In his experimental work he found that delamination areas were generally oblong shaped with their major axis being coincident with the fibre orientation of the layer below the interface. For 0/90 laminates the shape became a distinct peanut. These results have been widely reported elsewhere in the literature^{43,48,49,58-60}. He also stated that it is the bending induced stresses which are the major cause of delamination, as both experiment and analysis revealed that along the fibre direction the plate tends to bend concave, whilst the bend is convex in the transverse direction. Liu defined a bending mismatch coefficient between the two adjacent laminates which includes bending stiffness terms and predicts the peanut shape reported for 0/90 laminates. The greater the mismatch (0/90 is the worst case fibre orientation) the greater the delaminated area, which is also effected by material properties, stacking sequence, and laminae thickness⁶¹.

Dorey⁶²⁻⁶⁴ has worked widely in this field and provides a simple expression for the elastic strain energy absorbed at the point of delamination failure, which suggests that this damage mode is more likely to occur for short spans and thick laminates with low interlaminar shear strength.

$$\text{Energy} = \frac{2(\text{ILSS})^2 wL^3}{9E_f t} \quad (2.2)$$

[where t = thickness, ILSS = interlaminar shear strength, w = width, L = unsupported length, and E_f = flexural modulus]

(a) Delamination Initiation and Interaction with Matrix Cracking

Delamination caused by transverse impact only occurs after a threshold energy has been reached and it has been observed that delamination only occurs in the presence of a matrix

crack⁵⁰. Much detailed work has been performed to verify this and explain the stress states which could cause this interaction.

Takeda et al⁶⁵ revealed for the first time the association between matrix cracking and delamination, and showed that delaminations do not always run precisely in the interface region, but can run slightly either side. Joshi and Sun⁴³ studied the delamination-matrix crack interaction for 0/90/0 laminates subject to transverse point impact. They concluded that when the inclined shear crack in the upper layer (Figure 2.6a) reaches the interface it is halted (by the change in orientation of the fibres) and so propagates between the layers as a delamination. This delamination is generally constrained by the middle transverse crack (Figure 2.6b). The vertical bending crack (Figure 2.6b) is thought to initiate the lower interface delamination, whose growth is not constrained. Matrix cracks which lead to delamination are known as *critical matrix cracks*⁴⁹.

F-K. Chang and colleagues^{44,49,50,66} performed a series of line loading, low velocity impact tests and reported a typical damage pattern for a 0/90/0 composite as shown in Figure 2.8. Chang, Choi, and Jeng⁴⁹ simulated these matrix cracks in their three-dimensional finite element analysis to study the stress in the vicinity of the cracks. They concluded that delamination was initiated as a Mode I fracture process due to very high out-of-plane normal stresses caused by the presence of the matrix cracks and high interlaminar shear stresses along the interface. In his review on delamination, Garg⁶⁷ proposed that matrix crack initiated delamination was due to the development of the interlaminar normal and shear stresses at the interfaces.

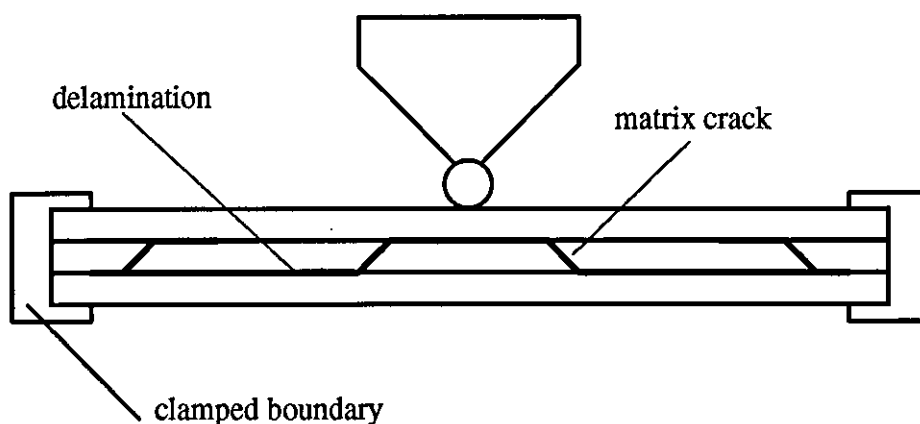


Figure 2.8 Typical matrix crack and delamination pattern from line load impact on a 0/90/0 composite.

Liu and co-workers⁶⁶ created an analytical model to study the interaction of damage mechanisms due to line load impact, utilising a fracture mechanics approach. They showed that both bending cracks and shear cracks could initiate delamination but that delamination induced by shear cracks is unstable, and that bending crack induced delaminations grow in a stable manner and proportional to the applied load.

Finn and Springer^{61,68} described in detail the stresses which they believed cause impact induced delamination. All the modes which could be induced by impact - bending, twisting, and transverse shear - were considered as were the restraints on the effected ply due to layers above and below. They concluded that if the cracked ply group was above the interface then σ_{12} (only if the upper interface of the ply group was unrestrained), and σ_{23} contributed to delamination, and if the cracked ply group was below the interface σ_{22} and σ_{12} contributed to delamination as long as the ply group lower interface was unrestrained.

Most fracture mechanics analyses of the initiation and growth of delamination are difficult to apply because they assume an initial flaw or crack size⁶⁹, however Davies⁴⁰ in a highly simplified isotropic axi-symmetric analysis for the threshold force for the growth of an internal circular delamination in the mid-plane, shows surprisingly that Mode II strain energy release rate is independent of delamination radius. Therefore an initial flaw size is not required and the threshold force is given by equation (2.3).

$$P_c^2 = \frac{8\pi^2 E h^3 G_{IIc}}{9(1 - \nu^2)} \quad (2.3)$$

[where, P_c = threshold load, G_{IIc} = critical strain energy release rate. ν = poison's ratio, h = plate thickness, and E = modulus] The predictions from this equation for delamination initiation agreed well with their experimental data on quasi-isotropic laminates.

Whilst most of the work relating matrix cracking and delamination has been performed for carbon/epoxy cross-ply or angle-ply laminates it was expected that the fundamental principles described above will also hold for pultruded laminates consisting of a unidirectional layer sandwiched between two layers of CFM.

(b) Delamination Growth

Many authors have proposed different theories on the stresses and fracture processes at work during the growth of delaminations. Choi and Chang⁵⁹ reported that delamination growth was governed by interlaminar longitudinal shear stress (σ_{13}) and transverse in-plane

stress (σ_{22}) in the layer below the delaminated interface and the interlaminar transverse shear stress (σ_{23}) in the layer above the interface.

Several investigators have introduced artificial delaminations by including a thin foil in between plies in the manufacturing stage to assess delamination growth from a known initial size⁷⁰. Doxsee et al⁷¹ calculated the energy absorbed per unit area of delamination growth and found that this was constant (595 J/m²). Jih and Sun⁴⁵ concluded that the interlaminar fracture toughness was independent of delamination size and that delamination area could be predicted from peak impact force generated. Wu and Shyu⁷² also found that there was a linear relationship between the peak force and delamination area and by extrapolating from the results they found a threshold force value for the onset of delamination.

In their numerical simulation of impact induced delamination growth Razi and Kobayshi⁷³ concluded that Mode II was the dominant failure mode for propagation, a view also put forward by Guild et al⁵⁸.

Therefore, whilst the basic nature of delamination, and initiation by matrix cracking is well understood, researchers are not in agreement regarding the stress states at initiation, and the propagation process is not well understood. Several authors try to describe the stresses which cause the delamination initiation and propagation with disagreement mainly being due to whether they are describing a thick or thin laminate which effects whether the global response is dominated by bending or shear.

2.2.2.3 Fibre Failure

This damage mode generally occurs much later in the fracture process than matrix cracking or delamination and as research has concentrated on the low energy modes of damage there is less information on this area. Fibre failure occurs under the impactor due to locally high stresses and indentation effects (mainly governed by shear forces) and on the non-impacted face due to high bending stresses. Fibre failure is a precursor to catastrophic penetration mode. A simple equation for the energy required for fibre failure due to back surface flexure is given by Dorey⁶³ as:

$$\text{Energy} = \frac{\sigma^2 wtL}{18E_f} \quad (2.4)$$

[where, σ = flexural strength, E_f = flexural modulus, w = width, L = unsupported length, and t = specimen thickness]

In the "plank" fibre failure will occur in both the CFM and the UD layer. The fibres are randomly oriented in the CFM layer and so it was expected that tensile failure would occur in the lower CFM layer whilst high local shear stresses in the upper CFM layer would cause fibre failure, whereas UD fibre failure would signal impending ultimate failure.

2.2.2.4 Penetration

Penetration is a macroscopic mode of failure and occurs when the fibre failure reaches a critical extent enabling the impactor to completely penetrate the material⁷⁴. Research into penetration impact has mainly concentrated in the ballistic range⁷⁵ however some low velocity impact work has been performed. Cantwell and Morton⁴⁷ showed that the impact energy penetration threshold rises rapidly with specimen thickness for carbon fibre composite. They also analysed the penetration process to calculate the energy absorbed by "shear-out" (i.e. removal of a shear plug), delamination and elastic flexure. This simplified analysis predicted shear-out as the major form of energy absorption (50 to 60% depending on plate thickness).

El-Habak⁷⁶ tested a variety of glass fibre composites at penetration loads and concluded that the glass fibre treatment played a key role in determining the perforation load whilst the matrix had little effect with polyester being preferable to epoxy. Dorey⁶³ provided a very simplified analytical model of penetration to give the energy absorbed as:

$$\text{Energy} = \pi \gamma t d \quad (2.5)$$

[where, γ = fracture energy, d = diameter of impactor, and t = plate thickness]

2.2.3 Damage Modes in Randomly Oriented Fibre Laminates

Most of the work reported above was performed on laminates consisting of unidirectional plies with varying fibre orientation. In layers in which the fibres are unidirectional it is quite straightforward to predict the orientation of matrix cracking. When the fibres are oriented randomly then crack patterns are less easy to establish. SMC panels and continuous filament mats used in pultrusions are common examples of randomly oriented short and long fibre layers respectively.

Clearly, a different approach to defining damage modes is required for these composites. In their research on SMC panels, Liu and Malvern³⁷ found that matrix cracks on the impacted surface were short and formed a series of rings away from the point of contact and deduced these were caused by the tensile strain wave moving out from the centre of impact. Both Chaturvedi and Sierakowski⁷⁷ and Khetan and Chang⁷⁸ performed work on glass/polyester SMC panels with air gun equipment (i.e. high velocity). Whilst the latter authors suggested that damage could be quantified by a "damage area", the former authors concluded from tensile residual strength tests that more information was required on failure modes to be able to predict stiffness and strength degradation. Liu et al⁷⁹ in their work on the Repairability of SMC composites for the automotive industry, defined three types of impact-induced damage: (1) indentation (crushing of matrix under the impactor), (2) bending fracture, and (3) perforation (i.e. damage resulting from penetration and associated fracture).

These damage modes are effected by the specific fibre and matrix type employed. This is a particularly important area to consider, as the "plank" consists of glass/polyester whereas the majority of published impact test data has been performed on carbon/epoxy combinations.

2.2.4 Influence of Constituents on the Impact Response of Composite Materials

A fibre reinforced composite consists of two major constituents (fibre and matrix) and the interphase region, which is the area of bond between fibre and matrix. The properties of each of these constituents effects the threshold energies and stresses required to initiate the different failure modes induced by impact, and indeed may alter the modes of damage which occur.

2.2.4.1 Fibres

This is the main load bearing constituent which provides the composite with the majority of its strength and stiffness. The most common fibres are glass, carbon and "Kevlar®". Carbon is widely used in the aircraft industry and many other structural applications as it has the highest strength and stiffness values, but it also is the most brittle with a strain to failure of 0.5 to 2.4%. Glass fibres have a lower strength and stiffness but higher strain to failure and are less expensive than carbon fibres, and they dominate the market⁸¹. The mechanical properties of kevlar lie between that of carbon and glass⁸². Carbon's design ultimate allowable strain is only 0.4% currently, whilst improvements in damage tolerance

performance would allow a 50% improvement on this⁸³. Thus a great deal of the fibre's superior performance characteristics cannot be taken advantage of due to its weakness with respect to impact.

For resistance to low velocity impact the ability to store energy elastically in the fibres is the fundamental parameter^{35,81}. This corresponds to the area under the stress-strain curve which is dictated by the fibre modulus and failure strain. E-glass can therefore absorb approximately three times the elastic energy of carbon. Hybrid composites are often formed by adding glass or kevlar^{42,69,82} to carbon composites to improve impact resistance, and take advantage of the "hybrid effect" which can induce considerable strength enhancements⁸⁴. Moduli mismatching between fibres however increases the complexity of the design of hybrids.

In the ACCS the fibres are E-glass⁶, which follow a basically linear stress-strain curve to failure⁸⁵. Vetrotex manufacture the E-glass used in the ACCS "plank", and give the fibre properties as having a tensile strength of 2480 MPa (for an impregnated roving), tensile modulus of 73 GPa, and a failure strain of 4.5%.

(a) Strain-Rate Sensitivity of Glass Fibres

There is conflicting information in the literature regarding the strain-rate sensitivity of glass fibres. In general, carbon fibres are thought of as not being strain-rate dependent^{33,62,86,87} and glass fibres as having a modulus and stiffness which increase with strain-rate^{62,87-89}. However, in their review in 1983, Sierakowski and Chaturvedi⁹⁰ concluded that there was not enough information available to fully assess the role of rate sensitivity of composite systems and this is still the case today.

In their impact tests from 1 to 5.5 m/s Caprino et al⁹¹ reported no strain-rate effects for glass cloth cloth/polyester. However, over a wider strain-rate range Sims⁹² reported increasing flexural strengths for a glass mat/polyester laminate (10^{-6} to 10^{-1} m/s displacement rate) for Charpy testing.

Hayes and Adams⁹³ constructed a specialised pendulum impactor to study tensile strain-rate effects, as impact speeds increased from 2.7 to 4.9 m/s, for glass/epoxy. They also performed static tensile tests. The elastic modulus and strength in general increased with impact velocity, but the trend was not consistent throughout the dynamic range, and the values at static loading did not support this trend. In contrast to the belief that carbon fibres are non-rate dependent they reported that graphite epoxy's modulus decreased with impact

speed and at dynamic loads the ultimate strength and energy to ultimate stress were lower than the static values.

Li et al⁹⁴ reported an increase in the tensile and compressive strength and stiffness for glass from quasi-static rates of strain (0.001/s to 10/s) to high velocity impact (350/s to 1100/s). They also noted through-thickness strength increases for glass weave. However, low velocity impact induces strain-rates which lie in a much narrower range than the work of Li.

In their investigation into the impact response of thick glass/polyester laminates, Zhou and Davies⁹⁵ compared their low velocity impact tests with static test performed in exactly the same configuration. They concluded that peak forces generated under impact loading were 36% higher for the 10mm thick plates than under static loading though the force-displacement curves were very similar up to the initiation of damage. This suggests that it is the damage growth mechanisms that are most strain-rate sensitive.

Testing the strain-rate dependence of the glass/polyester pultrusion in isolated stress states would require very specialised equipment and was beyond the scope of this investigation. Though the review indicates that glass fibres are strain-rate dependent it was not clear whether this would be apparent over the narrow range of impact velocities which the ACCS "plank" was be subject to, therefore some testing to ascertain this was required.

2.2.4.2 Matrix

In a FRP the polymeric matrix (usually a thermoset) provides several key functions: it transfers the load to the fibres, protects the fibres from damaging themselves and aligns/stabilises the fibres. The majority of structural applications employ epoxy resins as they meet the hot/wet compressive strength requirements. However, epoxy is brittle and has poor resistance to crack growth. Attempts to reduce matrix damage and improve the interlaminar fracture toughness of thermoset resins has involved incorporating plasticising modifiers, or adding rubber or thermoplastic particles to the resin⁸³. However, increased interlaminar fracture toughness invariably reduces mechanical properties and improvements made to the pure matrix are never transferred fully to the composite due to the presence of brittle fibres which prevent growth of plastic zones in the matrix³⁵. The inclusion of a thin discrete layer of very tough, high shear strain resin can also be employed to minimise delamination⁹⁶.

The use of thermoplastic resins (e.g. Polyetheretherketone PEEK) can give an order of magnitude increase in fracture toughness over thermoset composites. Low thermal stability

and chemical resistance, poor fibre/matrix interfacial bond, and creep problems have historically prevented the use of thermoplastic composites⁸³. The need for new production techniques still holds back the use of thermoplastics, but as these problems are overcome so thermoplastic based composite systems become more competitive.

Epoxy is a brittle matrix with a poorer resistance to flaw growth (leading to delamination and matrix cracking) than isophthalic polyester, which is used in the ACCS. Isophthalic polyester is a strain-rate dependent, visco-elastic material but only over a wide range of strain-rates does the rate loading effect its properties. Scott Bader manufactures the resin used in the ACCS, called Crystic D4847, and gives its mechanical properties as having a tensile strength of 42 MPa, tensile modulus of 4.3 GPa, and failure strain of 1.8%.

2.2.4.3 Interphase Region

The interphase region between fibre and matrix is of vital importance. Usually, the surface of carbon fibres are treated with an oxidative process in order to improve the level of adhesion between fibre and matrix, whilst glass fibres are treated with a coupling agent. The interphase region can effect the failure mode which occurs at a given load, i.e. poor adhesion results in failure at low transverse stress leaving clean fibres. The bond strength can be manipulated to improve the toughness by absorbing energy in fibre-matrix debond, however this reduces the mechanical properties.

2.2.4.4 Glass/Polyester Composites

As stated, the majority of testing has been on carbon/epoxy systems, however some glass/polyester impact test work has been reported. Svenson et al⁹⁷ performed line impact tests on glass/polyester and glass/vinylester pultrusions in their investigation into the application of pultruded composites as roadside safety structures. Plate specimens (all more than 6mm thick as compared to the 3.3mm skin sections on the ACCS) were cut from different pultruded sections and tested as bar specimens in a three-point bend test configuration. The pultrusions consisted of alternating layers of CFM and UD. Two major failure modes were observed - tensile failure on the lower surface followed by shear failure within the specimen. The shear induced failure was due to the relatively thick test samples with high bending stiffness. No delamination failure was mentioned.

Habib⁹⁸ also performed tests on 150mm square, 8mm thick glass/polyester flat panels and reported low energy damage in the form of delamination and transverse cracks, whilst at higher energies surface damage and fibre fracture were observed.

Further impact tests on thick glass/polyester flat panels were carried out by Zhou and Davies⁹⁵. They described a three stage sequential damage model: the first stage was an elastic response to the initial threshold and a static analysis was sufficient to describe this section using indentation laws. The second stage was dominated by bending with reduced stiffness due to delamination, the final stage was initiated by "shear-out" of the top plies causing extensive delamination. Initially the indentation was due to matrix cracking and surface micro-buckling which was observed visually as whitening. At higher energies the ply "shear-out" produced a much deeper indentation, as the uppermost layer cracked through.

2.2.5 Impact Performance of Complex Geometry Specimens

The "plank" cross-section is double-skinned with longitudinal webs which represents quite a complex geometry. In general little work on impacts on complex structures has been published, but the webs act as stiffeners and some work on impacts on stiffened panels has been performed.

Dorey⁶² reported that the energy to cause BVID dropped significantly near the stiffeners, where the structure was less compliant and that the stiffeners caused damage to spread asymmetrically, as would be expected over an area of non-uniform stiffness. Davies and co-authors^{40,60} stated that impact forces will be higher in the stiffened regions, but that reduced deflections may lead to smaller strains and therefore less strain induced failure. At the edge of the stiffeners delaminations were formed, whilst impacts directly over the stiffener caused debonding between plate and stiffener. The damage tended to extend down the stiffener which would have disastrous effects for a compression loaded panel. "Cratering" also occurred due to the very high forces induced in the stiffened regions. Due to fear of stiffener-panel debond, many manufacturers are using mechanical joining techniques to avoid this problem, indicating that it is an area of some concern.

Cheung et al⁹⁹ performed impacts on thin flat and blade stiffened carbon/epoxy panels. Tests were performed between, near, and directly over a stiffener and the extent of damage recorded. They concluded that the damage incurred depended on the impact location and that whilst flat panel damage remained local to the impact location, damage remote to the impact site was observed when the impacts were over a stiffener due to high stress concentrations at the skin-stiffener interface.

Tabiei et al¹⁰⁰ investigated the impact behaviour of pultruded box-beams for roadside safety structures. The materials used were glass fibres with polyester and vinyl ester, and the boxes were tested in a three-point bend set-up and line impactor. High speed film revealed that only shear failure was induced by the test configuration. The ultimate load was the same for both static and impact tests. The same workers¹⁰¹ also performed tests on more complex cross-sections but the selection of a simply supported three-point bend test reduced the usefulness of the exercise as the specimens did not fully fail.

Kelkar et al¹⁰² investigated the change in response as laminate thickness increased and they concluded that for the same impact energy the damage areas were larger for thick laminates than thin because the failure mechanisms were different for the different thicknesses. The thick laminates were stiffer and therefore absorbed less energy elastically and failed in transverse shear mode, whereas the thin laminate's failure was bending dominated. It was expected that the same change in failure mechanisms would occur in the ACCS "plank" when the point of impact changed, from between the webs to impact near or over a web.

2.2.6 Post Impact Residual Strength

As stated previously due to the susceptibility of composite materials to impact damage, dramatic loss in residual strength and structural integrity results. Even BVID can cause strength reductions by up to 50% whilst residual strengths in tension, compression, bending, and fatigue will be reduced to varying degrees depending on the dominant damage mode:

2.2.6.1 Residual Tensile Strength

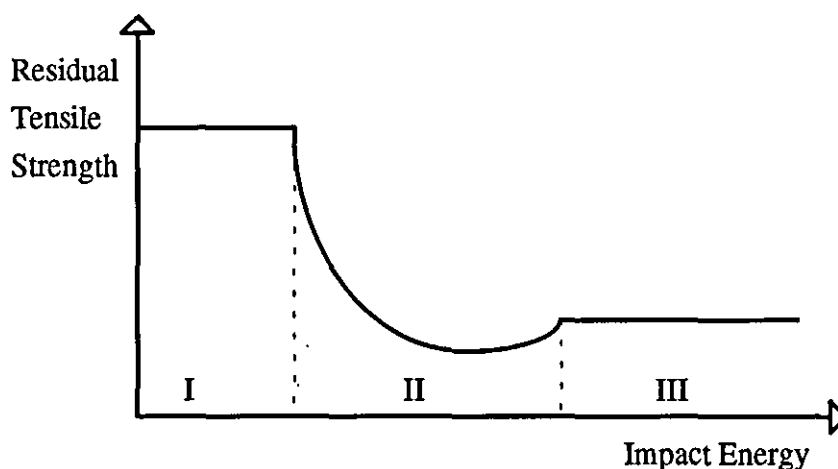


Figure 2.9 A characteristic residual strength versus impact energy curve.

Residual tensile strength³⁶ normally follows a curve as shown in Figure 2.9. In region I, no damage occurs as the impact energy is below the threshold value for damage initiation. The residual tensile strength reduces quickly to a minimum in region II as the extent of damage increases once the threshold has been reached. Region III sees a constant value of residual strength because the impact velocity has reached a point where clean perforation occurs leaving a neat hole. In this region the tensile residual strength can be estimated by considering the damage to be equivalent to a hole the size of the impactor. The minima in region II is less than the constant value in region III because the damage spreads over a larger area than is produced at a higher velocity when the damage is more localised. As the fibres carry the majority of tensile load in the longitudinal direction, fibre damage is the critical damage mode.

Caprino⁸⁷ developed a model to predict residual tensile strength as a function of impacting kinetic energy. Linear Elastic Fracture Mechanics was used to predict the strength degradation, as the damage was assumed to be a equivalent hole and behave as a stress concentrator. The expression is:

$$\sigma_r = \sigma_0 \left\{ \frac{U_0}{U} \right\}^\phi \quad (2.6)$$

[where U = impact energy, U_0 = threshold impact energy, σ_r = residual strength, σ_0 = undamaged strength, ϕ = geometric/material constant, and ϕ and U_0 are determined experimentally]. This equation fitted a number of experimental results with good correlation and was further confirmed by the work of Tui et al¹⁰³.

2.2.6.2 Residual Compressive Strength

Poor post impact compressive strength is the greatest weakness of composite laminates in terms of residual properties. This is mainly due to local instability resulting from delamination causing large reductions in compressive strength^{62,104}. As delamination can be produced by low energy impacts, large strength reductions in compression can occur for BVID. Delamination divides the laminate into sub-laminates which have a lower bending stiffness than the original laminate and are less resistant to buckling loads⁸³. Under a compressive load, a delamination can cause buckling in one of three modes³⁶: global instability/buckling of the laminate, local instability (buckling of the thinner sub-laminate), or a combination of the above. The mode of failure generally changes from global, to local, to mixed-mode as the delamination length increases.

PICS testing is often avoided due to the difficulty in providing a large enough gauge section to accommodate the damage. This necessitates the use of complex anti-buckling guides which must support the specimen to prevent global buckling, but at the same time must not prevent local instability¹⁰⁵.

2.2.6.3 Residual Flexural Strength

Less work has been done in this area, but it has been reported that both flexural modulus and strength decreased with increasing low velocity impact energy for ductile specimens (glass/epoxy) whilst brittle graphite/epoxy observed no losses until complete failure occurred³⁶. Flexural testing introduces a complex stress pattern in the specimen, therefore the effect of the damage on residual strength is less easy to analyse.

2.2.6.4 Residual Fatigue Life

Jones et al¹⁰⁶ reported that compression-compression and tension-compression are the critical fatigue loading cases, which corresponds to compression being the worst case static loading condition. The maximum residual compressive load divided by the static failure load (S) typically decreases from 1.0 to 0.6 in the range 1 to 10^6 cycles (N) depending on the initial damage size. The rate of degeneration is at its highest up to $N = 100$ cycles, and after 10^6 cycles no further degradation occurs, so $S = 0.6$ may be assumed to be the fatigue threshold. Therefore it is believed that fatigue loading is not a good way of characterising residual properties.

Having studied the impact and post-impact properties of composite laminates, the next section looks at the experimental techniques available for low velocity impact testing and damage assessment.

2.3 Experimental Procedures

In order to decide which test technique should be employed it was first necessary to decide whether to perform dynamic impact tests or whether static tests could be assumed to provide representative results for low velocity impact testing.

2.3.1 Static versus Dynamic Testing for Low Velocity Impact

Impact test results display a scatter wider than static testing (due to vibrations and dynamic effects) and therefore repeatability of results and result interpretation is less easy to achieve.

Quasi-static testing would be convenient, as it would allow the force to be increased to any level desired and the growth of damage noted in a much more controlled and repeatable way than could be achieved with impact testing.

Ganapathy¹⁰⁷ explained that low velocity impact can be treated as a quasi-static problem because the contact duration is much longer than the time required for the propagating waves to reach the specimen supports. However, this ignores potential strain-rate effects. Many authors^{33,34,45,46,72-74,87,108} have employed static testing when investigating the low velocity response and damage mechanisms of carbon fibre composites and shown the quasi-static assumption to be valid. However, unlike carbon, glass fibres are strain-rate sensitive as was discussed earlier, and so the above assumptions cannot automatically be made.

Liu and Malvern³⁷ studied both impact induced damage and quasi-static induced damage for glass/epoxy plates and concluded that completely different matrix cracking patterns existed for the two loading cases, whilst Collombet and colleagues¹⁰⁹ also observed different damage extents and modes in their comparison of the impact and static loading for glass/epoxy also. Zhou and Davies⁹⁵ clearly showed that the thick glass/polyester plates tested were both stronger and stiffer under low velocity impact loading than static loading.

In contrast, from their tests on glass fibre composite upper face sandwich panels, Robinson and Davies³⁹ concluded that IFWI was quasi-static as the damage was only a function of the impact energy and not mass or velocity individually, and the peak force correlated to impact energy. Lifshitz¹¹⁰ in his early work on the impact strength of glass fibres reported that failure under impact and static loads were basically the same but that strength values were higher in the dynamic case.

Whilst tentative conclusions can be drawn that quasi-static testing is valid for low velocity impact on non-rate sensitive carbon fibre composites, there is contradictory evidence for glass fibre composites. Therefore it was concluded that dynamic testing rather than static testing had to be employed to simulate low velocity impact.

2.3.2 Dynamic Impact Testing of Composite Materials

The impact test technique employed is dependent on the velocity range required, with low velocity testing generally involving a relatively large mass, whilst high velocity is mainly concerned with small masses. Applied to the aerospace industry, the larger mass impacts correspond to dropped tools whilst low mass impact simulates runway debris striking the underside of an aircraft, small arms fire etc. The test should ideally simulate the loading

condition of the in-service impact with respect to both dynamic and boundary conditions so that the same energy absorption, and damage levels and modes are induced.

For high velocity testing, high pressure gas guns are used to fire pellets at the specimen at ballistic rates of strain^{43,48,90}, and instrumented gas guns have been developed to enable more information to be measured (i.e. force/displacement data). The Hopkinson Bar is a technique for the analysis of basic material properties at different strain-rates (up to approximately 1000/s), whilst different test configurations can be used to isolate specific stress states¹¹¹. The elastic impact response of composites can be investigated using a non-destructive instrumented impact hammer technique and frequency analyser¹¹².

For low velocity impact testing, Charpy Pendulum and Izod tests can be employed. Both are easy to use and have the ability to be instrumented to give the impact force and energy absorbed as a function of time. The main disadvantage is that the specimen must be a short thick notched bar which is therefore not a typical component and so does not necessarily induce the damage modes which occur in a structure. This technique is therefore normally used to compare different materials or in quality control rather than in attempting to recreate "real" structural impacts³⁵.

The most widely used procedure for testing real components under low velocity impact is the instrumented falling weight impact (IFWI) test technique, which was also available to be used on this project.

2.3.2.1 Instrumented Falling Weight Testing

In instrumented falling weight impact testing a weight is dropped from a pre-set height onto the test specimen supported horizontally below it. Impact energy can be varied by altering the drop height or the impactor's mass, with the test resulting in failure by penetration or only inducing minimal damage with the impactor being caught on rebound.

An optical sensor is usually employed to measure the impact velocity and with the impactor being instrumented, force-time and energy-time characteristics are recorded. This technique allows a wide range of specimen configurations to be supported and tested. Impactors are generally hemi-spherical but in theory any design of contact geometry can be used, within the physical limitations of the machine.

Instrumented Falling Weight Impact has been employed by many authors^{108,114,115} to test composite materials. Due to the transient dynamic nature of the test, both specimen and

impactor vibrate to some extent which is seen as spurious noise on the force-time signal recorded. These oscillations in the force-time graph can hide information, (i.e. sudden drops in load due to a failure mode being reached), therefore a low pass filter is often required to remove the unwanted high frequency noise. However over filtering can remove significant peaks and reduces the peak values recorded^{114,116}, so filtering effects must be carefully monitored and a knowledge of the natural frequencies of the impactor and specimen is required. Johnson et al¹¹⁴ compared IFWI tests from five different laboratories to validate the technique and concluded that when correct filtering levels were used, the method was reliable and informative.

Several authors^{114,116-118} used high speed photography during IFWI tests to enable composite material failure modes to be identified and related to peaks on the force-time curve, whilst Lindsay and Wilkins¹⁰⁸ identified energy, load and displacement at damage initiation using this technique. In their IFWI investigation of the effects of impact mass and specimen geometry, Robinson and Davies³⁹ used the force-time signal to separate the energy absorbed in the damage process from that stored elastically.

There are clearly many ways that the information from IFWI testing can be analysed in order to further explain the impact event under consideration. Whilst this instrumented technique provides much data regarding the impact event, the damage induced by an impact must also be identified and quantified in order to fully characterise damage mode initiation, propagation, and interaction. The following section reviews the commonly employed techniques to do this.

2.3.3 Impact Damage Detection Techniques

It was shown in section 2.2.2, that the major modes of impact induced damage comprises of matrix cracking, fibre breakage and delamination. To identify the impact damage due to each mode, a combination of the following techniques is required: (For further information on damage detection techniques, the review by Cantwell and Morton¹¹⁹ is excellent.)

2.3.3.1 Non-Destructive Techniques

Visual Inspection enables the location and general severity of surface damage to be assessed. When epoxy laminates are being tested the transparency of the epoxy often allows strong back-lighting to allow the detection of matrix cracking and internal delaminations⁶⁵.

Ultrasonic scanning techniques^{120,121} are used to provide information regarding in-plane internal damage i.e. delamination. To ensure efficient transmission of energy, the

component is immersed in water, coated with gel or transmission is via a water jet. Viscoelasticity, inhomogeneity, and damage attenuate the signal, but by correct frequency selection the signal can reflect attenuation solely due to the damage. There are three general methods of ultrasonic testing: (1) *A-Scan* detects the severity and the through-thickness location of the damage at a single point only. It is therefore one-dimensional and so does not give information regarding the area of damage. (2) *B-Scan* is two-dimensional, in that it will render information through a section of the specimen. (3) *C-Scan* involves the transmitter sweeping over the surface of the component and it is the most widely used of the ultrasonic damage detection techniques. It provides a plan view of the area of damage but gives no through-thickness information and so does not distinguish between delaminated areas on different interfaces through the laminate¹²². Time-of-flight-analysis, combines A- and C-Scan, and therefore gives a complete three-dimensional map of damage, i.e. the damage area at each interface. However, the high attenuation of glass fibres makes this method difficult for glass fibre composites.

X-ray Radiography¹¹⁹ is also used to assess internal damage. Normally a radio-opaque penetrant is used to enhance the contrast between damaged and unaffected areas to increase the differential absorption of the radiation. Care must be taken in choosing the dye to ensure that there will be no reaction with the composite. In theory, all three modes of damage stated above can be detected, however resolution between damage modes can be a problem in areas of severe damage and in practice this technique is mainly used for detecting delamination areas. A three-dimensional damage zone can be viewed if two radiographs are taken at different angles to the x-ray beam.

Acoustic emission¹²³ is the noise which is emitted as a material is damaged by a particular mechanism and the technique employs a transducer to detect the stress waves (generated as a material responds so as to reduce its internal energy) when they reach the surface of the component undergoing deformation and fracture. Differentiation between damage modes is poor and in general it is a complex research technique only yielding reliable information in the hands of an experienced operator.

The **Thermography**¹¹⁹ technique employs an external heat source to cause a rapid temperature increase producing heat flow across the component. Flow across a damaged zone is reduced, thus impact damage can be detected with an Infra Red camera. The effectiveness of this technique strongly depends on the material's thermal properties, component thickness and type of damage. Whilst it detects large delaminations well, it is generally less accurate than x-ray radiography or ultrasonic techniques.

Edge Replication¹¹⁹ involves pressing softened cellulose acetate tape onto the edge of the component, thus reproducing the damage along the edge. The tape can be viewed in transmitted light or with Scanning Electron Microscopy (SEM). If internal damage is to be assessed then a section must be cut and so it becomes a destructive technique.

2.3.3.2 Destructive Testing Techniques

Whilst non-destructive techniques leave the component intact enabling residual strength testing or further damage assessment to be performed, this is not possible if destructive testing is employed.

Thermal Deply involves placing the component in an oven at a temperature which will remove the polymer matrix but not effect the fibres. After cooling and removal from the oven the plies can be separated and inspected for fibre breakage.

Optical Microscopy is the most common method of assessing matrix damage. The section is mounted, ground and polished for viewing. Delaminations can also be detected but only a two-dimensional damage map can be obtained from one cross-section. However an approximate three-dimensional map can be interpolated if several sections through the damaged area are inspected. Very careful section preparation is required to ensure that the damage introduced by the sectioning is minimised, thus the technique is time consuming.

When employing the **Scanning Electron Microscopy**¹¹⁹ technique, small specimens are normally coated in a very thin layer of gold or carbon particles⁶⁵ in order to conduct the electrons away and prevent the area under examination from over-heating. Fracture paths can be determined and all modes on the surface of the specimen can be detected. Internal damage is only detected by viewing the surface of sections cut through the plate.

For a full three-dimensional damage map to be constructed, two or more of the above techniques are required. The most common strategy in the literature was to use X-ray or C-Scan to detect delamination, in conjunction with optical microscopy, thermal deply and visual inspection to detect matrix damage, fibre breakage and macroscopic surface damage respectively.

2.3.4 Relating Experimental Impact Test Results to "Real" Structures

With the IFWI technique, whilst the support structure can be modified and different boundary conditions, and specimen and impactor sizes and shapes can be used, the variety is in practice limited. Impact testing of large "real" structures is not practical, physically or economically. It is therefore necessary to be able to relate coupon test results to impact on "real" structures, but this has proven difficult⁸⁸.

The key to relating impact damage from coupons to "real" structures is finding the characteristics of the coupon test which identifies the impact induced damage process. In trying to identify the key characteristics relating the damage in the specimen to the impact, most authors have related the impact energy to the damage area (i.e. delaminated area).

However, if specimens of different size or support conditions are employed, varying amounts of elastic energy will be stored in the coupon, therefore characteristic energy values cannot be related from one set of tests to another using impact energy⁴⁰. Davies and co-authors^{39,40,60,88} have been particularly active in attempting to relate coupon tests to "real" structures and reported good correlation between the peak force and the level of damage in a coupon due to low velocity impact. Jackson and Poe¹²⁴ concluded that for low velocity (high mass) impacts, the peak force could be used as the sole parameter to predict the resulting delamination size.

Whilst progress has been made in relating damage in flat plate specimens of one dimension to that of another dimension, it is clear that some analytical or computational technique is required to relate coupon impact test results to the response of complex "real" structures and the impactor shapes they will be subject to in-service, and this is the subject of the following sections.

2.4 Analytical Techniques Applied to Aspects of Impacts of Composites

Several different approaches to qualitatively assess aspects of the impact response of composite structures have been employed. Simple analyses allow the main features of the impact event to be more clearly understood, with the following two models being valid for elastic impacts only.

2.4.1 Spring-Mass Models

Caprino et al⁹¹ used a single degree of freedom (SDOF) model to predict elastic impact response of glass cloth/polyester, where the ratio of the mass of the structure to the impactor's mass (m_i) was small, as in Figure 2.10. For this case the ratio of vibration energy to total energy was small, enabling vibration effects to be ignored, and a linear elastic plate was represented by a linear spring of stiffness K , which can be determined experimentally or from laminate beam or plate theory.

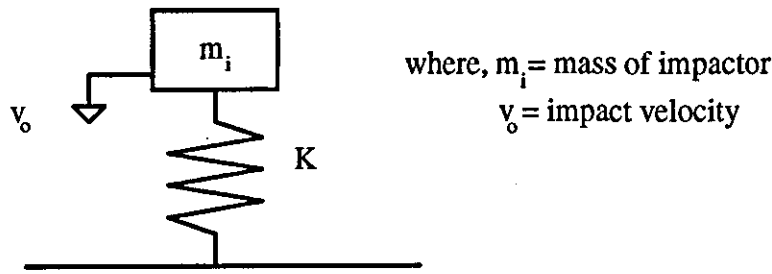


Figure 2.10 Single degree of freedom spring-mass model of impact.

Ignoring energy losses:

$$U_0 = U_i + U_p \quad (2.7)$$

[where U_0 = energy of impactor before impact, U_i = energy of impactor after impact at time t , U_p = strain energy in plate at time t]. This equation can be developed to give the contact force, and the contact time:

$$F = F_{\max} \sin \pi \frac{t}{t_c} \quad (2.8)$$

$$t_c = \pi \sqrt{\frac{m_i}{K}} \quad (2.9)$$

$$\text{where } F_{\max} = \sqrt{2U_0 K} = v_0 \sqrt{m_i K} \quad (2.10)$$

The analysis gives a sinusoidal shaped force-time curve assuming linear elasticity with F_{\max} being a linear function of impact velocity (v_0). Good experimental agreement was reported by the author with the plate behaving elastically even beyond first failure. The approximate strain-rate in the upper ply can also be found from this analysis¹²⁵.

Sjöblom et al³³ developed the above analysis to include the mass of both plate and impactor, with the plate and contact rigidity being modelled separately. More complex spring-mass models include the two degree of freedom model by Shivakumar et al¹²⁶ who used a spring to represent Hertzian contact stiffness (section 2.4.3) between the plate and the impactor, and separate springs for the bending, shear, and membrane stiffnesses of the plate. Choi and Hong¹²⁷ computed the impact duration from an eigenvalue analysis of the lumped mass system and then used the impulse-momentum law combined with the spring-mass model to predict the impact force history. In these analyses, thermal and acoustic losses, post-impact vibration and impact damage were ignored.

Spring-mass models therefore provide information on the history of the contact force and the displacement by integration of the equations of motion for an elastic event. The complexity of the model can be tailored to the analysis being performed, yielding useful trends of the impact event. However, if only the contact force and deflection are required then an energy balance model can be used.

2.4.2 Energy Balance Models

These analyses are based on the principle of conservation of total energy of the plate-impactor system. Shivakumar et al¹²⁶ compared an energy balance model to the spring-mass model described above, for impact on a circular laminated plate by a mass (m_i) with velocity (v_0). It was assumed that the energy in the plate was stored as contact deformation (U_c), strain energy due to bending and shear (U_{bs}), and strain energy due to membrane deformation (U_m). The energy balance (ignoring losses due to material damping, surface friction, and higher mode vibrations) gave:

$$\frac{1}{2} m_i v_0^2 = U_c + U_{bs} + U_m \quad (2.11)$$

The separate energies were calculated as follows:

$$U_c = \int_0^{\max} F d\alpha \quad (2.12)$$

[where α is the indentation given by the Hertzian relation, and $F = n\alpha^{3/2}$ and n is a material and geometry dependent stiffness parameter]. The reactive force F from the plate can be resolved into two components

$$F = F_{bs} + F_m \quad (2.13)$$

and using the force deflection relationship for circular plates:

$$F = K_{bs}\delta + K_m \delta^3 \quad (2.14)$$

[where δ = central transverse deflection and $1/K_{bs} = 1/K_b + 1/K_s$]. The stiffnesses, K_b , K_s , and K_m are dependent on the boundary conditions. U_{bs} , and U_m are obtained by integrating the forces F_{bs} and F_m with respect to δ .

$$U_{bs} = 1/2 K_{bs} \delta^2 \quad (2.15)$$

$$U_m = 1/4 K_m \delta^4 \quad (2.16)$$

which can be substituted into the energy balance equation

$$m_i v_0^2 = K_{be} \delta^2 + \frac{1}{2} K_m \delta^4 + \frac{4}{5} \left[\frac{(K_{be} \delta + K_m \delta^3)^5}{n^2} \right]^{1/3} \quad (2.17)$$

The central deflection, δ can therefore be found by solving equation 2.17 using the Newton-Raphson numerical technique, and F calculated by substituting δ into equation 2.14. The authors used this approach to show the increased significance of membrane effects as δ increases.

Simplified global elastic impact response can therefore be predicted from the two types of model described above. However, directly under the impactor local elastic indentation occurs which modifies the local stress field and alters the forces generated¹²⁵. The use of contact laws enables the local stress field analysis to be performed.

2.4.3 Contact Analyses

On impact, the stress field consists of local stresses in the vicinity of the impactor caused by the contact between the indenter and structure, and those resulting from the global dynamic response of the structure. The indentation must be described accurately in order to obtain an accurate local stress field and also because an appreciable amount of energy can be absorbed by the formation of the indentation¹²⁸. The local stress field is not taken into account in either of the above simplified models. Matrix cracks and delamination are often introduced into the contact zone even at low energy levels, but the indentation laws are only applicable up to first failure.

Experimentally determined static force-indentation relationships can be found, but they are time consuming to obtain and so contact/indentation laws are employed in most analyses with a semi-empirical unloading curve, to take into account permanent indentation.

The **Modified Hertz Contact Law** uses the classical Hertz contact law^{113,128-130} (equation 2.18) but applies a modified constant proposed by Yang and Sun¹³¹ and Tan and Sun¹³⁰ (equation 2.19).

$$F = K \alpha^{3/2} \quad (2.18)$$

[where K = contact stiffness parameter and α = indentation]. The Hertz Contact law was developed using the theory of elasticity for contact between two elastic isotropic spheres. However, experimentation has shown that the law also yields good correlation for contact of a rigid sphere on a laminated composite^{128,131} where:

$$K = \frac{4}{3} \sqrt{R_i} \left(\frac{[(1 - \nu_i^2)]}{E_i} + \frac{1}{E_{22}} \right)^{-1} \quad (2.19)$$

[where R_i = impactor radius, ν_i , E_i = Poisson's ratio and Young's modulus of the impactor, and E_{22} = Young's modulus of the top ply in the transverse direction to the fibres]. The most commonly used **Unloading Curve** is that developed by Yang and Sun¹³¹ where, the permanent deformation is taken into account by including the following unloading force-indentation relationship, with curve fitting of experimental results to the above equation giving the unknown variables¹³¹.

$$F = F_m \left[\frac{\alpha - \alpha_0}{\alpha_m - \alpha_0} \right]^q \quad (2.20)$$

[where q = best fit value for the experimental data ($q = 2.5^{68}$ and $1.5 - 2.5^{130}$), F_m = maximum contact force, α_m = maximum indentation during loading, and α_0 = permanent deformation, and $\alpha_0 = 0$ if $\alpha_m < \alpha_{cr}$, and $\alpha_0 = \alpha_m [1 - (\alpha_{cr}/\alpha_m)^{0.4}]$ if $\alpha_m > \alpha_{cr}$.]

Wu and Chang¹³² incorporated the modified Hertz contact law with the Yang-Sun unloading curve into their transient dynamic finite element (FE) code specifically developed for studying the impact response of composite plates. This code was used in several investigations: Choi and Chang⁵⁹, Finn and Springer⁶⁸, and Wu and Springer¹⁰⁴. Montemurro et al¹³³ also incorporated the Modified Hertz contact law with unloading, in their FE study of impact on composite plates and shells. Choi et al^{44,50} modified the above laws for incorporation into their FE analysis of cylindrical line loading impact. Gu and Sun¹³⁴ studied impact damage of SMC composites and they also used the Modified Hertz contact law with the unloading law in a dynamic FE analysis. In Aggour and Sun's¹³⁵ FE analysis of impact on thin laminated plates they neglected permanent deformation and used the loading contact law described above for both loading and unloading.

Whilst the spring-mass model, energy balance model and use of indentation laws can yield much important information regarding basic impact response, they are not applicable

beyond first failure (excepting indentation). Another useful analytical approach is to apply scaling laws to relate an impact from one specimen to that on a specimen of similar size.

2.4.4 Scaling Laws

It is uneconomical and impractical to test very large structures, therefore scaling laws have been developed to relate small specimen test results to impact on larger structures. However the laws can only be applied for simple geometry.

Morton¹³⁶ approached the problem of scaling of impact loaded composite materials by identifying the relevant parameters in the problem and applying Buckingham's π -theorem to obtain a complete set of non-dimensional groups. The central variable of interest was the transverse deflection, and the parameters were grouped into geometry, target material and impactor parameters. Morton calculated that if the linear dimensions were each scaled by a factor, S , from the model to the "real" structure then the velocity must be the same in both "real" structure and model for scaling laws generated by his analysis to be applicable. However if the material was rate sensitive, an exact scale model could not be reproduced. The author applied the scaling laws to test results on carbon/epoxy composites (non-rate sensitive) and concluded that impact duration and force scaled well before damage occurred, i.e. the laws held for linear structural response. However, impact damage did not scale according to the above laws and an important size effect was also noted: smaller specimens were always stronger than large ones, which was thought to be due to fracture phenomena and the absolute size of cracks. Swanson and colleagues¹³⁷⁻¹³⁹ obtained similar scaling rules to those obtained by Morton and also concluded that the scaling laws governing the formation of damage would be much more complicated than those governing the linear structural response.

The scaling laws can be utilised to predict global elastic impact responses between simple plates of different sizes, but cannot scale between more complex geometry. Scaling of damage remains an area of uncertainty and requires a detailed understanding of the underlying mode of failure before progress will be made.

The spring-mass, energy balance, and contact analyses are useful in understanding elastic impact response. However, none of the above analyses can be used beyond first failure, or to relate coupon tests to "real" structures. Therefore a more flexible predictive tool is

required and the next section deals with the application of finite element analysis to impact on composite structures.

2.5 Modelling the Impact Event

Due to the complexity of geometry, the dynamic nature of the local/global stress field produced, and damage modes, the problem is too complicated to be solved by analytical methods. A computational model is required to predict response beyond first failure and simulate impact on complex structures¹⁴⁰. Finite element analysis was chosen as the basis for the predictive analysis as it is the most powerful and commonly used method.

2.5.1 Finite Element Analysis

When a physical system has a finite number of degrees of freedom (DOF), equations can be derived to fully describe the system's behaviour, and so an exact solution can be found. However, most real systems have an infinite number of DOF and so the number of DOF must be reduced to enable a solution to be obtained. In FE analysis this process is called discretisation - the continuum or the domain (the object being modelled) is divided into smaller sub-domains or finite elements, thus reducing the problem to a finite number of DOF. Elements are connected together at their nodes and the simultaneous equations which arise from the assembly of the elements can then be solved and the solution found.

The FE method was developed for use as a stress analysis tool, but can now be applied to a wide variety of problems including structural dynamics, fluid flow, heat transfer, acoustics, etc. In each analysis an appropriate field variable is solved for from which other variables can be found. In stress analysis, the displacement method is normally used, in which the displacement is the field variable, the element properties are stiffness and the equilibrium equations are for the forces acting on the nodes. Once the nodal displacements of an element have been solved, they can be used via an interpolation function to give the displacement anywhere within the element. Once the field variable has been solved for over the domain, post processing facilities allow this information to be manipulated to give the stresses and strains throughout the object.

The element properties (e.g. stiffness) are obtained by standard procedures and the simultaneous equations solved over the domain by considering the equilibrium and compatibility between element boundaries, structure supports, and the loading applied to the domain. The equations can only be solved with a digital computer and so the method

has developed as computing power has advanced. There are a wide variety of elements available, formulated for different problems: two- or three-dimensional analyses, plate, shell, or beam assumptions, plane stress or strain conditions etc. Element shapes can be two-dimensional rectangular, triangular, or three-dimensional solid bricks etc.

2.5.2 Finite Element Analysis of Composite Materials

The structural analysis of fibre reinforced composite materials (often in the form of laminates) is more complicated than the analysis of metals due to the composite material's inhomogeneity and anisotropy¹⁴¹. There are two general approaches to the FE analysis of fibre reinforced composites^{142,143}:

In **Micro-mechanical** modelling the fibre and matrix, are defined individually with a number of elements modelling a fibre surrounded by elements representing the matrix. Thus the heterogeneous nature of the material is maintained. As the name suggests, this involves modelling the micro-structure of the material, and is used to investigate phenomena appropriate to this level, i.e. load transfer mechanisms between matrix and fibres¹⁴³. Only a few fibres surrounded by matrix are modelled with each constituent using many elements to describe it. Because the fibre dimensions are so small relative to the overall component or structure, this approach can only be used to study micro-structural behaviour and cannot be used to model a whole component due to the number of elements which would be required. Micro-mechanical modelling may be applied to determine three-dimensional material properties, which currently cannot be obtained experimentally.

In a **Macro-mechanical** analysis the heterogeneous nature of the composite is simplified by smearing the fibre and matrix properties to give anisotropic homogenous lamina properties. Less elements are therefore required to model the same area and so this method, as the name suggests, is used to model complete composite components. The disadvantage of this method is that the global properties assigned to the element clearly includes a simplification especially as the two media have such contrasting mechanical properties. Only the average stress over a lamina can be predicted rather than stresses carried by fibres or matrix. It is this type of analysis which was pursued in this project. With careful modelling and use of accurate constitutive equations, macro-mechanical modelling can be used to give informative global stress analysis data up to first failure. Post first failure the use of Progressive Failure Finite Element Analysis (PFFEA) as described in section 2.5.4 is required.

To perform a macro-mechanical analysis, theory describing anisotropic elasticity and mechanics of composite laminates is required. Fibre reinforced composites normally consist of layers of lamina bonded together by resin. Usually the thickness of the laminate is small compared to the in-plane dimensions and therefore two-dimensional stress state theories derived from three-dimensional elasticity are used to calculate the laminate properties from those of the laminae¹⁴⁴. Assumptions on the through-thickness variation of displacements and/or stresses therefore have to be made.

The first generation of elements formulated for FE analysis of composite materials were shells based on the classical laminated plate theory which applies Kirchhoff's plate theory (assuming plane stress) to an orthotropic material¹⁴¹. This hypothesis does not account for transverse deformation and the transverse stress states are neglected. However, the transverse properties of composite materials cannot be neglected because, even though these stresses (σ_{23} , σ_{13} , and σ_{33}) are generally an order of magnitude less than the in-plane stresses (σ_{11} , σ_{22} , and σ_{12}), the shear moduli and through-thickness modulus are also approximately an order of magnitude less, which results in interlaminar shear stresses causing major failure modes. Prasad et al¹⁴⁵ showed that transverse shear effects cannot be ignored even for an elastic transverse impact analysis.

The first order shear deformation theory was developed for shell elements to include transverse shear deformation¹⁴⁶. Interlaminar shear stress can be calculated¹⁴¹ with the displacements taken linearly over the thickness of each lamina assuming the normal to the mid-plane can stray from the perpendicular after deformation, though remaining straight¹⁴⁶. Elements formulated on these theories form the second generation of composite material finite elements. The next generation of shell elements were based on higher order bending theories which assume the displacement through the thickness varies according to a power series expression¹⁴⁴.

Three-dimensional elements, based on elasticity theory, are also available to model relatively thick laminates (compared to their span) or are used where accurate through-thickness stresses are essential¹⁴¹. Within either two- or three-dimensional elements, one element can be used to represent several laminae of varying material properties and orientations. Further advances are well covered in the literature^{144,146-149}.

2.5.3 Impact Analysis of Composite Materials with the FE Method

To model transverse impact events with the finite element method, a transient dynamic analysis capability is required. In general, impact events are characterised by large relative

displacements between two or more surfaces with possible intermittent contact, depending on the dynamic response of the structure¹⁵⁰. The code should be able to give the history of the contact force, displacement and velocity of the impactor and specimen, and the stresses and strains throughout the composite plate¹³².

Cook¹⁵¹ says that if the frequency of excitation applied to a structure is less than approximately one third of the structure's resonant frequency, then inertia effects can be ignored. This implies that the static equation $[F] = [k]\{x\}$ is sufficient despite the fact that the load $[F]$ and therefore displacements $\{x\}$ are varying (slowly) with time. If the excitation frequencies induced by the impact are higher than the above criteria then a dynamic solution is required with inertia being an important characteristic. Inertia is accounted for in the mass matrix in the equation of motion below, which also includes the stiffness and damping matrices.

$$[M]\{\ddot{x}\} + [C]\{\dot{x}\} + [K]\{x\} = [F] \quad (2.21)$$

Response to high velocity impact is dominated by high frequency components and therefore a very short time step is required in the analysis, which lends itself to an explicit temporal integration scheme. Explicit schemes do not require the governing equation to be solved at each time step, and so can be computationally more efficient for this type of problem as they avoid matrix assembly and inversion. Low velocity impact is governed by structural dynamics (lower frequency components) which enables larger time steps to be employed and so implicit (i.e., conventional static analysis) algorithms are acceptable¹⁵⁰.

To model the contact, one of two methods can be employed. Either the impact is approximated to a transient loading in which the analyst chooses a contact law (section 2.4.3) to define the loading pulse, or the structures of the two impacting bodies are fully modelled with contact elements¹⁵² employed between the two bodies. Several contact algorithms can be employed with the most common being the penalty method and direct method^{150,153,154}. The penalty method is relatively simple with the contacting surfaces being monitored at each time step and when contact occurs a penalty-constraint equation is inserted between the contacting nodes/elements.

In order to gain accurate through-thickness stresses and strains for a detailed failure and post-failure analysis three-dimensional elements are required for transverse impact analyses^{148,155} and damage representation may also be difficult in two-dimensional models, as delamination cannot be physically modelled, unless each layer in the laminate is represented separately. A three-dimensional analysis is therefore required and using solid

elements, fully orthotropic material data can be assigned. However, experimentally obtaining the through-thickness properties is not currently possible and so several simplifying assumptions are generally made. **Transverse isotropy** is the assumption that the material contains one plane in which the properties are equal in all directions ($E_{22} = E_{33}$, $\nu_{12} = \nu_{13}$, $G_{12} = G_{13}$, $G_{23} = E_{22}/\{2[1+\nu_{23}]\}$). Another approach is to use **two-dimensional data** where E_{11} , E_{22} , G_{12} and ν_{12} are known and it is assumed that $G_{12} = G_{13} = G_{23}$ and $\nu_{12} = \nu_{13} = \nu_{23}$ or that $G_{12} = G_{13}$ and $G_{23} = E_{22}/\{2[1+\nu_{23}]\}$ where $\nu_{12} = \nu_{13} = \nu_{23}$. Hellweg and Crisfield¹⁵⁶ concluded that, though one cannot generalise with so many loading, material, geometry and support conditions, the accuracy of the interlaminar stresses and also the in-plane stresses are effected by the assumptions made for the through-thickness data. The two-dimensional assumptions were the least accurate but the transverse isotropy assumption can also yield inaccurate results under certain loading conditions. In a similar analysis Griffin¹⁵⁷ concluded that the assumptions mentioned above only effected the interlaminar stresses and not the in-plane stresses significantly. As failure for composites is often dominated by interlaminar stresses this is a particularly important aspect of FE modelling of composites.

Both Sala and Anghileri¹⁵⁸ and Murphy¹⁵⁹ emphasised the importance of accurately modelling the boundary conditions. Rather than define the boundary conditions by fixing degrees of rotation within the model, both modelled the support conditions with solid elements. This is clearly a very expensive computational approach and was justified by the latter by the fact that the supports were relatively pliable, and the resulting analysis showed that it was the supports which primarily effected the high frequency response of the impactor force-time plot. Habib⁹⁸ found that his analysis of perfectly clamped boundary conditions yielded higher peak forces than his experimental results due to the rotation which occurred in the tests.

2.5.4 Progressive Failure Finite Element Analysis

An analysis which implements damage in the model when failure has occurred is called a Progressive Failure Finite Element Analysis (PFFEA)¹⁶⁰. PFFEA goes some way to bridging the gap between micro-mechanical analysis and the inherent simplification involved in smeared property macro-mechanical modelling, by recognising different failure modes characteristic of fibres, matrix and the interface between the lamina¹⁶⁰⁻¹⁶³. The two extra dimensions which a PFFEA requires in addition to a standard analysis are **Failure Criterion** which indicate the initiation of damage modes, and a **Damage Model**, which reflects the damage induced. These two aspects are discussed in detail in the following sections. Damage must be modelled within the analysis as it occurs, because it alters both

the structural and dynamic response, and because damage gives rise to stress concentrations which initiate further damage³¹. An accurate PFFEA can be a very powerful tool in that it enables damage mechanisms and the stress states and/or geometry which initiate them to be investigated, and illustrate the effect this damage has on a structures subsequent behaviour, which is not always easy to understand even from an IFWI test. However the complex nature of impact failure mechanisms and the effect of damage in an heterogeneous anisotropic composite laminate means that it is very difficult to achieve a representative model. Many authors have included failure criteria, and so have modelled quite accurately the impact event up to first failure and identified a mode of failure. However relatively few authors have included damage models and so have not been able to accurately model post-first failure behaviour.

A recent PFFEA was performed for static in-plane tensile and shear loads by Shahid and Chang¹⁶⁴, whilst Pavier and Chester¹⁶⁵ modelled delamination damage due to compression testing of impacted specimens from which they could predict residual strengths. They concluded that the discrepancy between model and test results was because damage due to matrix cracks and fibre breakage in the analysis was not included in the model. Huang et al¹⁶⁶ performed a static PFFEA with failure criteria identifying failure modes and the damage also reflecting the mode of failure.

However, authors have not identified the effect of mesh dependency on their results. Degrading elements produces stress concentrations, with failure propagating early for a fine mesh, whereas a coarse mesh will tend to smooth the gradient due to an averaging effect and delay damage growth. Any model developed should therefore investigate these effects. The following sections study in detail the failure criteria and damage models used in the literature.

2.5.4.1 Failure Concepts for Composites

A failure criterion usually relates critical combinations of stress or strain (or fracture mechanics properties) in a material in order to predict failure of a particular mode. It is of vital importance that the criterion used should be able to distinguish between failure modes as the damage which results is mode dependent¹⁶⁰. Many different failure criteria have been used in the literature¹⁶⁷, which in general were developed for static analyses but have been carried over to impact analyses. A failure criterion may be chosen for each different failure mode, which when combined, form the overall failure envelope. The concepts can generally be divided into intralaminar (matrix cracking, fibre breakage, fibre-matrix debond etc.) and interlaminar (delamination) failure.

(a) Matrix Cracking/Fibre Breakage Failure Criteria

These modes of failure are usually predicted using stress-strength based failure criteria of which there are three broad categories¹⁶¹.

The **Constant Stress or Strain Criteria**, also called the **maximum stress or maximum strain criteria**, is the simplest form of failure envelope, which is shown in Figure 2.11 (the diagram is shown in two dimensions for simplicity but in reality the failure volume is a rectangular parallelogram in three-dimensional stress-strain space with sides parallel to co-ordinate axes). This is called an independent failure mode criterion because it neglects stress interaction effects completely, and usually overestimates the strength. Fibre breakage is often modelled this way. Different compressive and tensile strengths can be taken into account, thus precisely identifying the mode of failure. Failure occurs when:

$$\sigma_{11} \geq X_T \quad \text{for } \sigma_{11} > 0 \quad (2.22)$$

$$|\sigma_{11}| \geq X_C \quad \text{for } \sigma_{11} < 0 \quad (2.23)$$

$$\sigma_{22} \geq Y_T \quad \text{for } \sigma_{22} > 0 \quad (2.24)$$

$$|\sigma_{22}| \geq Y_C \quad \text{for } \sigma_{22} < 0 \quad (2.25)$$

The subscripts T and C refer to tension and compression and X and Y are the strengths in the longitudinal and transverse direction respectively. Fibre strengths vary significantly within the same composite¹⁶⁸, and so some representation of the strength distribution (e.g. Weibull statistical strength theory) may be required to improve the accuracy of the criterion. When applied to finite elements, strain based criteria are more accurate as in-plane strains are continuous within displacement elements and the conversion of strains to stresses is avoided, whilst a point stress or average stress method can be employed⁵⁴. Mathematical singularities in the interlaminar stress field at free edges do occur, to which the average stress methods are less prone.

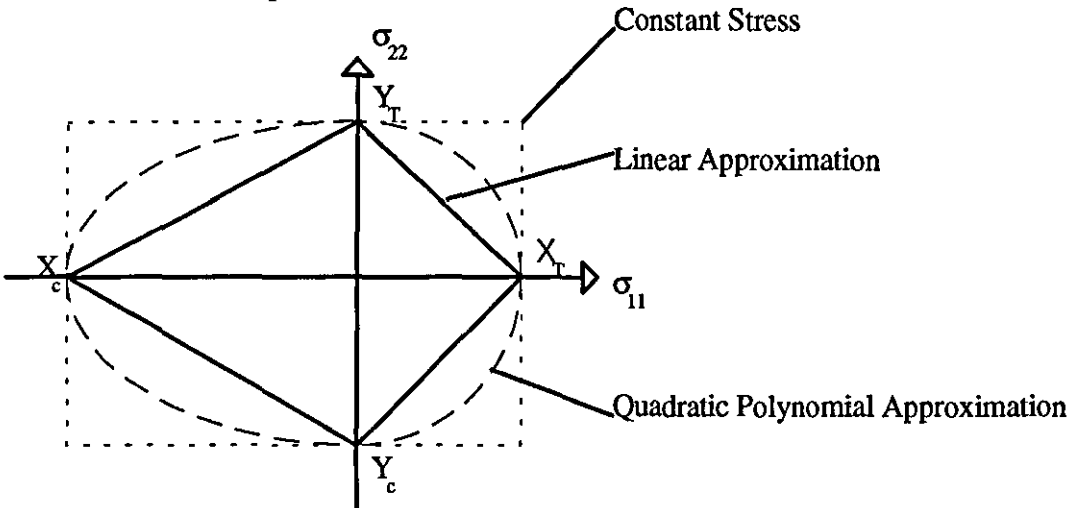


Figure 2.11 Diagrammatic representation of failure envelopes.

The **Linear Approximation Criterion** has failure planes intersecting the stress-strain axes at their ultimate uni-axial strengths (Figure 2.11). This clearly takes the interaction of stresses to the extreme, and as such, tends to underestimate the strength of the fibre composite material¹⁶¹. This approximation is not often used in the literature.

Polynomial Approximation Criteria cover a very wide range of concepts which consist of polynomial expressions chosen to best fit the experimental data. These criteria are derived mathematically and therefore do not have a direct physical basis, in contrast to the maximum stress and strain criteria. In general, quadratic polynomials are chosen as they have been found to adequately represent failure data, rendering higher terms unnecessary. These criteria agree with each other where uni-axial stress states exist in the principal material direction of a lamina, as can be seen from the points of intersection with the stress axes in Figure 2.11. However, uni-axial stress states rarely exist in-service (impact events involve three-dimensional stress states), and for bi-axial stress states and higher, different polynomial approximation criteria will provide different failure predictions. Some commonly used quadratic polynomial failure criteria are described below (for further information on failure theories for both isotropic and composite materials see the review paper by Nahas¹⁶⁷):

Hashin¹⁶¹ developed interactive criteria for unidirectional (and therefore transversely isotropic) fibre composites which identify fibre and matrix tensile and compressive failure modes. The form of the equations shown are for a three-dimensional stress state but plane stress failure criteria are obtained by neglecting the transverse shear terms.

$$\text{Fibre Tension :} \quad \left(\frac{\sigma_{11}}{X_T} \right)^2 + \left(\frac{\sigma_{12} + \sigma_{13}}{S_{12}} \right)^2 \geq 1 \quad \text{for } \sigma_{11} > 0 \quad (2.26)$$

$$\text{Fibre Compression :} \quad |\sigma_{11}| \geq X_c \quad \text{for } \sigma_{11} < 0 \quad (2.27)$$

$$\text{Matrix Tension :} \quad \left(\frac{(\sigma_{22} + \sigma_{33})}{Y_T} \right)^2 + \left(\frac{(\sigma_{23}^2 - \sigma_{22}\sigma_{33})}{S_{13}^2} \right) + \left(\frac{(\sigma_{12} + \sigma_{13})}{S_{12}} \right)^2 \geq 1$$

$$\text{for } \sigma_{22} + \sigma_{33} > 0 \quad (2.28)$$

Matrix Compression :

$$\left[\left\{ \frac{Y_c}{2S_{13}} \right\}^2 - 1 \right] \frac{(\sigma_{22} + \sigma_{33})}{Y_c} + \frac{(\sigma_{22} + \sigma_{33})^2}{4S_{13}^2} + \frac{(\sigma_{23}^2 - \sigma_{22}\sigma_{33})}{S_{13}^2} + \frac{(\sigma_{12}^2 + \sigma_{13}^2)}{S_{12}^2} \geq 1$$

$$\text{for } \sigma_{22} + \sigma_{33} < 0 \quad (2.29)$$

The **Tsai-Hill**¹⁶⁹ equation 2.30 is based on the Von Mises failure criterion, which Hill modified for anisotropic bodies and was applied to composites by Tsai.

$$\left(\frac{\sigma_{11}}{X}\right)^2 - \left(\frac{\sigma_{11}\sigma_{22}}{X^2}\right) + \left(\frac{\sigma_{22}}{Y}\right)^2 + \left(\frac{\sigma_{12}}{S_{12}}\right)^2 \geq 1 \quad (2.30)$$

The **Tsai-Wu**¹⁶⁹ failure criterion is in the form of a tensor polynomial from which all the other failure theories can be derived (equation 2.31). A major disadvantage is that bi-axial testing is required to give some of the strength tensors (F_1 to F_{66} in equation 2.31)¹⁶⁷, and neither the Tsai-Wu or Tsai-Hill interactive criteria, in isolation, will identify the mode of failure.

$$F_1\sigma_{11} + F_2\sigma_{22} + F_{11}\sigma_{11}^2 + F_{22}\sigma_{22}^2 + F_{12}\sigma_{11}\sigma_{22} + F_{66}\sigma_{12}^2 \geq 1 \quad (2.31)$$

The **Modified Tsai-Wu** is obtained by eliminating σ_{11} terms in the Tsai-Wu criteria above and can therefore be used to identify matrix failure¹⁶⁹:

$$F_{22}\sigma_{22} + F_{22}^2\sigma_{22}^2 + F_{66}\sigma_{12}^2 \geq 1 \quad (2.32)$$

Chang and Chang⁵³ modified Hashin's fibre breakage, matrix cracking, and matrix compressive failure criteria to involve non-linear shear behaviour, giving equations 2.33 to 2.36:

$$\text{Fibre Breakage:} \quad \left(\frac{\sigma_{11}}{X_T}\right)^2 + \tau \geq 1 \quad \text{for } \sigma_{11} > 0 \quad (2.33)$$

$$\text{Matrix cracking:} \quad \left(\frac{\sigma_{22}}{Y_T}\right)^2 + \tau \geq 1 \quad \text{for } \sigma_{22} > 0 \quad (2.34)$$

$$\text{Matrix compression:} \quad \left(\frac{\sigma_{22}}{2S_{12}}\right)^2 + \left[\left(\frac{Y_C}{2S_{12}}\right)^2 - 1\right] \frac{\sigma_{22}}{Y_C} + \tau \geq 1 \quad \text{for } \sigma_{22} < 0 \quad (2.35)$$

$$\text{where } \tau = \frac{\left(\frac{\sigma_{12}}{S_{12}}\right)^2 \left(1 + \frac{3\alpha G_{12}\sigma_{12}^2}{2}\right)}{\left\{1 + \frac{3\alpha G_{12}S_{12}^2}{2}\right\}} \quad (2.36)$$

[where α is an experimentally determined constant which accounts for the non-linear shear stress behaviour]. The Chang-Chang criteria were developed for notched tensile testing of composite laminates but have been applied to many impact problems.

Many authors have adopted one of the criteria above or modified them for use in impact failure analyses of composite laminates. The choice of criteria used is often based on that which fits the experimental data most closely and not for physical reasons or an in-depth understanding of the stress states induced by the impact.

Reddy and Pandey¹⁶³ compared the Hill, Tsai-Wu, and Hoffman criteria and used failure indices associated with each stress component to identify the mode of failure in a FE analysis of composite laminates subjected to in plane and/or bending loads.

Yener and Wolcott¹⁶⁰ used the maximum stress theory including an additional fibre failure mode in transverse compression, in their study of impact on composite pressure vessels. Kerth and Maier¹⁷⁰ also employed a detailed series of stress/strength based failure criteria corresponding to the different modes of fibre and matrix failure, combined with an undisclosed damage degradation model in a crash worthiness investigation of axial crushing of composite tubes.

Hashin formulated his criteria for unidirectional composites undergoing off axis tensile testing, but it has also been adopted for many other loading conditions. Ambur and co-workers¹⁷¹ used the Hashin criteria in their low velocity analysis of composite laminates. Ochoa and Engblöm¹⁷² used the Hashin fibre failure criterion in tension and matrix failure criteria in tension and compression to predict failure due to uni-axial tension and four-point bending. Choi et al^{44,50} used Hashin's matrix failure criteria to predict matrix cracking in transversely impacted laminates, but simplified it for the two-dimensional case of line loading impact. Liu et al⁶⁶ used the same approach in their similar analysis, whilst Choi and Chang^{51,59} used the three-dimensional stress state version of the criteria for point impact modelling.

Pavier and Chester¹⁶⁵ used a modified Tsai-Hill criteria which neglected transverse cracking as a failure mode for their investigation of the effects of delamination on post impact compression strength:

$$\left(\frac{\sigma_{11}}{X_c}\right)^2 - \left(\frac{\sigma_{11}\sigma_{22}}{X_c^2}\right) + \left(\frac{\sigma_{12}}{S_{12}}\right)^2 \geq 1 \quad (2.37)$$

Shivakumar et al³⁴, Lakshminarayana et al¹⁴⁰ and Ganapathy et al¹⁰⁷ used the Tsai-Wu criterion to predict failure in their studies on the impact behaviour of composite laminates. Once failure was predicted, the maximum stress theory was applied to indicate the mode of failure which was a strategy followed by many researchers. Montemurro et al¹³³ compared Tsai-Wu and Hashin criteria in their FE impact analysis which suggested that failure occurred at a higher load for the latter.

Davies et al⁶⁰ and Edlund¹⁷³ used the Chang-Chang criteria to model in-plane failure in their simulations to predict damage in composite aircraft structures due to low velocity impact.

(b) Delamination Initiation

Delamination initiation has also usually been predicted using a stress/strength based approach. The strength based delamination criterion of Huang et al¹⁶⁶ was based on the shear stresses only, and occurred when

$$\sqrt{(\sigma_{13}^2 + \sigma_{23}^2)} \geq \text{ILSS} \quad (2.38)$$

Liu et al⁶⁶ used the following strength based criterion to predict the onset of delamination due to line load impact:

$$\left(\frac{\sigma_{33}}{Y_T}\right)^2 + \left(\frac{\sigma_{23}^2 + \sigma_{13}^2}{\text{ILSS}^2}\right) \geq 1 \quad (2.39)$$

Many FE models have predicted the initiation of delamination as being coincident with the formulation of a critical matrix crack as described in section 2.2.2.1 and so have postulated that the load at which transverse matrix cracking occurs can be used as the delamination initiation criteria also^{59,68}.

Becker¹⁷⁴ employed a complex stress based delamination failure criteria based on the approaches of Tsai-Wu, Hashin, and Chang. which considered the stresses in the layers above and below the interface in his solid element model. Hwang and Sun¹⁷⁵ used an interactive quadratic strength formula to predict delamination in their three-dimensional FE analysis.

$$\left(\frac{\sigma_{33}}{Z_T}\right)^2 + \left(\frac{\sigma_{23} + \sigma_{13}}{\text{ILSS}}\right)^2 \geq 1 \quad (2.40)$$

Lagace⁵⁴ used equation 2.41 to predict the initiation of delamination due to various static loads, which included all the interlaminar stresses, whilst Edlund¹⁷³ used a simplified version of this criterion in his low velocity impact study.

$$\left(\frac{\sigma_{13}}{S_{13}}\right)^2 + \left(\frac{\sigma_{23}}{S_{23}}\right)^2 + \left(\frac{\sigma_{33}^t}{Z_T}\right)^2 + \left(\frac{\sigma_{33}^c}{Z_C}\right)^2 \geq 1 \quad (2.41)$$

Lagace concluded showed that the stress/strength approach was better than a fracture mechanics (FM) approach but different authors have reached contrasting conclusions. Cui and Wisnom⁵⁵ proposed that where there is no macroscopic singularity (such as dropped plies, free edges etc.) then stress based criteria are better, but where there is a macro-singularity then a FM base approach is more appropriate. However FM generally requires knowledge of where the crack propagation will occur and assumes the presence (and therefore estimate of the size) of an initial crack. Fracture mechanics involves the behaviour of cracked components, with either stress intensity factors or fracture energy being computed^{176,177}.

(c) Delamination Propagation

When matrix cracking is predicted, because each ply is thin, all authors assume that the crack instantaneously extends from the ply above to the ply below, therefore the analyses do not have matrix crack propagation models. Because a delamination area may be quite large (involving a high energy absorption and change in stiffness) it is important in a PFFEA to model the growth of the delamination, which has proved a difficult task for researchers, who have followed varied approaches.

Crack propagation lends itself to being modelled by a FM approach and one such method is to predict delamination growth by employing fracture energy or strain energy release rate (SERR). FE analysis can calculate the SERR within an element and compare it to the relevant critical value for the mode of propagation - Mode I (opening), Mode II (shear), or Mode III (anti-plane shear) or a mixture of the three. However, the experimental tests performed to calculate the critical strain energy release rates, G_{Ic} , G_{IIc} , and G_{IIIc} have varying degrees of accuracy which Jones et al¹⁰⁶ have outlined. There is no agreed test for Mode III and it has not been included in any of the delamination models in the literature, whilst generally, the double cantilever beam and end notched flexure tests are used to experimentally determine Mode I and II critical strain energy release rates. In most structures the loading will not induce a pure mode, therefore mixed-mode loading must be taken into account, and Reeder and Crews¹⁷⁸ reviewed the mixed-mode tests available and proposed a new mixed-mode bending test method. Chapters 4 and 6 contain a more

detailed discussion on the critical strain energy release rate tests described above. Fracture energy failure criteria governing the initiation and propagation of impact induced delamination are often of the form:

$$\left(\frac{G_I}{G_{IC}}\right)^m + \left(\frac{G_{II}}{G_{IIC}}\right)^n = 1 \quad (2.42)$$

[m and n are constants which are chosen to best fit the experimental data and as such do not have a physical basis]. After identifying delamination initiation as described previously, Liu et al⁶⁶ inserted a delamination into the two-dimensional model (line load impact) and a fracture analysis was applied to model the propagation. The mixed-mode criterion in equation 2.42 (with $m = n = 1$) was used to predict propagation. As the crack advanced the model was re-meshed, by releasing the relevant nodes and creating new free surfaces.

Ruiz and Xia⁹⁶ used a FM approach in studying the effect of interfaces between layers in reducing impact damage. The SERR was calculated using the J-integral method to predict delamination. Finn and Springer⁶¹ assumed that when their matrix crack criteria was satisfied, delamination was initiated. The growth of delamination was predicted by comparing the strain energy available for delamination with a critical value. A detailed analysis of which stresses cause impact induced delamination was described and only the strain energy due to those stresses were then made available for delamination in the FE model. Razi and Kobayashi⁷³ developed a FE model to predict delamination due to low velocity impact of graphite/epoxy and concluded that Mode II was dominant and that delamination growth occurred when $G_{II} \geq G_{IIC}$ and was halted when $G_{II} \leq G_{IIa}$ (an arrest strain energy release rate).

Bonini et al¹⁵³ performed a three-dimensional FE analysis of low velocity impact in which the interlaminar nodes were separated according to a failure criteria based on the components of the interlaminar nodal forces. Thus physically modelling the opening of a delamination. Zheng and Sun¹⁷⁹ treated a delaminated specimen as two separate plates with fixed constraints imposed in the undamaged region and contact restraints in the damaged region (to ensure non-penetration). The modified crack closure method was employed to calculate the strain energy release rate at the crack front, and the analysis yielded excellent agreement with experimental data.

(d) Interface Element Modelling of Delamination Initiation and Propagation

Interface elements can be employed to bridge the gap between stress/strength based criteria and fracture mechanics approaches to physically model delamination by combining stress

failure theory with fracture energy in the creation of new free surfaces. Interface elements have zero thickness with the variables being the tractions (forces) and relative displacements between node pairs¹⁷⁶. Either discrete nodal spring elements or continuum interface elements can be employed. Cui and Wisnom⁵⁵ developed a two-dimensional FE model by employing horizontal and vertical non-linear spring elements between the plies. The springs had a high initial stiffness but once a threshold force was reached the stiffness was reduced and the springs opened fully to physically represent delamination initiation and growth. However this type of model is computationally expensive and would only be possible with relatively small models. Collombet et al¹⁰⁹ employed a double-node assembly at the interface to enable delamination to be modelled. The node pairs were linked and when both a matrix crack initiation criterion was met and the threshold force was exceeded, the nodes separated and propagation occurred.

Li and Wisnom¹⁸⁰ used a line interface element in a two-dimensional analysis to model the initiation and propagation of delaminations produced by cut or dropped plies for glass/epoxy composite laminates. Normal and shear forces were transmitted across the interface via normal and tangential 'springs' at each node. The element had the stress/displacement model illustrated in Figure 2.12.

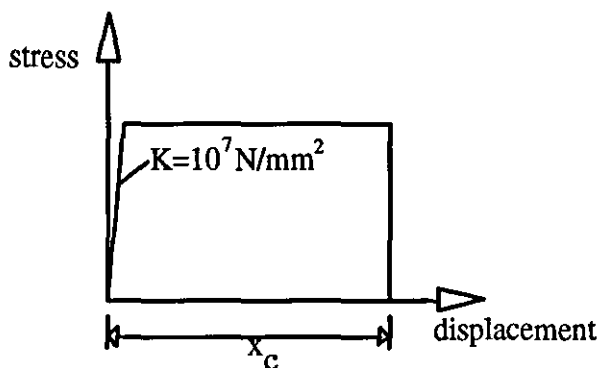


Figure 2.12 Stress-displacement relationship for interface element material model employed by Li and Wisnom.

The normal and shear forces were uncoupled and each node behaved elastic-perfectly plastic until failure. The energy absorbed at failure corresponded to the energy absorbed by the element under the curve above. The authors also assessed the effect of the value of friction used between the two delaminated surfaces.

Lo and colleagues¹⁸¹ also employed non-linear interface elements to model delamination growth from the tip of a matrix crack in thick composite laminates, subjected to low velocity impact in a two-dimensional analysis. The interface elements obeyed a complex

failure criterion based on a continuum mechanics approach. They also used the interface elements to model matrix cracking, but convergence problems were encountered during damage growth for the coarse mesh employed. Schellekens and de Borst¹⁸² studied free edge delamination under uni-axial tension with a cubic line element and various softening models in their two-dimensional analyses. They concluded that mesh refinement had no effect on laminate strength though all the meshes were quite fine.

(e) Prediction of Penetration

Lee and Sun⁴⁶ used double nodes (and gap elements) through the thickness of their two-dimensional static FE model to simulate penetration by a blunt impactor. As the "plug-crack" developed the gap elements were removed and the SERR was calculated by a crack closure integral scheme at the crack tip. The code incrementally increased the impactor displacement as in the test and as soon as the crack reached the bottom layer the plug was pushed out (as no friction was considered). However plug initiation could not be predicted with this analysis.

Penetration analyses lend themselves to explicit methods of solution, as they involve extreme non-linear behaviour. Very few composite impact analyses have successfully gone beyond first failure let alone proceeded to penetration. Therefore this research will focus on the damage evolution prior to penetration.

2.5.4.2 Composite Damage Models

The damage modes which are induced by low velocity impact (section 2.2.2) reduce the material properties in different ways, therefore the damage introduced into the FE model must be dependent on the mode of failure which has occurred, and may involve altering stiffness values and/or creating new free surfaces. Normally for intralaminar damage, a ply discount method is used, in which one or more of the elastic constants of the failed ply are reduced or set to zero. Only the element, or the ply in the element, in which failure has occurred is degraded.

Chang and Chang⁵³ formulated a property degradation model which has been widely implemented. The degradation, as in all of the models described below depends on the failure mode:

- (a) If *matrix cracking* occurred then E_{22} and ν_{12} were set to zero.
- (b) If *fibre breakage* occurred then E_{22} and ν_{12} were set to zero, with the longitudinal modulus E_{11} and the shear modulus G_{12} degraded according to the size of the damage zone.

Davies et al^{60,88}, Shivakumar et al³⁴, Ganapathy et al¹⁰⁷, Murray and Schwer¹⁶⁹ applied similar matrix and fibre damage degradation models to the Chang-Chang property degradation model. Shahid and co-workers¹⁶⁴ performed a PFFEA with in-plane tensile and shear loads using the Chang-Chang fibre damage model. Matrix cracking was modelled by degrading the ply properties as a function of crack density.

Instead of reducing individual material properties to zero, in their damage model Hwang and Sun¹⁷⁵ reduced specific components of the stiffness matrix to zero. Huang et al¹⁶⁶ and Ochoa and Engblom¹⁷² also reduced the element stiffness of the failed ply in such a way as to reflect fibre, matrix, or delamination damage in their model of uni-axial tension and four-point bending.

Most of the work described above involved reducing the ply properties to zero instantaneously once the appropriate failure criterion was met, which is illustrated by (i) in Figure 2.13. However Murray and Schwer¹⁶⁹ investigated three different ways of applying the degradation which are shown in Figure 2.13. The authors implemented gradual unloading, (ii) for fibre breakage (the Petit-Waddoups model), whilst for matrix failure in tension or compression the degradation was instantaneous (i) (the Chui model). Line (iii) represents the ability of the damaged element to hold a constant stress after failure (the Hahn-Tsai model). The three methods illustrated in Figure 2.13 are expanded in Nahas's review¹⁶⁷ where several further post-failure theories for composite materials are also described. It is expected that convergence difficulties were encountered for material damage models (i) and (ii) due to the sudden change in stiffness of adjacent elements. These difficulties and mesh dependence were not mentioned in the literature.

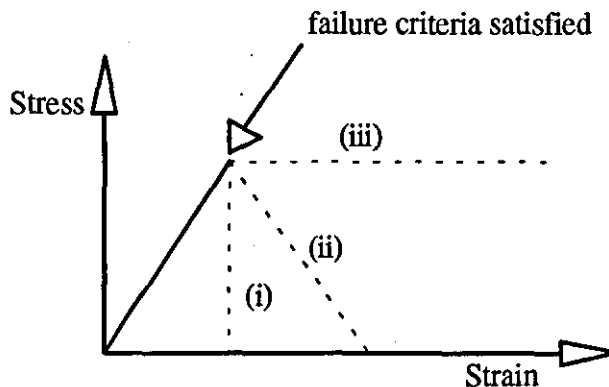


Figure 2.13 Methods of applying material degradation in a PFFEA.

2.5.5 Modelling Residual Strength

Pavier and Chester¹⁶⁵ artificially introduced a central delamination in a series of experiments on residual compressive strength and the growth of the delamination. However the model simplified the impact damage by assuming it was only a delamination and illustrated that it was also necessary to model matrix cracking and fibre breakage in order to accurately model the damage. Guild et al⁵⁸ also modelled a post impact compression test with FE but based their model on the hypothesis that the damage gives rise to a soft zone of reduced laminae stiffness which results in local stress magnification.

Ideally, following a PFFEA, the resulting damaged model could then be "loaded" in compression, tension, or flexure and further failure criteria applied to give its residual strength. Given the difficulties encountered in the literature regarding post first failure analyses, this is not a realistic goal for this project.

2.6 Conclusions

Due to opportunities which have arisen in the container industry and technological advances in the pultrusion process it has been shown that pultruded composite materials can, and are being, utilised in relatively small components, panel sections, flooring, or complete freight containers. Various agencies, including Maunsell Structural Plastics Ltd., have carried out extensive design work concluding that pultruded components similar to the ACCS could satisfy the ISO strength and stiffness standards and would certainly be attractive in the European Swap-body market in which the specifications are slightly less demanding. However, it is the area of impact resistance which must be better understood before composite materials will be accepted more fully in the freight container market. The ACCS "plank", the panelling section providing the majority of surface area in ACCS constructions, and being representative of a typical pultruded composite section, has been employed to investigate the impacts properties.

In-service, freight containers are open to low velocity impacts, which corresponds to those ordinarily introduced in the laboratory by mechanical test machines such as the IFWI test technique, whilst static testing is not representative of low velocity impact of glass/polyester composites. In low velocity impact, the contact period is such that the whole structure has time to respond to the loading, therefore dynamic structural response is important. The modes of impact damage induced ranges from matrix cracking and delamination through to fibre failure and penetration, requiring several damage assessment techniques. Damage

mode interaction must also be understood when attempting to predict initiation and growth of a particular form of damage.

In terms of the effect of constituents, toughened resins or thermoplastics can reduce matrix dominated damage but the fibres have the most bearing on impact response, and it was uncertain whether over the narrow velocity range under consideration, the strain-rate sensitivity of glass fibres can be ignored. Whilst the majority of reported impact test work has been on carbon/epoxy, it was expected that the glass/polyester system to be investigated would respond in a less brittle manner, but with the same general damage modes corresponding to the generic weaknesses of fibre composites.

Much research has been performed on simple geometry laminates consisting of UD plies at various fibre orientation. The low velocity impact response of random fibre/unidirectional laminate combinations (such as are found in pultrusions) and impacts on complex geometry are less well documented. Therefore it was not clear how the CFM and UD layers will interact in the initiation of delamination and how the low transverse strength will effect final failure. Therefore this review has highlighted the need for a detailed impact test and damage analysis programme to identify damage modes and interactions in the typical CFM/UD/CFM pultruded lay-up and effect of the typical double/skin web pultruded design.

The development of accurate predictive tools are required to relate coupon impact test results to "real" structures. Whilst simple analytical models to predict elastic impact response are available, the finite element method will be necessary to model post first failure impact events. Elastic FE impact analysis of composite laminates is well established, however, analyses which go beyond first failure are complex. Many theories have been applied to predict inter- and intralaminar failure with authors generally applying the theory which best fits the experimental data, thus doing little to further the understanding of the conditions which cause the onset and growth of the various modes of damage. Therefore there is a need for more physically representative models to improve the understanding of damage initiation and propagation. The literature review stressed the need for a physically representative interlaminar damage model to simulate delamination and to provide this, the interface element method was chosen.

Most of the PFEEA involving impact of composites have been performed on special-purpose programs designed by academic researchers¹⁴⁰, whilst this research was focused on a more accessible commercial code. The number of commercially available FE packages (pre- and post-processors and solver) capable of inputting the required data, solving, and then presenting the output in a meaningful way, for impact analyses of laminated

composites is limited¹⁸³. NAFEMS have produced a report comparing a number of packages and gives a good outline of their capabilities and limitations¹⁸⁴. Due to the industrial collaborations involved with this project, the LUSAS finite element system including pre-and post- processing software (MYSTRO), was employed. The LUSAS system includes an impact module allowing slidelines (contact elements) for contacting surfaces to be defined for modelling impact as well as including a composite laminated shell model formulation¹⁵⁰, and a solid element¹⁷⁶, enabling several laminae to be defined within one shell or brick element. A new interface element designed specifically to model delamination was developed by Hellweg¹⁷⁶ and was focus of the damage model development in this research. The following chapters describe the experimental and FE research performed during this research.

PART II

METHODOLOGY

Chapter 3

Static Mechanical Testing

The ACCS "plank" was the focus for this research as described in section 2.1.1, therefore all the experimental work performed was based on this section. A series of static mechanical tests were performed to provide both elastic and failure data to be employed in defining the ACCS "plank" material within the FE model. In addition to the tests described below, compression and interlaminar shear strength tests were also conducted, but ultimately the data obtained was not used in the FE material definition and so a description of these test methods employed and results have been consigned to Appendix II and IV respectively.

3.1 Materials and Environmental Conditioning

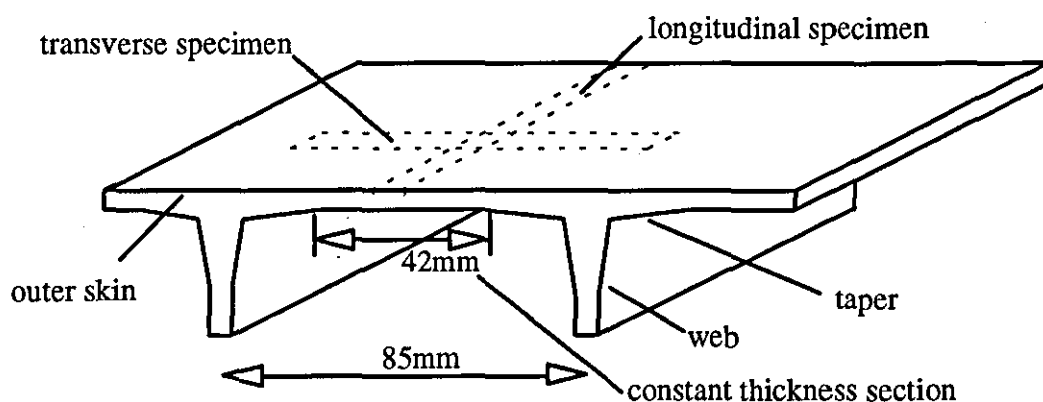


Figure 3.1 Static mechanical test specimens cut from ACCS plank.

All the tests were performed on specimens cut from the outer skins of the ACCS "plank" (Figure 3.1), whilst in some cases individual plies of CFM peeled from the outer skin laminates were also tested (Appendix II and IV). Longitudinal specimens were cut parallel

to the webs and therefore also parallel to the UD fibres in the central ply, whilst transverse specimens were cut perpendicular to the webs.

Isophthalic polyester absorbs a negligible quantity of water vapour from the atmosphere and so the only conditioning applied to these samples was to ensure they were at room temperature for 48 hours prior to testing.

3.2 Test Equipment and Data Acquisition

3.2.1 "Dartec" Servo Hydraulic Test Machine

Tension and in-plane shear tests were performed on this machine (shown in Figure 3.2) which had a maximum load of 50KN. The jaws were hydraulically operated to grip the tabbed tensile specimens and in-plane shear rail assembly. The strain was measured using either an extensometer or strain gauge as described in section 3.3, with the signal from the strain gauge bridge circuit or the extensometer being fed into a Si-Plan Amplifier (Figure 3.3). The load was fed from the load cell, directly to the computer, where the load signal was divided by the specimen cross sectional area to give the stress. The data acquisition program, Workbench, was employed to log three channels of data from the amplifier- load, strain, and elapsed time. The data from the tests performed on the "Dartec" was stored on disc, and transferred to a spreadsheet package for further manipulation. A least squares linear regression algorithm was employed to calculate the moduli and other gradients of interest, from the stress-strain curves.

3.2.2 "Lloyd" Materials Testing L1005 Machine

Flexural, double cantilever beam (DCB), and end notch flexure (ENF) tests were performed on this machine (Figure 3.4), with the load cell varying from 500N to 5KN depending on the test being performed. Standard three-point bend jigs were employed for the flexural and ENF tests, whilst a tensile load was applied to the DCB specimens via hinges bonded to the specimens as detailed in section 3.4.4.1 For each of the tests, the crosshead displacement and load were fed directly to an OP4 XY plotter to record load-displacement graphs, for further analysis.

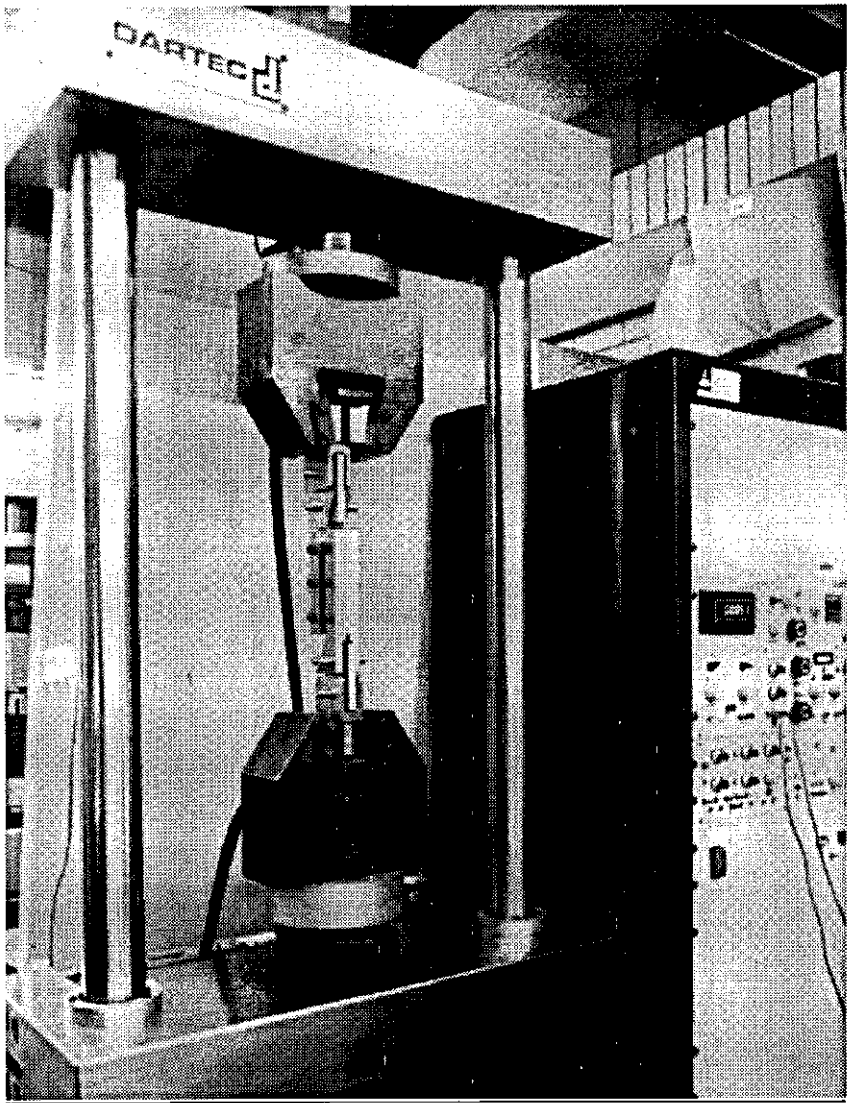


Figure 3.2 Photograph of the Dartec servo hydraulic test machine and in-plane shear assembly.

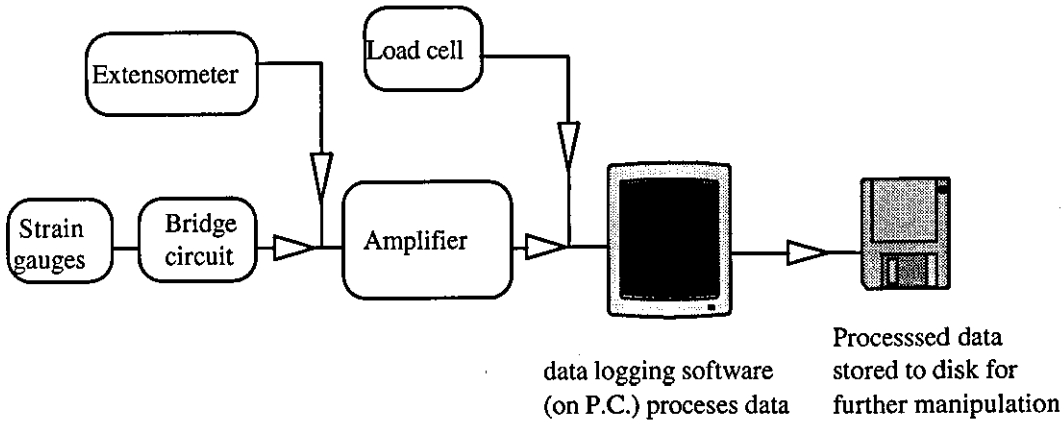


Figure 3.3 Flow of data from test specimen to disc storage.

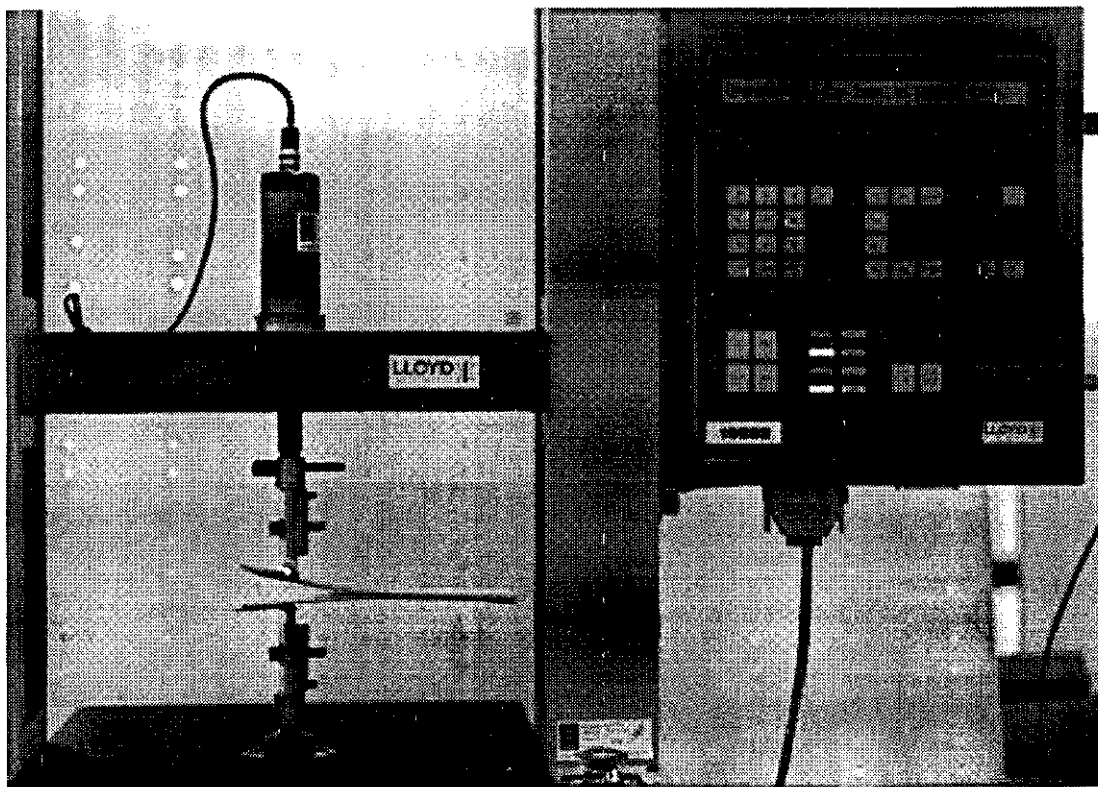


Figure 3.4 Photograph of "Lloyd" materials testing 11005 machine performing a DCB test.

3.2.3 In-Plane Shear Rail Assembly

In-plane shear data is usually obtained by laying-up a $\pm 45^\circ$ laminate and applying a tensile load as described in CRAG 101¹⁸⁵. However, this was clearly not possible for specimens cut from the ACCS "plank", therefore the Two Rail Shear Assembly test jig (Figure 3.5) detailed in ASTM Standard D4255-83¹⁸⁶ was manufactured, as this test is valid for symmetric orthotropic laminates containing UD or randomly oriented fibres. It should be noted however that this is only a "Standard Guide" and not a "Standard Test Method" due to the poor inter-laboratory repeatability for this procedure¹⁸⁷.

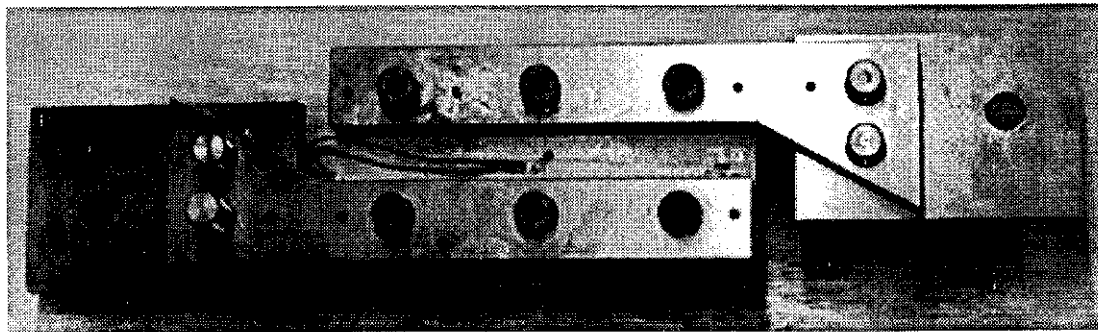


Figure 3.5 Photograph of In-Plane Shear Assembly specified in ASTM D4255-83.

The fixture consists of two pairs of rails bolted along both long edges of the shear specimen. When a tensile load was applied to the rails (Figure 3.2) an in-plane shear load was induced in the specimen. The aspect ratio of the specimen (i.e., the area exposed between the rails), was high to ensure as near a pure state of shear stress as possible and to minimise edge effects¹⁸⁸. On the surface of each of the four rails which gripped the specimen, 250 grit silicon carbide paper was adhered, in order to improve the contact between rails and specimen.

3.3 Strain Measurement Techniques

Three different methods of measuring specimen strain or displacement were employed.

3.3.1 Crosshead Displacement

Crosshead displacement was used on the "Lloyd" testing machine to record the central deflection for the three-point bend tests (flexural and ENF tests), and the vertical displacement in the DCB tests. However, crosshead displacement was not employed for the tension or in-plane shear test due to the excessive slippage which generally occurs between the grips and 'tabbed' specimens and also because this method would give the extension of the whole specimen and not the strain exclusive to the gauge length.

3.3.2 Extensometer

The strain in the direction of load application was measured using the extensometer (Figure 3.6) for both longitudinal and transverse tensile specimens.

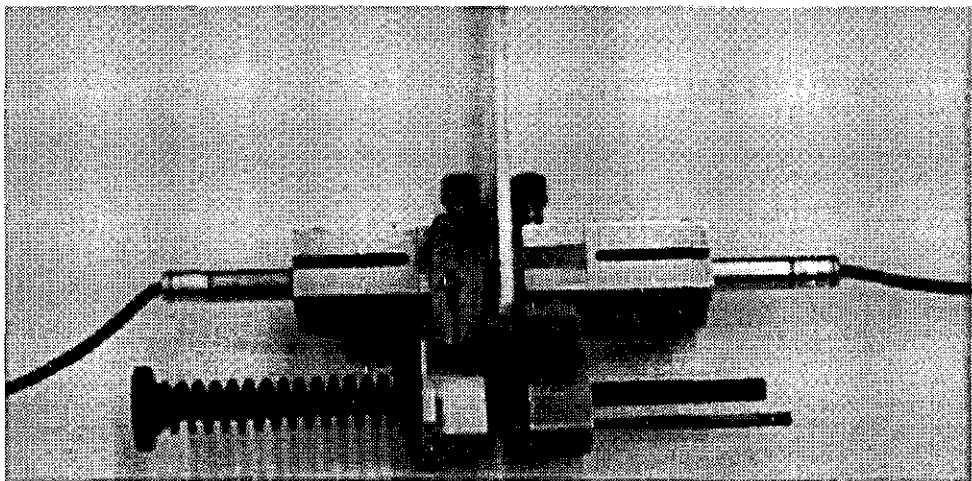


Figure 3.6 Photograph of the extensometer employed in static mechanical tests.

The extensometer consisted of two sets of knife edges 25mm apart which contacted either side of the specimen, therefore as the specimen strained so the knife edges were deflected. The system effectively averaged the strain on both sides of the specimen, thus eliminating errors due to bending effects. The extensometer gripped the specimen by means of a spring which was adjusted so that the extensometer was just self-supporting. Excessive spring tension can cause the knife edges to dig into the specimen and so become stress raisers. Because of the manner in which the extensometer 'clips' onto the specimen, it could only be positioned so as to measure strain along the specimen's long axis, thus the need for strain gauges arose for measuring the strain at 90° to the direction of the load.

3.3.3 Strain Gauge

Strain gauges were employed to measure transverse strain in the tensile specimens and shear strain in the in-plane shear specimens. Bending effects were accounted for by placing a strain gauge on each side of the specimen. The signal was then averaged and the true strain obtained from equation 3.1, by employing the gauge factor as given by the manufacturer¹⁸⁹.

$$\Delta\epsilon = \Delta R / \text{Gauge factor} \quad (3.1)$$

Appendix II contains the Wheatstone Bridge circuit employed and detailed installation instructions¹⁹⁰. The circuit ensured that resistance changes due to ambient temperature variations were minimised, I^2R losses in each arm were equal, and the circuit also contained an in-built strain gauge calibration circuit. Strain gauge size was maximised for ease of installation and accuracy, with the gauges used made by TML:

Tensile specimens:	FLA-5-11 (gauge length = 5mm)
Compressive specimens:	FLA-2-11 (gauge length = 2mm)
In-Plane Shear specimens:	PRS-5-11 (gauge length = 5mm, $\pm 45^\circ, 0^\circ$ strain rosettes)
	FLA-5-11 (gauge length = 5mm)

A strain gauge/extensometer calibration exercise was performed in which the longitudinal strain of a tensile specimen was measured using both the extensometer and a strain gauge and compared to Classical Laminated Plate Theory predictions for the solution. The measure values were within 2-3% of each other and within 3-4% of the theoretical solution, thus justifying the use of these strain measuring techniques.

3.4 Test Specimen Preparation, Geometry and Procedures

All the specimens were cut with a diamond tipped rotary wheel, employing a simple jig to ensure that the edges of the specimens were exactly parallel or perpendicular to the webs so that the UD fibres were at 0° or 90° respectively. Where possible the specimens were cut so that the gauge length fell within the constant thickness section between the webs (Figure 3.1). The edges were then smoothed on a linisher followed by 240-grit silicon-carbide hand polishing. Specimen dimensions were recorded at intervals in each direction with either a micrometer or a vernier calliper (to two decimal places) to ensure that each specimen was within the defined tolerances. All the laminate specimens had a gauge length thickness of approximately 3.3mm, which was the nominal thickness of the constant thickness section. A linear vernier microscope was used to measure the separate ply thicknesses in the gauge length of each specimen.

When end tabs were required, they were cut using a guillotine from a sheet of 1mm thick standard grade aluminium. All the tabs used were 50mm long and the same width as the specimen. The bottom front edge of each tab was chamfered on a linisher to ensure that the edge did not dig into the specimen and thus induce failure at or under the tab. After "roughing" both bonding surfaces with coarse grit paper and cleaning the surfaces, the tabs were bonded to the specimens using a thin film of Loctite Prism Gel 454 Adhesive.

3.4.1 Tensile Tests

3.4.1.1 Longitudinal

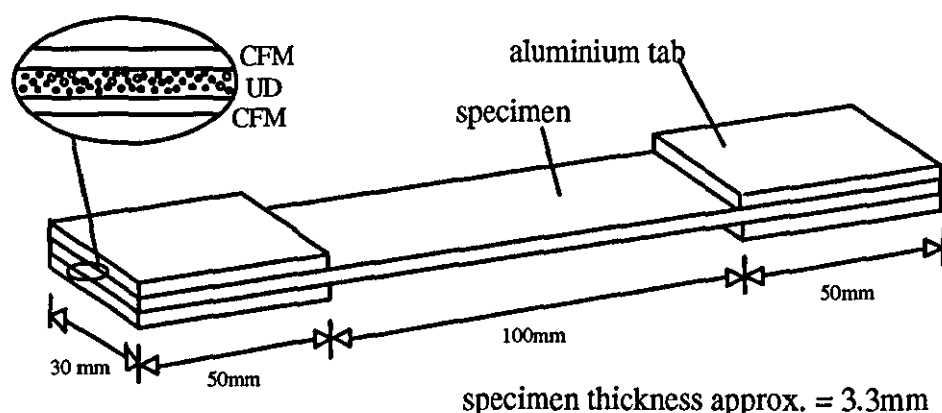


Figure 3.7 Longitudinal tensile specimen.

The specimens were cut from the constant thickness section between the webs in accordance with CRAG 302¹⁸⁵ (Method of test for the tensile strength and modulus of

multi-directional fibre reinforced plastics) as shown in Figure 3.7, with the unidirectional rovings parallel to the long specimen edge. Five specimens were strain gauged with the gauges aligned at 90° to the load to measure the transverse strain enabling Poisson's ratio to be calculated.

3.4.1.2 Transverse

Due to the geometry of the "plank" it was not possible to follow the CRAG 302 specimen specification precisely. Initially specimens were cut to the stipulated dimensions at 90° to the UD fibre axis with the middle of the specimen falling halfway between the webs. The webs were then cut off and finished until a uniform thickness specimen was achieved. However due to excessive voids under the web the specimens all failed in this region. It was therefore decided to leave a 20mm high web "stub" on the specimen, which resulted in failure occurring in the gauge length (Figure 3.8). It was believed that the stubs only had a minimal effect on the stress field in the gauge length where failure had to occur for the result to be valid. The gauge length was the constant thickness section, which had the smallest cross sectional area. In order to be able to bond the tabs to a flat surface, these specimens were longer than the longitudinal tensile specimens. Again, five specimens were strain gauged for Poisson's ratio calculations.

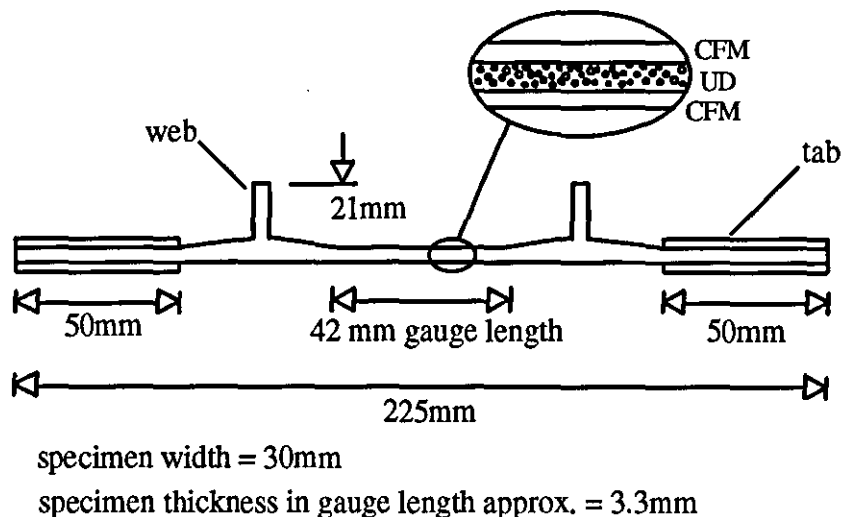


Figure 3.8 Cross-section of a transverse tensile specimen.

The specimens (both longitudinal and transverse) were hydraulically gripped over the tabbed area, and a crosshead displacement of 5mm/minute applied by the "Dartec". With the exception of those for Poisson's ratio measurement, all the specimens were tested until catastrophic failure.

The amplifier could only accept one strain input, therefore it was not possible to record longitudinal and transverse strain concurrently. Therefore for Poisson's ratio measurement, specimens were initially loaded to half the failure load and unloaded whilst recording the transverse strain using the strain gauges. Then the extensometer was clipped onto the specimen to record longitudinal strain and loaded to failure. The initial modulus was then calculated, and Poisson's ratio given by the gradient of the stress-strain curves:

$$\nu = \frac{\text{stress} / \text{strain parallel to load}}{\text{stress} / \text{strain } 90^\circ \text{ to load}} \quad (3.2)$$

3.4.2 In-Plane Shear Tests

Specimens were cut, with the UD fibres at 0° to the long edge of the specimen, from the outer skin of the ACCS "plank", to the dimensions specified in ASTM Standard D4255-83¹⁸⁶. In order to achieve a uniform thickness specimen the thicker sections along the edges of the specimen (i.e. where the taper to the web begins) were finished down to the thickness of the central section ($\pm 0.05\text{mm}$) and the holes drilled (Figure 3.9).

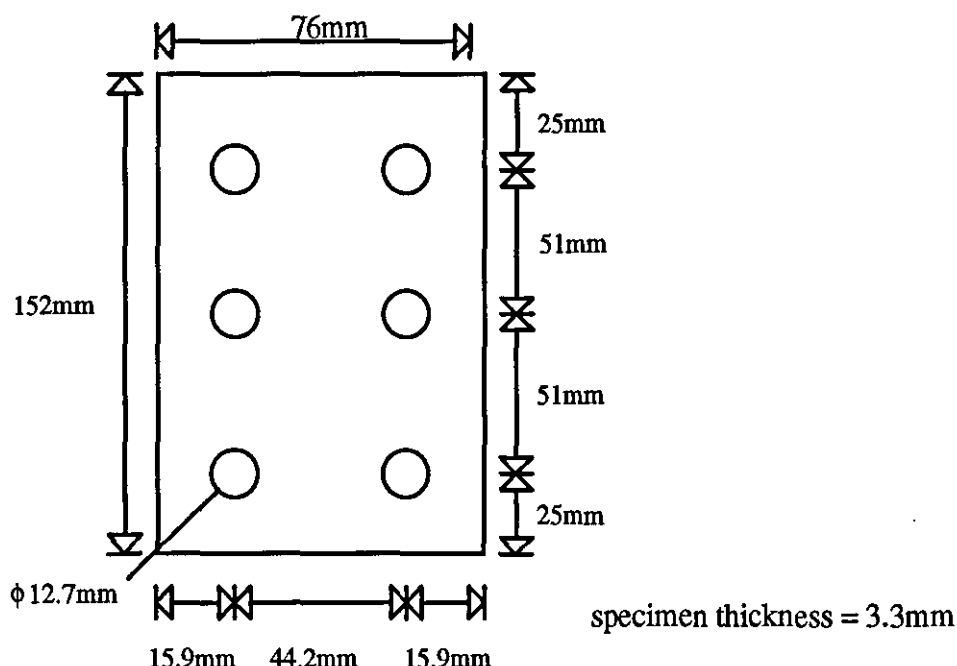


Figure 3.9 In-plane shear test specimen.

When the rails were bolted on, a gauge width of approximately 19mm remained. The standard recommends a specimen thickness between 1.27mm and 3.17mm, which some of the specimens exceeded, however the upper limit was only suggested to ensure the rail

clamping capacity was not approached, therefore the results were still valid. Strain gauge rosettes ($+45^\circ$, 0° and -45°) were attached to either side of three specimens, whilst eight further specimens had a single strain gauge on either side, enabling one component of the strain to be measured.

In all of the in-plane shear tests, the rail edges were aligned with the edges of the specimen and secured by finger tightening the bolts. A torque wrench was then employed to tighten each bolt to 80Nm. A torque of 100Nm was specified in the standard, but 80Nm gripped the specimen adequately and at higher torque it was possible to twist and damage the specimen. A specified crosshead speed of 1.5 mm/minute was applied until failure.

3.4.3 Flexural Tests

3.4.3.1 Longitudinal

CRAG 200¹⁸⁵ (Method of test for flexural strength and modulus of fibre reinforced plastics) was used for this series of tests in which specimens were cut from the "plank" with a span to depth ratio of 20:1 as suggested in the specification for glass fibre composites. Longitudinal test specimens were cut from the constant thickness section between webs to the dimensions and tolerances as specified in CRAG 200. Support rollers of 10mm diameter and a loading roller of 25mm diameter were employed.

3.4.3.2 Transverse

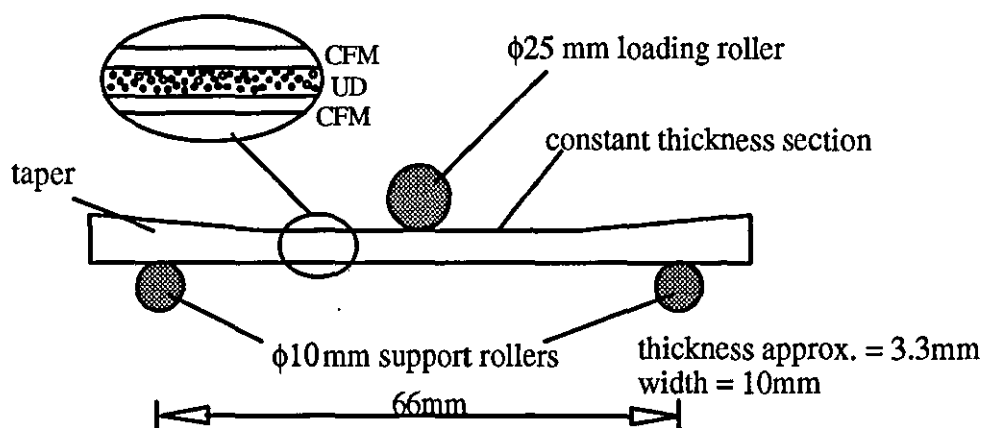


Figure 3.10 Cross-section of transverse flexural specimens illustrating tapers.

These specimens were cut from the "plank" (Figure 3.10) with the unidirectional fibres at 90° to the specimen axis, and were prepared as closely as possible to the CRAG 200 specification. However the transverse specimens had an increasing thickness at either end

on the upper surface due to the tapers on the outer skin (Figure 3.1). It was believed that this only had a minimal effect on the stress distribution at the centre of the beam where the bending stress was at a maximum, and where failure occurred.

The longitudinal and transverse tests employed a simple variable span three-point bend fixture which was attached to the "Lloyd" test machine with a 5KN load cell for the longitudinal specimens and 500N load cell for the transverse specimens. A cross head speed of 5mm/minute was employed, which caused failure within the 30-180 second time interval defined.

3.4.4 Critical Strain Energy Release Rate Tests

The Mode I and II critical strain energy release rates were required as part of the definition of the material model for the interface element employed to simulate delamination in the FE analyses (see Chapter 5).

3.4.4.1 Double Cantilever Beam Tests for Mode I

Mode I characterisation most commonly uses the Double Cantilever Beam technique, which is well documented^{191,192}, and is considered to be the most accurate method of determining Mode I critical strain energy release rate, G_{Ic} . Tests were performed as near as possible to that described in CRAG 600¹⁸⁵ (Method of test for interlaminar fracture toughness of fibre reinforced plastics). Constant width specimens were employed (Figure 3.11) with the analysis based on the area under the force-deflection curve, rather than on beam theory or a semi-empirical compliance method^{191,193}.

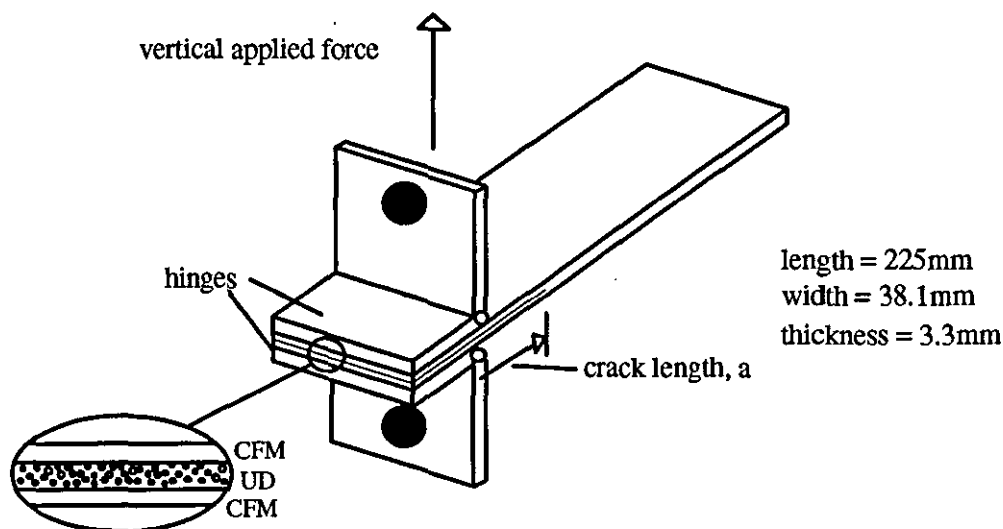


Figure 3.11 Double cantilver beam test specimen.

This test requires a symmetric lay-up of an even number of plies so that the starter crack can be centrally located to ensure that bending in each arm is balanced. The starter crack is usually induced by inserting a thin Teflon¹⁸⁵ sheet at the central interface during lay-up. However, there being only three layers, the "plank" does not have a central interface, nor was it possible to start the crack in the usual way as it was necessary to test the pultruded product. Therefore, the specimens described below do not conform exactly to CRAG 600.

Two test specimen types were employed. The first with a central crack (though this was not along an interface) which was started by cutting a 3mm deep notch along the centreline on the end of the specimen with a CO₂ laser. A razor was then inserted into the notch and forced into the material to initiate the crack. This was far from satisfactory as an exactly centrally located central crack was difficult to achieve and the crack itself was quite wide.

The second batch of tests was performed on specimens with a crack at one of the interfaces. However, this gave rise to such a large stiffness mismatch between the two arms, that if the thinner arm was not "stiffened-up", then it simply bent until it "creased" without the interface crack propagating. Support for this arm was provided by bonding a layer of CFM, peeled from another specimen to the weaker arm. Because the two bonded layers had the same stiffness the interface crack propagated, rather than the two newly bonded layers peeling apart. This method, whilst crude, meant that the arms were reasonably balanced and so allowed some approximate data to be obtained. The initial crack was easily initiated by flexing a notched specimen and the steel hinges were bonded either side as shown in Figure 3.11 with epoxy adhesive. The tensile force was provided by bolting the "Lloyd" test machine crosshead to the hinges (Figure 3.4).

The specimen was initially loaded to elongate the crack to 50mm from the hinge pivot, and then unloaded and removed from the machine. The crack length was then marked with a razor on either side of the specimen with the assistance of an optical microscope. The specimen was then relocated in the machine and loaded at 5mm/minute crosshead speed until the crack had extended to the desired length. The CRAG method suggested extending the crack from 50mm initially to 125mm, but for these specimens the bending became excessive when the crack length exceeded 100mm so this was taken as the limit. Either one crack of 50mm or two successive cracks of 25mm each were formed in order to be able to take two measurements of G_{Ic} from the specimen (i.e. after 25mm extension the specimen was removed from the machine, the crack length marked as described previously and re-tested). The CRAG method specifies only one reading per sample, but many researchers¹⁹³ have performed several crack extension increments per specimen thus justifying this

technique. Load extension graphs were recorded for each test, whilst a 2.5KN load cell was used throughout.

3.4.4.2 End Notched Flexure Tests for Mode II

The choice of test method to determine G_{IIc} was less straightforward than for Mode I, with different methods providing markedly different values¹⁰⁶. One of the most widely used techniques is the End Notched Flexure test^{191,192,194} which was chosen as it best meets the two most important criteria for a Mode II test:

- (1) Whilst preventing crack opening (to ensure pure Mode II) the friction between cracked surfaces is minimised.
- (2) The specimen dimensions ensure a sufficiently large change in compliance with crack length so that this can be experimentally determined.

This technique involved a three-point bend test on a pre-cracked laminate, thus inducing shear stresses at the crack tip. The crack is ideally situated at the mid-plane of a symmetric laminate, as this is where the shear stress is at a maximum. However, having no interface at the mid-plane, these tests were performed with a crack at the lower UD/CFM interface. Figure 3.12 shows the experimental set-up employed based on references^{191,192}. Specimens were again cut from the midsection between webs of the outer skin, and the initial crack generated in the same way as for the DCB interface specimens. There were two stages to this experiment:

(a) Calibration of Compliance Equation

Initially the change in compliance of the specimen with cracked length (dC/da) was experimentally obtained for use in equation 3.3¹⁹¹:

$$G_{IIc} = \frac{P_c^2}{2w} \cdot \frac{dC}{da} \quad (3.3)$$

[where P_c = peak load, and w = specimen width]. To this end a series of three-point bend tests were performed on the "Lloyd" test machine on twelve specimens with the initial crack lengths increasing from 22mm to 29mm at approximately 0.5mm intervals. For each test, load (P) was plotted versus central displacement (δ), from which the compliance for the specimen was obtained from equation 3.4. The data was then plotted in a graph of compliance against crack length and a best fit straight line calculated by linear regression to give the value of dC/da . For all the tests within this section a load cell of 500N and crosshead speed of 5mm/minute were employed.

$$C = \frac{\delta}{P} \quad (3.4)$$

(b) Crack Growth Test

A second series of tests was then performed, in which a specimen of initial crack length of 25mm was loaded in the three-point bend jig until the crack extended. The load at which extension occurred (P_e) was recorded along with the load deflection curve, the initial slope of which yielded the individual specimen compliance.

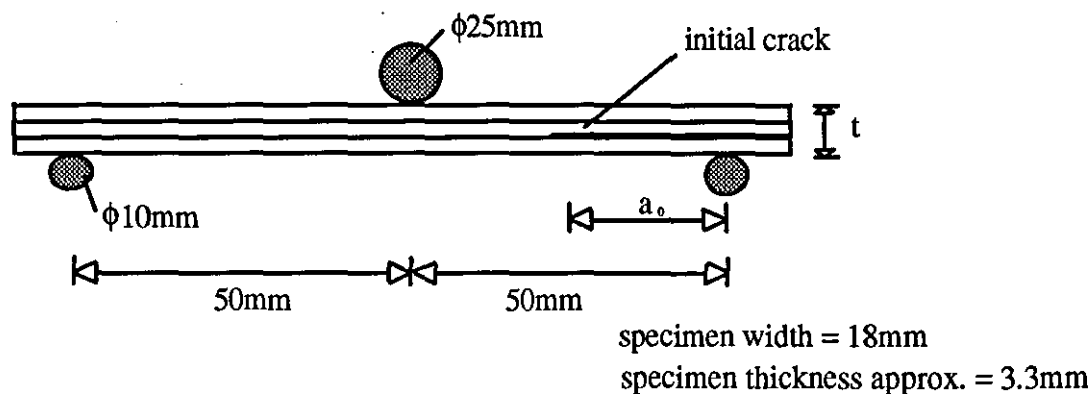


Figure 3.12 End notched flexure test specimen and supports.

Chapter 4

Impact Testing and Damage Assessment

This chapter details the equipment, test configurations, and methodology for the experimental impact tests and damage analysis of the resulting impacted specimens. The methodology employed in designing the test strategy was that of a building-block approach¹²⁴. First, tests concerned with understanding the fundamentals of the test technique and material characteristics were conducted. A series of simple geometry coupon tests followed, which induced all failure modes. Specimen geometry complexity was increased from the coupons to sub-components (the box sections) to testing of full-scale components (the "plank"). Thus understanding of the system was steadily improved as the complexity of impact specimens increased, with each progression building on the knowledge gained from the previous work.

4.1 Materials and Environmental Conditioning

All the material employed was taken from the ACCS "plank", and each test was performed at room temperature, therefore no environmental conditioning was applied to these specimens (section 3.1).

4.2 Test Equipment and Techniques

4.2.1 Instrumented Falling Weight Impact Test Machine

The literature review revealed the need for a dynamic test technique for low velocity impact. The equipment employed for these tests was a Rosand Precision Impact Test Machine IFW 5, which is an Instrumented Falling Weight Impact (IFWI) Test machine

capable of employing variable mass and geometry impactors and with a second-strike prevention facility for sub-penetration energy impacts (i.e. when the impactor bounces on the specimen). The impactor carriage unit falls down the tower under gravity (Figure 4.1) along guiding rods to impact the specimen.

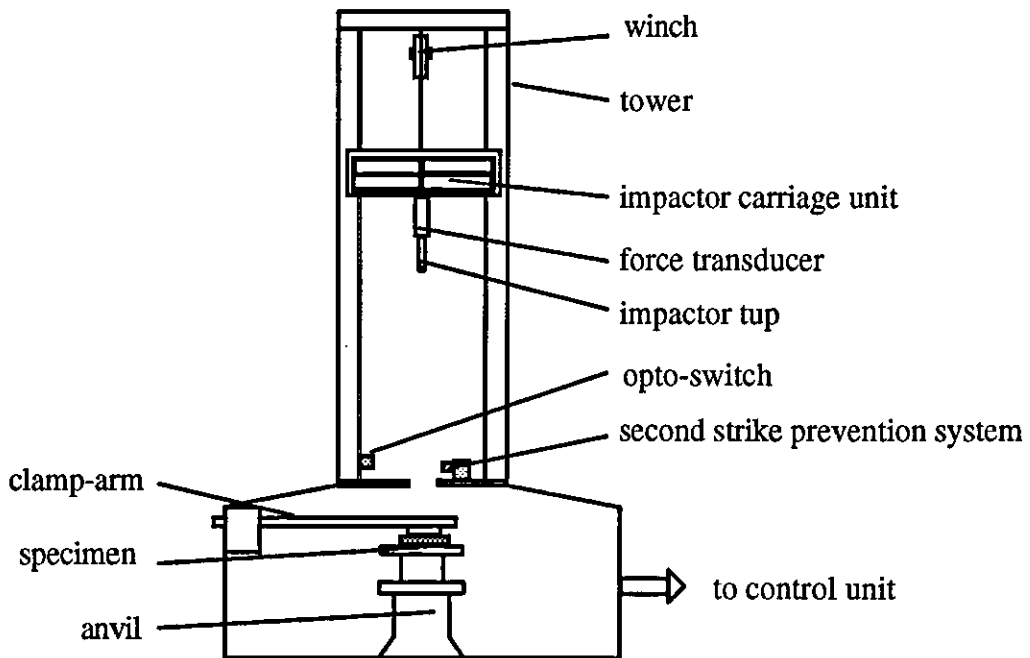


Figure 4.1 Simplified diagram of IFWI test tower employed for all the experimental impact tests.

Data from a piezo-electric force transducer (calibrated from 10 to 50,000N) in the impactor was logged at a constant time interval over the sweep time specified and the software automatically calculated the impactor's acceleration from Newton's first law (i.e. it is assumed that the mass of the impactor is significantly greater than the target's mass such that its inertia can be ignored). From integration and double integration of the acceleration, the velocity and deflection respectively under the impactor were obtained.

The initial impact velocity (v_0) was recorded by an opto-switch which was positioned to measure the impactor's velocity just before contact was made with the specimen. The opto-switch consisted of an accurately machined 'flag' attached to the impactor carriage which passed through an optical gate on the tower. From the time taken to pass through the gate, the velocity was calculated. The same system was also used to trigger data capture.

The variable mass option enabled impacts with masses from 1Kg to 25Kg to be performed. For an impact mass of 10Kg or greater, the whole carriage system was part of the impact mass, however, for a mass under 10Kg a floating mass system was employed which sits

within the carriage when dropped, but moves independently on contact with the specimen. Second-strike prevention was performed with a pneumatically driven mechanical system which flicked a catching device under the impactor carriage as it rebounded from the specimen following a non-penetrative impact. Because the system catches the carriage unit, it could not be used for floating masses or with the 25Kg mass (to prevent damage to the catching device).

There were a number of ways that the impact specimen could be supported and in this research, simple and clamped supports were employed (clamping pressure was achieved pneumatically). Almost any geometry specimen can be accommodated by customising the conventional anvil or by using a different support system entirely. All the simply supported specimens were located on a table designed especially for the ACCS "plank" as illustrated in Figure 4.2, which replaced the anvil at the bottom of the tower. The anvil and clamp-arm were used for the clamped specimens.

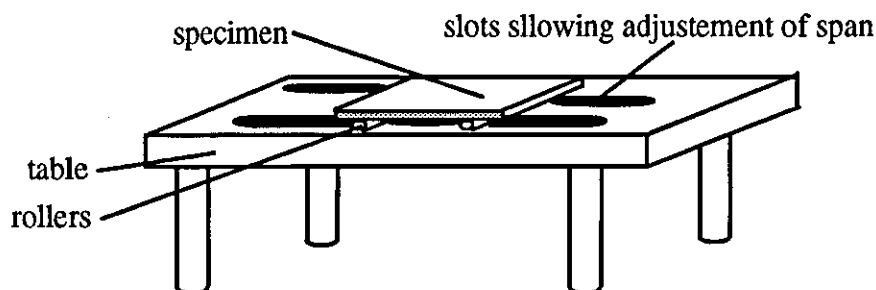


Figure 4.2 Table for simply supported impact test specimens with adjustable span.

After the impact test, the impactor mass was automatically lifted to the prescribed height by an electrically powered winch. Further capabilities of the machine include safety rods, shock absorbers, sample strippers (to pull the impactor out of a penetrated specimen), and environmental cabinets for temperature controlled testing.

The Control Unit contained the electronics and software to drive the test machine and to perform calculations on the captured data. The output from a test was wide ranging including graphs plotting combinations of force, time, deflection, energy, and impactor velocity. From these curves discrete data was also provided including peak force, peak deflection, deflection at peak force, and energy absorbed at peak deflection.

The test method employed was as described in the user manual¹⁹⁵. For each support condition, the anvil height was adjusted so that on rebound the second-strike prevention mechanism caught the impactor carriage just above the top surface of the specimen. Once

the specimens height was fixed, the opto-switch was adjusted to trigger data capture and record the impact velocity just prior to impact. The correct impact energy level was set by defining the drop height, impact velocity or impact energy. The following variables were also set:

Force Range - the full scale force value effectively set the amplifier gain. The lowest full scale value was chosen to include the highest expected peak force, thus maximising the accuracy of the force transducer.

Data Filter - following the exercise described in section 7.1.2, the data filter was turned off which set the filter to the highest reasonable value (half the sampling frequency - Nyquist frequency). Filtering could still be performed after data capture.

Delay - this function effectively delayed or brought forward the trigger point. After the investigation described in section 7.1.3, the delay function was always set to zero and instead the opto-switch was manually adjusted to move the trigger point.

The data gathered from the IFWI tests to characterise the impact events is defined below:

1. **Impact Velocity** (m/s) - the velocity of the impactor on contact with the specimen calculated by the opto-switch.
2. **Impact Energy** (J) - calculated from the impact velocity and the impactor mass.
3. **Peak Force** (N) - the highest force during the impact.
4. **Deflection at Peak Force** (mm) - the deflection under the impactor at peak force.
5. **Energy at Peak Force** (J) - the energy under the force-deflection curve up to peak force.
6. **Peak Deflection** (mm) - maximum deflection under the impactor.
7. **Energy at Peak Deflection** (J) - the energy under the force-deflection curve up to peak deflection (corresponds in magnitude to the Total Impact Energy).
8. **Total Impact Energy- TIE** (J) - as defined below.
9. **Damage Energy** (J) - the energy absorbed in producing damage during the impact.
10. **Elastic Energy** (J) - the elastic energy absorbed (= TIE - damage energy).
11. **Time to Peak force** (m/s) - the elapsed time from first contact to the peak force.
12. **Time to Peak Deflection** (m/s) - the elapsed time from contact to peak deflection.
13. **Contact Time** (m/s) - the duration of the impact.
14. **t_p Stiffness** (KN/mm) - the stiffness response calculated from the modified spring-mass model (section 4.3.2) and using double the time to peak force.
15. **t_d Stiffness** (KN/mm) - the stiffness response calculated from the modified spring-mass model and using double the time to peak deflection.

16. **t_c Stiffness (KN/mm)** - the stiffness response calculated from the modified spring-mass model and using the contact time.
17. **Initial Stiffness (KN/mm)** - the initial slope measured from the force-deflection curve.

The term "total impact energy" requires explanation. During initial testing it was observed that in most cases the energy at peak deflection (i.e. when the impactor had been brought to rest for non-penetration tests), was greater than the initial impact energy as given by $1/2mv_0^2$. In all the literature which was reviewed $1/2mv_0^2$ was termed the impact energy without elaboration. However, if an energy balance analysis is performed on an impact the following is revealed (Figure 4.3).

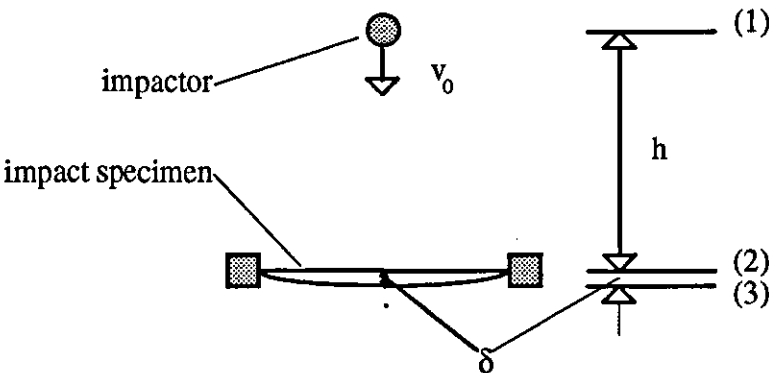


Figure 4.3 Energy balance of an impact event taking into account the deflection of the impact specimen.

If the deflection of the specimen is ignored, then it is assumed that at the heights (1) and (2) the following energy balance applies:

(1)	KE = 0	(2)	KE = $1/2mv_0^2$
	PE = mgh		PE = 0
	SE = 0		SE = 0
Total = mgh		Total = $1/2mv_0^2$	

[where PE = potential energy, KE = kinetic energy, and SE = strain energy in the plate]. Therefore the impact energy (IE) = $mgh = 1/2mv_0^2$ and when the impactor has been brought to rest, then the strain energy in the plate is therefore given by equation (4.1):

$$SE = 1/2K\delta^2 = mgh = 1/2mv_0^2 \quad (4.1)$$

However, if the deflection of the plate under the impactor, δ , is taken into account, an energy balance referring to Figure 4.3 gives:

(1) $KE = 0$ $PE = mg(h+\delta)$ $SE = 0$	(2) $KE = 1/2mv_0^2$ $PE = mg\delta$ $SE = 0$	(3) $KE = 0$ $PE = 0$ $SE = 1/2F\delta = 1/2K\delta^2$
Total = $mg(h+\delta)$	Total = $1/2mv_0^2 + mg\delta$	Total = $1/2F\delta = 1/2K\delta^2$

The strain energy absorbed by the plate is greater than the impact energy and therefore the Total Impact Energy (TIE) has been defined as:

$$TIE = mg(h+\delta) = 1/2mv_0^2 + mg\delta \quad (4.2)$$

This definition is far more satisfactory in explaining the energy balance throughout the impact event. As can be seen in the tables of impact test results in Appendix V the values of TIE correspond almost exactly to the energy under the force-deflection curve up to the peak deflection (the strain energy) as would be expected. Despite not being able to quantify the TIE until after the event, this definition is very important. The TIE was crucial in explaining the strain-rate test results, as discussed in section 7.2.

The initial tests and the coupon tests were performed with impactor masses from 10.82 to 10.92Kg (this varied because the length of the impactor tup had to be adjusted for the different supports heights dictated by the various coupon geometry and supports conditions). The strain-rate tests were performed with masses ranging from 1.63 to 25.9Kg. All the tests were performed with a 10mm diameter hemi-spherical tup. At each energy level, approximately six specimens were tested to enable a meaningful average and standard deviation to be calculated.

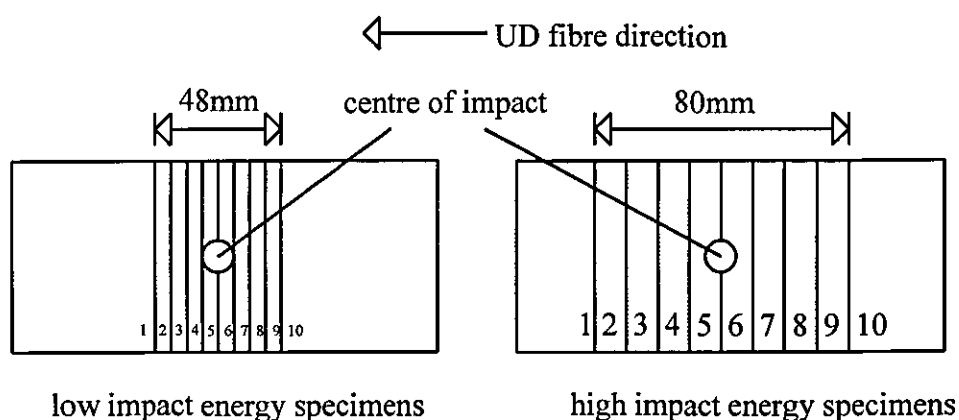
4.2.2 Damage Assessment

As explained in the literature review, in order to assess all the possible damage modes resulting from a low velocity impact event on a composite laminate, several techniques were required. In addition to the visual inspection, optical microscopy, and ultrasonic C-scan performed by Zhou and Davies⁹⁵, thermal deply testing was also performed to assess fibre breakage.

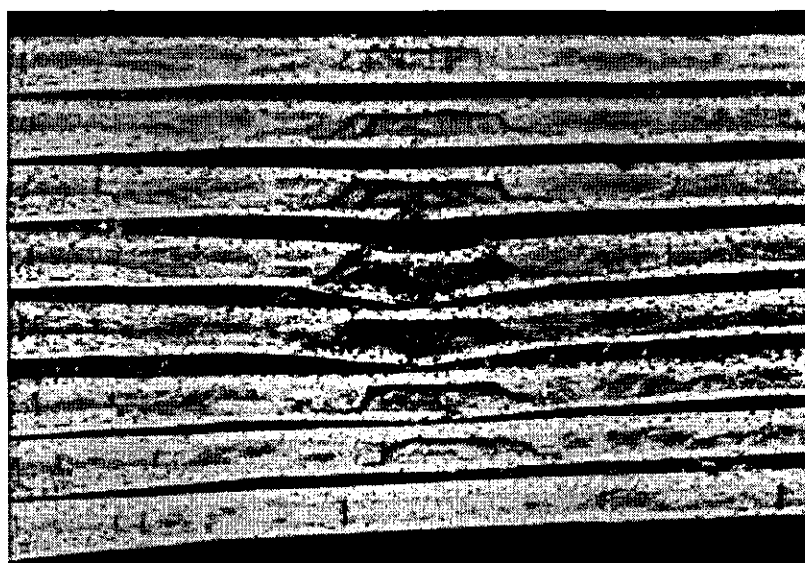
Only modes of damage on the surface of a coupon could be observed by **visual inspection**. The CFM ply on the tensile face (i.e. non-impacted surface) was often the first form of damage to be noted. The tensile crack length was measured to the nearest millimetre. The permanent indentation on the impacted surface was measured using a displacement dial

gauge accurate to 0.01mm, and any local shear cracking under the impactor on the impacted surface was also noted.

For the **optical microscopy (OM)** inspection of sections cut from the damaged area, a Vickers Stereo Microscope with variable magnification (x1 to x4) was employed. Optical microscopy provided quantitative and qualitative information on matrix cracking and delamination patterns. This was a destructive technique, because in order to obtain a three-dimensional map of matrix cracking and delamination, the impacted specimens were cut into transverse strips (a similar approach is described by Hong and Liu¹⁹⁶). The number of surfaces inspected was maintained at approximately eight, therefore for the higher energy tests the damaged area was sectioned at wider intervals (see Figure 4.4).



(a)



(b)

Figure 4.4 (a) Sectioning technique for impact specimens for OM inspection, and (b) sections from a shear coupon.

The specimens were cut into strips using a diamond tipped rotary wheel followed by polishing of the through-thickness surface of each strip with progressively finer grades of silicon carbide paper (240-, 400-, 600-, 1000-grit). A fluorescent green highlighter pen was then drawn across the polished surface and the excess ink removed by wiping with a clean cloth. The remaining ink highlighted the matrix cracks (tensile and shear) and delaminations (Figure 4.4 (b)). The delamination length on the upper and lower interfaces and positions of the matrix cracks (both tensile and shear) were noted. By plotting the delamination lengths and matrix crack positions for each section, a three-dimensional picture of the damage was obtained, enabling the upper and lower delamination areas to be calculated. An equivalent "damage area" which would be seen by ultrasonic C-Scan was also calculated. This was essentially the plan view of the total delamination area and included the shear cracks running at approximately 45° through the UD layer if present. The method of calculating an area from the one-dimensional information was not very precise, therefore minimum, maximum, and average values were calculated, but only the average values are included in the assembled damage assessment tables in Appendix V. Where possible, four test specimens from each energy set were inspected by OM to provide meaningful average values. The average UD vertical tensile matrix crack spacing was calculated as follows:

$$\text{average crack spacing} = \{\text{total inspected length/ number of cracks}\} \text{ (mm)} \quad (4.3)$$

Ultrasonic C-Scan amplitude plots were obtained via a 2.25 MHz alpha type transmitter employed with a Wells Krautkramer Flaw Detector USIP 12 system. A method employing reflection from a glass plate mirror beneath the specimens submerged in the water bath was used. Every impact specimen was submitted to a scan as it was a non-destructive technique. This technique provided a global delamination area. A time-of-flight analysis would have provided through-thickness information and therefore given the delamination area at each interface, however the method could not be employed because it relies upon a strong back-face reflected signal, which cannot be achieved with glass fibre composites due to the associated high level of attenuation.

Specimens were placed in a tank of water over the glass sheet with the impacted surface uppermost. The ultrasonic transmitter was then programmed to scan over the surface of the specimen. The system was very sensitive, therefore care was taken to ensure that conditions (i.e. the amplifier gain, height of the transmitter above the test specimen etc.) were kept constant. Once the scan had been performed the data was transferred to the Wells Krautkramer Mark II software for analysis of the amplitude plot. The plots were then visualised graphically by splitting the range into seven bands of attenuation from -24dB to 0dB. The -24dB band corresponded to the greatest attenuation and therefore the zone of

greatest damage in the specimen (Figure 4.5). Using a zoom facility it was possible to calculate the absolute damage area corresponding to each level of attenuation. An initial investigation to obtain the contours which should be included in the damage area was performed by comparing the OM and C-Scan results (section 7.3.1). In the damage results tables in Appendix V the damage areas were calculated by including successive contours from the -24dB contour through to the area calculated by adding the -24dB, IF, -20dB, -12dB, and -8dB contours. The IF contour refers to zero attenuation which only occurred in "holed" (penetrated sample) specimens.

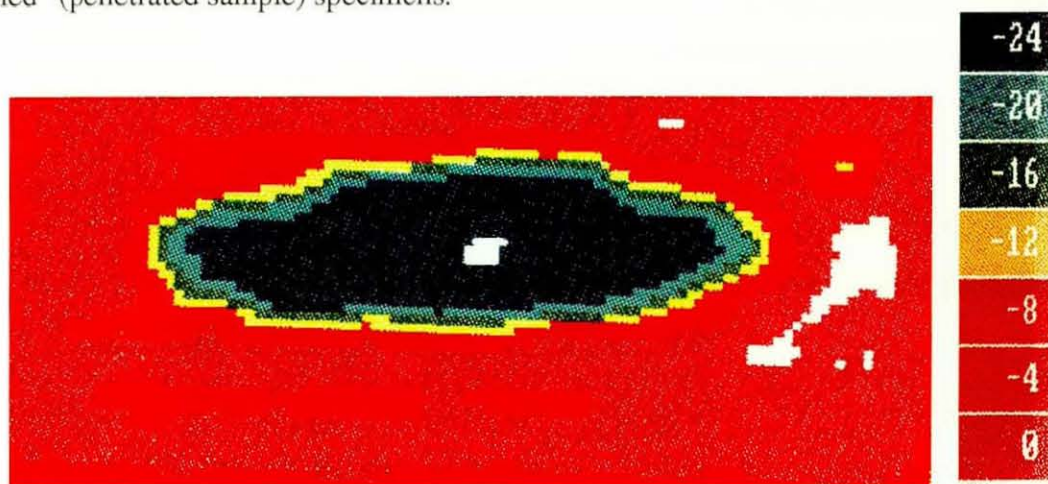


Figure 4.5 C-Scan of 15J TIE shear coupon and dB scale.

The specimens chosen for **thermal deply analysis** were placed in a Eurotherm Muffle Furnace, situated in a standard fume cupboard, to burn off the resin. The technique was employed to obtain the extent of fibre breakage in the impacted specimen. Specimens were placed in a vented furnace at 600°C for approximately three hours and then inspected visually and under the Vickers microscope. Due to the high filler content the UD fibres remained bound together preventing easy inspection of the fibres (Figure 7.19). To overcome this the fibres were gently plied apart with fine tweezers and splayed out, allowing broken fibres to be identified. Two specimens from each energy set were deplyed and the results used qualitatively only.

4.2.3 High Speed Video Camera

A Solid State Kodak Ektapro EM™ Motion Analysis System was used to film several impact events. The data was stored in solid state memory and replayed at slow speed or frame by frame and was permanently recorded on standard VHS video tape at the desired speed. The high speed video camera was used to film several impact events, in two different modes. Firstly, the camera was positioned so as to film the global deflection of the ACCS

"plank", and secondly the camera was zoomed in to record the local deflection under the impactor (section 7.5).

4.3 Test Strategy

The experimental impact work can be divided into five sections: preliminary tests, an analysis of strain-rate effects, testing of simple geometry coupons taken from the "plank", tests of box sections, and high speed video recordings of impacts on the whole "plank" cross-section. Thus the complexity was steadily increased with the initial tests investigating material response through to an investigation of complex geometry impacts. The following sections describe the test strategy, specimen geometry and support conditions employed within each series of tests.

4.3.1 Preliminary Impact Tests

Before embarking on the main body of the investigation, it was necessary to assess the effect of three variables on the impact response - specimen thickness, filtering of the force-time and force-deflection curves, and the delay function within the Rosand software.

4.3.1.1 Specimen Thickness

The thickness within the constant thickness section between the webs which was directly under the impactor for these tests, varied from 3.1mm to 3.6mm, however the majority of specimens fell in the region of 3.25 to 3.45mm. In order to properly define a test procedure in which sets of results could be compared it was necessary to understand the effect of specimen thickness on the impact response. Therefore a "flat" coupon was cut from between the webs of the ACCS "plank", 135mm long by 85mm wide, as shown in Figure 4.6(a). There was a taper along the two long sides of the specimen with the 42mm constant thickness section in the middle. When a specimen thickness is referred to, this was the average specimen thickness in the central section under the impactor and was calculated from several micrometer readings from within this area.

The specimens were clamped by a ring as shown in Figure 4.6(b). The top clamp was a simple steel ring of 60mm internal diameter and 80mm external diameter. The bottom plate consisted of a 150mm diameter steel plate with a central hole of 60mm diameter and reverse taper to accommodate the tapers on the specimen. The lower plate was located on the anvil of the impact test machine. The impact site was at the centre of the circular support.

In order to assess the effect of the thickness variation, two series of tests were performed under identical conditions of impactor mass (10.8Kg) and velocity (1.01m/s). Six specimens with thicknesses at the lowest end of the spectrum (average = 3.13mm) and six specimens at the upper extreme of the range (average = 3.57mm) were tested and the impact characteristics compared.

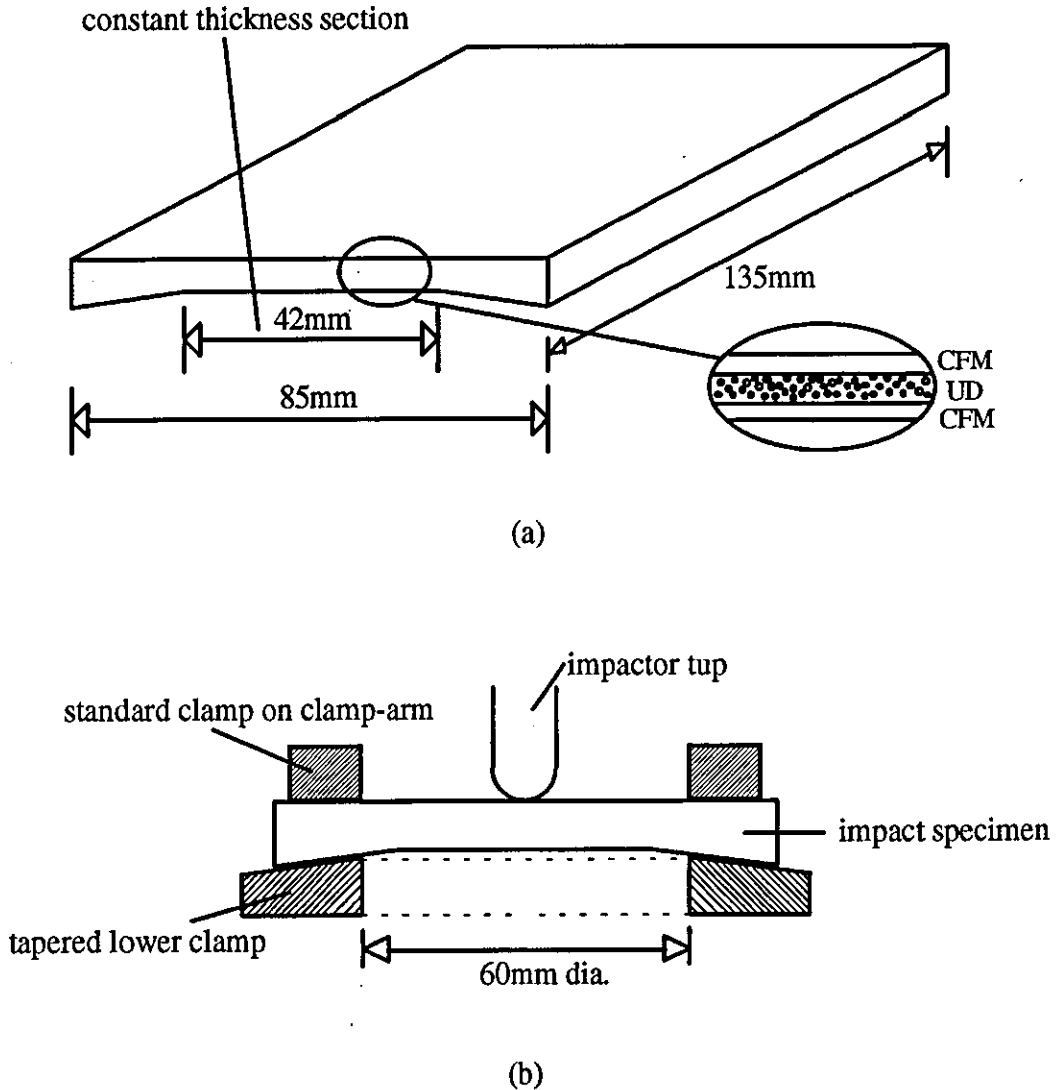


Figure 4.6 (a) Specimen employed, and (b) clamped support conditions for preliminary, strain-rate, and shear coupon impact tests.

4.3.1.2 Filtering of the Characteristic Impact Curves

When two bodies suddenly contact, vibrations are initiated in both objects. The amplitude and frequency of the vibrations depend upon the velocity of the impact, the physical characteristics of the two bodies, and the support conditions. As discussed in the literature review, there is some debate concerning the place of filtering the results in impact

testing^{114,116}. Filtering effectively removes the vibration curve which oscillates about, and is superimposed upon, the "overall response". These vibrations can hide the material response of interest, however over-filtering can lose much valuable information.

In order to investigate the effect of filtering on the force-deflection and force-time response, selected impact curves were progressively filtered, and the effect on the impact characteristics of peak force, and deflection and energy at peak force was observed. The data which was filtered was the impact test data from the four lowest energies tested in the strain-rate test series. The filtered data and unfiltered data were then compared.

4.3.1.3 Delay function

The opto-switch was set to trigger data capture, however, the start or end of the impact can be missed and so the software allows the trigger to be delayed or brought forward with the delay function (rather than resetting the opto-switch) within the software. This function was not supposed to effect the results, however it was noticed early on in the project that when the delay function was altered the calculated impact variables within the software were effected.

In order to assess the quantitative effect of the delay function, four tests were performed on 8mm thick, flat, woven aramid/polyester laminated plates. The specimens were clamped with an internal diameter of 40mm, the impactor mass was 10.9Kg, and the impact energy was set to 13.4J. The delay was varied from -80% to +25% (with the opto-switch being altered so as to enable all the impact data to be captured). All other impact variables were kept constant.

4.3.2 Strain-Rate Impact Tests

The strain-rate tests were performed in order to understand the material behaviour under different velocity impacts, so that the test strategy for the coupon tests could be planned. Impacts of the same energy, but with different mass and velocity combinations were compared in order to assess strain-rate effects. As stated in section 2.2.4.1, generally, researchers are agreed that glass fibre composites are strain-rate sensitive, but the effect on stiffness or strength, and the strain-rate range over which the effect is important, is not defined. Therefore it was necessary to determine the importance of these effects over the range of tests to be performed in this project.

Tests at impact energies of 0.4, 0.8, 3, 6, 8 and 15J were performed. These values were chosen because the first two energies induced very little damage, the middle three contained some damage but did not ultimately fail, and the final energy was above the penetration threshold. At each energy three sets of tests were performed with varying impactor masses (1.63, 2.13, 3.13, 10.8 or 25.9 Kg) and varying impact velocities. The same specimens were employed for this series as were used in the preliminary specimen thickness tests and are described in section 4.3.1.1.

For the masses under 10kg and for the 25.65Kg mass, the second-strike prevention option on the Rosand could not be used, therefore below the penetration threshold, tests performed with these masses bounced repeatedly on the specimen, thus preventing a comparison of impact damage between tests to be performed. Instead, comparison between the different tests was achieved by assessing the effect on several key variables: peak force, peak deflection of the plate under the impactor, and contact time, time to peak force and time to peak deflection.

It is useful at this stage to refer to Caprino et al's⁹¹ single degree of freedom spring-mass model of impact described in section 2.4.1, and illustrated in Figure 4.7.

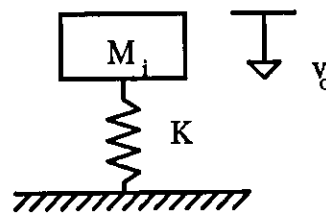


Figure 4.7 Single degree of freedom spring-mass model of elastic impact

The model is only valid for elastic impacts and non-strain-rate dependent materials, yielding the following relationships:

$$F_{\max} = \sqrt{(2U_0 K)} \quad (4.4)$$

$$\delta_{\max} = \sqrt{\left(\frac{2U_0}{K}\right)} \quad (4.5)$$

$$t_c = \pi \sqrt{\frac{M}{K}} \quad (4.6)$$

[where, F_{\max} = peak force, δ_{\max} = peak deflection, K = plate stiffness, t_c = contact time, and U_0 = impact energy] This model implies the following:

1. The peak force generated and deflection at peak force, are dependent only on the impact energy and not on the impact velocity or mass independently.
2. The contact time is dependent only on the impactor mass and is independent of the impact velocity. This implies that for the same energy impact, as the velocity increases (and therefore the mass decreases), the contact time decreases, therefore the plate must be capable of absorbing the same amount of energy in a shorter time.

This spring-mass model was used in the analysis of the strain-rate tests and coupon tests along with a newly developed modified spring-mass model which employed the total impact energy rather than the impact energy, giving:

$$F_{\max} = \sqrt{(2 \cdot TIE \cdot K)} \quad (4.7)$$

$$\delta_{\max} = \sqrt{\left(\frac{2TIE}{K}\right)} \quad (4.8)$$

4.3.3 Coupon Tests

A coupon is a simple geometry specimen on which initial studies can be performed before a more complex structure is examined. The coupons were taken from the ACCS "plank" and were each designed and supported so as to respond in a different primary mode on impact: shear, transverse bending, and longitudinal bending. By reducing the geometrical complexity to a minimum, the material behaviour in each response mode dominated thus enabling a clearer understanding of the material. The coupon specimens were also modelled using FE analysis, therefore the simple geometry reduced the model size which had to be employed.

The impactor mass (10.8Kg) was kept constant throughout the tests and the impact energy altered by varying the impactor velocity (by altering the drop height) from very low energies up to final failure (penetration or "creasing" depending on the specimen).

The second-strike prevention system was employed, therefore it was possible to perform a detailed damage analysis on all the impacted specimens. In this way the initiation, propagation, and interaction of and between the main damage modes was studied from first

damage through to ultimate failure. The following support conditions and specimen geometry were employed for each of the three coupon tests.

4.3.3.1 Shear Coupon

Exactly the same coupon geometry and support conditions were employed for these test as was used for the preliminary and strain-rate tests (see section 4.3.1.1). The clamped supports introduced high shear forces, hence the coupon's name.

4.3.3.2 Transverse Coupon

Specimens 135mm by 170mm were cut from the ACCS "plank" and simply supported, with a span of 140mm, as shown in Figure 4.8. This cross-section responded as if it was a transverse flexural test. The specimen was stiff in the longitudinal direction due to the stiffeners and UD fibres, whilst being relatively compliant in the transverse direction because the only fibres in this direction were those randomly oriented in the CFM plies. The impact site was exactly at the centre of the upper surface of the coupon.

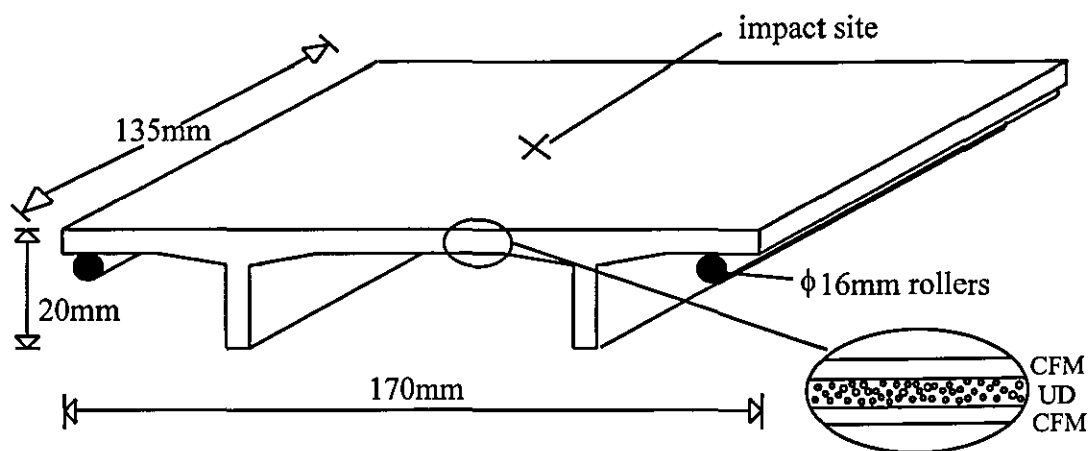


Figure 4.8 Transverse coupon geometry and support conditions.

4.3.3.3 Longitudinal Specimen

Plates 135mm by 76mm were cut from between the webs of the "plank" and simply supported, with a span of 120mm, as shown in Figure 4.9. The unidirectional fibres were parallel with the long edge of the coupon, therefore on central impact, the specimen flexed primarily in the longitudinal direction. The impact site was again central on the coupon.

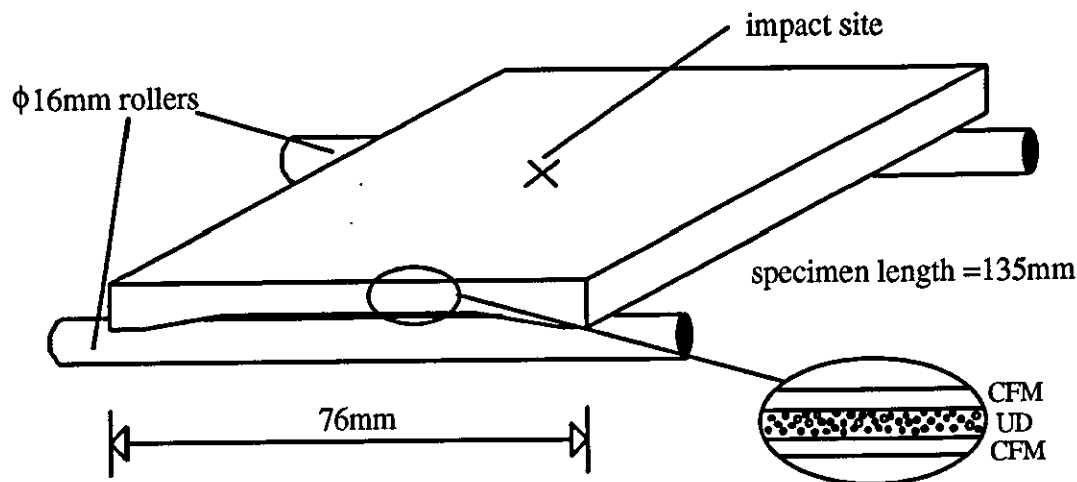


Figure 4.9 Longitudinal coupon geometry and support conditions.

4.3.4 Box Section Tests

The box sections consisted of either three- or five-box sections cut from the ACCS "plank", and therefore consisted of the inner and outer skins joined by the webs. The box sections are the unit cell from which the plank is built. The three-box section was 200mm wide by 255mm long, whilst the five-box section was 200mm by 425mm. Both were simply supported on 16mm diameter rollers midway between the webs of the end boxes (span = 170mm and 340mm as shown in Figures 4.10 and 4.11 respectively).

Three different series of tests were performed on each section by altering the position of the impactor strike as described below, along the same principles as Phan and Kesack¹⁹⁷ and Cheung et al⁹⁹ in their work on residual strength and damage growth of impacted stiffened composite panels respectively.

4.3.4.1 "Central" Impact Site

The impactor struck the box section precisely mid-way between the webs of the central box, which was therefore halfway along the length of the section, and is shown as impactor position (a) in Figures 4.10 and 4.11.

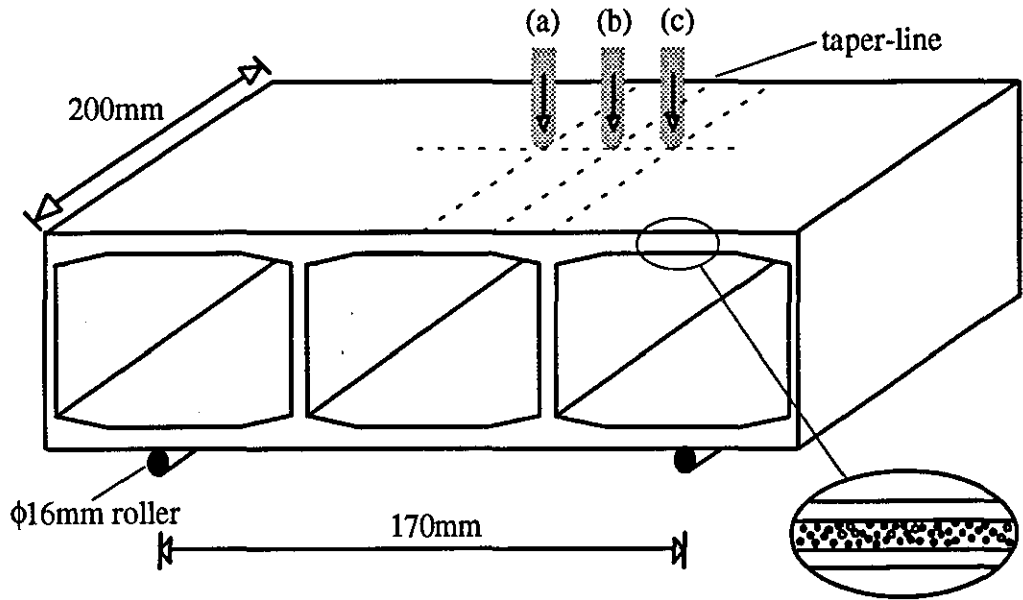


Figure 4.10 "Three-box section" impact test geometry and support conditions.

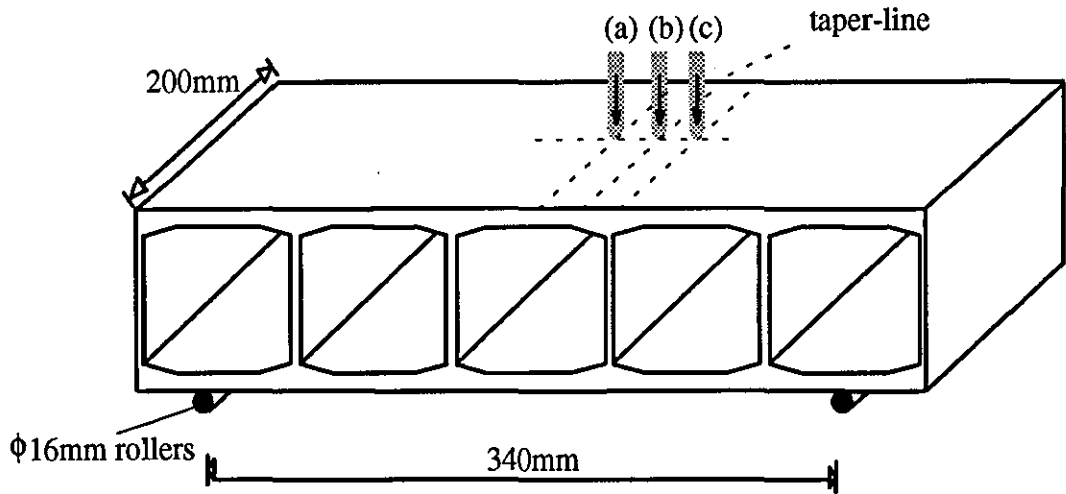


Figure 4.11 "Five-box section" impact test geometry and support conditions.

4.3.4.2 "Intermediate" Impact Site

The impactor struck the box section precisely over the taper-line which was one quarter of the distance from the right central web to the left central web, and is shown as impactor position (b) in Figures 4.10 and 4.11.

4.3.4.3 "Web" Impact Site

The impactor struck the box section precisely over the right central web, and is shown as impactor position (c) in Figures 4.10 and 4.11.

4.3.5 Full "Plank" Cross-Section Tests

Five tests were performed on the full "plank" cross-section whilst simultaneously recording the event impact with a high speed video camera. Only a small number of tests could be recorded due to the limited time for which the camera was available.

The mass of the impactor used was 10.8Kg with a 20mm diameter tup. The plank was simply supported on 16mm diameter rollers as in Figure 4.12 which positioned the support rollers directly underneath the two outer webs.

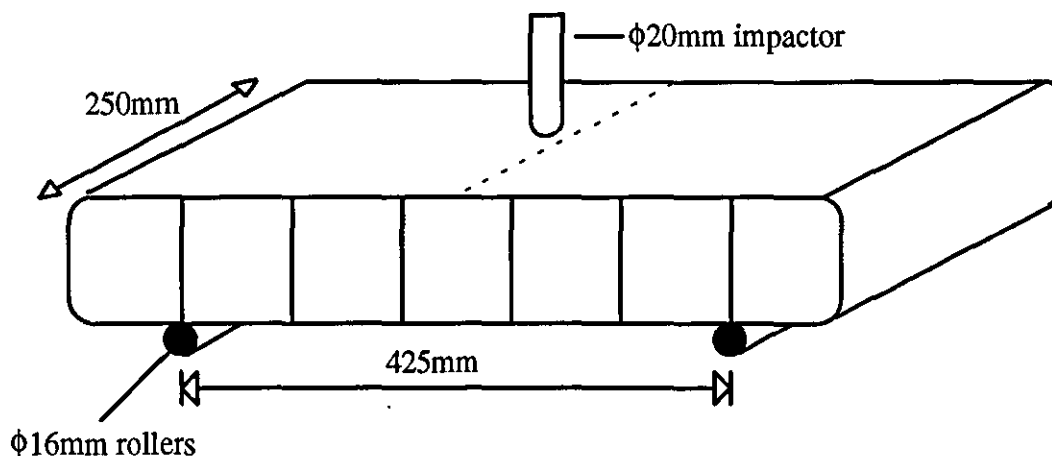


Figure 4.12 ACCS "plank" support conditions for high speed video camera impact tests.

The camera view was either set to show the whole plank cross section and therefore the global deformation of the plank under impact or the view was zoomed in on the local deformation directly under the impactor. The objective of the test was to provide a visual correlation of the global and local dynamic response of the plank with the recorded force-time traces.

Chapter 5

Finite Element Analysis of Impact

The literature review clearly highlighted that a model was required to relate coupon test results to impacts on real structures. In order to accurately model the impact event, a computational method must be employed due to the complexity of geometry, the dynamic nature of the local/global stress field produced, and damage initiation and propagation. The finite element method was chosen as the basis for the predictive analysis as it is the most powerful and commonly used tool.

In order to model an impact event above the initial damage threshold energy of the structure, a progressive failure approach must be undertaken. The damage must be modelled within the analysis as it occurs, because it alters the dynamic response of the structure and initiates further damage. However, the first requirement is for a representative elastic model to be constructed which is then the foundation upon which the various damage models can be added. The three coupon experimental impact tests provided relatively simple geometry and support conditions to be analysed, therefore the elastic finite element models focused on these specimens.

The remainder of the chapter deals with the development of the interface element modelling technique to simulate delamination. Models are described to verify the two- and three-dimensional interface elements under Mode I, Mode II and mixed-mode loading. The final section details analyses of intralaminar crack induced delamination on the ACCS "plank".

5.1 Elastic Impact Models

The models were created for comparison with the experimental impact test data at the lowest energies tested - where the least damage was induced. In order for the elastic model to be compatible with interface element modelling, it was necessary to define the layers discreetly and the out-of-plane stiffnesses are important when solving transverse impact problems, therefore the use of solid elements was required.

5.1.1 Geometric Configurations and Boundary Conditions

Three coupon models were created using precisely the same dimensions as the experimental impact test coupons as described in section 4.3.3. A total laminate thickness of 3.30mm was employed with the CFM and UD layers being 0.89mm and 1.52mm respectively. Each specimen had two planes of symmetry therefore a quarter model was analysed for computational efficiency, with symmetry boundary conditions being applied to the relevant planes. Figures 5.1 to 5.3 show the meshes employed, and support conditions, whilst Figure 5.1 also shows the symmetry boundary conditions applied.

The longitudinal and transverse test coupons were simply supported and this was modelled by restraining the supported edges (Figures 5.1 and 5.2). The shear coupon was clamped, which was modelled by restraining out-of-plane motion only on the top and bottom surfaces at two concentric rings of radius 30 and 40mm from the point of impact, thus modelling the 10mm anvil support ring (Figure 5.3).

In the impact tests the mass contacted the sample via a hemispherical impactor. A quarter model of the tip of the impactor was therefore employed, as shown in the Figures, with symmetry boundary conditions. Only the tip, i.e. the contacting area, was modelled in order to minimise the number of elements. The impactor was initially positioned 0.1mm above the specimen surface.

5.1.2 Modelling Strategy

(a) Elements

The 8-noded HX8 brick element was employed enabling orthotropic material properties to be assigned to it. The tip of the impactor was also modelled using standard HX8 solid elements.

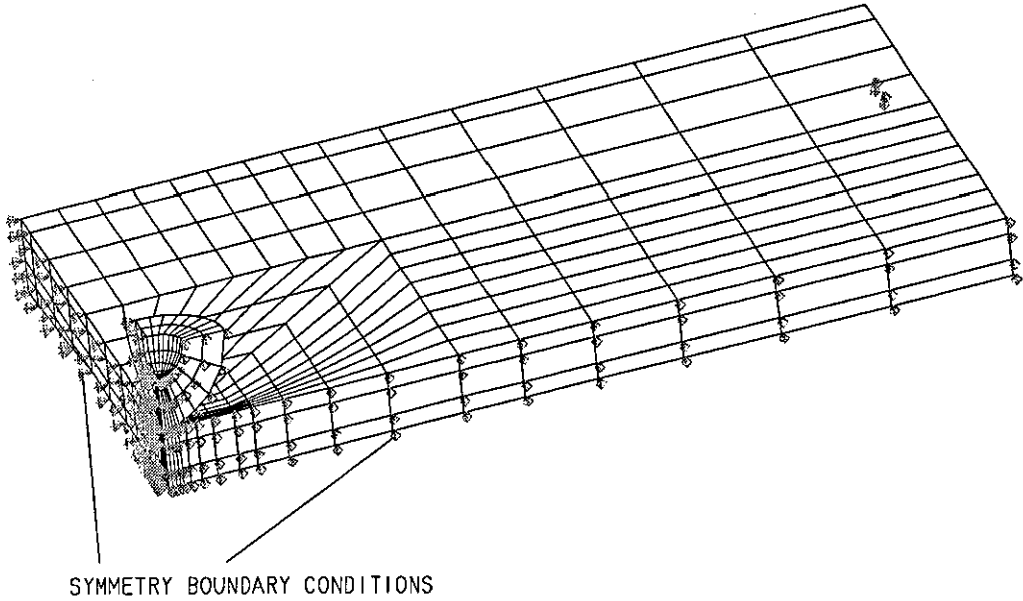


Figure 5.1 Mesh, symmetry supports, and boundary conditions for the longitudinal coupon model.

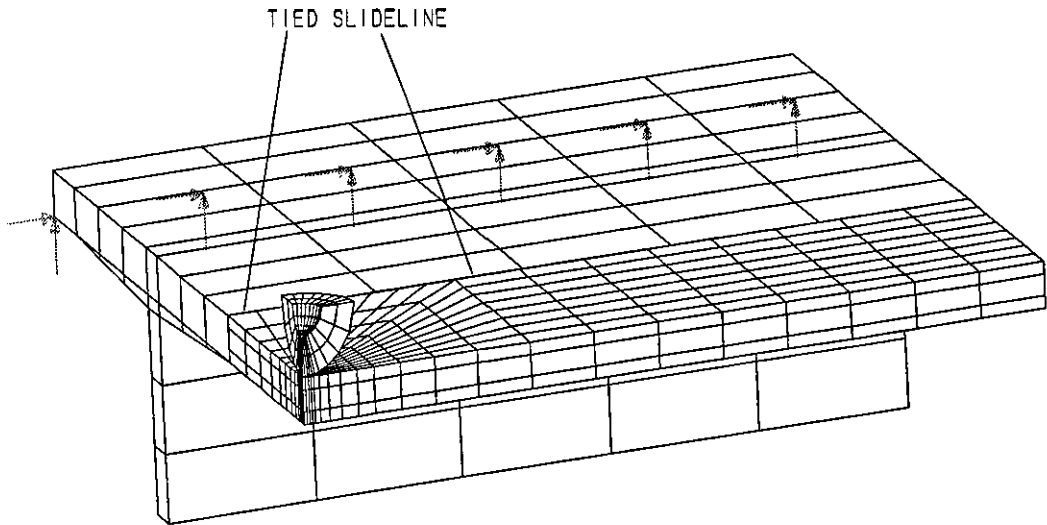


Figure 5.2 Mesh and supports for the transverse coupon model showing the tied slideline surface.

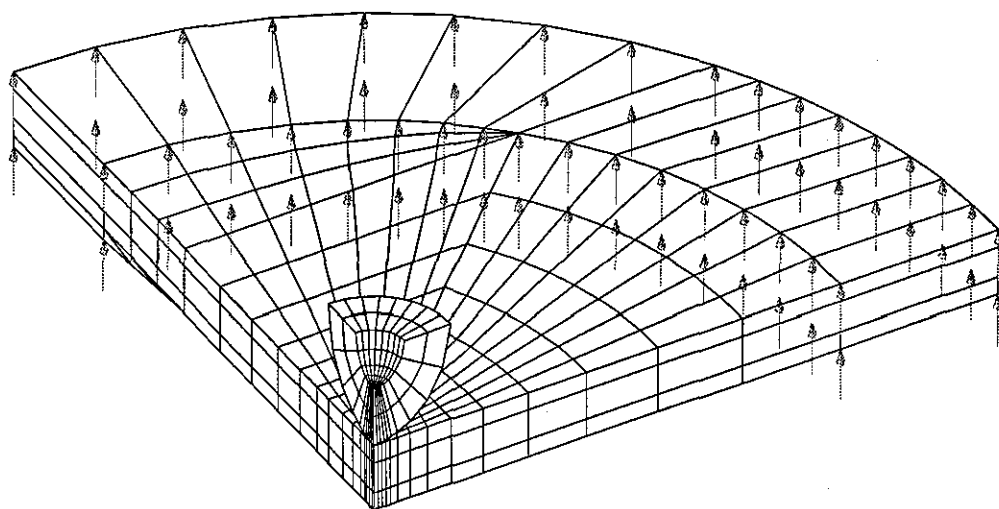


Figure 5.3 Mesh and supports for the shear coupon model.

(b) Mesh

The models employed one brick element per layer (i.e. three through the constant thickness section and four through a tapered section). The web in the transverse model was represented by one element through the thickness, which was satisfactory as the web was parallel to the plane of bending and therefore not contributing greatly to the stiffness response of the specimen.

A mesh density convergence exercise was performed, which involved three areas of mesh discretisation for the elastic analyses:

- (1) the impactor mesh needed to be fine enough to model the curvature of the tip and also to provide sufficient contacting nodes for the contact slideline to operate effectively.
- (2) the mesh on the coupon directly under the impactor had to have the same density as on the tip of the impactor for the contact slideline to operate effectively.
- (3) the mesh defining the coupon away from the contact region needed to be refined to reduce CPU time.

Following this convergence exercise (section 8.1.1), the impactor tip was modelled in each case with 160 elements, the shear coupon with 648, the transverse coupon with 714, and the longitudinal coupon with 640 elements.

(c) Slidelines

The slideline facility within LUSAS was employed in two different ways. Contact slidelines were assigned to the two contacting surfaces to enable the software to model the contact between impactor and coupon. The tied slideline facility was used to reduce the number elements by eliminating the need for a transition mesh between two areas of varying mesh refinement. This option was used in the transverse coupon model, as it was the largest, and most complex specimen. An exercise in varying the slideline stiffness in the transverse coupon model was performed in order to quantify the effect.

5.1.3 Material Properties

The HX8 elements representing the impactor tip were given the following isotropic material properties, $E = 210,000 \text{ N/mm}^2$, $\nu = 0.3$, and $\rho = 4.90\text{e}7 \text{ Kg/m}^3$ to $4.92\text{e}7 \text{ Kg/m}^3$. The density was artificially high to represent one quarter of the mass of the impactor, and was calculated from the experimental impactor mass and the volume of the impactor in the model. Changing the density of the impactor in the model therefore effectively altered the impactor mass.

Chapter 6 describes the results from the static mechanical tests and the reduction of the laminate properties to determine both the CFM and UD ply properties as listed in Table 5.1. In LUSAS different tension and compression ply properties cannot be assigned, therefore the values used below were obtained from the tensile and flexural testing.

	CFM	UD
E_{11}	7626 N/mm ²	49,548 N/mm ²
E_{22}	7626 N/mm ²	5600 N/mm ²
E_{33}	5600* N/mm ²	5600* N/mm ²
G_{12}	2926 N/mm ²	2438 N/mm ²
G_{13}	1203* N/mm ²	2438* N/mm ²
G_{23}	1203* N/mm ²	2135* N/mm ²
ν_{12}	0.3033	0.3115
ν_{13}	0.3033*	0.3115*
ν_{23}	0.3033*	0.3115*
Density	0.186E-8 Kg/mm ³	0.186E-8 Kg/mm ³

Table 5.1 Material Properties for the CFM and UD plies.

The values marked with an * are assumed values as through-thickness testing was not possible. Various assumptions were tested, with only a relatively small effect on the elastic

response, therefore the following was employed: For the UD layer, from transverse isotropy assumptions (see section 2.5.3): $E_{33} = E_{22}$, $G_{13} = G_{12}$, $G_{23} = E_{22}/2(1+\nu_{23})$, and as ν_{23} was unknown, two-dimensional assumptions gave $\nu_{23} = \nu_{13} = \nu_{12}$. For the CFM layer the matrix shear modulus was employed for G_{13} , and G_{23} , and $\nu_{23} = \nu_{13} = \nu_{12}$.

5.1.4 Loading

The impactor was given an initial velocity corresponding to the impact velocity of the test being simulated. The impactor contacted then deflected the coupon, and after reaching peak deflection, was flicked off the surface of the plate as the coupon flexed back to its start position. A variety of initial velocities were tested for each coupon model ranging from below the lowest TIE experimentally tested for that coupon, to a mid-range impact test velocity.

5.1.5 Software

(a) Pre- and Post-Processing

The models were created and results analysed using MYSTRO mounted on a SUN server at Loughborough University. Pre-processing involved 3D model creation, meshing, applying boundary conditions and material, loading, and slideline. Post-processing was employed, amongst other things, to graphically display the deformed mesh and to plot force-time, force-deflection graphs for the impact event.

(b) Analysis

Each analysis was performed using LUSAS, also mounted on the SUN server at Loughborough University. Step-by-step implicit dynamic analyses were performed to model the impact tests with a time step varying from 0.06 to 0.2ms.

An implicit, rather than explicit, method was employed which therefore required inversion of the stiffness matrix at every time step and was therefore relatively computationally expensive, but was conditionally stable (i.e. for a linear elastic material, convergence to a solution is guaranteed independent of the time step). The implicit method allows the use of a larger time step which is acceptable when the low frequency components govern the problem response as in the high mass low velocity impacts being considered. The Hilber-Hughes integration scheme was employed within the implicit dynamic analyses, which is a dissipative algorithm, providing high dissipation in the highest frequency modes which are not integrated accurately anyway due the relatively long time step. No numerical dissipation occurs in the lower modes governing the response of the structure. The default

convergence criterion were adopted throughout the exercise. Further details regarding the solution techniques employed are contained in the LUSAS user and theory manuals^{198,199}.

5.2 Development of the Damage Model - Delamination

Unless the initiation and propagation of damage is modelled accurately, a FE analysis of an impact above the elastic limit will predict much higher forces generated than would be seen in reality (note the non-linearity of the peak force-TIE graphs in Chapter 7). The experimental program provided detailed information regarding damage modes and interactions for the three coupon tests, from which it was apparent that there were four damage mechanisms which should be modelled:

- (a) **transverse and shear matrix cracking**
- (b) **tensile cracking of the CFM layer**
- (c) **delamination** - induced by transverse matrix or shear cracking in the UD layer or lower CFM cracking.
- (d) **UD fibre breakage** - signalled imminent "creasing" in the longitudinal test.

Modelling (a), (b) and (d) requires an intralaminar brittle cracking model and (c) requires an interlaminar failure model. Developing a brittle damage model was beyond the scope of this research, but work is being progressed at Imperial College to achieve this goal. This research has therefore concentrated on an interlaminar failure model.

A newly developed type of interface element was added to the LUSAS finite element library. The formulation of the element is described in detail in the PhD thesis of Hellweg¹⁷⁶. This project has involved research into the behaviour of this element under various loads and understanding the effect of the parameters used to define the highly non-linear material model in order to implement the element into an impact analysis.

The element, of zero thickness, can be placed between layers in the laminate model. For two-dimensional problems, a quadratic line element is employed whilst in three dimensions, a plane element is used (Figure 5.4). Both elements consist of sets of double nodes which obey separate material models for the three modes of fracture as shown in Figure 5.5.

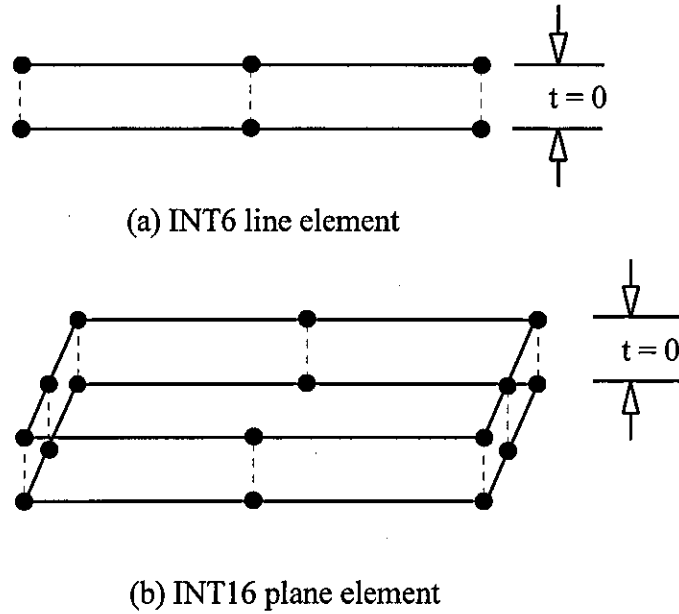


Figure 5.4 One- and two-dimensional interface element node structures.

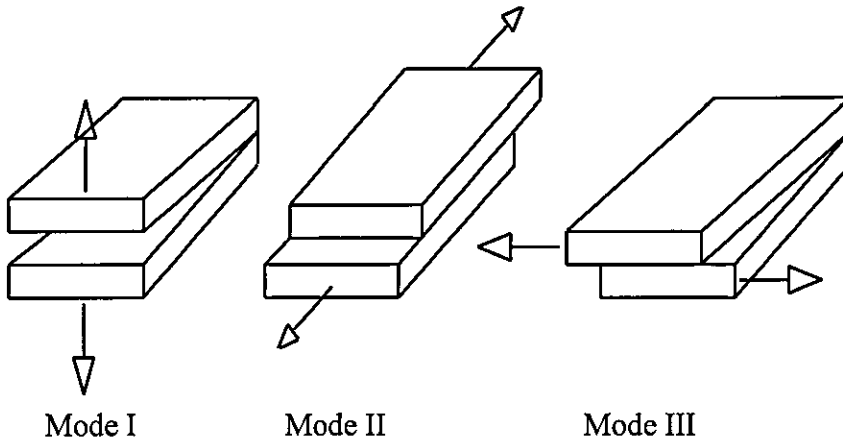


Figure 5.5 The three modes of delamination.

The basic material model form is illustrated in Figure 5.6 showing the three material parameters which are assigned to the interface element for each mode: fracture energy (critical strain energy release rate - G_c), strength (S), and relative thickness (t_{rel}). The fracture energy or critical strain energy release rate, can be obtained from experiment, however the strength value in the material model is less easy to define physically. The element has a very high initial stiffness (strength/relative thickness) to avoid deformation prior to the initiation of failure and in compression to avoid inter-penetration of elements either side of the interface. The fracture energy, G_c , is absorbed before failure finally occurs, with the overall shape of the model dictating the plastic behaviour

(deformation prior to failure). Crack initiation and propagation is highly non-linear and for a robust solution the material model shape is critical. The material model for each mode is defined separately but can be coupled in an analysis.

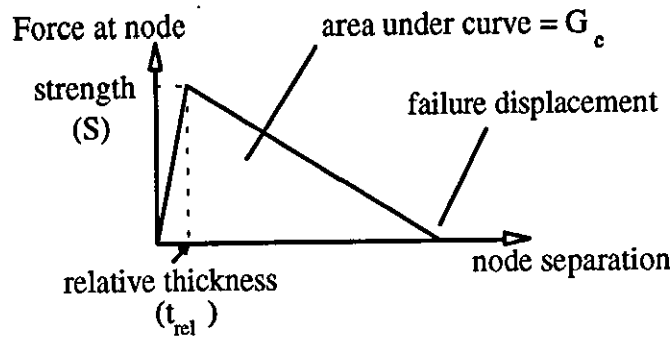


Figure 5.6 The material model for the interface element.

Figure 5.7 illustrates how the node pairs behave on application of a Mode I load. As the force on the node pair increases, they move up the very stiff linear portion of the material model (node d in Figure 5.7) and the relative displacement between the two nodes is still very small. Once the defined strength, S_I has been exceeded the node pair soften (node c). Node b in Figure 5.7 has just failed and can carry no load and so the two nodes have completely separated, as has node a, which has also failed. Therefore, as the external load is increased the crack will absorb energy as defined by G_c and will extend along the interface.

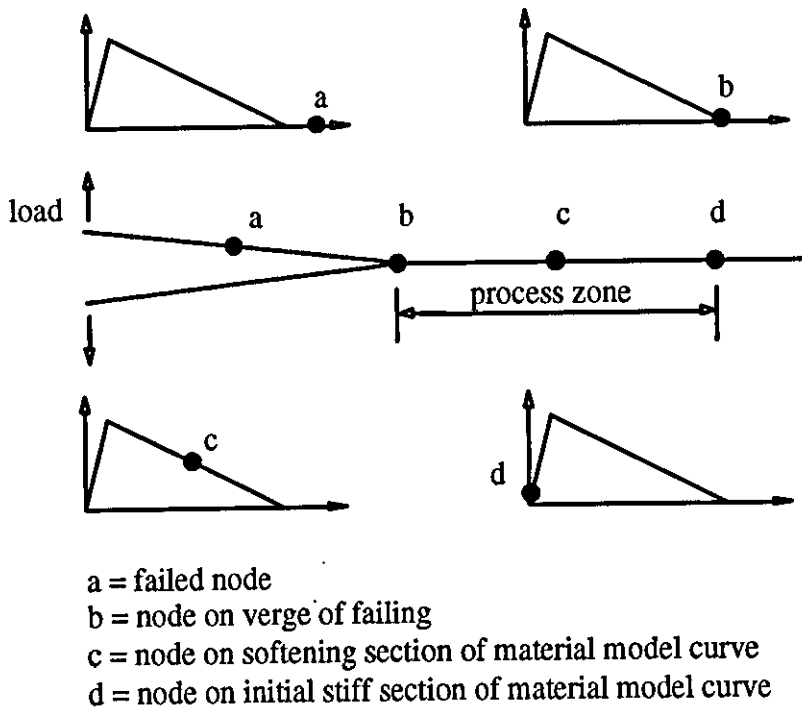


Figure 5.7 Nodal movement through the material model under Mode I loading.

The interface element formulation requires the parent material (i.e. elements defining the bulk of the test specimen) to be integrated using fine numerical integration (option 18) and the root selection for the arc length solution switched to that of the minimum residual norm (option 261), which overcomes potential convergence problems in trying to follow a non-linear load path¹⁷⁶. These options have therefore been employed in all the models.

Initially, the research involved investigating the effect of varying the material properties and mesh density. An analysis of the basic mechanics of node behaviour provided a framework to employ the element correctly. In "real" structures the loading is generally a complex combination of modes. For simplicity, the element has been verified initially under pure Mode I and Mode II loading, and finally under controlled ratio mixed-mode loading.

5.2.1 Two-Dimensional Models

There were two interface elements, INT6 and INT16, for two- and three-dimensional models respectively. To minimise complexity, the INT6 element was investigated first in two-dimensional models. The following sections describe the models used to research the element's nodal behaviour under each mode of loading.

5.2.1.1 Test for Mode I Delamination - The DCB Model

The double cantilever beam (DCB) test provides a pure Mode I loading (section 3.4.4.1), and so was modelled to investigate the element's Mode I response. A two-dimensional DCB model 100mm long and 3mm thick was created (Figure 5.8). The initial crack length was 30mm at the mid-thickness of the beam, with INT6 elements positioned along the centreline of the beam.

A prescribed displacement (or load) was applied to the cracked end of the beam as shown in Figure 5.8. QPN8 plane strain elements with the isotropic material properties (chosen for ease of comparison with the three-dimensional models - section 5.2.2) listed below, were employed to model the beam. The material properties were as follows :

Parent Material: $E_{11} = 135,500 \text{ N/mm}^2$, and $\nu_{12} = 0.25$.

Interface 1: $G_{Ic} = 0.5 \text{ to } 16 \text{ N/mm}^2$ $S_I = 14.25 \text{ to } 57\text{N}$, $t_{rel} = 1\text{e-}3 \text{ to } 1\text{e-}7\text{mm}$, and mode interaction = uncoupled.

The beam was regularly meshed with four QPN8 elements through the thickness and from fifty to two hundred along the beam length. The same number of INT6 elements were employed along the centreline of the beam as there were QPN8 elements along the length.

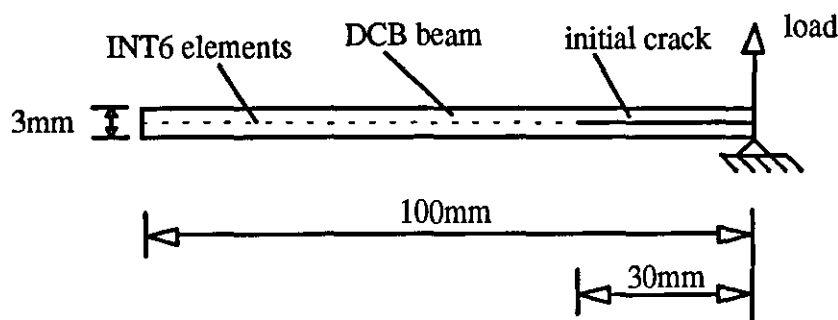


Figure 5.8 The DCB model for the analysis of Mode I response of the INT6 element.

5.2.1.2 Test for Mode II Delamination - The ENF Model

In order to verify the behaviour of the interface element under Mode II loading, a model of the end notched flexure (ENF) specimen was created as shown in Figure 5.9. The ENF specimen is the most effective test for pure Mode II loading as explained in section 3.4.4.2.

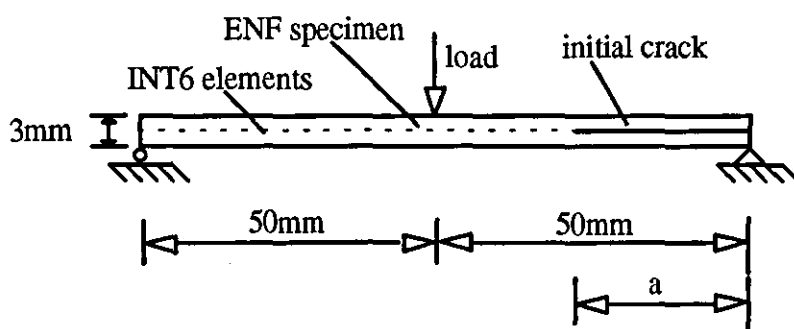


Figure 5.9 The ENF model for analysis of Mode II response of the INT6 element.

The ENF beam was modelled with QPN8 elements with isotropic material properties to model the body of the beam, and INT6 interface elements positioned along the centreline of the beam. The initial crack was modelled by placing INT6 elements with very low G_{Ic} and strength values, so that on the first load increment they all failed thus creating an initial crack of the desired length. The remaining interface elements were then given material properties appropriate to the test under consideration. The initial crack length, a , varied

from 15 to 35mm. The parent material properties employed in these tests were as for the DCB models with the following interface properties:

Interface 1*: $G_{IIC} = 1e-10$ N/mm, $S_{II} = 1e-3$ N, $t_{rel} = 1e-7$ mm, and mode interaction = uncoupled.

Interface 2*: $G_{IIC} = 0.5$ to 4 N/mm, $S_{II} = 10$ to 80 N, $t_{rel} = 1e-3$ to $1e-7$ mm, and mode interaction = uncoupled.

[*Interface 1 refers to the interface which failed on the first increment forming the initial crack. Interface 2 was the interface along which the initial crack grew.]

In all the models (except the mesh density tests) the mesh consisted of one hundred elements along the beam length, and two elements through the thickness, with one hundred interface elements along the beam centreline. The load was applied centrally using displacement or load control, whilst the beam was simply supported in the conventional way at either end.

5.2.1.3 Test for Mixed-Mode Delamination - The MMB Model

The mixed-mode bending (MMB) method proposed by Reeder and Crews¹⁷⁸ was adopted (Figure 5.10). The test method is a combination of the DCB test, inducing Mode I, and the ENF test inducing Mode II and can be used to measure delamination toughness over a wide range of Mode I/Mode II ratios. A single load, P is applied via the loading arm (Figure 5.10(a)), which results in the central and end load as shown in Figure 5.10(b). For fixed L , the length e , dictates the ratio of the two loads, and therefore the ratio of Modes I and II at the crack front. Reeder and Crews¹⁷⁸ reported the relationships in Table 5.2 (for $L = 50$ mm).

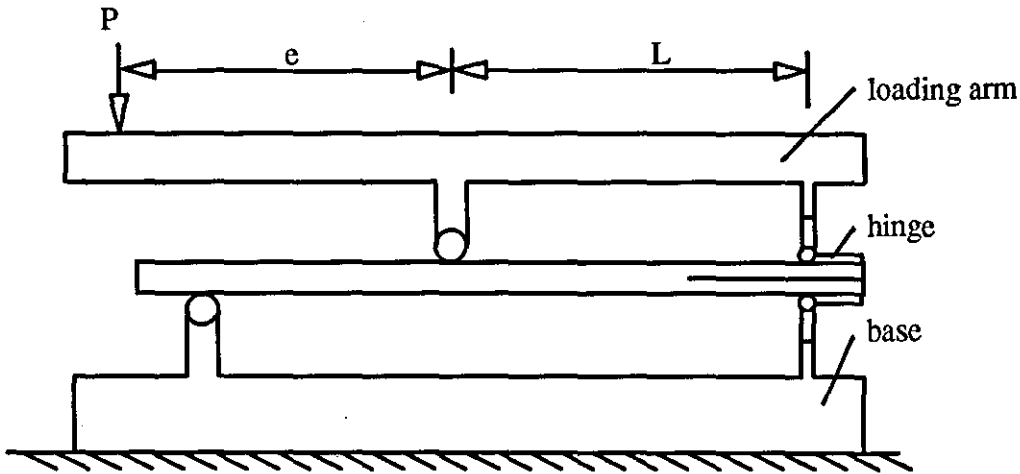
An analysis of the loading from Figure 5.10(b) reveals the following relationship between the total applied load, P and the loads X and Y .

$$\text{Mode I load, } Y = \frac{(3e - L)}{(4L)} P \qquad \text{Mode II load, } X = \left(\frac{e + L}{L} \right) P$$

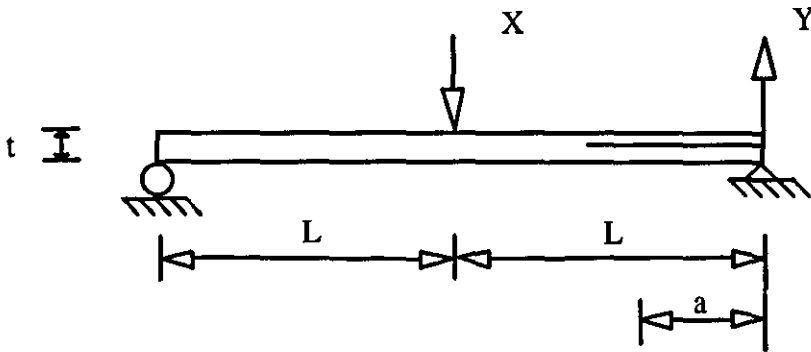
From the FE analysis, the total load, P was recovered and using these equations the Mode I and Mode II forces were calculated. In all the graphs drawn in the Chapter 8, the separate Mode I and II loads were therefore employed.

e (mm)	Load Ratio, B (X/Y)	G_I/G_{II}
95	1.53	4
75	1.67	3
60	1.83	2
41	2.22	1
27	2.85	1/4

Table 5.2 Relationship between e, load, and mode ratio for the MMB tests.



(a) MMB test apparatus



(b) The MMB model

Figure 5.10 Mixed-mode bending (MMB) test apparatus, specimen and loading.

The mode coupling option was selected which implements a linear combination of Modes I and II (Figure 5.11). Reeder and Crews²⁰⁰ in their analysis of various coupling models, concluded that for the epoxy systems under investigation, a bi-linear failure envelope modelled their experimental data most closely as they obtained a change in failure mechanism at a mode ratio of 1/1 but was relatively linear either side of this point (Figure

5.11). However, linear coupling is the simplest model and in the absence of more detailed material information regarding mode coupling, was sufficient in this case.

A model of the MMB test was created along similar lines to both the ENF and DCB models. Figure 5.10(b) shows the basic model employed with one hundred equally spaced QPN8 elements were employed along the 100mm length with four elements through the thickness of 3mm. Seventy-five INT6 interface elements were positioned along the horizontal centreline, and an initial crack of 25mm length was used throughout. The isotropic material properties described for the previous two models were assigned as the parent material properties, with the interface properties as below:

Interface - Mode I: $G_{Ic} = 2 \text{ N/mm}$, $S_I = 15 \text{ to } 20\text{N}$, $t_{rel} = 1\text{e-}7\text{mm}$, and mode interaction = coupled.

Interface - Mode II: $G_{IIc} = 2 \text{ to } 3\text{N/mm}$, $S_{II} = 20 \text{ to } 40\text{N}$, $t_{rel} = 1\text{e-}7\text{mm}$, and mode interaction = coupled.

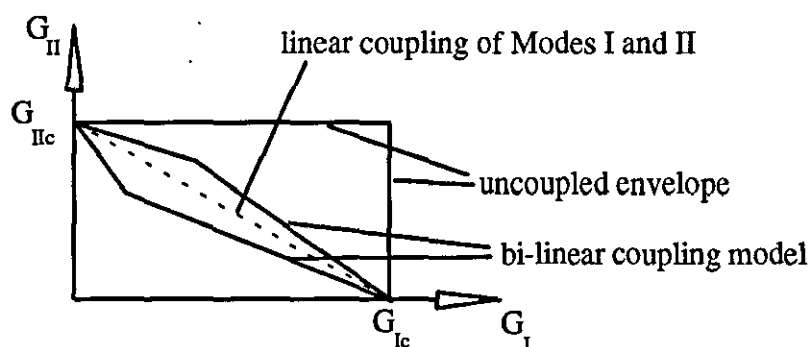


Figure 5.11 Failure envelope for coupling models for Modes I and II.

A concentrated load was specified at the end and centre of the specimen with the load ratio (X/Y) set at the desired value for the particular mode ratio being tested. To aid convergence a non-symmetric frontal solution method was adopted (option 64 within LUSAS).

5.2.2 Three-Dimensional Models

The three-dimensional models were created with 16-noded HX16 brick elements and the INT16 plane element to define the interface. Unless otherwise stated, the three-dimensional DCB, ENF, MMB models were identical to the two-dimensional models (including the parent material properties) but with a thickness of 1mm, allowing direct comparison with the two-dimensional tests.

5.2.2.1 Test for Mode I Delamination

In order to *minimise* the number of elements employed in the three-dimensional models, the DCB model length was reduced to 50mm with a thickness of 3mm, width of 1mm, and initial crack length of 15mm. Fifty elements were used along the length and two elements through the thickness, whilst the number of elements across the width was varied from one to four. A two-dimensional model of the same geometry was created for comparison with the three-dimensional results. A second model was also created, but with a width of 10mm in order to study the three-dimensional nature of the crack front. The number of elements across the width was varied in this case from one to six. The interface properties used in all the models were, $G_{Ic} = 4\text{N/mm}$, $S_{II} = 14.25\text{N}$, and $t_{rel} = 1\text{e-}7\text{mm}$.

5.2.2.2 Test for Mode II Delamination

The same geometry as for the two-dimensional models was employed with a width of 1mm and one element across the width. The interface properties were, $G_{IIc} = 4\text{N/mm}$, $S_{II} = 57\text{N}$, and $t_{rel} = 1\text{e-}7\text{mm}$.

5.2.2.3 Test for Mixed-Mode Delamination

The same geometry as for the two-dimensional models was employed with a width of 1mm and one element across the width. The interface properties were, $G_{Ic} = 4\text{N/mm}$, $S_I = 14.25\text{N}$, and $t_{rel} = 1\text{e-}7\text{mm}$, $G_{IIc} = 4\text{N/mm}$, $S_{II} = 57\text{N}$, and $t_{rel} = 1\text{e-}7\text{mm}$ for both modes. The modes were coupled as for the two-dimensional analyses.

5.2.3 Delamination in the ACCS "Plank"

Having verified INT6 and INT16 over a range of material data and mesh densities, this exercise was performed to assess the behaviour of the element with the experimental ACCS "plank" material data. This investigation was undertaken to check the use of the element's behaviour with genuine composite laminate elastic and failure data, and to develop a full material property interface definition for use in the impact induced delamination studies (section 5.3) for the "plank".

DCB, ENF, and MMB models were created with one hundred elements along the beam length. Both two and three-dimensional models were tested, with the three-dimensional models having a thickness of 1mm. The ACCS "plank" parent material properties employed were as follows:

Orthotropic plane strain: - $E_{11} = 25140 \text{ N/mm}^2$, $E_{33} = 6867 \text{ N/mm}^2$, $G_{12} = 2702 \text{ N/mm}^2$, $\nu_{12} = 0.3145$, $\nu_{23} = 0.1014$, $\nu_{13} = 0.3145$.

Orthotropic solid: - $E_{11} = 25140 \text{ N/mm}^2$, $E_{22} = 6867 \text{ N/mm}^2$, $E_{33} = 6867 \text{ N/mm}^2$, $G_{12} = 2702 \text{ N/mm}^2$, $G_{23} = 2438 \text{ N/mm}^2$, $G_{13} = 2438 \text{ N/mm}^2$, $\nu_{12} = 0.3145$, $\nu_{23} = 0.1014$, $\nu_{13} = 0.3145$.

G_{Ic} was set at 0.57 N/mm which was the average experimentally determined value (section 6.1.5 - where $J/m^2 = 10^{-3} \text{ N/mm}$) and strength values of 7 and 14N were tested in accordance with the findings of section 8.2.1.1. Only the 7N test was repeated for the three-dimensional model. Also in line with the initial findings, the relative thickness was set at $1e-7 \text{ mm}$.

From the experimental tests (section 6.1.5.2) a G_{Ic} value between 0.35 N/mm and 0.8 N/mm was obtained, therefore for this exercise, G_{Ic} was set at 0.5 N/mm . Three mixed-mode models were run with mode ratios of 1/4, 1 and 4/1, with $G_{Ic} = 0.57 \text{ N/mm}$, $S_I = 14 \text{ N}$, $G_{IIc} = 0.5 \text{ N/mm}$, $S_{II} = 15 \text{ N}$, and $t_{rel} = 1e-7 \text{ mm}$ for both modes.

5.3 Non-Linear Impact Models

As explained in Chapter 7, in the experimental impact tests all the delaminations were initiated by a stress concentrating crack. As explained previously, a brittle failure model was not available, therefore a pre-crack was inserted in the model to provide the stress concentration to initiate delamination. This crack was created by providing free surfaces at the correct location within the model. The same approach was carried out by Liu²⁰¹ who loaded pre-cracked models to test his delamination growth model in graphite epoxy under quasi-static transverse loads.

Ideally the models created would have been based on the coupon specimens from the experimental tests to allow qualitative comparisons to be drawn, however this was not practical for two reasons. Firstly, the number of elements required would be far too large for the computer power available resulting in unmanageable run times. Secondly, comparisons would be limited due to the lack of a brittle crack model. Therefore, simple models were chosen based on the "plank" geometry to represent impact induced delamination growth from both bending and shear cracks. The ACCS "plank" material properties were employed as described in section 5.2.3.

During the creation of these models, several more problems were encountered. When contact sidelines were employed option 261 could not be used, which necessitated a much

smaller step size. More importantly, option 64 cannot be employed during a dynamic analysis, resulting in insurmountable convergence problems under dynamic loading therefore only static loading was considered.. Meshing difficulties were also encountered in three-dimensional models, whereby graded meshes could not be employed, and adjacent volumes with and without interface elements created problems. These difficulties are currently being resolved at FEA Ltd.

The two-dimensional models employed QPN8 and INT6 elements, whilst the three-dimensional models used HX16 and INT16. Loading for the two-dimensional models was via a 10mm diameter impactor, which was given a prescribed displacement, and contact with the beam was modelled via contact slidelines. To maintain manageable run times for the three-dimensional models, a concentrated load was applied directly to the model to simulate the contact of the impactor tip.

5.3.1 Lower Interface Delamination Induced by Longitudinal Bending

This model was designed to simulate longitudinal bending in the ACCS "plank", with lower interface delamination growth being induced from the lower CFM crack as reported in the experimental work. The crack was situated in the lower layer as shown in Figure 5.12. Models with pre-crack but no delamination, and no pre-crack were also run for comparison. An identical three-dimensional model was also created, but with a width of 60mm, the lower CFM crack closed at one end, and a half model employed taking advantage of symmetry.

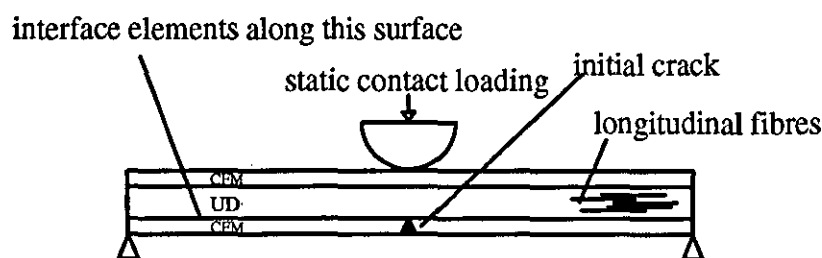


Figure 5.12 Two-dimensional model for lower interface delamination under longitudinal bending.

5.3.2 Upper Interface Delamination Induced by Transverse Bending

This model was created to simulate the experimentally observed delamination growth at the upper interface due to transverse bending associated with lower CFM cracking and matrix cracking of the UD layer. In this case a crack through both the UD layer and lower CFM

layer was included in the model (Figure 5.13) and the interface elements situated along the upper interface. Uncracked and non-delamination growth models were also run as above. The three-dimensional half-model was created with a width of 60mm, and the lower CFM crack closed at one end.

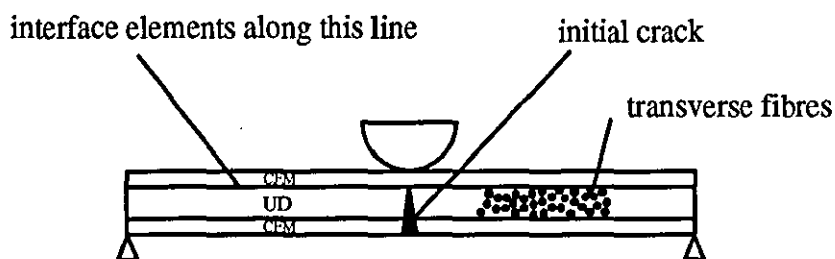


Figure 5.13 Two-dimensional model for upper interface delamination under transversal bending.

5.3.3 Lower Interface Delamination Induced by Shear Loading

A half model was used in this case to reduce the model size (Figure 5.14). Several models with varying shear crack positions relative to the centreline were tested. Interface elements were placed along both interfaces and the model loaded as for the above two cases. Clamped supports were employed to generate the shear loading. A three-dimensional quarter model, was also created representing a total width of 60mm and with the shear crack closed at one end.

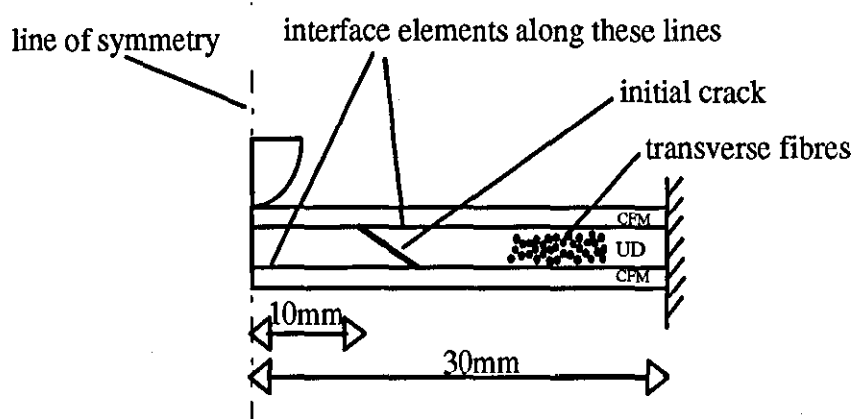


Figure 5.14 Two-dimensional half model for shear induced lower interface delamination.

PART III

RESULTS AND DISCUSSION

Chapter 6

Static Mechanical Test Results and Analysis

This chapter contains the results from the tests described in Chapter 3 and the analysis of the laminate results to obtain the individual ply properties for the material definition in the FE models. Definitions of the statistics employed are contained in Appendix III, whilst the individual specimen test results for all the static mechanical tests are contained in Appendix IV. Appendix IV also contains results from the compression and interlaminar shear strength tests which were not employed in the FE analysis. Failure strengths were also noted for all the tests performed and Appendix IV also contains an analysis to calculate the ply strengths from the laminate failure strengths. This extra data is included in the Appendix so that it may be employed as modelling strategies are refined in follow-on projects

6.1 Static Mechanical Test Results

6.1.1 Tensile Tests

6.1.1.1 Longitudinal

A summary of the data from this series of tests is contained in Table 6.1. Figure 6.1 contains typical stress-longitudinal strain and stress-transverse strain curves. The slope of the stress-longitudinal strain graphs (Figure 6.1(a)) steadily decreased which is illustrated by the slopes calculated between 0-0.25% (initial modulus), 0.25-1% and 1-1.6% strain in Table 6.1. It was concluded that the CFM layer introduced the non-linearity as the UD layer can be assumed to be linear to failure in the longitudinal direction⁸⁰. The Poisson's ratio was calculated as described in section 3.4.1 with the results showing good repeatability.

	Average	Coefficient of Variation (%)
Initial Modulus (N/mm ²)	25,139	6.37
Strength (N/mm ²)	423.00	5.69
Failure Strain (%)	1.84	3.53
Slope (0.25-1.0 % strain)	23,673	5.97
Slope (1.0-1.6 % strain)	22,476	6.12
Poisson's ratio	0.3145	4.43
Total Specimen Thickness (mm)	3.15	3.52
% Thickness of each CFM ply	29.09	22.3
% Thickness of the UD ply	41.82	18.5
Total number of specimens	14	

Table 6.1 Longitudinal tensile results from specimens (Figure 3.7) taken from the ACCS "plank".

All the specimens failed in the gauge length and the strength was calculated from the highest load supported by the specimen. Tests at very low crosshead speed (0.5mm/sec.) showed that the CFM layers were the first to fail, followed by the UD. The secondary failure of the central ply was characteristically brush-like with the longitudinal fibres becoming separated as fibre breakage occurred.

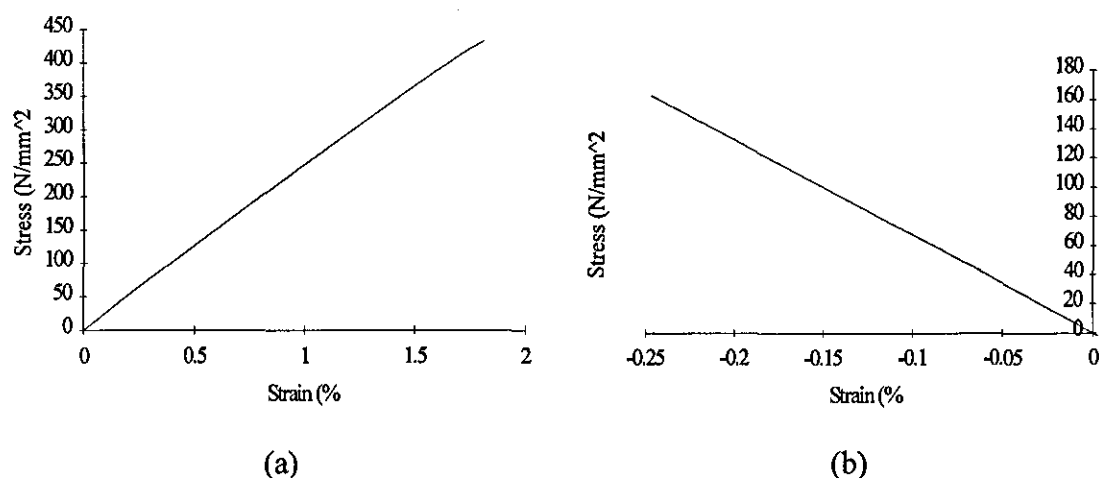


Figure 6.1 A typical stress-strain (a) and stress-transverse strain graphs (b) for a longitudinal tensile specimen taken from the ACCS "plank".

6.1.1.2 Transverse

Table 6.2 contains a summary of the data from this series of tests with Figure 6.2 containing an example of a stress-strain curve.

	Average	Coefficient of Variation (%)
Initial Modulus (N/mm ²)	6,867	7.31
Strength (N/mm ²)	45.43	8.63
Failure Strain (%)	1.46	8.78
Slope (0.4-1.2 % strain)	2,674	12.3
Poisson's ratio (calculated)	0.086	-
Position of Knee: stress (N/mm ²)	19.97	8.27
Position of Knee: strain (%)	0.358	8.80
Total Specimen Thickness (mm)	3.33	3.17
% Thickness of each CFM ply	25.50	17.54
% Thickness of the UD ply	49.00	19.36
Total number of specimens	15	

Table 6.2 Transverse tensile test results from specimens (Figure 3.8) taken from the ACCS "plank".

The stress-strain curve in Figure 6.2 can be approximately represented by an initial linear section, a "knee", and a further linear section. The statistics in Table 6.2 indicate that the occurrence of the "knee" in the stress-strain curve and its position was very repeatable. The position of the knee was approximated by calculating the intercept of the two best fit straight lines on either side, as illustrated graphically in Figure 6.3. The initial modulus was calculated using points lying from 0-0.15% strain.

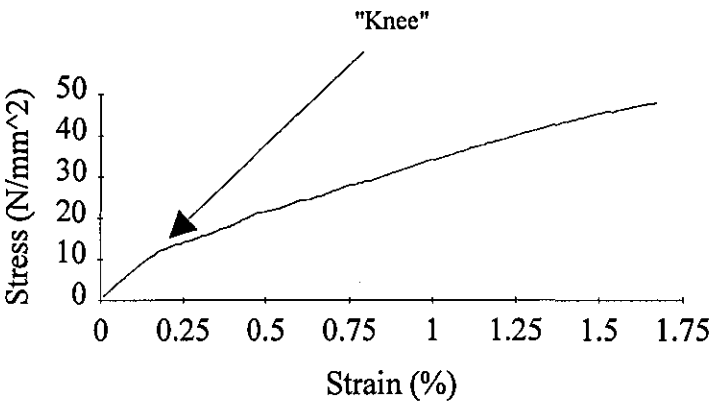


Figure 6.2 A typical stress-strain graph for a transverse tensile specimen taken from the ACCS "plank".

Only eight specimens failed in the gauge length (the 42mm long constant thickness section), whilst the other specimens failed either at the web or at the end of the tabs. The failure was instantaneous through the thickness and width of the specimen.

When a tensile load is applied to a cross-ply laminate consisting of two outer layers of longitudinal fibres surrounding an inner layer of transverse fibres, the literature reports that a characteristic "knee" is produced in the stress-strain curve which corresponds to the onset of matrix cracking in the central layer⁸⁰. The CFM/UD/CFM lay-up will behave in the same manner as that described above under transverse tension and so it can be deduced that the "knee" corresponds to the onset of transverse tensile matrix cracking. On microscopic examination it was noted that the matrix crack density was higher in specimens tested to just beyond the knee than before the "knee", therefore the stress in the inner layer at the knee was taken as the transverse matrix cracking strength.

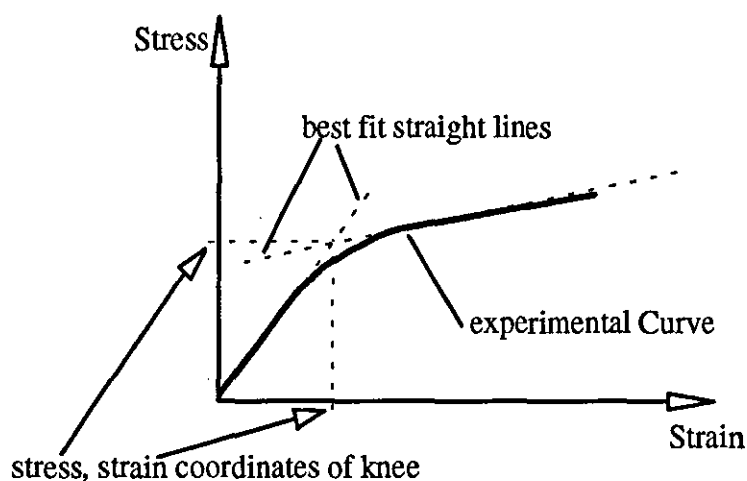


Figure 6.3 Calculation to give "knee" position from transverse tensile test

The damage introduced at the "knee" prevented a representative second test to the same specimen being performed to measure the transverse strain to calculate Poisson's ratio. Instead, ν_{21} was calculated from equation 6.1⁸⁰ using the experimentally determined values for E_{11} , E_{22} , and ν_{12} giving a calculated value of $\nu_{21} = 0.086$.

$$\frac{E_1}{E_2} = \frac{\nu_{12}}{\nu_{21}} \quad (6.1)$$

6.1.2 In-Plane Shear Tests

6.1.2.1 Commissioning the In-Plane Shear Rail Assembly

Standard Guide D4255-83 suggests that when a new jig is built, it should be tested to check where the major shear strains occur (nominally at $\pm 45^\circ$). Therefore three specimens were prepared with strain rosettes positioned with gauges at $\pm 45^\circ$ and 0° . Because there was only one strain box, it was necessary to do three tests separately to record strain in each

direction. The load was increased to approximately 4KN ($\approx 0.1\%$ strain) for each reading, which was about $1/5^{\text{th}}$ of the failure load, and was within the linear section of the stress-strain curve. The following equations²⁰² were then employed to calculate the principal shear strains and the principal angle:

$$\epsilon_1 = \frac{1}{2}(\epsilon_A + \epsilon_C) + \frac{1}{2}\sqrt{(\epsilon_A - \epsilon_C)^2 + (2\epsilon_B - \epsilon_A - \epsilon_C)^2} \quad (6.2)$$

$$\epsilon_2 = \frac{1}{2}(\epsilon_A + \epsilon_C) - \frac{1}{2}\sqrt{(\epsilon_A - \epsilon_C)^2 + (2\epsilon_B - \epsilon_A - \epsilon_C)^2} \quad (6.3)$$

$$\tan 2\phi = \frac{(2\epsilon_B - \epsilon_A - \epsilon_C)}{(\epsilon_A - \epsilon_C)} \quad (6.4)$$

where ϵ_A , ϵ_B , and ϵ_C = strain measured at -45° , 0° and $+45^\circ$ respectively, ϵ_1 , ϵ_2 = principal strains, and ϕ = principal angle.

In each case the principal shear strains were found to be within 0.5° of $\pm 45^\circ$, which was inside the accuracy with which the gauge can be positioned. Therefore, following this commissioning exercise the single strain gauges were positioned as accurately as possible at 45° to the longitudinal axis.

6.1.2.2 In-Plane Shear Test Results

The calculations performed in these analyses were as specified in the standard:

$$\text{Shear Modulus} = (\text{slope of stress-strain curve})/2 \text{ (N/mm}^2\text{)} \quad (6.5)$$

$$\text{Shear Strength} = \text{maximum stress supported by the specimen (N/mm}^2\text{)} \quad (6.6)$$

$$\text{Stress} = \frac{P}{Lt} \text{ (N/mm}^2\text{)} \quad (6.7)$$

[where P = Load (N), L = specimen length (mm), and t = specimen thickness (mm)]. The curve was linear to approximately 0.1% , but was then highly non-linear to failure (Figure 6.4). The initial modulus was therefore calculated from 0 - 0.1% , whilst further slopes between 0.6 - 0.8% , and 1.2 - 1.4% were calculated to illustrate the reducing stiffness (Table 6.3). The standard specifies out-of-plane failure to be the normal case, but this was not observed, possibly due to the high thickness of the specimens. Complete failure occurred instantaneously with a crack running down the specimen at 0° between longitudinal fibres in

the central layer and a crack in the CFM layers following the 0° crack but in a crooked path.

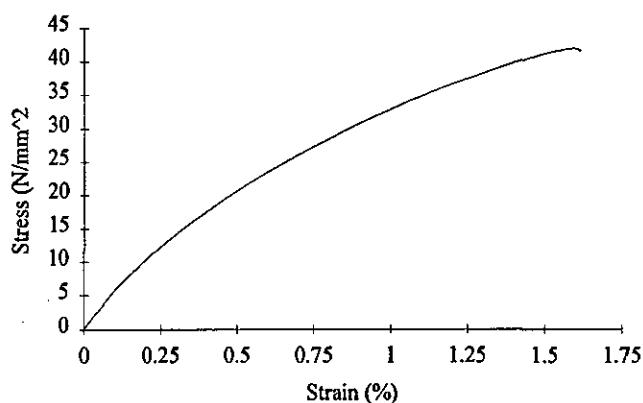


Figure 6.4 A typical stress-strain graph for an in-plane shear specimen taken from the ACCS "plank".

	Average	Coefficient of Variation (%)
Initial Modulus (N/mm ²)	2,702	9.69
Strength (N/mm ²)	41.12	5.25
Failure Strain (%)	1.56	10.06
Slope (0.6-0.8 %)	2,560	6.79
Slope (1.2-1.4 %)	1,683	26.94
Total Specimen Thickness (mm)	3.48	4.34
% Thickness of each CFM ply	27.07	17.90
% Thickness of the UD ply	45.86	16.41
Total number of specimens	14	

Table 6.3 In-plane shear test results from specimens (Figure 3.9) taken from the ACCS "plank".

6.1.3 Flexural Tests

For small deflections, the flexural strength is given by equation 6.8¹⁸⁵:

$$\sigma_f = 1.5PS/wt^2 \text{ (N/mm}^2\text{)} \quad (6.8)$$

Where deflections in excess of 10% of the support span occurred, the equation given in ASTM Standard D790M-86²⁰³ was used to account for large deflections:

$$\sigma_f = \left(\frac{1.5PS}{wt^2} \right) \left(1 + 6 \left[\frac{D}{S} \right]^2 - 4 \left[\frac{t}{S} \right] \left[\frac{D}{S} \right] \right) \quad (\text{N/mm}^2) \quad (6.9)$$

The flexural modulus is given by¹⁸⁵

$$E_f = S^3m/4wt^3 \quad (\text{N/mm}^2) \quad (6.10)$$

[where P = load at failure (N), S = span (mm), w = width at the middle of the specimen (mm), t = thickness at the middle of the specimen (mm), m = slope of linear load/deflection graph (N/mm), and D = central deflection (mm)].

6.1.3.1 Longitudinal

Table 6.4 contains the results for these tests. Failure occurred in the lower CFM layer under tension, which cracked across the width of the beam and through the thickness of the CFM ply. This immediately caused a delamination to spread from this central point towards the support rollers along the lower interface (Figure 6.5(a)).

	Average	Coefficient of Variation (%)
Flexural Modulus (N/mm ²)	11,350	13.89
Strength (N/mm ²)	308.67	14.02
Total Specimen Thickness (mm)	3.30	5.16
% Thickness of each CFM ply	28.22	12.87
% Thickness of the UD ply	43.56	11.68
Total number of specimens	18	

Table 6.4 Longitudinal flexural results from specimens taken from the ACCS "plank".

6.1.3.2 Transverse

Initial failure in the transverse specimens occurred in the tensile CFM layer also, but the crack then travelled through the matrix in the central layer, rather than initiating lower interface delamination (Figure 6.5(b) and Table 6.5).

	Average	Coefficient of Variation (%)
Flexural Modulus (N/mm ²)	6,578	9.21
Strength (N/mm ²)	113.81	12.75
Total Specimen Thickness (mm)	3.23	4.19
% Thickness of each CFM ply	27.66	16.91
% Thickness of the UD ply	44.68	16.62
Total number of specimens	19	

Table 6.5 Transverse flexural results from specimens (Figure 3.10) taken from the ACCS "plank".

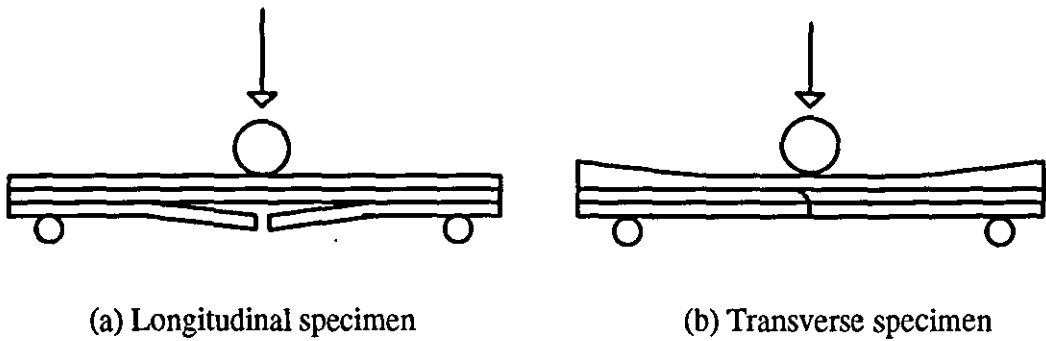


Figure 6.5 Typical failure of flexural specimens.

6.1.4 Critical Strain Energy Release Rate Tests

6.1.4.1 Double Cantilever Beam Test for Mode I

As stated in section 3.4.4.1 the data reduction scheme chosen was based on the area under the force-deflection graphs. Typical plot shapes are shown in Figure 6.6 depending on whether the single or double crack growth tests were performed on the same specimen.

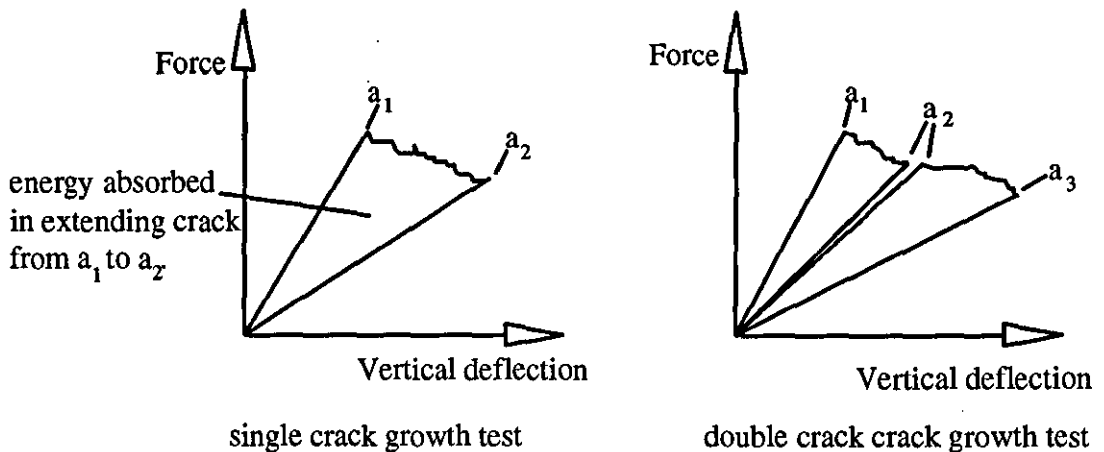


Figure 6.6 Typical force-deflection graphs from DCB tests.

The area within the "loop" (Figure 6.6) is the energy absorbed in extending the crack, and was manually calculated from the graphs. G_{Ic} was then calculated as given by the CRAG Standard:

$$G_{Ic} = \text{Area under graph (Nm)} / (\text{width} \times \text{crack extension}) \quad \text{J/m}^2 \quad (6.11)$$

The results from these tests are contained in Table 6.6, and exhibit wide scatter (high coefficient of correlation), especially from the central crack specimens. Several problems

existed with the central crack specimens which gave rise to the above: non-symmetrical stiffness in the two arms gave rise to unbalanced bending, (in the central crack specimen this was due to the crack not being exactly central initially and deviating further as the crack propagated), the crack did not propagate in a clean plane but became very jagged and irregular, and fibre bridging occurred to a greater degree in the central crack specimens because there was no natural interface. For these reasons the central crack specimen results have been disregarded.

	Average	Co. of Variation (%)
G_{Ic} - Interface Specimen (J/m^2)	573.28	12.60
G_{Ic} - Central crack Specimen (J/m^2)	1314.9	23.19
Total number of specimens	6 (interface) and 9 (central crack)	

Table 6.6 Mode I test results from specimens (Figure 3.11) taken from the ACCS "plank".

In order for the area method data reduction scheme to be valid the unloading and subsequent loading curves must be linear and follow a very similar path¹⁹³, which in general was exhibited by the interface specimens. After visually inspecting the cracked surfaces of each interface specimen it was clear that as the "cleanness" of the crack increased, the value of G_{Ic} decreased. The average value can be used as an upper limit to G_{Ic} . It is expected that the actual G_{Ic} is nearer the lowest value obtained ($484 J/mm^2$). However, even the lowest values obtained for the interface specimens are well above the range of G_{Ic} values reported by previous researchers¹⁰⁶ ($80 - 240 J/m^2$), which indicates the low confidence level which could be applied to these results.

6.1.4.2 End Notched Flexure Tests for Mode II

(a) Experimental Compliance Equation

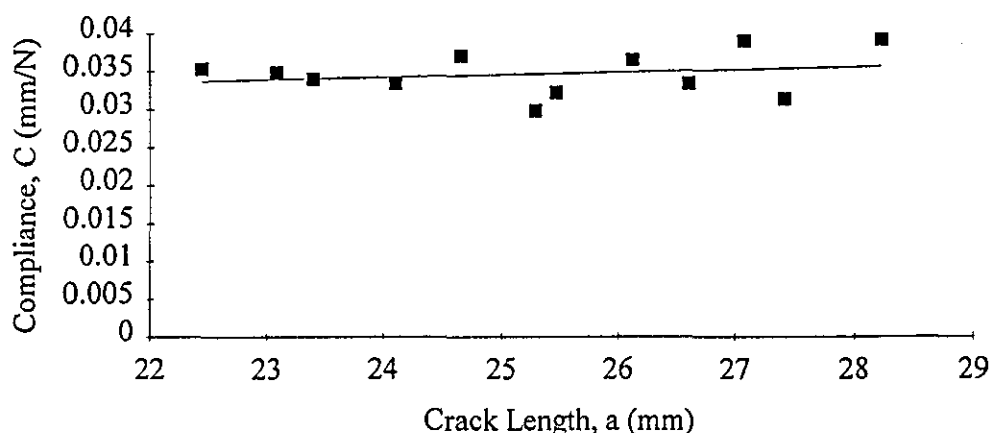


Figure 6.7 Compliance versus crack length for the ENF specimens from specimens taken from the ACCS "plank"

The experimental results are displayed in Figure 6.7 showing the best fit curve to the data giving $dC/da = 0.000323$. However, this figure must be treated with some caution due to the spread of results.

(b) Crack Growth Results and Analysis

In each case the crack growth was unstable, as reported by previous authors^{191,192} with the crack extending to the central loading roller. There were several ways that these results (Table AIV.12 in Appendix AIV) could be analysed. The first technique (Method 1) was the experimental approach, in which the experimentally determined value of dC/da and the recorded values of P_c were substituted into equation 6.12 (equation 3.3 from Chapter 3) giving the results shown in Table 6.7.

$$G_{IIc} = \frac{P_c^2}{2w} \cdot \frac{dC}{da} \quad J/m^2 \quad (6.12)$$

Method 2 was the theoretical approach based on theoretical compliance calculations for the cracked ENF specimen from beam theory. The analysis has only been performed for centrally cracked specimens in the literature^{192,194}, therefore the following describes the analysis adapted for a crack at any depth in the specimen. Noting Figure 6.8 it can be seen that:

$$\delta = \frac{\Delta AB + \Delta BC + \Delta CD}{2} \quad (6.13)$$

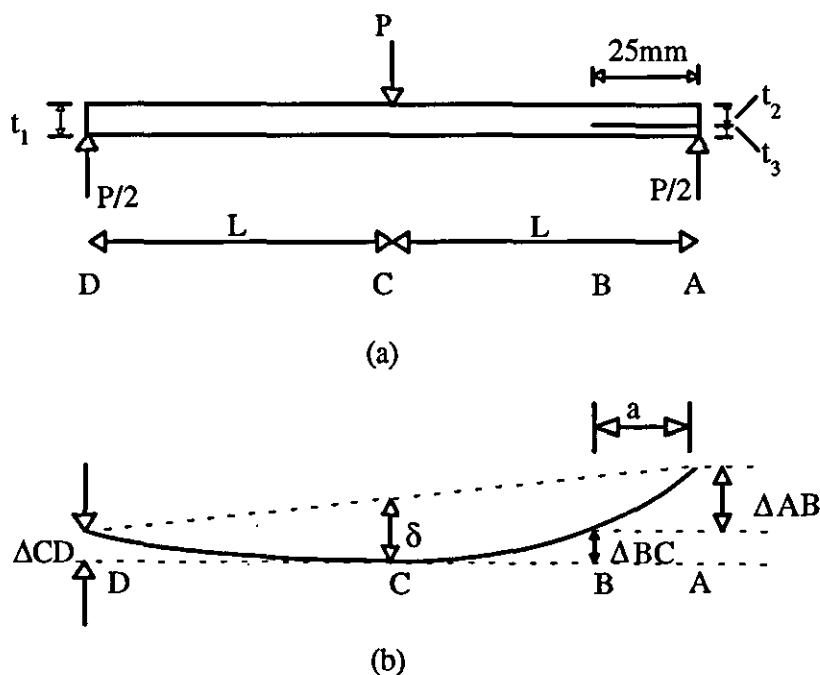


Figure 6.8 Schematic of the Mode II Specimen

The analysis is based on the assumption that the shear deformations and cross-sectional distortions can be ignored. The section BC and CD are assumed to behave as cantilever beams (fixed at C - Figure 6.8) with an applied point end load and moment and point end load respectively. Therefore using standard equations from Timoshenko²⁰⁴:

$$\Delta_{CD} = \frac{(P/2)L^3}{3E_1I_1} \quad (6.14)$$

$$\Delta_{BC} = \frac{(P/2)(L-a)^3}{3E_1I_1} + \frac{(Pa/2)(L-a)^2}{2E_1I_1} \quad (6.15)$$

which reduces to
$$\Delta_{BC} = \frac{P(2L^3 - 3aL^2 + a^3)}{12E_1I_1} \quad (6.16)$$

[where, $I_1 = wt_1^3/12$ and E_1 and I_1 refer to the un-cracked section of the beam, and all the E values refer to flexural moduli]. The displacement Δ_{AB} in the cracked region has two components. The first is due to bending and the second due to rotation of the cross-section at B. The latter (Δ_{AB_r}) is unchanged from the previous author's work, as the position of the crack does not alter the analysis, which is calculated from the vertical and horizontal displacements of the cross-section at B²⁰⁵.

$$\Delta_{AB_r} = \frac{P(aL^2 - a^3)}{4E_1I_1} \quad (6.17)$$

The deflection due to bending (Δ_{AB_b}) of the delaminated region, is effected by the depth of the crack and it was assumed that the curvatures of arms 2 and 3 are compatible (Figure 6.9) and the stress concentration at the crack tip can be ignored.

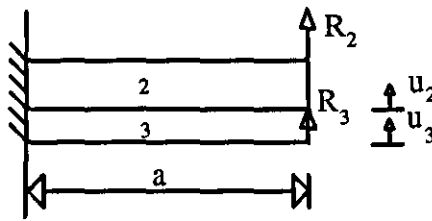


Figure 6.9 Cracked section of the ENF beam.

From Figures 6.8 and 6.9 and, for equilibrium:

$$R_2 + R_3 = P/2 \quad (6.18)$$

For compatibility:

$$u_2 = u_3 \quad (6.19)$$

Considering each arm as a cantilever:

$$u_2 = \frac{R_2 a^3}{3E_2 I_2} \quad \text{and} \quad u_3 = \frac{R_3 a^3}{3E_3 I_3} \quad (6.20(a) \text{ and } (b))$$

On substitution into equation 6.19 gives:

$$R_2 = (R_3) \frac{E_2 I_2}{E_3 I_3} \quad (6.21)$$

[where E_2 and I_2 refer to the upper arm and E_3 and I_3 refer to the lower arm of the delaminated region]. Substituting from equation 6.21 into equation 6.18 gives:

$$R_3 = \left(\frac{P}{2}\right) \cdot \frac{1}{\left(\frac{E_2 I_2}{E_3 I_3} + 1\right)} \quad (6.22)$$

$$\text{and} \quad R_2 = \left(\frac{P}{2}\right) \cdot \frac{\frac{E_2 I_2}{E_3 I_3}}{\left(\frac{E_2 I_2}{E_3 I_3} + 1\right)} \quad (6.23)$$

Substituting from equation 6.22 and 6.19 into equation 6.20(b):

$$\Delta AB_b = \frac{Pa^3}{6(E_2 I_2 + E_3 I_3)} \quad (6.24)$$

Therefore each component ΔAB_b , ΔAB_r , ΔBC , and ΔCD have been found and so can be substituted into equation 6.13, which on simplification becomes

$$\delta = \frac{P(2L^3 - a^3)}{12E_1 I_1} + \frac{Pa^3}{12(E_2 I_2 + E_3 I_3)} \quad (6.25)$$

And as $C = \delta/P$, the compliance of the specimen is:

$$C = \frac{(2L^3 - a^3)}{12E_1 I_1} + \frac{a^3}{12(E_2 I_2 + E_3 I_3)} \quad (6.26)$$

By differentiating with respect to a , the crack length:

$$\frac{dC}{da} = \frac{a^2}{4} \left(\frac{1}{(E_2 I_2 + E_3 I_3)} - \frac{1}{E_1 I_1} \right) \quad (6.27)$$

By substituting from equation (6.25) for the compliance into equation (6.27):

$$\frac{dC}{da} = \frac{3}{a} \left(C - \frac{L^3}{6E_1I_1} \right) \quad (6.28)$$

The following values were used in this analysis: $t_1 = 3.29\text{mm}$, $t_2 = 2.32\text{mm}$ (consisting of 0.92mm of CFM and 1.40mm of UD), $t_3 = 0.97\text{mm}$, and $w = 18.28\text{mm}$. All the above values were the average of the specimens tested, and were used to calculate the second moment of areas, which gave: $I_1 = 54.24\text{mm}^4$, $I_2 = 1.3903\text{mm}^4$, and $I_3 = 19.022\text{mm}^4$.

Lamanal software²⁰⁶, based on the classical laminated plate theory, was used to calculate the flexural moduli E_1 , E_2 and E_3 using the in-plane longitudinal tensile moduli of 7626 N/mm^2 and $49,548\text{ N/mm}^2$ for the CFM and UD respectively (as calculated in section 6.2.2), which gave: $E_1 = 10,860\text{ N/mm}^2$, $E_2 = 19,603\text{ N/mm}^2$, and $E_3 = 7626\text{ N/mm}^2$.

Applying this data to equations (6.26) and (6.27) yielded:

$$C = 0.03655\text{ mm/N}$$

$$dC/da = 0.000142$$

It should be noted that the theoretical value of dC/da calculated above was less than half the experimentally determined value, underlining the level of uncertainty in this series of tests.

The theoretical analysis described above was used in two ways:

(a) Method 2a: The theoretical value of dC/da from equation 6.27 was substituted into equation 6.12 to give G_{IIC} , using the experimentally recorded load values (which were used in each of the analyses).

(b) Method 2b: In a semi-empirical approach the experimentally measured compliance of the specimen was inserted into the theoretically derived equation 6.28 to calculate dC/da which was then used in equation 6.12.

The predicted values of G_{IIC} from each of the three methods are contained in Table 6.7. The spread in load values (P_c) obtained was due to the variation in specimen thickness, individual layer proportions (which also effected the measured dC/da and C values), but possibly more importantly by the crack surface produced. It was apparent that the greater the crack path veered into the UD from the interface, and the greater the extent of fibre bridging the higher was the P_c value and therefore G_{IIC} . The different analysis methods resulted in different values of G_{IIC} . In Method 1, the inaccuracy was mainly due to the experimentally determined dC/da value. Method 2a was the theoretical analysis incorporating the experimental P_c values and provided a lower limit to G_{IIC} . Method 2b incorporated the measured compliance of the specimens as well as the experimental P_c values into the theoretical analysis, and not surprisingly produced an average value between

that of Methods 1 and 2a and is the technique most employed by previous investigators^{191,192}.

Due to the spread of results, they should be treated with some caution. However, it was concluded that the value calculated by analysis Method 2b of 424 J/m² was probably the most accurate. Jones et al¹⁰⁶ reviewed the procedures adopted by previous research for G_{IIc} testing and the range of G_{IIc} values is quoted as being from 154 - 1200 J/mm², into which the above values fit. However, normally¹⁰⁶ G_{IIc} is greater than G_{Ic} , which was not the case with these results.

	Average	Coefficient of Variation (%)
Experimental Compliance (mm/N)	0.0368	2.30
G_{IIc} - Method 1 (J/m ²)	797.6	9.18
G_{IIc} - Method 2a (J/m ²)	351.2	9.18
G_{IIc} - Method 2b (J/m ²)	424.4	9.18
Total number of tests	12	

Table 6.7 G_{IIc} test results from specimens taken from the ACCS "plank".

6.2 Reduction of Laminate Moduli to obtain Individual Ply Properties

From the tension, in-plane shear and flexural tests, elastic moduli were obtained for the three ply laminate, however it was necessary to reduce these moduli to obtain the individual ply properties for input to the FE model. The laminae were thin enough for 2D theories to be employed in analysing the composite stresses, therefore the classical laminated plate theory was used for the reduction^{80,144,207}.

6.2.1 Classical Laminated Plate Theory

This analysis assumed that the three ply laminate was orthotropic. For a layer in a laminate, the in-plane stress-strain relations (in the principal material directions) of an orthotropic lamina are:

$$\begin{Bmatrix} \sigma_{11} \\ \sigma_{22} \\ \sigma_{66} \end{Bmatrix}^k = \begin{bmatrix} Q_{11}^k & Q_{12}^k & 0 \\ Q_{12}^k & Q_{22}^k & 0 \\ 0 & 0 & Q_{66}^k \end{bmatrix}^k \begin{Bmatrix} \epsilon_{11} \\ \epsilon_{22} \\ \epsilon_{66} \end{Bmatrix}^k \quad (6.29)$$

$[\sigma_{66}$, and ϵ_{66} correspond to the in-plane shear and strain respectively]. The Q_{ij}^k 's are the in-plane reduced stiffnesses for the k^{th} lamina, and are related to the engineering constants as follows:

$$Q_{11} = \frac{E_1}{1 - \nu_{12}\nu_{21}} \quad (6.30)$$

$$Q_{22} = \frac{E_2}{1 - \nu_{12}\nu_{21}} \quad (6.31)$$

$$Q_{12} = \frac{\nu_{21}E_1}{1 - \nu_{12}\nu_{21}} = \frac{\nu_{12}E_2}{1 - \nu_{12}\nu_{21}} \quad (6.32)$$

$$Q_{66} = G_{12} \quad (6.33)$$

The laminate constitutive equations shown below relate the force (F_i) and moment (M_i) resultants to the membrane strains (ϵ_i) and curvatures (γ_i), and refer to the principal material directions.

$$\begin{bmatrix} F_1 \\ F_2 \\ F_6 \\ M_1 \\ M_2 \\ M_6 \end{bmatrix} = \begin{bmatrix} A_{11} & A_{12} & A_{16} & B_{11} & B_{12} & B_{16} \\ A_{12} & A_{22} & A_{26} & B_{12} & B_{22} & B_{26} \\ A_{16} & A_{26} & A_{66} & B_{16} & B_{26} & B_{66} \\ \hline B_{11} & B_{12} & B_{16} & D_{11} & D_{12} & D_{16} \\ B_{12} & B_{22} & B_{26} & D_{12} & D_{22} & D_{26} \\ B_{16} & B_{26} & B_{66} & D_{16} & D_{26} & D_{66} \end{bmatrix} \begin{bmatrix} \epsilon_1 \\ \epsilon_2 \\ \epsilon_6 \\ \gamma_1 \\ \gamma_2 \\ \gamma_6 \end{bmatrix} \quad (6.34)$$

where,

$$A_{ij} = \sum_{k=1}^N Q_{ij}^k (z_{k+1} - z_k) = \text{membrane (in-plane) stiffness matrix} \quad (6.35)$$

$$B_{ij} = \frac{1}{2} \sum_{k=1}^N Q_{ij}^k (z_{k+1}^2 - z_k^2) = \text{membrane-plate coupling stiffness matrix} \quad (6.36)$$

$$D_{ij} = \frac{1}{3} \sum_{k=1}^N Q_{ij}^k (z_{k+1}^3 - z_k^3) = \text{plate (bending) stiffness matrix} \quad (6.37)$$

[where z_{k+1} , z_k = thickness co-ordinates on the top and bottom of the k^{th} lamina, and N = total number of layers]. For the case of an orthotropic laminate¹⁴⁴:

$$B_{ij} = A_{16} = A_{26} = D_{26} = 0. \quad (6.38)$$

The **[A]** matrix therefore consists of the reduced stiffnesses, summed in direct proportion to their thicknesses, the **[B]** matrix is empty as this lay-up is orthotropic, and the **[D]** matrix takes into account the position of each lamina in the laminate in proportion to the second moment of inertia of the layer (i.e. z^3).

The reduced stiffnesses for the laminate are therefore related to the A_{ij} and D_{ij} values as described in equations 6.39 to 6.46, with the subscript c denoting the composite properties and t referring to the laminate thickness. The superscript f refers to flexural properties.

$$A_{11} = Q_{11c} \cdot t = \frac{E_{1c} t}{1 - \nu_{12c} \nu_{21c}} \quad (6.39)$$

$$A_{22} = Q_{22c} \cdot t = \frac{E_{2c} t}{1 - \nu_{12c} \nu_{21c}} \quad (6.40)$$

$$A_{12} = Q_{12c} \cdot t = \frac{\nu_{21c} E_{1c} t}{1 - \nu_{12c} \nu_{21c}} = \frac{\nu_{12c} E_{2c} t}{1 - \nu_{12c} \nu_{21c}} \quad (6.41)$$

$$A_{66} = G_{12c} \quad (6.42)$$

$$D_{11} = \frac{E_{1c}^f t^3}{3(1 - \nu_{12c}^f \nu_{21c}^f)} \quad (6.43)$$

$$D_{22} = \frac{E_{2c}^f t^3}{3(1 - \nu_{12c}^f \nu_{21c}^f)} \quad (6.44)$$

$$D_{12} = \frac{\nu_{21c}^f E_{1c}^f t^3}{3(1 - \nu_{12c}^f \nu_{21c}^f)} = \frac{\nu_{12c}^f E_{2c}^f t^3}{3(1 - \nu_{12c}^f \nu_{21c}^f)} \quad (6.45)$$

$$D_{66} = \frac{G_{12c}^f t^3}{3} \quad (6.46)$$

Hence the above equations can be used to calculate the overall laminate properties (E_{1c} , E_{2c} , G_{12c} etc.) if the laminae properties are known. It is also possible to perform the reverse calculation, in order to calculate individual ply properties from the global laminate behaviour which was how the theory was used in this analysis. The following section is concerned with calculating the ply moduli within the initial linear section of the laminate's behaviour. The same calculations were performed from the laminate moduli at higher strains and the results from these calculations are in Appendix IV.

6.2.2 Moduli Calculations

6.2.2.1 Initial Tensile Ply Properties

From the tensile experiments on the laminate the following initial moduli and Poisson's ratios were obtained (section 6.1): $E_{1c} = 25,139 \text{ N/mm}^2$, $E_{2c} = 6,867 \text{ N/mm}^2$, $\nu_{12c} = 0.3145$, and (calculated) $\nu_{21c} = 0.086$. The results tables in section 6.1 contain the average lamina thickness for each of the series of tests in the form of a percentage of the total value of the laminate thickness. These values were substituted into equations 6.39 to 6.41 to obtain A_{11} , A_{12} , and A_{22} .

From the flexural tests the following moduli were obtained: $E_{1c}^f = 11,350 \text{ N/mm}^2$, and $E_{2c}^f = 6,578 \text{ N/mm}^2$. The flexural tests did not yield Poisson's ratios therefore it was assumed that ν_{12c}^f was 0.3 which gave ν_{21c}^f as 0.17. Substituting these flexural properties into equations 6.42 to 6.43 gave D_{11} , D_{22} , and D_{12} .

Referring to equations 6.35 and 6.37 for the three ply laminate, the A_{ij} and D_{ij} values were equated to the individual laminae reduced stiffnesses as follows

$$A_{11} = Q_{11}^{cfm} (z_2 - z_1)^{T/L} + Q_{11}^w (z_3 - z_2)^{T/L} + Q_{11}^{cfm} (z_4 - z_3)^{T/L} \quad (6.47)$$

$$A_{22} = Q_{22}^{cfm} (z_2 - z_1)^{T/T} + Q_{22}^w (z_3 - z_2)^{T/T} + Q_{22}^{cfm} (z_4 - z_3)^{T/T} \quad (6.48)$$

$$A_{12} = Q_{12}^{cfm} (z_2 - z_1)^{T/L} + Q_{12}^w (z_3 - z_2)^{T/L} + Q_{12}^{cfm} (z_4 - z_3)^{T/L} \quad (6.49)$$

$$D_{11} = \frac{1}{3} \left\{ Q_{11}^{cfm} (z_2^3 - z_1^3)^{F/L} + Q_{11}^w (z_3^3 - z_2^3)^{F/L} + Q_{11}^{cfm} (z_4^3 - z_3^3)^{F/L} \right\} \quad (6.50)$$

$$D_{22} = \frac{1}{3} \left\{ Q_{22}^{cfm} (z_2^3 - z_1^3)^{F/T} + Q_{22}^w (z_3^3 - z_2^3)^{F/T} + Q_{22}^{cfm} (z_4^3 - z_3^3)^{F/T} \right\} \quad (6.51)$$

$$D_{12} = \frac{1}{3} \left\{ Q_{12}^{cfm} (z_2^3 - z_1^3)^{F/L} + Q_{12}^w (z_3^3 - z_2^3)^{F/L} + Q_{12}^{cfm} (z_4^3 - z_3^3)^{F/L} \right\} \quad (6.52)$$

The superscripts T/L, T/T, F/L, and F/T refer to tensile/longitudinal, tensile/transverse, flexural/longitudinal, and flexural/transverse respectively, and define which ply thicknesses were used to calculate each particular set of thickness co-ordinates, i.e. equation 6.47 refers to longitudinal tensile properties therefore the ply thicknesses from this series of tests were employed. A_{12} and D_{12} were used to calculate the laminae Poisson's ratios, therefore the thickness co-ordinates for equations 6.49 and 6.52 were taken from the tensile longitudinal

tests (as it was from these that ν_{12c} was determined) and flexural longitudinal tests (being the more reliable flexural results) respectively. Table 6.8 contains the percentage ply thicknesses summarised from section 6.1, and the calculated thickness co-ordinates, which were then used in the calculations.

Equations 6.47 and 6.50, 6.48 and 6.51, and 6.49 and 6.52 form three sets of simultaneous equations, which were solved to give the reduced stiffnesses of each layer. It was also assumed the CFM was planar isotropic and therefore $Q_{11}^{cfm} = Q_{22}^{cfm}$. On substitution of the ply reduced stiffnesses into equations 6.30 to 6.33, the individual ply engineering constants were obtained, which are contained in Table 6.9.

	% Thickness		Thickness Co-ordinates			
	CFM	UD	z_1	z_2	z_3	z_4
T/L	29.09	41.82	-0.5	-0.2091	0.2091	0.5
T/T	25.5	49.0	-0.5	-0.245	0.245	0.5
F/L	27.66	44.68	-0.5	-0.2234	0.2234	0.5
F/T	28.22	43.56	-0.5	-0.2178	0.2178	0.5
C/L	27.30	45.40	-0.5	-0.2270	0.2270	0.5
C/L	23.25	53.50	-0.5	-0.2675	0.2675	0.5
S	27.07	45.86	-0.5	-0.2293	0.2293	0.5
AV.	26.87	46.26				

Table 6.8 Ply Thicknesses for laminate reduction calculations.

6.2.2.2 Initial In-Plane Shear Ply Properties

For the planar isotropic CFM the following equation²⁰⁷ holds:

$$G_{12}^{cfm} = \frac{E^{cfm}}{2(1+\nu^{cfm})} \quad \text{N/mm}^2 \quad (6.53)$$

Therefore substituting in the relevant tensile CFM properties from Table 6.9, gave $G_{12}^{cfm} = 2926 \text{ N/mm}^2$. From equation 6.35, with the superscript, S, denoting that the in-plane shear ply thickness were to be employed, equation 6.54 was derived:

$$A_{66} = G_{12}^{cfm} (z_2 - z_1)^S + G_{12}^w (z_3 - z_2)^S + G_{12}^{cfm} (z_4 - z_3)^S \quad (6.54)$$

A_{66} ($= G_{12c}$) and G_{12}^{cfm} were known, therefore equation 6.54 was solved which gave $G_{12}^w = 2438 \text{ N/mm}^2$.

		Initial Modulus
CFM	E_{11}	7626 N/mm ²
	E_{22}	7626 N/mm ²
	G_{12}	2926 N/mm ²
	ν_{12}	0.3033
	ν_{21}	0.3033
UD	E_{11}	49548 N/mm ²
	E_{22}	5600 N/mm ²
	G_{12}	2438 N/mm ²
	ν_{12}	0.3115
	ν_{21}	0.0352

Table 6.9 All UD and CFM calculated ply moduli and Poisson's ratios.

Therefore the static mechanical tests supplied all the required elastic and critical strain energy release rate data for the FE material model. Chapter 8 describes how this data was employed in the various analyses performed.

Chapter 7

Impact Test Results and Discussion

The experimental impact test work undertaken during this project is detailed in this chapter, with the first section describing the preliminary tests to establish basic test techniques and strategy. There was much data generated, therefore the individual specimen impact test and damage analysis results for each section are contained in Appendix V.

7.1 Preliminary Impact Tests

7.1.1 Effect of Specimen Thickness

A summary of the results for the two sets of different specimen thickness tests are contained in Table 7.1 with the full data in Table AV.1 in Appendix V. The thicker plate was marginally stiffer as expected, but despite an increase in plate thickness of 14%, the peak force generated in the thicker plates was only 2.3% higher, with the mean peak forces being within one standard deviation of each other. However, the deflection at peak load was 10% higher for the thinner plates, resulting in the energy absorbed at peak load being greater for the thinner specimens corresponding to a higher TIE.

The separate ply thicknesses of the impact specimens were measured and a percentage variation of ply thickness of only 1 to 2% was observed. Therefore it was concluded that ply thickness could be neglected as a variable.

The specimen thickness had only a minimal effect due to the pultrusion process, which maintains a constant fibre content (the main load bearing constituent and therefore dictating specimen stiffness) along the length of the pultrusion, whilst the thickness

variation is mainly due to excess resin. As the specimen thickness had some effect on the impact response, it was decided that because direct comparisons were to be made between sets of results, the specimens would be grouped so that the average thickness of each set within a series was as close as possible.

	Specimen Thickness (mm)	Impact Velocity (m/s)	Impact Energy (J)	Peak Force (KN)	Defl. at Peak Force (mm)	Energy at Peak Force (J)	Total Impact Energy (J)
Average	3.57	1.01	5.37	2.18	4.08	5.64	5.73
Std Dev	0.01	0.03	.30	0.06	0.29	0.53	0.30
Co. of Var.	0.40	2.80	5.54	2.85	7.11	9.33	5.26
Average	3.13	1.02	5.47	2.13	4.49	5.93	5.94
Std Dev	0.02	0.02	0.17	0.09	0.20	0.14	0.16
Co. of Var.	0.61	1.52	3.04	4.03	4.52	2.40	2.78

Table 7.1 Effect of specimen thickness on impact response.

7.1.2 Effect of Filtering the Characteristic Impact Curves

Section 4.3.1.2 explained the need to investigate the effect of electronically filtering the force signal. In this exercise, by steadily increasing the level of filtering, the impact characteristics (peak force, deflection and energy at peak force) did not follow a consistent trend. As the filter level was increased (i.e. the value of the low pass filter reduced), the peak force reduced to a minimum and then rose again at very high filter levels. Therefore the choice of filter level was not straightforward. A filter level of 2.5KHz was finally chosen because it was this point that the vibrations on the highest velocity tests disappeared, allowing the steady response to be observed. The filtered data from the strain-rate tests is contained in Appendix V, Table AV.2 (the unfiltered data in Table AV.4). The effect of filtering at this level on the peak force, deflection at peak force, and energy at peak deflection was as follows:

Peak Force - only for the highest velocity tests did the filtering have a marked effect (4 to 6% reduction). In all the other cases, the peak force only dropped by 1 to 2% when filtered.

Deflection at Peak Force - filtering always increased the deflection at peak force (by 1 to 7%), because as the periodic vibration peaks were removed the peak load recorded tended to move up the force - deflection curve.

Energy at Peak Force - was unaffected by filtering except for the two highest velocities (5 to 6% variation).

It was concluded that only at the highest velocities tested does the filtering have a major effect on the force-deflection curve and the associated characteristics. On the lower velocity curves the material response was quite clear even before filtering, therefore considering the difficulty in deciding the level of filtering to be employed, and the relatively readable unfiltered curves it was decided that the test data would be analysed in its unfiltered form.

7.1.3 Effect of the Delay Function

Table AV.3 in Appendix V contains the data obtained from the four impact tests. Figure 7.1(a) shows that the peak force generated was not effected by the delay, as expected because this was a directly measured value rather than a calculated value. However, as the delay became more positive both the calculated deflection at peak force and deflection at failure decreased in a linear manner. Because the calculated deflections were effected the energies were also altered as the energy corresponds to the area under the force-deflection curve (Figure 7.1(b)).

The Rosand software integrates the force twice as described in section 4.2.1. In order to check that the calculations were correct for a delay of zero, the double integration routine was created, based on the Rosand user manual¹⁹⁵ and the work of Svenson and colleagues²⁰⁸. On integrating the measured data the same derived values were obtained, confirming that the Rosand software was functioning correctly when the delay was at zero.

It was clearly shown that if the delay was given a non-zero value, the calculated values were seriously effected. The software is currently being investigated by the manufacturers to eliminate this problem. As a result of this investigation, it was decided to perform impact tests with the delay set at zero and if data was not captured, to adjust the opto-switch rather than using the delay.

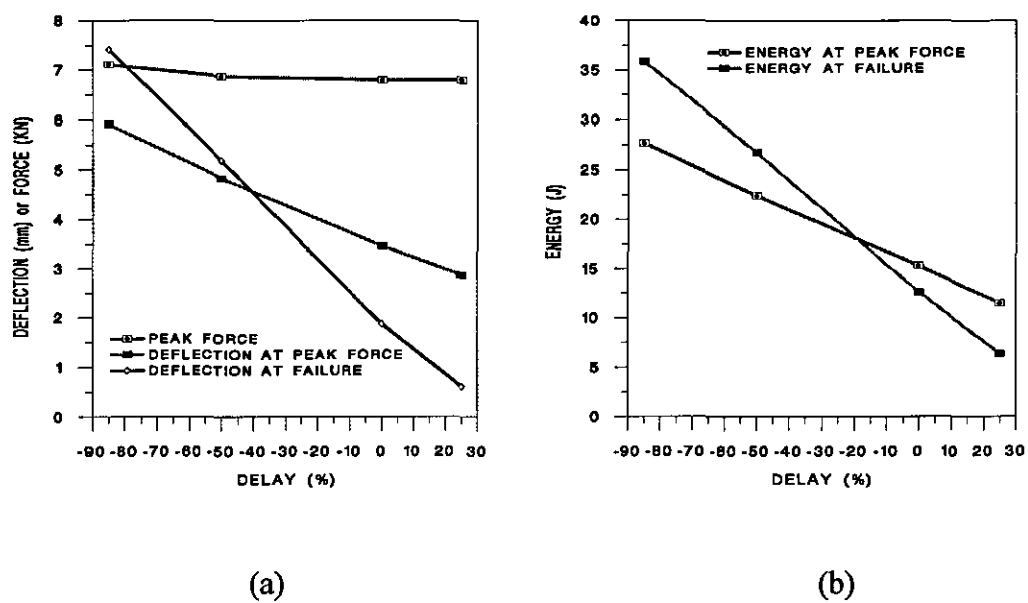


Figure 7.1 Effect of delay function on impact characteristics.

7.2 Strain-Rate Tests

The individual test results can be found in Table AV.4 in Appendix V. In this and the following sections, the data will be presented in a series of graphs, with each point representing the average value from a set of tests, and the error bars referring to ± 1 standard deviation.

At each energy three sets of tests were performed with varying mass and velocity combinations as described in Chapter 4, except at penetration where interference between the floating mass and carriage prevented the lower mass tests being performed. At penetration the force-time graph (Figure 7.2) show that a load was still being carried as the impactor passed through the plate, which was due to the friction between plate and impactor as reported by Lee and Sun⁴⁶.

Figure 7.3 shows the peak force and peak deflection plotted against impact energy. Figure 7.3(a) displays a constant trend over the energy range that at the same impact energy, the greater the mass, the higher the peak force generated. This cannot be explained as a statistical anomaly because the different impactor mass curves generally lie more than one standard deviation from each other as indicated by the error bars. Figure 7.3(b) suggests that at the same impact energy, the higher the mass, the greater the peak deflection.

However, for the impacts to be of the same energy, the above two observations cannot be true.

The term total impact energy (TIE) was introduced in Chapter 4, and is used to explain these results. Figure 7.4 shows the peak force and peak deflection plotted against TIE respectively, and the trends described previously disappear or at least are greatly reduced. Even though different masses may have the same impact energy ($1/2mv_0^2$), the higher the mass the greater the TIE ($1/2mv_0^2 + mg\delta$) which will ultimately be absorbed as strain energy. This is a very important concept, because if only the impact energy is considered, strain-rate effects would appear to be present. The spring-mass model does not take this into account either, and therefore, as described in Chapter 4, has also been modified to include the term TIE rather than IE.

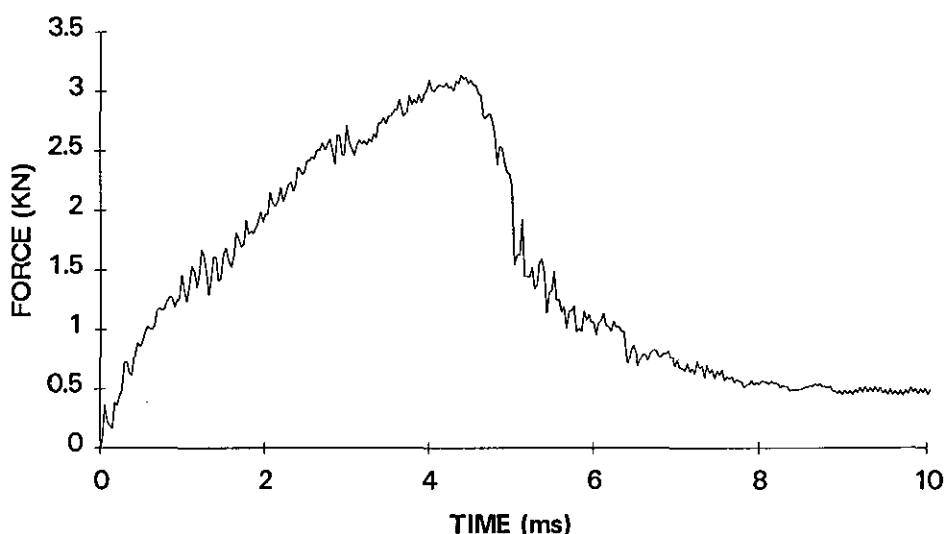


Figure 7.2 Force-time curve for a penetrated strain-rate test specimen.

Figure 7.5 shows the contact time versus TIE for each mass impact. The general trend (which is also repeated for the time to peak force and time to peak deflection versus TIE curves) was for the periods to be dependent on the impactor mass alone, as predicted by the spring-mass model (equation 4.6). Prasad et al¹⁴⁵ reached similar conclusions from their impact tests on graphite/epoxy systems - the response of plates at the same energy but different masses was dominated by the impactor mass which dictated the contact duration. For impacts with the same mass impactor it was the velocity which dictated the plate response (i.e. deflection, force) without affecting the time at which these events occurred.

Each period was shorter for the lowest energy impacts, because very little damage was induced at this stage resulting in a stiffer overall response, leading to a lower period. In effect, the graphs exhibit two characteristic periods - a shorter "elastic period", and a longer "damage period" reflecting the reduction in stiffness due to the damage in the specimen.

It was therefore concluded that over the velocity and mass range tested there were no detectable strain-rate effects, either in elastic stiffness response or in damage initiation/propagation levels. The impact energy was therefore varied in the following sections by varying the drop height, and therefore impact velocity, whilst keeping the mass constant. In all the following sections the impact data is plotted against TIE rather than IE.

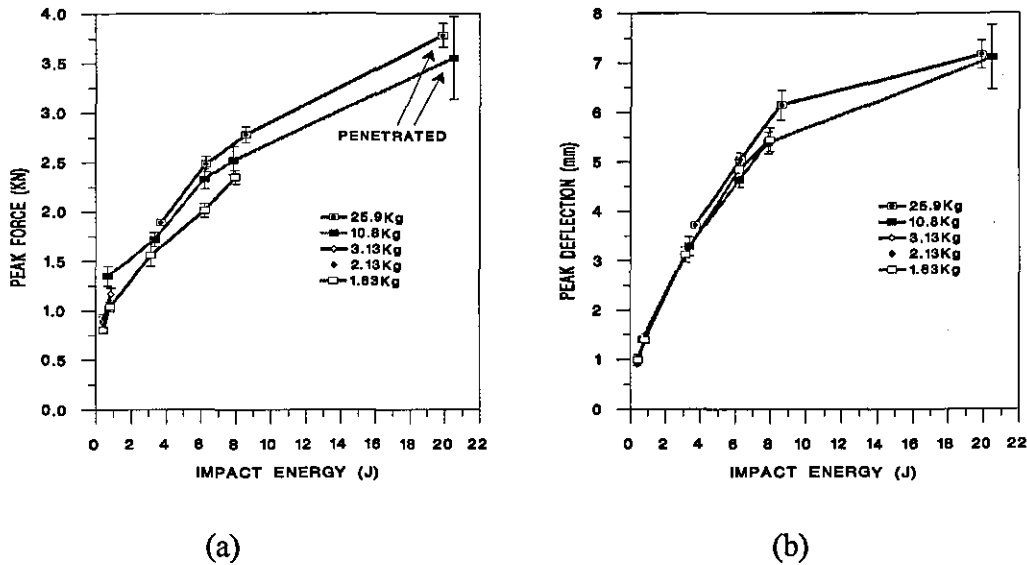


Figure 7.3 Peak force (a) and peak deflection (b) versus IE for the strain-rate impact tests.

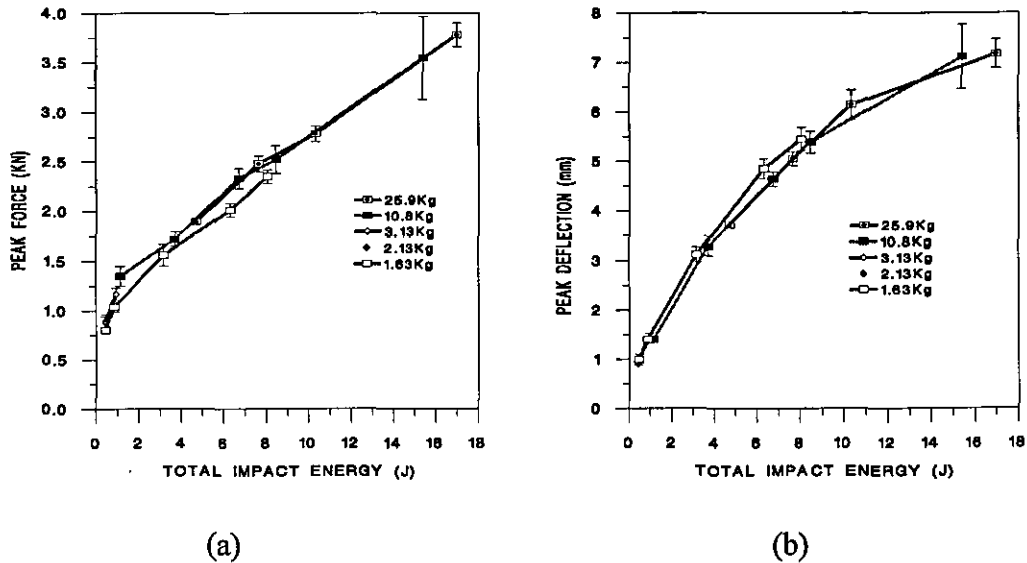


Figure 7.4 Peak force (a) and peak deflection (b) versus TIE for the strain-rate impact tests.

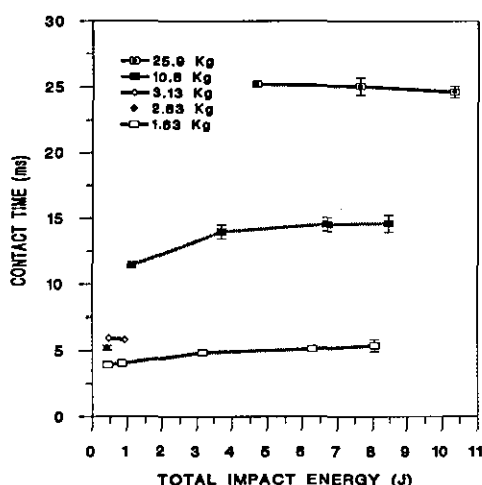


Figure 7.5 Contact time versus TIE for the strain-rate impact tests.

7.3 Coupon Tests

The individual specimen impact test data and damage assessment data is contained in Tables AV.5 to AV.15 and Figures AV.1 to AV.4 in Appendix V for the shear, longitudinal and transverse coupons.

7.3.1 Shear Coupon

The force-deflection and force-time curves were sufficiently smooth that the most obvious change in stiffness (at approximately 1.3KN) during the impact event could be pinpointed and this is referred to as the "knee" (Figure 7.6). The oscillations which were present were due to the coupon vibrating against the impactor during the period of contact. The basic shape of the curve was very similar to that reported by Zhou and Davies⁹⁵ and Jackson and Poe¹²⁴ with an initial knee followed by a less stiff response up to the peak load. The latter suggested that the second linear section was due to stable delamination growth. Non-linear bending occurred for these tests as the deflection was well over double the plate thickness, which explained the increasing stiffness after the "knee" which sometimes occurred.

Figures 7.7 and 7.8 contain the four major graphs of impact test data plotted against TIE. All four graphs are related to each other with effects sometimes being more pronounced in one graph than another. For the following sections, only the peak force-TIE graph will be included in the text, whilst the others will be in Appendix V for reference.

The impactor penetrated for the two highest energy impacts, and the peak force flattened off at 3.3KN (Figure 7.7(a)), which was therefore the penetration threshold for this test configuration. The error bars on each graph indicate that there was a good level of repeatability within each set of tests. The continuous line plotted in Figure 7.7. corresponds to the modified spring-mass model prediction of the elastic relationship between peak force (equation 4.7) and peak deflection (equation 4.8) versus TIE. The initial stiffness measured from the force-deflection graphs was used for K in the equations. The graphs clearly show that the reduction in stiffness due to damage was dramatic, and even at the lowest energy some damage was induced.

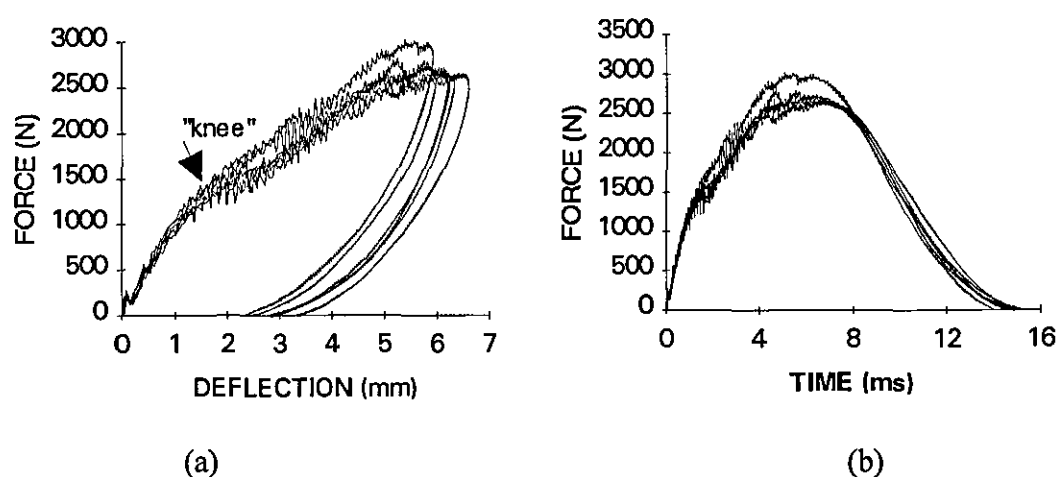


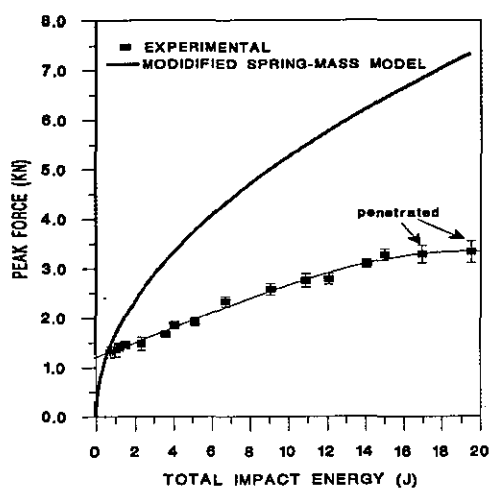
Fig 7.6 Force-deflection (a), and force-time (b) curves for the 10.9J TIE shear coupons (Figure 4.6).

The peak deflection and deflection at peak force (Figure 7.7(b)) lie close to each other over the energy range. This is because in these tests the force still rose as the damage grew (Figure 7.7(a)) and so the peak force and peak deflection generally occurred at approximately the same point in the event. This damage growth could be termed stable, in contrast to the damage growth in both the longitudinal and transverse coupons.

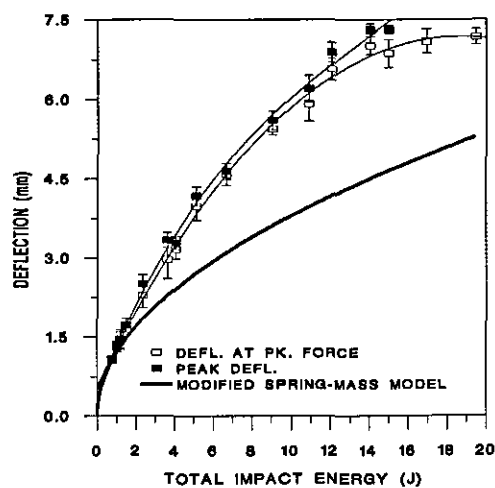
The contact time, time to peak force and time to peak deflection rose up to 5J TIE (Figure 7.8(a)) and then levelled off, due to the effect of damage as described for the strain-rate tests. The time to peak force reduced for the penetrated coupons due to the increased impact velocity and therefore the shorter time to reach the penetration force.

Figure 7.8(b) shows the damage energy, energy at peak deflection, and elastic energy plotted against TIE. The graph illustrates quite clearly that there is a maximum level of

elastic energy which can be absorbed ($\approx 2.5\text{J}$) shown by the relatively flat elastic energy curve, above approximately 4J TIE.

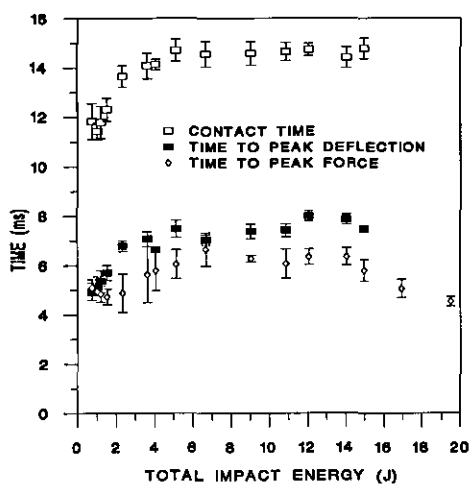


(a)

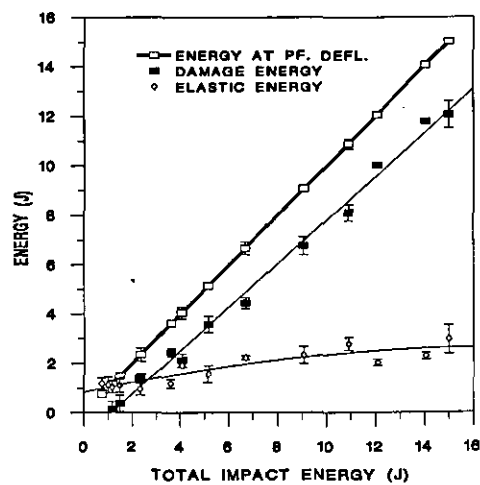


(b)

Figure 7.7 Peak force (a) and deflection data (b) versus TIE for the shear coupon, and modified spring-mass model prediction.



(a)



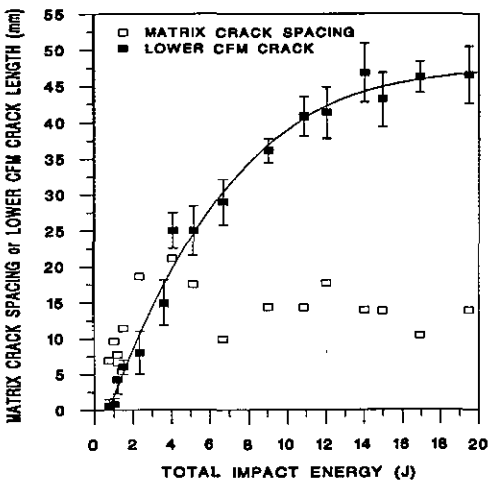
(b)

Figure 7.8 Temporal (a) and energy data (b) versus TIE for the shear coupon.

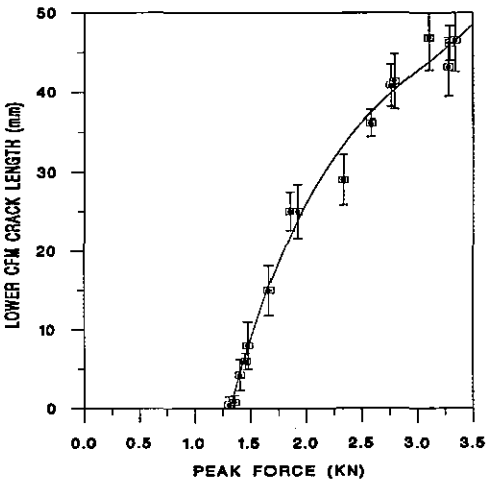
Figures 7.9 to 7.11 summarise the results of the damage analyses. Figure 7.9(a) shows the lower CFM crack length and average vertical UD matrix crack spacing versus TIE. For clarity, the error bars are not shown for the matrix crack spacing because the variation was very wide and there was no visible trend in the results. It was concluded that the lowest energy impacts performed were still above the onset of matrix cracking and that over the energy range tested the matrix crack density did not increase. Therefore the non-linearity in the force-deflection curve (Figure 7.6(a)) before the knee could be due to matrix cracking. For some specimens, no matrix cracks were visible, due to poorly wetted out material in the central ply. However, the poorly wetted out material did not seem to alter the specimens' overall impact response greatly, as the force-deflection curves still exhibited the same characteristics. The average UD transverse matrix crack spacing showed great variation for all of the impact tests on the coupons and box sections, therefore it is believed that this type of damage was introduced at an energy below that tested for all these sections and this form of damage will not be considered further in this chapter.

The lower CFM crack grew longitudinally as the coupon was less stiff in the transverse direction. The rate of lower CFM crack growth (Figure 7.9(a)) was constant up to approximately 25mm length, but then the growth rate decreased and levelled off at approximately 45mm, due to the clamped supports (60mm diameter). Figure 7.9(b) shows the crack length plotted against peak force, which exhibits the same trends as Figure 7.9(a) but is more consistent suggesting that the lower CFM crack was more dependent on the peak force than the TIE. The onset of the lower CFM cracking occurred at 1.3KN, which coincides with the "knee" on the force-deflection curve.

In comparison to the simply supported coupons in section 7.3.2 and 7.3.3, due to the clamped supports the shear coupon's response was relatively stiff and therefore the permanent indentation could not be ignored as a damage energy absorbing mode. Figure 7.10(a) illustrates that permanent deformation of the impacted surface occurred at approximately 1.5KN, from which point the indentation deepens, as the peak force increased. The jump in indentation depth above 2.4KN corresponded to the first sign of shear cracking on the upper CFM surface directly under the edge of the impactor. The large error bar for the final point indicates that the penetration threshold was being approached (the indentation of the penetrated coupons could not be measured). The initial indentation was observed as stress-whitening (matrix cracking and surface micro-buckling) as described by Zhou and Davies⁹⁵ who also observed ply "shear-out" which corresponds to the shear cracking of the impacted ply.

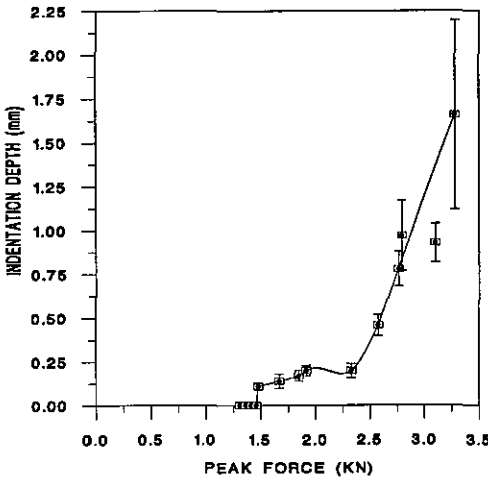


(a)

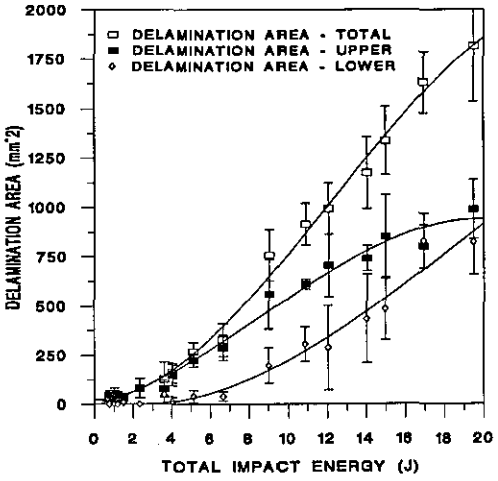


(b)

Figure 7.9 Lower CFM crack length and UD matrix crack spacing versus TIE (a) and lower CFM crack length versus peak force (b) for the shear coupon



(a)



(b)

Figure 7.10 Indentation depth (a) and delamination areas (b) versus peak force for the shear coupon.

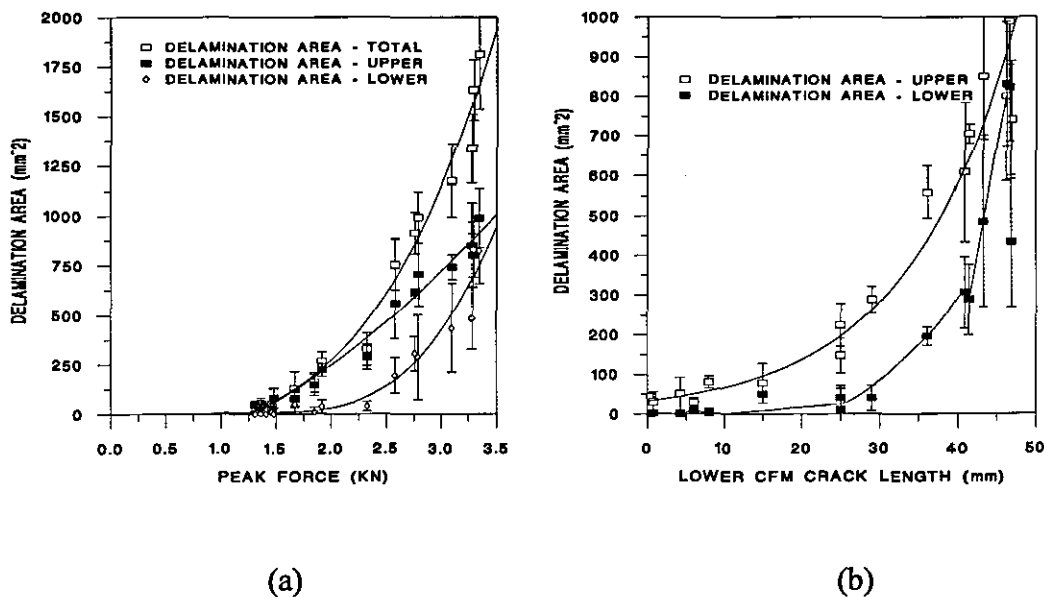


Figure 7.11 Delamination areas versus peak force (a) and delamination areas versus lower CFM crack length (b) for the shear coupon.

Figures 7.10(b) and 7.11 show delamination areas as calculated from optical microscopy versus TIE, peak force, and lower CFM crack length respectively. The total delamination area was the sum of the lower and upper interface delamination areas. The delamination of the upper interface occurred at the lowest energy tested which generated a peak force of 1.3kN and was therefore another damage mode contributing to the "knee". Shear cracks and/or vertical tensile cracks in the UD ply were almost always found at the edges of the upper interface delamination (Figure 7.12).

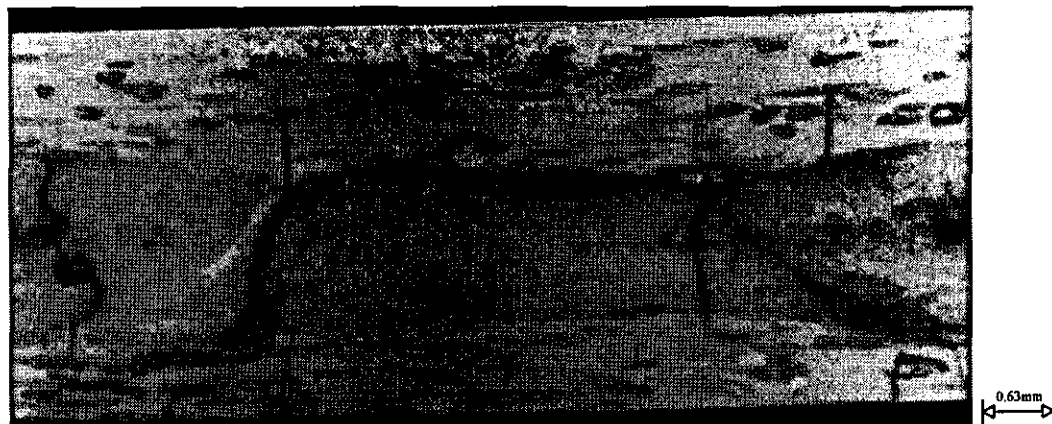


Figure 7.12 Photograph of upper interface delamination and associated shear/tensile UD matrix cracks of a 1.02 J TIE shear coupon.

The upper interface delamination grew longitudinally (Figure 7.13) spreading to a width of approximately 10mm corresponding to the impactor diameter and the "generator strip" referred to by Malvern et al²⁰⁹. From their impact tests on cross-ply glass/epoxy with a

blunt ended impactor, they reported a delamination, of width corresponding to the impactor diameter, bounded by two through thickness shear cracks. The "generator strip" lengthened parallel to the fibres as result of the upper layer being forced through the laminate by the impactor, which describes closely the observations for the shear coupon.

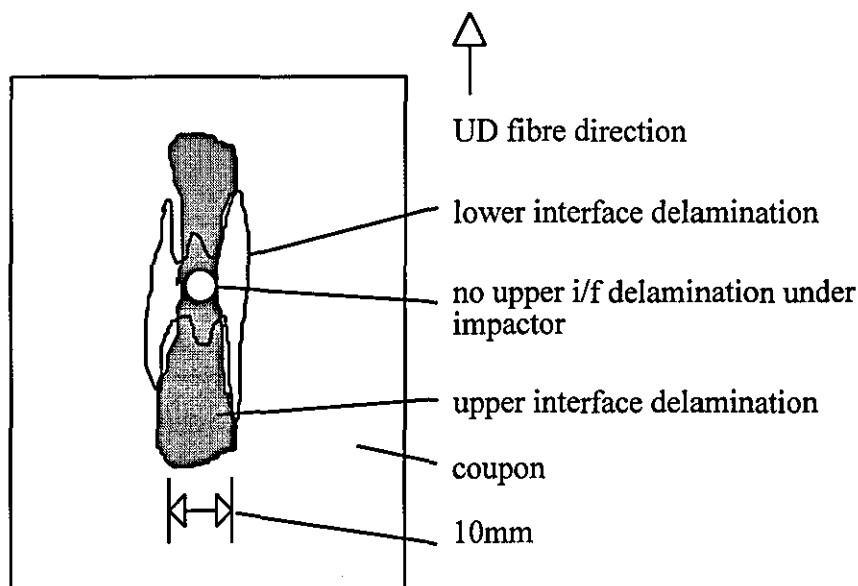


Figure 7.13 Upper and lower interface delamination patterns in the shear coupon.

The growth in delamination corresponds to the softer section of the force-displacement graph (Figure 7.6(a)) above the "knee", correlating well with the findings of Zhou and Davies⁹⁵. Upper interface delamination was in general not found directly under the impactor due to the high compressive normal forces generated, but much shear cracking in the UD layer was present due to the high contact forces.

At the highest energies, the delamination size was less predictable as growth was hindered by the clamped supports. Jackson and Poe¹²⁴ refer to the need for the maximum extent of damage to remain a minimum distance away from the boundary or other discontinuity for specific relationships to hold, which was seen to be the case in this work also.

The upper interface delamination was initiated by the high shear stresses induced by the clamped supports and it is believed by a transverse UD matrix crack.. The growth was relatively linear with both TIE (Figure 7.10(b)) and peak force (Figure 7.11(a)) but less so with lower CFM crack length (Figure 7.11(b)). This crack assisted delamination growth because the crack propagated through the UD layer in the form of a longitudinal UD matrix crack, increasing the Mode I energy available for opening the upper interface

delamination (Figure 7.14). Figure 7.11(b) suggests that above a lower CFM crack length of 25mm, the rate of upper interface delamination increased, due to this effect.



Figure 7.14 Photograph of lower CFM crack propagated through UD layer to promote upper interface delamination for 6.69J TIE shear coupon.

The lower interface delamination area was small up to approximately 7J TIE (2.3KN) as shown in Figures 7.10(b) and 7.11(a). Two separate forms of lower interface delamination were observed which merged at higher energies:

Firstly, **shear induced lower interface delamination** initiated from the 45° UD shear cracks dropping down from the upper interface delamination as shown in Figure 7.15(a). This type of delamination formed outside the upper interface delamination (Figure 7.13). Up to 4J TIE all the observed lower interface delamination was induced by this mechanism (Figure 7.16).

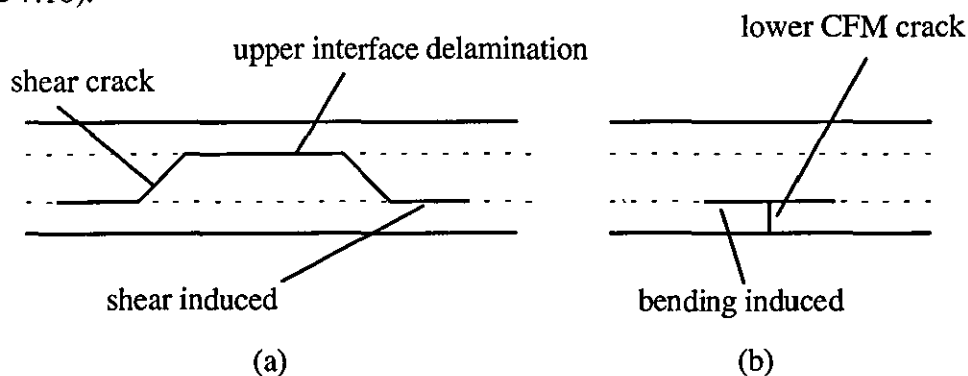


Figure 7.15 Types of delamination in the shear coupon.

Secondly, **bending induced lower interface delamination** originated under the impactor due to the lower CFM crack (Figure 7.15(b)). As this form of lower interface delamination developed, it grew as an oval with its long axis in the UD fibre direction as illustrated in Figure 7.13. AT 4J TIE the bending induced lower interface delamination was first observed by optical microscopy (OM), and was seen to follow the lower CFM crack. The lower CFM crack formed due to transverse bending, and the delamination due to

longitudinal bending as both occur under the circular support conditions. At 4J TIE the lower CFM crack had reached 15mm, the critical crack length for initiating the bending induced lower interface delamination. At a lower CFM crack length of 25mm lower interface delamination growth increased rapidly in parallel with the upper interface delamination (Figure 7.11(b)).



Figure 7.16 Photograph of lower interface delamination induced by 45° UD shear cracks in the 14J TIE shear coupon.

As the TIE increased, the number of shear cracks in the UD layer under the impactor increased. When allied to the crushing caused by the compressive forces this resulted in considerable UD fibre-matrix debond. As the support from the UD layer reduced, the upper CFM layer collapsed under the impactor leading to complete penetration (Figure 7.17). The area of UD fibre-matrix debond increased up to penetration by spreading away from the impact site under the upper interface delamination, and was therefore a large mode of damage energy absorption at high TIE.

Table AV.7 in Appendix V contains all the information gathered from the thermal depley exercise. 9J TIE (2.6KN) was the lowest energy at which specimens contained fibres in the upper CFM layer which were broken in a circle approximately 5-8mm diameter, under the impactor (Figure 7.18), which corresponds with the jump in measured indentation on the top face (Figure 7.10(a)) and the recorded onset of upper CFM shear cracking during the visual inspection.



Figure 7.17 Photograph of collapsed upper CFM layer and considerable UD shear cracking under the impactor in 12J TIE shear coupon.



Figure 7.18 Photograph of fibre breakage under the impactor in the upper CFM layer above 9J TIE for the shear coupon from thermal deply exercise.

In the penetrated specimens, the UD fibre breakage extended to a width corresponding approximately to the diameter of the impactor. Only a very small amount of fibre breakage in the UD layer was found in unpenetrated coupons (Figure 7.19), where it was limited to the lower tensile surface of the UD layer. For 4J TIE specimens and above, on thermal deply, the lower CFM crack was clearly visible (Figure 7.20). Whilst the crack ran approximately longitudinally it was not perfectly straight due to the random fibre orientation in the CFM layer. The crack length could only be crudely measured, but as the figures in Table AV.7 indicate, good agreement was found with the crack lengths reported by visual inspection.

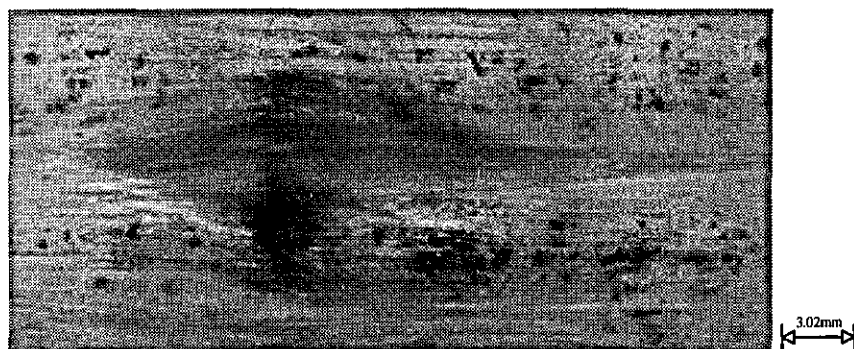


Figure 7.19 Photograph of UD fibre breakage on the lower (tensile) surface prior to penetration in the shear coupon.



Figure 7.20 Photograph of lower CFM crack for the shear coupon from thermal deply exercise.

From optical microscopy a global "damage area" (as described in Chapter 4) was calculated (upper and lower delamination and associated shear cracks) for comparison with the C-Scan which reports this as the damage area. From Table AV.6 it was clear that the C-scan contour which gave the closest results to the optical microscopy damage area was the area calculated by including all the attenuation contours down to and including -16dB. Figure 7.21 shows both the resulting C-Scan damage area and the damage area predicted by optical microscopy. The correlation between the two was very close and well within one standard deviation of each other over the energy range. Figure 7.22 shows a 15J TIE damage area as given by C-Scan illustrating a similar outline shape as shown in Figure 7.13, with the colour dB scale shown applying to all further C-Scans contained in this work.

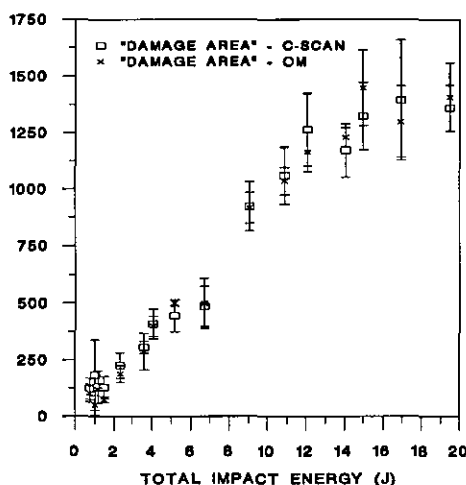


Figure 7.21 Comparison of C-Scan and OM "Damage areas" for the shear coupon.

Throughout the impact test programme, a C-Scan of every specimen was performed and the OM and C-Scan damage areas compared. For each series of tests the correlation was satisfactory, therefore only the OM results will be included in the main body of the report with the correlation graph for each section within Appendix V for reference.

The results presented have described in detail the damage modes and interactions for the shear coupon with respect to the force-deflection curves and peak force-TIE curve in particular. Changes in stiffness have been shown to correlate with the onset of particular forms of damage energy absorption. A summary of the threshold forces and energies for the various modes of damage observed, and damage interactions is contained in Table AV.8 in Appendix V.

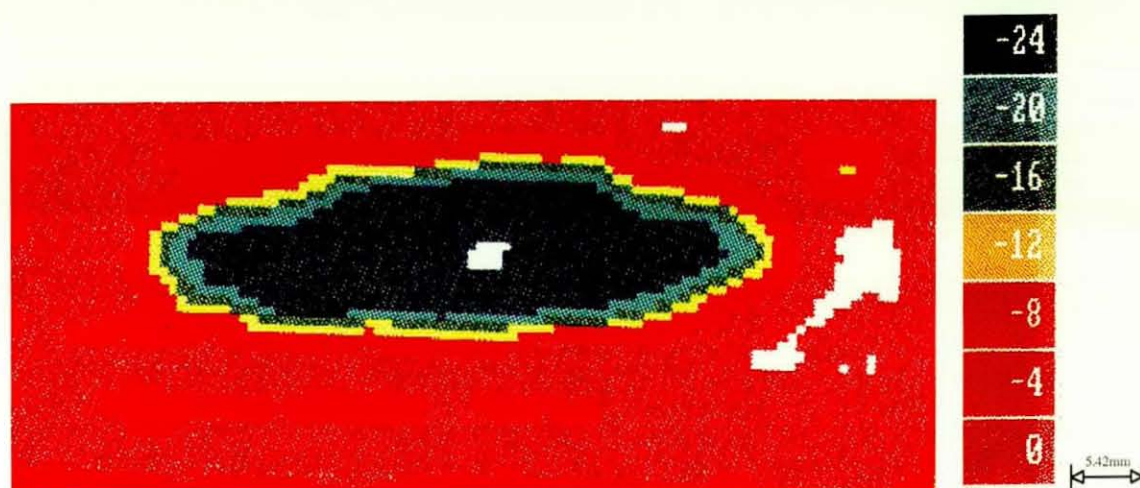


Figure 7.22 C-Scan of 15J TIE shear coupon and dB colour contour scale.

7.3.2 Transverse Coupon

It is clear from Figure 7.23(a) showing a typical force-deflection curve at 6.4J TIE, that the vibration response on top of the curve was quite prominent making it difficult to interpret damage initiation directly. In contrast to the shear coupon, the majority of damage occurred at peak force when there was a large load drop, therefore the damage can be termed unstable. This coupon was a lot less stiff than the shear coupon due to the geometry, supports and because there were no UD fibres in the major plane of bending. The peak forces generated were therefore much lower than the previous tests.

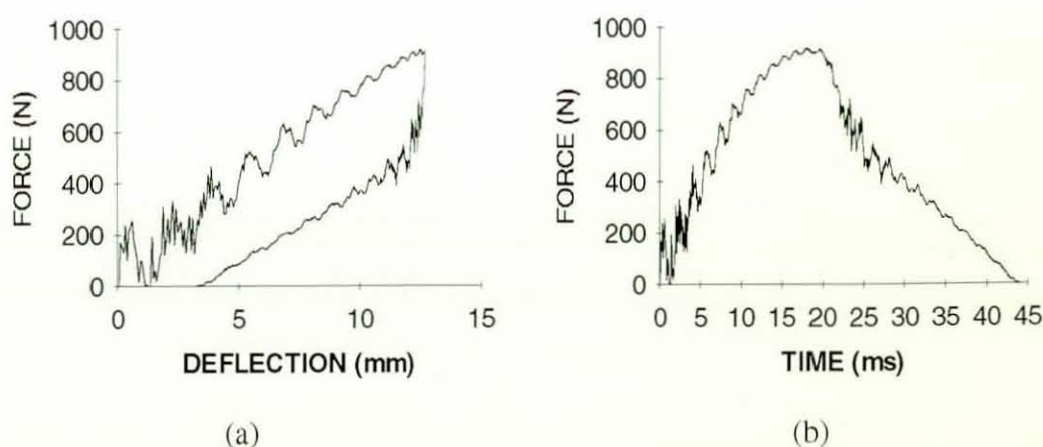


Figure 7.23 Force-deflection (a) and force-time (b) curves for the 6.4J TIE transverse coupons (Figure 4.8).

Figure 7.24 displays good correlation between the experimental results and the peak force predicted by the modified spring-mass model for the first three points. At higher energies the curve deviated from an elastic response and flattened off at a peak force of approximately 0.9KN. Final failure occurred in the form of "creasing" and not penetration for the two highest energy tests in this series. "Creasing" occurred when the lower CFM crack had traversed the width of the specimen which then folded along the crack because only the upper CFM had any remaining strength. The deflection, energy, and temporal data graphs (Figures AV.1 and AV.2 in Appendix V) all indicated that the major damage absorption occurred above 5.5J TIE, comparing well with Figure 7.24.

Due to the simple supports and there being only one plane of bending, the damage analysis was less complex than in the previous section. The damage response was dominated by the lower CFM crack and associated upper interface delamination and the damage analysis very clearly explained the impact test data. Figure 7.25(a) shows the lower CFM crack length versus TIE and illustrates that the crack was initiated between 4.5 and 5.5J. The graph also illustrates that once lower CFM cracking began, growth was rapid (and therefore less stable and less repeatable hence the jumps in the curve) corresponding to the unstable nature of the load drop in Figure 7.23. At the highest crack length the specimen width limited crack growth.

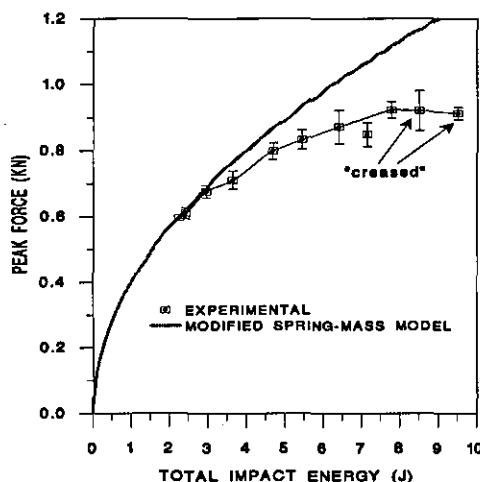


Figure 7.24 Peak force versus TIE for the transverse coupon, and modified spring-mass model prediction.

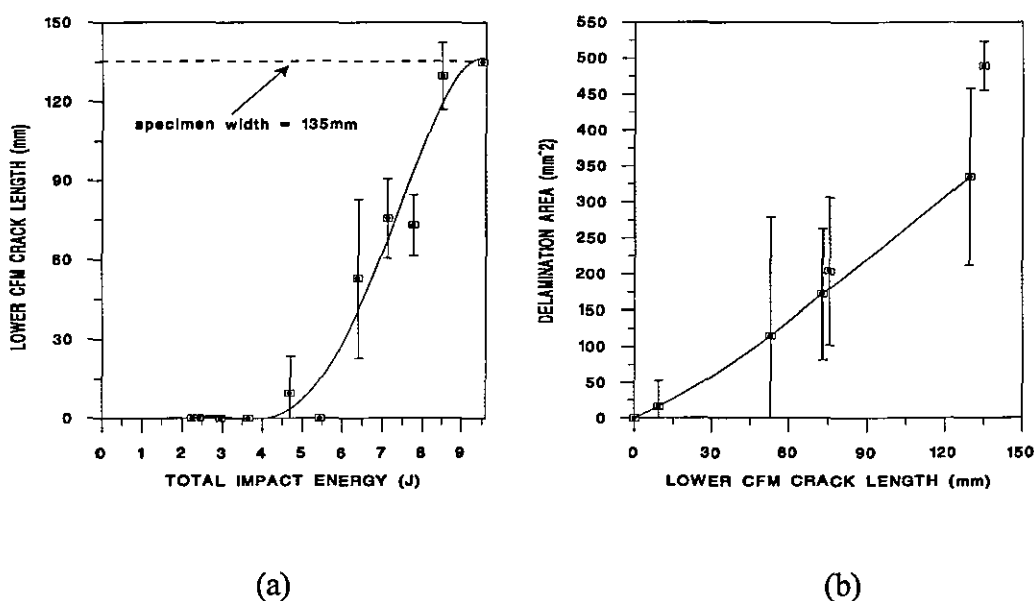


Figure 7.25 Lower CFM crack length versus TIE (a) and delamination area versus lower CFM crack length (b) for the transverse coupon.

Figure 7.25(b) indicates the linear relationship between lower CFM crack length and upper interface delamination area, except for the final point where the CFM crack had reached the edge of the specimen. This relationship arises because the CFM crack propagates straight through the UD layer and as the crack reaches the upper interface, it is redirected into a delamination (Figure 7.26). Upper interface delamination was initiated as soon as a lower CFM crack occurred and it was these two forms of damage which caused the flattening of the curve in Figure 7.24. The delamination extended along the length of the crack but remained thin as illustrated by the C-Scan in Figure 7.27.

Specimens from the two highest energy sets of tests were tested for fibre breakage using the thermal deply technique and no fibre failure was found in the UD layer or upper CFM layer, which was in keeping with the visual inspection which did not detect any indentation or shear failure on the upper surface. This is because the indentation and other upper CFM damage directly under the impactor is governed by the peak force, but the peak forces generated were quite low, and certainly below the 1.5KN force at which permanent indentation was first observed during the shear tests. Throughout the energy range there was no shear cracking in the UD layer, which was due to the simple supports inducing bending rather than shear forces.

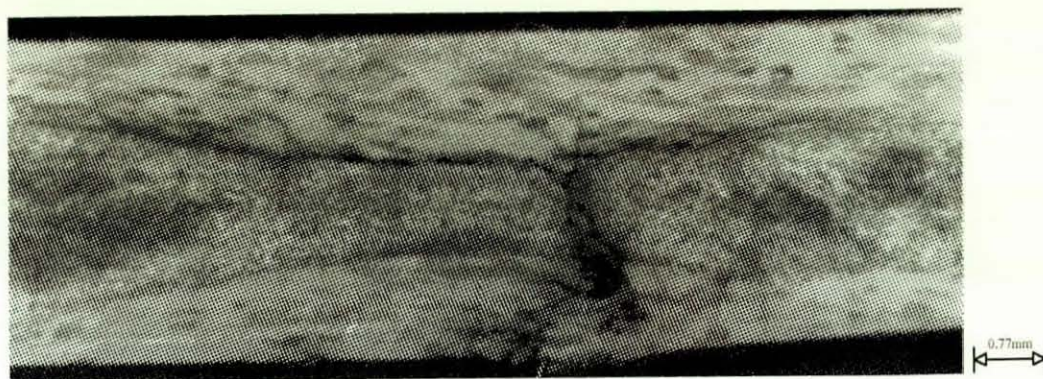


Figure 7.26 Photograph of upper interface delamination initiated by lower CFM crack and transverse UD matrix crack for 7J TIE transverse coupon.



Figure 7.27 C-Scan plot from a 8J TIE transverse coupon (the attenuation along the edges are due to the tapers/webs and not damage).

7.3.3 Longitudinal Coupon

Figure 7.28 contains typical 27J TIE force-deflection and force-time responses with damage occurring at peak force in the same way as the transverse coupon but with a stiffer response (Figure 7.29(a)).

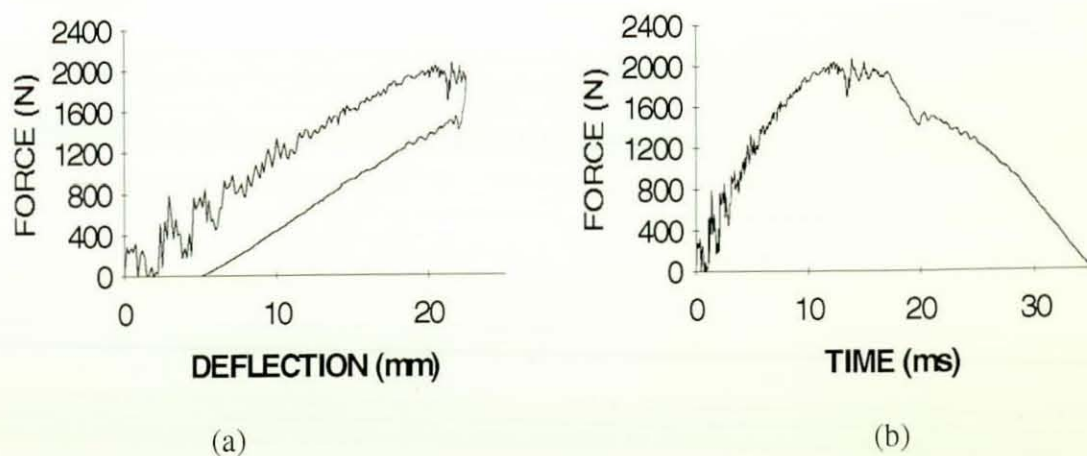


Figure 7.28 Force-deflection (a) and force-time (b) curves for a 27J TIE longitudinal coupon (Figure 4.9).

Figure 7.29(a) shows that the peak force rose in agreement with the predicted elastic response curve to approximately 5J and then the gradient gradually reduced up to 21J, above which the peak force flattened off at 2.0KN. Figures AV.3 and AV.4 in Appendix V underline the change in nature of the impact above 21J due to the increased damage energy absorbed. Final failure occurred in a "creasing" mode for the two highest energies tested, as a consequence of the lower CFM crack extending across the width of the specimen.

The various forms of lower surface cracking in Figure 7.29(b) and 7.30 (the error bars have been omitted for clarity), were the first signs of visible damage and were complex due to the tapers on the lower surface:

Lower CFM crack - tensile crack formed under the impactor.

Taper crack - a transverse tensile crack through the wrap-around ply forming the taper.

Taper-line crack - a longitudinal tensile crack caused by the ply-drop-off at the end of the wrap-around ply, running along the taper-line.

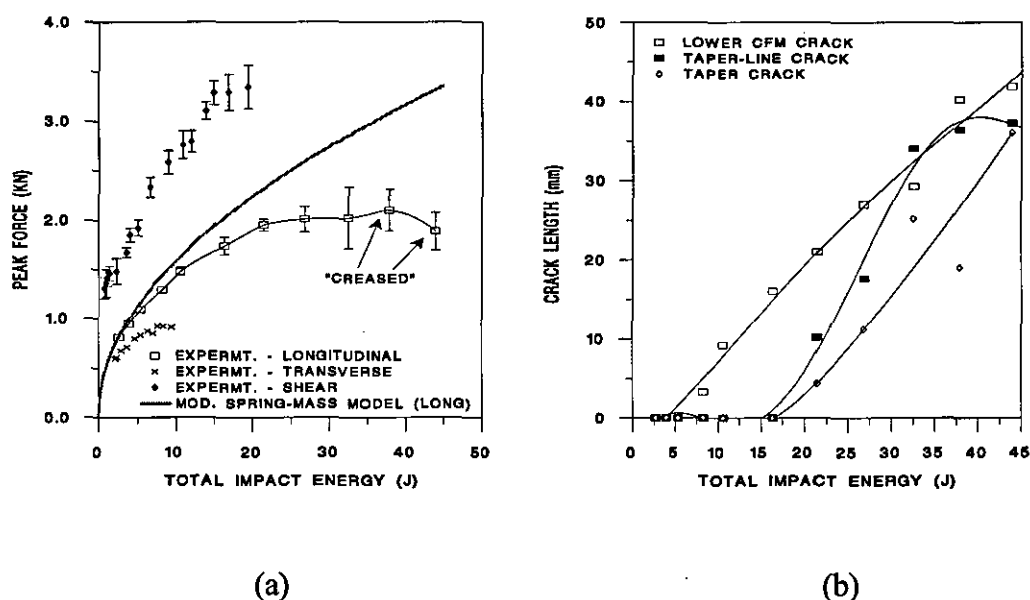


Figure 7.29 Peak force versus TIE for the longitudinal coupon, and modified spring-mass model predictions, in comparison with the shear and transverse coupon experimental results (a) and crack lengths versus TIE for the longitudinal coupon (b).

The lower CFM crack was initiated at approximately 5J (Figure 7.29(b)) and grew quite linearly with TIE, which corresponds to the reduction in stiffness response at 5J in Figure 7.29(a). The taper crack and taper-line crack were initiated between the 16 and 21J TIE sets of tests. It is these forms of cracking and associated delamination which were a prime cause of the reduction in stiffness response above 21J.

Figure 7.31(a) shows the delamination areas plotted against TIE, with rapid delamination growth above 27J TIE, which corresponds to the flattening off in the peak force above this energy. Figure 7.32 contains two typical C-Scan plots, with scan (a) showing the individual side and central delaminations whilst (b) shows how they merged at higher energies. Figure 7.33 shows the central lower delamination and taper delamination overlapping, and merging.

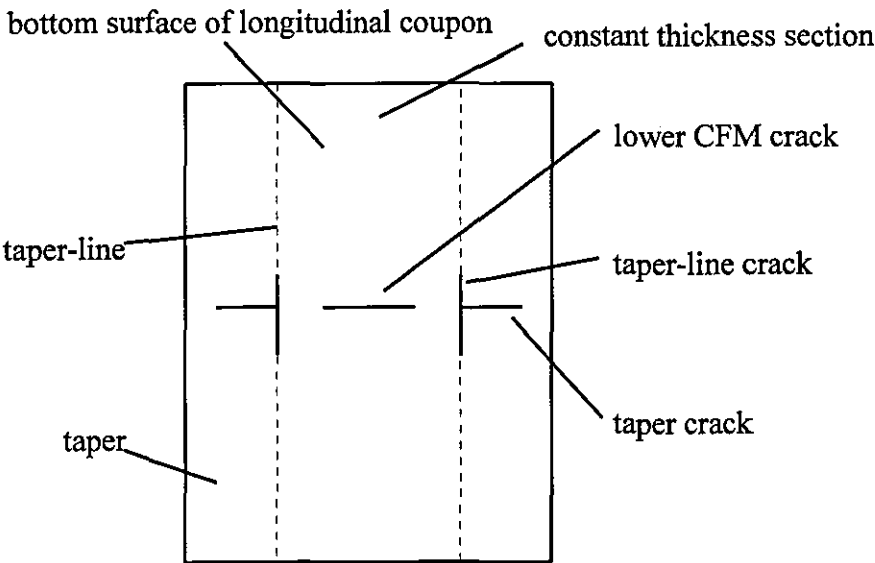


Figure 7.30 Cracking on lower surface of the longitudinal coupon.

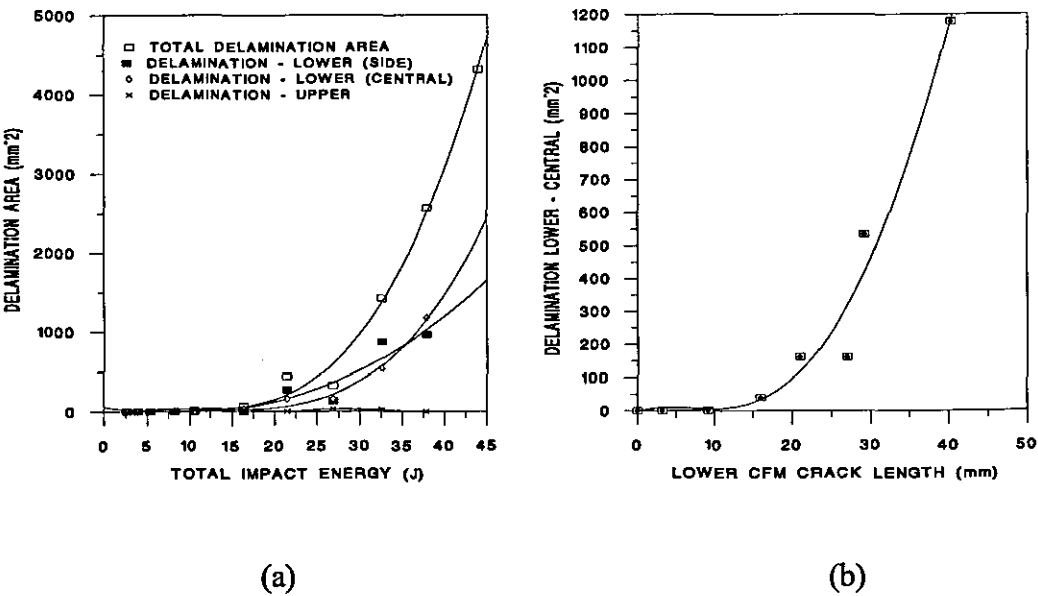


Figure 7.31 Delamination areas versus TIE (a) and lower interface delamination (central) versus lower CFM crack length for the longitudinal coupon (b).

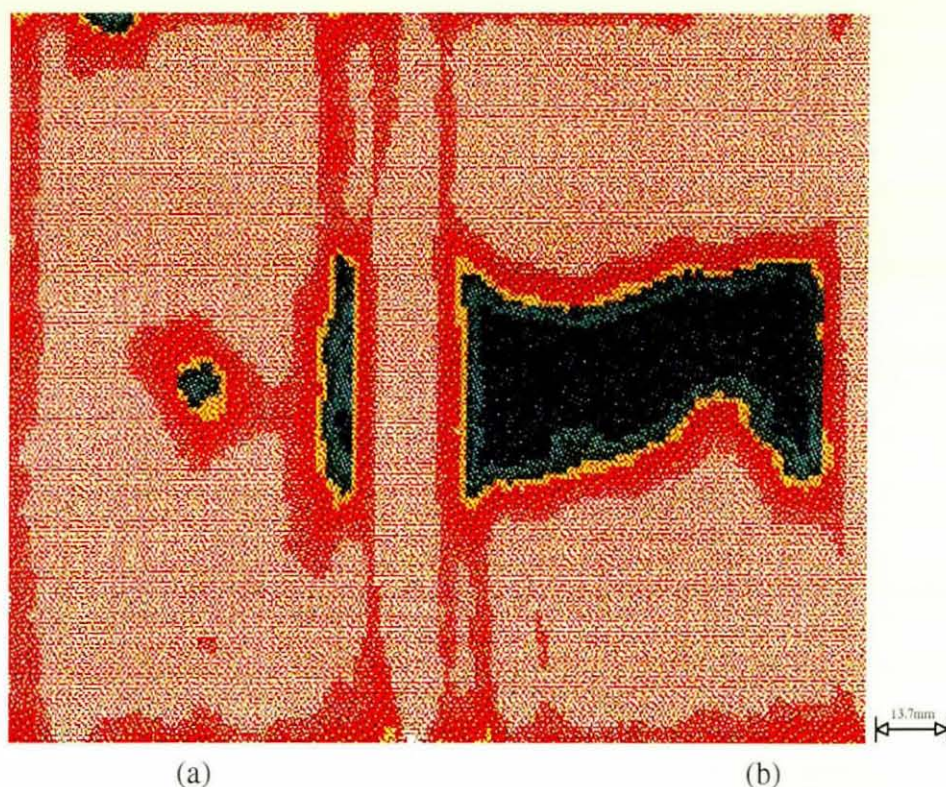


Figure 7.32 Typical 27J (a) and 33J TIE (b) C-Scan plots for the longitudinal coupon.

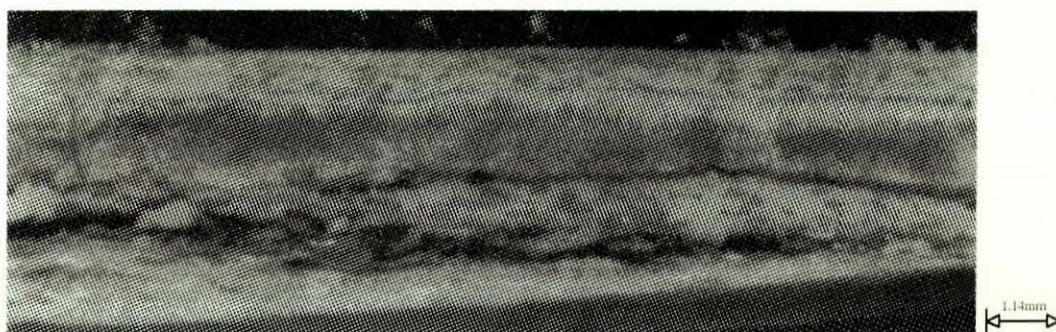


Figure 7.33 Photograph of central lower interface delamination and taper delamination overlapping and merging in a 33J TIE longitudinal coupon.

The most significant form of delamination was at the lower interface (delamination lower (central)) and along the interface between lower CFM and wrap-around ply (delamination lower (side)). The delamination lower (side) could also be considered to be a "debond" of the web from the skin. The lower CFM crack initiated the lower interface delamination (central) because when the crack reached the lower interface it was redirected by the longitudinal fibres in the UD layer into a delamination (Figure 7.34). Figure 7.31(b) shows the relationship between the lower CFM crack and lower interface delamination (central) and suggests an initiation crack length of 10mm above which delamination growth increased rapidly.

Figure 7.31(a) indicates that there was some upper interface delamination but this remained very small, and was due to the high shear stresses local to the impactor, as this form of delamination was only found adjacent to the impact site.

Under the impactor, upper CFM damage consisted initially of permanent indentation and then shear cracking. An indentation was just visible at 8J TIE (1.3KN - as compared to 1.5KN for the shear tests) and increased to approximately 0.15mm before shear cracking occurred at 32J (2KN). "Creasing" failure occurred before the shear cracks had passed through the upper CFM layer.

At higher energies, as the deflection of the coupon increased, compressive failure of the upper CFM layer occurred along the crease line in the form of whitening (surface fibre micro-buckling).

Table AV.14 in Appendix V contains the fibre breakage results from thermal deply tests, showing that considerable UD fibre breakage occurred before final failure. As the lower surface CFM crack grew, the stresses in the UD layer increased dramatically especially in the lowermost fibres, producing UD fibre breakage prior to final failure (Figure 7.34).



Figure 7.34 Photograph of lower interface delamination initiated by a lower CFM crack and UD fibre failure in a 44J TIE longitudinal coupon.

There were a large number of damage modes for this impact configuration, due to the tapers on the lower surface. The interactions in the higher energy tests could not be described sufficiently due to their complexity. However, the initial onset of central lower CFM cracking and associated delamination was clearly identified and correlated with the change in stiffness response in Figure 7.29(a).

The coupon tests have thus provided a great deal of information regarding the behaviour of the basic pultruded composite in shear, and transverse and longitudinal bending. Lower CFM cracking was critical as it directly initiated lower interface delamination under longitudinal bending and indirectly initiated, via transverse UD matrix cracking, upper interface delamination under transverse bending. Under shear loading upper interface delamination was induced by high shear forces and a transverse UD matrix crack prior to promotion via a lower CFM crack. Thus for this lay-up the lower CFM crack can be likened to the critical matrix crack referred to by Chang and co-workers⁴⁹ which initiated delamination in 0/90 laminates. UD shear cracking also occurred, which under shear loading only initiated lower interface delamination. Shear cracks in the UD layer initiated lower interface delamination, as reported by Joshi and Sun⁴³ for 0/90 lay-ups. Thus, delamination only occurred in the presence of an initiating crack as was first reported by Takeda⁶⁵. Transverse UD matrix cracking occurred at energy levels below that tested, whilst only limited UD fibre breakage was observed prior to final failure. When very high contact forces were induced (e.g. in the shear coupon), and the indentation under the impactor reached a critical level, the upper CFM cracked through. This form of upper CFM failure was labelled ply "shear-out" by Zhou and Davies⁹⁵ in their impact work on thick glass/polyester laminates. For the shear coupon at high energy levels UD shear cracking was so dense under the impactor that considerable fibre-matrix debond occurred in the UD layer. The understanding of these damage modes and interactions was applied to explaining the response of the structurally complex impact configurations described in the following sections.

7.4 Box Section Tests

Two series of box section tests (three- and five-box sections) were performed with three impact locations tested for each section as described in Chapter 4. Being much larger sections, less specimens were tested due to restrictions on the quantity of material available. Comparison between the responses of these configurations and the coupon test are made in section 7.6.

7.4.1 Three-Box Section

7.4.1.1 "Central" Impact Tests

Figure 7.35 contains the force-deflection and force-time curves for all the impacts in the 21J TIE set of tests, showing a high vibration content but also a very repeatable response. Figure 7.36(a) shows a steady rise in peak force up to 8J, a less steep rise between 8J and

21J and a flattening off thereafter. The 38J tests penetrated the upper skin, but penetration of the lower skin did not occur because the impactor was not long enough. With respect to the modified spring-mass model predictions, it is clear that only the lowest energy impact approached an elastic response. The remaining three impact test data graphs (Figures AV.5 and AV.6 in Appendix V) correlate well with Figure 7.36(a), showing changes in response at 8J and 21J TIE.

The damage analysis results are included in Figures 7.36(b) and 7.37. The first macroscopic damage was cracking of the lower CFM layer, which was initiated above 2J and grew with TIE (Figure 7.36(b)) to approximately 150mm at which point penetration occurred. This crack initiated upper interface delamination by the mechanism described in section 7.3.2 for the transverse coupon. Figure 7.37(a) shows the close relationship between lower CFM crack length and upper interface delamination area and gives the CFM crack length required for upper interface delamination as 25mm approximately. The relationship was less consistent at the highest energies due to both the penetration threshold being reached and the crack length approaching the width of the specimen.

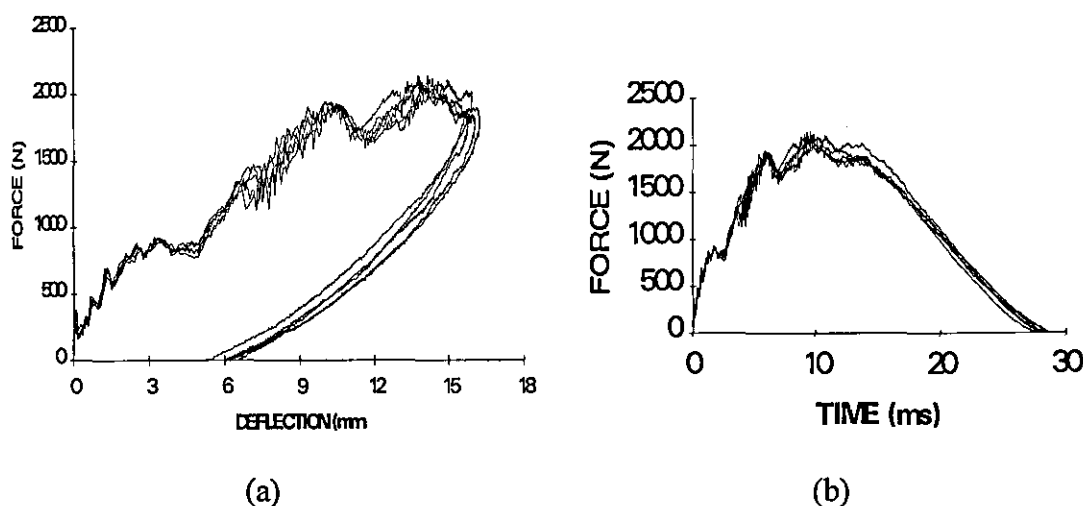


Figure 7.35 Force-deflection (a) and force-time (b) curves for the 21J TIE central impacts from the three-box section (Figure 4.10).

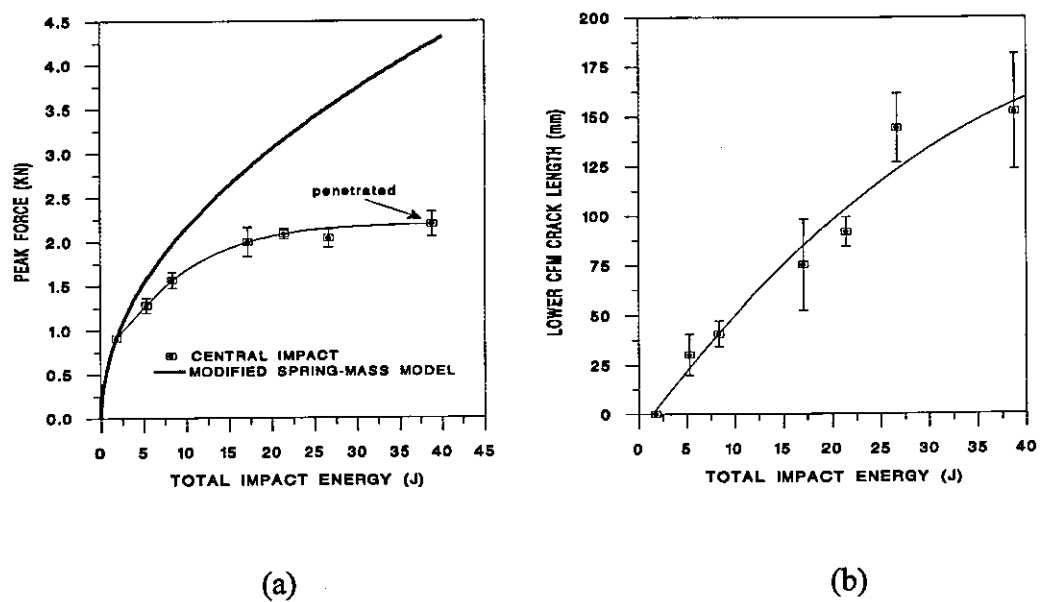


Figure 7.36 Peak force (a) and lower CFM crack length (b) versus TIE for the central impacts from the three-box section and modified spring-mass model prediction.

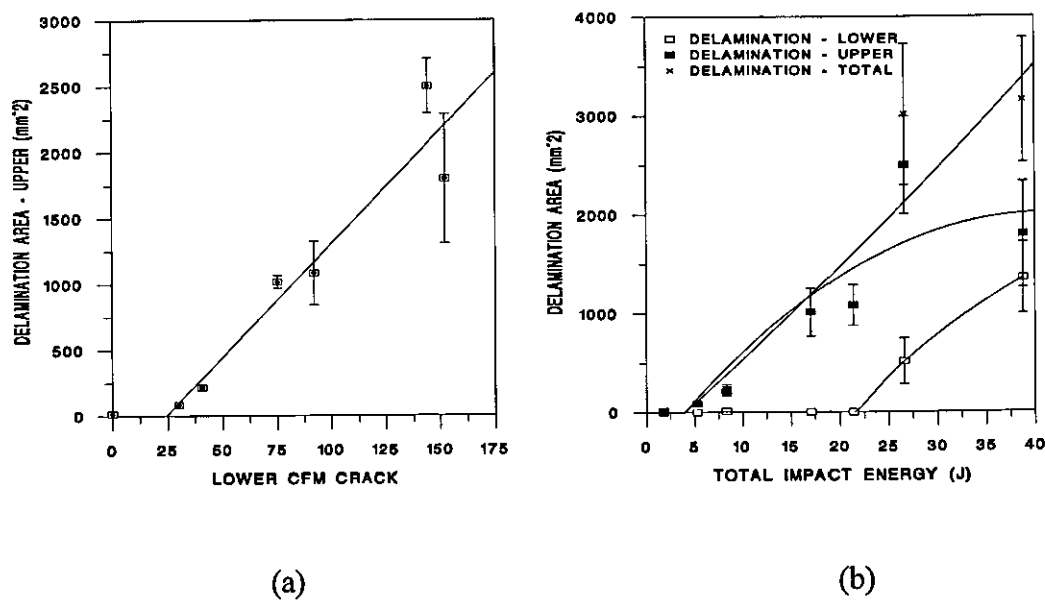


Figure 7.37 Upper interface delamination area versus lower CFM crack length (a) and delamination areas versus TIE for the central impacts from the three-box section.

Figure 7.37(b) shows that upper interface delamination growth was relatively linear with TIE up to 21J, at which point lower interface delamination was initiated which then increased linearly to penetration. The upper interface delamination, which was first detected at 5J, was usually accompanied by a vertical (transverse) or inclined (shear) UD crack at or near its edge. (Figure 7.38).

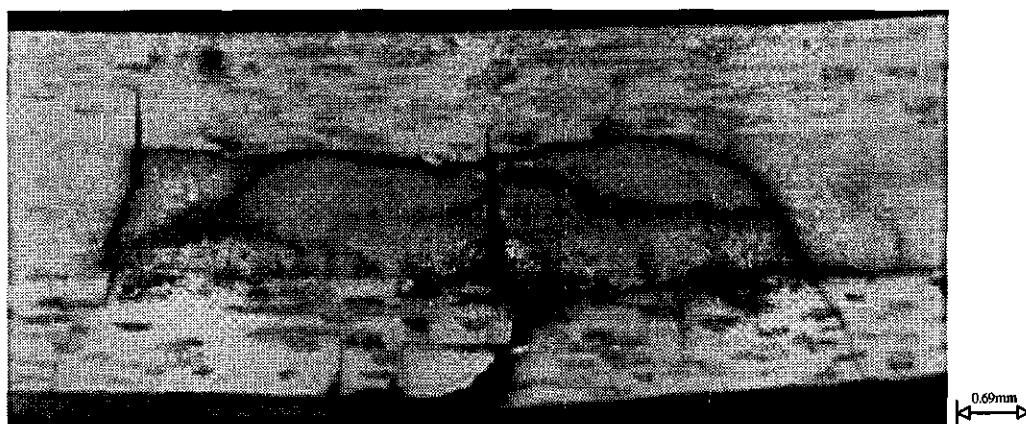


Figure 7.38 Photograph of UD cracking associated with upper interface delamination for 5J TIE central impacts from the three-box section.

The shear cracks in the UD layer, induced by the high shear forces generated by the double skin/web section, initiated lower interface delamination as described in section 7.3.1 for the shear coupons and illustrated in Figure 7.39. Lower interface delamination only occurred when quite considerable deformation of the lower CFM layer had taken place (Figure 7.40) and did not always form on both side of the upper interface delamination depending on the global deformation present. However, due to this large deformation on the lower CFM surface of the 27J specimens, it was apparent that "hinges" were forming as shown in Figure 7.41, due to the CFM cracking through its thickness.

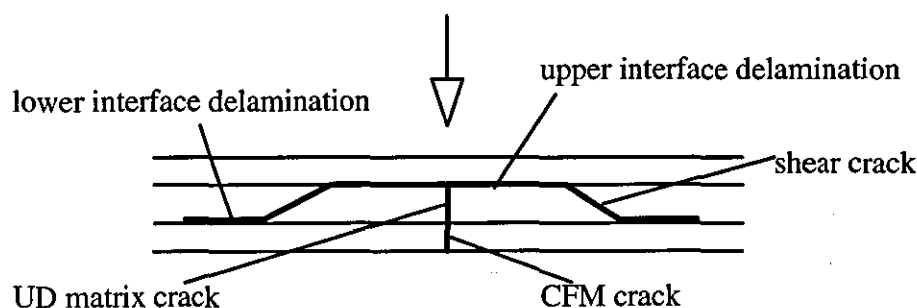


Figure 7.39 Shear cracking and delamination in central impacts from the three-box section.

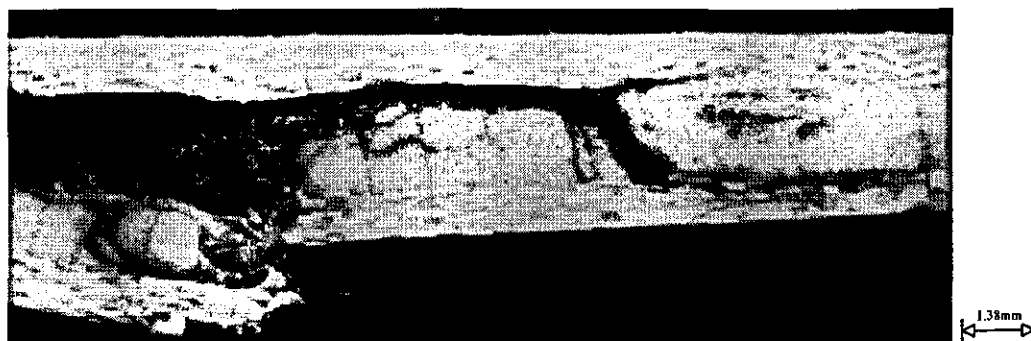


Figure 7.40 Photograph of large deformations and lower interface delamination in 27J TIE central impact specimen from the three-box section.

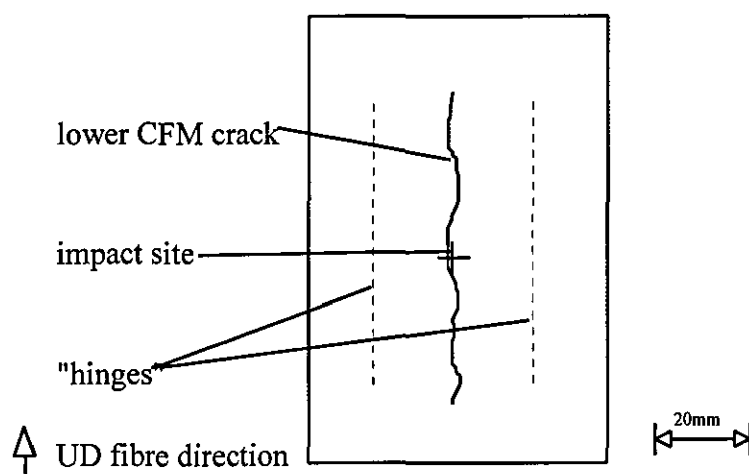


Figure 7.41 "Hinging" on the bottom surface of central impact specimens from the three-box section.

Figure 7.42 shows a diagrammatic plan view of the typical upper and lower interface delamination shapes for a high energy impact, with the upper interface delamination following the CFM crack and the lower interface delamination forming outside the upper. From OM the classic "peanut" shape was observed, with upper interface delamination suppressed directly under the impactor as explained for the shear coupons.

Other forms of damage which occurred were shear cracking of the upper CFM layer and UD fibre breakage on penetration. The shear cracking was initiated in the 8J set of tests and by 27J the upper CFM layer was completely cracked through, therefore this form of damage also contributed to the lower peak forces above these energies.

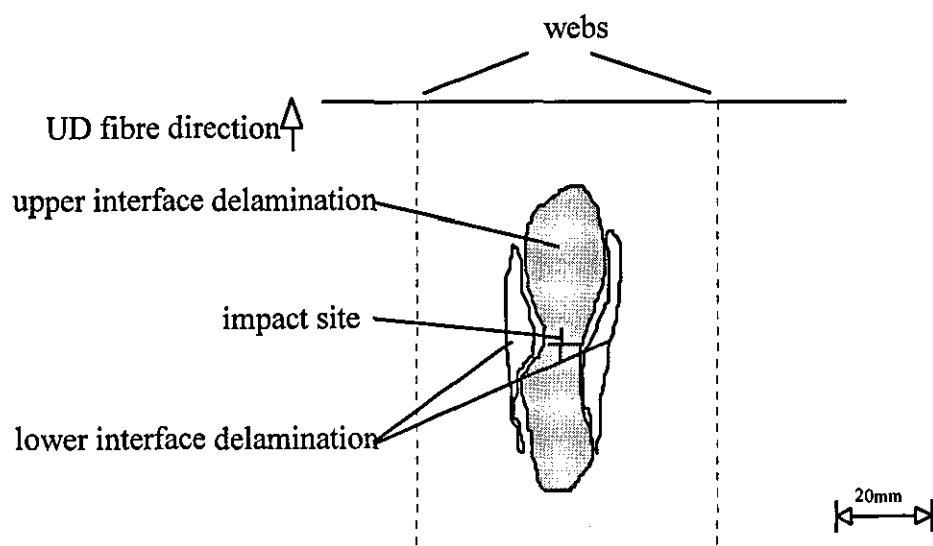


Figure 7.42 Upper and lower interface delamination shapes in central impacts from the three-box section.

7.4.1.2 "Intermediate" Impact Tests

The force-deflection and force-time curves for the intermediate and web impacts were similar to the responses in Figure 7.35 and so have not been repeated. The structural response and resulting damage progression of these specimens was quite complex due to the non-symmetry of geometry and lay-up. In order to understand the results it is first necessary to study the exact lay-up at the web/skin join (Figure 7.43). The fibres of the lower CFM ply and the wrap-around ply made of needle-mat do not intermesh, so the bond is dependent on the resin strength and was therefore an area of weakness.

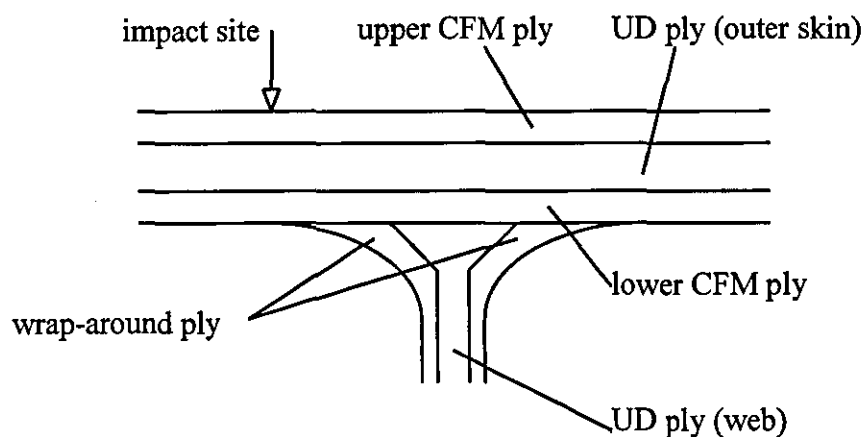
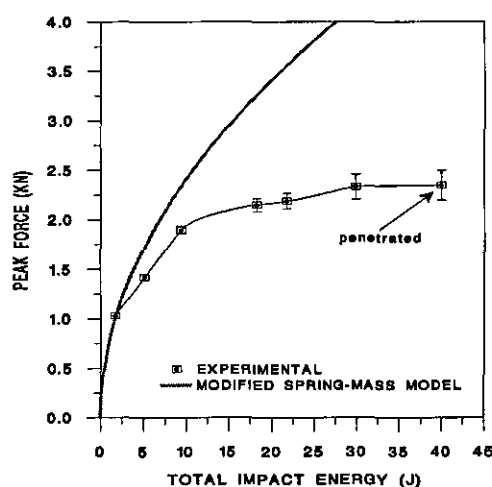


Figure 7.43 Typical transverse section through web-skin join of the ACCS "plank".

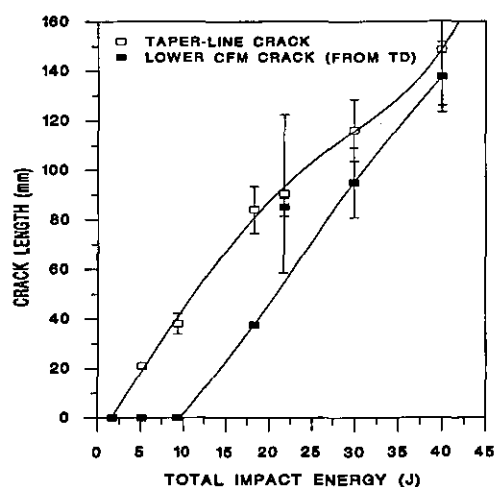
Figure 7.44(a) shows the peak force rising linearly to 9J, flattening off thereafter at approximately 2.2KN with penetration occurring for 38J TIE tests. Only the lowest energy response correlated well with the elastic response prediction.

The first form of visible damage was a longitudinal crack between the wrap-around ply and the lower CFM layer - a taper-line crack. The thermal deply exercise showed that there was no lower CFM crack at this point. The taper-line crack was not vertical and so did not directly initiate a matrix crack through the UD layer. Instead, it travelled between the CFM and needle-mat layers (Figures 7.45 and 7.46) contributing towards the reduction in peak force from elastic predictions up to 9J TIE.

Figure 7.44(b) shows that the taper-line crack grew linearly with TIE. This form of damage initiated a debond between the wrap-around ply and lower CFM layer, but even with optical microscopy it was not possible to identify the interface and so it was not possible to follow the crack growth. This form of damage will greatly reduce the compressive stiffness and strength of the section as stated by Davies and Robinson⁴⁰.



(a)



(b)

Figure 7.44 Peak force (a) and crack lengths versus TIE for the intermediate impacts from the three-box section.

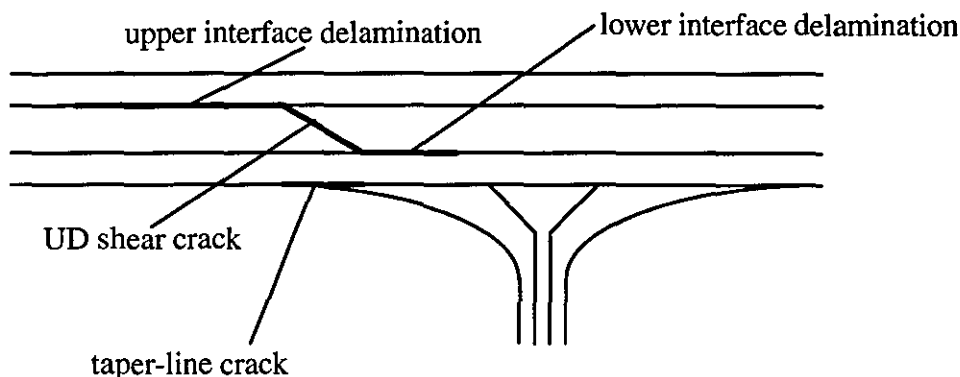


Figure 7.45 Damage progression in the intermediate impacts from the three-box section.



Figure 7.46 Photograph taper-line crack at 9J TIE for an intermediate impact from the three-box section.

Optical microscopy revealed that both upper and lower interface delamination was initiated above 2J and both increased steadily up to penetration though the area of lower interface delamination was much lower than the upper (Figure 7.47). The delaminations were initiated by a single shear crack in the UD layer under the impactor at approximately 45° pointing down towards the web (Figure 7.48). The UD shear crack was present in the 2J test specimens but with little or no associated delamination. Due to the non-symmetrical geometry and the much stiffer response on the web side of the impact site, high shear stresses were developed which initiated the shear crack and upper and lower interface delamination.

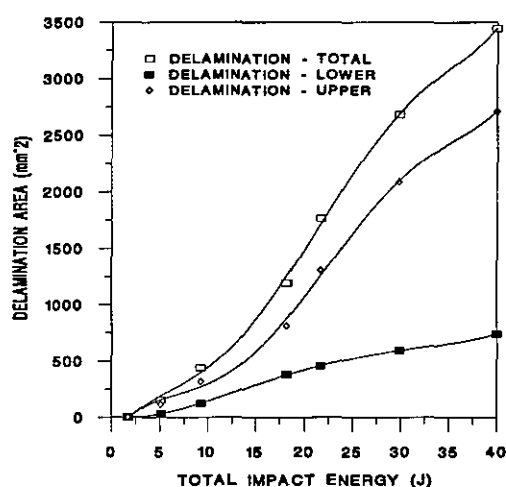


Figure 7.47 Delamination areas versus TIE for the intermediate impacts from the three-box section.

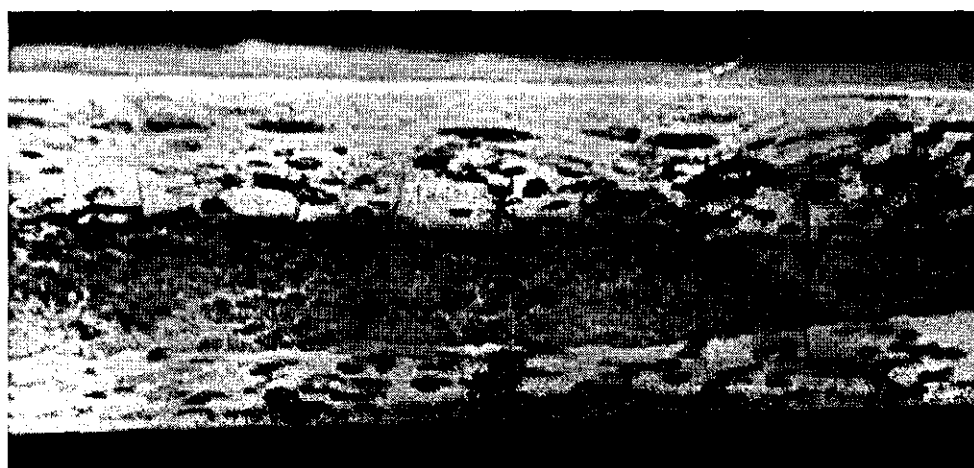


Figure 7.48 Photograph of upper interface delamination initiated by a UD shear crack for a 5J TIE intermediate impact from the three-box section.

The upper interface delamination grew at a greater rate above 18J (Figure 7.47) whilst thermal deply (Table AV.21 in Appendix V) showed that lower CFM cracking was first observed 9J and 18J (Figure 7.44(b)). Due to the taper, the lower CFM crack could not be observed visually. The lower CFM crack, induced a UD matrix crack, which further promoted the propagation of the upper interface delamination (Figure 7.49). Lower CFM crack growth and greater rate of upper interface delamination correspond to the reduction in stiffness present in Figure 7.44(a) between 9J and 18J TIE.

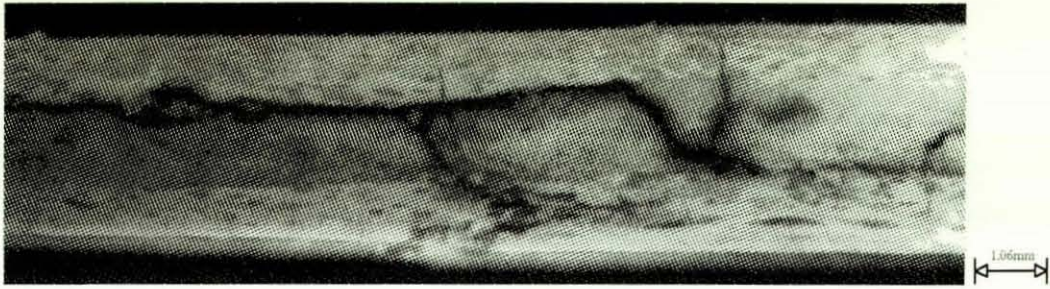


Figure 7.49 Photograph of lower CFM crack and UD matrix crack promoting upper interface delamination in a 18J TIE intermediate impact from the three-box section.

The initiation of lower CFM cracking was very dependent on the exact location of the impact. If the impact site was outside the wrap-around ply then lower CFM cracking occurred earlier, and behaviour tended towards that observed for the central impacts. When the impact site was over the wrap-around ply, the damage forms discussed above postponed lower CFM cracking until later in the damage process.

A C-Scan of a specimen from the highest energy set of tests is shown in Figure 7.50, and Figure 7.51 shows how the upper and lower interface delamination areas developed at higher energies. Clearly the damage was non-symmetrical along the impact site (i.e. the taper line), due to the non-symmetry of the geometry and therefore stiffness in the impact locality.

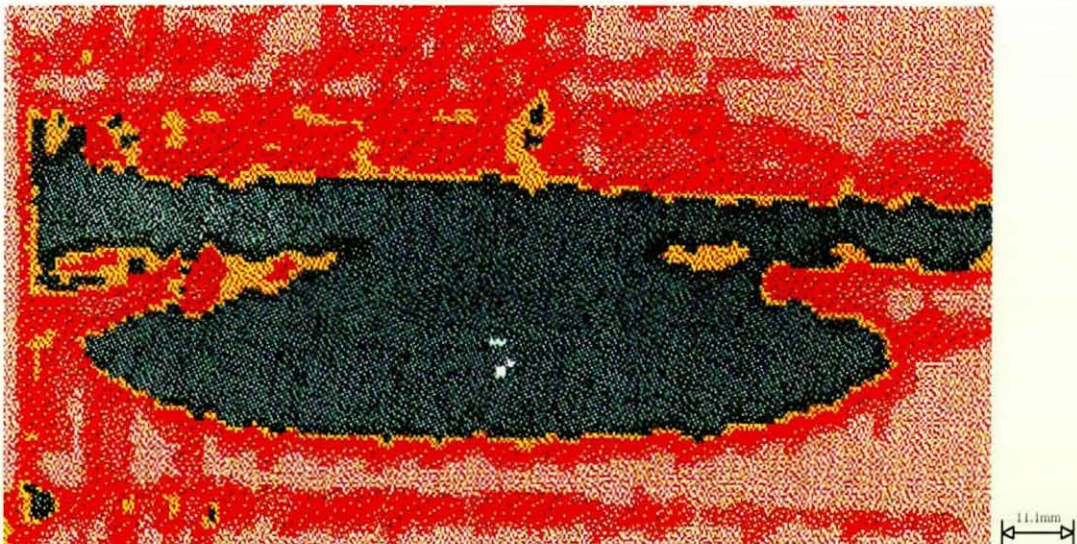


Figure 7.50 C-Scan of 40J TIE showing damage area blending into the area indicating the web for an intermediate impact from the three-box section .

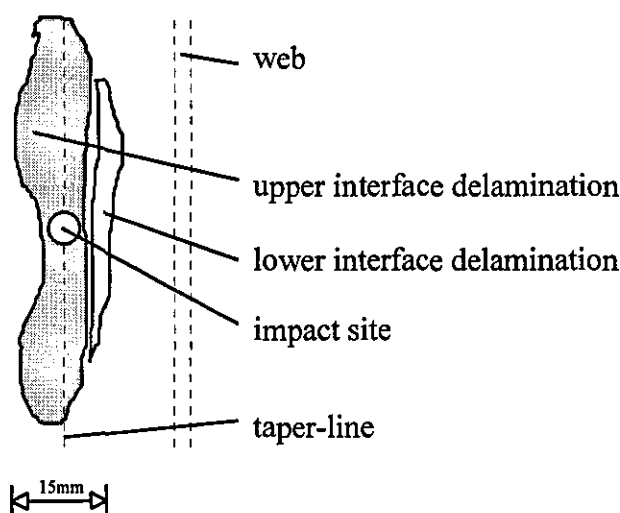


Figure 7.51 Delamination areas at high energy for intermediate impact from the three-box section.

The non-symmetry of structural and damage responses was also seen on the impacted surface. Little damage was induced on the CFM layer under the impactor on the side furthest from the web up to 22J, but on the stiffer side nearest the web, shear cracking occurred and this side of the impact site collapsed at 18J, which contributed to the flat curve above this TIE in Figure 7.44(a).

7.4.1.3 "Web" Impact Tests

The impacts performed directly over the webs from the three-box sections elicited a completely different damage response from the central or intermediate impacts. Due to the nature of the damage the results have been treated descriptively rather than quantitatively.

Figure 7.52 contains the peak force versus TIE graph for all three test locations for the three-box section and clearly the forces generated in the web specimens were much greater than either the central or intermediate impacts indicating an entirely different response. The graph also shows that the peak force steadily departed from the elastic response curve, and flattened off above 40J TIE ($\approx 5\text{KN}$).

For a strike directly over the web, due to the web itself, penetration cannot take place, whilst the impact damage was unpredictable because the response was critically dependent on the exact strike location, as there was a very large stiffness variation over a few mm's either side of the web.

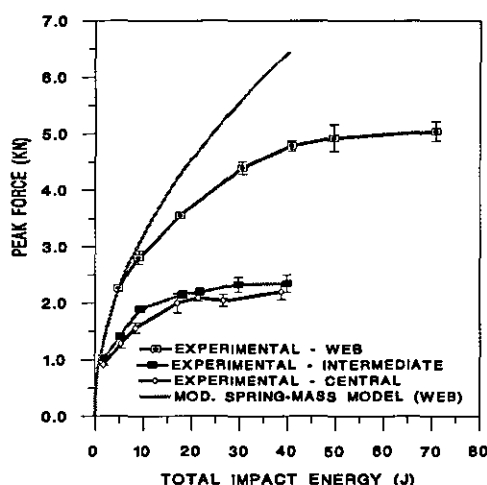


Figure 7.52 Peak force versus TIE for web, intermediate, and central impacts from three-box sections, and modified spring-mass model prediction for the web impacts.

In all the previous tests, local deformation under the impactor was superimposed on the global bending of the entire structure. For the strike location directly over the web, due to the high stiffness directly under the impactor very little local deformation occurred. Instead high stresses were transferred from the impact site on the upper skin throughout the structure via the webs. Because there was little local deformation and therefore very low strains directly under the impactor, there was less local damage initially which agreed with that suggested by Davies⁶⁰. The first damage, visible on the lowest energy tests, was a small permanent indentation under the impactor which arose due to the very high contact force.

The global deformation was responsible for absorbing the impact energy and therefore the damage, rather than originating and growing from under the impactor as previously, was initiated at remote sites as reported by Cheung⁹⁹. The web/skin sections act as shear boxes and therefore the web/skin joins were particularly susceptible to damage. In addition to the geometry making these joins areas of stress concentration, the tight radii resulted in poor material and/or lay-up quality. Often resin rich or poorly wetted out fibres were found in these areas. Due to being both areas of high stress and often poor material quality, it was along these joins where the second form of visible damage occurred - matrix cracking and/or fibre whitening. Thermal deply revealed that the resin rich areas were caused by the wrap-around layer being forced into the area where the web UD should have been (Figure 7.53) and resulting in matrix cracks (Figure 7.54). Often the fibres were poorly wetted out on the opposite

join, resulting in fibre whitening. Both these forms of damage were noted on all test specimens from 5J TIE upwards. At 50J each section was permanently bowed due to the extent of this remote damage.

Cheung and colleagues⁹⁹ identified the peeling stress on the skin/stiffener join due to bending as the reason for the remote delamination which they identified. In this work it was the tensile forces across the joins due to shear distortion of the boxes, which generated the cracking. The tensile forces caused matrix cracking whilst the compressive forces on the opposite join caused surface fibre buckling seen as fibre whitening.

On one of the specimens at 20J TIE, there was a crack along the taper-line to the right of the impacted web due to a lay-up problem through the section at this point. One of the 70J specimens for which the impact was directly over the web, had no local damage on the web/skin join under the impactor, but instead the web buckled along its length about halfway down its height. Both these examples illustrate how these impacts exploited local or remote weaknesses to a much greater degree than any of the others impact configurations.

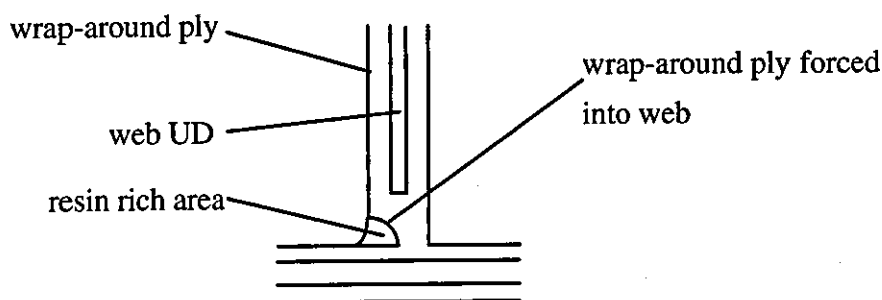


Figure 7.53 Resin rich area along skin/web join.

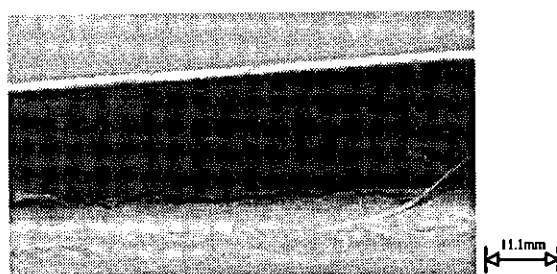


Figure 7.54 Photograph of matrix crack along skin/web join for a web impact from the three-box section.

At 20J TIE half the specimens exhibited a small crease/crack (approximately 10mm long) on the web/skin join under the impactor, with a semi-circular crack on the web below it or on the opposite side of the web (Figure 7.55). The sides that these appeared on was not consistent but usually the crease/crack was on the side to which the impactor had struck. As the TIE increased this crease/crack combination grew in length to approximately 35mm at 70J. The reason for this form of damage is explained below. The exact nature of the lay-up at the joints was inconsistent and had some bearing on the damage induced under the impactor, and Figure 7.56 shows three types of lay-up commonly observed.

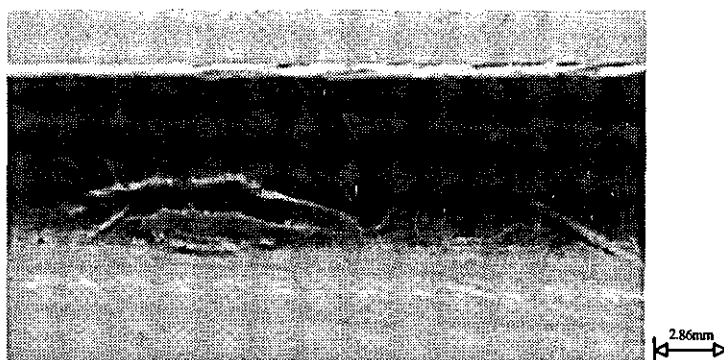


Figure 7.55 Photograph of crease/crack under the impact site for the web impacts from the three-box section.

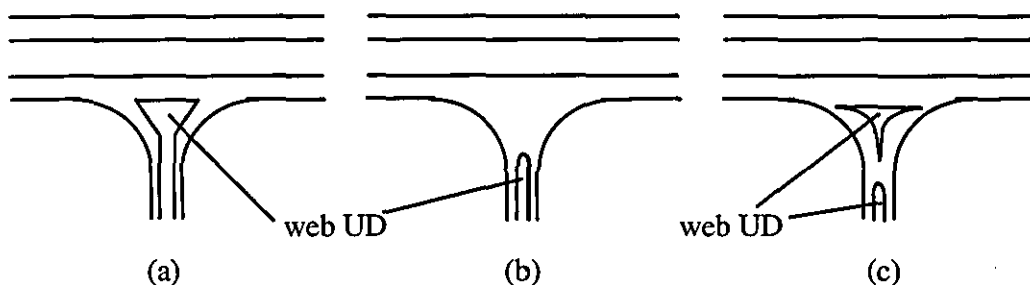


Figure 7.56 Transverse section through web-skin join showing three major lay-up types.

At 20J TIE the first form of internal damage under the impactor (other than transverse matrix cracking in the skin UD layer) was observed. Small delaminations at either interface and shear cracking in the UD layer were noted as shown in Figure 7.57(a). As the TIE increased so the matrix damage parallel to the fibres in the skin UD layer increased (Figure 7.57(b)) due to the very high contact forces. At 40J the first signs of shear cracking on the upper CFM layer were observed.

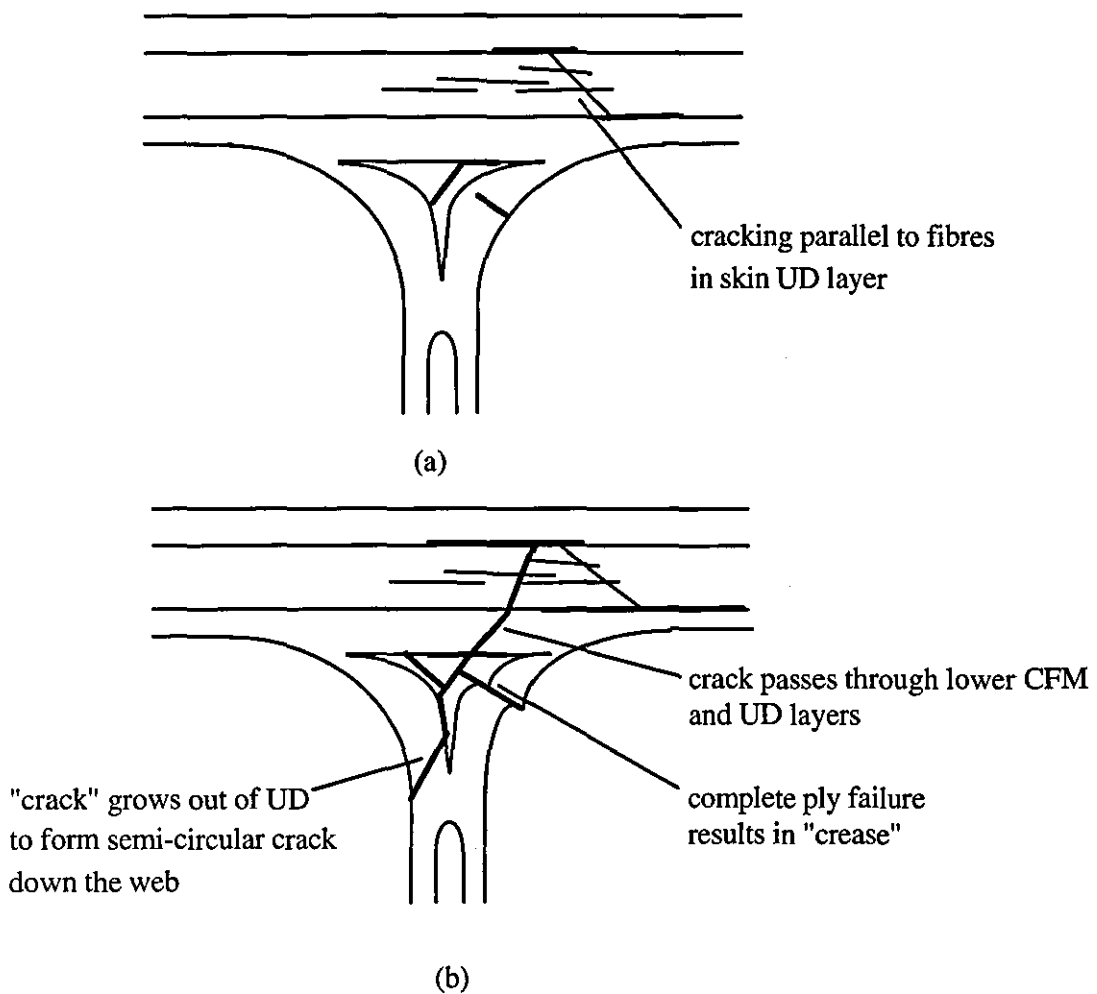


Figure 7.57 Damage progression revealed by OM for the web impacts from the three-box section.

The damage observed at the skin/web join was dependent on the type of lay-up at the join. If there was a triangle of web UD (Figure 7.56(a and c)), then a pattern of internal crack growth was observed. As in Figure 7.57(a) the damage initiated as a matrix crack in the triangle of UD. This crack continued to grow within the UD as the TIE increased and a crack in the wrap-around layer then grew into the triangle of UD, thus cracking completely through the outer layer of the join (Figure 7.57(b)). As the impact was often just to the right of the web, this caused the upper section of the cracked ply to move down over the lower section - giving the appearance of overlapping or creasing. On the other side of the web, the matrix crack eventually grew out of the bottom of the UD triangle and passed through the wrap-around ply on the left side of the web. This crack was further down the web and therefore explains the semi-circular crack described previously. The matrix crack also grew out of the top of the UD triangle, through the lower CFM layer, and skin UD layer to promote delamination along upper and lower interfaces. If there was no UD at the join (Figure 7.56(b)) then

there was only cracking in the wrap-around layer (Figure 7.58). Because of the random nature of both the needle mat and CFM in this area, it was impossible to establish a pattern of crack growth as the TIE increased for this type of lay-up.

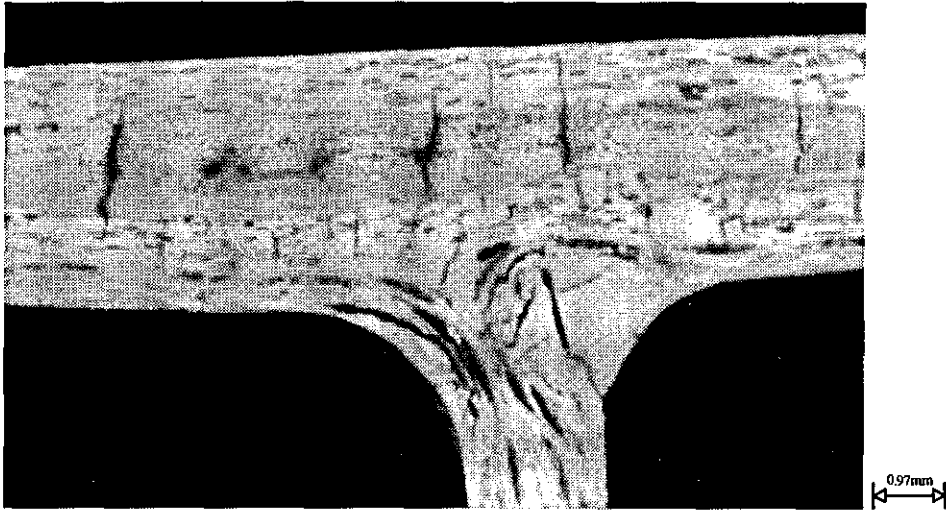


Figure 7.58 Photograph of cracking under impactor in type (b) web/skin join in web impacts for the three-box section.

At 70J TIE, the specimen response fell into two clear categories. If the strike was directly over the web, then there was little upper CFM damage and C-Scan revealed little damage around the impact site. If however, the impact was slightly off centre, the impactor penetrated through the upper skin, causing complete failure of the upper CFM layer, and a huge area of debond/delamination was shown by the C-Scan. These specimens also had a long crack (50-60mm) running along the join on the debonded side of the web. Thermal depley and optical microscopy showed that this crack passed through the wrap around ply, lower CFM layer, and UD. Generally the C-Scans were difficult to interpret as they showed various forms of attenuation along the web, due to the web, varying thickness (over the taper), and material quality as well as impact damage.

The central impacts from the three-box section exhibited damage which could be related to the response of the coupon tests, because there was no local complex geometry. However, as the impact site neared the web the response changed from local damage initiation, to a response dominated by remote damage at locations of stress concentration or poor material/lay-up quality. In the latter case the damage sites were unpredictable and far reaching, which has grave implications for residual strength of the whole structure and makes post-impact repair virtually impossible.

7.4.2 Five-Box Section

Three specimens per set were tested for these tests due to the availability of material for this size of specimen, which resulted in larger standard deviations on the averages calculated, therefore the error bars have been omitted for clarity on the graphs. As for the three-box sections tests, central, intermediate and web impact site tests were performed. The analysis of the results is briefer than previously as many of the damage modes and interactions have been explained in detail before.

7.4.2.1 "Central" Impact Tests

Figure 7.59 shows examples of the force-deflection and force-time graphs from this series of tests, and like the three-box sections, the response was dominated by a high vibration content.

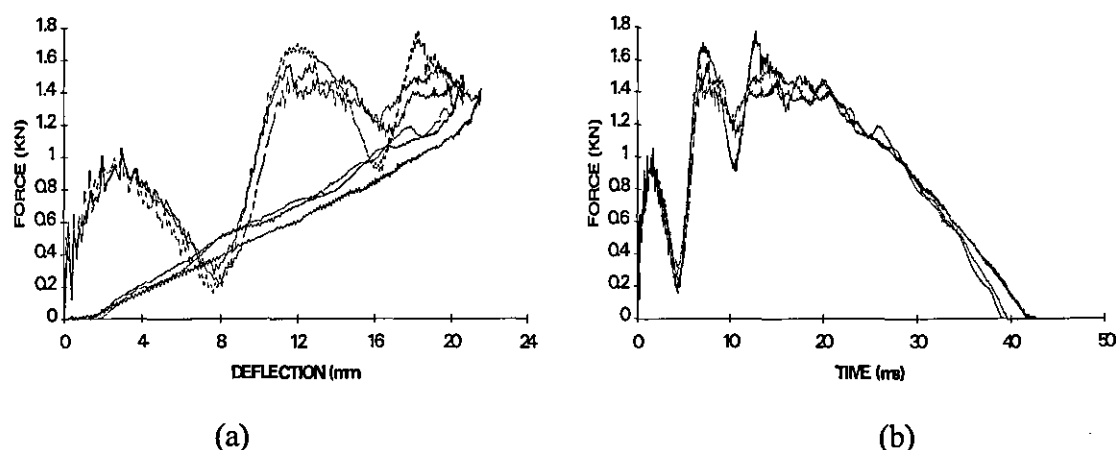


Figure 7.59 Force-deflection (a) and force-time (b) curves at 21J TIE for the central impacts from the five-box section (Figure 4.11).

Figure 7.60(a) contains the peak force data from all three impact sites. There is only one modified spring-mass model curve because all three impact sites had almost exactly the same initial stiffness response. The peak force for the central impacts flattened off at 1.9kN, though final failure, which would have been in the form of "creasing", was not reached.

Figure 7.60(b) shows the delamination areas indicating that there was no lower interface delamination present. OM inspection revealed the absence of shear cracks in the UD layer from which lower interface delamination would be induced.

In the same way as for the other specimens in which transverse bending occurred, the upper interface delamination grew proportionally with the lower CFM crack (Figure 7.61). The delamination areas were again "peanut" shaped, centred around the impact site, as reported previously.

Shear cracking on the upper CFM layer was first observed for the 43J TIE (1.9KN) tests, and was the only other visible damage local to the impact site. Some cracking along the skin/web joins occurred at the higher energies due to the lower stiffness of the section and therefore greater deflections compared to the three-box section. All three impact site test specimens were permanently bowed due to the skin/web join damage.

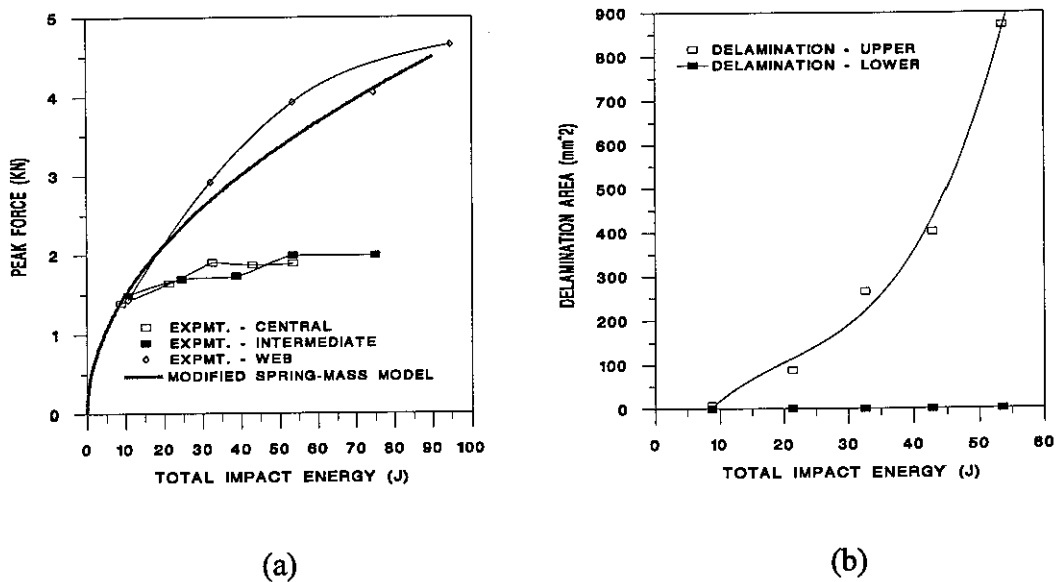


Figure 7.60 Peak force (a) and delamination areas (b) versus TIE of all three site locations from the five-box section.

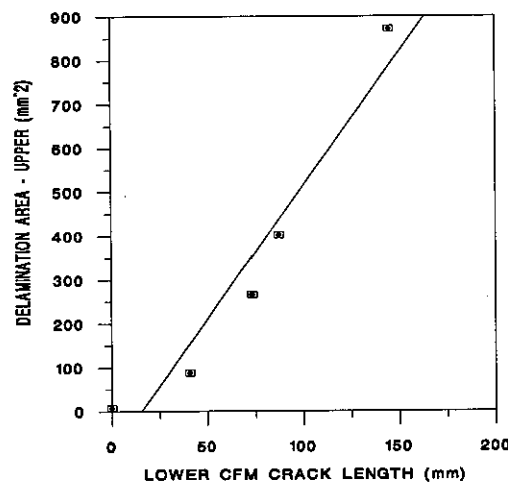


Figure 7.61 Upper delamination area versus lower CFM crack length for the central impacts from the five-box section.

7.4.2.2 "Intermediate" Impact Tests

The force-deflection and force-time graphs were very similar to the central impacts shown in Figure 7.59, and so are not repeated here. The peak force-TIE graph for the intermediate site location follows a very similar path to the central impacts, but flattens out at 2KN and at a higher energy (Figure 7.60(a)). One reason for the similarity in the curves is that the distance between impact locations as a fraction of the span length was much lower than for the three-box sections. So, for these tests, the slightly off-centre intermediate impacts response was more closely related to the central impacts, than was the case for the three-box section. The highest energy impacts did not totally fail, due to the prominence of bending induced damage rather than shear, though some of the specimens had cracked completely across the width along the taper-line.

The damage was generally of the same form as for the corresponding tests on the three-box sections. Shear cracking occurred first in the UD layer, which induced upper interface delamination and, at a higher energy, lower interface delamination. Figure 7.62 shows both the upper and lower interface delamination and taper-line crack versus TIE for this series of tests. It was very hard to distinguish between the taper-line crack and lower CFM crack for these specimens so only one crack length is shown.

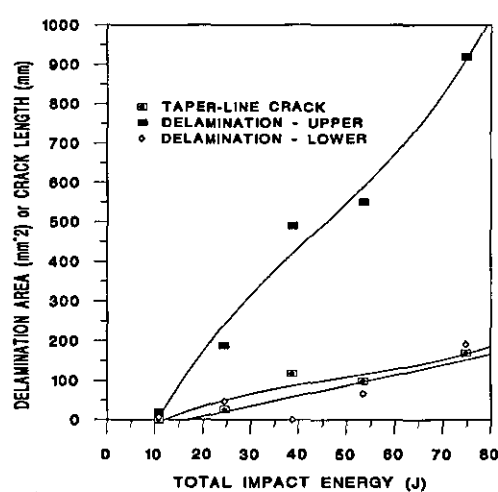


Figure 7.62 Delamination areas and crack length versus TIE for the central impacts from the five-box section.

The lower interface delamination area was low due to the lower shear forces. In more of the specimens, lower CFM cracking occurred in contrast to taper-line cracking, resulting in a transverse UD crack initiating upper interface delamination in the same way as for the

central impacts for the five-box section. Thus the upper interface delamination was more bending than shear crack induced, which is another reason for the similarity between central and intermediate peak force - TIE curves. Despite the impacts being nearer the webs, the shear forces were only slightly higher in the intermediate tests than the central impacts, and therefore the damage induced between the two impact sites was more comparable.

7.4.2.3 "Web" Impact Tests

Each of the impact sites for the five-box section produced a force-deflection curve with a relatively high inertial spike, but this was far more exaggerated in the web tests due to the stiffer contact region (Figure 7.63). In Figure 7.64 the force associated with the inertial spike and the peak force in the vicinity of the peak deflection are shown. Because of the "spiky" curve, the other impact characteristics were very erratic also, making analysis of the impact data difficult. The inertial peak force following the elastic model prediction is believed to be coincidental.

No damage was visible local to the impact site except for a little local cracking at the skin/web join in a few of the specimens. No upper CFM shear cracking occurred due to the slightly lower contact forces than were present in the three-box section. The majority of the damage energy was therefore absorbed by cracking along the skin/web joins throughout the section, though there was no particular pattern to report, strengthening the argument that this form of damage was material/lay-up quality dominated. Due to the higher deflections recorded the cracking and creasing along the joins was more widespread than for the three-box sections.

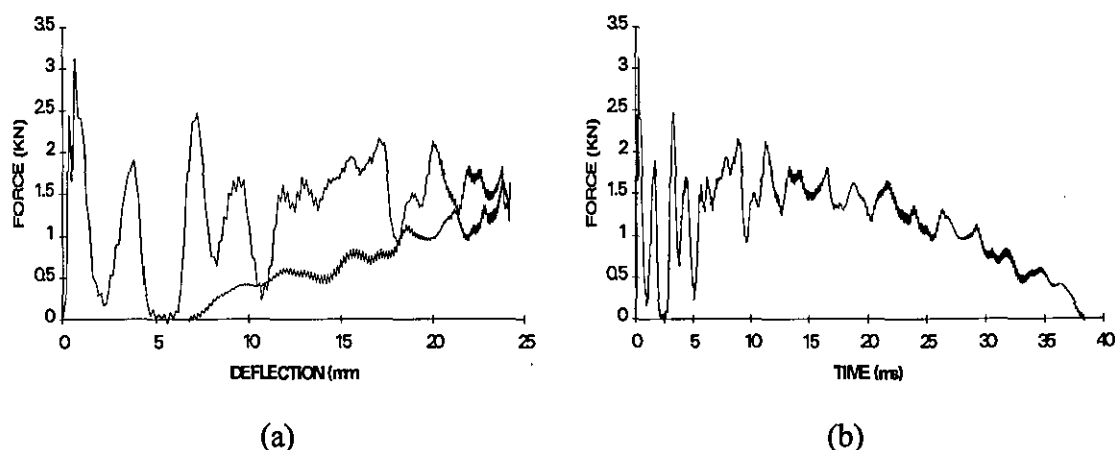


Figure 7.63 Force-deflection (a) and force-time (b) curves at 32.1J TIE for web impacts from the five-box section displaying a high inertial spike.

Figure 7.63 Force-deflection (a) and force-time (b) curves at 32.1J TIE for web impacts from the five-box section displaying a high inertial spike.

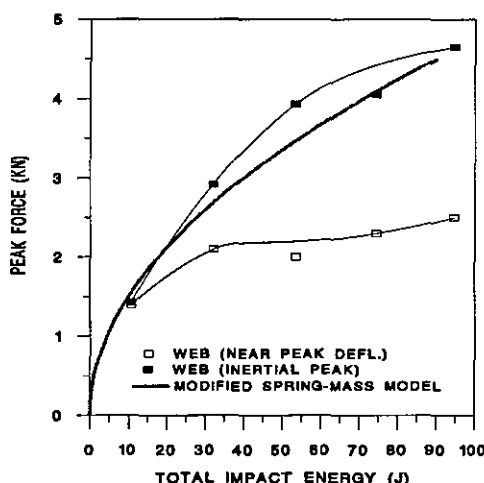


Figure 7.64 Peak force (near peak deflection and inertial peak) versus TIE for web impacts from the five-box section, and modified spring mass-model prediction.

7.5 Full Plank Cross-Section Tests

This section involved correlation of observations from the video recording with the force-time curves. Figure 7.65 contains the force-time trace for a test at 1m/s, an almost elastic impact, which clearly shows five peaks. The corresponding zoomed in video recording of this test (Figure 7.66) showed the upper skin under the impactor flexing five times, superimposed on the global deflection of the plank (the diameter of the flexed area was approximately 35mm), thus providing excellent correlation between the video recording and the force data as logged by the Rosand software.

The video recordings of the 3m/s and 4m/s impacts were also instructive. On both tests the global deflection of the plank was large (for the 4m/s test the plank bottomed out on the support plate underneath), and the video recording of the global deflection of the ACCS "plank" clearly showed the seven connected boxes acting as shear cells (Figure 7.67), and confirming why the skin/web joins were so prone to damage.

Due to the cellular nature of the plank it was not possible to view the underside of the top skin, therefore the lower CFM tensile crack initiation and propagation could not be viewed.

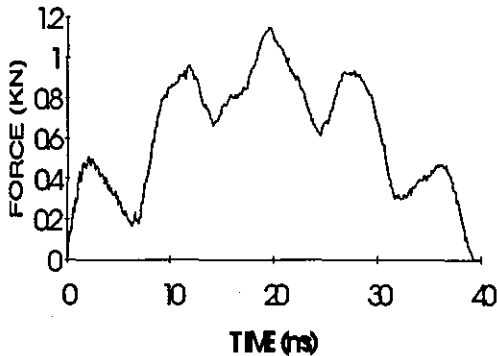


Figure 7.65 Force-time curve of 1m/s impact on full plank cross-section.

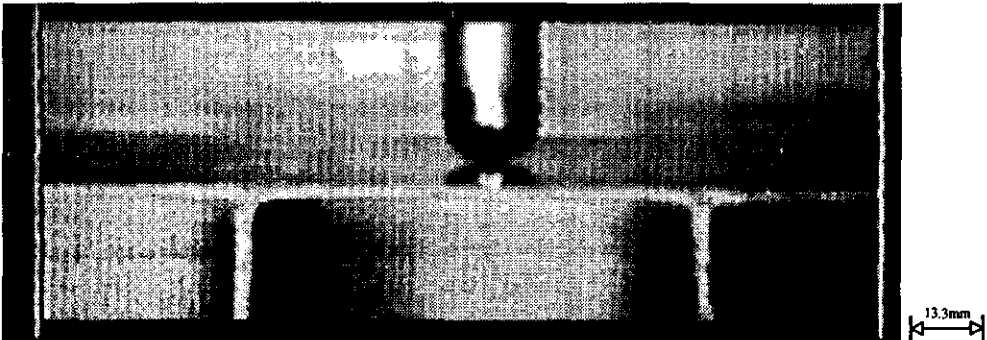


Figure 7.66 Photograph from zoomed in view from video recording of the local deflection during the 1m/s impact on the full plank cross-section.

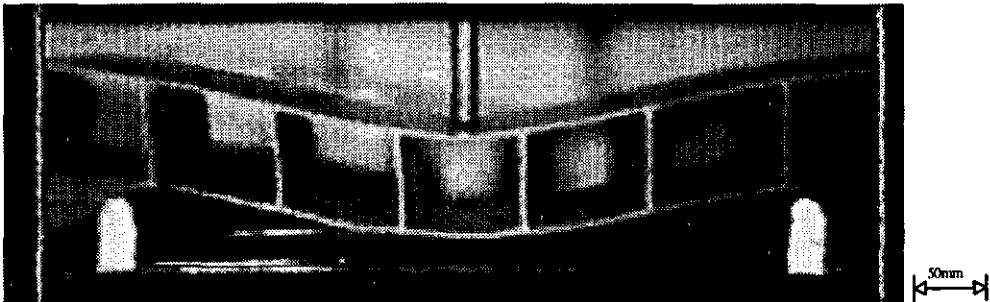


Figure 7.67 Photograph from video recording of the global deflection during the 4m/s impact on the full plank cross-section.

7.6 Comparisons Between Impact Test Configurations

This section concentrates on those areas where a relationship between different impact configurations existed, thus providing a deeper understanding of the damage mechanisms involved.

7.6.1 Comparison of Damage Data for all the Impact Specimens

Davies^{39,40,60,88} in particular has attempted to relate impact damage from one coupon to another. The standard method has been to plot damage against impact energy, but for different specimen sizes and support conditions different amounts of elastic energy are absorbed prior to the onset of damage therefore a relationship cannot be found between them. However, by plotting the damage against peak force, rather than against impact energy, for different size specimens under clamped or simply supported boundary conditions, Davies reported that the damage results fall into single groupings dependent only on specimen thickness. This enabled predictions of damage initiation from one specimen size to another. Davies et al⁶⁰ went further to say that the induced force would be expected to control the through-thickness and shear-stresses, whilst the bending strains would control back- and front-face tensile and compressive damage modes respectively. Bending strains are not readily available so the following analyses are based on relating damage in different configurations using the peak force generated.

Figures 7.68 and 7.69 contain the total delamination areas and back-face crack lengths plotted against TIE (a) and peak force (b) respectively for all the impact configurations. The back-face crack corresponds to the lower CFM crack in all cases except for the intermediate impacts in which case it refers to the taper-line crack. Figure 7.68 (a) shows a variation in delamination initiation TIE from 0.5J to 15J, with the growth dependent on the configuration - the shear coupon and five-box section tests are at either extreme, being the stiffest and most compliant specimens respectively. When plotted against peak force (Figure 7.68(b)), delamination initiation lies in the range 0.8 to 1.25KN, with growth generally occurring rapidly between 1.75 and 2.0KN. The transverse and shear coupon growth curves are the exceptions, with the former displaying very unstable delamination growth on initiation, and the latter displaying the most stable propagation.

Figure 7.69(a) displays back-face cracking as initiating over a wide range from 0.5J to 11J TIE, whilst in Figure 7.69(b), initiation was between 0.85 and 1.5KN, which as above is a much narrower range. The growth curves when mapped using the peak force were more varied than was the case for delamination area, with the transverse and shear coupons again providing the extremes. This agrees with Davies⁶⁰ as back-face cracking would be expected to be governed more closely by the bending strains than the peak force.

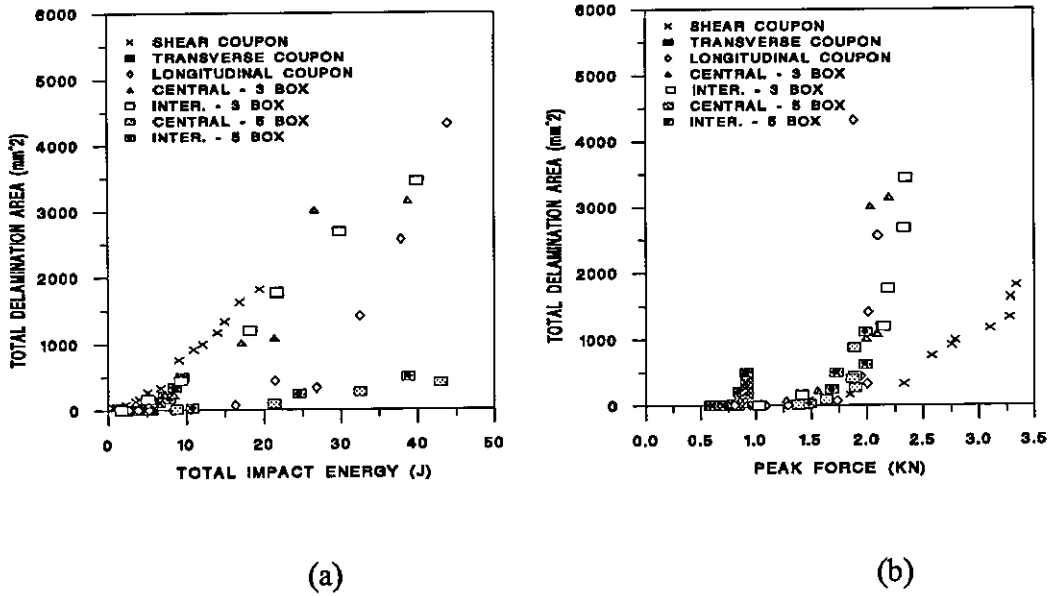


Figure 7.68 Total delamination area versus TIE (a) and peak force (b) for all the impact configurations.

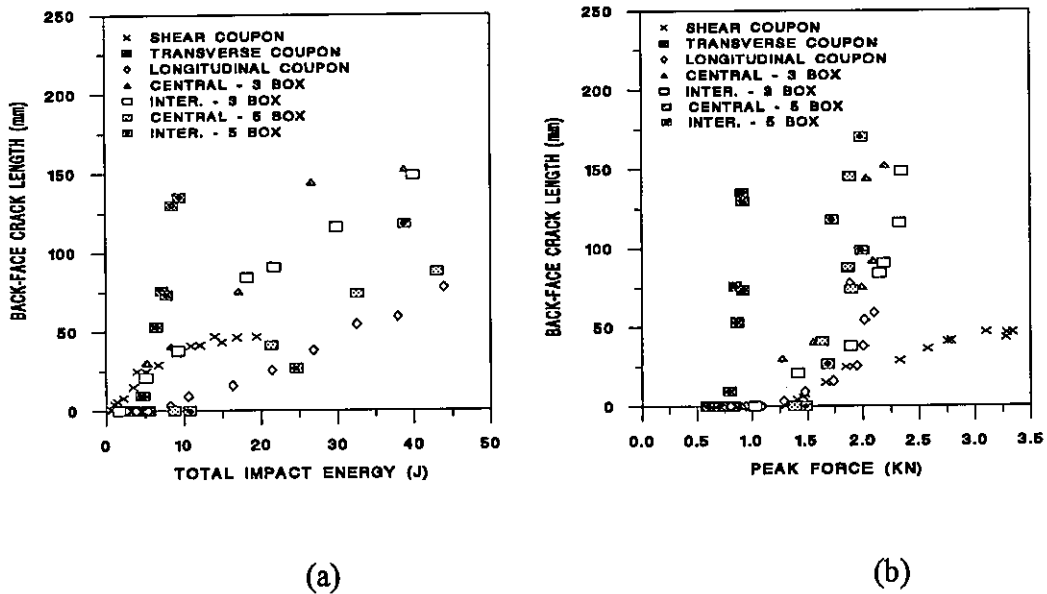


Figure 7.69 Back-face crack length versus TIE (a) and peak force (b) for all the impact configurations.

Whilst not completely causing the results to converge, the peak force seems to be a better parameter than TIE with which to relate damage between varying impact specimens. Therefore, by employing FE analysis or some other technique to predict the elastic peak force, the onset of failure for a complex structure could be predicted, within limits, from coupon impact damage results. The peak force cannot define the damage completely

because it does not define the relative dominance of shear and bending induced damage which was so dramatically different between specimens.

The form of damage which was most dependent on the peak force was the upper CFM damage directly under the impactor. This is illustrated by considering shear cracking of the upper CFM layer which was initiated between 6 and 43J, but in the much narrower peak force range of 1.9 and 2.3KN for the specimens tested. The peak force will therefore be used in the comparison of impact damage in various configurations in the following sections

7.6.2 Comparison between the Transverse Coupon, and Central Impacts from Three- and Five-Box Sections

Each of these impact specimens, whilst having different geometry, were all simply supported with the UD fibres parallel to the major plane of bending. From the individual analysis of each of these impact specimens there were many similarities, but it was also clear that there were important contrasts in impact response. The three-box sections generated much higher shear forces than either of the other two configurations under consideration. This can be deduced from the UD shear cracking leading to lower interface delamination and penetration failure, which was present in the three-box section but not in either the transverse coupon or five-box-section. The five-box-section generated much lower shear forces because of the much greater span-to-depth ratio of this section compared to the three-box section, resulting in transverse bending being more dominant.

Figure 7.70 shows the peak force versus TIE for the three specimens. The transverse coupons clearly suffered final failure at a relatively low TIE, because they did not absorb much elastic energy relative to the box sections. It was clear that if damage mode onset was to be compared between these specimens then some variable other than TIE must be used. Figure 7.71 contains the lower CFM crack lengths and delamination areas versus peak force for the three configurations being considered. Figure 7.71(a) shows that lower CFM cracking was initiated at a very similar peak force for the transverse and central impacts from the three-box section though the crack growth curves were quite different. Crack initiation for the central impacts from the five-box section was at a higher peak force, possibly due to the fact that this section was less stiff, and the higher deflections resulted in remote skin/web join damage delaying back-face cracking.

When the upper interface delamination areas are plotted against peak force the difference between unstable (transverse coupon) and relatively stable (three- and five-box sections) growth is emphasised (Figure 7.71(b)). The upper interface delamination area was much

greater for the three-box section than the directly comparable (in terms of area available for delamination) five-box section. It is believed that this was a result of the higher Mode II fracture energy available for delamination due to the higher shear forces in this section. With the two layers below it being cracked, and the upper CFM layer being relatively compliant, the bending forces tend to cause the upper CFM layer to deflect rather than to promote extensive delamination, hence a higher Mode II content will accelerate delamination considerably.

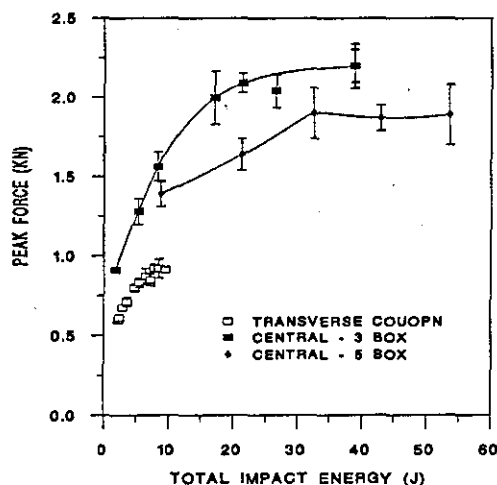


Figure 7.70 Peak force versus TIE for the transverse coupon, and central impacts from the three- and five-box sections.

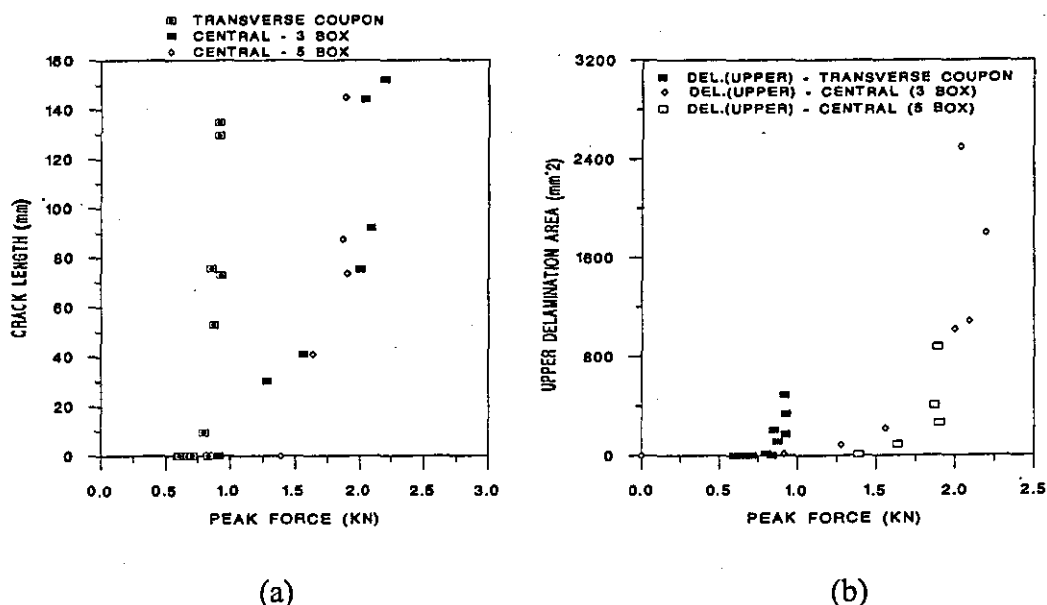


Figure 7.71 Lower CFM crack length (a) and delamination area (b) versus peak force for the transverse coupon, and central impacts from the three- and five-box sections.

7.6.3 Comparison of Three- and Five-Box Sections

Figure 7.72(a) shows the peak force versus TIE for the three impact locations from both the three- and five-box sections. The peak forces for the web impacts for the five-box sections are in some doubt as explained in section 7.4.2.3, with the inertial spike values shown here. The peak forces generated in the shorter specimens (the three-box section) were, for each impact site, higher than for the longer specimens in the same location, due to the longer specimens being less stiff. The deflections at a given impact energy were therefore that much greater for the five-box section, which resulted in the impacts at all three locations causing more remote damage than for the three-box sections.

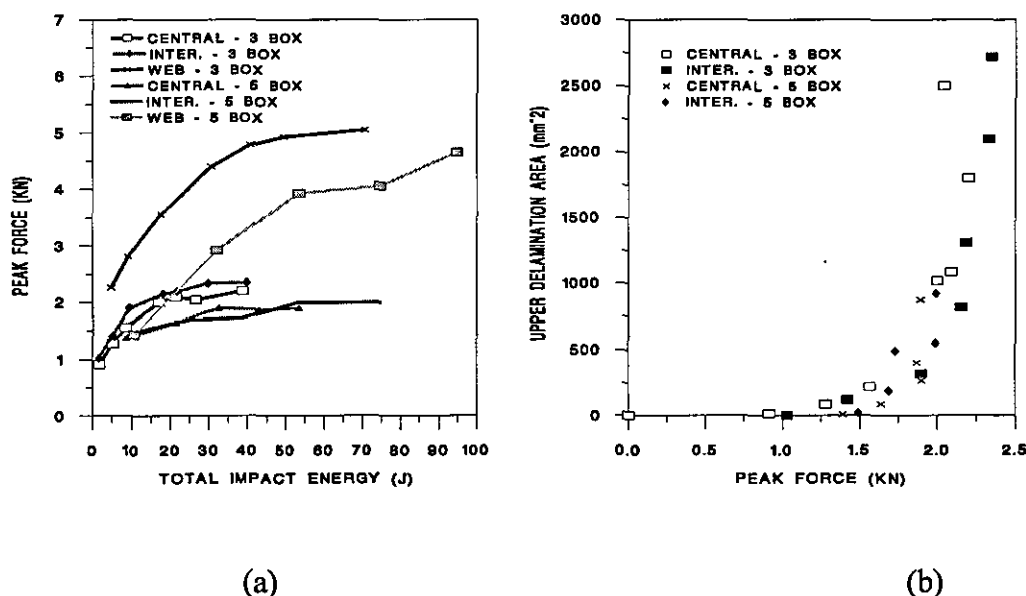


Figure 7.72 Peak force versus TIE from both the three- and five-box sections (a), and upper interface delamination area versus peak force for the central and intermediate impacts from the three- and five-box sections (b).

Figure 7.72(b) shows the upper interface delamination areas plotted against peak force. Upper interface delamination for both the central and intermediate impacts was initiated at a lower peak force for the three-box section, whilst the growth curves were indistinguishable. The delayed delamination initiation of the longer five-box section could again be due the greater remote damage in these sections. Provided the impact site is not directly over a web, peak force seems to be an excellent indication of upper interface delamination area independent of strike location.

This comparison exercise has assisted in explaining the individual results for each section, with the shear forces in the three-box section confirmed as being higher than in the five-box section. Delamination area and back-face crack length maps plotted against peak force have provided a better method of relating impact damage between specimen configurations than was achieved using TIE. These maps could be used as a first approximation to predict initiation of delamination or back-face crack damage on ACCS "plank" profiles.

Overall, the experimental impact test programme has provided a great deal of information regarding the basic material response of a typical (CFM/UD/CFM) pultruded lay-up and the more complex response of impacts at various locations on a typical double-skin/web pultrusion. The damage analyses have highlighted weaknesses in the system regarding damage originating under the impactor, and also the danger of remote, extensive and unpredictable damage resulting from impacts in the vicinity of the webs.

Chapter 8

FE Results and Discussion

This chapter contains the results and findings of the all the finite element work performed during the research. Firstly, elastic impact analyses of the three coupon models are compared with experimental data. The results of a full investigation into the interface elements is then presented, and finally the interface elements are employed to model the three major modes of impact induced delamination that were observed for the ACCS "plank".

8.1 Elastic Impact Models

The elastic impact model is the foundation on which to build any non-linearity to model impact induced damage, therefore it is very important that the elastic impact model reflects the elastic impact characteristics accurately. In order to minimise complexity, models of the relatively simple geometry coupon tests were created as described in Chapter 5. The results of these analyses are discussed below compared with the experimental results.

8.1.1 Convergence Exercise

A fine mesh was required under the impactor so that enough nodes defined the contact region, therefore the convergence exercise, performed on the longitudinal coupon model, involved refining the mesh away from this area. As the number of elements, and therefore the degrees of freedom, was increased the stiffness of the model reduced, resulting in the model with 640 elements being the best compromise between a converged solution and CPU time. The same refinement was therefore employed in the transverse and shear coupon models. The final meshes chosen are shown in Figures 5.1 to 5.3 in chapter 5, each

having an identical contact region, i.e. impactor mesh and coupon mesh directly under the impactor.

The transverse coupon model mesh was slightly different as it contained a tied slideline along the taper-line, through the thickness of the model as shown in Figure 5.2. The tied slideline stiffness parameter was varied from 1 to 10,000, resulting in only a 1% change in overall stiffness response. The stress gradients across the slideline were also seen to be continuous, therefore it was concluded that the slideline was performing correctly and the stiffness parameter was set at 1,000.

8.1.2 Correlation of Coupon Impact Analyses with Experimental Data

The initial analyses were run at the lowest impact velocities tested because this was when the least damage was introduced in the experimental tests, therefore allowing comparison with the elastic FE models. Figures 8.1 to 8.3 show the FE predicted response and experimental curves obtained for the longitudinal, transverse, and shear coupons respectively at the lowest impact velocity. Table 8.1 contains the discrete impact characteristic data.

The best correlation with the experimental data was provided by the longitudinal model where the peak force, peak deflection, time to peak force and initial stiffness were within 0.5, 3.5, 1.6, and 3.2% of the experimental data respectively. This model provided the best correlation because the longitudinal experimental impact data most clearly represented an elastic response as very little damage was induced.

The shear and transverse models provided less close agreement with the experimental data. In the case of the shear coupon this was almost entirely due to extent of damage absorbed even at the lowest TIE. The experimental data therefore did not represent an elastic impact, and the only comparison that can be meaningfully made is between initial stiffnesses, where excellent agreement to 1.5% was achieved. The relatively poor comparison between FE and experimental data for the transverse coupon was due to the 5.8% discrepancy in initial stiffness, which suggests that the transverse in-plane ply properties were not as accurate as the other material data.

Elastic FE impact analyses were also run over a range of velocities for the three coupon models. Figures 8.4 to 8.6 contain the peak forces predicted from these models compared to the experimental data and the modified elastic spring-mass model predictions (see section 7.3.1). Comparison with the spring-mass model was excellent except at the higher

velocities due to non-linear bending being taken into account in the FE models. As expected, agreement with the experimental data was only close at the lowest energies tested.

Where comparisons can be made, the elastic FE results provided excellent correlation with the experimental data. Over the range of velocities tested, when compared to the modified spring-mass model, the results confirmed that the impact analyses run in LUSAS were performing correctly and gave the dynamic responses expected. These results also provided excellent evidence that the static mechanical tests performed gave accurate elastic moduli data for the FE model.

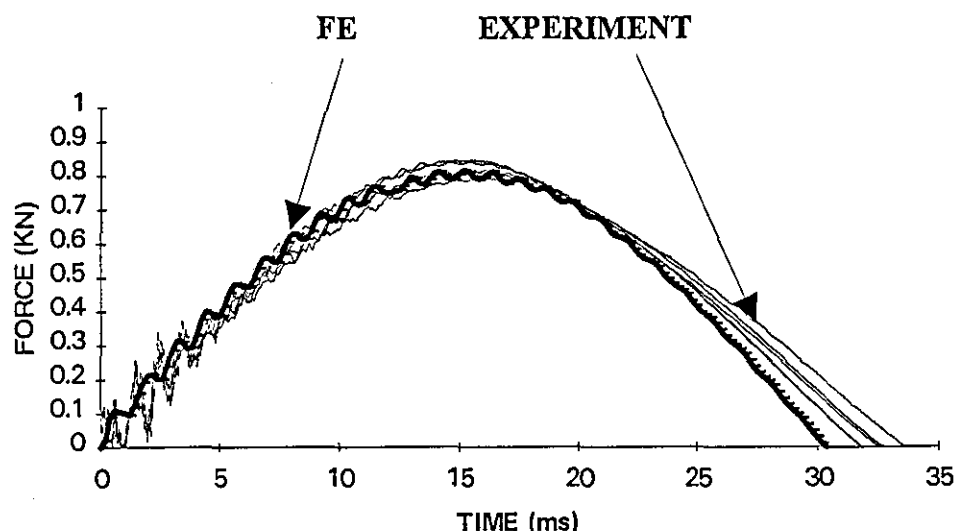


Figure 8.1 Finite element and experimental force-time curves for the longitudinal coupon at the lowest TIE tested (2.69J).

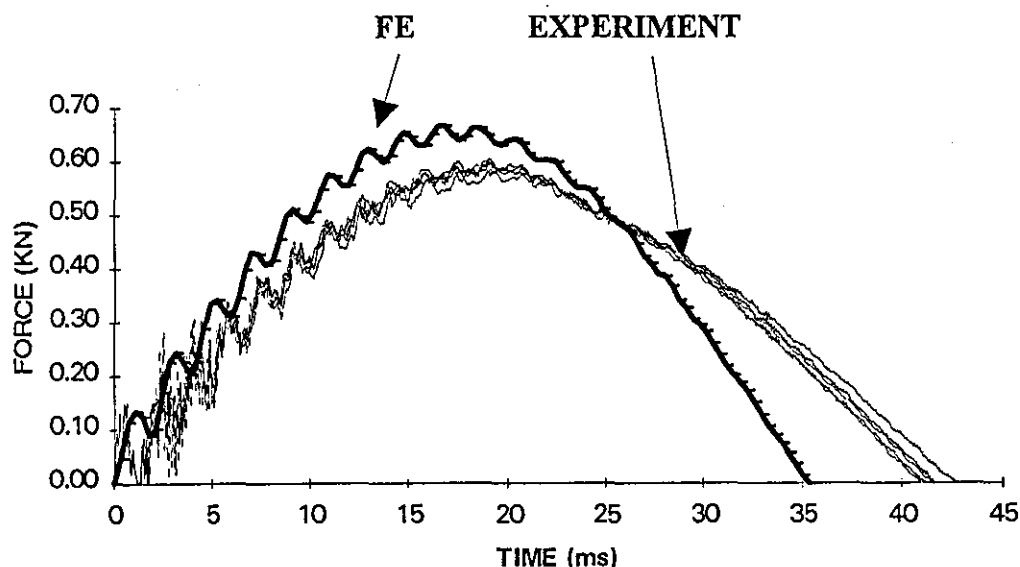


Figure 8.2 Finite element and experimental force-time curves for transverse coupon at the lowest TIE tested (2.25J).

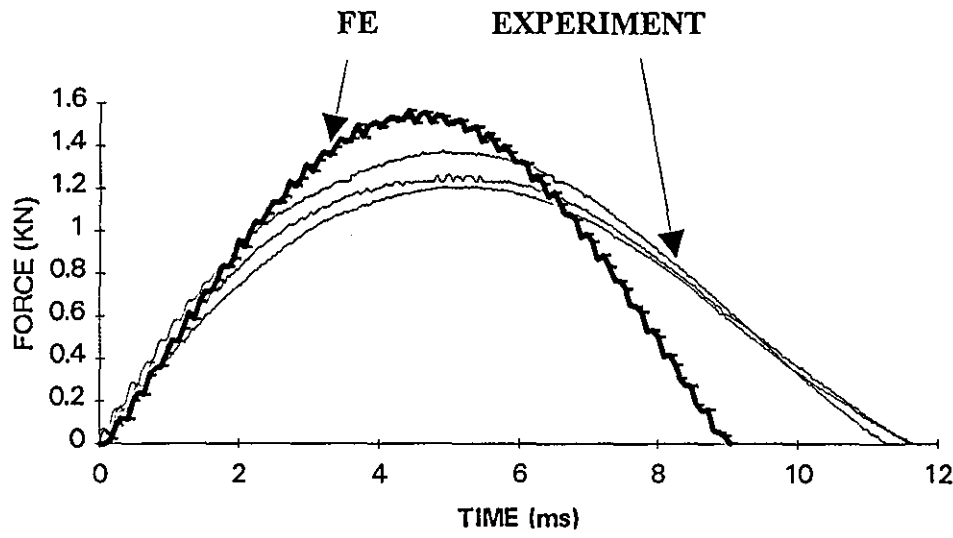


Figure 8.3 Finite element and experimental force-time curves for the shear coupon at the lowest TIE tested (0.75J).

	Shear			Transverse			Longitudinal		
	Expt	FE	Error (%)	Expt	FE	Error (%)	Expt	FE	Error (%)
TIE (J)	0.75	0.75		2.25	2.25		2.69	2.69	
Peak Force (kN)	1.31	1.56	+19.1	0.60	0.67	+11.7	0.820	0.816	-0.5
Peak Defl. (mm)	1.08	1.07	-0.9	7.24	7.33	+1.2	6.53	6.76	+3.5
Time to Pk Force (ms)	5.10	4.56	-10.6	18.92	17.85	-5.6	15.38	15.14	-1.6
Contact Time (ms)	11.83	9.04	-23.6	41.60	35.7	-14.2	32.56	30.28	-6.9
Initial Stiff. (kN/mm)	1.36	1.34	-1.5	0.084	0.089	+5.8	0.125	0.121	-3.2

Table 8.1 Characteristic impact data from finite element analysis and experiment at the lowest TIE tested for the three coupons.

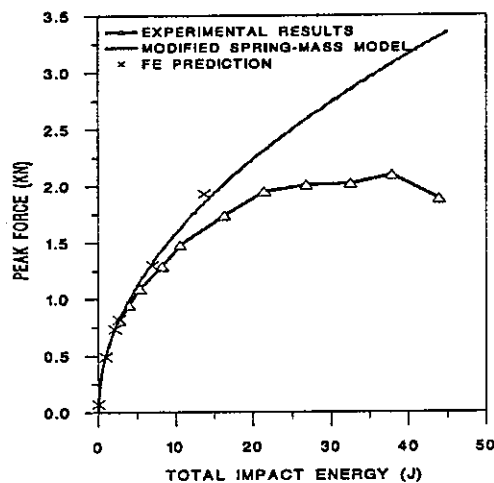


Figure 8.4 FE impact analyses from 0.06 to 1.5 m/s for the longitudinal coupon model compared with modified spring-mass model predictions and experimental results.

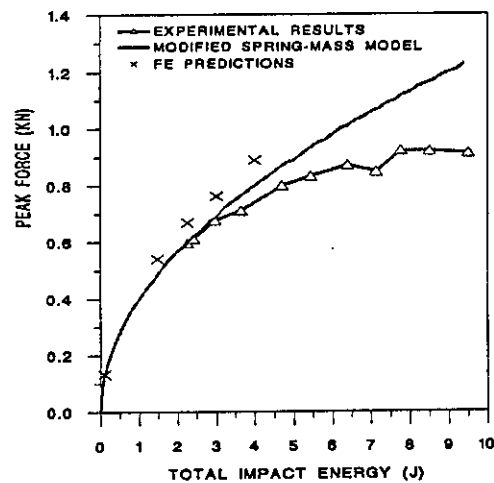


Figure 8.5 FE impact analyses from 0.13 to 0.86 m/s for the transverse coupon model compared with modified spring-mass model predictions and experimental results.

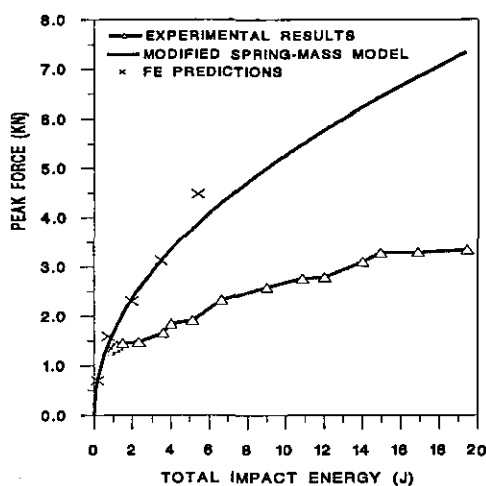


Figure 8.6 FE impact analyses from 0.18 to 1.0 m/s for the shear coupon model compared with modified spring-mass model predictions and experimental results.

8.2 Development of the Damage Model - Delamination

As described in chapter 5, the aim of this aspect of the research was to employ the newly formulated interface elements to model delamination in composite laminates. This section describes the verification of the element under Mode I, Mode II and mixed-mode loading. As part of the process it was necessary to perform a detailed investigation into the element's behaviour at a nodal level. For simplicity the research first focused on two-dimensional models and later on three-dimensional models. Two- and three-dimensional models were then developed to model Mode I, II and mixed-mode delamination in the ACCS "plank" employing the experimentally determined elastic and failure data obtained in the static mechanical testing as described in Chapters 3 and 6. The work culminated in the implementation of the interface element into real, mixed-mode analyses to model impact induced delamination in the "plank".

On commencing this work it was known that the interface elements were difficult to implement and that convergence problems were common. Force-deflection crack growth curves (Figure 8.8) were usually very jagged leading to unstable solutions, very small step lengths, and/or aborted analyses. Crack growth is a continuous process, but when modelled with interface elements, the process becomes discontinuous as defined by the node spacing. Therefore node behaviour is very important, and it was at this level that the investigation was begun.

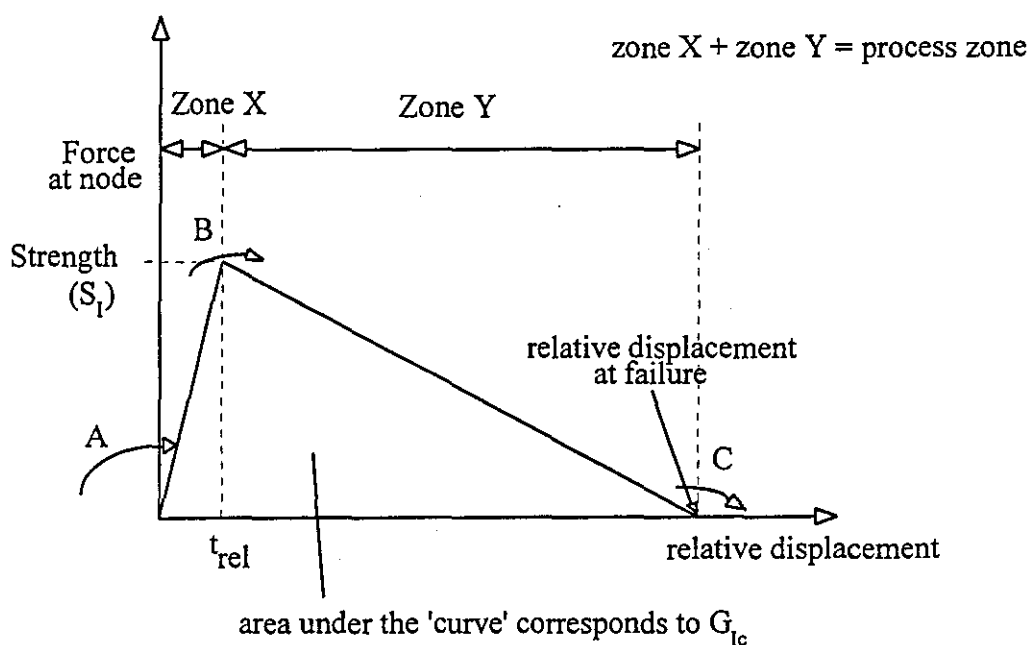
8.2.1 Two-Dimensional Models

The two-dimensional models employed the INT6 line element to simulate crack initiation and propagation under plane strain conditions. The line element made the initial investigation of node behaviour much simpler than that of the plane interface element (INT16) which is considered in section 8.2.2.

8.2.1.1 Test for Mode I Delamination - The DCB Model

Being the first series of tests involving the INT6 element, this section contains the most data regarding nodal behaviour. The findings from each set of tests were used in the next set of tests, resulting in a gradual evolution in understanding of the element's behaviour, and improvement in performance.

Figure 8.7 shows a typical deformed mesh for a DCB model and also explains the terms referred to in this section regarding the analysis of node positions and movement through the interface material model (see section 5.2).



(a)

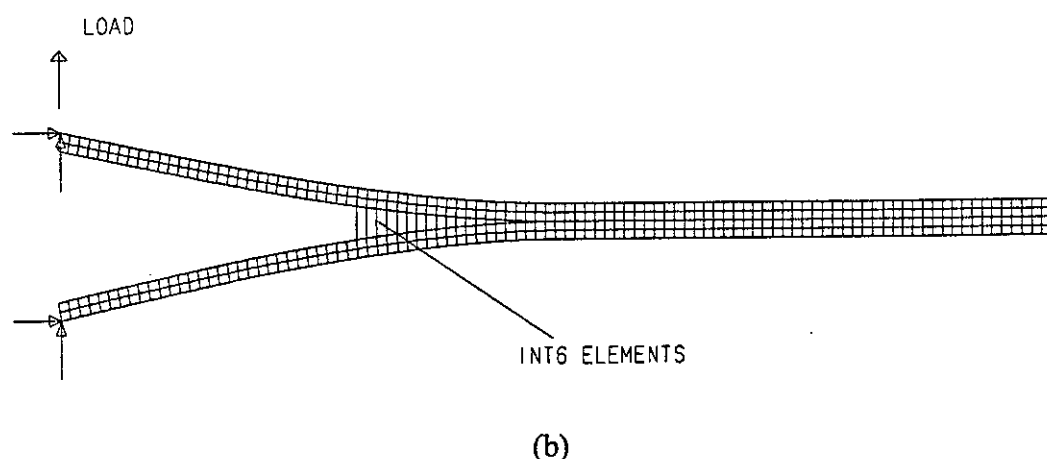


Figure 8.7 Material model and terms used to define node positions and movement (a), and deformed mesh of a two-dimensional DCB model employing INT6 elements (b).

Nodes in zone X refers to the nodes on the up-slope of the material model, whilst those in zone Y are on the softening curve. When the movement of nodes is referred to, there are three categories:

- A = a node moves onto the up-slope of the model
- B = a node passes from the up-slope to the softening curve as the strength, is exceeded (and the relative displacement exceeds the relative thickness).
- C = a node fails and no longer carries a load.

The following sections describe the effect of the mesh and material parameters on node behaviour and convergence to a smooth/stable crack growth solution.

(a) Effect of Mesh Density

Six models were investigated, each with the same interface material properties ($G_{Ic} = 4\text{N/mm}$, $S_I = 57\text{N}$, $t_{rel} = 1\text{e-}3\text{mm}$) but with varying mesh densities, whilst only regular meshes (rather than graded) were tested. Figure 8.8 contains the force deflection curves for the six tests, with the curves being incrementally displaced along the x-axis for clarity. The load rises as the beam halves are forced apart, with crack initiation occurring at the peak force, and the down-slope corresponding to crack propagation. All the curves were jagged at certain points and to varying degrees except for test F1 (see Table 8.2) where a very smooth crack growth curve was achieved. A chart containing the detailed node positions and movements was created for all the tests referred to in this section (a typical chart is shown in Table AVI.1 of Appendix VI) which has been summarised in Table 8.2.

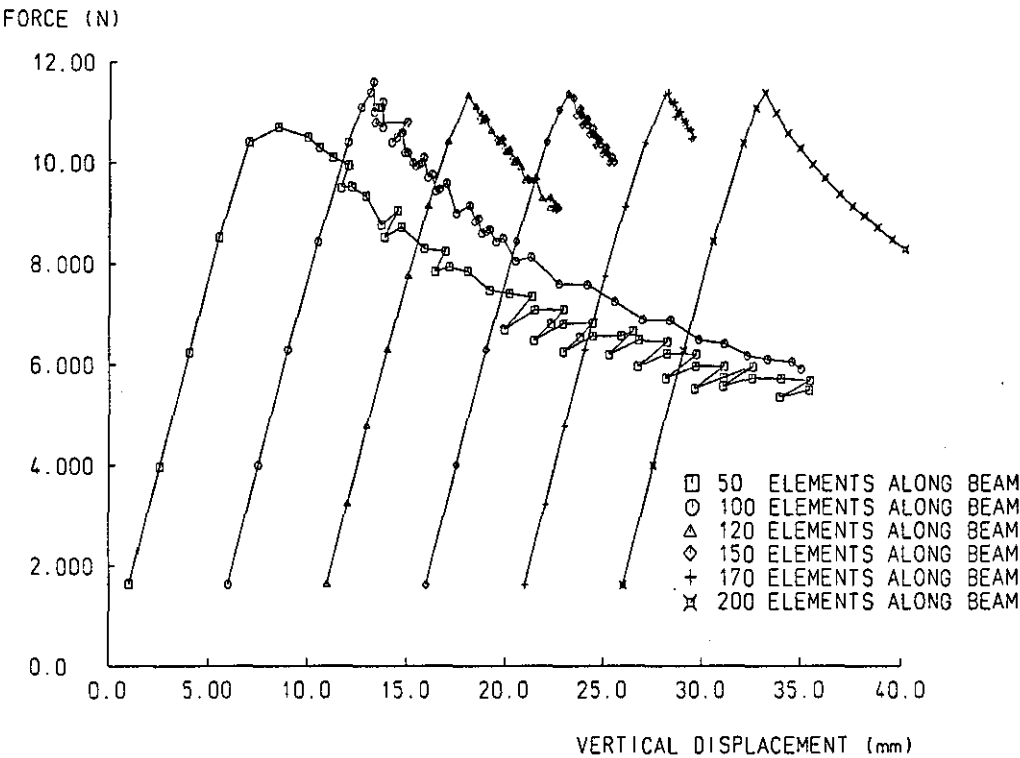


Figure 8.8 Effect of mesh density on Mode I force-deflection response.

Test Model	N ^o . of Elements along length	N ^o . of Elements through thickness	Average N ^o . of nodes in X	Average N ^o . of nodes in Y	Total nodes in X and Y
A1	50	4	0.83	2.06	2.90
B1	100	4	0.97	4.68	5.65
C1	120	4	1.00	6.21	7.21
D1	150	4	1.36	7.11	8.47
E1	170	4	1.63	8.26	9.89
F1	200	6	2.00	9.86	11.86

Table 8.2 Nodal data from mesh density analysis of INT6 DCB models.

When the average number of nodes in X or Y (Table 8.2) was not close to a whole number this indicated that a stable pattern of nodes in zones had not been achieved, i.e. for test B1 the average number of nodes in Y varied between 4 and 5. This was one reason for a jagged crack growth response.

Analysis of node movements for these tests revealed that in the jagged sections, load drops corresponded to nodes failing (movement category C) and load jumps (increases) were due to increments in which no nodes failed and the nodes simply move along the material model either within zones X and Y or with movements A and/or B. In this instance the crack was not growing and so the stiffness response corresponded to bending of the two beam halves.

For test F1, on every increment several nodes (4 or 5) failed and therefore the crack growth curve was smooth as the response was the same in nature for each increment, therefore it can be concluded that to ensure a smooth response, at least one node must fail each increment. To achieve this on average more than one node must fail, therefore the number of nodes in zone Y must be high. In confirmation of this, for the curves which exhibited smooth and jagged sections (e.g. B1), the smooth sections corresponded to nodes failing on each increment and the jagged sections corresponded to node failure followed by increments of non-failure.

From these tests it was concluded that simply increasing the mesh density will not cause a steady improvement in the crack growth curve. The mesh density must be sufficient for there to be enough nodes in Y for (several) nodes to fail on each increment, and the number of nodes in zones X and Y must establish a stable pattern. Some element lengths did not allow the solution to find a stable failure pattern, resulting in oscillations in the numbers of nodes in X and Y.

(b) Effect of Relative Thickness, t_{rel}

Three models each with 100 elements along the length were compared as shown in Figure 8.9 (with each curve staggered along the x-axis for clarity as before). Each model had $G_{lc} = 4\text{N/mm}$ and $S_I = 57\text{N}$. All three tests exhibited smooth and jagged sections, but as t_{rel} decreased the curves became slightly smoother. In general the initial smoother curves in B2 and B3 corresponded to several more nodes failing on each increment. After the initial crack growth, nodes did not fail on each increment and so a jagged response occurred, confirming the findings of the previous section.

Test	Relative thickness (mm)	Average N ^o . of nodes in X	Average N ^o . of nodes in Y	Total nodes in X and Y
B1	$t_{rel} = 1\text{e-}3$	0.97	4.68	5.65
B2	$t_{rel} = 1\text{e-}4$	0.88	5.00	5.88
B3	$t_{rel} = 1\text{e-}5$	0.88	5.00	5.88

Table 8.3 Nodal data from the relative thickness analyses of INT6 DCB models.

In summary, decreasing the relative thickness from 1e-3mm to 1e-4mm smoothed the initial crack growth curve slightly by enabling the number of nodes in Y to stabilise at five (Table 8.3). This suggests that the number of nodes in Y is more important than the number in X. The change from 1e-4mm to 1e-5mm had only a very small effect on crack growth. Clearly the effect of this parameter is less important than the mesh density.

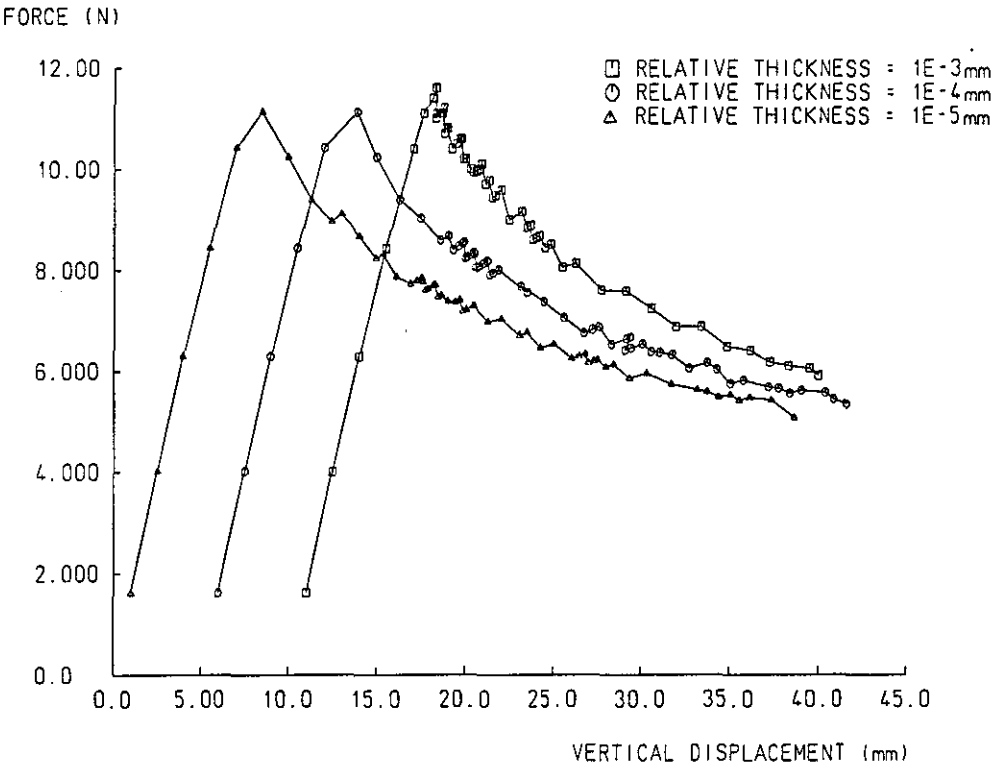


Figure 8.9 Effect of relative thickness on Mode I force-deflection response for INT6 DCB models.

(c) Effect of Strength, S_I

Four models were tested, with $G_{Ic} = 4\text{N/mm}$ and $t_{rel} = 1\text{e-}3\text{mm}$ using the model with 100 elements along the model length. The initial slope of the material model corresponds to the strength divided by the relative thickness (Figure 8.7(a)). Therefore, if the relative thickness is constant, by reducing S_I the initial slope of the material model is also reduced. Figure 8.10 shows the material models employed.

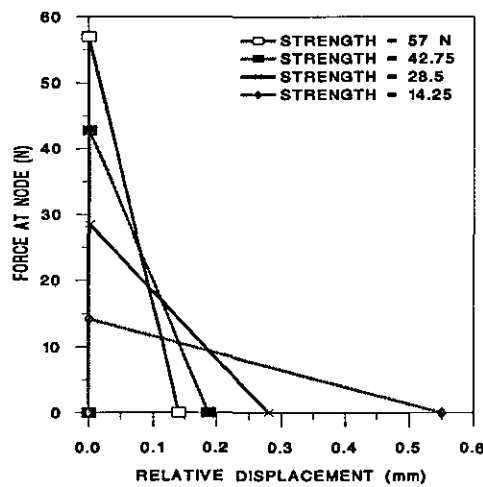


Figure 8.10 Interface element material models for constant G_{Ic} and various strengths.

Test Model	Strength, S_I (N)	Peak Force (N)	Average No. of nodes in X	Average No. of nodes in Y	Total nodes in X and Y
B1	57	11.6	0.97	4.68	5.65
B4	42.75	11.2	0.97	6.08	7.06
B5	28.5	10.9	0.86	8.50	9.36
B6	14.25	10.3	0.78	14.22	15.00

Table 8.4 Nodal data from strength analysis of INT6 DCB models.

Figure 8.11 contains the force-deflection curves for the five tests, incremented along the x-axis, whilst Table 8.4 contains the nodal results. There was a general trend that as the strength decreased the crack growth curves became smoother.

The peak force reduced as the strength reduced as expected, however a reduction in strength by a factor of four only reduced the peak force by approximately 10%. The number of nodes in zone Y increased as the strength reduced and the material model became flatter (Figure 8.10). As a result of the large process zone, two or three nodes failed on each increment for B6 which resulted in the smoothest curve observed. The average number of nodes in X reduced but this did not prevent smooth crack growth.

S_I is therefore a key parameter in achieving a smooth crack growth curve, and the peak force was relatively unaffected by S_I , so it could be varied to aid smooth crack growth. These tests again confirmed that both a reasonably stable number of nodes in zones and a large number of nodes in Y must be achieved for smooth crack growth.

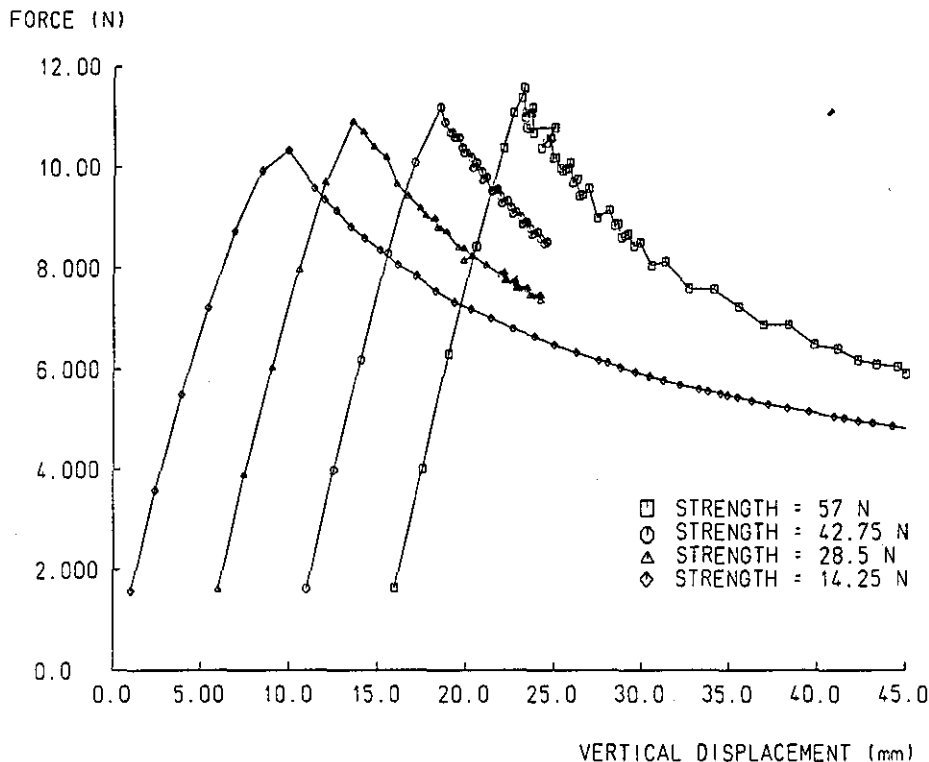


Figure 8.11 Effect of strength on Mode I force-deflection response for INT6 DCB models.

(d) Effect of Critical Strain Energy Release Rate, G_{Ic}

Six models were tested, with $S_I = 57\text{N}$ and $t_{rel} = 1\text{e-}3\text{mm}$, using the model with one hundred elements along the model length. Figure 8.12 shows the material models for these tests, Figure 8.13 contains the force-deflection curves, and Table 8.5 contains further analysis results.

Altering G_{Ic} did not have a great effect on the size of the process zone as increasing G_{Ic} by a factor of 16 only increased the total number of nodes in the zone 2.5 times, however in general a smoother curve resulted. B8 had a stable number of nodes in X and Y and therefore despite the low number of effected nodes it had a reasonably smooth curve. B1 and B7 did not achieve this stability and B7 in particular was very jagged. With regard to the peak force generated, it was clear that G_{Ic} is a much more important factor than S_I , however increasing G_{Ic} had a much smaller effect on the process zone than decreasing the strength by the same factor.

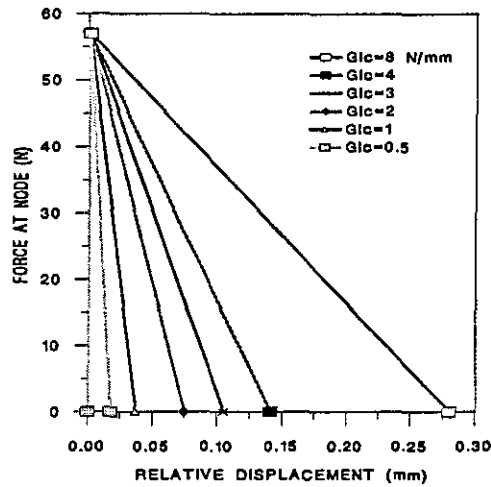


Figure 8.12 Interface element material models for various G_{Ic} but constant S_I .

Test Model	G_{Ic} (N/mm)	Peak Force (N)	Average No. of nodes in X	Average No. of nodes in Y	Total nodes in X and Y
B7	8	15.5	0.91	6.62	7.53
B1	4	11.6	0.97	4.68	5.65
B8	3	9.8	1	4.06	5.06
B9	2	8.0	0.97	3.16	4.14
B10	1	5.5	1.44	2.31	3.74
B11	0.5	4.6	1.9	1.13	3.03

Table 8.5 Nodal data from G_{Ic} analysis of the INT6 DCB models.

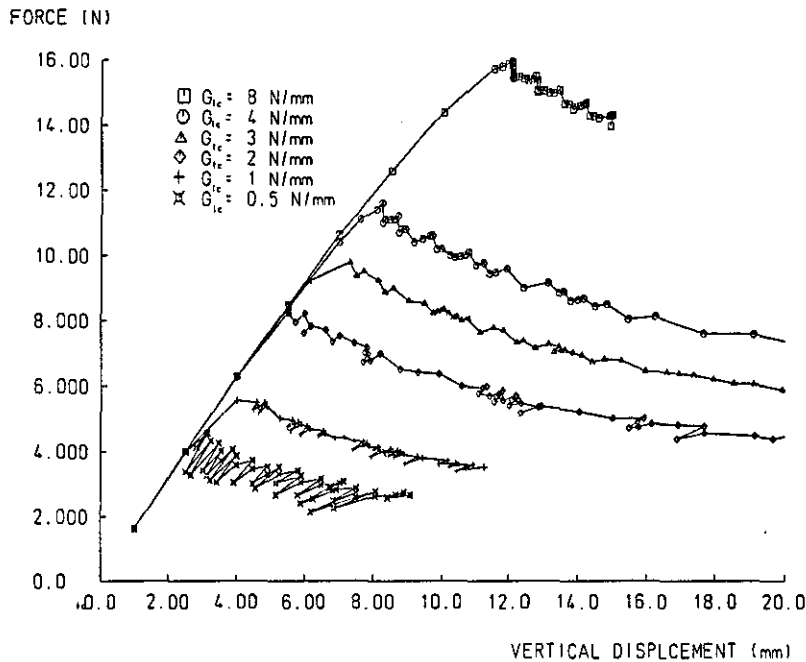


Figure 8.13 Effect of G_{Ic} on Mode I force-deflection response for INT6 DCB models.

(e) Comparison of $G_{Ic-input}$ and $G_{Ic-output}$

$G_{Ic-output}$ value was calculated using the area under the curve as shown in Figure 8.14 in equation 8.1 (equation 6.11) as described in section 6.1.4.1:

$$G_{Ic-output} = \frac{A}{w(a_2 - a_1)} \quad \text{N/mm} \tag{8.1}$$

[where A = area indicated in diagram below (N/mm), a_1 = initial crack length (mm), a_2 = final crack length (mm), and w = specimen width (mm)]

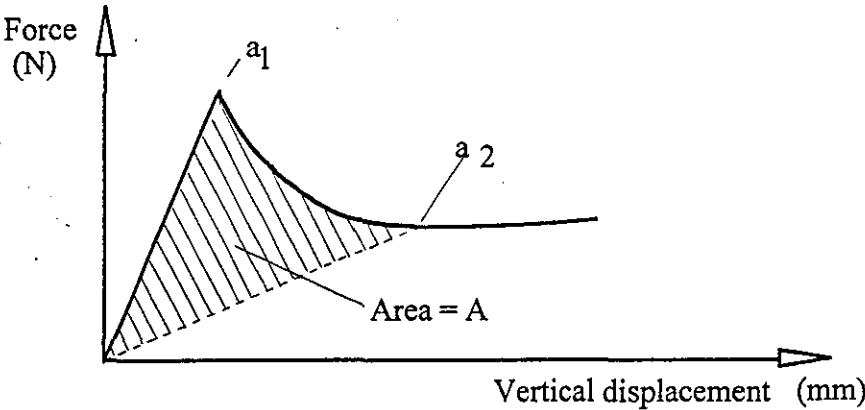


Figure 8.14 The area under the force displacement curve employed in the calculation of $G_{Ic-output}$

The fracture energy calculated from the force-displacement curve ($G_{Ic-output}$) by the method described above, should correspond to the G_{Ic} value used in defining the interface element ($G_{Ic-input}$). Three models with different mesh densities were chosen to calculate $G_{Ic-output}$ to test this relationship.

Near identical force-deflection curves were obtained for the different meshes, illustrating that given a smooth response, the interface elements behaviour is independent of mesh density which is crucially important.

Test	N ^o . of elements along length	$G_{Ic-input}$ (N/mm)	$G_{Ic-output}$ (min)	$G_{Ic-output}$ (max.)	$G_{Ic-output}$ (average)	$G_{Ic-output}/G_{Ic-input}$
A2	50	16	18.0	16.4	17.2	1.08
B6	100	4	3.95	4.15	4.05	1.01
F1	200	4	3.9	4.4	4.1	1.03

Table 8.6 Results of comparison between $G_{Ic-input}$ and $G_{Ic-output}$ for INT6 DCB models

$G_{Ic-output}$ depends on the final crack length taken from the FE model which is not straightforward to define. The crack front can be assumed to lie between the last failed node and the end of the process zone, which can be considered to be the plastic zone at the crack tip. These two extremes give the minimum and maximum $G_{Ic-output}$ values quoted in Table 8.6. The average of the two extremes would seem to give a good estimate and this is given as the average in the above table.

A coarser mesh (A2) will have a less accurate $G_{Ic-output}$ as the crack length can only be as precise as the nodal spacing. B6 had the longest crack length and therefore the length of the process zone was smaller in relation to the total length which resulted in a more accurate estimate of $G_{Ic-output}$. The error between $G_{Ic-input}$ and $G_{Ic-output}$ for B6 and F1 is in the range 1-3% which is very satisfactory.

(f) Summary

- A jagged crack growth curve was due to increments alternating between node failure steps and nodes simply moving through the model without failing completely. The load drops when nodes fail as the crack propagates. The load increases when nodes move within the material model without failing, as this is the same as forcing the beam apart without any crack growth, resulting in a stiffness response dependent on the crack length at the beginning of the increment.
- a smooth curve was obtained by having nodes fail on each increment, which was achieved by satisfying two conditions:
 1. having a stable ratio of nodes in X and Y
 2. exceeding a threshold number of nodes in Y
- increasing the mesh density, increasing G_{Ic} and reducing the S_I all have the effect of increasing the number of nodes in the process zone and therefore creating a smoother crack growth response. However, S_I was the dominant factor in increasing the process zone length.
- over the range of values tested, the relative thickness had the least effect of the material parameters on the interface element's behaviour.
- the peak force was heavily dependent on G_{Ic} , but was relatively insensitive to S_I . Therefore, S_I , the key parameter in increasing the process zone, can be varied with little effect on the global response.

- the correlation between $G_{Ic-input}$ and $G_{Ic-output}$ was excellent, verifying the ability of this element to quantitatively model delamination growth under Mode I loading.

8.2.1.2 Test for Mode II Delamination - The ENF Model

Having gained an understanding of the nodal behaviour of the INT6 element under Mode I loading, the following tests were performed in order to assess the effect of mesh density and the element's material variables in Mode II response. The ENF models described in section 5.2.1.2 were employed to produce pure Mode II loading. As nodal behaviour and its effect on crack growth response was thoroughly analysed in the previous section, the effect of the material parameters on the force-deflection curve will be the focus of these tests.

(a) Effect of Mesh Density

Models with either one or two hundred elements along the beam length, and with identical material variables ($G_{IIc} = 4\text{N/mm}$, $S_{II} = 57$, $t_{rel} = 1\text{e-}7\text{mm}$, and initial crack length = 25mm), were compared (Figure 8.15). The finer mesh had a negligible effect on the force-deflection response and therefore is a less important variable under Mode II loading than for Mode I loading. The coarser mesh was adopted for the remainder of the exercise for computational efficiency. As expected for this model, the shear force along the interface under this loading was almost constant, thus leading to a long process zone. The factors effecting the process zone length under Mode I loading were therefore not influential in the same way in the ENF test.

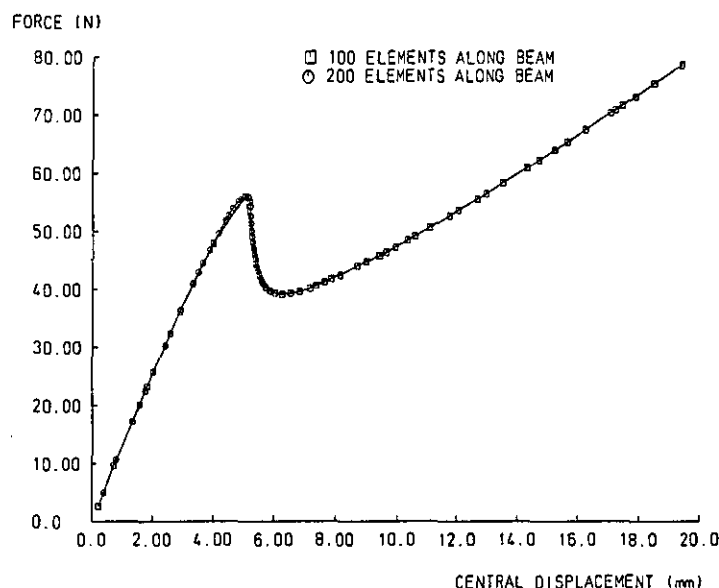


Figure 8.15 Effect of mesh density along the beam length on Mode II force-deflection response for the INT6 ENF models.

(b) Effect of Relative Thickness, t_{rel}

The two extremes of relative thickness tested ($1e-3$ and $1e-7$ mm) had little effect on the force-deflection curve ($G_{IIc} = 4\text{N/mm}$, $S_{II} = 57$, and initial crack length = 15mm) as was the case for Mode I loading. Under Mode II opening the elements were still in contact after failure unlike the DCB test, and it was therefore advantageous to set the relative thickness as low as possible to reduce inter-penetration of failed and partially failed elements. Figure 8.16 shows the limitations of the method employed to prevent penetration of failed elements showing failed overlapping elements from the loaded tip of the beam.

The high compressive normal stiffness prevented movement together in the normal direction (in the diagram a line is drawn between the nodes in the pair which remained horizontal illustrating this) but when the beam was curved the nodes in the node pairs moved apart in the plane resulting in the penetration shown.

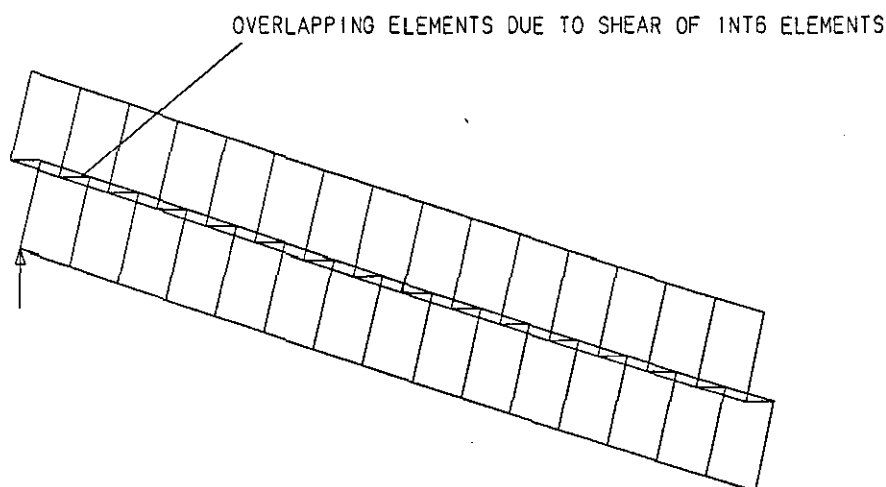


Figure 8.16 Deformed mesh at the cracked end of an INT6 ENF model displaying interpenetrated element.

(c) Effect of Critical Strain Energy Release Rate, G_{IIc}

Five models were run with G_{IIc} values of 0.5 , 1 , 2 , 3 , and 4 N/mm ($S_{II} = 57\text{N}$, $t_{rel} = 1e-7\text{mm}$, and initial crack length = 25mm), with the resulting curves contained in Figure 8.17. As expected the peak force reduced as G_{IIc} was reduced and the higher the G_{IIc} value the easier the convergence (longer step lengths). However, all the curves exhibited smooth crack growth rather than the jagged response which was common amongst the Mode I tests. This was because the shear stress along the centreline of the beam was relatively constant and so the plastic zone was large, as stated previously.

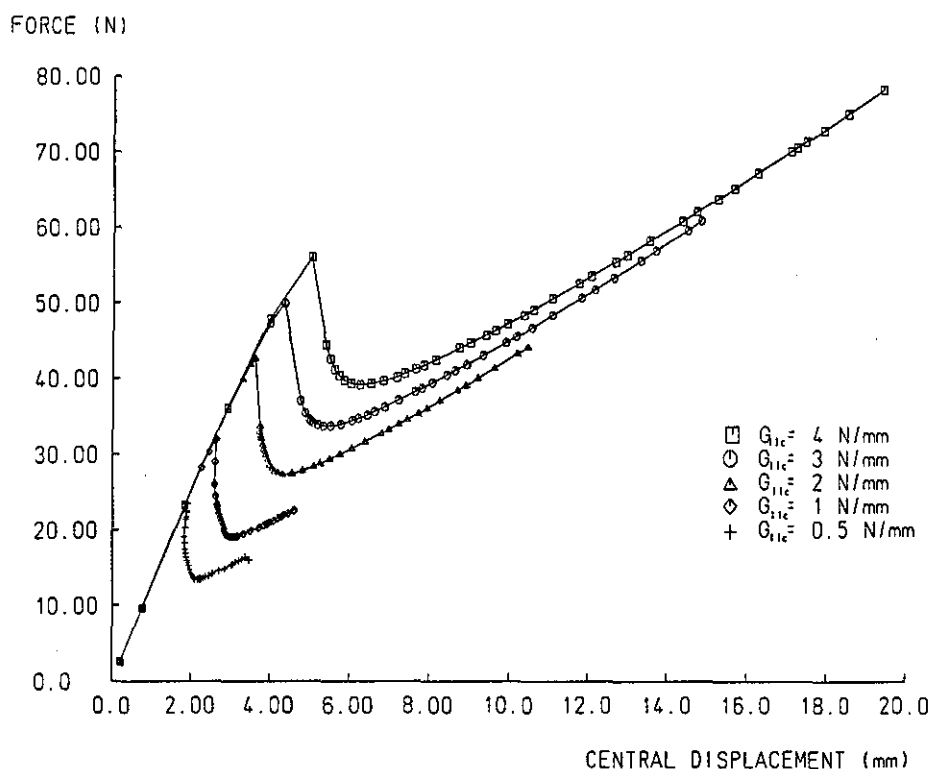


Figure 8.17 Effect of G_{IIc} on Mode II force-deflection response for INT6 ENF models.

(d) Effect of Strength, S_{II}

Figure 8.18 contains the force-deflection curves from six tests in which the only variable was the strength parameter, which was increased from 15 to 80N whilst a constant value of $G_{IIc} = 4 \text{ N/mm}$, $t_{rel} = 1 \text{ e-}7 \text{ mm}$ and initial crack length of 25mm were employed.

Whereas the strength value, S_I had little effect on the global force-deflection response for Mode I and could therefore be altered to improve convergence, S_{II} had a profound effect on the nature of the resulting curve for Mode II. The two highest strength values had a similar response with the peak force being slightly higher for the higher strength. When S_{II} was reduced to 30N, the load drop became much smoother and the peak force greatly reduced, and for a strength of 15N, no load drop was achieved at all, and convergence was only possible for very small load steps.

For the higher strengths the force-deflection response was linear before the load drop, but for the lowest strength, the initial response was quite non-linear. This was due to the softening of the extra nodes in the process zone and therefore more gradual failure at the interface. However, in ENF experiments unstable crack growth is usually reported as was the case for the ACCS "plank" tests (section 6.1.4.2). Therefore, for Mode II, S_{II} must be quite high in order to maintain the correct (i.e. unstable) nature of crack growth.

Fortunately, due to the nature of shear failure, a low strength value was not required to ensure smooth failure as described in the previous section for the DCB tests, therefore the strength can be maintained at a relatively high value without introducing convergence difficulties.

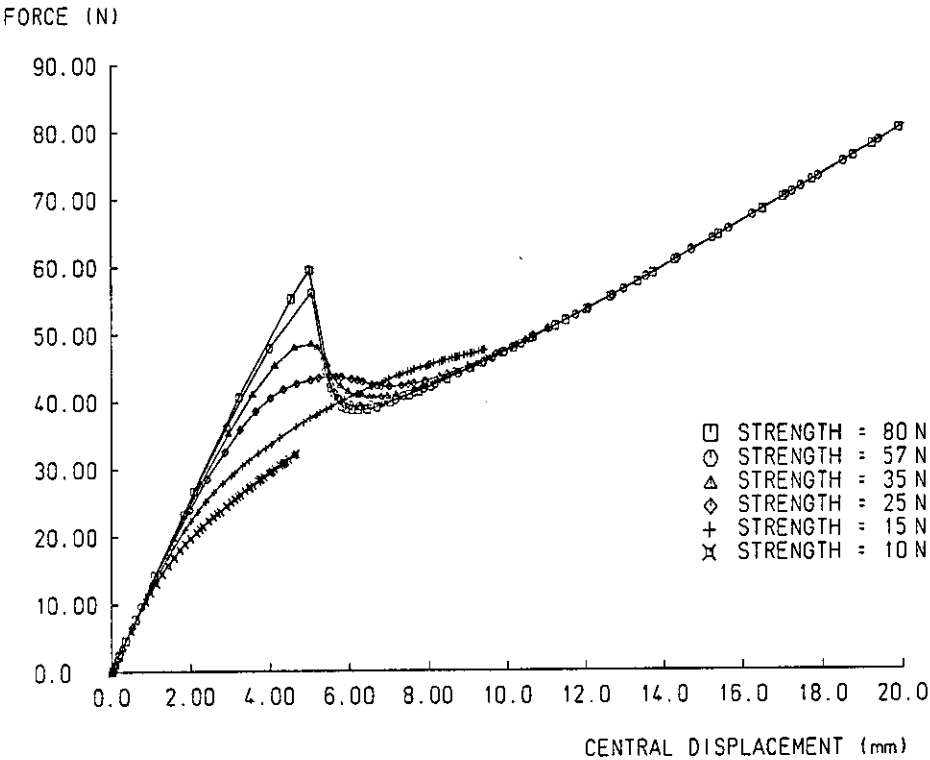


Figure 8.18 Effect of strength on Mode II force-deflection response for INT6 ENF models.

(e) Effect of Initial Crack Length

Figure 8.19 contains force-deflection curves of specimens with initial crack lengths varying from 15mm to 35mm ($G_{IIc} = 4\text{N/mm}$, $S_{II} = 57\text{N}$ and $t_{el} = 1\text{e-}7\text{mm}$). As expected the peak force reduced as the initial crack length increased as did the initial stiffness response of the beam. However, as would be expected, all five curves followed the same path when the cracks had grown to 35mm. The graph also displayed a transition from stable to unstable crack growth between 35 and 30mm. For initial crack lengths of less than 30-35mm, the force-deflection curves displayed a "snap-back" (i.e. where the displacement decreases) which indicates unstable crack growth. This exact same transition has been reported in the literature^{178,192}, and thus increases the level of confidence in the ability of this element to model crack growth under pure Mode II loading.

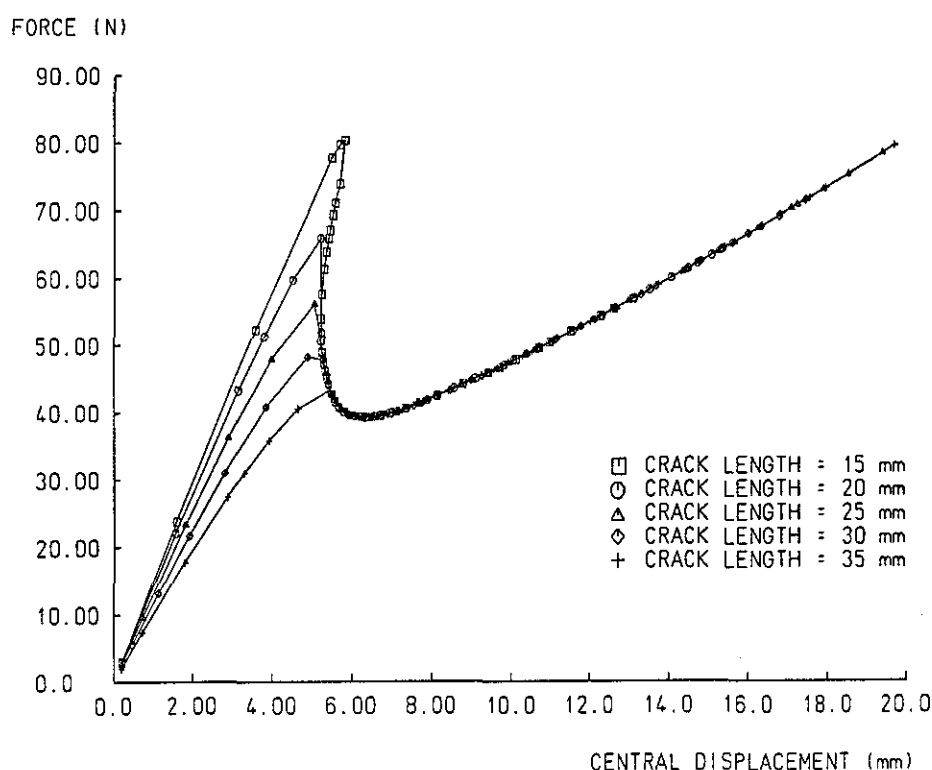


Figure 8.19 Effect of crack length on Mode II force-deflection response for the INT6 ENF models.

(f) Comparison of $G_{IIc-input}$ and $G_{IIc-output}$

It was decided to model the ENF test described by Gillespie et al.¹⁹² for this series of tests, as their work is well respected in this area. In their experiments a 100mm long, 25mm wide and 3.5mm thick beam was employed with $E_{xx} = 130$ GPa and initial crack length of 25mm. The experimentally determined G_{IIc} value was 1.4 N/mm which was therefore used in the material model (with $t_{rel} = 1e-7$ mm). As explained in Chapter 5, the strength value cannot be directly defined from experiment, so models were created with S_{II} varying from 57 to 150N (Figure 8.20).

The area method used for Mode I (Figure 8.14 - equation 8.1) was employed which provided a $G_{IIc-output}$ value varying from 1.35 to 1.44N/mm for the range of strengths employed, which correlated closely with the $G_{IIc-input}$ value of 1.4 N/mm defined for the interface element.

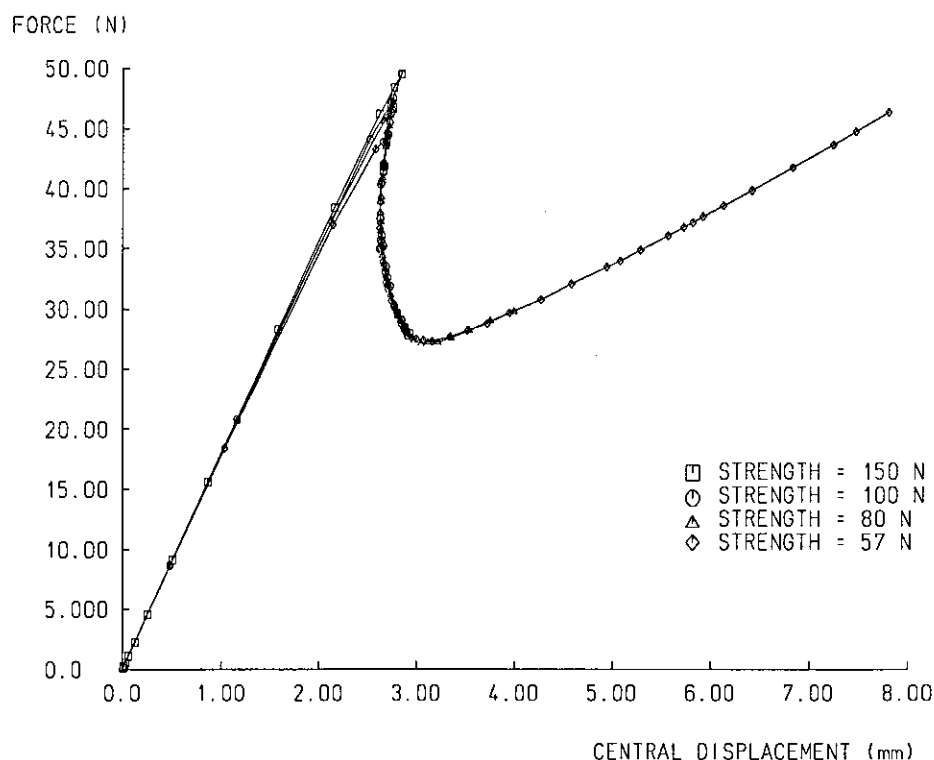


Figure 8.20 Comparison of $G_{IIc-input}$ and $G_{IIc-output}$ force-deflection responses for the INT6 ENF models.

(g) Summary

- In the range tested the Mode II force-deflection response was independent of mesh density and relative thickness.
- The strength parameter, S_{II} must be set relatively high to maintain the experimentally reported nature of the load displacement curve i.e. a considerable load drop associated with initial unstable crack growth followed by a steady load increase at reduced stiffness.
- The INT6 interface element predicted the same transition from unstable to stable crack growth as the initial crack length was increased, as has been reported experimentally and analytically in the literature.
- Inter-penetration of sheared elements highlighted a weakness of the element, whilst the high Mode I compressive stiffness prevented normal penetration.
- Comparison of $G_{IIc-input}$ and $G_{IIc-output}$ was acceptable.

This section has illustrated that under Mode II loading, due to the naturally longer process zone, the material parameters have different functions than would have been predicted from Mode I. Therefore careful consideration must be paid to the values employed in the interface specification, and Mode I material values should not be simply mirrored to Mode II.

8.2.1.3 Test for Mixed-Mode Delamination - The MMB Model

The MMB model as described in section 5.2.1.3 was employed to investigate the coupling model within the interface element definition for mixed-mode loading. The force-deflection graphs contain show two curves per model, referring to the force and deflection at the end and middle of the beam at the points of load application.

(a) Variable Mode ratio

Five tests were performed using the load ratios in Table 5.2 in chapter 5 to produce mode ratios at the crack tip from $G_I/G_{II} = 1/4$ to 4. $G_I = 2 \text{ N/mm}$, $S_I = 15\text{N}$, $G_{II} = 3 \text{ N/mm}$, $S_{II} = 40\text{N}$, and $t_{rel} = 1\text{e-}7\text{mm}$ for all the models. The resulting curves are contained in Figure 8.21 with Figure 8.22 showing a loaded mesh.

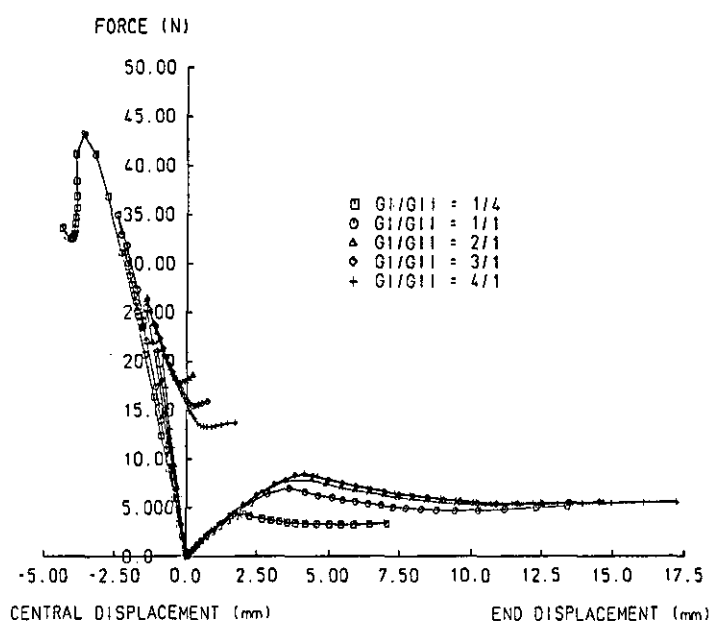


Figure 8.21 Effect of mode ratio on mixed-mode response for INT6 MMB models.

Throughout the mode range the solution converged to smooth curves for the mesh and material properties employed. As the Mode I content rose so the deflection at the centre was effected by the end load and so above a G_I/G_{II} ratio of 1, the central deflection became positive (Figure 8.21). The energy absorbed in each mode clearly altered in accordance with the mode ratio, with the higher the G_I/G_{II} ratio, the greater the energy absorbed by Mode I.

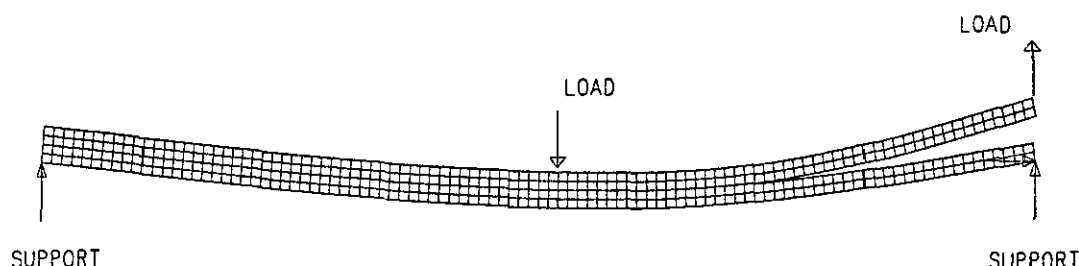


Figure 8.22 The deformed mesh of an INT6 MMB model prior to crack growth.

(b) Comparison of $(G_I/G_{II})_{\text{input}}$ to $(G_I/G_{II})_{\text{output}}$

Two tests were run, with exactly the same G_c value (3N/mm), strength (20N) and t_{rel} (1e-7mm) values for Modes I and II to simplify the calculation of the relative amounts of energy absorbed in the two modes. By using low mode ratios the end displacement did not interfere with the central displacement, making analysis easier, therefore the models had G_I/G_{II} ratios of 1/4, and 1. The resulting curves are shown in Figure 8.23.

The curves were analysed using the area under the force-deflection curve technique as employed for both the DCB and ENF tests. Due to coupling the final crack length in Mode I and II was always exactly the same - therefore a simple ratio of areas corresponded to the mode ratios. The results are contained in Table 8.7 and show correlation within 4% between the input and output mode ratios, illustrating that the areas under the force-deflection curves reflected the correct value of energy absorbed according to the mode ratio selected.

Model	Mode ratio input (G_I/G_{II})	Area ratio output (A_I/A_{II})	Mode ratio input/output
1	0.25	0.256	1.02
2	1	1.04	1.04

Table 8.7 Results of comparison between mode ratios input and output for the INT6 MMB models.

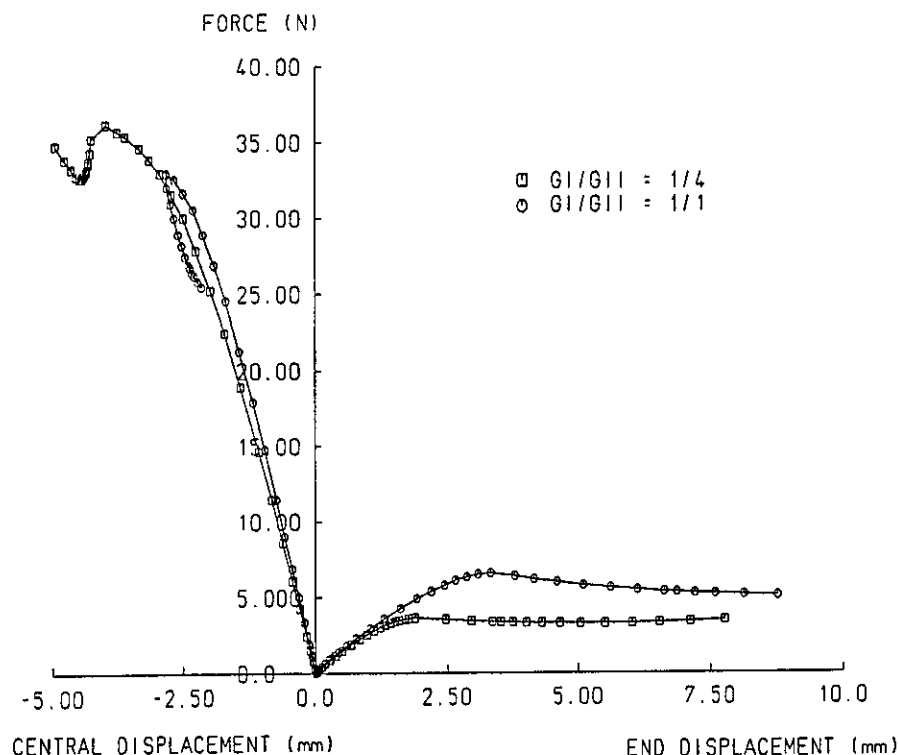


Figure 8.23 Comparison of G_{output} with G_{input} for the INT6 MMB models at different mode ratios.

(c) Summary

- These tests illustrated that the mixed-mode linear coupling model within the INT6 element, modelled crack initiation and propagation accurately both qualitatively and quantitatively.
- Knowledge gained regarding material parameter values during the DCB and ENF tests, when applied to these models, ensured convergence to smooth crack growth responses.

Over the previous three sections, the INT6 interface element has been shown to be mesh independent within reason, and with judicious material parameter selection, stable solution/smooth crack growth responses can be obtained whilst maintaining the correct nature of the response and accurate correlation to the fracture energy employed. This knowledge was then applied to the more complex INT16 plane interface element as described below.

8.2.2 Three-Dimensional Models

After detailed investigation, it was discovered that the three-dimensional interface element INT16 was incorrectly coded within the LUSAS software. The area of the element was not taken into account correctly, resulting in numerical inaccuracies in the failure load and fracture energy absorbed on crack growth. The results described below were obtained from the amended code containing the correct element area formulation. In three-dimensional models, Mode III values had to be assigned to the interface element. As stated in the literature review, tests for Mode III are not available, therefore Mode II values were employed.

8.2.2.1 Test for Mode I Delamination

Figure 8.24 shows the force-deflection curves from three 1mm wide three-dimensional models (with different numbers of elements across the width) and the same geometry two-dimensional model. The same material parameters as defined in section 5.2.2.1 were assigned to each model. The curves were identical confirming the correction to the INT16 coding, and illustrating that the response was insensitive to the number of elements across the width under pure Mode I loading. This was confirmed by a 10mm wide DCB model which, when the forces were scaled, produced identical curves to those in Figure 8.24.

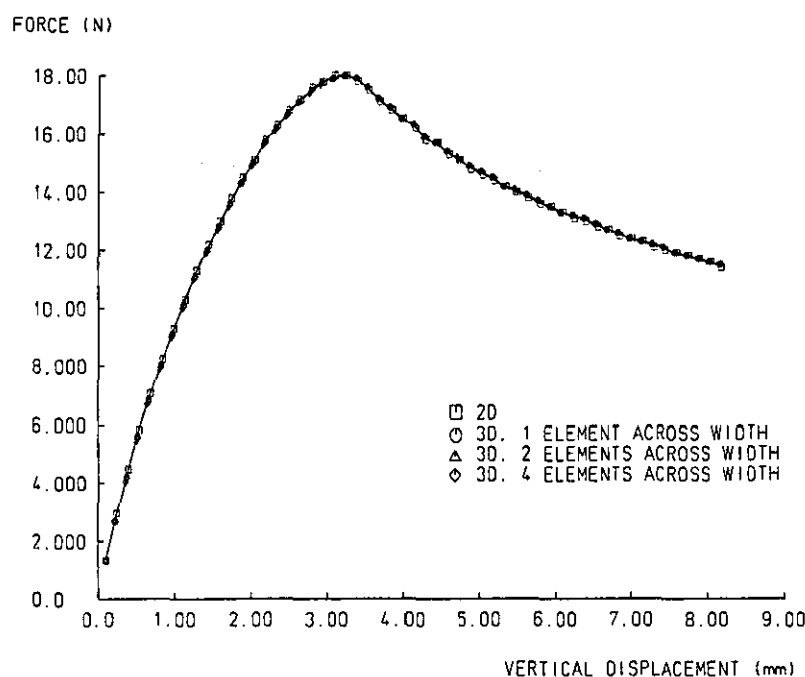


Figure 8.24 Comparison of two and three-dimensional DCB model force-deflection responses employing INT6 and INT16 elements respectively.

Figure 8.25 shows the global deformed mesh and the interface elements at the crack front from the 10mm wide DCB model. In Figure 8.25(b) the displacements were scaled-up to highlight the curved crack front which has been observed both experimentally and in other numerical analyses²¹⁰, confirming that the element was accurately qualitatively simulating the crack front. Anticlastic curvature in the width direction of the DCB arms develops due to the Poisson strain, which results in a variation in G_I across the crack width producing a curved crack front²¹⁰.

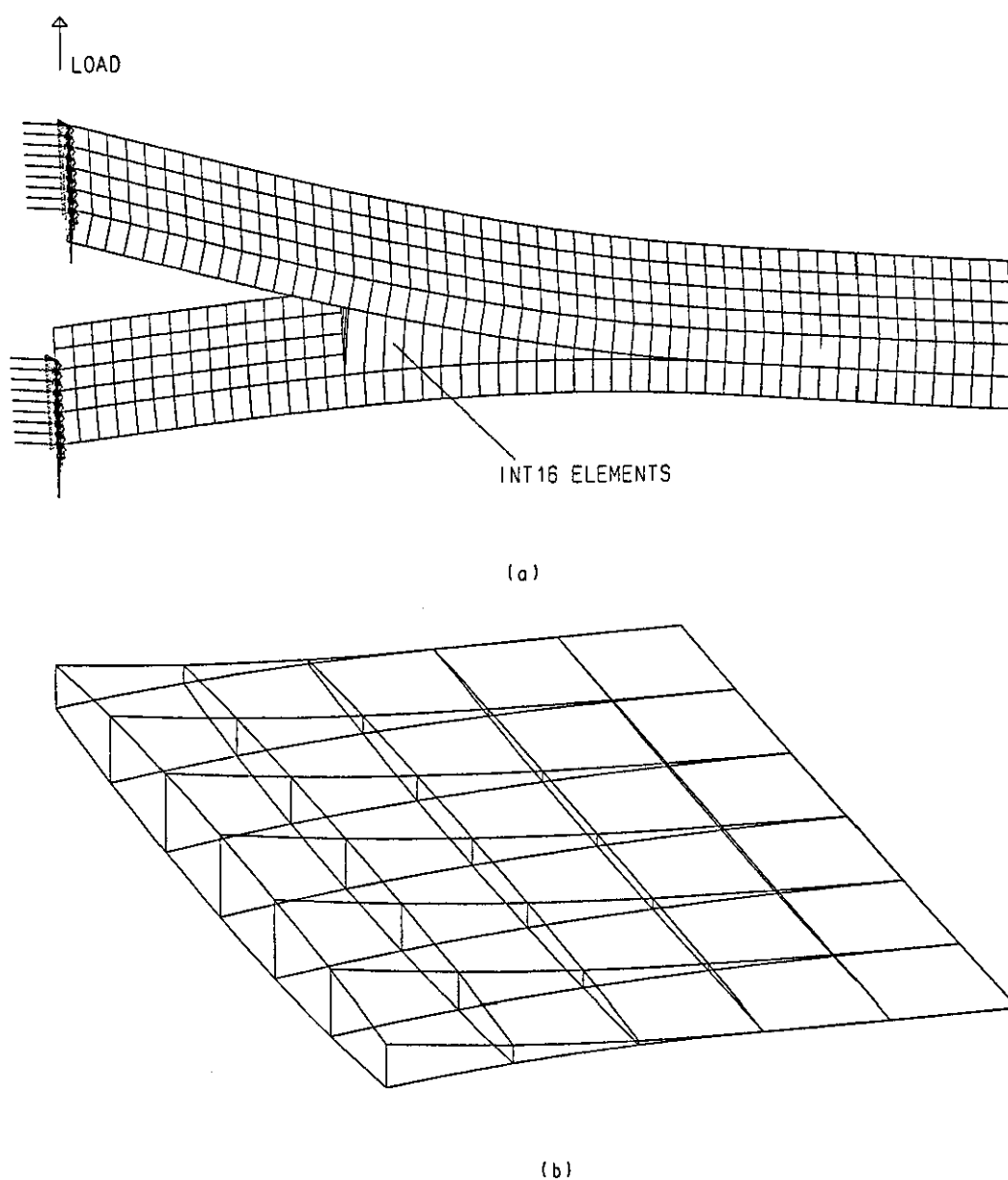


Figure 8.25 Global deformed mesh (a) and curved crack front (b) from 10mm wide three-dimensional DCB model, employing INT16 interface elements.

8.2.2.2 Test for Mode II Delamination

The three-dimensional and two-dimensional ENF models produced virtually identical force-deflection curves, however the three-dimensional model required a much smaller step length for convergence in the non-linear analysis.

8.2.2.3 Test for Mixed-Mode Delamination

A three-dimensional model with a mode ratio of G_I/G_{II} of 1, was compared to the appropriate two-dimensional MMB model. The force-deflection curves were again very similar confirming the accuracy of the INT16 response to mixed-mode crack initiation and propagation.

The close agreement between two and three-dimensional curves, confirmed that the correlation of $G_{c-input}$ and $G_{c-output}$ for Modes I, II and mixed-mode was excellent for INT16.

Each of the three-dimensional models described above required a much smaller load step to find a converged solution than the two-dimensional analyses. This could prove to have a very serious effect in terms of CPU time when modelling delamination in "real" structures with higher numbers of elements and more complex three-dimensional mixed-mode crack propagation.

Crack initiation and growth under pure Mode I, II and mixed-mode loading has been accurately modelled both qualitatively and quantitatively for two- and three-dimensional models employing the INT6 and INT16 interface elements respectively. Both elements have been fully verified and the correlation between two and three-dimensional results, the stable/unstable crack growth transition under Mode II loading, and the curved crack front from the three-dimensional DCB tests, all agree well with the literature, adding confidence to the concept of interface element modelling of delamination in composite laminates.

8.2.3 Delamination in the ACCS "Plank"

The previous sections have seen the verification of the INT6 and INT16 interface elements under Mode I, Mode II, and mixed-mode crack growth as simulated with the DCB, ENF and MMB models respectively. The same tests are reported here, but using the experimentally determined material data from the ACCS "plank", to provide verification of the elements when employing genuine material data, and interface material properties for use in the impact models described in section 8.3. G_{Ic} and G_{IIc} were obtained experimentally as described in section 5.2.3, but the strength values had to be determined by achieving a balance between the correct nature of response (stable/unstable crack growth) and smooth crack growth for each mode. The final values chosen are contained in Table 8.8.

The force-deflection curves from the respective tests are contained in Figures 8.26 to 8.28. The crack growth curves of both the two and three-dimensional tests agreed well and were relatively smooth for the DCB, ENF and MMB models. Therefore the mesh density corresponding to an element length of 1mm along the beam length provided a large enough process zone for both two and three-dimensional models.

S_I was chosen to be 7N as this gave the smoother crack growth response (Figure 8.26). Figure 8.27 contains the ENF force-deflection responses from five analyses with S_{II} varying from 5 to 20N. Higher strengths were also used but the crack growth response became very jagged. The three highest strengths maintained a consistent nature to the load drop, whilst the lowest strength smoothed the curve out almost completely. S_{II} was chosen at 15N as this maintained the correct nature of the ENF force-deflection response whilst still giving a smooth crack growth curve. When using the material parameter values in Table 8.8, for mode ratios (G_I/G_{II}) from 1/4 to 4 in the MMB models, smooth/stable solution responses were obtained (Figure 8.28). Good correlation of $G_{c-output}$ to $G_{c-input}$ was achieved with $G_{c-output}$ being within 5% of $G_{c-input}$ for both Modes I and II.

	Mode I	Mode II
Fracture energy (experimentally determined) - N/mm	0.57	0.50
Strength (determined by analysis) - N	7	15
t_{rel} (determined by analysis) - mm	1e-6	1e-6

Table 8.8 Final values chosen for material parameters for interface element definition to model delamination for the ACCS "plank".

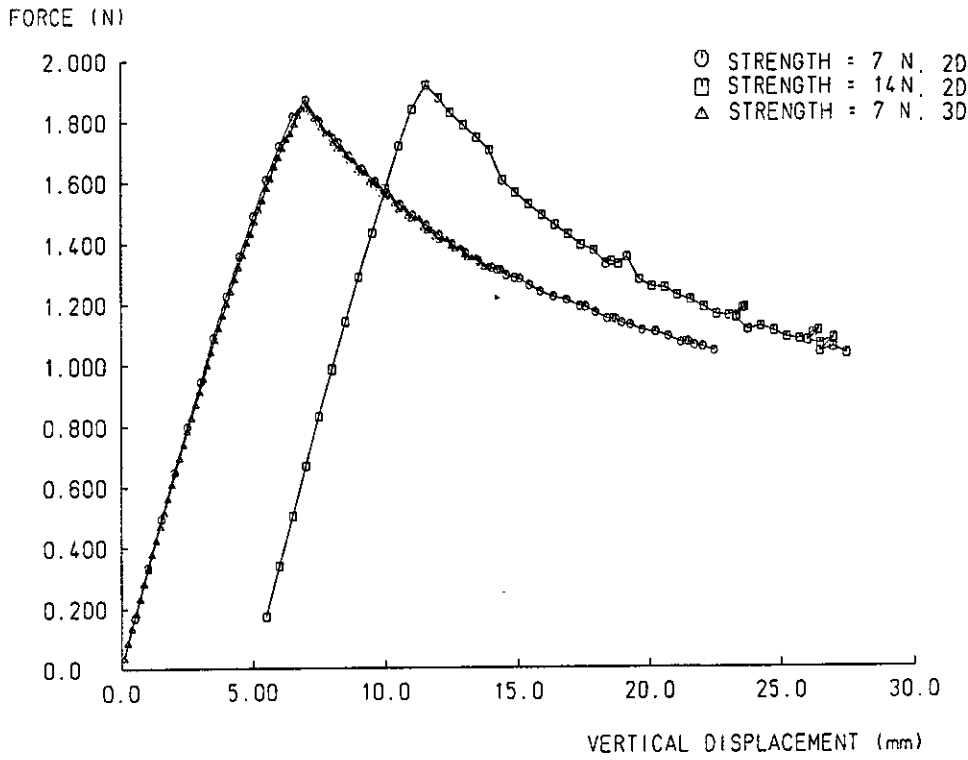


Figure 8.26 Effect on force-deflection response of varying S_I for ACCS "plank" material in two and three-dimensional DCB models.

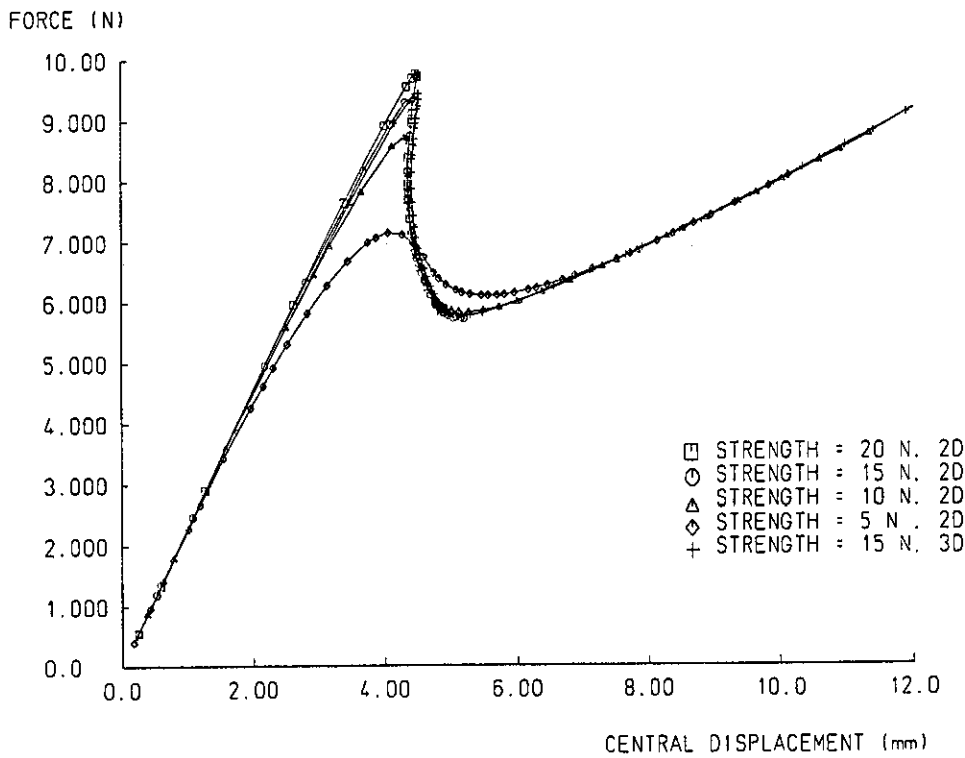


Figure 8.27 Effect on force-deflection response of varying S_{II} for ACCS "plank" material in two and three-dimensional ENF models.

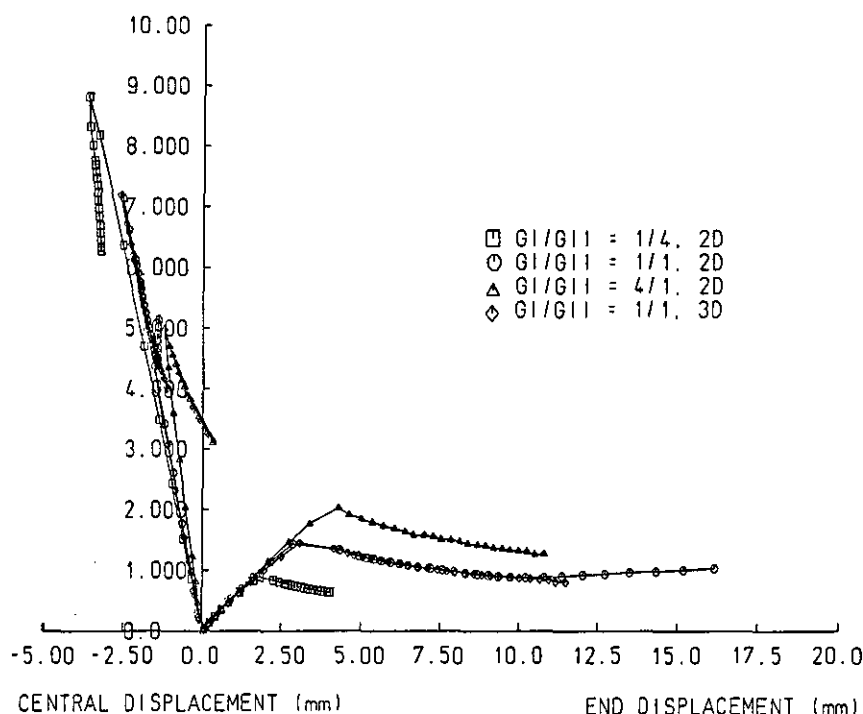


Figure 8.28 Effect of mode ratio on force-deflection response for ACCS "plank" material in two and three-dimensional MMB models.

This section has shown that with a reasonable mesh density, both the line and plane interface elements converged to smooth crack growth response curves provided the material parameters are carefully chosen. Complete interface element material parameter definitions were developed for use in "real", mixed-mode crack growth problems concerning the ACCS "plank". The next section details the results of models designed to simulate the types of delamination observed in the experimental impact test programme.

8.3 Non-Linear Impact Models

The models referred to in this section correspond to those described in section 5.3. After fully verifying the element's behaviour and ascertaining how to assign the material properties to ensure efficient convergence this section describes the implementation of the interface element to model delamination in the "plank". The types of delamination which were modelled were the three fundamental modes as observed in the experimental impact test work. It was concluded in Chapter 7 that each mode of delamination was observed to have been initiated by a critical crack which was therefore represented in the FE models, by artificially inserting a pre-crack.

8.3.1 Lower Interface Delamination Induced by Longitudinal Bending

Three two-dimensional models were run based on a three ply beam corresponding to the ACCS "plank" as described in section 5.1. The first model was un-cracked, the second had a central crack through the lower CFM layer, and the third model had INT6 elements along the lower interface to model delamination as initiated by the pre-crack.

Figure 8.29 shows the deformed beam at peak deflection from which the lower interface delamination initiation and propagation from the pre-crack was clear. Over the whole range the pre-cracked model was only slightly less stiff than the un-cracked model. However, the model which enabled delamination to extend along the lower interface had a much lower stiffness corresponding to the energy absorbed in delamination.

Section 2.2.2.2 illustrated that various researchers^{44,49,58,59,61,67,68,73} have proposed conflicting ideas regarding whether delamination initiation is dominated by Mode I or II. Inspection of the analysis output file containing the forces at the interface modes, clearly showed that failure was initiated by high interlaminar shear forces at the pre-crack tip, but Mode I dominated the crack propagation. This was true for both the delamination models loaded in bending.

At a central deflection of 6mm, the three-dimensional model provided a delamination area as shown in Figure 8.31, having grown to a considerable width under the impactor and tapering in to the end of the lower CFM crack (Figure 8.32). The delamination areas shown were for completely failed nodes and therefore were an underestimation of the area as they did not include any of the process zone.

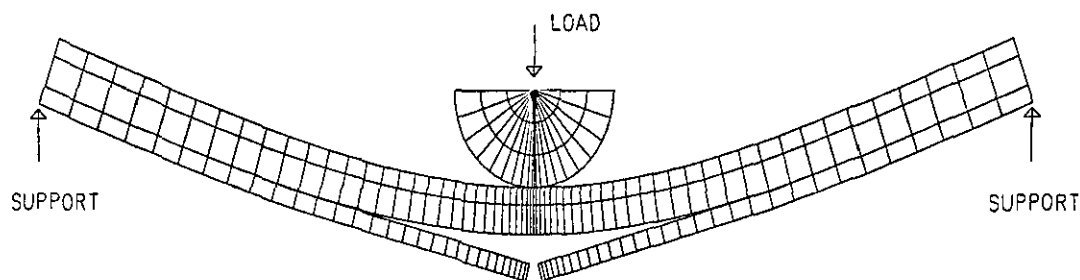


Figure 8.29 Deformed mesh for a two-dimensional model displaying lower interface delamination induced by lower CFM crack under longitudinal bending.

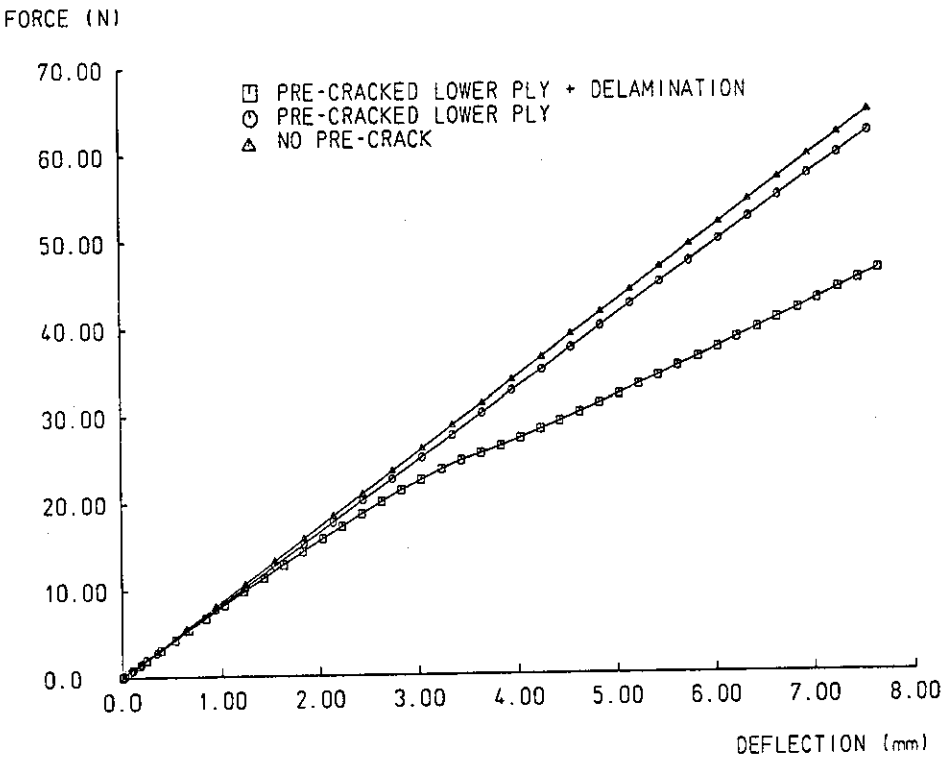


Figure 8.30 Force deflection curve for two-dimensional longitudinal bending models illustrating the stiffness reduction due to the pre-crack and delamination.

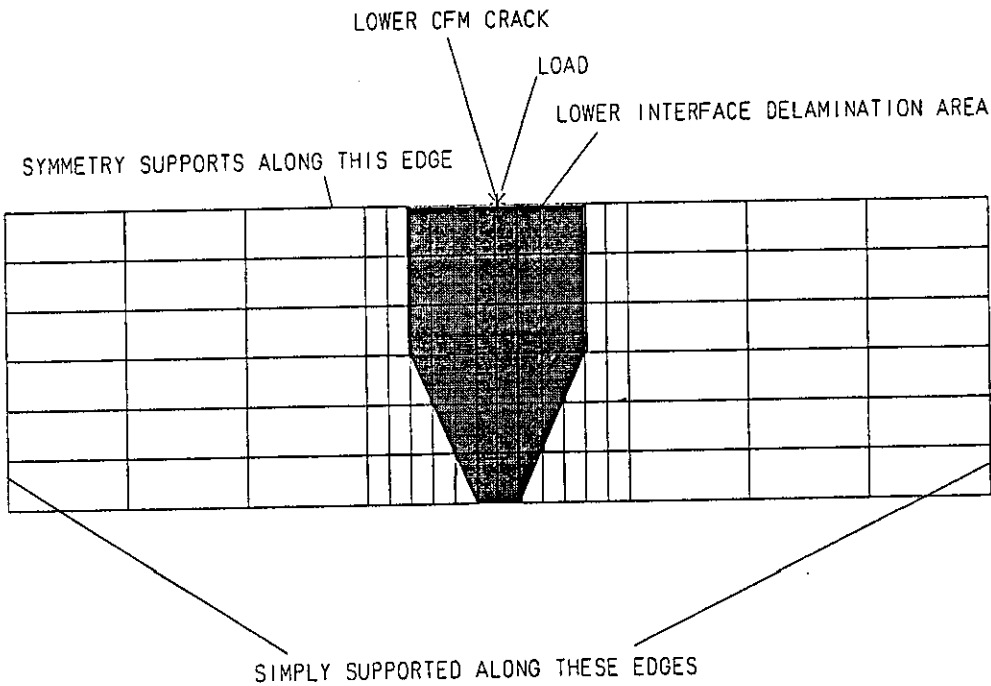


Figure 8.31 Plan view of lower interface delamination area from three-dimensional cracked longitudinal bending model.

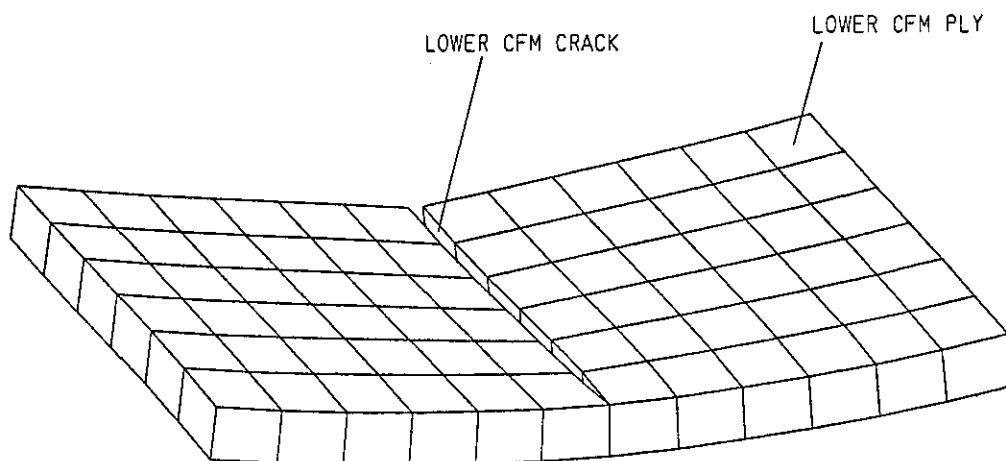


Figure 8.32 Lower CFM ply and "closed" crack from three-dimensional cracked longitudinal bending model.

8.3.2 Upper Interface Delamination Induced by Transverse Bending

Three two-dimensional models were run with the first being un-cracked and the second having a central crack through the lower CFM layer and the central UD layer. The third model had INT6 elements along the upper interface to model delamination. Figures 8.33 and 8.34 show the resultant force-deflection graph and deformed beam at maximum deflection respectively.

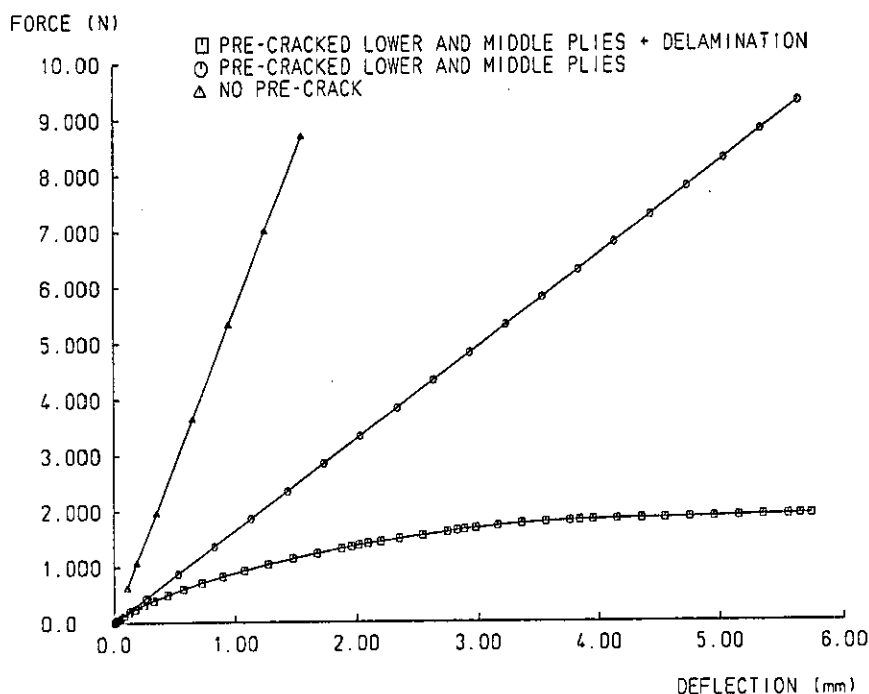


Figure 8.33 Force deflection curve for transverse bending models illustrating stiffness reduction due to the pre-crack and delamination.

The upper interface delamination width was less than for the longitudinal bending model which was due to the lack of stiffness in the upper CFM layer (Figure 8.33). The delamination was therefore thin, following the crack, which corresponded closely to experiment, where the transverse coupon displayed a thin upper interface delamination (section 7.3.2). Figure 8.33 illustrates that the pre-cracked model was much more compliant than the un-cracked model, whilst the model which allowed for delamination along the upper interface had the lowest stiffness. Figure 8.35 illustrates the "peanut" shaped upper interface delamination obtained from the three-dimensional test, which agreed with the experimental investigation, and the literature. Even for a point load the compressive through-thickness normal stress reduced the delamination in the vicinity of load application.

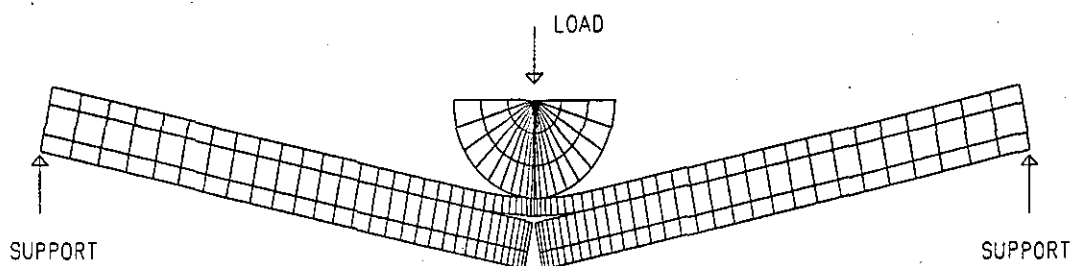


Figure 8.34 Deformed mesh of a two-dimensional model displaying upper interface delamination induced by lower CFM crack under transverse bending .

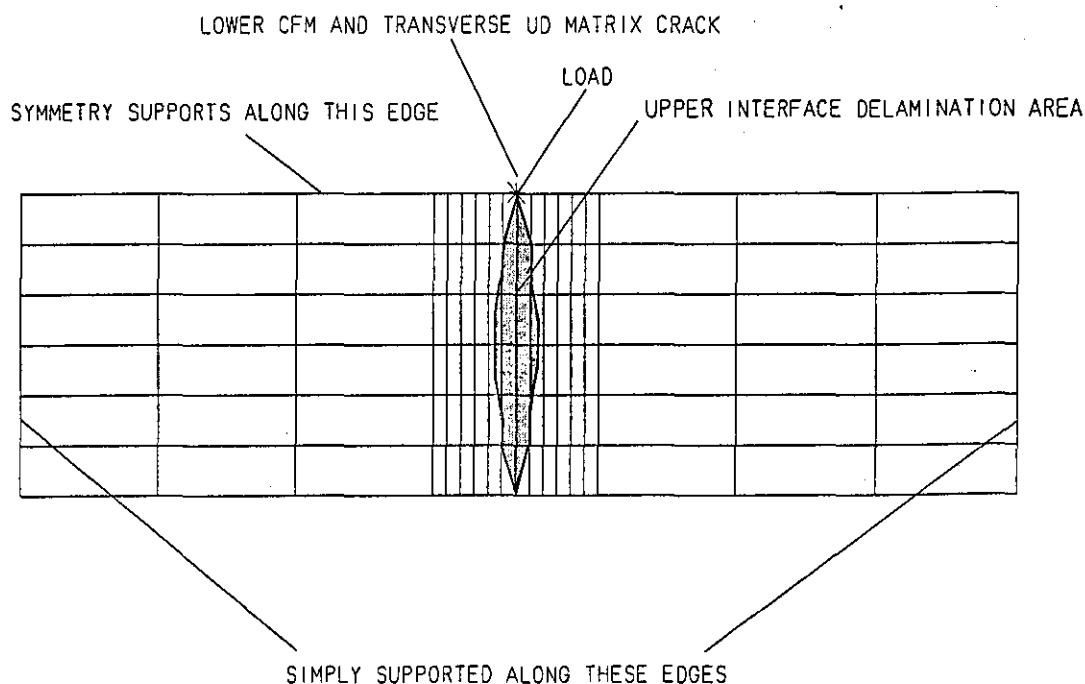


Figure 8.35 Plan view of upper interface delamination area from three-dimensional cracked transverse bending model.

8.3.3 Lower Interface Delamination Induced by Shear Loading

Figure 8.36 illustrates that the change in stiffness due to delamination growth induced by a UD shear crack was dramatic compared to the bending induced delamination growth described in the previous two sections. Figure 8.37 clearly illustrates the shear dominance in this model.

Several models were run with various positions of the shear crack, however neither the overall response nor the force-deflection curve were greatly effected, therefore just the one condition is reported.

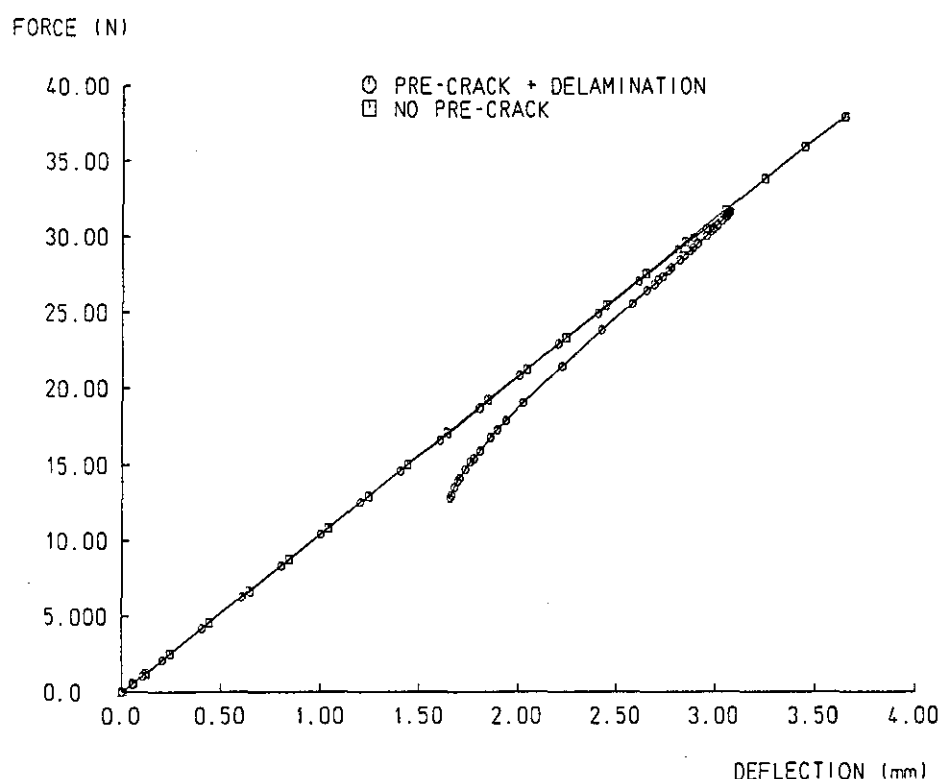


Figure 8.36 Force-deflection curves for the two-dimensional shear loaded models displaying lower delamination growth induced by a shear crack in the UD layer.

The equivalent three-dimensional model (Figure 8.38) provided a large lower interface delamination area centrally in the specimen, under the point of load application, which very quickly tapered off as the closed end of the shear crack was approached. This compared well with the experimental results where the shear induced lower interface delamination was usually concentrated in the centre of the specimen and ran out well before either the upper interface delamination or lower CFM crack stopped (Figure 7.13).

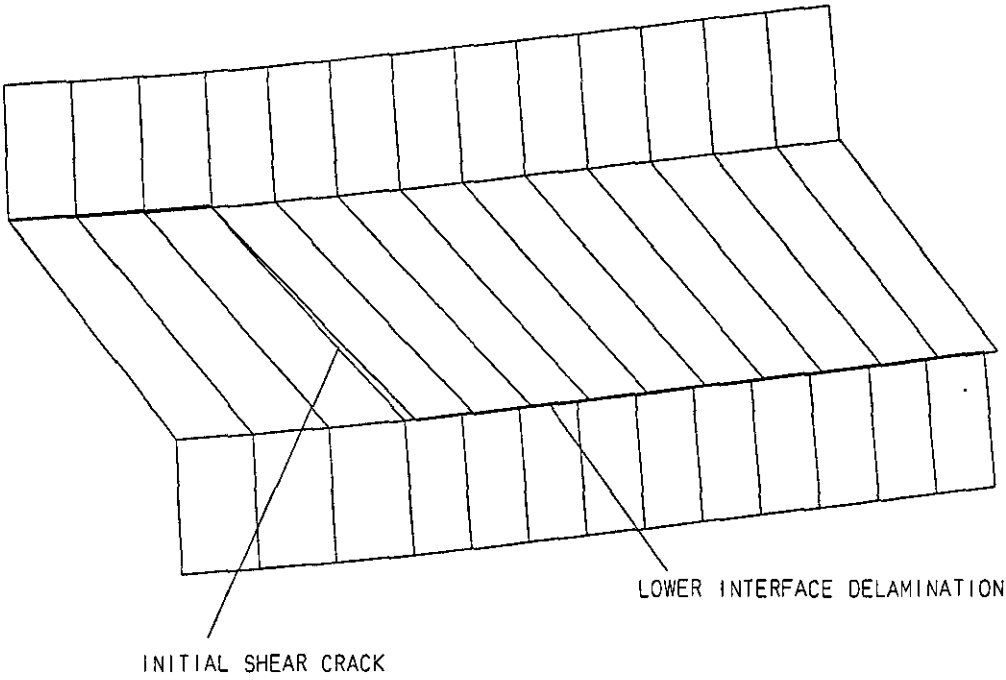


Figure 8.37 Deformed mesh of the two-dimensional model displaying shear dominated delamination growth from a UD shear crack.

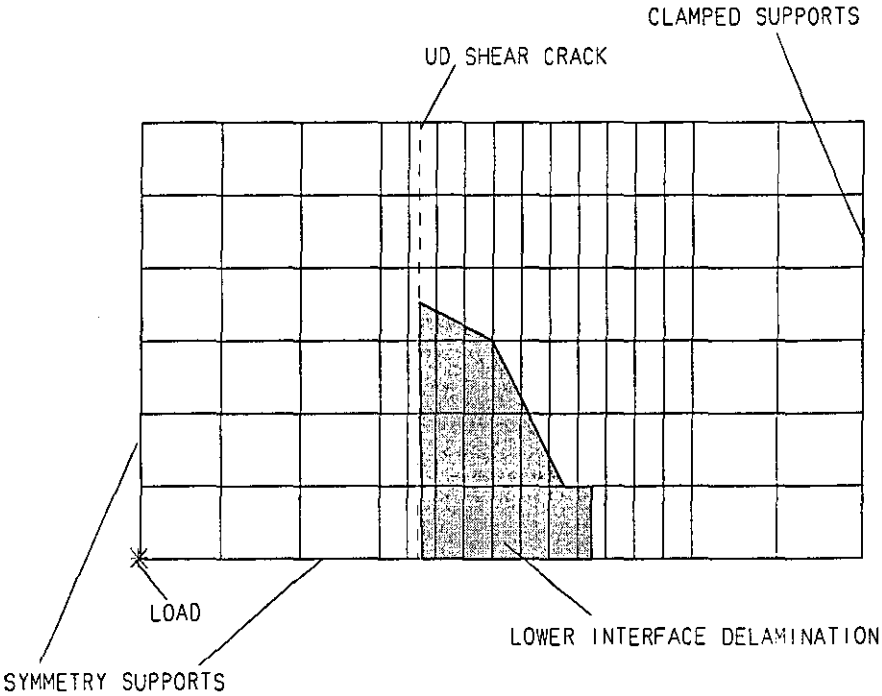


Figure 8.38 Plan view of lower interface delamination area from three-dimensional UD shear cracked model.

The two-dimensional models illustrated the considerable change in stiffness due to delamination, whilst the three-dimensional models have provided excellent qualitative correlation to the experimental observations of delamination shapes with respect to the impact site and the closed end of the crack. These models clearly illustrate that interface element modelling of delamination using the INT6 or INT16 elements within LUSAS was both qualitatively and quantitatively accurate, and will prove a useful technique in predicting damage areas and in furthering the understanding of delamination initiation and propagation.

PART IV

CONCLUSIONS

AND

FURTHER WORK

Chapter 9

Conclusions

9.1 Static Mechanical Testing and Elastic Finite Element Analysis

1. The static mechanical tests proved to be repeatable, despite not being able to use standards test specimens which was made inevitable by the geometry of the Advanced Composite Construction System (ACCS) "plank".
2. The elastic finite element models, employing the material properties derived from the static mechanical tests, accurately predicted the behaviour of the coupons under elastic loading. The initial stiffness response of the models were within 5.8% of those calculated from the experimental impact tests. The longitudinal coupon model was the most accurate, predicting the peak force to 0.5%, the peak deflection to 3.5%, and the time to peak force to 1.6% of the experimental data.

9.2 Experimental Impact Test Results

3. The results from the strain-rate series of tests could only be explained by introducing the parameter, "total impact energy" ($1/2mv_0^2 + mg\delta$), which takes into account the deflection of the specimen, and therefore corresponds exactly to the total strain energy absorbed by the plate, in contrast to the "impact energy" ($1/2mv_0^2$), which has traditionally been employed. This new term quantifies the effect that a heavier mass striking a specimen at the same impact energy as a lower mass will transfer a greater amount of energy to the plate.

4. Using impact energy to correlate the strain-rate test results indicated that a higher mass (lower velocity) produced a higher impact force at a given impact energy therefore suggesting a strain-rate effect. When the term total impact energy (TIE) was introduced, the different mass tests converged onto one line, with the TIE corresponding exactly to the energy absorbed at peak deflection. From this more detailed and accurate analysis it was concluded that there was no appreciable strain-rate effect over the velocity range (0.40 to 3.12 m/s) tested.
5. Prior to this research, the literature contained no detailed impact response and damage analysis regarding a typical pultruded lay-up. This thesis has reported in detail the low velocity impact damage modes and interactions for the typical pultruded lay-up - one unidirectional fibre (UD) layer sandwiched between two continuous filament mats (CFM). From each of the coupon tests the damage observed and the reduced stiffness response of the force-deflection curves were closely correlated. Interlaminar damage (delamination) was always initiated by some form of intralaminar damage (lower CFM cracking, vertical tensile matrix cracks and/or inclined shear cracks). The three basic forms of crack induced delamination were:
 - (a) lower interface delamination induced by a lower CFM crack
 - (b) lower interface delamination induced by a shear crack in the UD layer.
 - (c) upper interface delamination induced by a lower CFM crack associated with a matrix crack.
6. Classic "peanut" shaped upper interface delamination, as reported in the literature, was obtained with the compressive normal force suppressing delamination under the impactor.
7. Penetration, after collapse of the upper CFM layer, and UD fibre breakage of the central layer, only occurred for the shear coupons due to the high shear forces. "Creasing" was the final form of damage for the simply supported coupons.
8. Very little UD fibre breakage was present prior to ultimate failure, except in the longitudinal coupons, suggesting that a finite element analysis which accurately predicted the onset of UD fibre failure, could be assumed to have failed (i.e. therefore avoid modelling the UD fibre breakage). This is in contrast to a typical cross-ply laminate (common outside of the pultrusion manufacturing technique) in which much UD fibre breakage can occur prior to failure, which therefore must be accurately represented in the model.

9. The box sections introduced shear forces due to the double skin/webs design, with the span-to-depth ratio dictating the shear force levels, and therefore the modes of damage induced under impact loads.
10. An important transition in impact response was observed when the impact site was varied from between webs (simple geometry) to impacts over or near a web (complex geometry). When impacted between the webs, the impact response could be defined by superimposing a local deflection directly under the impactor on top of a global deflection of the whole section. Due to the local deflection, damage was only initiated directly under the impactor.

For impacts over a web there was very little local deflection and bending was due to global deflection alone, which resulted in remote and unpredictable areas of poor material quality and/or areas of stress-concentration (web/skin joins) being the first areas to absorb damage energy.

The transition from local to remote damage modes would have implications not only for residual strength but also repair of sections if employed in the construction of freight containers.
11. At high energies, cracking under the impactor occurred when the impact site was over a web. A crack propagation model was developed to explain this damage at the web/skin join.
12. Peak force was shown to be the best parameter for comparison of the initiation of delamination (0.8 to 1.25KN), lower CFM cracking (0.85 to 1.5KN), and upper CFM shear cracking (1.9 to 2.3KN) between the wide variety of impact specimens and support conditions tested during this research.
13. The hemi-spherical impactor employed throughout the impact test programme would be representative of the following point impacts which a freight container would be subject to in-service: a corner casting striking another container when being moved from one mode of transport to another; impact of a crane's hook; fork lift truck prong impact; or a corner of a pallet being dropped onto the container floor.

9.3 Non-Linear Finite Element Analysis

14. An innovative approach to simulating delamination was developed employing the interface element technique. A newly developed interface element was fully verified for Mode I, Mode II and mixed-mode loading in both two- and three- dimensional models.

The fracture energy absorbed in the modes was coupled in the mixed-mode analyses using a linear coupling model.

15. Previous to this research jagged crack growth was obtained and solution convergence was unstable often resulting in aborted analyses. This research highlighted how to assign material parameters to ensure smooth crack growth without sacrificing the accuracy in the nature of crack initiation and propagation.
16. Delamination was modelled in the ACCS "plank" using the material data gathered from the experimental double cantilever beam (DCB) and end notched flexure (ENF) tests. The energies absorbed in Mode I, Mode II, and mixed-mode crack growth correlated to within 4% of the fracture energy assigned to the element, therefore it was concluded that the element accurately quantitatively modelled delamination crack growth.
17. The ability of the interface element to qualitatively model delamination was illustrated by the curved crack-front in the three-dimensional DCB models, whilst under Mode II loading a transition from stable to unstable crack growth at a critical initial crack length of 30-35mm for the ENF test model was observed. Both these phenomena have been reported by many other investigators.
18. Provided a smooth crack growth response was achieved, interface element modelling of delamination initiation and growth was shown to be independent of mesh refinement.
19. Two- and three-dimensional models were run simulating the three major modes of delamination observed in the impact tests. Cracks were inserted to initiate growth, with delamination from the two bending models being initiated by high shear stress (Mode II) at the pre-crack tip, and propagation dominated by normal stresses (Mode I). Mode II dominated the onset and growth of lower interface delamination induced from a UD shear crack. The delamination shapes predicted were the same in nature as those observed experimentally.
20. The finite element research has created accurate elastic models and an interlaminar failure model. On development of a brittle damage (intralaminar model), the commercial finite element code LUSAS will be fully capable of a composite laminate impact analysis beyond first failure.
21. The above findings have furthered the understanding of the impact response, damage modes and interactions of a typical pultruded composite section and areas of weakness

highlighted for improvement. The finite element method has been advanced for modelling delamination, a key damage energy absorbing mode under transverse impact loading. As understanding of the impact properties of pultruded sections increases, and the ability to model important failure phenomena improves, so pultrusion will become more readily accepted in structurally demanding roles, such as in the construction of freight containers.

Chapter 10

Recommendations for Further Work

1. Whilst the predicted vibration response of the finite element models was adequate, more work could be performed regarding the levels of damping employed. The time step could be reduced also, but as explained this vastly increases the CPU time for an analysis, and also requires larger disk space.
2. The coupon finite element models were of very small specimens. Large and more complex specimen geometry could be investigated using the tied slideline technique by employing three-dimensional modelling under the impactor, whilst using shell elements to represent the remainder of the structure.
3. Further double cantilever beam and end notched flexure tests are required to obtain more accurate Mode I and II critical strain energy release rate data. Flat pultruded plates with an interface at the mid-plane of a balanced laminate need to be produced to avoid the difficulties encountered in testing specimens taken directly from the outer skins of the "plank".
4. Throughout the experimental impact tests, a 10mm diameter hemi-spherical impactor tip was employed to simplify the response, however in terms of describing impacts that a freight container would receive in-service, they were limited. The effect of different shaped impactors could be investigated, and some work in this area has been performed on the ACCS "plank"²¹¹.
5. The impact test programme was comprehensive, and highlighted areas of weakness in the ACCS "plank". When damage is induced under the impactor due to the local

deflection, tensile cracking of the lower CFM layer is normally the first form of damage to have a significant effect on the stiffness response. This form of damage will usually also initiate upper interface delamination as transverse bending is likely to be the dominant bending mode due to the structure of the "plank". An increased transverse strength of the lower CFM layer would delay the initiation of impact damage on strikes between the webs quite considerably. Research into CFM mats having a higher proportion of fibres in the transverse direction to be employed on the lower surface, and the effect on damage thresholds could be performed.

6. Another area of weakness was the lay-up at the skin/web joins on the inside surface of the plank, which were particularly susceptible to damage when the impact location was over or near a web. An investigation into improving the lay-up quality could potentially reduce damage at these joins.
7. The interface element, used to model delamination needs to be developed to enable it to be employed within a dynamic analysis, whilst some meshing problems, which arose when using graded meshes, remain to be solved.
8. A brittle damage model to simulate shear/transverse matrix cracking in the UD layer, and CFM tensile cracking needs to be developed. This model must simulate a crack closely enough that the required shear and normal interlaminar stresses at the crack-tip are generated to initiate delamination. From the mechanical tests performed all the strength data regarding the CFM and UD layers in the "plank" have been obtained which could be used directly in the brittle damage model.
9. Once a brittle damage model has been developed, predicted crack lengths and delamination areas can be compared with experimental data.

References

1. Maunsell Structural Plastics Ltd., "Data Pack", London, UK, April 1992.
2. Robbins, J., "Links to a tee", *New Civil Engineer*, August 1992, 20-23.
3. Richmond, B., "Bridge construction and beyond", *Reinforced Plastics*, October 1993, 26-30.
4. Anon., "Advanced Composites bridge the gap", *Materials World*, 1994, 2(9), 460.
5. Head, P.R. and Templeman, R.B., "Application of limit state design principles to composite structural systems", In: *Limit state design method - handbook of polymer composites for engineers*, Woodhead Publishing, 1994, 181-197.
6. Anon., "Specification for pultrusion of structural glass reinforced plastic for the advanced composite construction system", Designer Composites Technology, Internal Document of Maunsell Structural Plastics Ltd.
7. Meyer, R.W., *Handbook of pultrusion technology*, London, Chapman and Hall, 1985.
8. Holloway, L., "Current developments in materials technology and engineering-pultrusion", *Rapra Review No 3*, 1989, 2 (3).
9. Sumerak, J.E. and Martin, J., "Pultruded products - new capability on the horizon", Advanced Composites Conference Proceedings, Dearborn, MI, USA, 2-4 Dec. 1985, 133-138.
10. Starr, T.F., "Structural applications for pultruded products", In: I.H. Marshall ed., *Composite Structures 2*, 1983, Applied Science Pub., UK, 192-213.
11. Michaeli, W. and Jürss, D., "Thermoplastic pull-braiding: pultrusion of profiles with braided fibre lay-up and thermoplastic matrix system (PP)", *Composites*, 27(1), 1996, 3-7.

12. Tooth, E.S., "Container standardisation: Its impact on shipping and port operations", *Dock and Harbour Authority*, 1990, 70(816), 299-303.
13. Anon., ISO Standards Handbook, *Freight Containers*, Second Edition, International Organisation for Standardisation, Switzerland, 1992.
14. Anon., "Domestic container prospects assessed", *Cargo Systems International: The Journal of the ICHCA*, 1986, 13(6), 81-83.
15. Gooden, C.W., "Intermodal operators raise efficiency", *Railway Gazette International*, 1991, 147(12), 885-888.
16. Munford, C., "Box floor prices hit the roof", *Cargo Systems*, August 1993, 61-63.
17. Anon., "Hitting the floor", *Container Management*, July/August 1993, 15-17.
18. Anon., "Floors under the spotlight", *Container Management*, January 1994, 34-35.
19. Anon., "Wanted: new floor for new flat", *Container Management*, December 1993, 5-6.
20. Davis, R., "The protective alternative for cargo containers", *Product Finishing*, 1988, 41(12), 26-27.
21. Barbero, E. and Fu, S-H., "Local buckling as failure initiation on pultruded composite beams", Impact of Buckling and Structures ASME Conference, Aerospace Division, 1990, AD Vol 20, N.Y., USA, 41-45.
22. Plecnik, J. M., Diba, A., Koppam, V., and Azar, W., "Composite tanker trucks: design and fabrication", *Transportation Research Record 1118*, 1987, 83-87.
23. Anon., "Plastic on the rebound", *Reefer Systems - Cargo Systems Supplement*, March 1996, 13.
24. Grey, J., "Boarding with bamboo", *Container Management*, June 1995, 55-57.
25. Thomas, R., "From little acorns", *Cargo Systems*, February 1996, 25-27.
26. Thomas, R., "More from the floor", *Cargo Systems*, September 1994, 37-39.
27. Anon., "Envirodek funded", *Cargo Systems*, March 1995, 15.
28. Damas, P., "Genstar do-it-all", *Containerisation International*, April 1995, 78-79.
29. Grey, J., "Looking to a plastic future", *Container Management*, June 1995, 57.
30. Anon., "Composite box unveiled", *World Cargo News*, March 1995, 16.

31. Lagace, P.A., Ryan, K.F., and Graves, M.J., "Effect of damage on the impact response of composite laminates", *AIAA Journal*, 1994, **32**(6), 1328-1330.
32. Majeed, O., Worswick, M.J., Straznicky, P.V., and Poon, C., "Numerical modelling of transverse impact on composite coupons", *Canadian Aeronautics and Space Journal*, 1994, **40**(3), 99-106.
33. Sjöblom, P.O., Hartness, J.T. and Cordell, T.M., "On low-velocity impact testing of composite materials", *Journal of Composite Materials*, 1988, **22**, 30-52.
34. Shivakumar, K.N., Elber, W., and Illg, W., "Prediction of low-velocity impact damage in thin circular laminates", *AIAA Journal*, 1985, **23**(3), 442-449.
35. Cantwell, W.J. and Morton, J., "The impact resistance of composite materials - a review", *Composites*, 1991, **22**(5), 347-362.
36. Abrate, S., "Impact on laminated composite materials", *Applied Mechanics Review*, 1991, **44**(4), 155-190.
37. Liu, D. and Malvern, L.E., "Matrix cracking in impacted glass/epoxy plates", *Journal of Composite Materials*, 1987, **21**, 594-609.
38. Joshi, S.P. and Sun, C.T., "Impact-induced fracture initiation and detailed dynamic stress field in the vicinity of impact", Proceedings for the American Society of Composites 2nd Technical Conference, Delaware, September 23-25, 1987, 177-185.
39. Robinson, P. and Davies, G.A.O., "Impactor mass and specimen geometry effects in low velocity impact of laminated composites", *International Journal of Impact Engineering*, 1992, **12**(2), 189-207.
40. Davies, G.A.O. and Robinson, P., "Predicting failure by debonding/delamination, AGARD: 74th Structures and Materials Meeting", 1992.
41. Sierakowski, R.L., "High strain rate loading of composites", In: J.N. Reddy and A.V. Krishna Murty eds., *Composite Structures: Testing, Analysis and Design*, New Delhi, 1992, Springer-Verlag, 222-259.
42. Agarwal, B.D. and Broutman, L.J., *Analysis and performance of fiber composites*, 2nd Edition, John Wiley and Sons, NY, 1990.
43. Joshi, S.P. and Sun, C.T., "Impact induced fracture in a laminated composite", *Journal of Composite Materials*, 1985, **19**, 51-66.
44. Choi, H.Y., Wu, H-Y.T. and Chang, F-K., "A new approach toward understanding damage mechanisms and mechanics of laminated composites due to low-velocity impact: Part II - Analysis", *Journal of Composite Materials*, 1991, **25**, 1012 - 1038.
45. Jih, C.J. and Sun, C.T., "Prediction of delamination in composite laminates subjected to low velocity impact", *Journal of Composite Materials*, 1993, **27**(7), 684-701.

46. Lee, S-W.R. and Sun, C.T., "A quasi-static penetration model for composite laminates", *Journal of Composite Materials*, 1993, 27(3), 251-271.
47. Cantwell, W.J. and Morton, J., "Geometrical effects in the low velocity impact response of CFRP", *Composite Structures*, 1989, 12, 39-59.
48. Wu, H.-Y.T. and Springer, G.S., "Measurements of matrix cracking and delamination caused by impact on composite plates", *Journal of Composite Materials*, 1988, 22, 518-532.
49. Chang, F-K., Choi, H.Y., and Jeng, S-T., "Study on impact damage in laminated composites", *Mechanics of Materials*, 1990, 10, 83-95.
50. Choi, H.Y. , Downs, R.J. and Chang, F-K., "A new approach toward understanding damage mechanisms and mechanics of laminated composites due to low-velocity impact: Part I - Experiments", *Journal of Composite Materials*, 1991, 25, 992 - 1011.
51. Choi, H.Y. and Chang, F-K., "Impact damage threshold of laminated composites, Failure criteria and analysis in dynamic response", ASME, Applied Mechanics Division AMD Vol 107, Dallas, Texas, November 1990, 31-35.
52. Choi, H.Y., Wang, H.S. and Chang, F-K., "Effect of laminate configuration and impactor's mass on the initial impact damage of graphite/epoxy composite plates due to line-loading impact", *Journal of Composite Materials*, 1992, 26(6), 804-827.
53. Chang, F-K. and Chang, K-Y., "A progressive damage model for laminated composites containing stress concentrations", *Journal of Composite Materials*, 1987, 21, 834-855.
54. Lagace, P.A., "On delamination failures in composite laminates", In: J.N. Reddy and A.V. Krishna Murty eds., *Composite Structures: Testing, Analysis and Design*, New Delhi, 1992, Springer-Verlag, 111-132.
55. Cui, W. and Wisnom, M.R., "A combined stress-based and fracture-mechanics-based model for predicting delamination in composites", *Composites*, 1993, 24(6), 467-474.
56. Wang, S.S., "Delamination crack growth in unidirectional fiber-reinforced composites under static and cyclic loading", In: S.W. Tsai, ed., *Composite Materials: Testing and Design* (Fifth Conference) ASTM STP 674, American Society for Testing and Materials, 1979, 642-663.
57. Liu, D., "Impact-induced delamination - a view of bending stiffness mismatching", *Journal of Composite Materials*, 1988, 22, 674-692.
58. Guild, F.J., Hogg, P.J. and Prichard, J.C., "A model for the reduction in compression strength of continuous fibre composites after impact damage", *Composites*, 1993, 24(4), 333-339.

59. Choi, H.Y. and Chang, F-K., "A model for predicting damage in graphite/epoxy laminated composites resulting from low-velocity point impact", *Journal of Composite Materials*, 1992, 26(14), 2134-2169.
60. Davies, G.A.O., Zhang, X. and Edlund, A., "Predicting damage in composite aircraft structures due to low velocity impact", Aerotech Conference, Birmingham, Jan.1994
61. Finn, S.R., He, Y-F., and Springer, G.S., "Delaminations in composite plates under transverse impact loads - experimental results", *Composite Structures*, 1993, 23, 191-204.
62. Dorey, G., "Impact damage tolerance and assessment in advanced composite materials", Seminar on Advanced Composites - Cranfield Institute of Technology, 1986.
63. Dorey, G., "Impact damage in composites - development, consequences, and prevention", 6th International Conference on Composite Materials, 2nd ECCM, Imperial College, London, 1988, 3, 3.1-3.26.
64. Dorey, G., Sigety, P., Stellbrink, K., and 't Hart, W.G.J., "Impact damage tolerance of carbon fibre and hybrid laminates", RAE Technical Report 87057, 1987.
65. Takeda, N., Sierakowski, R.L. and Malvern, L.E., "Microscopic observations of cross sections of impacted composite laminates", *Composites Technology Review*, 1982, 4(2), 40-44.
66. Liu, S., Kutlu, Z. and Chang, F-K., "Matrix cracking and delamination in laminated composite beams subjected to a transverse concentrated line load", *Journal of Composite Materials*, 1993, 27(5), 436-470.
67. Garg, A.C., Delamination - "A damage mode in composite structures", *Engineering Fracture Mechanics*, 1988, 29(5), 557-584.
68. Finn, S.R. and Springer, G.S., "Delaminations in composite plates under transverse static or impact loads - a model", *Composite Structures*, 1993, 23, 177-190.
69. Dorey, G., Sidey, G.R. and Hutchings, J., "Impact properties of carbon fibre/kevlar 49 fibre hybrid composites", *Composites*, 1978, 9, 25-32.
70. Clarke, M.P. and Pavier, M.J., "Artificial damage techniques for low velocity impact in carbon fibre composites", *Composite Structures*, 1993, 25, 113-120.
71. Doxsee, L.E., Rubbrecht, P., Li, L., Verpoest, I., and Scholle, M., "Delamination growth in composite plates subjected to transverse loads", *Journal of Composite Materials*, 1993, 27(8), 764-781.

72. Wu, E. and Shyu, K., "Response of composite laminates to contact loads and relationship to low-velocity impact", *Journal of Composite Materials*, 1993, 27(15), 1443-1464.
73. Razi, H. and Kobayashi, A.S., "Delamination in cross-ply laminated composite subjected to low-velocity impact", *AIAA Journal*, 1993, 31(8), 1498-1502.
74. Lee, S.M. and Zahuta, P., "Instrumented impact and static indentation of composites", *Journal of Composite Materials*, 1991, 25, 204-222.
75. Lee, S.-W.R. and Sun, C.T., "Dynamic penetration of graphite/epoxy laminates impacted by a blunt-ended projectile", *Composites Science and Technology*, 1993, 49(4), 369-380.
76. El-Habak, A.M., "Effect of impact perforation load on GFRP composites", *Composites*, 1993, 24(4), 341-345.
77. Chaturvedi, S.K. and Sierakowski, R.L., "Effects of impactor size on impact damage-growth and residual properties in an SMC-R50 composite", *Journal of Composite Materials*, 1985, 19, 100-113.
78. Khetan, R.P. and Chang, D.C., "Surface damage of sheet molding compound panels subject to a point impact loading", *Journal of Composite Materials*, 1983, 17, 182-194.
79. Liu, D., Lee, C.Y., and Lu, X., "Repairability of impact-induced damage in SMC composites", *Journal of Composite Materials*, 1993, 27(13), 1257-1271.
80. Hull, D., *An introduction to composite materials*, Cambridge University Press, 1981.
81. Bader, M.G., Reinforcing fibres: the strength behind composites, *Materials World*, 1993, 1(1), 22-26.
82. Jang, B.Z., Chen, L.C., Hwang, L.R., Hawkes, J.E., and Zee, R.H., "The response of fibrous composites to impact loading", *Polymer Composites*, 1990, 11(3), 144-157.
83. Sela, N. and Ishai, O., "Interlaminar fracture toughness and toughening of laminated composite materials: A review", *Composites*, 1989, 20(5), 423-435.
84. Pitkethly, M.J. and Bader, M.G., "Failure modes of hybrid composites consisting of carbon fibre bundles dispersed in a glass fibre epoxy resin matrix", *Journal of Applied Physics : D - Applied Physics*, 1987, 20, 315-322.
85. Holmes, M. and Just, D.J., *GRP in structural engineering*, Applied Science Pub. Ltd., 1983.
86. Moon, F.C., "Wave propagation and impact in composite materials", In: L.J. Broutman and R.H. Krock eds., *Composite Materials: Vol. 7: Structural Design and Analysis - Part I*, Academic Press, London, 1975, 259-332.

87. Caprino, G., "Residual strength prediction of impacted CFRP laminates", *Journal of Composite Materials*, 1984, 18, 508-518.
88. Davies, G.A.O., Zhang, X., Zhou, G., and Watson, S., "Numerical modelling of impact damage", *Composites*, 1994, 25(5), 342-350.
89. Broutman, L. J. and Rotem, A., "Impact strength and toughness of fiber composite materials", In: *Foreign Object Impact Damage to Composites*, ASTM STP 568, American Society for Testing and Materials, 1975, 114 - 133.
90. Sierakowski, R.L. and Chaturvedi, S.K., "Impact loading in filamentary structural composites", *Shock and Vibration Digest*, 1983, 15(10), 13-31.
91. Caprino, G., Crivelli Visconti, I., and Di Ilio, A., "Elastic behaviour of composite structures under low velocity impact", *Composites*, 1984, 15(3), 31-234.
92. Sims, G.D., "Understanding Charpy impact testing of composite materials", 6th International Conference on Composite Materials/2nd ECCM, Imperial College, London, 1988, 3.494-3.507.
93. Hayes, S.V. and Adams, D.F., "Rate sensitive tensile impact properties of fully and partially loaded unidirectional composites", *Journal of Testing and Evaluation*, 1982, 10(2), 61-68.
94. Li, Y.L., Harding, J., and Ruiz, C., "Modelling of the impact response of fibre reinforced composites", University of Oxford Department of Engineering Science, OU-DES-OUEL 1863/90, 1990.
95. Zhou, G. and Davies, G.A.O., "Impact response of thick glass fibre reinforced polyester laminates", *International Journal of Impact Engineering*, 1995, 16(3), 357-374.
96. Ruiz, C. and Xia, Y.R., "The significance of interfaces in impact response of laminated composites", *Composite Material Technology - 1991 ASME*, Petroleum Division, PD Vol. 37, ASME, NY, USA, 1991, 161-166.
97. Svenson, A.L., Hargrave, M.W., and Bank, L.C., "Impact behaviour of pultruded composites", *Engineering Plastics*, 1994, 7(3), 173-186.
98. Habib, S.S., "Impact response of glass fibre reinforced composite plates", *Journal of Reinforced Plastics and Composites*, 1995, 14(8), 799-803.
99. Cheung, A.K.H. and Scott, M.L., "Impact damage of thin skinned fibre composite panels", Australian Aeronautical 5th Conference, Sept. 1993, Melbourne, 155-160.
100. Tabiei, A., Svenson, A.L., and Hargrave, M.W., "Impact behaviour of pultruded box-beams for roadside safety structures", 50th Annual Conference, Composites Institute, The Society of the Plastics Industry, Jan. 30 - Feb. 1 1995, Session 10-D, 1-6.

101. Svenson, A. L., Hargrave, M.W., Tabiei, A., Bank, L.C., and Tang, Y., "Design of pultruded beams for optimisation of impact performance", 50th Annual Conference, Composites Institute, The Society of the Plastics Industry, Jan. 30 - Feb. 1 1995, Session 10-E 1-7.
102. Kelkar, A.D., Craft, W.J., and Sandhu, R.S., "Study of progressive damage in thin and thick composite laminates subjected to low velocity impact loading", Recent Advances in Structural Mechanics, ASME Winter Annual Meeting 1993, PVP-Vol 269, 67-73.
103. Tui, W.P., Gott, J., and Breckell, T.H., "Residual static strength prediction of impacted composite laminates", In: C.A. Brebbia, W.P. de Wilde, W.R. Blain eds., *Computer Aided Design in Composite Material Technology*, Springer-Verlag, 1988, 337-351.
104. Wu, H-Y.T. and Springer, G.S., "Impact induced stresses, strains, and delaminations in composite plates", *Journal of Composite Materials*, 1988, **22**, 533-560.
105. Nettles, A.T. and Hodge, A.J., "Compression-after-impact testing of thin composite materials", 23rd International SAMPE Technical Conference, Covina, USA, October 21-24, 1991, 177-183.
106. Jones, R., Paul, J., Tay, T.E., and Williams, J.F., "Assessment of the effect of impact damage in composites: some problems and answers", *Composite Structures*, 1988, **10**(1), 51-73.
107. Ganapathy, S., Tripathy, B., and Rao, K.P., "Damage and its growth in laminated composite circular/rectangular plates undergoing large deformations", *Composite Structures*, 1995, **32**(1-4), 367-373.
108. Lindsay, T.C. and Wilkins, D.J., "The role of instrumented impact testing in the design of composite structures for low-velocity impact resistance", 23rd International SAMPE Technical Conference, Covina, USA, October 21-24, 1991, 72-90.
109. Collombet, F., Bonini, J., and Lataillade, J.L., "A three dimensional modelling of low velocity impact damage in composite laminates", *International Journal for Numerical Methods in Engineering*, 1996, **39**(9), 1491-1516.
110. Lifshitz, J.M., "Impact strength of angle ply fiber reinforced materials", *Journal of Composite Materials*, 1976, **10**, 92-100.
111. Harding, J. and Li, Y.L., "Determination of interlaminar shear strength for glass/epoxy and carbon/epoxy laminates at impact rates of strain", *Composites Science and Technology*, 1992, **45**(2), 161-171.
112. Pal, N.C. and Ghosh, A.K., "An experimental investigation on impact response of laminated composite beams", *Experimental Mechanics*, 1993, **33**(2), 159-163.

113. Greszczuk, L.B., "Damage in composite materials due to low velocity impact", In: J.A. Zukas et al. eds., *Impact Dynamics*, John Wiley and Sons, NY, USA, 1982.
114. Johnson, A.E., Moore, D.R., Prediger, R.S., Reed, P.E., and Turner, S., "The falling weight impact test applied to some glass-fibre reinforced nylons. Part 1 - Appraisal of the method", *Journal of Materials Science*, 1986, 21, 3153-3161.
115. Kessler, S.L., Adams, G.C., Driscoll, S.B., and Ireland, D.R., "Instrumented impact testing of plastics and composite materials", ASTM STP 936, American Society for Testing and Materials, Philadelphia, 1987.
116. Chivers, R.A. and Moore, D.R., "Further developments in the interpretation of signals from instrumented falling weight impact (IFWI)", *Measurement Science and Technology*, 1990, 1, 313-321.
117. Jones, D.P., Leach, D.C., and Moore, D.R., "The application of instrumented falling weight impact techniques to the study of toughness in thermoplastics", *Plastics and Rubber Processing and Applications*, 1986, 6(1), 67-79.
118. Moore, D.R. and Prediger, R.S., "A study of low-energy impact of continuous carbon-fiber-reinforced composites", *Polymer Composites*, 1988, 9(5), 330-336.
119. Cantwell, W.J. and Morton, J., "The significance of damage and defects and their detection in composite materials: A review", *Journal of Strain Analysis*, 1992, 27(1), 29-42.
120. Krautkrämer, J. and Kräutkramer, H., *Ultrasonic testing of materials*, Third Edition, Springer-Verlag, Heidelberg, 1983.
121. Hull, B. and John, V., *Non-destructive testing*, Macmillan Education Ltd, London, 1988.
122. Joshi, S.P. and Sun, C.T., "Impact-induced fracture in a quasi-isotropic laminate", *Journal of Composites Technology and Research*, 1987, 9(2), 40-46.
123. Richardson, M.O.W., "Damage assessment in fatigue of reinforced structural composites", ASI/NATO Conference, Advances in fatigue science and technology, Algarve, Portugal, 4-13 April, 1988, 1-20.
124. Jackson, W.C. and Poe, C. C. Jr., "The use of impact force as a scale parameter for the impact response of composite laminates", *Journal of Composites Technology and Research*, 1993, 15(4), 282-289.
125. Mines, R.A.W., "Impact on laminated polymer composites", In: C.Y. Chiem ed., *Behaviour and dynamics of materials and structures in severe environment*, Ouest Editions, France, 1993.

126. Shivakumar, K.N., Elber, W., and Illg, W., "Prediction of impact force and duration due to low-velocity impact on circular composite laminates", *Journal of Applied Mechanics* - Transactions of the ASME, 1985, 52, 674-680.
127. Choi, I.H. and Hong, C.S., "New approach for simple prediction of impact force history on composite laminates", *AIAA Journal*, 1994, 32(10), 2067-2072.
128. Goldsmith, W., *Impact*, Edward Arnold, London, 1960.
129. Greszczuk, L.B., "Response of isotropic and composite materials to particle impact", In: *Foreign object impact damage to composites*, ASTM STP 568, American Society for Testing and Materials, 1975, 183-211.
130. Tan, T.M. and Sun, C.T., "Use of statical indentation laws in the impact analysis of laminated composite plates", *Journal of Applied Mechanics* - Transactions of the ASME, 1985, 52, 6-12.
131. Yang, S.H. and Sun, C.T., "Indentation law for composite laminates", Nasa CR - 165460, 1981.
132. Wu, H-Y.T. and Chang, F-K., "Transient dynamic analysis of laminated composite plates subjected to transverse impact", *Computers and Structures*, 1989, 31(3), 453-466.
133. Montemurro, M.P., Hansen, J.S., and Houde, M.J.L., "Finite element analysis of the impact response of composite plates and shells", AIAA/ASME Structures, structural dynamics and materials 34th Conference, 1993, 3, 1245-1253.
134. Gu, Z.L. and Sun, C.T., "Prediction of impact damage region in SMC composites", *Composite Structures*, 1987, 7, 179-190.
135. Aggour, H. and Sun, C.T., "Finite element analysis of a laminated composite plate subjected to circularly distributed central impact loading", *Computers and Structures*, 1988, 28(6), 729-736.
136. Morton, J., "Scaling of impact-loaded carbon-fiber composites", *AIAA Journal*, 1988, 26(8), 989-994.
137. Quian, Y., Swanson, S.R., Nuismer, R.J., and Bucinell, R.B., "An experimental study of scaling rules for impact damage in fiber composites", *Journal of Composite Materials*, 1990, 24, 559-570.
138. Swanson, S.R., "Dynamic and scaling effects in impact of composite structures", ICCM9, Madrid, July 1993, 291-298.
139. Swanson, S.R., "Scaling of impact damage in fiber composites from laboratory specimens to structures", *Composite Structures*, 1993, 25, 249-255.

140. Lakshminarayana, H.V., Boukhili, R. and Gauvin, R., "Impact response of laminated composite plates: prediction and verification", *Composite Structures*, 1994, **28**, 61-72.
141. Sastry Putcha, N., "FEA eases composites design", *Advanced Materials and Processes*, 1990, **138**(3), 49-53.
142. Gibson, R.F., "Dynamic mechanical properties of advanced composite materials and structures: A review", *Shock and Vibration Digest*, 1987, **19**(7), 13-22.
143. Kwon, Y.W. and Byun, K.Y., "Development of a new finite element formulation for the elasto-plastic analysis of fiber-reinforced composites", *Computers and Structures*, 1990, **35**(5), 563-570.
144. Ochoa, O.O. and Reddy, J.N., *Finite element analysis of composite laminates*, Kluwer Academic Publishers, Netherlands, 1992.
145. Prasad, C.B., Ambur, D.R., and Starnes, J.H. Jr., "Response of laminated composite plates to low-speed impact by different impactors", *AIAA Journal*, 1994, **32**(6), 1270-1277.
146. Rao, K.M. and Meyer-Piening, H.-R., "Analysis of thick laminated anisotropic composite plates by the finite element method", *Composite Structures*, 1990, **15**(3), 185-213.
147. Yang, H.T.Y., Saigal, S., and Liaw, D.G., "Advances of thin shell finite elements and some applications - version I", *Computers and Structures*, 1990, **35**(4), 481-504.
148. Griffin, O.H. Jr., "The use of computers in the evaluation of three dimensional stress effects in composite materials products", In: W.P. de Wilde and W.R. Blain eds., *Composite Materials: Design and Analysis*, Computational Mechanics, Belgium, 1990, 171-185.
149. Moser, K. and Schmid, A., "Composite structures - modelling, finite element analysis and evaluation", *Composite Structures*, 1989, **11**, 33-56.
150. Lyons, L.P.R., Kent, A.J., Bell, A.P., and Crook, A.J.L., "Recent developments in the Lusas finite element system", *Computers and Structures*, 1991, **41**(6), 1273-1280.
151. Cook, R.D., Malkus, D.S., and Plesha, M.E., *Concepts and applications of finite element analysis*, Third Edition, John Wiley and Sons, 1989.
152. Cui, W.C. and Wisnom, M.R., "Contact finite element analysis of three- and four-point short-beam bending of unidirectional composites", *Composites Science and Technology*, 1992, **45**, 323-334.
153. Bonini, J., Collombet, F., and Lataillade, J.L., "Numerical modelling of contact for low velocity impact damage in composite laminates", In: M H Aliabadi and C A

- Brebbia eds., *Contact Mechanics*, 1st International Conference on Contact Mechanics, Southampton, July 1993, 453-461.
154. Banerjee, R., "Numerical simulation of impact damage in composite laminates", *Proceedings of the American Society for Composites*, 1992, 539-552.
 155. Glance, P.M., "Computer-aided engineering analysis of composite laminate structures", *Advanced Composites - Conference Proceedings*, Dearborn, MI, USA, 1985, 277-284.
 156. Hellweg, H-B. and Crisfield, M.A., "Role of material properties in the finite element solution for three-dimensional composites - a sensitivity study", *Proceedings of the Institution of Mechanical Engineers, Part G: Journal of Aerospace Engineering*, 1995, 209(2), 157-160.
 157. Griffin, O.H. Jr., "The use of proper shear moduli in the analysis of laminated composites", *Composites Technology Review*, 1984, 6(1), 22-24.
 158. Sala, G. and Anghileri, M., "Analytical and experimental evaluation of finite element models for crash analysis", *Structures under shock and impact - 2nd Conference 1992*, Portsmouth, 155-173
 159. Murphy, D., "Non-linear analysis provides new insights into impact damage of composite structures", *Composites*, 1994, 25(1), 65-69.
 160. Yener, M. and Wolcott, E., "Damage assessment analysis of composite pressure vessels subjected to random impact loading", *Journal of Pressure Vessel Technology* - Transactions of the ASME, 1989, 111, 124-129.
 161. Hashin, Z., "Failure criteria for unidirectional fiber composites", *Journal of Applied Mechanics* - Transactions of the ASME, 1980, 47, 329-334.
 162. Lakshminarayana, H.V., Boukhili, R. and Gauvin, R., "Numerical and experimental impact damage evaluation of laminated composite plates", *ICCM9*, Madrid, July 1993, 422-429.
 163. Reddy, J.N. and Pandey, A.K., "A first-ply failure analysis of composite laminates", *Computers and Structures*, 1987, 25(3), 371-393.
 164. Shahid, I., Chang, F-K., and Ilcewicz, L.B., "Progressive failure analysis for laminated composite plates under multiple in-plane loads", *ICCM9*, Madrid, July 1993, 105-112.
 165. Pavier, M.J. and Chester, W.T., "Compression failure of carbon fibre-reinforced coupons containing central delaminations", *Composites*, 1990, 21(1), 23-31.
 166. Huang, C., Cheikh Saad Bouh, A.B., and Verchery, G., "Progressive failure analysis of laminated composites with transverse shear effects", *ICCM9*, Madrid, July 1993, 97-104.

167. Nahas, M.N., "Survey of failure and post-failure theories of laminated fiber-reinforced composites", *Journal of Composites Technology and Research*, 1986, 8(4), 138-153.
168. Zhou, G. and Davies, G.A.O., "Characterization of thick glass woven roving/polyester laminates: Part 2, flexure, and statistical consideration", *Composites*, 1995, 26(8), 587-596.
169. Murray, Y. and Schwer, L., "Implementation and verification of fiber - composite damage models, failure criteria and analysis in dynamic response", ASME Applied Mechanics Division AMD Vol 107, Dallas, Texas, November 1990, 21-30.
170. Kerth, S. and Maier, M., "Numerical simulation of the crashing of composite tubes", *Computer aided design in composite materials technology IV*, 1994, Ch.47, 141-148.
171. Ambur, D.R., Starnes Jr., J.H., and Prasad, C.B., "Low-speed impact damage-initiation characteristics of selected laminated composite plates", *AIAA Journal*, 1995, 33(10), 1919-1925.
172. Ochoa, O.O. and Engblom, J.J., "Analysis of progressive failure in composites", *Composites Science and Technology*, 1987, 28, 87-102.
173. Edlund, A., "Finite element modelling of low velocity impact damage in composite laminates", ICCM9, Madrid, July 1993, 334-341.
174. Becker, W., "Mathematical simulation of external and internal damage due to low velocity impact", *Computer aided design in composite materials technology IV*, 1994, Ch.47, 149-156.
175. Hwang, W.C. and Sun, C.T., "Failure analysis of laminated composites by using iterative three-dimensional finite element method", *Computers and Structures*, 1989, 33(1), 41-47.
176. Hellweg, H.B., "Non-linear failure simulation of thick composites", PhD Thesis, Department of Aeronautics, Imperial College, London, 1995.
177. Rybicki, E.F. and Kanninen, M.F., "A finite element calculation of stress intensity factors by a modified crack closure integral", *Engineering Fracture Mechanics*, 1977, 9, 931-938.
178. Reeder, J.R. and Crews, J.H. Jr., "Mixed-mode bending method for delamination testing", *AIAA Journal*, 1990, 28, 1270-1276.
179. Zheng, S. and Sun, C.T., "Prediction of impact induced delamination in composite laminates using plate finite elements", ASME Aerospace Division Publication, 1994, 43, 137-148.
180. Li, D.S. and Wisnom, M.R., "Modelling damage initiation and propagation in composites using interface elements", *Computer aided design in composite materials technology IV*, 1994, Ch.47, 213-220.

181. Lo, D. C., Costanzo, F., Zocher, M.A., and Allen, D.H., "Modelling of damage evolution in thick laminates subjected to low velocity impact", *Mechanics of Thick Composites*, Applied Mechanics Division ASME Summer Annual Meeting 1993, AMD-Vol 162, 137-150.
182. Schellekens, J.C.J. and De Borst, R., "Numerical simulation of free edge delamination in graphite-epoxy laminates under uniaxial tension", *Proceedings ICCS-6*, Paris, 1991, Elsevier Applied Science, 647-657.
183. Anon., "Selecting the Software", *Advanced Composites Engineering*, 1987, 2(3), 24-25.
184. Taig, I. C., "Finite element analysis of composite materials", NAFEMS-R0003, 1991.
185. Curtis, P.T., "CRAG Test methods for the measurement of the engineering properties of fibre reinforced plastics", RAE Technical Report 88012, 1988.
186. "Standard guide for testing inplane shear properties of composite laminates", ASTM D 4255 - 83.
187. Lockwood, P.A., "Results of the ASTM round-robin on the rail shear test for composites", *Composites Technology Review*, 1981, 3(2), 83-86.
188. Whitney, J.M., Stansbarger, D.L., and Howell, H.B., "Analysis of the rail shear test - applications and limitations", *Journal of Composite Materials*, 1971, 5, 24-34.
189. Window, A.L., "An introduction to strain gauges", Measurements Group UK Ltd., Tenth Edition, 1993.
190. Anon., "Strain gauge installations with M-Bond 200 Adhesive", M-Line Accessories, Measurements Group UK Ltd., Instruction Bulletin B-127-12, 1979.
191. Russell, A.J. and Street, K.N., "Moisture and temperature effects on the mixed-mode delamination fracture of unidirectional graphite/epoxy", In: W.S. Johnson, ed., *Delamination and debonding of materials*, ASTM STP 876, American Society for Testing and Materials, Philadelphia, 1985, 349-370.
192. Gillespie, J.W. Jr., Carlsson, L.A., Pipes, R.B., Rothschilds, R., Trethewey, B., and Smiley, A., "Delamination growth in composite materials - final report", NASA-CR-176416, December 1985.
193. Whitney, J.M., Browning, C.E., and Hoogsteden, W., "A double cantilever beam test for characterising mode I delamination of composite materials", *Journal of Reinforced Plastics and Composites*, 1982, 1, 297-313.
194. Carlsson, L.A., Gillespie, J.W. Jr., Pipes, R.B., "On the analysis and design of the end notched flexure (ENF) specimen for mode II testing", *Journal of Composite Materials*, 1986, 20, 594-604.


195. Anon., "Rosand precision impact tester software manual", Version 1.3.
196. Hong, S. and Liu, D., "On the relationship between impact energy and delamination area", *Experimental Mechanics*, 1989, 29, 115-120
197. Phan, N.D. and Kesack, W.J., "Effects of damage on post-buckled skin-stiffener composite skin panels", American Helicopter Society, 45th Annual Forum, May 1989, Boston, 1083-1090.
198. Anon., *LUSAS user manual*, Version 11, Finite Element Analysis Ltd.
199. Anon., *LUSAS theory manual*, Version 10.0, Finite Element Analysis Ltd, 1990.
200. Reeder, J.R., "An evaluation of mixed-mode delamination failure criteria", Nasa TM 104210, 1992.
201. Liu, S., "Damage mechanics of cross-ply laminates resulting from transverse concentrated loads", ICCM9, Madrid, July 1993, 121-128.
202. Dally, J.W. and Riley, W.F., *Experimental stress analysis*, Third edition, McGraw-Hill, USA, 1991.
203. "Standard methods for flexural properties of unreinforced and reinforced plastic and electrical materials", ASTM Standard D790M - 86.
204. Timoshenko, S.P. and Young, D.H., *Elements of Strength of Materials*, Fifth Edition, D. Van Nostrand Co., Canada, 1968.
205. Timoshenko, S.P. and Goodier, J.N., *Theory of Elasticity*, Third Edition, McGraw-Hill, 1987.
206. Butler, R.J. and Butler A.L., *Lamanal users manual*, Cranfield Press, Bedford, 1986.
207. Tsai, S.W. and Hahn, H.T., *Introduction to composite materials*, Technomic Publishing Company, Lancaster, PA, USA, 1982.
208. Svenson, A.L., Hargrave, M.W., Bank, L.C., and Ye, B.S., "Data analysis techniques for impact tests of composite materials", *Journal of Testing and Evaluation*, 1994, 22(5), 431-441.
209. Malvern, L.E., Sierakowski, R.L., and Ross, C.A., "Impact failure mechanisms in fiber-reinforced composite plates", High velocity deformation of solids conference, Aug. 24-27 1977, Tokyo, 1978, 120-131.
210. Crews J.H. Jr., Shivakumar, K.N., and Raju, I.S., "Strain energy release rate distributions for double cantilever beam specimens", *AIAA Journal*, 1991, 29(10), 1686-1691.

211. Lay, M.R., "Instrumented falling weight and impact testing of pultruded section, using electronic speckle pattern interferometry (ESPI) for different impactors", M.Sc. Thesis, Institute of Polymer Technology and Materials Engineering, Loughborough University, 1996.
212. Standard test method for compressive properties of unidirectional or crossply fibre - resin composites, ASTM Standard D3410-87.
213. Determination of apparent interlaminar shear strength of reinforced plastics, BS:2782: Part 3: Method 341A : 1977.


Appendix I

Detailed Data Sheet of the Advanced Composite Construction System (ACCS)


DATA SHEET




Plank (Ref P)




3-Way Connector (Ref B)




Groove Connector (Ref C)



Toggle Connector (Ref T)



Flat Trimmer (Ref F)



Channel Connector (Ref U)

Geometric Properties

		Overall Dimensions (mm)	Typical Wall Thickness (mm)	Weight (Kg.m)
Plank	Ref P	600 x 80	3.5	11.0
3-Way Connector	Ref B	80 x 80	3.5	2.2
Groove Connector	Ref C	80 x 40	4.0	2.3
Toggle Connector	Ref T	Not Applicable	N/A	0.5
Flat Trimmer	Ref F	80 x 10	4.0	0.9
Channel Connector	Ref U	80 x 88	3.5	1.8

Material Properties

Axial Modulus	20-25000 MPa
Transverse Flexural Modulus	10-13000 MPa
Surface Spread of Flame (BS 476 : Part 7)	Class 0-2
Thermal Resistance, U-Value (when foam filled)	0.3-0.45 W/m ² K

General Information

The components shown are from the ACCS for which worldwide patents are held by Designer Composites Technology Limited. Sections are manufactured by the pultrusion process with full quality assurance procedures to BS 5750 in operation. Components comprise E-Glass embedded in isophthalic polyester resin, typically 60% glass by weight. Sections are pigmented and may be painted where required. Further profiles may be developed to suit specific client requirements.

Designer Composites Technology Limited, Unit 25, Coker Stream Road, Mill Lane, Alton, Hampshire, UK, GU34 2QF
Telephone: 0420 542760 Fax: 0420 541124

Appendix II

Additional Static Mechanical Test Equipment, Specimens, and Procedures

Compression Testing

CRAIG 400¹⁸⁵ (Method of Test for Longitudinal Compressive Strength and Modulus of Unidirectional Fibre Reinforced Plastics) was chosen for the compression testing, which calls for the use of a Celanese jig to provide lateral restraint on the test specimen. The jig was made in accordance with ASTM Standard D3410-87²¹² and is shown in Figure AII.1.

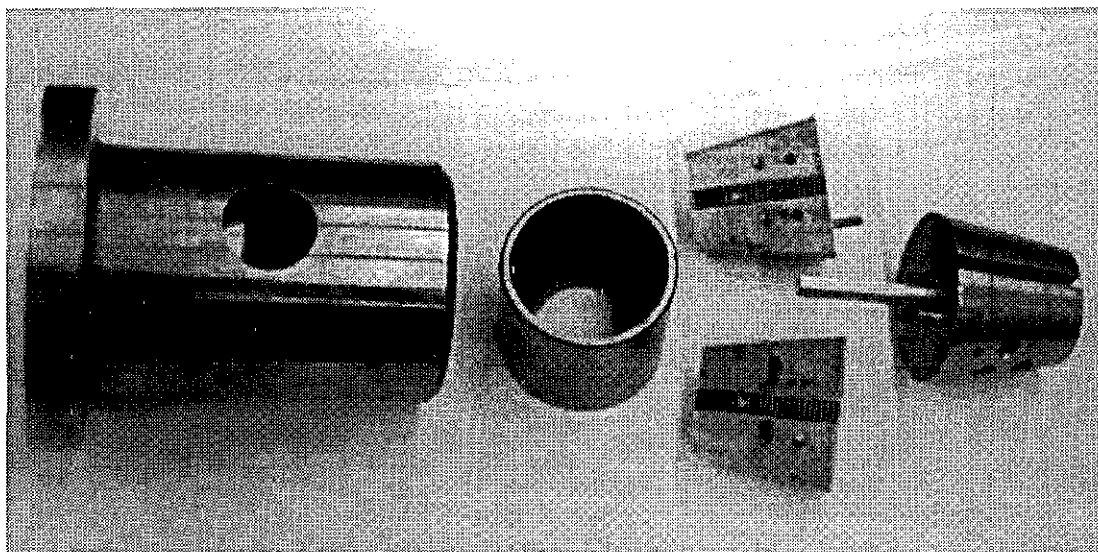


Figure AII.1 Photograph of Celanese Jig Compression Test Fixture.

Two pairs of conical collets were bolted onto the tabbed specimen on either side of the gauge length, via serrated steel grips. Different thickness shims were placed behind the adjustable jaws (the jaws described in the standard are not adjustable) to ensure that on tightening the collet halves closed together to produce a perfect cone. Dowels assisted in locating all four collets together. The assembly was then placed on the lower tapered sleeve within the cylindrical shell. The upper tapered sleeve was slid over the top cone and the lid put in place. The shell/sleeve/cone combination minimised lateral movement, whilst the geometry of the jig ensured that the jaws increased their grip on the specimen as the load applied increased. The gauge length was visible through windows in the shell through which strain gauge connection wires were passed.

Longitudinal specimens were cut with fibres at 0° from the uniform thickness section of the plank to dimensions according to CRAIG 400¹⁸⁵. The tabbed specimen is shown in Figure

AII.2 and strain gauges were bonded in the longitudinal direction on eight of the samples so that the modulus could be determined.

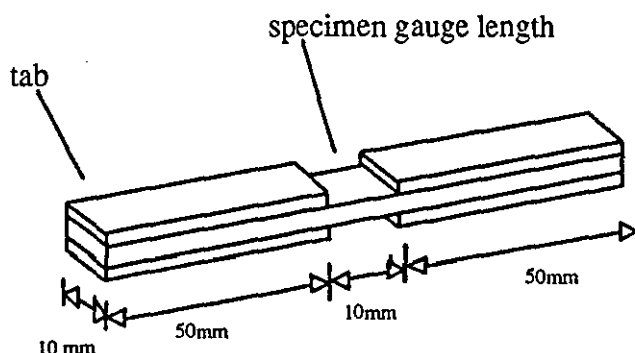


Figure AII.2 Longitudinal/transverse compressive specimen.

Transverse specimens were also prepared to CRAG 400, but with the specimens cut with the unidirectional rovings at 90° to the main specimen dimension, with the 10mm gauge length falling in the centre of uniform thickness region between the webs. The specimens were then finished down (in the area under the tabs) to a uniform thickness ($\pm 0.05\text{mm}$). Individual CFM ply specimens were cut from the outer skin as described for the compressive longitudinal laminate specimens. The thickest possible specimens were chosen so as to avoid buckling failure. The outer CFM layers were peeled away using a razor blade, and any remaining unidirectional fibres adhering to the CFM were then stripped off and the rough inner surface of the CFM smoothed down on a finisher.

The lower jaw of the Dartec machine was removed to provide a flat surface for the Celanese jig and self levelling device, and the compressive force applied by lowering the top jaw directly onto the jig. The same crosshead speed (2 mm/minute) was used however for both longitudinal and transverse specimens within each series of tests so as not to introduce any possible strain-rate effects.

Interlaminar Shear Strength Testing

The British Standard Test Method BS:2782²¹³ was adopted as this method can be used for both unidirectional and mat/cloth woven roving laminates (the term 'apparent' is used because the measured ILSS has been found to have a strong dependence on specimen geometry). This test method employed a span to depth ratio of 5:1 with a 10mm width specimen of length 6t, and produced consistent interlaminar shear failures in the longitudinal specimens. A short, stiff three point bend jig was employed with loading and support rollers of diameter 6mm. The crosshead speed was set at 2mm/minute with the crosshead

displacement representing the central deflection of the specimen. A 2.5KN load cell was employed.

Strain Gauge Procedures

The Wheatstone Bridge Circuit employed (Figure AII.3) added the strain on either side of the specimen, therefore dividing the strain recorded by two gave the average strain. The dummy gauges consisted of strain gauges mounted on the ACCS "plank" material, and placed within the strain gauge box containing the circuit. This ensured that resistance changes due to ambient temperature variations were minimised as each arm in the bridge was effected equally. The length of wires between gauges in the bridge were also the same despite the active gauges being remote, so that I^2R losses in each arm were equalised. The set-up also contained a calibration circuit in which a variable resistor was set to represent 1% strain when the calibration circuit was switched in, thus allowing the output voltage to be calibrated. The zero adjust circuit allowed any resistance unbalance (i.e., due to variation in the nominal strain gauge resistance or strain induced during the installation process) in the bridge to be zeroed.

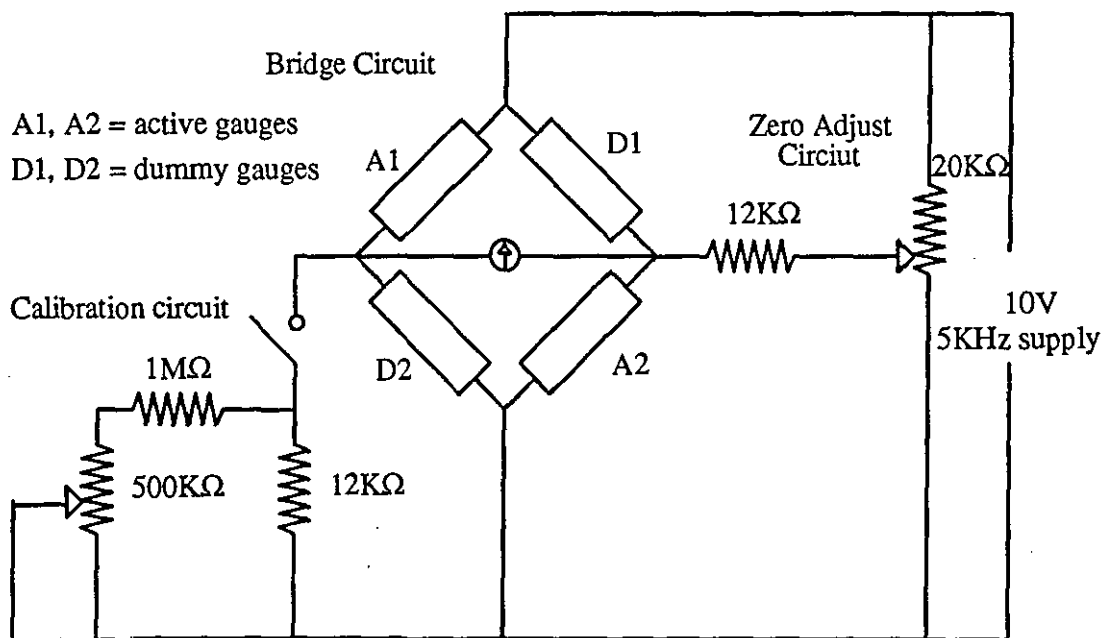


Figure AII.3 The Strain Wheatstone Bridge Circuit

Achieving a good bond between strain gauge and specimen was crucial in obtaining accurate results, and to this end the guidelines provided by M-line Accessories¹⁹⁰, were followed closely and are briefly described below.

1. *Degreasing* of the specimen using CSM-1 Degreaser.

2. **Initial dry abrading** using 240-grit silicon-carbide paper.
3. **Final wet abrading** using 400- and then 600-grit silicon-carbide paper with lubrication by M-Prep Conditioner A, with excess conditioner wiped away with a lint free cotton cloth.
4. **Marking** of the specimen with a 4H pencil so that the gauge was accurately positioned at the desired location.
5. **Swabbing** with M-Prep Conditioner 5 and cotton swabs until a clean swab was not discoloured.
6. **Neutralising** of the specimen by swabbing with M-Prep Neutraliser 5A, followed by a single wipe clean with a lint free cotton cloth.
7. **Initial alignment** of the strain gauge relative to the CPF-38C Bondable Terminal was then achieved by placing them bonding side down on a chemically clean glass plate and overlaying a length of cellophane tape (PCT-2A) on top of the aforementioned, to fix their position.
8. **Positioning** of the strain gauge and terminal on the specimen was then achieved by lifting the tape with attached gauge and terminal off the glass plate and sticking down onto the surface of the specimen. Adjustment was possible as the cellophane tape was designed to leave no mastic behind.
9. **Application of the catalyst** followed by carefully peeling back the tape, with both gauge and terminal still attached, from the specimen leaving one end firmly attached so as not to lose the position. M-Bond 200 Catalyst was then applied sparingly to the bonding side of the gauge and terminal
10. **Adhesion** was achieved by placing a drop of M-Bond 200 Adhesive at the join of the cellophane tape to the specimen, and then holding the tape taut at a shallow angle over where it was to be positioned. A cloth was then used to wipe down the cellophane, thus spreading the adhesion in a thin even layer under the gauge and terminal.
11. **Hardening of the adhesive** occurred due to the application of thumb pressure for a minute over the gauge and terminal, after which the cellophane tape was carefully peeled back, leaving the bonded apparatus.

The strain gauge wires were then soldered to the terminals at the same time as soldering in two short thin lead wires from the gauge to the terminal, as shown in Figure AII.4. The strain gauges on each side of the specimen were then wired into the Wheatstone Bridge Circuit as the active gauges as shown in Figure AII.3.

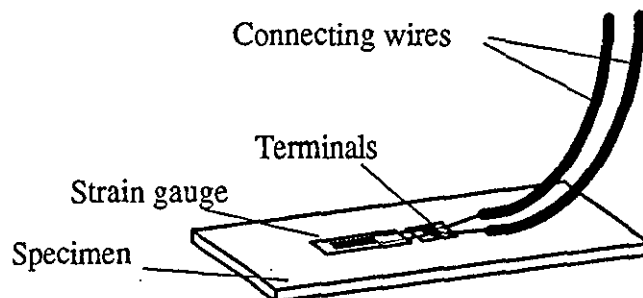


Figure AII.4 Connections to the strain gauge.

Appendix III

Statistics Employed to Analyse the Mechanical and Impact Test Results

Average :

$$\bar{X} = \frac{\sum_{k=1}^N x_k}{N}$$

Standard Deviation:

$$S = \sqrt{\frac{\sum_{k=1}^N (x_k^2 - N(\bar{X})^2)}{N-1}}$$

Coefficient of Variation:

$$C = 100 \left(\frac{S}{\bar{X}} \right)$$

where, N = total number of specimens tested
 x = individual specimen result

Appendix IV

Static Mechanical Individual Specimen Test Results and Analyses To Obtain Further Ply Moduli and Strengths

Specimen	Width (mm)	Thickness (mm)	Initial Modulus (N/mm ²)	Strength (N/mm ²)	Failure Strain (%)	Slope 0.25-1.0 (%)	Slope 1.0-1.6 (%)	Slope Stress/Trsv Strain	Poisson's Ratio
TL6B	30.10	3.15	27224	447.66	1.74	26194	24821	851.15	0.32
TL14B	30.17	3.12	27491	445.15	1.81	25370	24091	864.47	0.32
TL12B	30.12	3.18	24848	430.97	1.87	24123	22662	840.11	0.30
TL15B	30.13	3.49	24025			23230		783.84	0.31
TL10B	30.11	3.14	21958			21322		660.62	0.33
TL26	29.92	3.13	26085	445.69	1.96	24524	22738		
TL25	29.73	3.09	26283	416.02	1.81	23734	22083		
TL17	29.83	3.04	26477	460.41	1.95	24840	23578		
TL23	29.82	3.15	25408	412.64	1.78	23886	22357		
TL22	29.61	3.09	24521	392.69	1.77	22825	21571		
TL21	29.64	3.22	23144	386.69	1.87	21543	19830		
TL20	29.40	3.15	25802	431.85	1.81	24525	23297		
TL19	29.75	3.08	23366	399.19	1.85	22112	21073		
TL18	29.88	3.04	25318	407.09	1.82	23192	21615		
Average	29.87	3.15	25139	423.00	1.84	23673	22476	800.04	0.3145
Std Dev	0.23	0.11	1602.09	24.06	0.06	1412.75	1375.02	83.77	0.01
Co. of Var	0.78	3.52	6.37	5.69	3.53	5.97	6.12	10.47	4.43

Table AIV.1 Longitudinal tensile tests results.

Specimen	Width (mm)	Thickness (mm)	Initial Modulus (N/mm ²)	Strength (N/mm ²)	Failure Strain (%)	Slope Strss/trnsv Strain	Slope 0.4-1.2%	Position of Knee	
								Strain (%)	Stress (N/mm ²)
tt21	30.09	3.35	6530				2857	0.21	14.12
tt22	29.92	3.45	6172	46.23	1.70		2418	0.21	12.82
tt18	30.04	3.35	6677				2528	0.20	13.83
tt13	30.17	3.21	7519				3052	0.19	14.74
tt12	30.10	3.36	6471	39.14	1.34		2341	0.22	14.53
tt11	30.10	3.18	7263	48.53	1.42		2830	0.21	15.62
ttr1	30.18	3.41	6823	48.18	1.55		2608	0.21	14.60
tt10	29.88	3.20	7650				3037	0.18	14.41
tt24	30.12	3.46	6694	42.26	1.31		2677	0.21	14.17
tt17b	30.02	3.36		46.20	1.53	591.78	2517	0.37	19.98
tt23b	29.79	3.47		42.12	1.47		2292	0.33	17.66
tt19b	29.65	3.36				689.61	2523	0.40	19.35
tt16b	30.08	3.21		50.79	1.39	767.56	3042	0.32	20.70
tt20b	29.75	3.20				659.75	2996	0.38	22.13
Average	29.99	3.33	6867	45.43	1.46	677.17	2674	0.36	19.96
Std Dev	0.17	0.11	502.04	3.92	0.13	72.85	328.82	0.03	1.65
Co. of Var	0.56	3.17	7.31	8.63	8.78	10.76	12.30	8.80	8.27

Table AIV.2 Transverse Tensile Tests Results.

Specimen	Width (mm)	Thickness (mm)	Initial Modulus (N/mm ²)	Strength (N/mm ²)	Slope 0.8-1.1 (%)	Failure Strain (%)
cl3b	10.02	3.35		405.41		
cl4	9.95	3.25		450.55		
cl8	10.30	3.22		416.18		
cl11	10.20	3.05		423.05		
cl14	10.27	3.24		482.61		
cl15	10.00	3.51		415.41		
cl1	10.09	3.35	30699	368.65	25439	1.31
cl6	10.00	3.40	33172	402.94	26933	1.40
cl7	10.00	3.40	35404	433.79	31055	1.32
cl9	10.18	3.26		412.15		0.81
cl10	10.07	3.37		383.40		
cl13	10.11	3.10				
cl13b	10.11	3.10	30193	362.34	27019	1.16
cl16	10.16	3.30	29123		31357	
cl16b	10.16	3.30	32772	425.59	31195	
cl17	10.26	3.20	28757	340.19	28907	1.18
cl18	9.72	3.25	37747	453.63	38484	1.19
Average	10.09	3.27	32233	411.72	30049	1.19
Std Dev	0.14	0.12	3160	37.28	4082	0.19
Co. of Var	1.41	3.68	9.80	9.06	13.58	16.04

Table AIV.3 Longitudinal Compression Tests Results.

Specimen	Width (mm)	Thickness (mm)	Initial Modulus (N/mm ²)	Strength (N/mm ²)	Slope 0.6-1 (%)	Slope 1-1.4 (%)
ct2	9.77	3.17		98.38		
ct4	9.84	3.26		109.08		
ct5	9.78	3.27		80.89		
ct6	9.81	3.25		121.54		
ct7	9.86	3.22		95.25		
ct11	9.80	3.08		126.96		
ct14	9.91	3.03		119.69		
ct1	9.80	3.25		105.71		
ct3	9.84	3.12	6818	97.00	4810	4279
ct8	9.79	3.19	7068	103.62	5936	3872
ct9	9.83	3.01	7224	102.00	5079	3950
ct10	9.85	3.02	7055	87.81	5125	4172
ct12	10.01	3.11	7330	100.35		
ct13	9.86	3.11	6151	81.14	5040	4111
Average	9.84	3.15	6941	102.10	5198	4077
Std Dev	0.06	0.09	424	14.01	430	165
Co. of Var	0.63	2.96	6	13.72	8	4

Table AIV.4 Transverse Compression Tests Results.

Specimen	Thickness (mm)	Width (mm)	Load (N)	Strength (N/mm ²)
CFM/1	1.13	10.18	1444	125.53
CFM/3	1.43	10.12	1660	114.71
CFM/5	1.90	9.99	2153	113.43
CFM/6	1.46	10.02	1619	110.67
CFM/12	1.55	10.16	2400	152.40
CFM/14	1.59	10.14	1702	105.57
Average	1.51	10.10		120.38
Std Dev	0.25	0.08		17.01
Co. of Var	16.58	0.77		14.13

Table AIV.5 Individual CFM ply Compression Tests Results.

Specimen	Length (mm)	Thickness (mm)	Modulus (N/mm ²)	Strength (N/mm ²)	Failure Strain (%)	Slope 0.6-0.8 (%)	Slope 1.2-1.4 (%)
s11e	152.24	3.55	3168	37.89	1.23	2656	
s12e	152.36	3.56	2858	42.58	1.62	2839	2731
s13	152.57	3.67	2754	43.63	1.79	2507	1795
s1a	151.60	3.41	2466	40.35	1.55	2396	1491
s2	151.65	3.24	2378	41.76		2332	2015
s3	151.45	3.55		40.86	1.53	2367	1593
s4	151.70	3.15	2846	43.21	1.58	2711	1456
s5b	150.70	3.50	2295				
s5e	150.70	3.50		37.68	1.63	2482	1369
s8	152.20	3.69	2784	41.88		2752	1290
s10	152.12	3.49	2648	39.32		2558	1409
s6	152.12	3.45		38.73			
s7	152.34	3.35		43.71			
s9	152.94	3.58	2823	42.99	1.55		
Average	151.91	3.48	2702	41.12	1.56	2560	1683
Std Dev	0.65	0.15	262	2.16	0.16	174	453
Co. of Var	0.43	4.34	10	5.25	10.06	7	27

Table AIV.6 In-Plane Shear Tests Results.

Specimen	Thickness (mm)	Length (mm)	Load (N)	Strength (N/mm ²)
CFM/20	1.15	153.00	6164	35.03
CFM/21	1.20	153.90	8700	47.11
CFM/22	1.05	153.15	8013	49.83
CFM/23	1.00	153.10	7770	50.75
CFM/24	1.10	152.50	7654	45.63
CFM/25	1.09	152.63	8213	49.37
Average	1.10			46.29
Std Dev	0.07			5.83
Co of Var	6.45			12.59

Table AIV.7 Individual CFM Ply In-Plane Shear Test Results.

Specimen	Span (mm)	Width (mm)	Thickness (mm)	Load (N)	Deflection (mm)	Gradient (N/mm)	Max. Strain (%)	Modulus (N/mm ²)	Strength (N/mm ²)
F/L/B/2	64.80	9.91	3.24	259.8	5.60	51.61	1.68	10,416	242.74
F/L/6	62.80	9.74	3.14	335.7	5.75	65.39	1.73	13,426	329.29
F/L/7	62.40	9.79	3.12	296.4	5.60	59.74	1.68	12,204	291.11
F/L/g/5	68.80	9.92	3.45	410.1	7.55	61.86	2.27	12,363	376.45
F/L/10	64.35	10.15	3.17	355.9	6.00	65.22	1.77	13,437	336.81
F/L/12	64.35	10.24	3.26	365.4	6.45	71.09	1.96	13,350	337.05
F/L/13	70.00	10.12	3.51	317.0	8.00	50.00	2.41	9,797	281.77
F/L/14	74.30	10.11	3.70	379.6	6.15	53.67	1.84	10,747	305.67
F/L/15	64.35	10.15	3.18	323.9	6.45	55.56	1.91	11,339	316.93
F/L/16	68.10	10.13	3.42	296.0	8.85	46.72	2.67	9,107	274.53
F/L/17	64.35	10.11	3.20	344.5	5.95	63.33	1.77	12,795	322.21
F/L/18	70.00	10.14	3.53	438.5	8.15	63.22	2.47	12,154	385.47
F/L/19	70.00	10.17	3.47	300.2	8.40	46.25	2.50	9,333	273.52
F/L/21	68.10	10.20	3.40	321.2	7.15	52.04	2.14	10,249	290.83
F/L/22	68.10	9.95	3.38	294.9	6.70	48.21	2.00	9,908	265.01
F/L/23	66.80	10.25	3.31	371.9	8.05	58.23	2.39	11,726	353.90
F/L/25	62.04	10.15	3.11	283.1	5.50	56.71	1.65	11,147	269.36
F/L/26	63.85	10.11	3.17	249.5	6.45	45.16	1.92	9,130	245.01
F/L/27	63.85	10.09	3.22	413.1	6.35	72.73	1.92	14,122	379.55
F/L/28	62.04	10.09	3.09	288.0	7.55	51.10	2.26	10,247	296.17
Average		10.08	3.30				2.05	11,350	308.67
Std dev		0.14	0.17				0.32	1576.20	43.2888
Co. of Var		1.39	5.16				15.44	13.89	14.02

Table AIV.8 Longitudinal Flexural Tests Results.

Specimen	Span (mm)	Width (mm)	Thickness (mm)	Load (N)	Deflection (mm)	Gradient (N/mm)	Max. Strain (%)	Strength (N/mm ²)	Modulus (N/mm ²)
F/T/1	68.00	9.8	3.42	107.00	3.90	32.43	1.18	95.2	6503
F/T/2	68.00	9.98	3.41	143.10	4.90	35.63	1.47	125.8	7077
F/T/3	68.00	9.95	3.4	126.20	4.90	30.34	1.47	111.9	6099
F/T/5	68.00	9.91	3.39	113.40	4.90	29.38	1.47	101.6	5981
F/T/8	66.80	10.04	3.36	155.70	5.05	34.58	1.52	137.6	6765
F/T/10	61.20	9.94	3.07	122.90	4.50	31.96	1.35	120.4	6367
F/T/11	61.20	10.035	3.085	105.20	3.70	32.92	1.12	101.1	6402
F/T/12	61.20	9.99	3.065	94.03	3.75	30.75	1.13	92.0	6126
F/T/13	66.80	10.11	3.345	101.80	3.75	29.65	1.13	90.2	5839
F/T/15	61.20	9.985	3.08	98.72	3.15	37.50	0.95	95.7	7366
F/T/16	66.80	10.035	3.355	140.40	5.10	26.04	1.54	124.5	5120
F/T/18	61.20	9.995	3.07	125.10	4.20	35.00	1.26	121.9	6935
F/T/19	66.80	9.97	3.34	147.00	5.30	35.06	1.59	132.4	7034
F/T/20	63.38	9.8	3.15	129.70	4.85	32.79	1.45	126.8	6814
F/T/21	63.38	9.795	3.16	124.40	4.20	36.54	1.26	120.9	7524
F/T/22	63.38	10.02	3.155	110.20	3.70	33.41	1.11	105.0	6758
F/T/23	63.38	10.025	3.17	122.40	4.50	33.93	1.35	115.5	6762
F/T/24	63.38	10.025	3.165	134.20	4.25	36.75	1.27	127.0	7360
F/T/25	63.38	10.005	3.18	124.20	4.65	31.05	1.40	116.7	6142
Average		9.97	3.23				1.32	113.8	6578
Std dev		0.09	0.14				0.18	14.5	606
Co. of Var		0.88	4.19				13.64	12.7	9

Table AIV.9 Transverse Flexural Tests Results.

Specimen	Width (mm)	Thickness (mm)	Span (mm)	Load (N)	ILSS (N/mm ²)
IL/33	9.77	3.09	15.50	870.5	21.66
IL/31	9.76	3.09	15.50	905.6	22.52
IL/32	9.90	3.12	15.50	939.2	22.80
IL/20	9.90	3.13	15.50	1104.0	26.76
IL/27	10.00	3.14	15.50	1047.0	25.01
IL/22	10.00	3.15	15.50	1201.0	28.60
IL/26	9.94	3.20	16.00	1097.0	25.91
IL/19	10.00	3.21	16.00	1206.0	28.18
IL/34	9.87	3.41	17.18	1052.0	23.44
IL/37	9.70	3.41	17.18	949.9	21.54
IL/38	9.72	3.43	17.18	1044.0	23.49
IL/16	9.93	3.46	17.34	1112.0	24.32
IL/18	10.02	3.47	17.34	1284.0	27.70
IL/15	9.92	3.48	17.34	1177.0	25.62
IL/23	10.00	3.48	17.56	951.0	20.53
IL/30	9.79	3.48	17.18	1091.0	24.05
IL/17	10.01	3.48	17.34	1260.0	27.13
IL/24	10.00	3.50	17.56	1030.0	22.07
IL/28	10.02	3.51	17.56	952.0	20.30
IL/29	9.98	3.52	17.56	973.1	20.80
Average	9.91	3.34			24.12
Std Dev	0.11	0.17			2.64
Co. of Var	1.08	5.07			10.93

Table AIV.10 Interlaminar Shear Stress Tests Results.

Interface Crack				Central Crack			
Specimen	Length (mm)	Width (mm)	G _{Ic} (J/m ²)	Specimen	Length (mm)	Width (mm)	G _{Ic} (J/m ²)
5	220	38.30	499	1	223	36.50	1630
5	220	38.30	485	1	223	36.50	1682
6	225	38.65	652	3	225	38.28	811
9	204	38.01	598	3	225	38.28	1082
10	218	38.38	649	4	225	38.65	1635
10	218	38.38	557	8	225	38.56	1236
				8	225	38.56	1044
				11	232	38.45	1268
				11	232	38.45	1446
Average			573				1315
Std dev			72				305
Co. of Var			13				23

Table AIV.11 Double Cantilever Beam (Mode I) Test Results.

Specimen	Thickness (mm)	Width (mm)	Expt. Compl. (mm/N)	Critical Load (N)	G _{IIC}		
					Method 1 (J/m ²)	Method 2a (J/m ²)	Method 2b (J/m ²)
GII/1	3.15	18.16	0.0364	284.8	721	318	384
GII/2C	3.21	18.58	0.0357	310.7	839	370	446
GII/2D	3.21	18.58	0.0357	301.6	791	348	421
GII/4	3.44	18.11	0.0362	315.1	885	390	471
GII/8	3.42	18.54	0.0382	292.9	747	329	398
GII/8C	3.42	18.54	0.0382	282.1	693	305	369
GII/10	3.19	18.05	0.0364	312.0	871	384	463
GII/10C	3.19	18.05	0.0364	279.8	700	308	373
GII/11C	3.47	18.11	0.0373	315.7	889	391	473
GII/11D	3.47	18.11	0.0373	306.7	839	369	446
GII/12	3.18	18.4	0.0367	301.4	797	351	424
GII/12C	3.18	18.4	0.0367	280.8	692	305	368
Average	3.29	18.30	0.04		798	351	424
Std Dev	0.13	0.22	0.00		73	32	39
Co. of Var	4.07	1.22	2.30		9	9	9

Table AIV.12 End Notched Flexure (Mode II) Crack Growth Test Results.

Calculation of Initial Compressive Laminae Properties

The initial compressive moduli for each lamina was ascertained using the same method as described in section 6.2, but by substituting the experimentally determined compressive longitudinal and transverse values and thickness co-ordinates for the equivalent tensile values. It was also assumed that the tensile Poisson's ratio was equal to the compressive Poisson's ratio and the same estimates for laminate flexural Poisson's ratios were used. The results of this analysis are also shown within Table AIV.13.

Calculation of Individual Ply Moduli at Higher Strains

The tensile and compressive stress-strain curves were, in general, not linear, therefore further moduli were calculated to fully describe the ply behaviour at higher strains. Using the same method as in section 6.2 and the following assumptions, the higher strain ply moduli were obtained.

- the central layer of unidirectional fibres in tension was linear to failure⁸⁰, and therefore the laminate non-linearity was attributed to the CFM layers
- the CFM and UD Poisson's ratios remain constant.
- the "knee" in the transverse tension test, was due to the onset of transverse matrix cracking in the central layer, therefore it was possible to calculate a new modulus for the UD layer.
- the UD layer was assumed to be linear to failure in longitudinal compression.
- The transverse compression stress-strain curve was highly non-linear. The planar isotropic CFM was assumed to behave in the same way as in the longitudinal compressive tests, therefore it was concluded that the UD layer was behaving non-linearly also (as expected, because the matrix dictates the transverse behaviour of the UD).
- it was not obvious which layer contributed more to the non-linear nature of the in-plane shear modulus, therefore it was decided to reduce the each modulus by the same proportion.

			Modulus (N/mm ²)		
			Initial	Slope 1	Slope 2
CFM	Tension	Long.	(0-0.25%) 7626	(0.25-1%) 5275	(1-1.6%) 3354
		Trans.	(0-0.15%) 7626	(0.25-1%) 5275	(1-1.6%) 3354
	Comp.	Long.	(0-0.7%) 6112	(0.8-1.1%) 2844	
		Trans.	(0-0.25%) 6112	(0.8-1.1%) 2844	
	In-Pl. Shear		(0-0.1%) 2926	(0.6-1%) 2772	(1-1.4%) 1823
UD	Tensile	Long.	(0-0.25%) 49548	(0.6-0.8%) 49548	(1.2-1.4%) 49548
		Trans.	(0-0.15%) 5600	(0.4-1.2%) 1744	
	Comp.	Long.	(0-0.7%) 63607	(0.8-1.1%) 63607	63607
		Trans.	(0-0.5%) 7093	(0.6-1%) 6788	(1-1.4%) 4952
	In-Pl. Shear		(0-0.1%) 2438	(0.6-0.8%) 2310	(1.2-1.4%) 1519

* Figures in parenthesis refer to strain range of applicability for moduli.

Table AIV.13 All calculated ply moduli.

Calculation of Individual Ply Strengths

The modulus of each individual layer was known, therefore it was possible to calculate the stress in each layer of the laminate. As it was also known or assumed which layer failed first, the failure stress for the individual ply under various loading modes was calculated.

Analysis - The Parallel Spring Model

The three layers were assumed to be perfectly bonded to each other and to be a balanced laminate. Therefore the laminate can be assumed to be equivalent to three springs, of stiffness K_i , in parallel sharing the total load (P), with each experiencing the same extension (u) as shown in Figure AIV.1.

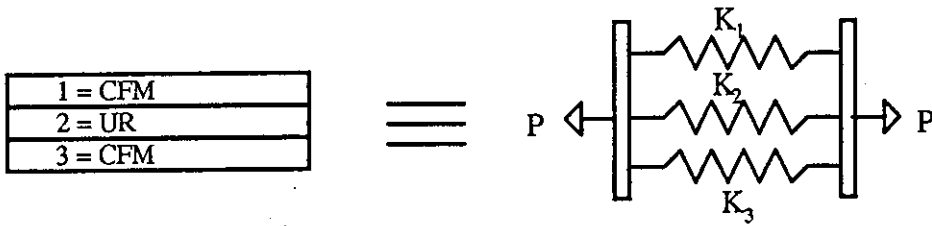


Figure AIV.1 The spring model representation of the laminate.

From Hooke's law, the load in each layer (spring) is given by

$$\begin{aligned} P_1 &= K_1 u \\ P_2 &= K_2 u \\ P_3 &= K_3 u \end{aligned} \quad (\text{AIV.1})$$

where

$$K_i = \frac{A_i E_i}{L_i} \text{ etc.} \quad (\text{AIV.2})$$

with $A_i = wt_i$, L_i = gauge length and E_i = modulus of layer i , and

$$P = P_1 + P_2 + P_3 \quad (\text{AIV.3})$$

Substituting from equation AIV.1, into equation AIV.3 gives

$$P = u \sum_{i=1}^3 K_i \quad (\text{AIV.4})$$

Substituting back into equation AIV.1 gives

$$P_i = P \frac{K_i}{\sum_{i=1}^3 K_i} \quad (\text{AIV.5})$$

as layer 1 is identical to layer 3, equation AIV.5 can be simplified to give:

$$\sigma_{\text{CFM}} = \sigma_1 = \sigma_3 = \sigma_c \frac{E_1 t_1}{2E_1 t_1 + E_2 t_2} \quad (\text{AIV.6})$$

$$\sigma_{\text{UR}} = \sigma_2 = \sigma_c \frac{E_2 t_2}{2E_1 t_1 + E_2 t_2} \quad (\text{AIV.7})$$

[where σ_c = global stress in the laminate calculated from total laminate cross-section.]

Strength Calculations

Therefore, using the moduli calculated, and the relevant percentage thicknesses, various failure strengths for the plies were calculated, using the global failure stresses (σ_f) quoted for each series of tests. The strengths calculated are contained in Table AIV.14. Some points are to be noted:

- the CFM tension failure test was calculated to within 3N/mm² from the transverse and longitudinal tests., thus a high level of confidence can be attributed to the results.
- the tensile longitudinal strength of the UD was calculated from theory⁸⁰. As a first approximation, the simplest rule of mixtures equation for a UD layer was employed. Assuming the fibre failure strain was higher than the matrix failure strain (section 2.2.4.1), and $v_f = 0.55$, $\sigma_f = 2480\text{MPa}$, the failure stress of a UD layer is given by:

$$\sigma_{UR} = v_f \sigma_f = 1364 \text{ N/mm}^2.$$

- neither the longitudinal or transverse compression tests yielded the CFM compressive strength (as the UD failed first), therefore it was ascertained experimentally as being 120.4 N/mm². This explained why the CFM did not fail first, in either of the above tests, as its strength was almost double the stress calculated for the CFM layer at UD failure for either longitudinal or transverse tests.
- the in-plane shear tests were performed on the individual CFM specimens in order to ascertain the CFM in-plane shear strength which was recorded as 46.3 N/mm², which again was a higher stress than was calculated to be in the UD layer at failure in the laminate test.

			Strength (N/mm ²)
CFM	Tension		59.4
	Compression		120.4
	In-plane shear		46.3
UD	Tension	Fibre Breakage	1364
		Transverse Matrix Cracking	16.9
	Compression	Longitudinal	860.6
		Transverse	127.3
	In-plane shear		44.5

Table AIV.14 Experimentally and theoretically determined ply strengths.

Appendix V

**Individual Specimen Impact Test, Damage Assessment Results and
Characteristic Impact Graphs**

Specimen	Specimen Thickness (mm)	Impact Velocity (m/s)	Impact Energy (J)	Peak Force (KN)	Defl. at Peak Force (mm)	Energy at Peak Force (J)	Total Impact Energy (J)
IB182E	3.56	0.96	4.85	2.16	3.881	5.22	5.25
IB159E	3.58	1.04	5.69	2.18			
IB177E	3.55	1.03	5.58	2.26	4.165	6.01	6.01
IB198E	3.59	1.02	5.47	2.19	4.46	6.20	5.93
IB178E	3.57	1.00	5.26	2.08	3.701	4.97	5.64
IB186E	3.57	1.01	5.37	2.23	4.189	5.82	5.8
Average	3.57	1.01	5.37	2.18	4.08	5.64	5.73
Std Dev	0.01	0.03	.30	0.06	0.29	0.53	0.30
Co. of Var.	0.40	2.80	5.54	2.85	7.11	9.33	5.26
IB124E	3.15	1.00	5.26	2.04	4.508	5.71	5.72
IB120E	3.15	1.04	5.69	2.14	4.534	6.08	6.16
IB109E	3.14	1.03	5.58	2.12	4.711	6.00	6.07
IB190E	3.12	1.03	5.58	2.21	4.106	5.82	6.00
IB116E	3.11	1.01	5.37	2.24	4.505	6.04	5.83
IB201E	3.11	1.01	5.37	2.03	4.576	5.90	5.84
Average	3.13	1.02	5.47	2.13	4.49	5.93	5.94
Std Dev	0.02	0.02	0.17	0.09	0.20	0.14	0.16
Co. of Var.	0.61	1.52	3.04	4.03	4.52	2.40	2.78

Table AV.1 Effect of specimen thickness on impact response.

Table AV.2 Effect of filtering - filtered data (2.5KHz)

	Specimen	Specimen Thickness (mm)	Impact Energy (J)	Impact Velocity (m/s)	Peak Force (N)	Defl. at Peak Force (mm)	Energy at Peak Force (J)	Time to Peak Force (ms)	Contact Time (ms)
25.9 Kg	IB72	3.35	3.74	0.54	1.85	3.631	4.61	10.70	24.80
	IB79	3.35	4.31	0.58	2.01	3.953	5.15	10.30	25.10
	IB150	3.33	3.60	0.53	1.83	3.551	4.31	10.40	25.30
	IB155	3.32	3.60	0.53	1.93	3.631	4.52	10.30	24.60
	IB100	3.30	3.74	0.54	1.93	3.557	4.52	9.80	24.30
	IB74E	3.34	3.47	0.52	1.79	3.488	3.94	8.80	26.00
	IB73E	3.33	3.34	0.51	1.76	3.541	3.96	9.60	26.10
	Average	3.33	3.69	0.54	1.87	3.62	4.43	9.99	25.17
	Std Dev	0.02	0.31	0.02	0.09	0.15	0.42	0.64	0.68
	Co. of Var.	0.53	8.47	4.15	4.74	4.27	9.41	6.42	2.71
10.8 Kg	IB131	3.35	3.30	0.79	1.71	3.254	3.56	6.20	14.30
	IB127	3.36	3.30	0.79	1.68				
	IB136	3.35	3.14	0.77	1.85	2.627	2.85	4.30	13.50
	IB128	3.32	3.22	0.78	1.65			4.90	13.20
	IB126	3.35	3.35	0.81	1.73	3.366	3.75	6.30	14.10
	IB141	3.35	3.39	0.80	1.62	2.330	2.18	3.30	14.50
	IB118	3.29	3.30	0.79	1.68	3.342	3.54	6.20	14.60
	Average	3.34	3.29	0.79	1.70	2.98	3.18	5.20	14.03
	Std Dev	0.02	0.08	0.01	0.07	0.47	0.65	1.24	0.56
	Co. of Var.	0.74	2.53	1.63	4.36	15.92	20.57	23.90	4.02
1.63 Kg	IB99	3.31	3.14	1.96	1.41	1.934	1.48	1.20	5.10
	IB122	3.35	3.11	1.95	1.41	2.692	2.38	1.70	5.00
	IB71	3.36	3.14	1.96	1.66	2.900	2.90	2.00	4.60
	IB91	3.33	3.23	1.99	1.35	3.132	2.86	2.10	5.20
	IB83	3.35	3.07	1.94	1.51	3.017	2.73	2.10	5.00
	IB133E	3.29	3.11	1.95	1.36	2.980	2.54	1.90	5.30
	IB87	3.35	3.07	1.94	1.54	2.806	2.66	1.90	4.70
	Average	3.33	3.12	1.96	1.46	2.78	2.51	1.84	4.99
	Std Dev	0.03	0.06	0.02	0.11	0.40	0.49	0.32	0.25
	Co. of Var.	0.77	1.77	0.88	7.69	14.38	19.43	17.12	5.10
25.9 Kg	IB145	3.28	8.62	0.82	2.86	5.680	9.23	9.50	24.90
	IB147	3.23	8.21	0.80	2.64				
	IB106	3.21	8.62	0.82	2.83	5.876	9.55	10.10	24.40
	IB97	3.21	8.84	0.83	2.90	5.417	8.95	8.80	24.00
	IB143	3.22	8.01	0.79	2.85	5.434	8.59	9.30	24.50
	IB140	3.22	8.62	0.82	2.61	5.736	9.47	10.30	24.90
	IB138E	3.25	8.62	0.82	2.74	6.115	9.63	10.60	25.50
	Average	3.23	8.51	0.81	2.78	5.71	9.24	9.77	24.70
	Std Dev	0.03	0.29	0.01	0.11	0.27	0.40	0.68	0.52
	Co. of Var.	0.79	3.41	1.72	4.11	4.67	4.35	6.96	2.10

Table AV.2 Effect of filtering - filtered data (2.5KHz)

	Specimen	Specimen Thickness (mm)	Impact Energy (J)	Impact Velocity (m/s)	Peak Force (N)	Defl. at Peak Force (mm)	Energy at Peak Force (J)	Time to Peak Force (ms)	Contact Time (ms)
10.8 Kg	IB11	3.20	7.73	1.21	2.70	5.045	7.71	6.10	13.90
	IB13E	3.21	7.86	1.22	2.63	5.184	7.68	6.10	14.70
	IB65E	3.24	7.60	1.20	2.98	5.000	7.53	6.10	14.20
	IB14E	3.23	7.88	1.22	2.36	4.927	6.66	5.10	15.60
	IB32E	3.27	7.62	1.20	2.41	5.053	7.53	6.20	15.00
	IB45	3.27	7.49	1.19	2.45	4.914	7.32	6.00	14.30
	Average	3.24	7.70	1.21	2.59	5.02	7.41	5.93	14.62
	Std Dev	0.03	0.15	0.01	0.23	0.10	0.39	0.41	0.62
Co. of Var.	0.91	1.99	1.00	8.99	1.97	5.27	6.96	4.23	
1.63 Kg	IB152	3.24	7.90	3.11	2.30	5.305	7.24	2.30	5.30
	IB153	3.21	8.42	3.21	2.28	5.736	7.75	2.40	6.40
	IB148	3.21	7.95	3.12	2.24	5.406	7.58	2.50	5.30
	IB135	3.22	7.90	3.11	2.35	5.209	7.39	2.30	5.20
	IB130	3.22	7.80	3.09	2.25	5.022	6.96	2.20	5.30
	IB93E	3.28	8.00	3.13	2.12	5.523	7.21	2.40	5.50
	IB94	3.26	7.80	3.09	2.26	5.223	7.22	2.30	5.30
	Average	3.23	7.97	3.12	2.26	5.35	7.34	2.34	5.47
Std Dev	0.03	0.21	0.04	0.07	0.23	0.26	0.10	0.42	
Co. of Var.	0.83	2.66	1.32	3.14	4.37	3.58	4.17	7.66	
10.8 Kg	IB68	3.39	0.89	0.41	1.20				
	IB76	3.40	0.98	0.43	1.41	1.417	1.11	4.70	11.70
	IB80	3.37	0.89	0.41	1.37	1.362	1.02	5.00	11.40
	IB101	3.43	1.02	0.44	1.40	1.441	1.16	5.10	11.50
	Average	3.40	0.95	0.42	1.35	1.41	1.10	4.93	11.53
	Std Dev	0.03	0.07	0.01	0.10	0.04	0.07	0.21	0.15
	Co. of Var.	0.74	7.12	3.55	7.30	2.88	6.47	4.22	1.32
	3.13 Kg	IB69	3.42	0.81	0.72	1.07	1.409	0.83	2.80
IB102		3.39	0.86	0.74	1.19	1.321	0.86	2.50	5.70
IB114		3.37	0.95	0.78	1.19	1.460	0.96	2.60	5.90
IB88		3.38	0.98	0.79	1.19	1.552	0.99	2.70	5.90
Average		3.39	0.90	0.76	1.16	1.44	0.91	2.65	5.93
Std Dev		0.02	0.08	0.03	0.06	0.10	0.08	0.13	0.21
Co. of Var.		0.64	8.69	4.36	5.17	6.73	8.46	4.87	3.48
1.63 Kg		IB146	3.37	0.83	1.01	0.99	1.475	0.82	2.00
	IB67	3.39	0.83	1.01	1.01	1.419	0.79	1.90	4.20
	IB151	3.38	0.85	1.02	0.95	1.487	0.82	2.00	4.30
	IB134	3.39	0.83	1.01	1.02	1.382	0.79	1.80	4.10
	IB129	3.38	0.85	1.02	1.08	1.342	0.78	1.70	4.00
	IB156	3.41	0.83	1.01	1.11	1.308	0.79	1.70	3.90
	Average	3.39	0.84	1.01	1.03	1.40	0.80	1.85	4.13
	Std Dev	0.01	0.01	0.01	0.06	0.07	0.02	0.14	0.16
Co. of Var.	0.40	1.02	0.51	5.75	5.11	2.16	7.45	3.95	

Table AV.2 Effect of filtering - filtered data (2.5KHz)

	Specimen	Specimen Thickness (mm)	Impact Energy (J)	Impact Velocity (m/s)	Peak Force (N)	Defl. at Peak Force (mm)	Energy at Peak Force (J)	Time to Peak Force (ms)	Contact Time (ms)
3.13 Kg	IB200	3.35	0.44	0.53	0.88	0.954	0.42	2.30	5.70
	IB199E	3.31	0.42	0.52	0.79	1.113	0.44	3.00	6.50
	IB189	3.34	0.41	0.51	0.89	0.998	0.44	3.00	5.90
	IB185	3.32	0.42	0.52	0.88				
	IB172	3.30	0.47	0.55	0.94	1.172	0.54	2.90	6.00
	IB193	3.38	0.46	0.54	0.97				
	Average	3.33	0.44	0.53	0.89	1.06	0.46	2.80	6.03
	Std Dev	0.03	0.02	0.01	0.06	0.10	0.05	0.34	0.34
	Co. of Var.	0.88	5.59	2.79	7.12	9.51	11.77	12.02	5.65
2.63 Kg	IB211	3.33	0.40	0.55	0.92	0.817	0.40	2.30	5.00
	IB205	3.35	0.41	0.56	0.93	0.947	0.73	2.40	5.20
	IB206	3.30	0.44	0.58	0.91	0.955	0.45	2.30	5.20
	IB171	3.34	0.40	0.55	0.88	0.902	0.39	2.20	5.40
	IB184	3.35	0.36	0.52	0.82	0.855	0.38	2.50	5.40
	IB194E	3.34	0.40	0.55	0.82	0.977	0.41	2.60	5.60
	Average	3.34	0.40	0.55	0.88	0.91	0.46	2.38	5.30
	Std Dev	0.02	0.03	0.02	0.05	0.06	0.13	0.15	0.21
	Co. of Var.	0.56	7.00	3.52	5.53	6.89	29.23	6.18	3.96
1.63 Kg	IB196	3.35	0.47	0.76	0.82	1.023	0.44	1.80	4.00
	IB188	3.34	0.37	0.67	0.76	0.912	0.36	1.90	4.00
	IB177	3.31	0.42	0.72	0.80	1.049	0.43	2.00	4.20
	IB158	3.34	0.44	0.73	0.80	1.010	0.41	1.80	4.00
	IB161	3.31	0.45	0.74	0.80	1.058	0.43	1.90	4.10
	IB192	3.35	0.41	0.71	0.80	1.004	0.41	1.90	4.10
	Average	3.33	0.43	0.72	0.80	1.01	0.41	1.88	4.07
	Std Dev	0.02	0.04	0.03	0.02	0.05	0.03	0.08	0.08
	Co. of Var.	0.56	8.38	4.24	2.52	5.17	6.96	4.00	2.01

Table AV.3 Effect of Delay Function on Impact Response.
Characteristic Data

Delay Setting (%)	Impact Energy (J)	Defl. at Pk. Force (mm)	Defl. at Pk. Force (mm)	Energy at Pk. Force (J)	Peak Defl. (mm)	Energy at Failure (J)
-85	13.39	5.91	5.91	27.68	7.41	35.83
-50	13.39	4.83	4.83	22.37	5.19	26.76
0	13.39	3.46	3.46	15.30	1.87	12.61
25	13.39	2.87	2.87	11.48	0.61	6.35

Table AV.4 Strain-Rate Impact Test Results.

Nominal 0.4J Impact	Specimen	Specimen Thickness (mm)	Impact Energy (J)	Impact Velocity (m/s)	Peak Force (N)	Defl. of Peak Force (mm)	Energy at Peak Force (J)	Damage Energy (J)	Peak Defl. (mm)	Energy at Peak Defl. (J)	Total Impact Energy (J)	Time to Peak Force (ms)	Time to Peak Defl. (ms)	Contact Time (ms)
3.13 Kg	B200	3.35	0.44	0.63	0.906	0.917	0.42	0.20	0.982	0.47	0.47	2.2	2.9	5.7
	B199E	3.31	0.42	0.62	0.790	1.065	0.44	0.17	1.082	0.45	0.46	2.9	3.3	6.4
	B189	3.34	0.41	0.61	0.894	0.960	0.44	0.12	0.960	0.44	0.44	2.9	2.9	5.9
	B185	3.32	0.42	0.62	0.877									
	B172	3.30	0.47	0.65	0.948	1.046	0.51	0.20	1.089	0.55	0.51	2.4	3.0	6.9
	B193	3.38	0.46	0.54	0.970									
	Average	3.33	0.44	0.63	0.90	0.997	0.45	0.17	1.03	0.48	0.47	2.600	3.025	5.98
2.63 Kg	B206	3.35	0.41	0.56	0.925	0.882	0.41	0.10	0.901	0.43	0.44	2.2	2.5	5.1
	B208	3.30	0.44	0.58	0.913	0.931	0.46	0.15	0.936	0.46	0.47	2.4	2.6	5.1
	B171	3.34	0.40	0.55	0.899	0.871	0.39	0.11	0.909	0.42	0.42	2.1	2.6	5.2
	B184	3.35	0.36	0.52	0.824	0.855	0.38	0.09	0.862	0.38	0.38	2.4	2.5	5.3
	B194E	3.34	0.40	0.56	0.824	0.950	0.40	0.10	0.942	0.42	0.42	2.5	2.8	5.5
	Average	3.34	0.40	0.55	0.89	0.898	0.41	0.11	0.91	0.42	0.42	2.320	2.620	5.24
	Std Dev	0.02	0.03	0.02	0.05	0.041	0.03	0.02	0.03	0.03	0.03	0.164	0.110	0.17
1.63 Kg	B196	3.35	0.47	0.78	0.831	0.952	0.43	0.33	1.015	0.49	0.49	1.7	2.2	3.8
	B188	3.34	0.37	0.67	0.781	0.822	0.34	0.21	0.870	0.38	0.38	1.6	2.1	3.9
	B177	3.31	0.42	0.72	0.810	0.947	0.41	0.25	0.988	0.44	0.44	1.8	2.2	4.1
	B158	3.34	0.44	0.73	0.805	0.993	0.44	0.31	1.014	0.45	0.45	1.9	2.2	3.9
	B161	3.31	0.45	0.74	0.798	1.007	0.43	0.32	1.046	0.46	0.46	1.9	2.3	4.0
	B192	3.35	0.41	0.71	0.802	0.940	0.40	0.25	0.979	0.43	0.43	1.8	2.2	4.0
	Average	3.33	0.43	0.72	0.80	0.944	0.41	0.28	0.99	0.44	0.44	1.783	2.200	3.95
10.82 Kg	B68	3.39	0.92	0.41	1.20									
	B76	3.40	1.00	0.43	1.41	1.417	1.14	0.30	1.431	1.16	1.15	4.8	5.3	11.6
	B80	3.37	0.91	0.41	1.38	1.354	1.04	0.08	1.361	1.05	1.05	4.9	5.3	11.3
	B101	3.43	1.05	0.44	1.40	1.409	1.17	0.21	1.422	1.19	1.20	4.6	5.3	11.3
	Average	3.40	0.97	0.42	1.35	1.393	1.12	0.20	1.40	1.13	1.13	4.633	5.300	11.40
	Std Dev	0.03	0.07	0.01	0.10	0.034	0.07	0.11	0.04	0.07	0.07	0.056	0.000	0.17
	Co. of Var.	0.74	6.74	3.36	7.36	2.462	6.10	56.24	2.71	6.50	6.50	1.195	0.000	1.52
3.13 Kg	B69	3.42	0.81	0.72	1.08	1.351	0.82	0.36	1.377	0.85	0.85	2.7	3.1	6.1
	B102	3.39	0.86	0.74	1.20	1.272	0.66	0.38	1.293	0.68	0.90	2.8	2.8	5.6
	B114	3.37	0.95	0.78	1.21	1.445	0.97	0.45	1.468	1.00	1.00	2.7	3.0	5.9
	B88	3.38	0.98	0.79	1.19	1.486	0.98	0.56	1.533	1.03	1.02	2.6	3.1	5.8
	Average	3.39	0.90	0.75	1.17	1.389	0.91	0.44	1.42	0.94	0.94	2.625	3.000	5.85
	Std Dev	0.02	0.08	0.03	0.06	0.096	0.08	0.09	0.10	0.09	0.08	0.096	0.141	0.21
	Co. of Var.	0.64	8.69	4.36	5.18	6.918	8.79	20.65	7.40	9.40	8.57	3.647	4.714	3.56
1.63 Kg	B146	3.37	0.83	1.01	1.000	1.406	0.83	0.60	1.447	0.87	0.86	2.0	2.4	4.2
	B67	3.39	0.83	1.01	1.020	1.298	0.72	0.59	1.447	0.86	0.86	1.8	2.3	4.2
	B151	3.38	0.85	1.02	0.981	1.317	0.77	0.63	1.428	0.87	0.87	1.7	2.4	4.3
	B134	3.39	0.83	1.01	1.030	1.294	0.77	0.61	1.382	0.86	0.86	1.7	2.3	4.0
	B129	3.38	0.85	1.02	1.080	1.312	0.81	0.59	1.378	0.88	0.87	1.7	2.2	3.9
	B156	3.41	0.83	1.01	1.110	1.234	0.76	0.58	1.323	0.86	0.85	1.6	2.1	3.8
	Average	3.39	0.84	1.01	1.04	1.310	0.78	0.60	1.40	0.87	0.86	1.717	2.283	4.07
25.9 Kg	B127	3.35	3.78	0.54	1.88	3.491	4.41	2.60	3.627	4.66	4.70	9.2	11.3	24.7
	B179	3.38	4.36	0.58	2.02	3.958	5.19	3.01	4.011	5.30	5.38	10.3	11.6	25.1
	B150	3.33	3.64	0.53	1.85	3.538	4.35	2.55	3.643	4.54	4.56	9.7	11.6	25.2
	B155	3.32	3.64	0.53	1.93	3.625	4.57	2.48	3.666	4.63	4.57	10.4	11.4	25.2
	B100	3.30	3.78	0.54	1.94	3.545	4.56	2.64	3.635	4.73	4.70	9.5		24.2
	B174E	3.34	3.50	0.52	1.81	3.490	4.03	2.42	3.730	4.46	4.45	8.9	11.8	25.9
	B135E	3.33	3.57	0.51	1.81	3.584	4.06	2.34	3.702	4.27	4.31	10.0	12.0	26.1
10.82 Kg	Average	3.33	3.72	0.54	1.89	3.604	4.45	2.58	3.71	4.66	4.67	9.71	11.62	25.20
	Std Dev	0.02	0.32	0.02	0.08	0.162	0.39	0.22	0.14	0.32	0.34	0.56	0.25	0.65
	Co. of Var.	0.53	8.47	4.16	4.07	4.506	8.77	6.43	3.66	6.91	7.32	6.74	2.21	2.59
	B131	3.35	3.38	0.79	1.72	3.239	3.62	2.21	3.297	3.72	3.73	6.1	7.0	14.2
	B127	3.36	3.38	0.79	1.68									
	B136	3.35	3.21	0.77	1.87	2.711	3.08	2.00	2.971	3.54	3.52	4.6	6.5	13.5
	B128	3.32	3.29	0.78	1.66									
1.63 Kg	B126	3.35	3.35	0.81	1.74	3.373	3.83	2.49	3.414	3.90	3.71	6.4	7.1	14.1
	B141	3.35	3.46	0.80	1.65	2.296	2.21	2.60	3.365	3.83	3.82	3.3	7.3	14.4
	B118	3.29	3.58	0.79	1.73	3.209	3.41	2.19	3.413	3.72	3.74	5.6	7.2	14.5
	Average	3.34	3.35	0.79	1.72	2.966	3.23	2.30	3.29	3.74	3.70	6.200	7.020	13.98
	Std Dev	0.02	0.08	0.01	0.07	0.451	0.63	0.24	0.19	0.14	0.11	1.263	0.311	0.52
	Co. of Var.	0.74	2.39	1.63	4.31	15.203	19.63	10.54	5.64	3.65	2.95	24.287	4.437	3.71
	B137	3.35	3.07	1.04	1.65	2.526	2.49	2.53	2.935	3.12	3.12	1.7	2.6	4.6
1.63 Kg	B122	3.35	3.11	1.95	1.55	2.422	2.19	2.62	3.117	3.15	3.16	1.6	2.8	4.9
	B171	3.36	3.14	1.96	1.74	2.662	2.74	2.61	2.938	3.18	3.19	1.8	2.6	4.5
	B191	3.33	3.23	1.99	1.42	2.843	2.66	2.80	3.300	3.27	3.29	1.9	3.0	5.1
	B183	3.35	3.07	1.94	1.56	2.792	2.58	2.54	3.149	3.13	3.12	1.9	2.8	4.9
	B133E	3.29	3.11	1.95	1.44	2.990	2.74	2.59	3.294	3.14	3.16	2.1	3.0	5.2
	B167	3.35	3.07	1.04	1.65	2.526	2.49	2.53	2.935	3.12	3.12	1.7	2.6	4.6
	Average	3.33	3.12	1.95	1.56	2.688	2.56	2.63	3.12	3.17	3.17	1.800	2.800	4.87
10.82 Kg	Std Dev	0.03	0.06	0.02	0.11	0.196	0.19	0.10	0.15	0.06	0.06	0.191	0.163	0.26
	Co. of Var.	0.77	1.77	0.88	7.18	7.299	7.50	3.71	4.74	1.62	1.77	10.638	5.832	5.13

Table AV.4 Strain-Rate Impact Test Results.

Nominal ΔJ Impact	Specimen	Specimen Thickness (mm)	Impact Energy (J)	Impact Velocity (m/s)	Peak Force (N)	Defl. at Peak Force (mm)	Energy at Peak Force (J)	Damage Energy (J)	Peak Defl. (mm)	Energy at Peak Defl. (J)	Total Impact Energy (J)	Time to Peak Force (ms)	Time to Peak Defl. (ms)	Contact Time (ms)
1.63Kg	B317E	3.30	6.13	2.74	2.07	4.120	5.30	5.62	4.592	6.20	6.21	2.0		5.0
	B366E	3.35	6.18	2.75	1.94	4.819	5.23	5.74	5.073	6.23	6.26	2.2		6.4
	B358E	3.36	6.13	2.74	2.06	4.240	4.92	5.60	4.932	6.20	6.21	2.0		5.2
	B330	3.48	6.13	2.74	2.00	4.436	5.76	5.67	4.677	6.20	6.21	2.3		5.0
	B318	3.43	6.22	2.76	2.10	4.639	5.95	5.65	4.823	6.31	6.30	2.4		5.1
	B341	3.43	6.31	2.78	2.00	4.248	5.55	5.77	4.674	6.36	6.39	2.1		6.0
	B389	3.43	6.22	2.76	1.90	3.825	4.43	5.74	4.854	6.27	6.30	1.7		6.2
	B378	3.44	6.36	2.79	2.04	4.683	5.54	5.89	5.172	6.44	6.44	2.2		5.3
	Average	3.40	6.21	2.76	2.01	4.339	5.34	5.71	4.85	6.28	6.29	2.11		5.15
	Std Dev	0.06	0.09	0.02	0.07	0.288	0.49	0.10	0.20	0.09	0.09	0.22		0.15
	Co. of Var.	1.75	1.39	0.69	3.37	6.637	9.10	1.66	4.19	1.29	1.39	10.26		2.94
10.82Kg	B208E	3.36	6.85	1.04	2.28	4.532	6.24	4.19	4.588	6.37	6.34	6.5		14.5
	B173	3.28	6.43	1.09	2.43	4.612	6.66	4.61	4.709	6.88	6.93	6.2		14.5
	B163	3.24	6.31	1.08	2.37	4.707	6.80	4.66	4.711	6.80	6.81	7.1		14.4
	B221E	3.48	6.43	1.09	2.28	4.792	6.90	4.66	4.796	6.91	6.94	7.2		16.0
	B244E	3.50	6.85	1.04	2.18	4.649	6.33	4.14	4.654	6.34	6.35	7.3		16.2
	B291	3.46	6.31	1.08	2.42	4.198	6.36	4.59	4.360	6.74	6.77	5.6		13.7
	Average	3.39	6.20	1.07	2.33	4.582	6.65	4.44	4.64	6.67	6.69	6.66		14.56
	Std Dev	0.11	0.27	0.02	0.10	0.207	0.27	0.22	0.15	0.25	0.26	0.67		0.52
	Co. of Var.	3.25	4.39	2.21	4.17	4.627	4.20	4.96	3.28	3.80	4.13	10.10		3.60
25.9Kg	B637E	3.39	6.71	0.72	2.46	4.958	7.19	5.77	5.278	7.97	8.06	9.2		25.0
	B387E	3.37	6.53	0.71	2.46	4.811	6.76	5.59	5.302	7.95	7.87	8.6		25.0
	B364	3.41	6.53	0.71	2.52									
	B374E	3.43	5.81	0.67	2.46									
	B382	3.41	5.99	0.68	2.36	4.271	5.94	4.61	4.645	6.81	7.17	8.0		25.2
	B376	3.41	6.16	0.69	2.64	4.802	7.25	4.16	4.816	7.41	7.39	10.2		24.4
	B381E	3.41	6.34	0.70	2.46	4.731	6.55	4.79	5.191	7.68	7.66	8.6		25.6
	Average	3.40	6.30	0.70	2.48	4.715	6.74	4.96	5.05	7.56	7.63	8.92		26.04
	Std Dev	0.02	0.32	0.02	0.08	0.261	0.53	0.69	0.30	0.48	0.36	0.83		0.43
	Co. of Var.	0.56	5.14	2.58	3.42	5.544	7.92	13.97	5.90	6.34	4.69	9.33		1.73
25.9Kg	B146	3.28	8.71	0.82	2.87	5.672	9.30	7.39	6.002	10.23	10.23	9.3	11.9	24.7
	B147	3.23	8.29	0.80	2.64									
	B106	3.21	8.71	0.82	2.84	6.025	10.06	7.42	6.124	10.34	10.26	10.6	12.1	24.4
	B97	3.21	8.92	0.83	2.92	5.547	9.50	7.33	5.628	10.31	10.40	9.2	11.6	23.8
	B143	3.22	8.08	0.79	2.85	5.479	8.82	5.76	6.610	9.20	9.76	9.3	11.7	24.5
	B140	3.22	8.71	0.82	2.62	5.817	9.79	7.47	5.967	10.17	10.22	10.3	12.2	24.8
	B138E	3.25	8.71	0.82	2.75	6.233	10.05	7.33	6.349	10.37	10.32	10.9	12.4	25.4
	Average	3.23	8.59	0.81	2.78	5.796	9.59	7.12	6.15	10.10	10.20	9.933	11.983	24.60
	Std Dev	0.03	0.29	0.01	0.12	0.290	0.48	0.67	0.29	0.45	0.23	0.756	0.306	0.53
	Co. of Var.	0.79	3.41	1.72	4.20	6.011	5.02	9.36	4.66	4.44	2.21	7.605	2.554	2.14
10.82 Kg	B111	3.20	7.90	1.21	2.72	5.149	8.21	6.32	5.268	8.53	8.46	6.1	7.1	14.0
	B13E	3.21	8.04	1.22	2.65	5.275	8.07	6.44	5.475	8.64	8.62	6.0	7.4	14.7
	B65E	3.24	7.77	1.20	2.43	5.095	7.96	5.02	5.206	8.29	8.32	6.0	7.0	14.1
	B14E	3.23	8.05	1.22	2.39	5.099	7.17	6.82	5.786	8.71	8.67	5.3	8.0	15.7
	B32E	3.27	7.79	1.20	2.44	5.190	7.96	6.33	5.355	8.40	8.36	6.2		14.9
	B45	3.27	7.66	1.19	2.46	4.936	7.52	6.15	5.223	8.25	8.22	5.7	7.4	14.2
	Average	3.24	7.87	1.21	2.52	5.124	7.82	6.18	5.39	8.47	8.44	5.883	7.380	14.60
	Std Dev	0.03	0.16	0.01	0.14	0.114	0.39	0.61	0.22	0.19	0.18	0.331	0.390	0.64
	Co. of Var.	0.91	1.99	1.00	5.39	2.218	5.01	9.68	4.08	2.21	2.09	5.629	5.283	4.42
1.63 Kg	B152	3.24	7.90	3.11	2.37	4.995	7.03	6.79	5.416	7.98	7.99	2.200	3.000	5.20
	B153	3.21	6.42	3.21	2.40	5.440	7.59	6.73	5.849	8.51	8.51	2.300	3.100	6.40
	B148	3.21	7.95	3.12	2.36	4.695	6.49	6.92	5.387	8.01	8.04	1.900	3.000	5.20
	B136	3.22	7.90	3.11	2.45	4.891	7.15	6.82	5.240	7.95	7.98	2.200	2.900	6.10
	B130	3.22	7.80	3.09	2.36	4.630	6.57	6.78	5.226	7.89	7.88	2.000	2.900	5.20
	B93E	3.28	8.00	3.13	2.21	4.923	6.41	7.13	5.719	8.08	8.09	2.000	3.100	5.50
	B94	3.26	7.80	3.09	2.33	5.164	7.57	6.72	5.303	7.87	7.88	2.500	3.000	5.20
	Average	3.23	7.97	3.12	2.35	4.963	6.97	6.84	5.45	8.04	8.05	2.157	3.000	5.40
	Std Dev	0.03	0.21	0.04	0.07	0.276	0.50	0.14	0.24	0.22	0.22	0.207	0.082	0.46
	Co. of Var.	0.63	2.66	1.32	3.15	5.570	7.13	2.10	4.45	2.72	2.67	9.597	2.722	8.49
Penetration Impact	Specimen	Specimen Thickness (mm)	Impact Energy (J)	Impact Velocity (m/s)	Peak Force (N)	Defl. at Peak Force (mm)	Energy at Peak Force (J)	Damage Energy (J)	Peak Defl. (mm)	Energy at Peak Defl. (J)	Total Impact Energy (J)	Time to Peak Force (ms)	Time to Peak Defl. (ms)	Contact Time (ms)
	B231	3.47	18.96	1.21	3.42	6.633	13.71				15.45	6.6		
	B277	3.42	19.91	1.24	3.90	6.994	14.15				16.93	6.6		
	B218	3.43	19.27	1.22	4.06	7.340	16.63				18.49	7.4		
	B226	3.46	20.56	1.26	4.03	7.632	17.40				19.39	7.6		
	B213	3.44	20.23	1.25	3.45	6.713	13.49				16.20	6.2		
	B241	3.44	20.23	1.25	3.80	7.307	15.37				17.23	6.8		
	Average	3.44	19.86	1.24	3.78	7.170	15.13				16.95	6.650		
	Std Dev	0.02	0.62	0.02	0.28	0.410	1.62				1.72	0.543		
	Co. of Var.	0.50	3.12	1.57	7.43	5.714	10.71				10.15	7.929		
10.82 Kg	B232E	3.47	21.00	1.97	3.33	6.111	11.00				11.66	3.5		
	B176	3.42	20.78	1.96	3.23	6.613	12.77				13.47	3.9		
	B272	3.43	20.36	1.94	3.78	7.346	15.71				16.49	4.6		
	B263	3.45	20.16	1.93	4.26	7.237	16.39				17.16	4.7		
	B149	3.44	20.15	1.93	3.55	7.402	16.74				16.53	4.7		
	B170	3.44	20.36	1.94	3.15	7.935	16.06				16.90	5.1		
	Average	3.44	20.47	1.95	3.55	7.107	14.61				15.37	4.417		
	Std Dev	0.02	0.35	0.02	0.42	0.645	2.20				2.25	0.596		
	Co. of Var.	0.50	1.69	0.84	11.74	9.081	15.05				14.72	13.466		

Table AV.5 Shear Coupon Impact Test Results.

Specimen	Specimen Thickness (mm)	Impact Energy (J)	Impact Velocity (m/s)	Peak Force (kN)	Defl. of Peak Force (mm)	Energy at Peak Force (J)	Damage Energy (J)	Elastic Energy (J)	Peak Defl. (mm)	Peak Defl. (mm)	Total Impact Energy (J)	Time to Peak Force (ms)	Time to Peak Defl. (ms)	Contact Time (ms)	Knee (kN)	Initial Stiffness (kN/mm)	Stiffness from tp (kN/mm)	Stiffness from td (kN/mm)	Stiffness from to (kN/mm)
B409	3.31	0.63	0.34	1.22	1.113	0.75	-0.53	1.3	1.119	0.75	0.74	5.5	5.2	12.9		1.42	0.88	0.99	0.64
B266	3.53	0.63	0.34	1.38	0.995	0.73	-0.46	1.2	1.009	0.75	0.73	5.1	4.6	11.4		1.74	1.03	1.26	0.82
B170	3.38	0.63	0.34	1.21	1.148	0.73	-0.09	0.8	1.150	0.74	0.75	5.1	5.3	11.6		1.17	1.03	0.95	0.79
B407	3.37	0.66	0.35	1.42	1.042	0.76	-0.42	1.4	1.042	0.76	0.77	4.7	4.7	11.4		1.50	1.21	1.21	0.82
Average	3.40	0.63	0.34	1.31	1.07	0.74	-0.43	1.18	1.08	0.75	0.75	5.10	4.95	11.63			1.04	1.10	0.77
Std Dev	0.09	0.02	0.00	0.11	0.07	0.02	0.23	0.24	0.07	0.01	0.02	0.33	0.35	0.72			0.13	0.16	0.09
Co. of Var.	2.75	2.94	1.46	8.27	6.42	2.02	-54.76	20.54	6.07	1.27	2.30	6.40	7.09	6.11			12.89	14.15	11.22
B648	3.39	0.78	0.38	1.20											1.05				
B410	3.46	0.82	0.39	1.54	1.181	0.94	-0.47	1.4	1.182	0.94	0.95	4.9	4.7	11.0		1.46	1.11	1.21	0.88
B355	3.46	0.87	0.40	1.26	1.402	1.00	0.29	0.7	1.423	1.03	1.02	5.0	5.6	11.6	1.22		1.07	0.85	0.79
B407	3.56	0.91	0.41	1.44	1.316	1.05	-0.29	1.3	1.316	1.05	1.05	5.0	5.1	11.8		1.44	1.07	1.03	0.77
B80	3.37	0.91	0.41	1.38	1.354	1.04	0.08	1.0	1.361	1.05	1.05	4.9	5.3	11.3		1.26	1.11	0.95	0.84
Average	3.45	0.86	0.40	1.36	1.31	1.01	-0.10	1.12	1.32	1.02	1.02	4.95	5.18	11.43			1.09	1.01	0.82
Std Dev	0.07	0.06	0.01	0.14	0.09	0.05	0.35	0.32	0.10	0.05	0.05	0.06	0.38	0.35			0.03	0.15	0.05
Co. of Var.	2.06	6.51	3.28	10.02	7.23	4.95	-364.04	28.33	7.74	5.16	4.79	1.17	7.29	3.06			2.33	14.97	6.18
B405E	3.35	0.95	0.42	1.49	1.260	1.07	-0.14	1.2	1.281	1.10	1.09	4.4	5.0	11.3		1.40	1.38	1.07	0.84
B406	3.45	0.95	0.42	1.53	1.255	1.07	-0.31	1.4	1.264	1.07	1.09	4.7	4.8	11.2		1.47	1.21	1.16	0.85
B245	3.52	0.95	0.42	1.44	1.309	1.08	-0.17	1.3	1.309	1.08	1.09	5.0	5.0	11.7		1.60	1.07	1.07	0.78
B310	3.47	1.00	0.43	1.31	1.495	1.13	0.39	0.8	1.607	1.14	1.16	5.2	5.6	11.8	1.22	1.16	0.99	0.85	0.77
B369	3.45	1.15	0.46	1.32	1.556	1.21	0.27	1.1	1.654	1.33	1.32	4.5	5.9	13.1	1.30	1.17	1.32	0.77	0.62
B311	3.45	1.20	0.47	1.34	1.743	1.35	0.58	0.8	1.770	1.39	1.38	5.3	6.0	12.3	1.23	1.04	0.95	0.74	0.71
B176	3.40	1.00	0.43	1.41	1.417	1.14	0.30	0.9	1.431	1.16	1.15	4.8	5.3	11.6	1.25	1.36	1.16	0.95	0.79
B101	3.43	1.05	0.44	1.40	1.409	1.17	0.21	1.0	1.422	1.19	1.20	4.8	5.3	11.3	1.18	1.29	1.16	0.95	0.84
Average	3.44	1.03	0.44	1.41	1.43	1.15	0.14	1.04	1.46	1.18	1.19	4.84	5.36	11.79		1.36	1.16	0.94	0.77
Std Dev	0.05	0.09	0.02	0.08	0.16	0.10	0.31	0.23	0.18	0.12	0.11	0.32	0.44	0.64		0.19	0.15	0.15	0.08
Co. of Var.	1.45	8.95	4.41	5.68	11.49	8.43	220.74	22.17	12.47	9.96	9.35	6.53	8.16	5.41		13.71	12.99	15.90	9.99
B340	3.45	1.35	0.50	1.40	1.716	1.34	0.74	0.8	1.849	1.52	1.55	4.5	6.0	12.2	1.25		1.32	0.74	0.72
B342	3.53	1.35	0.50	1.44	1.651	1.42	0.29	1.2	1.715	1.51	1.53	4.6	5.7	12.8			1.29	0.82	0.65
B401E	3.53	1.25	0.48	1.53	1.592	1.40	0.07	1.3	1.595	1.40	1.42	5.1	5.4	11.9			1.03	0.91	0.75
Average	3.51	1.32	0.49	1.46	1.65	1.39	0.37	1.11	1.72	1.48	1.50	4.73	5.70	12.30			1.20	0.83	0.71
Std Dev	0.04	0.06	0.01	0.07	0.06	0.04	0.34	0.29	0.13	0.07	0.07	0.32	0.30	0.46			0.15	0.09	0.05
Co. of Var.	1.15	4.65	2.34	4.57	3.75	3.09	93.14	26.22	7.39	4.51	4.87	6.79	5.26	3.73			12.88	10.54	7.32
B338	3.30	1.88	0.59	1.34	2.458	2.08	1.32	0.9	2.539	2.18	2.15	5.9	7.1	14.2	1.10		0.77	0.53	0.53
B347	3.47	1.82	0.58	1.35	2.094	1.77	1.29	0.8	2.323	2.07	2.07	4.7	6.8	13.6	1.33		1.21	0.58	0.58
B329	3.30	2.01	0.61	1.49	2.179	1.94	1.37	0.9	2.389	2.24	2.27	4.7	6.6	13.1	1.22		1.21	0.63	0.62
B360	3.48	2.29	0.65	1.58	2.089	1.90	1.72	0.9	2.653	2.59	2.56	3.8	6.7	13.4	1.55		1.85	0.59	0.59
B359E	3.48	2.43	0.67	1.62	2.616	2.47	1.33	1.4	2.750	2.58	2.72	5.3	6.8	13.9	1.55		0.95	0.58	0.55
Average	3.41	2.09	0.62	1.48	2.29	2.03	1.41	0.95	2.51	2.35	2.35	4.88	6.78	13.64			1.20	0.58	0.57
Std Dev	0.10	0.26	0.04	0.13	0.24	0.27	0.18	0.23	0.17	0.27	0.28	0.78	0.22	0.43			0.41	0.04	0.04
Co. of Var.	2.84	12.56	6.26	8.71	10.45	13.22	12.65	24.20	6.62	11.37	11.77	16.03	3.20	3.14			34.22	6.33	6.26
B327	3.47	3.21	0.77	1.67	2.672	2.75	2.10	1.5	3.518	3.61	3.58	6.6	6.7	14.7	1.45				
B323	3.45	3.38	0.79	1.69	3.059	3.30	2.51	1.2	3.304	3.70	3.73	5.2	7.1	15.8	1.23				
B345	3.32	3.21	0.77	1.68	2.416	2.27	2.50	1.0	3.197	3.53	3.55	3.7	7.0	13.9	1.21				
B344E	3.33	3.29	0.78	1.65	3.217	3.53	2.52	1.1	3.264	3.61	3.64	6.3	7.1	13.9	1.13				
B342	3.41	3.21	0.77	1.58	3.448	3.50	2.45	1.2	3.518	3.61	3.58	6.6	7.6	14.7	1.18				
B361	3.42	3.29	0.78	1.73	3.035	3.31	2.52	1.1	3.228	3.64	3.64	5.3	6.9	13.4	1.18				
Average	3.40	3.25	0.78	1.67	2.97	3.11	2.43	1.18	3.34	3.62	3.62	6.62	7.07	14.07					
Std Dev	0.05	0.07	0.01	0.05	0.37	0.50	0.17	0.17	0.14	0.05	0.05	1.13	0.30	0.52					
Co. of Var.	1.82	2.11	1.05	3.00	12.55	16.01	6.80	14.32	4.31	1.52	1.76	20.05	4.26	3.73					
B202	3.29	3.73	0.83	1.75															
B214	3.49	3.73	0.83	1.78															
B243E	3.40	3.91	0.85	1.85															
B261	3.47	3.73	0.83	1.90	3.254	4.04	2.05	2.0	3.269	4.07	4.08	6.2	6.6	14.0	1.48				
B160	3.36	3.64	0.82	1.85	3.084	3.62	1.99	2.0	3.266	3.95	3.99	5.2	6.6	14.2	1.20				
B191	3.36	4.00	0.86	1.95	3.371	4.20	2.52	1.9	3.459	4.37	4.37	6.7	6.7	13.9	1.45				
B220	3.45	3.46	0.80	1.88	2.953	3.41	1.97	1.8	3.182	3.81	3.80	5.0	6.6	14.4	1.20				
Average	3.40	3.74	0.83	1.85	3.17	3.82	2.13	1.92	3.29	4.05	4.05	5.78	6.63	14.13					
Std Dev	0.07	0.18	0.02	0.07	0.18	0.37	0.26	0.09	0.12	0.24	0.24	0.81	0.05	0.22					
Co. of Var.	2.10	4.69	2.35	3.71	5.82	9.58	12.22	4.55	3.56	5.88	5.84	14.02	0.75	1.57					
B321	3.33	4.58	0.95	1.91	3.617	4.43	3.80	1.3	3.980	5.11	5.10	5.2	7.3	14.1	1.35				
B306	3.40	4.58	0.92	1.92	3.981	4.66	3.47	1.5	4.166	5.01	5.02	6.1	7.6	14.8	1.16				
B370	3.40	4.48	0.91	1.80															
B309E	3.31	4.78	0.94	1.85	4.243	4.93	3.88	1.4	4.413	5.24	5.25	6.4	7.9	15.2	1.42				
B315	3.48	4.99	0.96	1.94															
B162	3.24	4.78	0.94	2.05	4.063	5.12	3.16	2.1	4.312	5.22	5.22	6.5	7.1	14.7	1.50				
B294	3.45	4.99	0.95	2.00															
Average	3.37	4.75	0.94	1.92	3.98	4.79	3.58	1.57	4.17	5.15	5.15	6.05	7.48	14.70					
Std Dev	0.08	0.19	0.02	0.08	0.26	0.30	0.33	0.34	0.18	0.11	0.11	0.59	0.35	0.45					
Co. of Var.	2.49	4.03	2.02	4.40	6.62	6.33	9.23	21.87	4.35	2.07	2.04	9.78	4.68	3.09					
B208E	3.36	5.85	1.04	2.28	4.532	6.24	4.19	2.2	4.688	6.37	6.34	6.5	7.2	14.5	1.38				
B173	3.28	6.43	1.09	2.43	4.612	6.66	4.51	2.4	4.709	6.88	6.93	6.2	7.0	14.5	1.00				
B163	3.24	6.31	1.08	2.37	4.707	6.80	4.66	2.2	4.711	6.80	6.81	7.1	7.1	14.4	1.50				
B221E	3.48	6.43	1.09	2.28	4.792	6.90	4.66												

Table AV.5 Shear Coupon Impact Test Results.

Specimen	Specimen Thickness (mm)	Impact Energy (J)	Impact Velocity (m/s)	Peak Force (N)	Defl. of Peak Force (mm)	Energy of Peak Force (J)	Damage Energy (J)	Elastic Energy (J)	Peak Defl (mm)	Energy of Peak Defl (J)	Total Impact Energy (J)	Time to Peak Force (ms)	Time to Peak Defl (ms)	Contact Time (ms)	Knee (00)	Initial Stiffness (GN/mm)	Stiffness from tp (GN/mm)	Stiffness from td (GN/mm)	Stiffness from to (GN/mm)
B175	3.27	8.69	1.24	2.46															
B164	3.26	8.32	1.24	2.71															
B300E	3.36	8.46	1.26	2.46	6.400	8.40	7.22	1.9	6.792	9.12	9.07	6.1	7.7	16.0	1.20				
B217	3.48	8.46	1.26	2.64	6.464	8.74	6.60	2.6	6.600	9.09	9.06	6.3	7.3	14.6	1.34				
B250	3.47	8.46	1.26	2.46	6.512	8.64	6.87	2.2	6.682	9.06	9.06	6.4	7.6	14.8	1.27				
B236	3.47	8.46	1.26	2.72	6.282	8.63	6.40	2.7	6.367	9.06	9.03	6.3	7.0	13.9	1.28				
B210	3.28	8.46	1.26	2.61															
Average	3.37	8.46	1.26	2.68	6.44	8.66	6.77	2.31	6.61	9.08	9.06	6.28	7.38	14.68					
Std Dev	0.10	0.08	0.01	0.12	0.11	0.19	0.36	0.34	0.18	0.03	0.02	0.13	0.30	0.48					
Co. of Var	3.08	0.92	0.46	4.69	1.93	2.14	5.24	14.62	3.21	0.32	0.21	2.01	4.06	3.28					
B212	3.40	10.61	1.40	2.66	6.384	10.76	8.64	2.7	6.671	11.24	11.30	6.6	7.7	14.8	1.38				
B119	3.39	10.01	1.36	2.73	6.810	10.33	7.71	2.9	6.917	10.62	10.64	6.4	7.2	14.6					
B180	3.29	10.16	1.37	2.68	6.972	10.20	8.33	2.6	6.211	10.83	10.82	6.2	7.6	14.8	1.17				
B267	3.44	10.31	1.38	3.01	6.412	9.40	7.77	3.2	6.946	10.98	10.94	6.1	7.0	14.0	1.33				
B237	3.47	10.16	1.37	2.61	6.808	9.63	8.17	2.7	6.296	10.84	10.83	6.6	7.6	14.7	1.60				
B304	3.33	10.16	1.37	2.66	6.129	10.32	8.06	2.7	6.293	10.76	10.82	6.6	7.6	15.1	1.33				
Average	3.39	10.23	1.38	2.74	6.92	10.09	8.10	2.78	6.21	10.88	10.89	6.07	7.42	14.66					
Std Dev	0.07	0.21	0.01	0.14	0.33	0.62	0.32	0.26	0.26	0.21	0.22	0.69	0.26	0.37					
Co. of Var	1.98	2.01	1.00	4.98	5.67	6.16	3.96	8.88	3.96	1.96	2.06	9.76	3.66	2.64					
B314	3.40	11.22	1.44	2.77	6.246	10.88	9.96	2.0	6.634	11.94	11.93	6.9	7.8	14.6					
B292	3.33	11.38	1.46	2.72	6.821	11.16	10.14	1.9	7.164	12.08	12.14	6.6	8.3	15.2	1.34				
B319	3.44	11.22	1.44	2.77	6.492	11.28	10.03	1.9	6.736	11.94	11.94	6.6	7.9	14.6	1.38				
B360E	3.37	11.38	1.46	2.96	6.620	10.80	9.93	2.2	6.992	12.16	12.12	6.0	7.9	14.7	1.38				
B331	3.42	11.38	1.46	2.89	6.667	11.61	9.90	2.2	6.868	12.06	12.11	6.6	7.9	14.6	1.46				
B322	3.39	11.38	1.46	2.66	6.714	11.33	10.16	2.0	7.011	12.11	12.12	6.6	8.2	14.8					
Average	3.39	11.33	1.46	2.79	6.68	11.16	10.01	2.03	6.90	12.06	12.06	6.36	8.00	14.73					
Std Dev	0.04	0.08	0.01	0.11	0.20	0.27	0.11	0.13	0.19	0.09	0.10	0.31	0.20	0.26					
Co. of Var	1.14	0.71	0.34	3.96	3.09	2.46	1.11	6.16	2.82	0.75	0.82	4.96	2.60	1.70					
B337	3.46	13.34	1.67	3.20															
B343	3.44	13.17	1.66	2.96	7.141	13.28	11.79	2.2	7.381	13.98	13.96	6.6	8.0	14.7	1.60				
B363	3.46	13.34	1.67	3.16	6.900	13.12	11.77	2.4	7.232	14.16	14.11	6.1	7.7	14.1	1.62				
B364	3.44	13.17	1.66	3.10															
B332E	3.31	13.17	1.66	3.06															
B367	3.31	13.17	1.66	3.12															
Average	3.40	13.23	1.66	3.10	7.02	13.20	11.78	2.29	7.31	14.07	14.03	6.36	7.86	14.40					
Std Dev	0.07	0.09	0.01	0.09	0.17	0.11	0.01	0.13	0.11	0.12	0.11	0.36	0.21	0.42					
Co. of Var	2.06	0.66	0.33	2.78	2.43	0.86	0.12	5.88	1.44	0.86	0.77	5.67	2.70	2.96					
B288	3.34	14.03	1.61	3.23	6.663	12.79	12.30	2.6	7.223	14.87	14.79	6.3	7.4	14.7	1.22				
B222	3.48	14.20	1.62	3.27	7.044	14.09	11.91	3.1	7.319	14.98	14.98	6.2	7.4	14.6	1.30				
B278	3.42	14.20	1.62	3.26	6.999	13.89	12.06	2.9	7.346	14.97	14.98	6.0	7.5	15.1	1.21				
B167	3.26	14.38	1.63	3.49	6.842	13.71	11.63	3.6	7.266	16.14	16.16	6.7	7.3	14.2	1.28				
B263	3.46	14.20	1.62	3.12	6.671	12.76	12.97	2.1	7.366	15.06	14.98	6.3	7.7	15.4	1.24				
B216E	3.48	14.20	1.62	3.32	7.210	14.28	11.43	3.6	7.438	15.00	14.99	6.3	7.6	14.7	1.26				
Average	3.41	14.20	1.62	3.28	6.87	13.69	12.06	2.96	7.32	16.01	14.98	6.80	7.47	14.78					
Std Dev	0.09	0.11	0.01	0.12	0.27	0.66	0.66	0.67	0.07	0.09	0.11	0.44	0.14	0.42					
Co. of Var	2.59	0.78	0.39	3.73	3.87	4.86	4.63	19.33	1.02	0.61	0.75	7.56	1.83	2.82					
B302	3.38	16.67	1.76	3.66	7.163	14.49	17.18					6.3			1.22				
B169	3.27	17.34	1.79	3.17	7.066	13.29	18.33					4.8			1.13				
B168	3.27	16.96	1.77	3.18	6.920	13.34	17.86					4.8			1.26				
B287	3.46	17.16	1.78	3.39	7.443	16.61	17.47					5.6			1.16				
B263	3.46	16.67	1.76	3.16	6.921	12.61	17.21					4.8			1.19				
Average	3.37	16.92	1.77	3.29	7.10	13.87	17.66					5.06							
Std Dev	0.10	0.34	0.02	0.18	0.22	1.18	0.48					0.37							
Co. of Var	2.83	2.02	1.01	6.46	3.04	8.64	2.72					7.34							
B286	3.42	19.33	1.89	3.21															
B174	3.28	19.64	1.90	3.46															
B233	3.36	19.64	1.90	3.13	7.104	13.17	18.77					4.4			1.19				
B296	3.33	19.33	1.89	3.37	7.201	14.35	20.66					4.6			1.17				
B282	3.46	19.64	1.90	3.08	7.006	12.96	18.43					4.3			1.21				
B247	3.36	19.64	1.90	3.44	7.211	14.41	18.91					4.6			1.26				
B219	3.49	19.64	1.90	3.71	7.394	16.39	20.63					4.8			1.17				
Average	3.38	19.48	1.90	3.34	7.18	14.06	19.48					4.64			1.20				
Std Dev	0.07	0.10	0.00	0.22	0.14	1.00	1.08					0.19			0.14				
Co. of Var	2.16	0.61	0.26	6.69	2.01	7.09	6.63					4.29			10.68				

Table AV.6 Shear Coupon Damage Analysis Results

Specimen	Total Impact Energy (J)	C-scan contours - Damage Areas						Optical Microscopy - Delamination Areas						Matrix Crack Spacing (mm)	Lower CFM crack (mm)	Permanent Indent. (mm)
		24dB Area (mm ²)	+4F Area (mm ²)	+20dB Area (mm ²)	+16dB Area (mm ²)	+12dB Area (mm ²)	+8dB Area (mm ²)	Upper Total (mm ²)	Lower (shear) (mm ²)	Lower (tension) (mm ²)	Lower Total (mm ²)	Delam. Total (mm ²)	Damage Area (mm ²)			
IB409	0.74							54	0	0	0	54	77	8.6	0	0
IB266	0.73	5	5	91	133	275	419	23	2	0	2	25	151		0	0
IB70	0.75	0	0	39	71	122	383	21	4	0	4	25	69	6.6	2	0
IB402	0.77	1	1	98	164	255	479	74	0	0	0	74	115	5.5	0	0
Average	0.75	2	2	76	123	217	427	43	1	0	1	44	103	6.9	0.50	0.00
Std Dev	0.02	3	3	32	47	83	48	25	2	0	2	24	38	1.6	1.00	0.00
Co. of Var.	2.30	124	124	43	38	38	11	59	133		124	54	37	22.8	200.00	
IB68		63	63	115	167	233	531								1	0
IB410	0.95	0	0	45	103	242	688	28	0	0	0	28	50	4.9	0	0
IB355	1.02							8	0	0	0	8	48	16.4	1	0
IB407	1.06	34	34	212	407	817	1187	91	14	0	14	104	107		0	0
IB90	1.05	0	0	25	60	109	281	0	0	0	0	0	0	7.4	2	0
Average	1.02	24	24	99	184	350	672	31	3	0	3	35	51	9.6	0.80	0.00
Std Dev	0.05	30	30	85	155	317	382	41	7	0	7	48	44	6.0	0.84	0.00
Co. of Var.	4.79	126	126	85	84	91	57	131	200		200	137	85	63.2	104.58	
IB405E	1.09	75	75	100	260	378	449	42	0	0	0	42	114	7.7	6	0
IB406	1.09	1	1	101	219	423	644	40	0	0	0	40	122	4.0	2	0
IB245	1.09	0	0	71	117	205	441								4	0
IB310	1.16	21	21	68	99	151	229								2	0
IB369	1.32	7	7	51	95	139	271	57	0	0	0	57	117		6	0
IB311	1.38	20	20	55	99	157	384								2	0
IB76	1.15	0	0	17	44	84	142								6	0
IB101	1.20	0	0	64	115	176	325	66	0	0	0	66	130	11.5	6	0
Average	1.19	15	15	66	131	214	361	51	0	0	0	51	121	7.7	4.25	0.00
Std Dev	0.11	26	26	28	71	121	156	12	0	0	0	12	7	3.7	1.98	0.00
Co. of Var.	9.35	166	166	42	55	56	43	24				24	6	48.4	46.64	
IB340	1.55	0	0	41	73	118	304	14	5	0	4	17	82	16.4	6	0
IB342	1.53	0	0	78	153	252	519	30	23	0	23	53	93		5	0
IB401E	1.42	0	0	80	161	435	570	43	0	0	0	43	60	6.4	7	0
Average	1.50	0	0	67	129	268	464	29	9	0	9	38	78	11.4	6.00	0.00
Std Dev	0.07	0	0	22	49	159	141	15	12	0	12	18	17	7.1	1.00	0.00
Co. of Var.	4.87			33	38	59	30	51	129		140	49	22	62.4	16.67	
IB338	2.15	70	70	144	204	263	351	139	0	0	0	139	232	14.6	7	0.1
IB347	2.07	90	90	145	221	335	760	49	8	0	4	52	162		8	0.1
IB329	2.27	37	37	104	151	211	315	54	0	0	0	54	174	22.5	7	0.1
IB360	2.56	118	118	188	254	382	776								13	0.1
IB359E	2.72	45	45	160	302	587	1063								5	0.15
Average	2.35	72	72	148	226	356	653	80	3	0	1	82	189	18.6	8.00	0.11
Std Dev	0.28	33	33	30	57	145	316	50	4	0	2	49	37	5.6	3.00	0.02
Co. of Var.	11.77	46	46	20	25	41	48	63	173		173	61	20	30.1	37.50	20.33
IB327	3.58	254	254	258	265	293	469	20		40	40	60	230	16.2	10	0.15
IB323	3.73	290	290	293	300	334	503								15	0.1
IB365	3.55	297	297	303	310	341	503								15	0.15
IB344E	3.64	331	331	338	342	383	506	112	135	0	135	247	396		15	0.1
IB362	3.58	230	230	254	299	444	885	112	0	27	27	139	301	11.7	20	0.2
IB361	3.64	274	274	277	322	483	746	68	0	0	0	68	223	16.4	15	0.15
Average	3.62	279	279	287	306	380	602	78	45	17	50	128	287	14.8	15.00	0.14
Std Dev	0.06	35	35	32	26	72	172	44	78	20	59	87	81	2.7	3.16	0.04
Co. of Var.	1.76	13	13	11	8	19	29	56	173	119	117	68	28	18.0	21.08	26.57
IB202															27	0.15
IB214															20	0.2
IB243E		355	355	372	454	906	906	120	0	0	0	120	441	-	26	0.15
IB261	4.08	308	308	322	374	533	533								25	0.15
IB160	3.99	362	362	393	493	837	1636	121	48	0	48	169	340	8.4	26	0.2
IB191	4.37	265	265	275	324	547	965	126	0	0	0	126	391	35.0	24	
IB290	3.80	324	324	344	399	623	1133	228	0	0	0	228	423	20.0	27	0.15
Average	4.06	323	323	341	409	689	1035	148	12	0	12	160	399	21.1	25.00	0.17
Std Dev	0.24	39	39	46	66	171	401	53	24	0	24	50	44	13.3	2.45	0.03
Co. of Var.	5.84	12	12	13	16	25	39	36	200		200	31	11	63.1	9.80	15.49
IB321	5.10	400	400	454	520	681	1094	271		49	49	320	520	26.3	23	0.2
IB306	5.02	305	305	312	315	353	496	221	0	0	0	221	495	20.0	30	0.15
IB370		408	408	415	426	469	699	190		35	35	225	496	12.4	25	0.25
IB309E	5.25	403	403	417	470	603	848								25	0.2
IB315		476	476	476	480	518	743								27	0.2
IB162	5.22														26	0.2
IB294		198	198	344	459	712	1334	221	0	77	77	298	490	11.4	19	0.2
Average	5.15	370	370	403	445	556	869	225	0	40	40	266	500	17.5	25.00	0.20
Std Dev	0.11	101	101	63	70	136	301	33	0	32	32	50	13	7.0	3.42	0.03
Co. of Var.	2.04	27	27	16	16	24	35	15	80	80	19	3		39.9	13.66	14.43

Table AV.6 Shear Coupon Damage Analysis Results

Specimen	Total Impact Energy (J)	C-scan contours - "Damage Area"						Optical Microscopy - Delamination Areas						Matrix Crack Spacing (mm)	Lower CFM crack (mm)	Permanent Indent. (mm)
		24dB Area (mm ²)	+4F Area (mm ²)	+20dB Area (mm ²)	+16dB Area (mm ²)	+12dB Area (mm ²)	+8dB Area (mm ²)	Upper Total (mm ²)	Lower (shear) (mm ²)	Lower (tension) (mm ²)	Lower Total (mm ²)	Delam. Total (mm ²)	Damage Area (mm ²)			
IB208E	6.34	208	208	255	426	776	1311	205	0	34	34	239	376	10.2	25	
IB173	6.93	391	391	401	495	677	1079	270	0	15	15	285	436	6.8	31	0.15
IB163	6.81	346	346	364	421	546	695	320	0	38	38	358	605	14.0	34	0.25
IB221E	6.94	539	539	565	655	874	1240	355	0	74	74	429	581	8.6	27	
IB244E	6.35	397	397	418	478	606	797								28	0.2
IB291	6.77	353	353	363	444	575	834								29	0.2
Average	6.69	372	372	394	486	676	993	288	0	40	40	328	499	9.9	29.00	0.20
Std Dev	0.28	107	107	101	88	128	254	65	0	24	24	83	111	3.1	3.16	0.04
Co. of Var.	4.13	29	29	26	18	19	26	23		61	61	25	22	31.0	10.90	20.41
IB175		918	918	957	1097	1596	2548	816	38	60	98	913	965	8.4	38	0.5
IB164															37	0.4
IB300E	9.07														33	0.5
IB217	9.05	755	755	800	938	1368	2483	526			226	751	985	19.3	37	0.5
IB250	9.06	699	702	723	802	998	1405	436	116	44	176	611	836	15.4	35	0.5
IB235	9.03	785	785	806	885	1102	1415	460			306	766	885		36	0.35
IB210		788	788	813	888	1167	1770								37	0.45
Average	9.05	789	790	820	922	1247	1924	559	77	52	201	760	915	14.4	36.14	0.46
Std Dev	0.02	81	80	85	109	238	560	175	55	11	87	123	68	5.5	1.68	0.06
Co. of Var.	0.21	10	10	10	12	19	29	31	72	22	43	16	7	38.4	4.64	13.29
IB212	11.30	883	921	938	1011	1240	1613	630			360	990	1095	18.6	40	0.75
IB119	10.64	1004	1022	1069	1242	1634	1904	596			366	961	1070	7.9	41	0.8
IB180	10.82	1033	1044	1055	1066	1154	1424	631			320	951	1080	16.4	43	0.8
IB267	10.94	881	881	888	891	950	1183	581	110	68	178	758	1000		36	0.6
IB237	10.83	1068	1068	1075	1089	1160	1416								43	0.8
IB304	10.82														42	0.9
Average	10.89	974	987	1005	1060	1228	1508	609	110	68	306	915	1036	14.3	40.83	0.78
Std Dev	0.22	87	82	86	127	261	269	25			88	106	61	5.7	2.64	0.10
Co. of Var.	2.06	9	8	9	12	20	18	4			29	12	6	39.5	6.46	12.74
IB314	11.93	1239	1239	1267	1385	1753	2603	530			586	1116	1271	13.8	41	0.75
IB292	12.14	996	996	1007	1028	1105	1324	790			281	1071	1125	20.0	41	1.1
IB319	11.94	1065	1076	1100	1209	1479	2015	616			211	826	1066	19.3	42	0.85
IB350E	12.12	895	898	1162	1436	2067	2659	880	26	54	80	960	1200		44	0.9
IB331	12.11	1200	1222	1233	1262	1389	1734								45	0.9
IB322	12.12														35	1.3
Average	12.05	1079	1086	1154	1264	1557	2067	704	26	54	289	993	1165	17.7	41.33	0.97
Std Dev	0.10	143	146	105	161	363	571	160			215	129	89	3.4	3.50	0.20
Co. of Var.	0.82	13	13	9	13	23	28	23			74	13	8	19.2	8.47	20.60
IB337		698	718	945	1064	1240	1453	740			275	1015	1220	11.5	45	0.85
IB343	13.95	1065	1065	1096	1195	1411	1743	655			656	1311	1250		48	0.95
IB363	14.11	1054	1071	1119	1221	1527	2075	811			210	1021	1176	16.4	40	0.8
IB354		917	935	1128	1287	1528	1845	755			595	1350	1276		47	1.1
IB332E		861	878	1110	1273	1474	1767								49	0.9
IB357		636	667	847	992	1138	1342								52	1
Average	14.03	872	889	1041	1172	1386	1704	740			434	1174	1230	14.0	46.83	0.93
Std Dev	0.11	178	170	117	119	162	267	64			224	181	43	3.5	4.07	0.11
Co. of Var.	0.77	20	19	11	10	12	16	9			52	15	3	24.8	8.69	11.57
IB288	14.79	800	814	1030	1177	1351	1557								47	1.7
IB222	14.98	1247	1278	1316	1440	1853	2304	616			561	1176	1366	15.4	41	1.4
IB278	14.98	1209	1223	1262	1392	1702	2182	910			300	1210	1301	11.7	43	1.2
IB167	15.15	940	982	1209	1352	1604	2145	1116			420	1536	1446	7.9	45	1.2
IB283	14.98	760	773	965	1105	1283	1475								46	2.35
IB216E	14.99	878	909	1188	1474	1698	1909	761			661	1421	1681	20.0	37	1.5
Average	14.98	972	996	1162	1323	1582	1929	850			485	1336	1448	13.8	43.17	1.56
Std Dev	0.11	208	210	136	149	221	345	214			158	172	166	5.2	3.71	0.43
Co. of Var.	0.75	21	21	12	11	14	18	25			33	13	11	37.6	8.60	27.71
IB302															45	
IB169		861	881	1085	1245	1463	1806	926			766	1691	1310	9.1	50	
IB168		1079	1110	1141	1232	1563	1930	721			735	1456	1136	9.1	46	2.3
IB287		1509	1551	1593	1788	2338	3039	755			990	1745	1451	13.1	45	2.4
IB263		887	929	1156	1309	1550	1861								45	
Average		1084	1118	1244	1394	1729	2159	800			830	1631	1299	10.4	46.20	2.35
Std Dev		300	305	235	265	409	589	110			139	154	158	2.3	2.17	0.07
Co. of Var.		28	27	19	19	24	27	14			17	9	12	22.1	4.69	3.01
IB286		1191	1198	1222	1326	1572	1904	960			625	1585	1406	9.1	47	
IB174		1035	1053	1427	1523	1755	2039	1080			841	1921	1456	7.9	40	
IB233		1090	1124	1162	1252	1496	1891								49	
IB296															51	
IB282		1161	1182	1209	1319	1630	1987	791			796	1586	1205	23.5	43	
IB247															50	
IB219		1212	1241	1279	1382	1639	1974	1125			1030	2155	1565	15.0	46	
Average		1138	1159	1260	1360	1618	1959	989			823	1812	1408	13.9	46.57	
Std Dev		74	73	102	102	96	61	149			166	278	151	7.1	3.95	
Co. of Var.		6	6	8	8	6	3	15			20	15	11	51.4	8.49	

Table AV.7 Thermal Depley Results for the Shear Coupon.

TIE (J)	Specimen Number	Upper CFM Layer	UD fibre breakage	Lower CFM fibre breakage (mm)
1.02	IB68	none	none	- (1)*
1.19	IB311	none	none	- (2)
2.35	IB360	none	none	- (13)
2.35	IB359E	none	none	- (5)
3.62	IB323	none	none	15-20 (15)
3.62	IB365	none	none	15 (15)
4.06	IB261	none	some FB	25 (25)
4.06	IB214	none	some FB	15-20 (25)
5.15	IB162	some FB	none	25 (26)
5.15	IB315	none	none	20-25 (27)
6.69	IB244E	none	none	25 (28)
6.69	IB291	some broken fibres	some FB	25-30 (29)
9.05	IB164	circle of FB	none	40-45 (37)
9.05	IB300E	circle of FB	none	35-40 (33)
10.89	IB304	circle of FB	none	45 (42)
10.89	IB237	circle of FB	none	45-50 (43)
12.06	IB322	circle of FB	none	40-45 (35)
12.06	IB331	circle of FB	none	45 (45)
14.03	IB332	circle of FB	some FB	45 (49)
14.03	IB357	circle of FB	-	45-50 (52)
14.98	IB288	circle of FB	5mm width	45-50 (47)
14.98	IB283	circle of FB	some FB	40-45 (46)
16.92	IB302	circle of FB	10mm width	40-45 (45)
16.92	IB263	circle of FB	10mm width	45 (45)
19.48(IE)	IB296	circle of FB	10mm width	50-55 (51)
19.48(IE)	IB247	circle of FB	10mm width	40-45 (50)

* Figure in parenthesis refers to crack length recorded in visual inspection.

Table AV.8 Damage thresholds and interactions for the shear coupon.

Mode of damage	Threshold TIE (J)	Threshold Force (KN)	Interactions
UD transverse matrix cracking	< 0.75	< 1.3	
Upper i/f delamination	< 0.75	< 1.3	
UD shear cracking	< 0.75	< 1.3	
Lower i/f del. (shear)	< 0.75	< 1.3	by UD shear cracking
Lower i/f del. (bending)	≈ 3.6	≈ 1.7	lower CFM crack length = 15mm
Lower CFM crack	≈ 1.0	≈ 1.3	
Upper CFM permanent indentation	≈ 2.35	≈ 1.5	
Upper CFM shear failure	≈ 6.7	≈ 2.3	
Penetration	> 15	≈ 3.3	

Table AV.9 Transverse Coupon Impact Test Results.

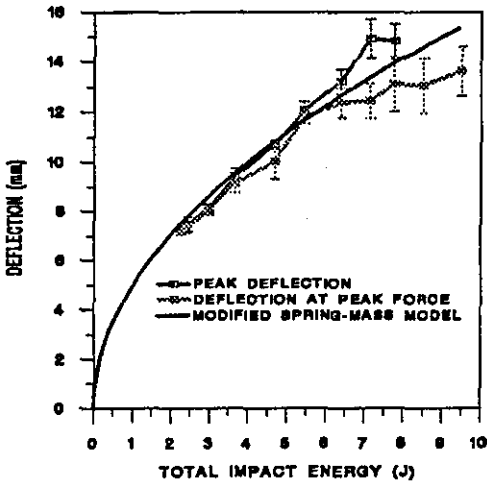
Specimen	Specimen Thickness (mm)	Impact Energy (J)	Impact Velocity (m/s)	Peak Force (N)	Defl. at Peak Force (mm)	Energy at Peak Force (J)	Damper Energy (J)	Elastic Energy (J)	Peak Defl (mm)	Energy at Peak Defl (J)	Total Impact Energy (J)	Time to Peak Force (ms)	Time to Peak Defl (ms)	Contact Time (ms)	Initial Stiffness (KN/mm)	Id Stiffness (KN/mm)	Ic Stiffness (KN/mm)	Iy Stiffness (KN/mm)
ID29	3.35	1.41	0.51	0.59	7.012	2.16	0.42	1.77	7.06	2.19	2.17	18.70	20.20	41.20	0.086	0.07	0.06	0.06
ID35	3.54	1.47	0.52	0.61	7.033	2.18	0.33	1.87	7.05	2.20	2.22	19.00	20.10	41.00	0.087	0.07	0.06	0.06
ID5	3.43	1.53	0.53	0.60	7.326	2.29	0.48	1.85	7.38	2.33	2.31	18.90	20.50	41.60	0.084	0.06	0.06	0.04
ID26	3.46	1.47	0.52	0.59	7.332	2.22	0.45	1.81	7.41	2.26	2.26	19.00	20.90	42.70	0.081	0.06	0.06	0.07
ID16	3.45	1.53	0.53	0.60	7.264	2.27	0.49	1.81	7.31	2.30	2.31	19.00	20.40	41.50	0.084	0.06	0.06	0.07
Average	3.49	1.48	0.52	0.60	7.193	2.22	0.43	1.82	7.24	2.26	2.25	18.92	20.42	41.60	0.084	0.06	0.06	0.07
Std Dev	0.05	0.05	0.01	0.01	0.158	0.06	0.06	0.04	0.17	0.06	0.06	0.13	0.31	0.66	0.00	0.00	0.00	0.00
Coef. of Var.	1.45	3.20	1.60	1.15	2.203	2.52	14.81	2.14	2.38	2.71	2.72	0.69	1.53	1.59	2.73	3.01	3.10	1.39
ID51	3.52	1.53	0.53	0.60	7.267	2.26	0.13	2.15	7.36	2.28	2.31	19.30	20.60	42.60		0.06	0.06	0.07
ID40	3.55	1.58	0.54	0.63	7.121	2.33	0.44	1.92	7.16	2.34	2.35	18.30	19.70	39.80		0.07	0.07	0.08
ID40	3.46	1.64	0.55	0.60	7.511	2.31	0.45	1.99	7.23	2.44	2.47	17.80	21.00	42.80		0.06	0.06	0.08
ID46	3.50	1.64	0.55	0.63	7.237	2.38	0.44	1.96	7.26	2.40	2.42	17.80	19.80	40.10		0.07	0.07	0.08
ID43	3.45	1.70	0.56	0.61	7.758	2.48	0.31	2.21	7.82	2.52	2.54	19.10	20.90	43.00		0.06	0.06	0.07
Average	3.51	1.62	0.55	0.61	7.379	2.35	0.35	2.05	7.46	2.40	2.42	18.64	20.40	41.70		0.06	0.06	0.08
Std Dev	0.06	0.07	0.01	0.02	0.255	0.08	0.14	0.13	0.30	0.09	0.09	0.61	0.61	1.52		0.00	0.00	0.01
Coef. of Var.	1.69	4.16	2.09	2.59	3.457	3.35	38.07	6.19	4.03	3.73	3.85	3.25	3.00	3.65		6.06	7.45	6.60
ID42	3.48	2.09	0.62	0.65	9.251	2.91	0.71	2.24	8.31	2.95	2.98	18.80	20.40	41.30		0.06	0.06	0.08
ID45	3.48	2.02	0.61	0.66														
ID52	3.54	2.09	0.62	0.69	7.923	2.89	0.66	2.26	7.98	2.92	2.94	17.90	19.40	39.20		0.07	0.07	0.08
ID10	3.56	2.09	0.62	0.68	7.907	2.86	0.74	2.21	8.05	2.95	2.95	17.90	19.50	39.40		0.07	0.07	0.09
ID21	3.56	1.77	0.57	0.68														
ID57	3.53	2.09	0.62	0.67	8.180	2.89	0.78	2.21	8.33	2.99	2.98	17.60	20.20	40.30		0.07	0.07	0.09
ID58	3.55	2.09	0.62	0.71	7.854	2.88	0.72	2.24	7.98	2.96	2.94	17.00	19.30	38.60		0.07	0.07	0.09
Average	3.53	2.03	0.61	0.68	8.023	2.89	0.72	2.23	8.13	2.95	2.96	17.70	19.76	39.76		0.07	0.07	0.09
Std Dev	0.03	0.12	0.02	0.02	0.179	0.02	0.04	0.03	0.18	0.03	0.02	0.71	0.50	1.05		0.00	0.00	0.01
Coef. of Var.	0.99	5.95	3.05	2.85	2.235	0.63	6.07	0.97	2.17	0.85	0.64	3.99	2.55	2.65		5.60	5.22	7.72
ID39	3.48	2.66	0.70	0.69	9.607	3.59	1.23	2.42	9.73	3.67	3.70	20.00	21.50	42.50				
ID50	3.52	2.66	0.70	0.71	9.258	3.45	1.18	2.49	9.58	3.67	3.69	17.40	20.80	41.60				
ID48	3.54	2.66	0.70	0.73	8.935	3.41	1.15	2.49	9.28	3.64	3.65	16.70	20.20	40.40				
ID47	3.60	2.66	0.70	0.75	8.572	3.39	1.16	2.41	8.83	3.57	3.60	16.40	19.50	39.00				
ID41	3.44	2.50	0.69	0.68	9.440	3.52	1.19	2.40	9.55	3.59	3.61	19.00	21.10	42.30				
Average	3.52	2.65	0.70	0.71	9.168	3.47	1.19	2.44	9.39	3.63	3.63	17.70	20.58	41.12				
Std Dev	0.06	0.03	0.00	0.03	0.411	0.08	0.04	0.04	0.35	0.05	0.04	1.24	0.73	1.42				
Coef. of Var.	1.73	1.28	0.64	3.76	4.488	2.38	3.30	1.82	3.77	1.07	1.21	7.01	2.56	3.45				
ID56	3.55	3.65	0.82	0.80	10.835	4.76	1.78	3.04	10.91	4.82	4.82	18.80	20.40	41.60				
ID55	3.55	3.48	0.80	0.84	9.065	3.53	1.80	2.84	10.51	4.64	4.60	13.20	20.10	39.80				
ID54	3.47	3.57	0.81	0.81	10.464	4.66	1.87	2.83	10.51	4.70	4.69	18.80	20.00	39.70				
ID53	3.49	3.57	0.81	0.77	9.834	4.02	2.73	1.96	10.82	4.66	4.72	15.10	21.80	44.90				
ID44	3.47	3.48	0.80	0.79	9.834	3.98	1.81	2.82	10.69	4.63	4.62	15.30	20.50	40.70				
Average	3.51	3.53	0.81	0.80	10.006	4.19	2.00	2.70	10.69	4.70	4.69	16.22	20.56	41.34				
Std Dev	0.04	0.07	0.01	0.02	0.679	0.51	0.41	0.42	0.18	0.08	0.09	2.49	0.72	2.13				
Coef. of Var.	1.17	2.07	0.04	3.07	6.781	12.25	20.55	15.66	1.68	1.61	1.87	15.33	3.52	5.16				
ID32	3.49	4.13	0.87	0.80	12.087	5.27	2.26	3.20	12.32	5.46	5.45	19.00	21.80	42.90				
ID21	3.50	4.23	0.88	0.84	11.640	5.15	2.33	3.21	12.12	5.34	5.32	17.20	21.10	41.60				
ID36	3.58	4.13	0.87	0.87	11.464	5.27	1.96	3.42	11.60	5.38	5.37	18.30	20.40	40.50				
ID33	3.50	4.13	0.87	0.85	11.680	5.26	2.16	3.26	11.87	5.42	5.40	18.30	20.80	41.00				
ID28	3.51	4.13	0.87	0.81	12.166	5.26	2.45	2.99	12.39	5.44	5.46	19.00	21.80	42.70				
Average	3.52	4.15	0.87	0.83	11.807	5.24	2.23	3.22	12.06	5.45	5.44	18.36	21.18	41.74				
Std Dev	0.04	0.04	0.00	0.03	0.304	0.05	0.19	0.13	0.33	0.06	0.06	0.74	0.62	1.05				
Coef. of Var.	1.04	1.03	0.51	3.52	2.572	0.99	8.29	4.79	2.74	1.09	1.07	4.01	2.92	2.50				
ID37	3.48	5.11	0.97	0.89	12.699	6.26	3.28	3.20	12.95	6.48	6.50	18.10	20.80	40.70				
ID7	3.44	5.01	0.96	0.84	12.735	5.97	3.04	1.43	13.56	6.49	6.46	17.40	24.10	51.80				
ID14	3.57	5.01	0.96	0.91	12.418	5.97	4.97	1.45	13.18	6.42	6.41	17.20	23.40	48.90				
ID1	3.51	5.01	0.96	0.92	12.591	6.19	3.81	2.56	12.79	6.37	6.37	18.10	20.50	44.10				
ID34	3.53	4.91	0.95	0.89	12.424	6.01	4.42	1.85	12.73	6.27	6.26	17.80	21.20	46.20				
ID15	3.46	4.93	0.95	0.78	11.161	4.75	4.93	1.33	14.00	6.46	6.42	13.80	26.00	57.40				
Average	3.50	5.00	0.96	0.87	12.338	5.86	4.41	2.01	13.20	6.42	6.40	17.07	22.70	48.18				
Std Dev	0.05	0.07	0.01	0.05	0.592	0.56	0.72	0.72	0.40	0.08	0.08	1.64	2.21	5.92				
Coef. of Var.	1.37	1.47	0.70	5.80	4.796	0.90	16.41	35.95	3.74	1.30	1.25	9.62	9.72	12.28				
ID31	3.54	5.54	1.01	0.82	12.080	5.36	5.95	1.22	15.66	7.17	7.21	14.70	27.50	54.80				
ID3	3.55	5.54	1.01	0.86	11.640	5.38	5.30	1.72	13.98	7.02	7.04	13.80	23.90	49.60				
ID25	3.44	5.54	1.01	0.90	13.196	6.36	5.46	1.66	14.53	7.12	7.09	17.10	23.00	48.80				
ID8	3.44	5.54	1.01	0.82	12.795	5.76	6.27	0.87	15.47	7.14	7.19	13.80	27.10	58.00				
Average	3.49	5.54	1.01	0.85	12.428	5.72	5.75	1.37	14.91	7.11	7.13	15.33	25.28	52.80				
Std Dev	0.06	0.00	0.00	0.04	0.699	0.47	0.45	0.40	0.79	0.07	0.08	1.42	2.26	4.37				
Coef. of Var.	1.74	0.00	0.00	4.26	5.626	8.18	7.76	29.22	5.30	0.91	1.18	9.28	8.90	8.28				
ID18	3.48	6.22	1.07	0.92	12.840	6.62	5.97	1.80	14.51	7.77	7.77	15.10	24.00	50.80				
ID22	3.53	6.22	1.07	0.90	13.226	6.54	6.49	1.43	15.60	7.92	7.89	15.40	25.80	55.20				
ID20	3.59	6.11	1.06	0.96	11.840	5.99	5.55	2.07	13.99	7.82	7.60	15.30	22.90	45.90				
ID43	3.43	6.22	1.07	0.92	14.449	7.46	6.73	1.02	15.10	7.85	7.83	14.40	24.60	53.40				
Average	3.51	6.19	1.07	0.92	13.089	6.65	6.19	1.61	14.80	7.79	7.77	15.60	24.23	50.83				
Std Dev	0.07	0.06	0.00	0.02	1.079	0.61	0.53	0.42	0.70	0.13	0.12	2.04	1.37	3.49				
Coef. of Var.	1.95	0.93	0.47	2.66	8.241	9.12	8.55	25.94	4.73	1.65	1.61	13.11	5.66	6.87				
ID2	3.55	7.15	1.16	0.89	11.527	5.24						11.10						
ID11	3.44	6.85	1.12	0.85	13.457	5.90						13.90						
ID42	3.47	6.85	1.12	0.93	12.806	6.39						13.90						
ID17	3.47	6.73	1.11															

Table AV.10 Transverse Coupon Damage Analysis Results.

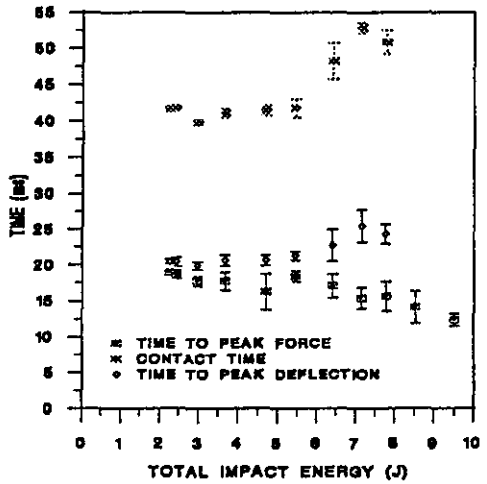
Specimen	Total Impact Energy (ft)	Crack content - "Damage Areas"						DM - Def. Area		Midline Crack Spacing (mm)	Lower CPD Crack (mm)
		24dB Area (mm ²)	+1P Area (mm ²)	+20dB Area (mm ²)	+10dB Area (mm ²)	+15dB Area (mm ²)	+A10 Area (mm ²)	Upper Area (mm ²)	Damage Area (mm ²)		
BT29	2.17	0	0	13	151	803	2556				0
BT15	2.22	0	0	0	20	608	2370				0
BT3	2.21	0	0	0	0	70	1109	0	0	131	0
BT26	2.26	0	0	31	706	854	2229				0
BT10	2.21	0	0	0	0	33	661	0	0	103	0
Average	2.25	0	0	13	99	434	1797	0	0	11.7	0
Std Dev	0.06	0	0	32	141	706	873	0	0	2.0	0
C.o. of Var.	2.72			134	142	31	48			16.9	
BT51	2.21	0	0	0	3	79	773	0	0	7.4	0
BT49	2.25	0	0	0	10	142	816	0	0	13.3	0
BT40	2.27	0	0	0	76	168	1378				0
BT46	2.42	0	0	30	143	376	1040				0
BT1	2.54	0	0	0	10	351	472				0
Average	2.42	0	0	48	73	315	1124	0	0	10.4	0
Std Dev	0.09	0	0	26	77	227	743	0	0	4.3	0
C.o. of Var.	3.85			149	106	48	15			40.3	
BT42	2.96	0	0	0	25	170	915	0	0	14.2	0
BT45		0	0	0	116	728	2315	0	0	9.1	0
BT52	2.94	0	0	70	62	196	604				0
BT10	2.95	0	0	0	0	252	2344				0
BT21		0	0	43	160	658	2143				0
BT57	2.98	0	0	34	136	1272	2899				0
BT48	2.94	0	0	0	23	791	2510				0
Average	2.96	0	0	14	75	274	1977	0	0	11.7	0
Std Dev	0.02	0	0	18	63	402	820	0	0	3.6	0
C.o. of Var.	0.64			131	84	39	43			31.0	
BT36	3.20	0	0	0	0	0	0	0	0	2.8	0
BT50	3.69	0	0	0	0	0	0	0	0	8.0	0
BT40	3.65	0	0	16	93	302	1187				0
BT47	3.60	0	0	0	0	0	0				0
BT41	3.61	0	0	0	0	0	0				0
Average	3.65	0	0	3	19	76	217	0	0	2.9	0
Std Dev	0.04	0	0	7	42	175	531	0	0	0.1	0
C.o. of Var.	1.21			224	224	224	224			1.8	
BT56	4.82	0	0	12	127	768	1897	2	2	7.6	15
BT55	4.60	1	3	29	220	805	3212	0	0	6.3	0
BT44	4.69	0	0	10	96	464	1300				0
BT53	4.72	0	0	87	193	497	794	73	73	28.0	32
BT44	4.62	0	0	4	15	348	1600	0	0	12.1	0
Average	4.69	1	1	24	134	507	1341	19	19	13.6	9
Std Dev	0.09	1	1	25	76	263	798	76	76	6.9	14
C.o. of Var.	1.87	224	224	105	35	40	36	195	195	73.3	155
BT42	5.43	0	0	0	33	432	2250	0	0	6.6	0
BT21	5.32	0	0	0	12	215	1531	0	0	7.7	0
BT46	5.37	0	0	0	5	512	2249				0
BT11	5.40	0	0	0	16	374	1582	0	0	7.6	0
BT36	5.46	0	0	0	0	76	1418	0	0	9.8	0
Average	5.44	0	0	13	329	1771		0	0	7.9	0
Std Dev	0.08	0	0	14	176	446		0	0	1.3	0
C.o. of Var.	1.07			94	53	25				17.0	
BT17	6.30	0	0	0	39	279	1818				0
BT7	6.46	13	17	172	499	1138	2793	56	56	7.9	65
BT14	6.41	0	53	203	567	1055	1928	113	113	14.3	60
BT1	6.37	0	0	76	285	941	2629	9	30	16.1	46
BT14	6.26	30	30	285	761	1768	2722	0	0	5.7	33
BT15	6.42	198	199	599	899	2138	2708	768	768	9.2	91
Average	6.40	70	48	221	406	1203	2476	113	120	10.6	53
Std Dev	0.08	70	76	198	294	650	471	166	158	4.4	20
C.o. of Var.	1.25	330	159	86	63	54	19	143	126	41.2	27
BT14	7.21	76	88	988	1334	3291	7052	276	280	5.4	88
BT4	7.04	29	29	420	678	1172	1627	300	315	6.8	66
BT25	7.09	0	0	278	431	868	1302	83	83	9.0	40
BT6	7.19	0	0	625	1108	1932	2643	138	253	6.0	95
Average	7.13	26	29	360	918	1493	2251	204	279	6.2	76
Std Dev	0.08	36	40	315	430	656	918	102	104	0.8	15
C.o. of Var.	1.16	137	141	54	48	44	40	20	42	13.6	20
BT16	7.27	0	0	551	990	1506	1817	296	315	6.5	70
BT22	7.49	1	1	763	706	1290	2252	127	127	6.2	83
BT20	7.60	0	0	244	430	840	1604	179	186	9.0	38
BT13	7.83	0	0	130	642	1111	1779	86	86	10.4	31
Average	7.27	1	1	320	795	1167	1869	172	179	8.0	73
Std Dev	0.12	2	2	79	110	282	322	91	100	2.0	12
C.o. of Var.	1.61	200	200	18	18	24	17	53	56	25.2	56
BT2								728	543	7.9	129
BT11								294	508	9.9	133
BT12								375	432	11.0	136
BT17								205	227	11.9	107
BT23								276	420	6.0	135
Average								335	424	8.5	130
Std Dev								123	123	3.6	13
C.o. of Var.								37	29	27.0	60
BT14								502	508	6.6	135
BT9								315	615	7.2	137
BT4								431	492	9.9	135
BT30											135
BT19											136
Average								480	578	8.8	135
Std Dev								54	76	1.4	1
C.o. of Var.								7	13	15.8	1

Mode of damage	Threshold TIE (J)	Threshold Force (KN)	Interactions
UD transverse matrix cracking	< 2.3	< 0.6	
Lower CFM crack	≈ 5.4	≈ 0.83	
Upper interface del.	≈ 5.4	≈ 0.83	initiated by lower CFM crack
Creasing	≈ 8	≈ 0.92	

Table AV.11 Damage thresholds and interactions for the transverse coupon.

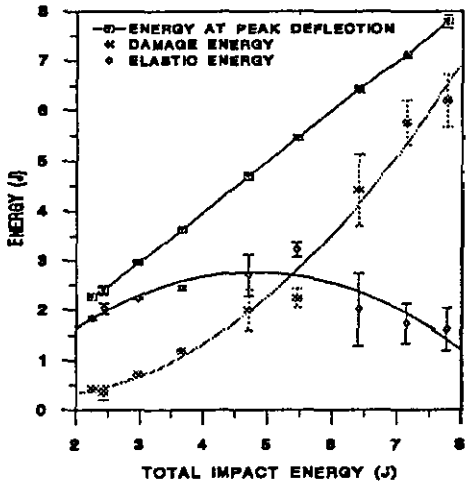


(a)

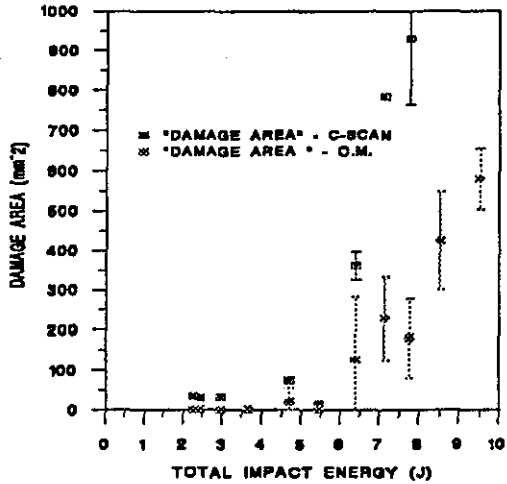


(b)

Figure AV.1 Deflection (a) and temporal data (b) versus TIE for the transverse coupon.



(a)



(b)

Figure AV.2 Energy data and "Damage areas" versus TIE for the transverse coupon.

Table AV.12 Longitudinal Coupon Impact Test Results.

Specimen	Specimen Thickness (mm)	Impact Energy (J)	Impact Velocity (m/s)	Peak Force (N)	Defl. at Peak Force (mm)	Energy at Peak Force (J)	Damage Energy (J)	Elastic Energy (J)	Peak Defl. (mm)	Energy at Peak Defl. (J)	Total Impact Energy (J)	Time to Peak Force (ms)	Time to Peak Defl. (ms)	Contact Time (ms)	Initial Stiffness (kN/mm)	1c Stiffness (kN/mm)	1d Stiffness (kN/mm)	1e Stiffness (kN/mm)
IC47	3.53	1.96	0.60	0.817	4.525	2.66	0.20	2.47	4.544	2.67	2.65	15.3	16.2	37.8	0.124	0.100	0.103	0.115
IC48	3.55	2.09	0.62	0.845	4.587	2.79	0.36	2.44	4.596	2.80	2.79	15.3	15.8	31.9	0.130	0.105	0.108	0.115
IC49	3.64	2.02	0.61	0.840	4.356	2.68	0.13	2.55	4.358	2.68	2.70	15.3	15.6	31.9	0.133	0.106	0.111	0.116
IC50	3.50	1.96	0.60	0.810	4.475	2.64	0.34	2.32	4.500	2.66	2.66	15.2	16.1	32.5	0.128	0.102	0.104	0.117
IC51	3.48	1.96	0.60	0.795	4.684	2.67	0.29	2.40	4.700	2.69	2.67	15.8	16.6	33.7	0.121	0.095	0.098	0.108
IC52																		
Average	3.54	2.00	0.61	0.82	4.53	2.69	0.26	2.44	4.540	2.70	2.69	15.38	16.06	32.56		0.10	0.10	0.11
Std Dev	0.05	0.06	0.01	0.02	0.12	0.06	0.10	0.09	0.126	0.06	0.06	0.24	0.38	0.75		0.00	0.00	0.00
Co. of Var.	1.75	2.97	1.48	2.55	1.88	2.19	36.78	3.49	1.976	2.11	2.18	1.55	2.40	2.29		4.50	4.76	3.02
IC17	3.55	3.06	0.75	0.901														
IC61	3.56	3.06	0.75	0.921	8.348	3.86	0.89	3.04	8.434	3.93	3.96	15.4	16.9	34.0	0.107	0.093		0.114
IC56	3.56	3.06	0.75	0.980	7.797	3.82	0.93	2.96	7.873	3.89	3.90	14.4	15.8	31.3	0.124	0.110		0.100
IC63	3.52	3.06	0.75	0.997														
IC59	3.57	3.14	0.76	0.960	8.158	3.93	1.00	2.98	8.211	3.98	4.01	15.1	16.3	32.4	0.118	0.103		0.118
IC62	3.57	2.98	0.74	0.975	7.802	3.75	0.88	2.94	7.870	3.82	3.82	14.6	15.9	31.4	0.126	0.109		0.126
Average	3.56	3.06	0.76	0.96	8.03	3.84	0.93	2.98	8.097	3.91	3.92	14.88	16.23	32.28		0.10		0.12
Std Dev	0.02	0.05	0.01	0.03	0.27	0.08	0.05	0.04	0.276	0.07	0.09	0.46	0.50	1.25		0.01		0.01
Co. of Var.	0.53	1.69	0.84	3.32	3.40	1.96	5.89	1.45	3.407	1.73	2.17	3.07	3.08	3.88		7.50		6.12
IC26	3.53	4.52	0.91	1.09	8.995	5.35	1.53	3.97	9.139	5.50	5.50	14.0	15.8	32.3	0.134	0.103	0.108	0.137
IC21	3.53	4.23	0.88	1.05	8.866	5.08	1.78	3.42	8.974	5.20	5.19	14.4	16.0	32.1	0.129	0.105	0.105	0.130
IC16	3.49	4.52	0.91	1.07	9.137	5.36	1.51	3.99	9.288	5.50	5.52	14.3	16.0	32.8	0.133	0.100	0.105	0.132
IC14	3.55	4.43	0.90	1.13	8.592	5.31	1.45	3.93	8.665	5.38	5.35	13.9	15.1	30.7	0.145	0.114	0.118	0.139
IC29	3.56	4.33	0.89	1.10	8.705	5.21	1.39	3.91	8.783	5.30	5.27	14.1	15.4	31.4	0.137	0.109	0.114	0.135
Average	3.53	4.41	0.90	1.09	8.86	5.26	1.53	3.84	8.966	5.38	5.37	14.14	15.66	31.86		0.11	0.11	0.13
Std Dev	0.03	0.13	0.01	0.03	0.22	0.12	0.15	0.24	0.248	0.13	0.14	0.21	0.40	0.82		0.01	0.01	0.00
Co. of Var.	0.76	2.90	1.45	2.79	2.47	2.24	9.73	6.22	2.762	2.42	2.66	1.47	2.54	2.57		5.22	5.16	2.92
IC55	3.53	7.10	1.14	1.29	12.400	8.27	3.19	5.27	12.610	8.46	8.45	15.2	16.9	33.2	0.107	0.098	0.094	0.117
IC60	3.55	6.98	1.13	1.32	11.838	8.03	3.57	4.70	12.027	8.27	8.26	14.4	16.3	31.8	0.116	0.107	0.101	0.130
IC58	3.56	6.98	1.13	1.29														
IC54	3.56	7.10	1.14	1.27	12.144	7.86	3.77	4.63	12.580	8.40	8.45	14.1	17.0	32.9	0.107	0.100	0.093	0.135
IC57	3.57	6.85	1.12	1.29	10.349	7.57	2.89	5.00	10.603	7.89	7.99	13.0	15.3	31.0	0.144	0.112		0.159
IC56	3.57	6.85	1.12	1.30	11.653	7.75	3.59	4.73	12.096	8.32	8.15	13.5	16.4	31.9	0.115	0.106	0.100	0.148
Average	3.56	6.98	1.13	1.29	11.69	7.90	3.40	4.87	11.984	8.27	8.26	14.04	16.36	32.16		0.125	0.10	0.10
Std Dev	0.02	0.11	0.01	0.02	0.81	0.27	0.36	0.27	0.817	0.22	0.30	0.84	0.68	0.89		0.01	0.01	0.00
Co. of Var.	0.43	1.58	0.79	1.26	6.92	3.39	10.46	5.47	6.817	2.70	2.40	6.01	4.13	2.77		9.20	5.55	4.22
IC9	3.63	8.95	1.28	1.47	13.581	10.33	4.43	5.96	13.821	10.39	10.41	15.6	16.5	31.9		0.105	0.099	0.111
IC31	3.47	8.95	1.28	1.42	12.793	10.12	4.51	5.84	12.956	10.35	10.34	14.4	16.1	32.3		0.103	0.104	0.130
IC25	3.44	9.38	1.31	1.52	13.697	10.17	4.21	6.73	14.217	10.94	10.90	13.7	16.6	32.9		0.100		0.143
IC13	3.55	8.95	1.28	1.47	11.708	9.06	4.66	5.70	12.608	10.36	10.30	11.7	15.5	30.7		0.114	0.112	0.197
IC33	3.56	9.52	1.32	1.50	14.372	10.91	3.92	7.11	14.655	11.03	11.07	15.6	16.7	32.8		0.100	0.097	0.111
Average	3.53	9.15	1.29	1.48	13.23	10.12	4.35	6.27	13.571	10.61	10.60	14.20	16.28	32.12		0.10	0.10	0.14
Std Dev	0.08	0.28	0.02	0.04	1.02	0.67	0.29	0.62	0.792	0.34	0.35	1.62	0.49	0.89		0.01	0.01	0.04
Co. of Var.	2.15	3.02	1.51	2.56	7.70	6.62	6.63	9.84	5.833	3.21	3.34	11.39	3.02	2.77		5.72	6.68	25.67
IC7	3.63	14.34	1.62	1.87	16.304	16.14	6.15	10.00	16.308	16.15	16.09	15.5	15.8	31.1				
IC10	3.47	14.51	1.63	1.65	17.537	15.55	7.08	9.38	18.092	16.46	16.45	14.6	17.5	34.9				
IC6	3.55	14.51	1.63	1.80														
IC35	3.53	14.51	1.63	1.73	17.145	15.56	6.53	9.83	17.608	16.36	16.40	14.4	16.9	33.7				
IC45	3.46	14.51	1.63	1.66	18.228	15.04	7.09	9.41	18.568	16.50	16.50	15.6	17.9	35.4				
Average	3.53	14.48	1.63	1.74	17.07	15.80	6.71	9.66	17.644	16.37	16.36	15.00	17.03	33.78				
Std Dev	0.07	0.08	0.00	0.09	0.80	0.29	0.46	0.31	0.973	0.16	0.19	0.61	0.91	1.92				
Co. of Var.	1.95	0.56	0.27	5.38	4.64	1.85	6.81	3.19	5.515	0.96	1.15	4.08	5.37	5.69				
IC3	3.60	19.31	1.88	2.05	16.175	19.87	9.69	11.32	16.750	21.01	21.10	12.2	15.8	31.2				
IC40	3.47	19.31	1.88	1.88														
IC1	3.49	19.31	1.88	1.95														
IC8	3.56	19.51	1.89	1.92														
IC2	3.57	19.72	1.90	1.95	19.570	21.06	9.98	11.85	19.981	21.84	21.86	14.5	17.9	33.5				
Average	3.54	19.43	1.89	1.95	17.87	20.46	9.84	11.59	18.366	21.43	21.48	13.35	16.85	32.35				
Std Dev	0.06	0.18	0.01	0.06	2.40	0.83	0.21	0.38	2.385	0.59	0.54	1.63	1.48	1.63				
Co. of Var.	1.57	0.95	0.47	3.22	13.43	4.08	2.09	3.29	12.449	2.74	2.50	12.18	8.81	5.03				
IC30	3.61	24.32	2.11	2.07	21.786	24.90	12.80	13.96	22.747	26.76	26.76	14.0	17.4	35.1				
IC32	3.44	24.32	2.11	1.97	22.192	24.14	14.41	12.46	23.734	26.87	26.87	13.8	18.5	37.9				
IC46	3.48	24.32	2.11	1.82														
IC11	3.55	24.55	2.12	2.05	22.657	26.03	13.63	13.31	23.113	26.94	27.03	15.2	17.5	35.6				
IC27	3.54	24.32	2.11	2.16	21.544	25.57	12.10	14.72	22.127	26.82	26.69	14.1	16.7	31.5				
Average	3.52	24.37	2.11	2.01	22.04	25.16	13.24	13.61	22.930	26.85	26.84	14.28	17.53	35.53				
Std Dev	0.07	0.10	0.00	0.13	0.49	0.82	1.00	0.96	0.673	0.08	0.15	0.63	0.74	1.82				
Co. of Var.	1.87	0.42	0.21	6.35	2.21	3.27	7.57	7.05	2.934	0.28	0.55	4.41	4.23	5.12				
IC37	3.64	29.66	2.33	2.42	22.694	30.22	18.56	13.56	23.613	32.12	32.19	13.5	16.8	34.9				
IC12	3.64	29.66	2.33	1.95	22.915	24.51	18.40	14.21	27.890	32.61	32.65	11.9	20.4	41.2				
IC73	3.28	29.66	2.33	1.68	21.072	18.94	25.99	7.07	31.844	33.06	33.07	10.2	26.3	61.4				
IC42	3.51	29.66	2.33	2.26	22.904	28.55	17.15	15.13	24.780	32.28	32.31	12.8	17.5	35.9				
IC5	3.49	29.66	2.33	1.79														
Average	3.51	29.66	2.33	2.02	22.40	25.56	20.03	12.49	27.032	32.52	32.56	12.10	20.90	40.85				
Std Dev	0.15	0.00	0.00	0.31	0.89	5.02	4.03	3.67	3.681	0.42	0.39	1.43	4.02	7.56				
Co. of Var.	4.20	0.00	0.00	15.48	3.99	19.64	20.11	29.39	13.618									

Table AV.13 Longitudinal Coupon Damage Analysis Results.

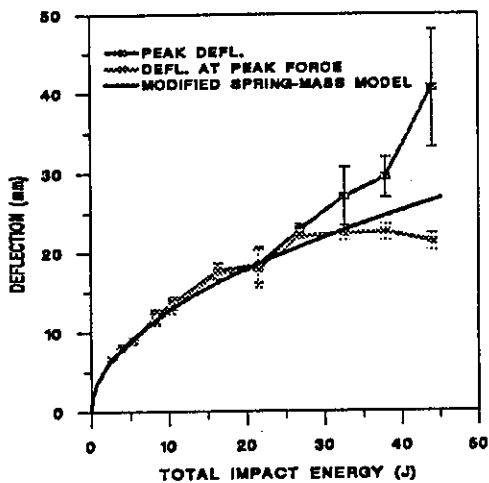
Specimen	Total Impact Energy (J)	C-scan contours - "Damage Area"						Optical Microscopy - Delamination Areas					Matrix Crack Spacing (mm)	Permanent Indent. (mm)	Lower CRM crack (mm)	Taper crack (mm)	Taper-line crack (mm)
		24dB Area (mm ²)	41F Area (mm ²)	+20dB Area (mm ²)	+16dB Area (mm ²)	+12dB Area (mm ²)	+8dB Area (mm ²)	Upper Av. (mm ²)	Central Lower Av. (mm ²)	Side Lower Av. (mm ²)	Total Delam. (mm ²)	Damage Area Av. (mm ²)					
IC47	2.65	0	0	0	0	0	0	0.00	0.00	0.00	0.00	0.00	6.8	0	0	0	0
IC48	2.79	0	0	0	0	0	0	0.00	0.00	0.00	0.00	0.00	6.1	0	0	0	0
IC49	2.70	0	0	0	0	0	0	0.00	0.00	0.00	0.00	0.00	6.9	0	0	0	0
IC50	2.66	0	0	0	0	0	0										
IC51	2.67	0	0	0	0	0	0										
IC52																	
Average	2.69	0	0	0	0	0	0	0	0	0	0	0	6.6	0.0	0.0	0.0	0.0
Std Dev	0.06	0	0	0	0	0	0	0	0	0	0	0	0.4	0.0	0.0	0.0	0.0
Co. of Var.	2.18												6.6				
IC17		0	0	0	0	0	0	0.00	0.00	0.00	0.00	0.00	5.9	0	0	0	0
IC61	3.96	0	0	0	0	0	0	0.00	0.00	0.00	0.00	0.00	4.9	0	0	0	0
IC56	3.90	0	0	0	0	0	0	0.00	0.00	0.00	0.00	0.00	5.8	0	0	0	0
IC63		0	0	0	0	0	0										
IC59	4.01	19	19	88	178	318	571										
IC62	3.82	0	0	0	65	403	758										
Average	3.92	3	3	15	44	120	221	0	0	0	0	0	5.5	0.0	0.0	0.0	0.0
Std Dev	0.09	8	8	36	74	188	348	0	0	0	0	0	0.6	0.0	0.0	0.0	0.0
Co. of Var.	2.17	245	245	245	169	167	157						10.0				
IC26	5.50	0	0	0	0	0	0	0.00	0.00	0.00	0.00	0.00	8.3	0	0	0	0
IC21	5.19	0	0	0	0	0	0	0.00	0.00	0.00	0.00	0.00	4.2	0	0	0	0
IC15	5.52	0	0	0	31	108	250	0.00	0.00	0.00	0.00	0.00	8.4	0	0	0	0
IC14	5.35	0	0	0	0	0	0	0.00	0.00	0.00	0.00	0.00		0	0	0	0
IC29	5.27	0	0	0	0	0	0										
Average	5.37	0	0	0	6	22	50	0	0	0	0	0	7.0	0.0	0.0	0.0	0.0
Std Dev	0.14	0	0	0	14	48	112	0	0	0	0	0	2.4	0.0	0.0	0.0	0.0
Co. of Var.	2.66				224	224	224						34.4				
IC55	8.45	0	0	16	64	204	374	0.00	0.00	0.00	0.00	0.00	5.8	0	2		
IC60	8.26	0	0	42	111	192	428	0.00	0.00	0.00	0.00	0.00	6.2	0	3		
IC58		0	0	26	76	218	519	0.00	0.00	0.00	0.00	0.00	5.1	0	3		
IC54	8.45	2	2	57	118	293	615							0	6		
IC57	7.99	0	0	16	66	178	558							0	3		
IC65	6.15	0	0	32	115	385	783							0	4		
Average	8.26	0	0	31	87	217	499	0	0	0	0	0	5.7	0.0	3.2		
Std Dev	0.20	1	1	18	26	45	97	0	0	0	0	0	0.6	0.0	1.1		
Co. of Var.	2.40	224	224	57	30	21	19						9.8		34.2		
IC9	10.41	0	0	0	0	7	20	42.00	0.00	0.00	42.00	42.00	5.8	0	5	0	0
IC31	10.34	0	0	0	0	0	0							0	8	0	0
IC25	10.90	0	0	0	0	0	0							0	16	0	0
IC13	10.30	0	0	0	0	0	38	0.00	0.00	0.00	0.00	0.00	7.5	0	10	0	0
IC33	11.07	0	0	0	0	0	0	0.00	0.00	0.00	0.00	0.00	16.8	0	8	0	0
Average	10.60	0	0	0	0	1	12	14	0	0	14	14	10.0	0.0	9.2	0.0	0.0
Std Dev	0.35	0	0	0	0	3	17	24	0	0	24	24	5.9	0.0	3.7	0.0	0.0
Co. of Var.	3.34					224	148	173			173	173	59.0		40.2		
IC7	16.09	0	0	10	41	124	330	18.50	55.00	0.00	73.50	55.00	5.2	0.1	13	0	0
IC10	16.45	0	0	16	33	84	147	35.63	47.63	0.00	83.26	65.63	4.2	0.05	16	0	0
IC6		0	0	7	40	93	158	24.38	18.75	0.00	43.13	37.50	4.5	0.1	12	0	0
IC35	16.40	0	0	0	0	6	117							0	15	0	0
IC45	16.50	0	0	0	18	73	131							0.05	26	0	0
Average	16.26	0	0	6	27	77	177	26	40	0	67	53	4.6	0.1	16.0	0.0	0.0
Std Dev	0.19	0	0	7	18	43	87	9	19	0	21	14	0.5	0.0	5.2	0.0	0.0
Co. of Var.	1.15			102	66	56	49	33	47	#DIV/0!	31	27	11.6	69.7	32.5		
IC3	21.10	89	89	221	371	597	963	18.00	29.50	199.50	247.00	233.50	7.5	0.2	20	0	10
IC40		42	42	97	186	272	411	0.00	96.00	212.50	308.50	308.50	9.5	0.15	25	10	17
IC1		156	156	303	394	529	685	0.00	361.50	402.00	763.50	763.50	13.2	0.15	30	12	16
IC8		0	0	14	72	182	416							0.16	16	0	0
IC2	21.66	0	0	8	33	71	146							0.1	15	0	8
Average	21.48	57	57	129	211	330	524	6	162	271	440	436	10.1	0.2	21.0	4.4	10.2
Std Dev	0.54	66	66	130	167	225	311	10	176	113	282	287	2.9	0.0	6.5	6.1	6.9
Co. of Var.	2.50	116	116	101	79	68	59	173	108	42	64	66	28.8	23.6	31.0	137.9	67.4
IC30	26.76	0	0	96	207	356	573							0.1	43	19	11
IC32	26.87	162	152	246	344	541	752							0.2	27	20	18
IC46		17	17	117	208	364	525	0.00	120.75	320.00	440.75	440.75	10.0	0.1	20	17	19
IC11	27.03	38	38	113	235	432	832	38.25	128.25	46.00	212.50	309.00	4.9	0.15	20	0	30
IC27	26.69	63	63	121	229	382	620	70.50	232.50	27.00	330.00	259.50	8.3	0.1	25	0	10
Average	26.84	54	54	139	243	416	660	36	161	131	328	336	7.8	0.1	27.0	11.2	17.6
Std Dev	0.15	60	60	60	58	76	128	35	62	164	114	94	2.6	0.0	9.5	10.3	8.0
Co. of Var.	0.55	111	111	43	24	18	19	97	39	125	35	28	33.5	34.4	35.0	91.8	45.6
IC37	32.19	367	367	599	831	1167	1507	22.00	345.00	815.00	1182.00	1160.00	8.9		25	41	40
IC12	32.65	212	212	470	712	1120	1848	43.25	90.00	617.50	650.75	650.75	5.5		24	28	19
IC23	33.07			2660				0.00	1167.50	1267.50	2425.00	2275.50			34	15	48
IC42	32.31	248	248	418	579	863	1114								35	21	19
IC5		1162	1162	1487	1812	2228	2663								28	21	44
Average	32.56	497	497	743	1319	1329	1783	22	534	863	1419	1362	7.2		29.2	26.2	34.0
Std Dev	0.39	448	448	501	894	620	659	22	563	372	911	831	2.4		5.1	10.0	14.0
Co. of Var.	1.21	90	90	67	68	47	37	99	105	43	64	61	33.4		17.4	39.5	41.1
IC38	37.85	493	493	1030	1342	1768	2193	0.00	1178.00	960.00	2138.00	2138.00	10.3		35	12	42
IC4	38.24	902	902	1209	1511	1909	2413				2179.00	2179.00			40	0	37
IC39	37.96	519	519	930	1263	1739	2220								45	38	32
IC41	37.79	2078	2078	2378	2635	2991	3313				3378.00	3378.00			40	26	36
IC28	37.66	1779	1779	2158	2432	2753	3097								41	20	35
Average	37.90	1194	1194	1541	1837	2232	2647	0	1178	960	2565	2565	10.3		40.2	19.0	36.4
Std Dev	0.22	692	692	676	647	594	522				704	704			3.6	14.2	3.6
Co. of Var.	0.58	58	58	44	35	27	20				27	27			8.9	74.8	10.0
IC36	43.01	144	144	431	844	1475	2561								55	50	29
IC20	43.01	1103	1103	1455	1704	2055	2468								40	70	32
IC22	44.55	2513	2513	2916	3259	3639	3964				4433.00	4433.00			33	10	43
IC44	44.64	2595	2595	2897	3146	3514	3911				3648.00	3648.00			37	26	40
IC43	44.46	640	640	1112	1548	2030	2634				4858.00	4858.00			44	26	42
Average	43.94	1399	1399	1792	2100	2543	3107				4313	4313			41.8	36.0	37.2
Std Dev	0.85	1108	1108	1108	105												

Specimen	TIE (J)	Width of UD fibre breakage (mm)
IC25	10.6	none
IC31	10.6	none
IC35	16.4	none
IC45	16.4	1
IC8	21.5	1
IC2	21.5	0
IC30	26.8	4
IC32	26.8	6
IC5	32.6	6
IC42	32.6	1.5
IC28	37.9	8
IC39	37.9	10
IC20	43.9	6
IC36	43.9	10

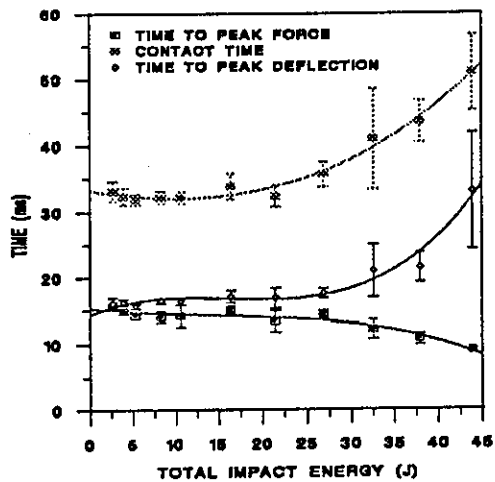
Table AV.14 Thermal Depley Results for the Longitudinal Coupon.

Mode of damage	Threshold TIE (J)	Threshold Force (KN)	Other (Interactions)
UD transverse matrix cracking	< 2.7	< 0.8	
Lower CFM crack (central)	5.4 - 8.3	1.1 - 1.3	
Taper crack	16.4 - 21.5	1.74 - 1.95	
Taper-line crack	16.4 - 21.5	1.74 - 1.95	
Lower i/f delamination (central)	16.4 - 21.5	1.74 - 1.95	initiated when lower CFM crack (central) = 15mm
Lower i/f delamination (side)	16.4 - 21.5	1.74 - 1.95	
Upper i/f delamination	≈ 16.4	≈ 1.74	
UD fibre breakage	≈ 16.4	≈ 1.74	
upper CFM compressive failure	≈ 21.5	≈ 1.95	
upper CFM permanent indentation	≈ 8.3	≈ 1.3	
Upper CFM shear cracking	≈ 32.6	≈ 2.0	

Table AV.15 Damage Thresholds and Interactions for the longitudinal Coupons.

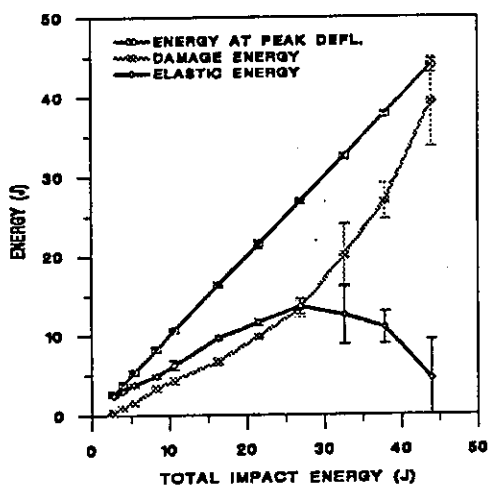


(a)

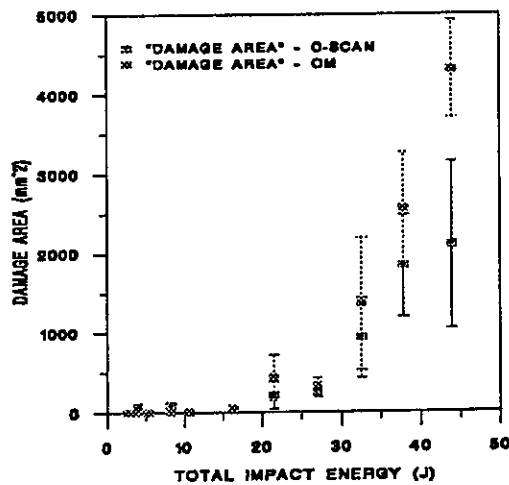


(b)

Figure AV.3 Deflection (a) and temporal data (b) versus TIE for the longitudinal coupon.



(a)



(b)

Figure AV.4 Energy data and "Damage areas" versus TIE for the longitudinal coupon.

Table AV.16 Central Impact Test Results from the Three-Box Section.

Specimen	Specimen Thickness (mm)	Impact Energy (J)	Impact Velocity (m/s)	Peak Force (kN)	Defl. of Peak Force (mm)	Energy at Peak Force (J)	Damage Energy (J)	Elastic Energy (J)	Peak Defl. (mm)	Energy at Peak Defl. (J)	Total Impact Energy (J)	Time to Peak Force (ms)	Time to Peak Defl. (ms)	Contact Time (ms)	Initial Stiffness (kN/mm)	1st Stiffness (kN/mm)	2nd Stiffness (kN/mm)	3rd Stiffness (kN/mm)
IT16A	3.46	1.29	0.49	0.92	3.600	1.66	0.17	1.63	3.65	1.69	1.68	9.20	11.30	23.00	0.261	0.21	0.20	0.31
IT27A	3.22	1.40	0.51	0.89	3.731	1.62	0.26	1.64	3.94	1.80	1.82	9.30	11.50	23.70	0.229	0.19	0.19	0.31
IT12A	3.46	1.46	0.52	0.92	3.908	1.66	0.31	1.66	4.06	1.87	1.88	9.20	11.90	23.70	0.229	0.19	0.19	0.31
IT26B	3.36	1.29	0.49	0.90														
IT21A	3.46	1.36	0.50	0.94														
IT21B	3.61	1.40	0.51	0.92	3.677	1.64	0.19	1.64	3.89	1.83	1.81	9.10	11.50	23.30	0.243	0.20	0.20	0.32
Average	3.40	1.36	0.50	0.91	3.680	1.62	0.23	1.67	3.88	1.80	1.80	9.20	11.66	23.43		0.20	0.19	0.31
Std Dev	0.13	0.07	0.01	0.02	0.130	0.04	0.06	0.06	0.17	0.08	0.09	0.08	0.30	0.34		0.01	0.01	0.01
Co. of Var.	3.81	4.81	2.41	1.83	3.520	2.49	27.74	3.36	4.38	4.29	4.79	0.89	2.58	1.45		6.19	2.93	1.78
IT37B	3.37	4.46	0.91	1.22	6.362	4.35	2.67	2.68	7.13	5.26	5.21	8.70	12.90	26.80	0.232	0.16	0.16	0.36
IT32A	3.30	4.56	0.92	1.18	7.477	5.33	2.60	2.73	7.48	5.33	5.35	13.20	13.20	26.70	0.227	0.16	0.16	0.16
IT37A	3.67	4.56	0.92	1.34	6.079	4.27	2.63	2.79	6.91	5.32	5.29	8.10	12.10	24.20	0.237	0.18	0.18	0.40
IT39B	3.47	4.56	0.92	1.56	6.229	4.51	2.44	2.82	6.90	5.26	5.28	8.70	12.10	24.20	0.224	0.18	0.18	0.36
IT39A	3.47	4.46	0.91	1.28	6.308	4.32	2.38	2.86	7.06	5.24	5.20	8.60	12.50	24.60	0.213	0.17	0.18	0.36
Average	3.44	4.52	0.92	1.28	6.499	4.56	2.52	2.76	7.10	5.28	5.27	9.46	12.56	25.10	0.233	0.17	0.17	0.32
Std Dev	0.10	0.06	0.01	0.08	0.562	0.44	0.12	0.11	0.24	0.04	0.06	2.11	0.49	1.11	0.01	0.01	0.01	0.10
Co. of Var.	3.02	1.19	0.60	6.01	8.661	9.70	4.64	3.96	3.32	0.79	1.12	22.26	3.88	4.42	6.78	7.67	8.64	30.37
IT30A	3.22	7.49	1.18	1.51	8.630	7.23	5.03	3.46	9.55	8.49	8.50	9.40	13.30	26.30		0.15	0.15	0.30
IT11A	3.67	7.37	1.17	1.72	7.787	7.76	4.47	3.73	8.07	8.20	8.22	9.30	11.40	22.40		0.20	0.21	0.31
IT13A	3.40	7.37	1.17	1.57	8.378	7.25	5.00	3.31	9.17	8.31	8.34	9.30	13.10	26.20		0.16	0.16	0.31
IT16A	3.46	7.37	1.17	1.51	8.594	7.50	4.87	3.42	9.17	8.29	8.34	9.80	13.00	26.50		0.16	0.16	0.28
IT28B	3.33	7.37	1.17	1.51	8.502	6.92	4.81	3.57	9.64	8.38	8.38	9.10	13.40	26.00		0.16	0.16	0.32
Average	3.42	7.39	1.17	1.56	8.378	7.33	4.84	3.50	9.10	8.33	8.35	9.38	12.94	26.28		0.16	0.17	0.30
Std Dev	0.17	0.06	0.03	0.09	0.346	0.31	0.22	0.16	0.61	0.11	0.10	0.26	0.82	1.64		0.02	0.02	0.02
Co. of Var.	4.88	0.77	0.58	5.82	4.112	4.26	4.63	4.56	6.67	1.30	1.22	2.76	6.39	6.48		14.42	14.67	5.36
IT23A	3.61	15.66	1.70	2.29	10.499	14.01	10.11	6.66	11.76	16.77	16.80	7.90	11.50	22.70				
IT34A	3.38	15.19	1.68	1.86	12.712	14.56	10.63	6.11	14.04	16.74	16.67	9.90	11.40	22.40				
IT30B	3.36	16.19	1.68	1.96	12.366	13.66	10.24	6.50	14.10	16.74	16.68	9.30	14.00	28.10				
IT13B	3.46	16.11	1.73	1.94	13.419	15.86	10.86	6.81	14.39	17.67	17.63	10.40	13.90	27.40				
IT28B	3.25	16.30	1.74	1.95	13.189	14.95	11.35	6.30	14.76	17.65	17.85	9.70	14.20	28.60				
Average	3.41	15.67	1.71	2.00	12.437	14.66	10.64	6.48	13.81	17.11	17.13	9.44	13.54	27.04				
Std Dev	0.13	0.51	0.03	0.17	1.158	0.89	0.50	0.28	1.18	0.60	0.57	0.95	1.16	2.47				
Co. of Var.	3.90	3.28	1.64	8.39	9.313	6.11	4.68	4.31	8.67	2.91	3.32	10.04	8.46	9.13				
IT22B	3.58	19.64	1.91	2.00	13.451	16.86	14.82	6.44	15.75	21.26	21.30	8.90	14.20	27.90				
IT49A	3.53	19.84	1.92	2.06	14.202	17.59	15.24	6.41	16.31	21.66	21.56	9.40	14.50	28.50				
IT36A	3.36	19.64	1.91	2.14	14.189	17.62	13.62	7.63	15.97	21.26	21.32	9.60	14.10	27.60				
IT46B	3.33	19.64	1.91	2.14	13.829	17.68	14.92	4.32	15.67	21.24	21.29	9.30	14.00	27.50				
IT48A	3.47	19.84	1.92	2.11	13.880	17.13	15.41	6.19	16.20	21.60	21.56	9.10	14.50	28.10				
Average	3.46	19.72	1.91	2.09	13.910	17.36	14.80	6.60	15.98	21.40	21.41	9.26	14.26	27.92				
Std Dev	0.11	0.11	0.01	0.06	0.309	0.36	0.70	0.69	0.28	0.21	0.14	0.27	0.23	0.40				
Co. of Var.	3.18	0.67	0.29	2.87	2.219	2.00	4.74	8.87	1.74	0.96	0.66	2.92	1.61	1.44				
IT12B	3.46	24.19	2.12	2.04	15.831	20.16	26.60					9.30						
IT15B	3.46	24.66	2.14	2.03	11.206	12.37	21.70	4.96	19.23	26.66	26.68	5.80	16.50	31.80				
IT28A	3.22	24.66	2.14	1.92	15.408	19.34	23.94	2.90	20.91	26.87	26.86	8.80	20.00	40.10				
IT18A	3.66	24.66	2.14	2.21	16.355	23.43	21.94	4.51	17.90	26.46	26.54	10.40	15.00	30.60				
IT27B	3.32	24.42	2.13	2.01	11.192	12.15	20.69	5.79	18.99	26.48	26.43	5.80	16.00	30.60				
Average	3.42	24.61	2.13	2.04	13.998	17.49	22.95	4.56	19.26	26.61	26.63	8.02	16.88	33.28				
Std Dev	0.16	0.21	0.01	0.11	2.577	5.01	2.31	1.20	1.24	0.19	0.19	2.11	2.17	4.59				
Co. of Var.	4.73	0.84	0.42	5.16	18.412	28.66	10.06	26.41	6.45	0.72	0.70	26.28	12.99	13.78				
IT31A	3.37	36.96	2.62	2.27	11.971	13.40			22.00		39.27	4.90						
IT11B	3.55	36.11	2.59	2.40	12.554	17.47			20.00		38.22	5.30						
IT14B	3.46	36.11	2.59	2.17	13.754	16.83			21.00		38.32	5.80						
IT16B	3.46	36.67	2.61	2.11	13.311	15.23			22.00		38.99	5.50						
IT34B	3.22	36.67	2.61	2.04	13.930	16.31			23.00		39.10	5.80						
Average	3.41	36.60	2.60	2.20	13.104	15.86			21.60		38.78	5.46						
Std Dev	0.12	0.38	0.01	0.14	0.827	1.60			1.14		0.48	0.38						
Co. of Var.	3.63	1.03	0.52	6.41	6.309	10.07			5.28		1.23	6.93						

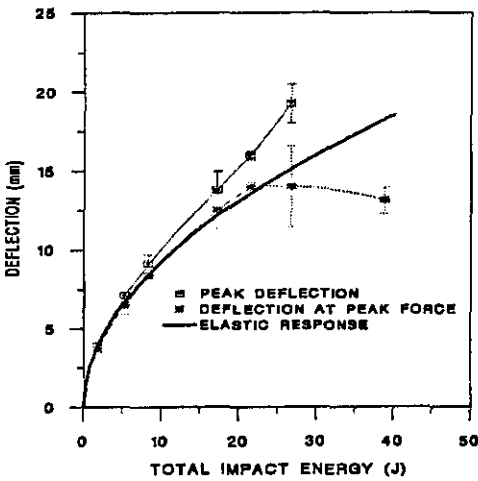
Table AV.17 Central Impact Damage Analysis Results from the Three-Box Section.

Specimen	Total Impact Energy (J)	C-Scan contours - "Damage Areas"						OM - "Delamination Areas"				Matrix Crack Spacing (mm)	Lower CFM Crack (mm)
		24dB Area (mm ²)	+1F Area (mm ²)	+20dB Area (mm ²)	+16dB Area (mm ²)	+12dB Area (mm ²)	+8dB Area (mm ²)	Upper Av. (mm ²)	Lower Av. (mm ²)	Total Av. (mm ²)	Damage Area (mm ²)		
IT15A	1.68	0	0	0	0	0	0	0	0	0	0	9.3	0
IT27A	1.82	0	0	0	0	0	0	0	0	0	0	0	0
IT12A	1.88	0	0	0	8	51	116	48	0	48	48	4.5	0
IT26B		0	0	0	7	40	87	0	0	0	0	0	0
IT21A		0	0	0	0	0	0	0	0	0	0	5.9	0
IT21B	1.81	0	0	0	0	0	0	0	0	0	0	0	0
Average	1.80	0	0	0	3	15	34	16	0	16	16	6.6	0
Std Dev	0.09	0	0	0	4	24	53	28	0	28	28	2.5	0
Co. of Var.	4.79				155	157	157	173		173	173	37.6	
IT37B	5.21	0	0	72	156	280	433						41
IT82A	5.35	0	0	0	25	207	337						42
IT37A	5.29	0	0	23	113	208	303	103	0	103	229	9.0	22
IT39B	5.28	0	0	63	162	273	472	85	0	85	156	5.3	25
IT39A	5.20	1	1	53	133	280	460	67	0	67	177	5.8	21
Average	5.27	0	0	42	118	249	401	85	0	85	187	6.7	30
Std Dev	0.06	0	0	30	55	39	76	18	0	18	37	2.0	10
Co. of Var.	1.12	224	224	71	47	16	19	21		21	20	30.0	35
IT30A	8.50	0	0	113	202	314	463	244	0	244	288	5.9	41
IT11A	8.22	3	3	222	332	467	588	160	0	160	380	-	32
IT13A	8.34	83	83	348	497	726	1003	244	30	274	372	4.7	50
IT16A	8.34	0	0	133	227	372	562						41
IT28B	8.38	0	0	172	286	410	564						40
Average	8.35	17	17	197	309	458	636	216	10	226	347	5.3	41
Std Dev	0.10	37	37	94	117	160	211	48	17	59	51	0.9	6
Co. of Var.	1.22	215	215	47	38	35	33	22	173	26	15	17.1	16
IT23A	16.80	17	17	276	438	631	918						35
IT34A	16.67	386	386	765	974	1208	1491	738	0	738	846	6.4	90
IT30B	16.68	0	0	601	849	1079	1334						87
IT13B	17.63	379	379	868	1076	1299	1526	1156	0	1156	1211	5.0	80
IT32B	17.85	472	472	912	1117	1314	1536	1158	0	1158	1266	7.1	85
Average	17.13	251	251	684	891	1106	1361	1017	0	1017	1108	6.1	75
Std Dev	0.57	224	224	258	274	282	261	242	0	242	228	1.1	23
Co. of Var.	3.32	89	89	38	31	25	19	24		24	21	17.4	30
IT82B	21.30	608	608	928	1168	1406	1649						85
IT49A	21.56	318	318	846	1145	1415	1645	1230	0	1230	1490	11.8	97
IT36A	21.32	128	128	518	744	1014	1282	938	0	938	1088	14.6	85
IT46B	21.29	704	704	1078	1339	1589	1850						91
IT48A	21.55	604	604	1004	1295	1579	1797					19.3	102
Average	21.41	472	472	875	1138	1400	1644	1084	0	1084	1289	15.2	92
Std Dev	0.14	241	241	217	235	233	222	206	0	206	284	3.8	7
Co. of Var.	0.65	51	51	25	21	17	14	19		19	22	24.9	8
IT12B		2372	2372	3992	4408	4819	5121	2940	660	3600	4040	4.3	168
IT15B	26.68	1043	1043	2193	2537	2929	3386	1970	248	2218	2635	6.3	128
IT28A	26.86	2185	2185	4172	4857	5823	6700	2580	640	3220	3450	5.7	157
IT18A	26.54	1010	1010	3135	3682	4255	4616						132
IT27B	26.43	660	664	2139	2511	2887	3237						136
Average	26.63	1454	1455	3126	3599	4143	4612	2497	516	3013	3375	5.4	144
Std Dev	0.19	771	770	960	1067	1259	1415	490	233	714	705	1.1	17
Co. of Var.	0.70	53	53	31	30	30	31	20	45	24	21	19.7	12
IT31A	39.27	6	6	3928	4373	4804	5152	2400	1240	3640	4180	5.9	190
IT11B	38.22	293	293	2089	2403	2744	3037	1370	1070	2440	2640	26.3	110
IT14B	38.32	0	0	3207	3685	4217	4603						150
IT16B	38.99	580	591	3168	3673	4298	4849						148
IT34B	39.10	1844	1844	4140	4556	4951	5345	1620	1760	3380	3610	8.9	163
Average	38.78	545	547	3306	3738	4203	4597	1797	1357	3153	3477	13.7	152
Std Dev	0.48	765	765	805	846	874	917	537	359	631	779	11.0	29
Co. of Var.	1.23	140	140	24	23	21	20	30	26	20	22	80.4	19

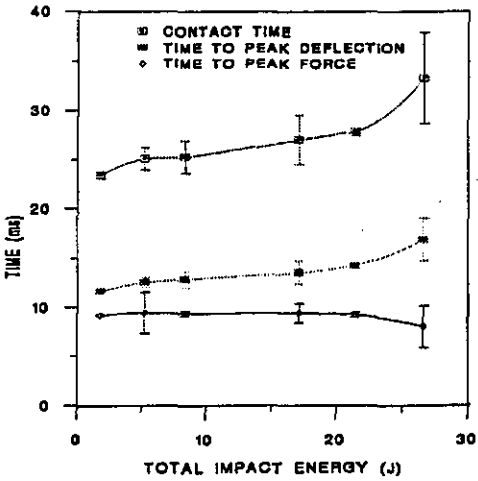
Specimen	TIE (J)	Lower CFM crack length (mm)	Upper CFM fibre breakage	UD fibre breakage
IT23A	17	30 (25)*	none	none
IT30B	17	80 (87)	v little	none
IT18A	27	120 (132)	a lot	none
IT27B	27	120 (136)	whole circle	none
IT16B	38	130 (148)	whole circle	8mm wide
IT14B	38	125 (150)	whole circle	3mm wide

* lower CFM crack length measured visually

Table AV.18 Thermal deply results for central impact tests from the three-box sections.



(a)



(b)

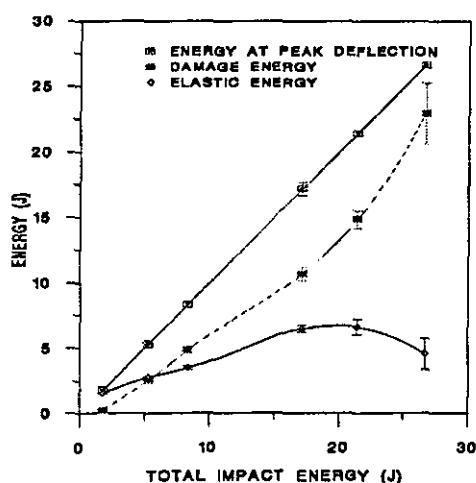
Figure AV.5 Deflection (a) and temporal data (b) versus TIE for central impacts from the three-box section.

Table AV.19 Intermediate Impact Test Results from the Three-Box Section

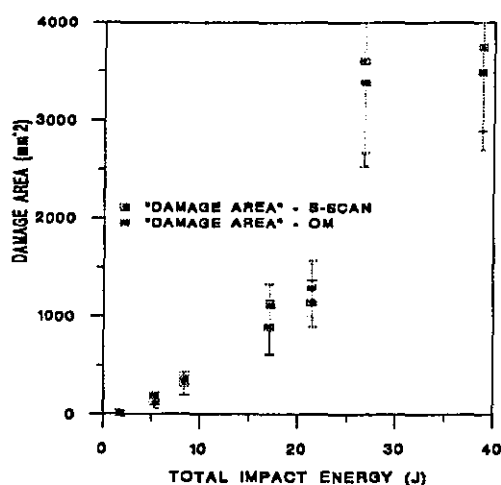
Specimen	Specimen Thickness (mm)	Impact Energy (J)	Impact Velocity (m/s)	Peak Force (N)	Defl. at Peak Force (mm)	Energy at Peak Force (J)	Damage Energy (J)	Elastic Energy (J)	Peak Defl (mm)	Energy at Peak Defl (J)	Total Impact Energy (J)	Time to Peak Force (ms)	Time to Peak Defl (ms)	Contact Time (ms)	Initial Stiffness (kN/mm)	Id Stiffness (kN/mm)	to Stiffness (kN/mm)	to Stiffness (kN/mm)
IT42B	3.37	1.40	0.61	1.01	3.340	1.69	0.20	1.67	3.43	1.77	1.76	8.80	10.30	21.10	0.297	0.26	0.24	0.34
IT43B	3.48	1.35	0.60	1.05	3.237	1.63	0.17	1.62	3.30	1.69	1.69	8.80	10.10	20.60	0.307	0.26	0.26	0.34
IT43A	3.44	1.46	0.62	1.02	3.507	1.78	0.25	1.57	3.55	1.82	1.83	9.40	10.40	21.10	0.296	0.26	0.24	0.30
IT53A	3.59	1.35	0.60	1.05	3.055	1.64	0.20	1.46	3.09	1.66	1.67	8.70	9.60	19.60	0.343	0.29	0.28	0.35
IT47A	3.43	1.40	0.61	1.06	3.237	1.71	0.22	1.53	3.28	1.75	1.75	8.80	9.90	20.40	0.318	0.27	0.26	0.34
Average	3.46	1.39	0.61	1.03	3.277	1.69	0.21	1.63	3.33	1.74	1.74	8.90	10.04	20.62		0.26	0.25	0.34
Std Dev	0.08	0.05	0.01	0.02	0.162	0.05	0.03	0.06	0.17	0.06	0.06	0.28	0.36	0.66		0.02	0.02	0.02
Co. of Var.	2.36	3.30	1.65	2.01	4.944	3.57	14.18	2.95	5.15	3.67	3.57	3.18	3.56	3.20		7.34	6.60	5.99
IT38B	3.38	4.46	0.91	1.48	5.962	4.85	2.34	2.79	6.15	5.13	5.11	9.10	10.90	21.60	0.286	0.22	0.23	0.32
IT52B	3.42	4.46	0.91	1.43	6.030	4.85	2.41	2.75	6.26	5.16	5.12	9.10	11.10	22.10	0.284	0.22	0.22	0.32
IT49B	3.35	4.46	0.91	1.42	6.384	4.93	2.48	2.72	6.58	5.20	5.15	9.70	11.60	23.00	0.251	0.20	0.20	0.28
IT50A	3.52	4.46	0.91	1.38	6.300	4.88	2.32	2.86	6.52	5.18	5.15	9.60	11.50	22.50	0.256	0.20	0.21	0.29
IT43B	3.55	4.46	0.91	1.40	6.305	5.05	2.29	2.88	6.40	5.17	5.13	10.00	11.30	22.10	0.258	0.21	0.22	0.27
Average	3.44	4.46	0.91	1.42	6.196	4.92	2.37	2.80	6.38	5.17	5.13	9.48	11.28	22.24	0.291	0.21	0.21	0.30
Std Dev	0.09	0.00	0.00	0.04	0.187	0.08	0.06	0.07	0.18	0.08	0.02	0.39	0.29	0.55	0.03	0.01	0.01	0.02
Co. of Var.	2.54	0.00	0.00	2.65	3.023	1.63	3.24	2.46	2.84	0.60	0.37	4.11	2.54	2.50	9.71	6.12	4.08	8.14
IT18B	3.52	8.41	1.25	1.93	8.254	8.73	6.31	2.98	8.55	9.29	9.31	9.20	11.30	21.90		0.21	0.22	0.31
IT22B	3.47	8.55	1.26	1.99	8.191	9.04	6.12	4.24	8.54	9.36	9.45	9.40	10.90	21.20		0.22	0.24	0.30
IT31B	3.33	8.28	1.24	1.83	8.608	8.88	5.45	3.77	8.79	9.22	9.20	10.00	11.60	22.40		0.20	0.21	0.27
IT24A	3.33	8.41	1.25	1.85	8.524	8.75	6.77	3.59	8.88	9.36	9.35	9.40	11.70	22.70		0.19	0.21	0.30
IT17B	3.45	8.41	1.25	1.88	8.400	8.85	5.28	4.01	8.64	9.29	9.32	9.50	11.30	21.90		0.21	0.22	0.29
Average	3.42	8.41	1.25	1.90	8.396	8.85	5.59	3.72	8.68	9.30	9.33	9.50	11.36	22.02		0.21	0.22	0.29
Std Dev	0.09	0.10	0.01	0.06	0.176	0.12	0.47	0.48	0.15	0.06	0.09	0.30	0.31	0.57		0.01	0.01	0.02
Co. of Var.	2.54	1.13	0.57	3.41	2.093	1.40	8.43	12.91	1.72	0.63	0.93	3.16	2.76	2.60		5.60	5.25	6.07
IT14A	3.53	16.48	1.75	2.14	12.308	16.55	11.97	5.97	12.98	17.94	17.85	9.80	12.60	25.20				
IT52A	3.36	16.86	1.77	2.17	12.447	16.28	11.81	6.43	13.42	18.24	18.28	9.50	12.80	25.20				
IT26A	3.36	16.86	1.77	2.25	11.918	16.84	11.93	6.33	12.59	18.26	18.19	9.30	12.10	23.80				
IT17A	3.46	16.86	1.77	2.14	11.974	16.69	12.39	5.76	12.70	18.15	18.20	9.40	12.40	24.90				
IT24B	3.37	17.05	1.78	2.04	12.804	15.58	12.65	5.85	14.24	18.51	18.54	9.40	13.50	26.40				
Average	3.42	16.83	1.77	2.15	12.290	16.41	12.15	6.07	13.18	18.22	18.22	9.48	12.68	25.14				
Std Dev	0.08	0.21	0.01	0.08	0.363	0.46	0.36	0.30	0.67	0.21	0.25	0.19	0.53	1.00				
Co. of Var.	2.24	1.24	0.62	3.66	2.955	2.79	2.95	4.89	5.10	1.13	1.38	2.03	4.15	3.97				
IT58A	3.35	20.05	1.93	1.98	8.530	8.99	17.55	4.09	15.45	21.65	21.68	4.80	14.60	27.30				
IT50A	3.30	20.26	1.94	2.17	12.518	18.01	16.45	5.29	14.34	21.74	21.77	8.40	13.00	26.40				
IT46A	3.57	20.26	1.94	2.25	8.787	9.69	15.61	6.15	14.55	21.76	21.79	5.00	13.00	26.40				
IT53B	3.47	20.26	1.94	2.32	13.285	19.56	15.97	5.74	14.32	21.71	21.77	9.40	12.90	25.10				
IT52A	3.50	20.05	1.93	2.21	13.259	18.77	15.49	6.18	14.70	21.67	21.60	9.10	13.20	25.60				
Average	3.44	20.17	1.94	2.19	11.278	16.00	16.22	5.49	14.67	21.71	21.72	7.34	13.34	25.75				
Std Dev	0.11	0.11	0.01	0.13	2.413	6.21	0.84	0.86	0.46	0.06	0.06	2.26	0.71	0.88				
Co. of Var.	3.22	0.57	0.28	5.85	21.394	34.69	5.17	15.71	3.16	0.21	0.37	30.75	5.34	3.41				
IT59A	3.40	27.98	2.28	2.31	10.550	13.18	25.17	4.90	18.90	30.07	29.98	5.10	15.40	30.70				
IT59B	3.46	27.98	2.28	2.35	10.878	13.78	22.89	7.27	18.34	29.95	29.92	5.30	14.40	29.70				
IT47B	3.54	27.98	2.28	2.52	9.814	12.63	24.20	6.55	17.90	29.76	29.87	4.70	14.40	27.70				
IT43A	3.29	27.74	2.27	2.10	10.430	11.51	24.67	8.24	19.95	29.91	29.84	5.00	16.10	30.40				
IT48B	3.52	27.74	2.27	2.37	9.872	11.83	20.22	9.48	17.83	29.70	29.62	4.70	13.70	28.00				
Average	3.45	27.88	2.28	2.33	10.309	12.59	23.39	6.49	18.59	29.88	29.85	4.95	14.80	29.30				
Std Dev	0.10	0.13	0.01	0.15	0.455	0.94	2.00	1.90	0.88	0.15	0.14	0.26	0.95	1.38				
Co. of Var.	2.97	0.48	0.24	6.49	4.425	7.44	8.55	29.34	4.71	0.50	0.45	5.25	6.39	4.70				
IT42A	3.56	37.51	2.64	2.39	11.678	16.01	39.92	-39.92	23.00		39.94	4.80						
IT53B	3.56	37.80	2.65	2.49	11.679	16.47	40.12	0.00	22.39	40.12		4.80	16.80	16.80				
IT50B	3.35	37.51	2.64	2.38	11.763	14.98	32.55	-32.55	20.00		39.63	4.80						
IT43A	3.33	37.80	2.65	2.18	11.574	14.87	34.07	-34.07	22.00		40.12	4.70						
IT45B	3.40	37.80	2.65	2.29	13.035	18.80	34.14	-34.14	20.00		39.91	5.50						
Average	3.44	37.68	2.65	2.35	11.945	16.23	36.16	-36.16	21.48	40.12	39.95	4.92	16.80	16.80				
Std Dev	0.11	0.16	0.01	0.12	0.612	1.59	3.58	16.98	1.39		0.21	0.33						
Co. of Var.	3.27	0.41	0.21	4.98	5.125	9.80	9.90	-56.79	6.49		0.53	6.65						

Table AV.20 Intermediate Impact Damage Analysis Results from the Three-Box Section.

Specimen	Total Impact Energy (J)	C-Scan contours - "Damage Area"						OM - Delamination Areas				Matrix Crack Spacing (mm)	Taper-line Crack (mm)	Lower CFM crack (mm)
		24dB Area (mm ²)	+1F Area (mm ²)	+20dB Area (mm ²)	+16dB Area (mm ²)	+12dB Area (mm ²)	+8dB Area (mm ²)	Upper Av. (mm ²)	Lower Av. (mm ²)	Total Av. (mm ²)	Damage Area (mm ²)			
IT42B	1.76	0	0	0	0	0	0						0	0
IT40B	1.69	0	0	0	0	0	0						0	0
IT40A	1.83	0	0	17	70	200	343	0	0	0	0	4.4	0	
IT53A	1.67	0	0	0	8	51	105	0	0	0	27	-	0	
IT47A	1.75	0	0	0	2	35	64	0	0	0	0	16.9	0	
Average	1.74	0	0	3	16	57	102	0	0	0	9	10.7	0	0
Std Dev	0.06	0	0	8	30	83	142	0	0	0	16	8.8	0	0
Co. of Var.	3.57			224	190	145	138				173	83.0		
IT38B	5.11	0	0	198	293	398	558						15	0
IT52B	5.12	0	0	46	132	239	388	75	0	75	162	10.8	20	
IT49B	5.15	0	0	113	240	379	524	192	0	192	280	7.8	20	
IT50A	5.15	0	0	377	552	795	939						25	0
IT43B	5.13	0	0	353	516	657	747	87	112	199	201	11.8	25	
Average	5.13	0	0	217	347	494	631	118	37	155	214	10.1	21	0
Std Dev	0.02	0	0	146	181	226	215	64	64	70	60	2.1	4	0
Co. of Var.	0.37			67	52	46	34	55	173	45	28	20.5	20	
IT18B	9.31												45	0
IT22B	9.45							332	83	415	608	4.6	30	
IT31B	9.20	0	0	861	1194	1773	2023	180	248	428	536	5.5	26	
IT24A	9.35	0	0	492	695	899	1210	445	38	483	555	6.7	47	
IT17B	9.32												42	0
Average	9.33	0	0	677	945	1336	1617	319	123	442	566	5.6	38	0
Std Dev	0.09	0	0	261	353	617	575	133	111	36	37	1.0	9	0
Co. of Var.	0.93			39	37	46	36	42	90	8	7	18.5	25	
IT14A	17.85	2	2	1264	1498	1745	1901	620	295	915	921	4.9	70	
IT32A	18.28	0	0	1822	2070	2342	2582	881	261	1141	1176	6.3	65	
IT26A	18.19	0	0	1647	1837	2049	2319	941	585	1526	1450	6.4	80	
IT17A	18.20	0	0	1835	2185	2727	3105						65	35
IT24B	18.56	0	0	2006	2268	2568	2842						140	40
Average	18.22	0	0	1715	1972	2286	2550	814	380	1194	1182	5.9	84	38
Std Dev	0.25	1	1	282	311	395	466	170	178	309	265	0.9	32	4
Co. of Var.	1.38	224	224	16	16	17	18	21	47	26	22	14.8	38	9
IT58A	21.68	0	0	2252	2564	2899	3313	1370	380	1750	2270	15.2	106	
IT56A	21.77												97	95
IT46A	21.79	0	0	2305	2694	3040	3272	1276	413	1689	2003	8.7	95	
IT53B	21.77	0	0	1875	2093	2333	2573						80	75
IT52A	21.60	0	0	2137	2541	2876	3150	1280	570	1850	2030	8.6	75	
Average	21.72	0	0	2142	2473	2787	3077	1309	454	1763	2101	10.8	90	85
Std Dev	0.08	0	0	192	262	311	343	53	102	82	147	3.8	12	14
Co. of Var.	0.37			9	11	11	11	4	22	5	7	34.9	14	17
IT59A	29.98	12	12	3207	3611	3975	4344	2570	810	3380	3470	9.5	135	
IT59B	29.92	774	774	2341	2644	2879	3083						115	85
IT47B	29.87	18	18	2897	3199	3597	3851						115	105
IT63A	29.84	1773	1773	2622	2993	3455	4008	2420	158	2578	3270	19.0	135	
IT48B	29.62	0	0	1993	2278	2618	2951	1280	810	2090	2070	12.4	80	
Average	29.85	515	515	2612	2945	3305	3647	2090	593	2683	2937	13.6	116	95
Std Dev	0.14	777	777	472	511	550	604	705	377	651	757	4.9	22	14
Co. of Var.	0.46	151	151	18	17	17	17	34	64	24	26	35.7	19	15
IT42A	39.94	65	65	4008	4357	4651	4902						150	115
IT63B	40.16	0	0	6428	6792	7184	7548						160	160
IT50B	39.63	0	0	4017	4413	4816	5163	2930	918	3848	4180	7.9	157	
IT43A	40.12	0	0	3262	3732	4179	4514	2550	620	3170	3460	12.3	145	
IT45B	39.91	13	19	3199	3527	3983	4356	2650	670	3320	3570	8.2	130	
Average	39.95	16	17	4183	4564	4963	5297	2710	736	3446	3737	9.5	148	138
Std Dev	0.21	28	28	1315	1303	1287	1298	197	159	356	388	2.5	12	32
Co. of Var.	0.53	181	167	31	29	26	25	7	22	10	10	26.0	8	23



(a)



(b)

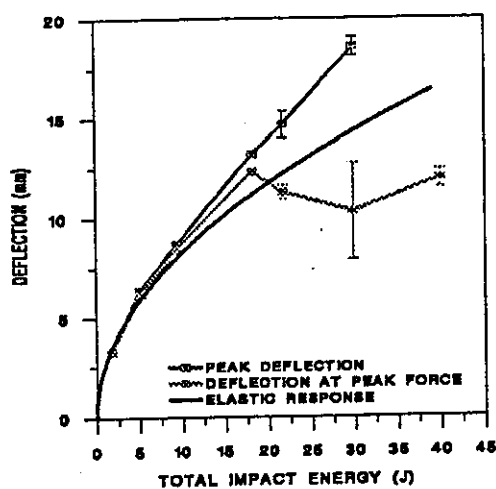
Figure AV.6 Energy data and "Damage areas" versus TIE for central impacts from the three-box section.

Specimen	TIE (J)	Taper-line crack length (mm)	Lower CFM crack length (mm)	Upper CFM fibre breakage	UD fibre breakage
IT40B	1.7	0 (0)	0	none	none
IT42B	1.7	2 (0)	0	"	"
IT38B	5.1	15 (15)	0	"	"
IT50A	5.1	25 (25)	0	"	"
IT17B	9.3	30 (42)	0	"	"
IT18B	9.3	45 (45)	0	"	"
IT24B	18.2	60 (140)	40	on web side	"
IT17A	18.2	-(65)	35	"	"
IT56A	21.7	-(97)	95	complete ring under impactor	"
IT53B	21.7	-(80)	75	"	"
IT47B	29.9	105 (115)	105	"	a little
IT59B	29.9	105 (115)	85	"	none
IT63B	40.2	-(160)	160	"	1-2mm
IT42A	40.2	130 (150)	115	"	4-5mm

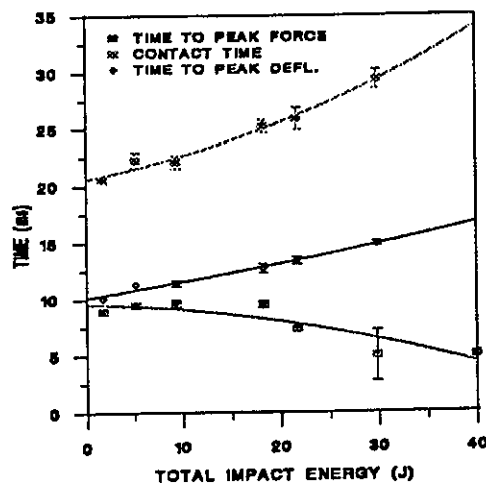
Table AV.21 Thermal depley results for intermediate impact tests.

Table AV.22 Web Impact Test Results from the Three-Box Section.

Specimen	Specimen Thickness (mm)	Impact Energy (J)	Impact Velocity (m/s)	Peak Force (N)	Defl. at Peak Force (mm)	Energy at Peak Force (J)	Damage Energy (J)	Elastic Energy (J)	Peak Defl (mm)	Energy at Peak Defl (J)	Total Impact Energy (J)	Time to Peak Force (ms)	Time to Peak Defl (ms)	Contact Time (ms)	Initial Stiffness (kN/mm)	1d Stiffness (kN/mm)	10 Stiffness (kN/mm)	1p Stiffness (kN)
I161A	3.31	4.46	0.91	2.24	4.329	4.87	1.66	3.24	4.343	4.90	4.92	8.0	7.6	16.2	0.617	0.46	0.46	0.41
I160B	3.55	4.46	0.91	2.25	4.231	4.84	1.59	3.28	4.249	4.87	4.91	7.1	7.5	15.0	0.634	0.47	0.47	0.53
I161A	3.34	4.36	0.90	2.24	4.097	4.74	1.66	3.18	4.143	4.84	4.80	8.1	7.4	14.3	0.634	0.48	0.62	0.40
I119B	3.50	4.26	0.89	2.30	4.077	4.59	1.57	3.18	4.152	4.75	4.70	8.3	7.4	14.4	0.556	0.48	0.51	0.39
Average	3.43	4.38	0.90	2.26	4.184	4.76	1.62	3.22	4.222	4.84	4.83	7.9	7.5	14.7		0.48	0.49	0.43
Std Dev	0.12	0.09	0.01	0.03	0.12	0.13	0.05	0.05	0.09	0.06	0.10	0.6	0.1	0.4		0.01	0.03	0.06
Co. of Var.	3.44	2.12	1.06	1.27	2.84	2.65	2.90	1.62	2.23	1.34	2.09	6.7	1.3	3.0		2.54	5.99	14.72
I126B	3.36	8.41	1.25	2.74	8.921	8.93	4.16	4.88	5.961	9.04	9.04	8.3	7.8	14.2	0.479	0.44	0.53	0.39
I133B	3.33	8.41	1.25	2.68	8.201	8.83	4.24	4.82	6.291	9.06	9.07	7.2	8.1	15.9	0.467	0.40	0.42	0.61
I129B	3.54	8.55	1.26	2.85	8.926	9.09	4.16	5.02	5.956	9.18	9.17	8.2	7.7	15.4	0.509	0.45	0.45	0.39
I129A	3.46	8.41	1.25	2.78	8.900	8.94	4.17	4.89	5.944	9.06	9.04	8.3	7.7	15.4	0.504	0.45	0.45	0.39
I121	3.45	8.55	1.26	2.99	8.814	6.70	4.37	4.76	5.708	9.13	9.16	4.6	7.4	14.7	0.555	0.48	0.49	1.25
Average	3.43	8.46	1.25	2.81	8.752	8.50	4.22	4.87	5.972	9.09	9.09	7.3	7.7	15.1	0.516	0.44	0.47	0.59
Std Dev	0.09	0.07	0.01	0.12	0.539	1.01	0.09	0.10	0.208	0.06	0.06	1.6	0.3	0.7	0.03	0.03	0.04	0.38
Co. of Var.	2.52	0.87	0.44	4.24	9.549	11.88	2.14	1.99	3.479	0.65	0.69	21.7	3.2	4.4	6.43	6.47	9.03	64.34
I125B	3.47	16.86	1.77	3.59	6.512	12.36	10.13	7.68	8.218	17.81	17.73	4.4	7.9	16.2		0.43	0.46	1.37
I120B	3.47	16.67	1.76	3.53	7.097	12.83	9.10	8.64	8.557	17.64	17.58	4.9	8.1	16.9		0.40	0.42	1.11
I125A	3.34	16.86	1.77	3.48	6.872	11.39	9.78	8.09	9.002	17.87	17.81	4.5	8.6	16.6		0.37	0.39	1.31
I122A	3.53	16.48	1.75	3.60	6.813	11.72	9.07	8.29	8.507	17.36	17.38	4.6	8.1	16.4		0.40	0.39	1.25
I133A	3.35	16.86	1.77	3.58	6.971	12.42	9.55	8.20	8.579	17.76	17.77	4.7	8.1	16.2		0.40	0.40	1.20
Average	3.43	16.75	1.76	3.55	6.853	12.14	9.53	8.16	8.573	17.69	17.65	4.6	8.1	16.1		0.40	0.41	1.26
Std Dev	0.08	0.17	0.01	0.05	0.219	0.68	0.46	0.32	0.280	0.20	0.18	0.2	0.2	0.5		0.02	0.03	0.10
Co. of Var.	2.35	1.01	0.51	1.41	3.194	4.76	4.75	3.87	3.272	1.14	1.00	4.2	2.7	3.4		5.23	7.05	8.16
I164A	3.33	29.47	2.34	4.43	9.073	21.68	17.96	12.90	11.316	30.87	30.67	4.7	8.2	16.1				
I165B	3.56	29.47	2.34	4.23	11.867	30.90	17.75	13.20	11.876	30.94	30.73	8.3	8.6	17.1				
I171B	3.35	29.47	2.34	4.45	9.121	21.50	18.56	12.10	11.320	30.66	30.67	4.7	8.2	16.7				
I165A	3.48	29.47	2.34	4.52	9.034	21.60	19.43	11.20	11.270	30.64	30.66	4.7	8.3	16.7				
I180B	3.44	29.22	2.33	4.37	9.171	20.65	17.88	12.80	11.735	30.68	30.46	4.7	8.6	16.7				
Average	3.43	29.42	2.34	4.40	9.653	23.27	18.32	12.44	11.503	30.76	30.64	5.4	8.4	16.7				
Std Dev	0.09	0.11	0.00	0.11	1.239	4.29	0.69	0.80	0.281	0.14	0.10	1.6	0.2	0.4				
Co. of Var.	2.76	0.38	0.19	2.48	12.831	18.43	3.79	6.45	2.439	0.45	0.33	29.7	2.2	2.1				
I179A	3.45	39.53	2.71	4.81	13.621	40.76	24.68	16.30	13.708	41.17	40.98	7.9	8.6	17.2				
I172B	3.50	39.53	2.71	4.65	10.072	26.34	25.37	15.80	13.419	41.12	40.95	4.4	8.5	17.0				
I144B	3.49	39.53	2.71	4.88	10.749	29.91	25.88	15.20	13.263	41.09	40.93	4.9	8.5	16.6				
I178B	3.32	39.24	2.70	4.85	10.468	28.31	25.64	15.10	13.239	40.80	40.64	4.7	8.4	17.0				
I156A	3.40	39.24	2.70	4.77	11.098	29.50	23.80	17.00	13.667	40.82	40.68	5.0	8.6	18.7				
Average	3.43	39.41	2.71	4.79	11.206	30.96	26.08	15.88	13.459	41.00	40.83	5.4	8.5	17.3				
Std Dev	0.07	0.16	0.01	0.09	1.400	5.45	0.85	0.79	0.220	0.18	0.16	1.4	0.1	0.8				
Co. of Var.	2.15	0.40	0.20	1.87	12.492	18.24	3.37	4.99	1.635	0.43	0.40	26.5	1.0	4.7				
I164B	3.49	47.16	2.96	5.12	11.649	34.17	20.97	27.80	14.688	48.77	48.71	4.8	8.6	18.7				
I167B	3.40	47.48	2.97	4.77	12.190	33.34	23.43	25.88	15.701	49.31	49.14	4.9	9.0	19.8				
I160B	3.32	47.48	2.97	4.59	12.194	33.21	29.53	19.78	15.905	49.31	49.16	4.9	9.3	18.9				
I181B	3.56	48.77	3.01	5.13	15.264	49.95	23.49	26.84	15.378	50.53	50.39	8.0	8.7	18.2				
I177A	3.41	48.77	3.01	5.05	15.612	50.10	17.84	32.74	15.709	50.58	50.42	8.2	8.4	19.2				
Average	3.44	47.93	2.98	4.99	13.382	40.15	23.09	26.61	15.476	49.70	49.56	6.2	8.8	19.0				
Std Dev	0.09	0.77	0.02	0.24	1.894	9.02	4.30	4.64	0.479	0.81	0.79	1.8	0.4	0.6				
Co. of Var.	2.67	1.62	0.81	4.84	14.154	22.46	18.63	17.45	3.098	1.63	1.59	28.8	4.0	3.1				
I176B	3.38	68.22	3.56	5.21	18.892	66.95	30.02	40.11	19.514	70.13	70.28	7.9	9.5	21.0				
I173B	3.51	68.60	3.57	4.95	14.880	45.98	53.25	17.74	20.576	70.99	70.77	5.0	10.6	22.2				
I162B	3.33	68.98	3.58	4.80	12.130	37.19	57.15	13.83	20.101	70.98	71.11	3.9	10.5	20.6				
I169A	3.57	68.60	3.57	5.16	14.768	46.66	52.68	18.24	19.877	70.92	70.70	5.0	10.2	20.8				
I174B	3.38	68.60	3.57	5.14	19.722	68.89	41.63	29.31	20.128	70.94	70.73	8.5	9.9	21.2				
Average	3.43	68.40	3.57	5.05	16.078	53.13	46.95	23.85	20.039	70.79	70.72	6.1	10.2	21.2				
Std Dev	0.10	0.27	0.01	0.17	3.160	14.02	11.08	10.76	0.388	0.37	0.30	2.0	0.4	0.6				
Co. of Var.	2.95	0.40	0.20	3.40	19.652	26.39	23.61	45.14	1.936	0.52	0.42	33.3	4.1	2.9				

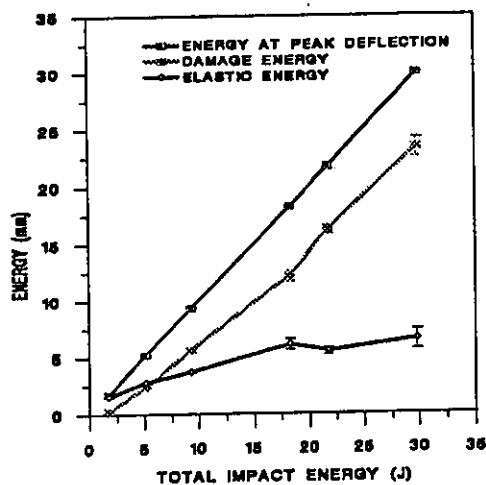


(a)

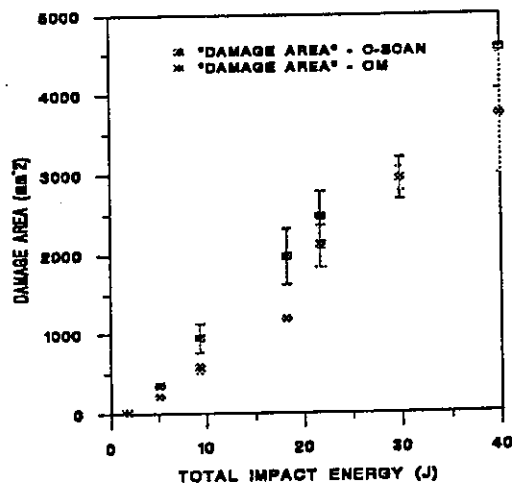


(b)

Figure AV.7 Deflection (a) and temporal data (b) versus TIE for intermediate impacts from the three-box section.



(a)



(b)

Figure AV.8 Energy data and "Damage areas" versus TIE for intermediate impacts from the three-box section.

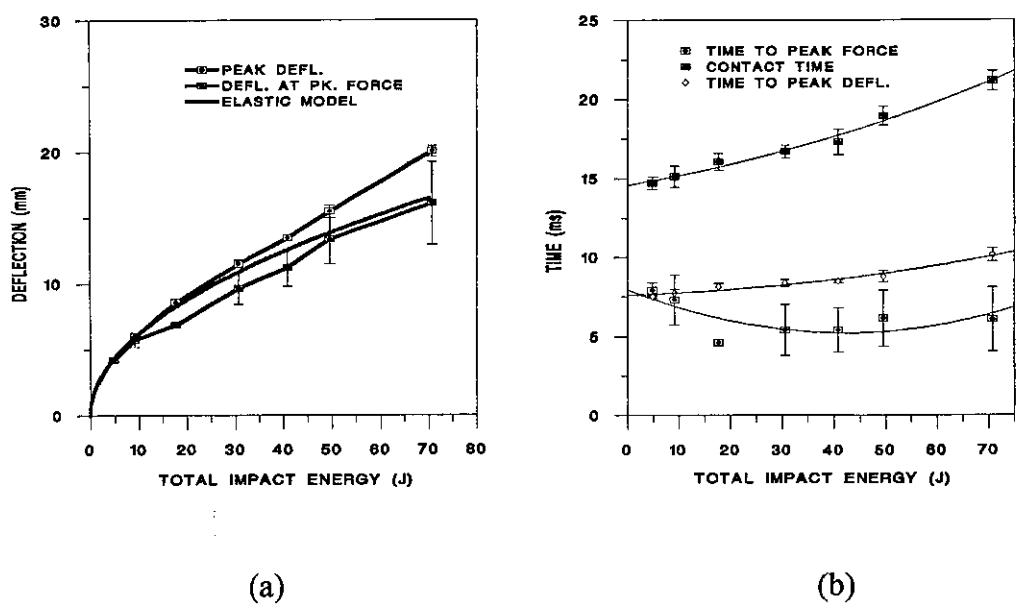


Figure AV.9 Deflection (a) and temporal data (b) versus TIE for web impacts from the three-box section.

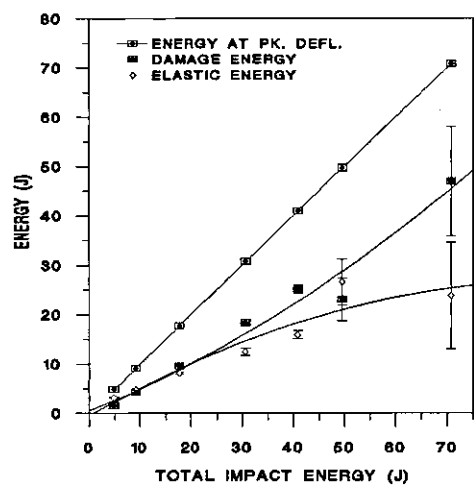


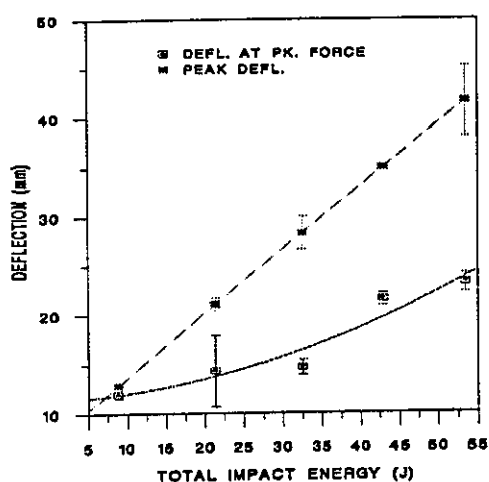
Figure AV.10 Energy data versus TIE for web impacts from the three-box section.

Table AV.23 Central Impact Test Results from the Five-Box Section

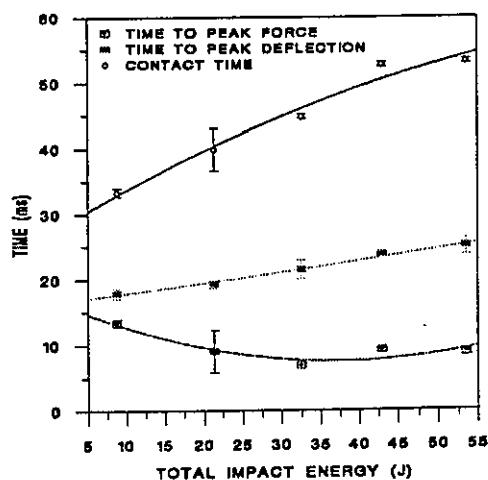
Specimen	Specimen Thickness (mm)	Impact Energy (J)	Impact Velocity (m/s)	Peak Force (N)	Defl at Peak Force (mm)	Energy at Peak Force (J)	Damage Energy (J)	Elastic Energy (J)	Peak Defl (mm)	Energy at Peak Defl (J)	Total Impact Energy (J)	Time to Peak Force (ms)	Time to Peak Defl (ms)	Contact Time (ms)	Inital Stiffness (kN)	Stiffness from tp (kN/mm)	Stiffness from td (kN/mm)	Stiffness from tc (kN)
IF5A	3.42	7.35	1.17	1.31	12.208	7.53	4.63	4.07	13.080	8.70	8.72	13.8	18.4	33.6		0.139	0.078	0.054
IF5B	3.41	7.47	1.18	1.46	11.655	7.69	2.43	6.34	12.518	8.77	8.79	12.9	17.3	33.0		0.159	0.098	0.097
IF4B	3.46	7.47	1.18	1.40														
Average	3.43	7.43	1.18	1.39	11.93	7.61	3.53	5.21	12.80	8.74	8.76	13.35	17.85	33.30		0.149	0.083	0.056
Std Dev	0.03	0.07	0.01	0.08	0.39	0.11	1.56	1.61	0.40	0.05	0.05	0.64	0.78	0.42		0.01	0.007	0.00
Co. of Var.	0.77	0.98	0.49	5.43	3.28	1.49	44.07	30.94	3.10	0.57	0.54	4.77	4.36	1.27		9.52	8.707	2.55
IF4A	3.43	19.17	1.89	1.59	13.066	9.74	9.26	12.19	21.800	21.45	21.47	7.7	20.0	42.3		0.448	0.066	0.059
IF8A	3.38	19.17	1.89	1.57	11.403	8.35	8.91	12.45	20.565	21.36	21.34	6.7	19.0	37.9		0.589	0.073	0.074
IF8B	3.48	19.97	1.89	1.76	18.347	17.53	8.31	12.87	20.745	21.18	21.15	12.7	19.0	39.1		0.164	0.073	0.069
Average	3.43	19.10	1.89	1.64	14.27	11.87	8.83	12.50	21.04	21.33	21.32	9.03	19.33	39.77		0.400	0.071	0.067
Std Dev	0.05	0.12	0.01	0.10	3.63	4.95	0.48	0.34	0.67	0.14	0.16	3.21	0.58	2.27		0.22	0.004	0.01
Co. of Var.	1.46	0.61	0.31	6.37	25.40	41.67	5.44	2.74	3.17	0.64	0.74	35.59	2.99	5.72		54.12	5.818	11.05
IT10A	3.22	29.64	2.35	1.96	14.070	12.03	16.32	16.19	28.025	32.51	32.59	6.6	21.3	43.7		0.607	0.059	0.055
IT10B	3.67	29.39	2.34	1.72	15.435	12.43	17.64	14.94	30.008	32.58	32.55	7.3	23.0	47.7		0.496	0.050	0.047
IT11B	3.43	29.64	2.35	2.03	14.305	12.55	15.99	16.45	26.689	32.44	32.45	6.7	20.2	42.9		0.589	0.065	0.058
Average	3.44	29.56	2.35	1.90	14.62	12.34	16.65	15.86	28.23	32.51	32.53	6.87	21.50	44.77		0.564	0.058	0.053
Std Dev	0.23	0.15	0.01	0.16	0.76	0.27	0.87	0.81	1.68	0.07	0.07	0.38	1.41	2.57		0.06	0.007	0.01
Co. of Var.	6.55	0.49	0.25	8.54	5.22	2.21	5.24	5.09	5.95	0.22	0.23	5.51	6.56	5.74		10.54	12.973	10.98
IF11A	3.44	39.13	2.70	1.92	21.089	21.47	23.93	18.78	34.848	42.71	42.79	8.9	23.5	50.2		0.334	0.048	0.042
IF24A	3.37	39.42	2.71	1.81	21.949	23.44	19.50	23.48	34.946	42.98	43.10	9.4	23.9	55.2		0.299	0.046	0.035
Average	3.41	39.27	2.71	1.87	21.52	22.46	21.72	21.13	34.90	42.95	42.95	9.15	23.70	52.70		0.317	0.047	0.038
Std Dev	0.05	0.21	0.01	0.08	0.61	1.39	3.13	3.32	0.07	0.19	0.21	0.35	0.28	3.54		0.02	0.001	0.01
Co. of Var.	1.45	0.52	0.26	4.17	2.93	6.20	14.43	15.73	0.20	0.45	0.50	3.86	1.19	6.71		7.72	2.387	13.38
IF12A	3.42	49.27	3.03	1.92	23.210	26.44	36.43	17.07	40.252	53.50	53.51	8.8	25.8	55.0		0.342	0.040	0.035
IF19B	3.48	48.95	3.02	2.06	22.206	24.90	31.88	21.00	38.862	52.98	53.04	8.3	24.0	50.8		0.384	0.046	0.041
IF30A	3.39	49.27	3.03	1.69	24.049	24.66	44.74	9.27	45.699	54.01	54.08	9.0		53.8		0.327		0.037
Average	3.43	49.17	3.03	1.89	23.16	25.33	37.68	15.78	41.59	53.46	53.55	8.70	24.90	53.20		0.361	0.043	0.038
Std Dev	0.05	0.19	0.01	0.19	0.92	0.97	6.52	5.97	3.59	0.57	0.52	0.36	1.27	2.16		0.03	0.004	0.00
Co. of Var.	1.47	0.38	0.19	9.88	3.99	3.81	17.30	37.84	8.63	1.06	0.97	4.14	5.11	4.07		8.49	10.210	8.33

Table AV.24 Central Impact Damage Analysis Results from the Five-Box Section.

Specimen	Total Impact Energy (J)	Crack contours - "Damage Area"						DM - "Delamination Areas"				Matrix Crack Spacing (mm)	Lower CFM Crack (mm)
		24dB Area (mm ²)	+1F Area (mm ²)	+20dB Area (mm ²)	+16dB Area (mm ²)	+12dB Area (mm ²)	+8dB Area (mm ²)	Lower Av. (mm ²)	Total Av. (mm ²)	Damage Area (mm ²)			
IF5A	8.72	0	0	0	36	34	167	0	0	70	3.3	0	
IF5B	8.73	0	0	37	79	153	270	0	24	96	5.2	0	
IF4B	0	0	0	31	73	159	237	0	0	48	7.0	0	
Average	8.76	0	0	23	63	132	224	0	8	61	7.4	0	
Std Dev	0.05	0	0	20	23	42	53	0	14	12	2.3	0	
Co. of Var.	0.54			88	37	31	24		173	19	31.9		
IF4A	21.47	1	1	94	207	374	551	0	72	264	7.1	43	
IF8A	21.34	0	0	43	93	176	297	0	125	250.5	6.8	50	
IF8B	21.15	8	8	101	174	309	504	0	66	213.5	6.2	30	
Average	21.32	3	3	80	158	286	450	0	88	243	6.7	41	
Std Dev	0.16	5	5	32	59	101	135	0	32	26	0.5	10	
Co. of Var.	0.74	136	136	40	37	35	30		37	11	7.1	25	
IT10A	32.59	122	122	584	861	1252	1826	0	157.5	630	4.3	70	
IT10B	32.55	44	44	167	275	403	505	0	295.5	375	5.5	71	
IT11B	32.45	343	343	782	1102	1511	2118	0	345.5	637.5	4.7	80	
Average	32.53	170	170	511	746	1055	1483	0	266	568	4.8	74	
Std Dev	0.07	155	155	314	426	580	859	0	97	170	0.6	6	
Co. of Var.	0.23	91	91	61	57	55	58		37	30	12.3	7	
IF11A	42.79	370	370	732	1028	1338	1600	0	607.5	810	7.6	55	
IF24A	43.10	82	82	291	530	775	933	0	195.5	335.5	6.0	120	
Average	42.95	226	226	512	779	1057	1267	0	402	573	6.8	88	
Std Dev	0.21	203	203	312	352	398	472	0	291	336	1.1	46	
Co. of Var.	0.59	90	90	61	45	38	37		73	58	16.6	53	
IF12A	53.51	663	663	1805	2403	3245	3990	0	1420	1560	5.0	195	
IF19B	53.04	214	214	663	862	1111	1450	0	720	1190	5.2	140	
IF30A	54.08	50	50	376	565	875	1212	0	472.5	652.5	6.8	100	
Average	53.55	309	309	948	1277	1744	2217	0	871	1134	5.7	145	
Std Dev	0.52	317	317	796	986	1306	1540	0	491	456	1.0	48	
Co. of Var.	0.97	103	103	80	77	75	69		56	40	18.1	33	

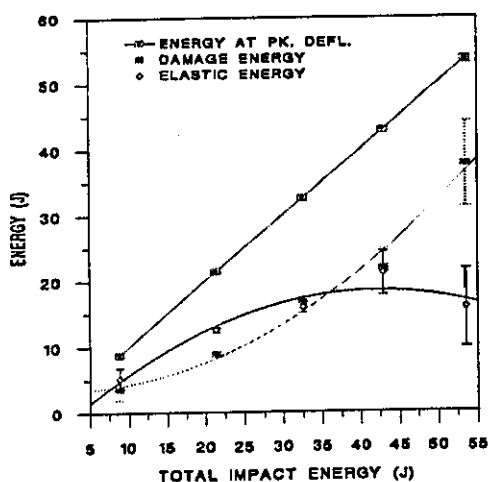


(a)

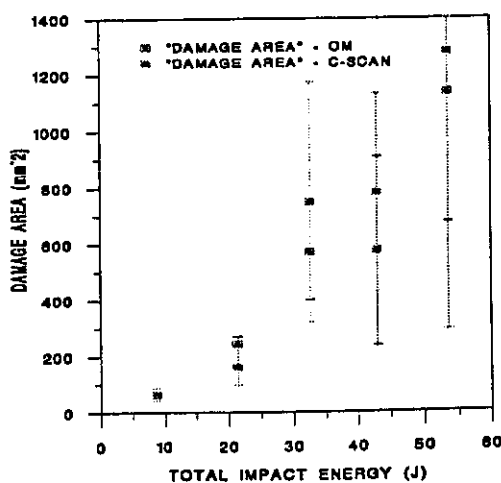


(b)

Figure AV.11 Deflection (a) and temporal data (b) versus TIE for central impacts from the five-box section.



(a)



(b)

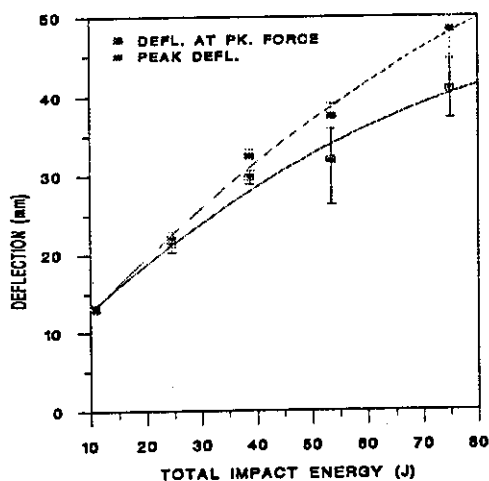
Figure AV.12 Energy data and "Damage areas" versus TIE for central impacts from the five-box section.

Table AV.25 Intermediate Impact Results from the Five-Box Section.

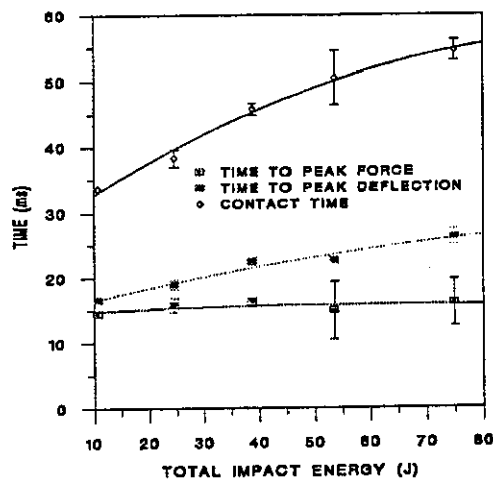
Specimen	Specimen Thickness (mm)	Impact Force (J)	Impact Velocity (m/s)	Peak Force (kN)	Defl. at Peak Force (mm)	Energy at Peak Force (J)	Damage Energy (J)	Elastic Energy (J)	Peak Defl. (mm)	Energy at Peak Defl. (J)	Total Impact Energy (J)	Time to Peak Force (ms)	Time to Peak Defl. (ms)	Contact Time (ms)	Initial Stiffness (kN/mm)	Stiffness from Id (kN/mm)	Stiffness from tp (kN/mm)	Stiffness from to (kN/mm)
F13B	3.38	9.21	1.31	1.81														
F3A	3.47	9.35	1.32	1.82	12.964	10.42	3.87	6.86	13.186	10.73	10.74	14.50	16.60	33.70		0.10	0.13	0.09
F3B	3.44	9.21	1.31	1.85														
Average	3.43	9.26	1.31	1.89	12.964	10.42	3.87	6.86	13.186	10.73	10.74	14.50	16.60	33.70		0.10	0.13	0.09
Std Dev	0.06	0.08	0.01	0.04														
Co. of Var.	1.34	0.88	0.44	2.54														
F13A	3.37	22.12	2.03	1.80	20.310	23.25	10.36	14.06	20.993	24.42	24.33	14.90	16.10	37.00		0.08	0.12	0.08
F26B	3.51	22.34	2.04	1.64	21.153	23.19	12.38	12.20	22.069	24.68	24.66	15.40	19.30	38.30		0.07	0.11	0.07
F28A	3.40	22.34	2.04	1.62	22.399	24.06	10.89	13.78	22.792	24.67	24.74	17.00	19.50	39.60		0.07	0.09	0.07
Average	3.43	22.26	2.04	1.69	21.287	23.60	11.21	13.35	21.951	24.65	24.57	15.77	18.97	38.30		0.07	0.11	0.07
Std Dev	0.07	0.13	0.01	0.10	1.051	0.49	1.05	1.00	0.905	0.13	0.22	1.10	0.76	1.30	#DIV/0!	0.01	0.01	0.00
Co. of Var.	2.15	0.57	0.28	6.85	4.937	2.07	9.34	7.51	4.124	0.52	0.88	6.96	3.99	3.39	#DIV/0!	8.24	13.28	6.79
F17A	3.38	35.45	2.57	1.79	29.166	35.21	22.35	16.48	31.386	38.83	38.75	16.20	21.90	45.00		0.06	0.10	0.06
F17B	3.41	35.17	2.56	1.70	30.660	34.95	23.60	16.09	33.016	38.69	38.65	16.90	23.00	46.70		0.06	0.09	0.06
F25A	3.50	35.45	2.57	1.70	29.289	33.69	22.74	16.18	32.650	38.92	38.89	15.60	22.70	45.70		0.05	0.11	0.05
Average	3.43	35.36	2.57	1.73	29.705	34.58	22.90	16.92	32.350	38.81	38.74	16.23	22.53	45.90		0.06	0.10	0.06
Std Dev	0.06	0.16	0.01	0.05	0.829	0.87	0.64	0.73	0.855	0.12	0.12	0.66	0.67	0.86		0.00	0.01	0.00
Co. of Var.	1.82	0.45	0.22	3.00	2.792	2.52	2.79	4.60	2.644	0.30	0.31	4.01	2.52	1.87		5.12	7.98	3.71
F16A	3.40	49.93	3.05	1.95	35.029	49.00	28.02	25.76	37.695	53.78	53.90	16.60	22.80	50.70				
F6B	3.39	49.27	3.03	1.96	25.441	30.98	25.02	28.42	38.924	53.44	53.37	9.90	23.70	54.40				
F9B	3.50	49.27	3.03	2.05	35.054	51.82	32.43	20.72	35.735	53.15	53.04	18.30	21.40	44.30				
Average	3.43	49.49	3.04	1.99	31.841	43.90	28.49	24.97	37.451	53.46	53.44	14.93	22.63	50.47				
Std Dev	0.06	0.38	0.01	0.06	5.543	11.31	3.73	3.91	1.608	0.32	0.43	4.44	1.16	4.05				
Co. of Var.	1.77	0.76	0.38	2.77	17.408	25.73	13.08	15.66	4.295	0.59	0.81	29.74	5.12	8.04				
F18B	3.36	69.55	3.60	1.94	38.280	54.31	59.63	16.11	50.517	74.74	74.88	13.50	27.00	55.60				
F20B	3.40	69.55	3.60	1.77	3.001	2.96	71.92		65.537	75.32	75.40		33.20	56.60				
F29B	3.52	69.55	3.60	2.25	43.453	70.47	59.05	16.24	45.846	74.30	74.38	18.60	25.30	53.40				
Average	3.43	69.56	3.60	1.99	28.248	42.58	63.54	16.18	50.633	74.79	74.89	16.05	28.50	54.87				
Std Dev	0.08	0.00	0.00	0.25	22.018	35.25	7.27	0.09	4.847	0.51	0.51	3.61	4.16	1.27				
Co. of Var.	2.43	0.00	0.00	12.50	77.944	82.79	11.44	0.61	9.572	0.68	0.68	22.47	14.50	2.32				

Table AV.26 Intermediate Impact Damage Analysis Results from the Five-Box Section.

Specimen	Total Impact Energy (J)	C-Scan contours - "Damage Area"						QM - Delamination Areas				Matrix Crack Spacing (mm)	Fiber-Line Crack (mm)
		24dB Area (mm ²)	+4F Area (mm ²)	+20dB Area (mm ²)	+16dB Area (mm ²)	+12dB Area (mm ²)	+8dB Area (mm ²)	Upper Av. (mm ²)	Lower Av. (mm ²)	Total Av. (mm ²)	Damage Area (mm ²)		
F13B		0	0	239	357	453	500	0	21	21	72	5.0	0
F3A	10.74	0	0	1	51	118	268	0	0	0	0	7.5	0
F3B		0	0	20	70	120	183	57	0	57	108	6.4	0
Average	10.74	0	0	87	159	230	348	19	7	26	40	6.3	0
Std Dev	#DIV/0!	0	0	132	172	193	216	33	12	29	55	1.3	0
Co. of Var.	#DIV/0!			152	108	84	62			92	19.9		
F13A	24.33	199	199	401	485	625	781	42	108	150	300	5.7	30
F26B	24.66	181	181	536	670	881	1262	332	0	332	396	6.0	25
F28A	24.74	85	85	536	800	1277	1805	192	34	226	312	4.9	25
Average	24.57	155	155	524	682	928	1283	189	47	236	336	5.5	27
Std Dev	0.22	61	61	118	203	328	513	145	55	91	52	0.6	3
Co. of Var.	0.88	40	40	22	30	35	40	77	117	39	16	10.4	11
F17A	38.75	351	351	1235	1820	2374	2777	465	0	465	638	3.8	80
F17B	38.65	204	204	748	1216	1691	2124	495	0	495	683	5.1	73
F25A	38.89	291	291	996	1333	1852	2413	510	0	510	820	6.0	200
Average	38.76	285	285	960	1456	1972	2438	490	0	490	713	5.0	118
Std Dev	0.12	78	78	250	320	357	327	23	0	23	95	1.1	71
Co. of Var.	0.31	27	27	26	22	18	13	5		5	13	22.2	61
F16A	53.90	194	194	1194	1615	2097	2498	220	35	255	365	4.8	70
F6B	53.37	51	51	1564	2488	3450	4137	541	165	706	901	4.7	115
F9B	53.04	340	340	1895	2397	2914	3392	800	0	800	1300	6.4	110
Average	53.44	195	195	1551	2167	2820	3342	550	67	617	855	5.3	98
Std Dev	0.43	144	144	351	480	682	820	335	87	327	469	1.0	25
Co. of Var.	0.81	74	74	23	22	24	25	61	130	53	55	18.2	25
F18B	74.88	830	830	1591	1785	2473	3351	970	375	1345	1350	4.5	110
F20B	75.40	1217	1217	2035	2500	3282	3942	758	200	958	1198	6.4	200
F29B	74.38	1702	1702	3433	4430	6024	6305	1030	0	1030	1600	5.1	200
Average	74.89	1250	1250	2363	2905	3593	4205	919	192	1111	1343	5.3	170
Std Dev	0.51	457	457	1154	1368	1304	998	143	188	205	203	0.9	52
Co. of Var.	0.68	35	35	49	47	35	24	16	98	19	15	17.8	31

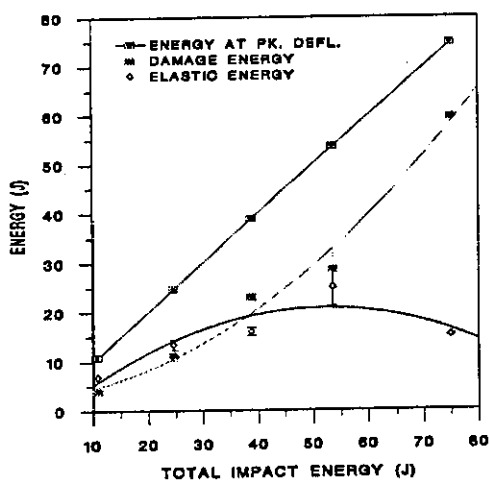


(a)

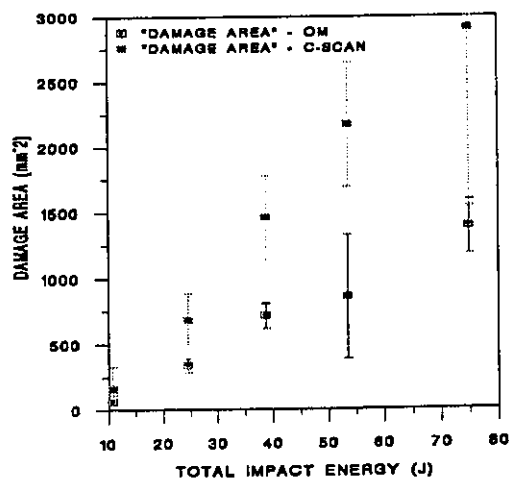


(b)

Figure AV.13 Deflection (a) and temporal data (b) versus TIE for intermediate impacts from the five-box section.



(a)



(b)

Figure AV.14 Energy data and "Damage areas" versus TIE for intermediate impacts from the five-box section.

Table AV.27 Web Impact Test Results from the Five-Box Section.

Specimen	Impact Energy (J)	Impact Velocity (m/s)	Peak Force (kN)	Def. at Peak Force (mm)	Energy at Peak Force (J)	Damage Energy (J)	Elastic Energy (J)	Peak Def (mm)	Energy at Peak Def (J)	Total Impact Energy (J)	Time to Peak Force (ms)	Time to Peak Def (ms)	Contact Time (ms)	Initial Stiffness (kN/mm)	Id Stiffness (kN/mm)	Ia Stiffness (kN/mm)	Ib Stiffness (kN/mm)
F258	9.21	1.31	1.44	13.648	9.93	6.08	4.65	14.279	10.73	10.72	14.5	18.0	33.7		0.08	0.09	0.13
F26A	9.21	1.31	1.48	12.538	10.14	4.33	6.16	12.815	10.49	10.55	14.4	16.7	33.0		0.09	0.10	0.13
F288	9.21	1.31	1.37	13.551	9.96	7.09	3.66	14.232	10.75	10.71	14.6	18.5	33.6		0.08	0.09	0.12
Average	9.21	1.31	1.43	13.246	10.01	5.83	4.82	13.776	10.66	10.67	14.5	17.7	33.4		0.08	0.09	0.13
Std Dev	0.00	0.00	0.06	0.61	0.11	1.40	1.26	0.83	0.14	0.09	0.1	0.9	0.4		0.01	0.00	0.00
Co. of Var.	0.00	0.00	3.89	4.64	1.13	23.94	26.10	6.04	1.36	0.82	0.7	5.2	1.1		10.81	2.29	1.38
F23A	29.39	2.34	3.13	0.655	0.57	19.40	12.63	24.338	32.03	31.96	0.3	19.3	38.4		0.07	0.07	293.98
F238	29.39	2.34	2.73	0.663	0.51	18.69	13.37	26.440	32.06	32.18	0.3	20.3	40.2		0.06	0.07	293.98
F27A	29.39	2.34	2.90	0.816	1.06	17.56	14.56	25.342	32.12	32.05	0.3	19.8	39.7		0.07	0.07	293.98
Average	29.39	2.34	2.92	0.708	0.71	18.55	13.62	26.373	32.07	32.07	0.3	19.8	39.4	#DIV/0!	0.07	0.07	293.98
Std Dev	0.00	0.00	0.20	0.094	0.30	0.93	0.97	1.051	0.06	0.11	0.0	0.5	0.9	#DIV/0!	0.00	0.00	0.00
Co. of Var.	0.00	0.00	6.87	13.211	41.69	5.00	7.20	4.144	0.14	0.35	0.0	2.5	2.4	#DIV/0!	5.06	4.78	0.00
F22A	49.60	3.04	4.08	0.849	1.04	39.03	14.48	37.465	53.51	53.56	0.3	23.8	49.7		0.06	0.04	293.98
F27B	49.27	3.03	3.78	0.847	0.81	36.77	16.68	39.397	53.45	53.43	0.3	24.3	49.7		0.04	0.04	293.98
Average	49.44	3.04	3.93	0.848	0.93	37.90	15.58	38.431	53.48	53.50	0.3	24.1	49.7		0.06	0.04	293.98
Std Dev	0.23	0.01	0.21	0.001	0.16	1.60	1.56	1.366	0.04	0.09	0.0	0.4	0.0		0.00	0.00	0.00
Co. of Var.	0.47	0.23	5.40	0.167	17.58	4.22	9.98	3.555	0.08	0.16	0.0	1.5	0.0		2.94	0.00	0.00
F18	70.33	3.62	3.93	1.012	1.44	37.43	37.66	43.924	75.09	74.97	0.3	22.1	47.5				
F2A	69.56	3.60	4.17	1.007	1.33	37.99	36.29	43.626	74.28	74.16	0.3	23.0	49.9				
F7B	69.56	3.60	4.06	1.256	2.26	55.69	18.80	45.577	74.49	74.37	0.3	24.5	51.7				
Average	69.81	3.61	4.06	1.092	1.68	43.70	30.92	44.376	74.62	74.60	0.3	23.2	49.7				
Std Dev	0.45	0.01	0.12	0.142	0.51	10.38	10.52	1.061	0.42	0.42	0.0	1.2	2.1				
Co. of Var.	0.64	0.32	2.96	13.099	30.31	23.76	34.01	2.368	0.56	0.56	0.0	5.2	4.2				
F14A	89.34	4.08	4.50	1.141	1.59	65.48	29.28	50.698	94.76	94.70	0.3	24.4	50.0				
F15B	89.34	4.08	4.86	1.422	2.91	69.17	25.59	50.654	94.76	94.69	0.4	23.4	48.3				
F21B	89.34	4.08	4.60														
Average	89.34	4.08	4.66	1.282	2.25	67.33	27.44	50.676	94.76	94.69	0.4	23.9	49.2				
Std Dev	0.00	0.00	0.19	0.199	0.93	2.61	2.61	0.031	0.00	0.00	0.1	0.7	1.2				
Co. of Var.	0.00	0.00	3.99	15.506	41.48	3.88	9.51	0.061	0.00	0.00	20.2	3.0	2.4				

Appendix VI

Typical chart detailing interface element node positions and movements for a DCB Model

Iterations	Increment	Load Change	A	B	C	Nodes In X	Nodes In Y	Total nodes In X and Y
2	0 to 1	5	2	0	0	2	0	2
2	1 to 2	5	0	1	0	1	1	2
2	2 to 3	5	0	0	0	1	1	2
2	3 to 4	5	0	0	0	1	1	2
2	4 to 5	5	1	1	0	1	2	3
4.0	5 to 6	4	2	2	2	1	2	3
4	6 to 7	2	2	2	2	1	2	3
6.4	7 to 8	2	1	1	1	1	2	3
4	8 to 9	2	1	1	1	1	2	3
4	9 to 10	2	1	1	1	1	2	3
6.3	10 to 11	1	0	1	0	0	3	3
3	11 to 12	3	1	1	1	1	2	3
4	12 to 13	2	1	1	1	1	2	3
6	13 to 14	1	2	2	2	1	2	3
2	14 to 15	5	0	0	0	1	2	3
6.3	15 to 16	1	0	1	0	0	3	3
3	16 to 17	5	1	0	1	1	2	3
6	17 to 18	2	2	2	2	1	2	3
4	18 to 19	2	1	1	1	1	2	3
6.3	19 to 20	1	0	1	0	0	3	3
3	20 to 21	4	1	0	1	1	2	3
4	21 to 22	2	1	1	1	1	2	3
6	22 to 23	2	2	2	2	1	2	3
4	23 to 24	2	1	1	1	1	2	3
4	24 to 25	2	1	1	1	1	2	3
3	25 to 26	1	0	1	1	0	2	2
3	26 to 27	5	1	0	0	1	2	3
4	27 to 28	3	1	1	1	1	2	3
6.3	28 to 29	1	0	1	0	0	3	3
2	29 to 30	1	0	0	0	0	3	3
3	30 to 31	5	1	0	1	1	2	3
4	31 to 32	3	1	1	1	1	2	3
6.3	32 to 33	1	0	1	0	0	3	3
2	33 to 34	1	0	0	0	0	3	3
3	34 to 35	5	1	0	1	1	2	3
4	35 to 36	3	1	1	1	1	2	3
6.2	36 to 37	4	0	0	0	1	2	3
3	37 to 38	1	1	1	1	1	2	3
2	38 to 39	5	0	0	0	1	2	3
4	39 to 40	3	1	1	1	1	2	3
3	40 to 41	1	1	1	1	1	2	3
2	41 to 42	5	0	0	0	1	2	3
4	42 to 43	3	1	1	1	1	2	3
3	43 to 44	1	1	1	1	1	2	3
2	44 to 45	5	0	0	0	1	2	3
4	45 to 46	3	1	1	1	1	2	3
3	46 to 47	5	0	1	0	0	3	3
3	47 to 48	1	1	0	1	1	2	3
					Average	0.83	2.06	2.90
Total no. of failed nodes					34			

Key

Load Change

- 1 big drop
2 drop
3 level
4 increase
5 big increase

Category

- A onto curve
B over the top
C failed

Zone

- X Initial slope
Y softening

Iterations : "." refers to step reduction

